Direct Synthesis of H_2O_2 and its Application in Water Purification

Rongjian Li

A thesis submitted for the degree of

Doctor of Philosophy

Cardiff University

Oct 2025

Summary

The primary goal of the work within this thesis is to develop novel catalysts capable of generating hydrogen peroxide (H_2O_2) in situ, along with other reactive oxygen species (ROS), for the oxidative degradation of organic pollutants in water (e.g., phenolic, pesticides, pharmaceuticals). Current industrial H_2O_2 production, dominated by the auto-oxidation of anthraquinone, is only practical at very large scale. This process is complex, requires the periodic replacement of organic carriers, and yields a highly concentrated solution (~70 wt.% H_2O_2). Shipping these hazardous materials necessitates the addition of stabilizers (acid or halide), creating safety and environmental concerns. Meanwhile, routine applications like Fenton-based water treatment only require low concentrations (3 to 5 wt.%) and dilution from the pre-formed H_2O_2 is needed for the purpose of use, highlighting a clear need for a smaller and more efficient method that can supply H_2O_2 locally while avoiding the concerns and issues mentioned above. The work presented here demonstrates that a catalytic system capable of producing H_2O_2 in situ, together with its full suite of ROS, can provide a credible alternative pathway for in situ water treatment.

The first part of this work primarily focused on the development of Fe-doped TiO_2-supported AuPd catalysts for the direct synthesis of H_2O_2 from molecular H_2 and O_2 in a batch regime. Initial studies into the effect of Fe loading on the catalytic performance towards the direct H_2O_2 synthesis revealed that the trimetallic AuPdFe catalysts, containing a minimal Fe loading (at 0.02 wt.%) could effectively promote the H_2O_2 productivity up to 120 mol_{H2O2} Kg_{Cat}^{-1} h^{-1} at an operational pressure of 39 bar. This was nearly double than that of the bimetallic AuPd (70 mol_{H2O2} Kg_{Cat}^{-1} h^{-1}) and Fe-rich trimetallic analogous (65 mol_{H2O2} Kg_{Cat}^{-1} h^{-1}) under the identical reaction conditons. The enhancement observed in H_2O_2 yield was mainly attributed to the increased activity towards H_2 activation rather than H_2O_2 selectivity. Further analysis through time on line and gas replacement experiments showed the excellent long-term operational potential of the optimal AuPdFe catalyst (0.3 wt.% H_2O_2 accumulated in time on line test and 0.76 wt.% H_2O_2 accumulated, respectively) compared to previously reported AuPd-based trimetallic series, in terms of the accumulated H_2O_2 concentration.

Based on the initial investigation on the trimetallic AuPdFe catalysts for H_2O_2 synthesis, subsequent research into the catalytic degradation of phenol was conducted under reaction conditions more realistic for real-world operation (a water-only solvent, ambient temperatures). Initial studies revealed the effect of Fe loading on the oxidative degradation of phenol, with 2

wt.% Fe loading on the AuPd catalyst outperforms other trimetallic AuPdFe formulations, with the optimal catalyst exhibiting a phenol degradation in excess of 80%, with hydroquinone, catechol, and ring-opening molecules existed as the main phenolic intermediates, which is over 10 times better than that of the bimetallic AuPd formulation. Detailed intermediates analysis (hydroxylated and ring-opening byproducts) and radical quenching experiments revealed that the hydroxyl radical (·OH) is the primary ROS in the oxidative degradation of phenol. Reactant control experiments were taken to exclude the contribution from H_2 and O_2, and also revealed the low efficiency in phenol degradation using bulk pre-formed H_2O_2, which only exhibited around 15% phenol conversion, compared to that offered by the in situ route. However, while the precious metal components were found to be stable, Fe leaching was considerable, as a result of the formation of many of the highly oxidised products of phenol degradation (hydroquinone, formic acid, oxalic acid, etc), highlighting the balance between activity and stability during the oxidative degradation of phenol.

Finally, a series of AuPd catalysts was prepared via the wet incipient method and pelleted utilised for the in situ treatment of contaminated water in a continuous flow reactor. Preliminary tests suggested that all bimetallic formulations (up to 80% conversion of phenol) outperformed the monometallic Pd (58% conversion of phenol) and Au (2% conversion of phenol) catalysts under the identical reaction conditions. Reaction parameter investigation over the ideal bimetallic AuPd catalyst revealed the relationship between in situ phenol conversion rate and liquid/gas flow rate, system pressure, catalyst loading, as well as pollutant concentration. Relatively long contact times were found to be essential for effective phenol removal. Long-term stability tests demonstrated over 50 hours of continuous and stable operation in phenol conversion over the bimetallic AuPd catalysts, with no detectable metal leaching and minimal morphology changes of the AuPd alloys. Although the investigation on the effect of reactant gases on phenol conversion excluded the contribution from H_2 and O_2 solely, extensive studies conducted on the in situ degradation of other various organic pollutants revealed that while there may be a minimal contribution from the oxidative pathway, catalytic hydrogenation is the primary cause for the observed conversion of these pharmaceutical and pesticide organic groups.

Acknowledgements

First, I would like to thank my academic supervisor, ***Professor Graham Hutchings***, who warmly welcomed me into the CCI (Cardiff Catalysis Institute) in 2022, providing excellent laboratory space and equipment, academic and research guidance, and endless knowledge over the past 3 years. Meanwhile, I would like to thank Cardiff University and the China Scholarship Council (CSC) for the joint scholarship scheme, which offered me this excellent opportunity to work within Prof. Graham Hutching's group and meet and collaborate with so many top-tier scientific researchers.

I would like to extend my sincere thanks to my PDRA, ***Dr. Richard Lewis***, for his exemplary leadership, patient guidance, and endless support throughout my research. His insight and encouragement sustained every stage of my work in the laboratory and beyond. Without his dedicated mentorship, I would not have completed my experimental studies successfully and achieved publication within three years.

I would like to thank ***Dr. Nicholas Dummer*** and ***Mr. Mark Reece*** for constructing the flow reactor used in the in situ water treatment projects; *Professor Jean-Yves Maillard* and ***Dr Rebecca Wesgate*** of for their help and support with the E. coli tests in the continuous flow reactor; ***Dr. David Morgan*** and ***Dr. Thomas Davies*** for assistance with XPS and electron microscopy (TEM, SEM, and STEM); ***Dr. Iulian Dugulan*** (Delft University of Technology) for the Mössbauer spectroscopy analysis; ***Mr. Simon Waller*** for inductively coupled plasma analyses; ***Dr. Greg Shaw***, ***Mr. Christopher Court-Wallace***, ***Dr. Wenjian Zhang***, and ***Mr. Evan Morton*** for support in TRH.

I would also like to thank everyone in the "**Hydrogen Peroxide**" Team: ***Dr. Dong Lin***, ***Dr. Fenglou Ni***, ***Dr.Ben Bayntun***, ***Dr. Alexander Stenner***, ***Dr. Joe Brehm***, ***Dr. Danyang Chen***, ***Lucy J. Fisher***, ***Dominic Conway***, and ***Qiyang Fan*** for all your help and support over the last three years. I would always remember the laughter on level 5 in TRH.

Finally, I would like to sincerely thank my family, especially ***Simon*** and ***my parents***, for their unconditional support, whatever decisions I have made. Their belief in me has enabled me to reach this stage.

Publication List

1. Promoting H_2O_2 direct synthesis through Fe incorporation into AuPd catalysts

R Li, R. J. Lewis, Á López-Martín, D. J. Morgan, T. E. Davies, D Kordus, A. I. Dugulan, B. R. Cuenya, and G. J. Hutchings, *Green Chem*., 2025, 27, 2065-2077.

DOI: https://doi.org/10.1039/D5GC00134J

Contribution: All experimental work held within this paper was undertaken by myself.

Please note: this paper is based on the work outlined in **Chapter 3**.

2. Balancing Activity and Stability in Phenol Oxidation via in situ H_2O_2 Generation over Fe-Modified AuPd Catalysts

R Li, R. J. Lewis, D. J. Morgan, E. Kitching, T. Slater, G. J. Hutchings, *Chemcatchem*, e01264.

DOI: https://doi.org/10.1002/cctc.202501264

Contribution: All experimental work held within this paper was undertaken by myself.

Please note: this paper is based on the work outlined in **Chapter 4**.

3. Oxidative Degradation of Phenol via in situ Generation of H_2O_2 in a Flow Reactor

R Li, R. J. Lewis, N. F. Dummer, D. J. Morgan, E. Kitching, T. Slater, G. J. Hutchings, *Catal Lett.*, 2025, 155, 373.

DOI: https://doi.org/10.1007/s10562-025-05221-3

Contribution: All experimental work held within this paper was undertaken by myself.

Please note: this paper is based on the work outlined in **Chapter 5**.

4. Benzyl Alcohol Valorization via the In Situ Production of Reactive Oxygen Species

G. Sharp, R. J. Lewis, J. Liu, G. Magri, D. J. Morgan, T. E. Davies, Á. López-Martín, **R. Li**, C.R. Morris, D. M. Murphy, A. Folli, A. I. Dugulan, L. Chen, X. Liu, and G. J. Hutchings, *ACS Catal.,* 2024, 14, 20, 15279–15293.

DOI: https://doi.org/10.1021/acscatal.4c04698

Contribution: Involved in catalyst synthesis, testing, and corresponding data analysis.

Table of Abbreviations

Abbreviation	Full name
5-FU	5-Fluorouracil
AC	active carbon
AC-STEM	Aberration Corrected-Scanning Transmission Electron Microscopy
AHQ	2-anthrahydroquinone
AO	Auto-oxidation
AOPs	Advanced oxidation process
AQ	2-alkyl anthraquinone
ATZ	Atrazine
BET	Brunauer-Emmett-Teller
BPA	Bisphenol A
CBZ	Carbamazepine
COD	Chemical oxygen demand
CO-DRIFTS	CO-Diffuse Reflectance Infrared Fourier Transform Spectroscopy
DFT	Density Function Theory
DMPO	5,5-dimethyl-1-pyrroline N-oxide
DMSO	Dimethyl sulfoxide
Ea	Active energy
EDX	energy-dispersive X-ray spectroscopy
EF	Electron Fenton
EPR	Electron paramagnetic resonance
GC	Gas Chromatography
GC2	gallic acid
g-C3N4	graphitic carbon nitride
HADDF	high-angle annular dark field
HAp	hydroxyapatite
HPLC	High-Performance Liquid Chromatography
ICP-MS	Inductively Coupled Plasma Mass Spectroscopy
LSV	Linear sweep voltammetry
MP-AES	Microwave Plasma Atomic Emission Spectroscopy
ORR	Oxygen reduction reaction
PCA	protocatechuic acid
PMS	Peroxymonosulfate
QMRC	Quinmerac
RhB	Rhodamine B
ROS	Reactive oxygen species
RRDE	Rotating ring-disk electrode
SEM	Scanning Electron Microscopy (
TBA	tert-Butanol
TC	Tetracycline
TEM	Transmission electron microscopy
TEMP	2,2,6,6-Tetramethylpiperidine
THAHQ	5,6,7,8-tetrahydroanthrahydroquinone
THAQ	tetrahydroanthraquinone

TOC	Total organic carbon
TPPMS	triphenylphosphine
UV	Ultraviolet
WOR	Water oxidation reaction
XAS	X-ray adsorption spectroscopy
XPS	X-ray Photoelectron Spectroscopy
XRD	X-ray Diffraction
ΔG	Gibbs free energy

Table of Contents

Chapter 1 - Introduction

1.1 Green Chemistry

Green chemistry is an area of chemistry that seeks to develop chemical products and processes that are safe for both humans and the environment.[1,2] The fundamental objective of this subfield is to improve atom efficiency and limit the use of hazardous materials by identifying more sustainable and efficient methods for synthesis and manufacturing.[1] The concept of green chemistry, as a discipline, was first introduced by Paul Anastas and John Warner, who authored the seminal publication "Green Chemistry: Theory and Practice" in 1998.[2] This influential text provided an extensive overview of the principles and practices of green chemistry and presented a set of 12 principles that established the foundation for the field. These principles are now widely accepted as guidelines for the development and implementation of green chemistry practices in scientific research and industrial applications:

1. Prevention: It is better to prevent waste than to treat or clean up waste after it is formed.

2. Atom Economy: Synthetic methods should be designed to maximise the incorporation of all materials used in the process into the final product.

3. Less Hazardous Chemical Synthesis: Whenever practicable, synthetic methodologies should be designed to use and generate substances that pose little to no toxicity to human health and the environment.

4. Designing Safer Chemicals: Chemical products should be designed to preserve the efficacy of the function while reducing toxicity.

5. Safer solvents and Auxiliaries: The use of auxiliary substances (e.g. solvents) should be made unnecessary whenever possible and, when used, innocuous.

6. Design for Energy Efficiency: Energy requirements of chemical processes should be recognised for their environmental and economic impacts and should be minimised. If possible, synthetic methods should be conducted at ambient temperature and pressure.

7. Use of Renewable Feedstocks: A raw material or feedstock should be renewable rather than depleting whenever technically and economically practicable.

8. Reduce Derivatives: Unnecessary derivatisation (use of blocking groups, protection/deprotection, temporary modification of physical/chemical processes) should be

minimised or avoided if possible because such steps require additional reagents and can generate waste.

9. Catalysis: Catalytic reagents (as selective as possible) are superior to stoichiometric reagents.

10. Design for degradation: Chemical products should be designed so that at the end of their function, they break down into innocuous degradation products and do not persist in the environment.

11. Real-Time Analysis for Pollution Prevention: Analytical methodologies need to be further developed to allow for real-time, in-process monitoring and control prior to the formation of hazardous substances.

12. Inherently Safer Chemistry for Accident Prevention: Substances and the form of a substance used in a chemical process should be chosen to minimise the potential for chemical accidents, including releases, explosions, and fires.

These principles serve as guides for designing sustainable and environmentally friendly chemical processes. The 2nd, 6th, and 9th principles addressed the importance of using catalytic technology to achieve ‘economic’, ‘greener’, and ‘efficient’ processes.

1.2 Catalysis and Catalysts

1.2.1 Brief history of catalysts

The practice of catalysis was a common but unrecognised phenomenon in early societies during the production of wine, beer, soap, cheese, sulfuric acid (oil of vitriol), and ether.[3] It was not until the scientific inquiry into the chemistry and origins of catalytic materials that the concept of catalysis emerged. Sir Humphrey Davy's discovery of the accelerated combustion of coal gas with oxygen through the use of a glowing Pt wire in 1817 represented a significant milestone in the understanding of catalysis and led to the invention of the Davy lamp.[4] Louis Jacques Thenard (research on alcoholic fermentation), Johann Wolfgang Döbereiner (observed the Pt black oxidation of alcohols), and others, all recognized the usefulness of various materials as catalysts, but did not explicitly identify them as such, nor did they describe the underlying principles.[5] Finally, in 1835, Jöns Jakob Berzelius introduced the term "*catalysis*" after observing a "*force*" in previous reports, but with no further explanation,[6] and Friedrich Wilhelm Ostwald first recognized catalysis as a phenomenon when investigating the oxidation

of hydrogen iodide by bromic acid and in 1901, he introduced the final definition of the nature of catalyst: "*A catalyst is a material that changes the rate of a chemical reaction without appearing in the final product*."[7]

1.2.2 Various Catalysis and Catalysts

In the realm of catalysis, three primary categories exist: homogeneous catalysis, enzymatic catalysis, and heterogeneous catalysis.[8] Homogeneous catalysis involves the use of catalysts and reactants in the same phase, where all active sites are accessible to the metal complex. Their chemo-selectivity, regioselectivity, and/or enantioselectivity could often be adjusted.[9] For example, the mono-sulfonated triphenylphosphine (TPPMS) acts as a ligand in $[RuCl_2(TPPMS)_2]$ for the selective hydrogenation of cinnamaldehyde.[10] Besides, the Fe^0 porphyrin catalyst electrochemically converts CO_2 to CO.[11] However, separating the catalyst from the reactants is a major challenge, as the distillation, chromatography, and extraction methods cause catalyst loss and decomposition due to the thermal sensitivity of most homogeneous catalysts.

Enzymatic catalysis involves the designed functional proteins or nucleic acids with catalytic ability through metabolic pathways, which are present in most living creatures, with the advantages of high selectivity and catalytic activity.[12,13] For example, Lipases (acylglycerol acylhydrolases, EC 3.1.1.3) are recognised as lipolytic enzymes belonging to the serine hydrolase group, with the catalytic abilities in hydrolysis, reverse reactions, and esterification reactions, making them versatile tools for applications such as organic synthesis, oil and fat modification, and racemate resolution.[14] Similarly, enzyme catalysts derived from cytochrome P450 achieved enantioselective amination of primary, secondary, and tertiary $C(sp^3)$–H bonds via a nitrene transfer mechanism.[15] Despite the numerous advantages, enzymes typically exhibit optimal catalytic activity within a very limited range of pH and temperature, as enzymes often undergo denaturation outside the specific conditions, leading to deactivation.[16,17]

Whereas heterogeneous catalysis involves catalysts and reactants in different phases (such as solid catalysts with liquid and/or gaseous reactants), where products could be separated from the catalysts and reaction solvents through relatively facile protocols.[18] Due to this advantage, heterogeneous catalysts have found wide-ranging applications across numerous industries, including petroleum refining, chemical synthesis, polymer production, environmental applications, and the food industry.[19–21] For instance, in the petroleum refining industry,

heterogeneous catalysts like zeolites,[22] and metal oxides[23] increase efficiency, leading to the production of higher-quality fuels. Fe-based[24] and Ru-based[25] catalysts play a vital role in the Haber-Bosch process for boosting fertiliser production. Environmental applications use noble metals such as Pt, Pd, and Rh, as well as transition metals like Cu, Co, and Fe, as catalytic converters in automobiles.[26] Advanced oxidation processes (AOPs) employ various metal[27] or metal-free catalysts[28,29] to generate radical and non-radical species to remove organic pollutants for environmental quality improvement.[30,31]

1.2.3 Reaction Mechanism of Heterogeneous Catalysis

Given the high activity and efficiency of heterogeneous catalysts, different fundamental models have been proposed to reveal the surface reaction mechanisms by which the surface reaction occurs, including the Langmuir-Hinshelwood mechanism, Eley-Rideal mechanism, and Mars-van Krevelen mechanism.[32]

The *Langmuir-Hinshelwood mechanism*, first proposed by Sir Cyril Hinshelwood, who expanded the earlier idea of Langmuir, describes simple catalytic routes including the adsorption and reaction of two reactants (R_A and R_B) and the generation and desorption of products (P) over a heterogeneous catalyst surface (**Eq. 1.1**).

$$R_{A(g)} + R_{B(g)} \rightarrow R_{A(ads)} \ldots R_{B(ads)} \rightarrow P_{(g)} \qquad \textbf{(Eq. 1.1)}$$

Besides, the *Eley-Rideal mechanism*, introduced by Gwyn Elwyn Eley and John Ralph Rideal in the 1930s, postulates that the catalytic reaction involves the adsorption of R_A. Meanwhile, R_B, which has not yet been adsorbed on the catalyst surface, reacts with R_A to form P, which subsequently desorbs from the catalyst surface (**Eq. 1.2**).

$$R_{A(ads)} + R_{B(g)} \rightarrow R_{A(ads)} \ldots R_{B(g)} \rightarrow P_{(g)} \qquad \textbf{(Eq. 1.2)}$$

Furthermore, the Mars-van Krevelen mechanism, developed by Jacobus Hendricus van't Hoff, Joannes Martinus van Bemmelen, and Frans Michiel Jaeger Mars in the 1950s, proposes that the catalytic reaction involves electron transfer between R_A and the catalyst. Specifically, R_A adsorbs onto the catalyst surface, forming adsorbed reactants, and the catalyst (depending on its oxidation state) donates or accepts electrons from the adsorbed reactants to form adsorbed intermediates (Catalyst…$R_{A(ads)}$). Then R_B interacts with Catalyst…$R_{A(ads)}$ to produce P, and the desorption of P leaves an empty site (Vac) on the catalyst surface, which will be filled with the succeeding reactant (**Eq. 1.3-1.4**).

$$R_{A(g)} + Catalyst \rightarrow Catalyst \ldots R_{A(ads)}\ R_{B(g)} + Catalyst \ldots R_{A(ads)} \rightarrow P_{(ads)} \rightarrow P_{(g)} + Vac \quad \textbf{(Eq. 1.3)}$$

$$R_{A(g)} + Vac \rightarrow Catalyst \ldots R_{A(ads)} \quad \textbf{(Eq. 1.4)}$$

1.2.4 Main Reaction Processes of Heterogeneous Catalysis

The key to heterogeneous catalysis lies in the interaction between the catalyst and the reactants. The reactants contact the surface of the catalyst, where they undergo a chemical reaction to form the desired products. The surface of the catalyst provides active sites where the reaction takes place, which can help lower the activation energy (**E_a**) required for the reaction to occur. Compared to the uncatalyzed pathway (Grey line), the catalysed pathways (Blue lines) involve more steps and intermediates, but increase the rate of chemical reactions by lowering the energy barriers in all steps without changing the Gibbs free energy (**ΔG**). More importantly, the catalyst does not influence the thermodynamic equilibrium composition after the cessation of the reaction. The overall catalytic pathway can be briefly separated into a number of elementary steps, including the adsorption and interaction of R_A and R_B on the catalyst surface and the formation and desorption of the final product P (**Figure 1.1**).[33,34]

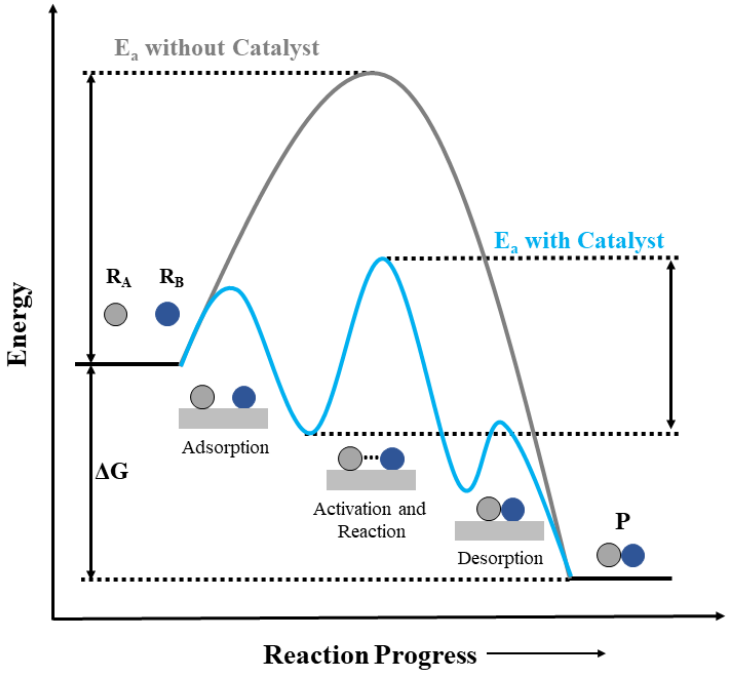

Figure 1.1. The relationship between active energy and reaction progress under catalysed and uncatalyzed pathways.[35]

Moreover, the rate of a catalytic reaction can be succinctly expressed using the Arrhenius Equation, introduced by Svante Arrhenius in 1889. By combining all the relevant reaction conditions (e.g. temperature), it yields a rate constant that quantifies the rate of any specific reaction (**Eq. 1.5**).[36]

$$k = Ae^{\frac{-E_a}{RT}} \qquad \textbf{(Eq. 1.5)}$$

Where k – Rate Constant (A proportional factor relating to the rate of a chemical reaction)

A – Pre-exponential Factor

E_a – Activation Energy

R – Gas Constant (8.3145 J mol^{-1} K^{-1})

T – Temperature (K)

The process of heterogeneous catalysis involving the interaction between heterogeneous catalysts and reactants is complex and depends on various factors, including the surface area, surface composition, surface chemistry of the catalyst, and reaction conditions. Therefore, the development and design of effective heterogeneous catalysts require a deep understanding of these factors and how they influence the reaction mechanism. A meticulous study and application of these factors can lead to the discovery and production of efficient and sustainable catalysts for boosting various industrial processes.

1.3 Hydrogen peroxide

Hydrogen peroxide (H_2O_2) is a simple form of peroxide that exists as a pale blue liquid, a versatile oxidant that has the capability to function optimally throughout a wide pH range with a high oxidation potential and water as the only coproduct. In an aqueous solution, it can undergo various reactions, including decomposition, oxidation, molecular addition, reduction, and substitution.[37] These characteristics make H_2O_2 an exceedingly vital commodity in various applications (**Figure 1.2**), with significant demand for both industrial and domestic purposes.[37,38] Globally, as of 2021, the H_2O_2 market was valued at USD 1.69 billion, and it is projected to grow annually at a rate of 3.8%, reaching USD 2.2 billion in 2028.[39]

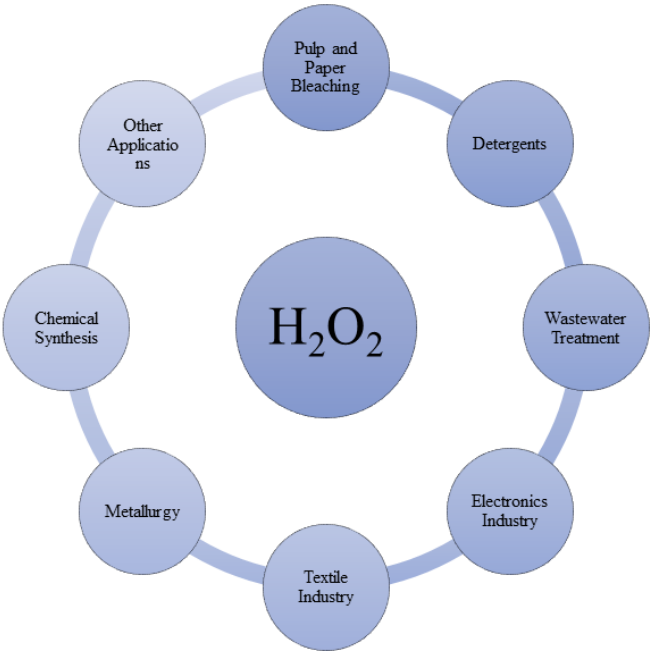

Figure 1.2. Principal uses of hydrogen peroxide.[37]

One of the most crucial applications of hydrogen peroxide is in pulp and paper bleaching, where it replaced chlorine-based bleaches to avoid the formation of dioxins and other hazardous chlorinated products during the reaction.[40] In chemical synthesis, H_2O_2 is also an essential component in oxidative organic reactions, such as epoxidation reactions.[41] Baeyer–Villiger oxidation,[42,43] and the oxidation of alcohols.[44,45] Additionally, H_2O_2 is commonly used for pollutant control.[46] The H_2O_2-based Fenton reaction is a classic and effective AOPs for the removal of toxic and non-degradable organic pollutants. In this reaction, hydroxyl radicals (·OH) with strong electron-capturing abilities are generated by H_2O_2 under the activation of Fe^{2+} via the Fenton pathway, non-selectively attacking most organic components and facilitating water restoration.[46,47]

1.4 Overview of H_2O_2 synthesis

1.4.1 Early stage study

The discovery of aqueous H_2O_2 can be attributed to the work of the French chemist Louis-Jacques Thénard, who identified and isolated it in the 19th Century using the reaction of barium peroxide with nitric acid via the following routes (**Eq. 1.6- 1.8**).[37]

$$BaO_2 + 2HCl \rightarrow BaCl_2 + H_2O_2 \qquad \textbf{(Eq. 1.6)}$$

$$BaCl_2 + H_2SO_4 \rightarrow BaSO_4 + 2HCl \quad \textbf{(Eq. 1.7)}$$

$$BaO_2 + H_2SO_4 \rightarrow BaSO_4 + H_2O_2 \quad \textbf{(Eq. 1.8)}$$

However, the low H_2O_2 production and affordability inhibited the development of Thenard's route, and further, in 1853, the discovery by Meidinger introduced an alternative way to produce H_2O_2 electrolytically from aqueous sulfuric acid, which became more economically feasible for high-purity and concentrated H_2O_2 synthesis (**Eq. 1.9 -1.12**).[48]

$$2H_2SO_4 \rightarrow H_2S_2O_8 + H_2 \quad \textbf{(Eq. 1.9)}$$

$$H_2S_2O_8 + H_2O \rightarrow H_2SO_5 + H_2SO_4 \quad \textbf{(Eq. 1.10)}$$

$$H_2SO_5 + H_2O \rightarrow H_2O_2 + H_2SO_4 \quad \textbf{(Eq. 1.11)}$$

$$2H_2O \rightarrow H_2O_2 + H_2 \quad \textbf{(Eq. 1.12)}$$

1.4.2 Anthraquinone Auto-oxidation (AO) Process

Large-scale production of H_2O_2 can be achieved under different routes, including the Anthraquinone autoxidation (AO) process, oxidation of alcohols (propanol, methyl-benzyl alcohol), and electrochemical synthesis.[37,49] Currently, the indirect anthraquinone process has replaced the alcohol oxidation and electrochemical processes and is responsible for more than 95% of H_2O_2 production.[50] In the 1940s, the first commercial AO Process was operated by IG Farbenindustrie in Germany, with the production of 1 metric ton of H_2O_2 per day. In the following decades, many endeavours have been involved in improving four major steps in the process, including hydrogenation, oxidation, extraction, and treatment of the working solution. The whole process involves Riedl–Pfleiderer reactions, in which 2-alkyl anthraquinone (AQ) is catalytically hydrogenated to 2-anthrahydroquinone (AHQ) in the presence of a hydrogenation catalyst such as supported Pd or Pt, and then AHQ is separated from the solution containing the hydrogenation catalyst and is oxidised in the air to re-form AQ and simultaneously produce H_2O_2. Meanwhile, AHQ could be over-hydrogenated to 5,6,7,8-tetrahydroanthrahydroquinone (THAHQ) via ring hydrogenation, and THAHQ will then be oxidised to tetrahydroanthraquinone (THAQ), with H_2O_2 produced at the same time (**Figure 1.3**).[37]

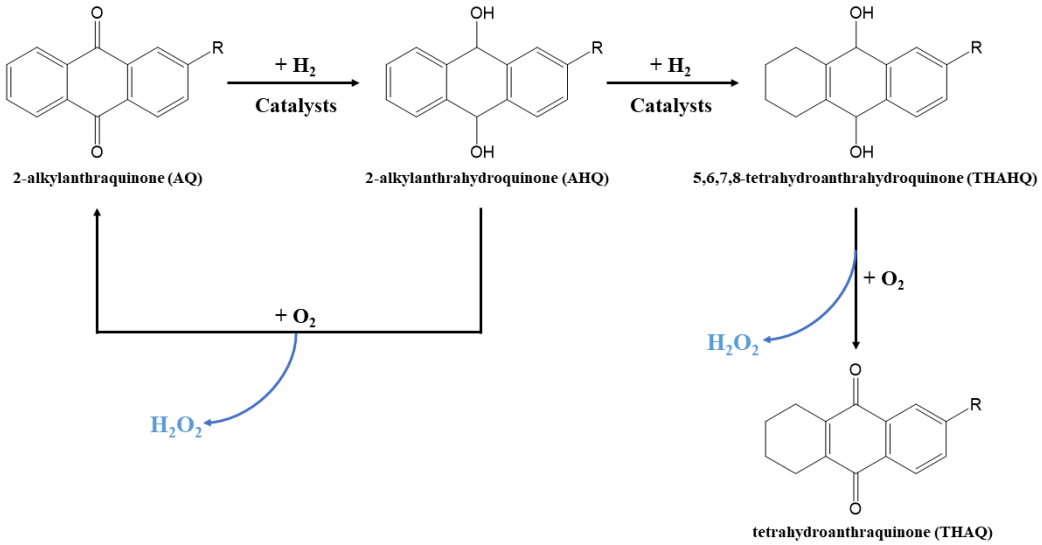

Figure 1.3. Simplified anthraquinone autoxidation (AO) process.[51]

Indeed, the AO process is widely used in the production of H_2O_2 as it avoids explosive H_2/O_2 gas mixtures.[51] However, there are still a number of problems associated with the indirect route to H_2O_2 production, including the use of complex and toxic solvents, costly periodic replacement of quinone derivatives due to non-selective hydrogenation, and deactivation of hydrogenation catalysts, and especially generating contaminated water (peroxide, organic solvent, and quinone residues).[38] Also, the high capital investment and operating costs associated with the AO process are only economically viable for large-scale production (>40 $\times$ 10^3 tons per year) instead of on-site production at the end-users facility.[38,51] Consequently, the centralised production of H_2O_2, followed by transportation, introduces additional safety concerns as the highly concentrated H_2O_2 is explosive when decomposing. Therefore, a more environmentally friendly and direct strategy for in situ H_2O_2 production attracts more attention, in terms of further implementing green and environmentally sustainable policies and for more economical and wider application.

1.4.3 In situ H_2O_2 production through catalytic synthesis

In addition to the traditional AO process for producing H_2O_2, electrocatalytic synthesis, photocatalytic synthesis, and direct synthesis of H_2O_2 have been considered as ideal and promising alternatives, from the perspective of energy saving and environmental protection.[52–54] Specifically, direct catalytic synthesis forms H_2O_2 via the reaction of H_2 and O_2 over heterogeneous catalysts, delivering superior atom economy to the AO route and achieving

selectivity above 95% on Pd-based materials under mild conditions.[55] Electrocatalytic synthesis employs the two-electron oxygen reduction reaction (2e$^-$ ORR) at the cathode, operates near ambient temperature and pressure, avoids concentrated acids or bases, and enables safe, decentralised, on-demand production driven by renewable electricity.[56,57] Photocatalytic synthesis harnesses solar photons to reduce O_2 or H_2O to H_2O_2 in aqueous media, eliminating external electricity input and further lowering capital and operating costs.[58,59] Both electro- and photocatalytic systems allow in situ coupling of H_2O_2 generation with downstream redox transformations, such as the oxidative degradation of organic pollutants, thereby reducing the need to transport and store bulk oxidant and improving overall process sustainability.[54]

1.4.3.1 Electrosynthesis of H_2O_2 from O_2 or H_2O

H_2O_2 synthesis via the electrochemical pathway offers an alternative but more economical and environmentally friendly approach to the AO process, by facilitating the electroreduction of O_2 or electrooxidation of H_2O or H_2 at ambient pressure and temperature, providing an efficient and uninterrupted generation of H_2O_2 on a small scale at the point of use and to mitigate the transportation cost and safety concern. Furthermore, it presents notable safety and environmental merits by circumventing the formation of carbonaceous secondary products. H_2O_2 electrosynthesis predominantly unfolds via two principal routes, namely oxygen reduction reaction (ORR, **Figure 1.4**) and water oxidation reaction (WOR, **Figure 1.5**).[60]

ORR process refers to the reduction half-reaction and takes place in several electrochemical and chemical reaction conditions, involving the electrochemical reduction of molecular oxygen by 2 e$^-$ or 4 e$^-$ to form H_2O_2 or H_2O. The electrochemical H_2O_2 synthesis via the 2 e$^-$ ORR process was first reported via the Huron–Dow process (**Eq. 1.13**).[61] However, insufficient selectivity limits the overall efficiency. The 2 e$^-$ ORR pathway is the desired path to produce H_2O_2 but is also thermodynamically unfavourable compared to the competitive 4 e$^-$ ORR pathway (**Eq. 1.14**). Meanwhile, the in situ generated H_2O_2 is subsequently involved in the electrochemical H_2O_2 reduction reaction (H_2O_2RR) and H_2O_2 decomposition, significantly affecting H_2O_2 yield. So far, some highly efficient electrocatalysts (e.g. Pt, Pd-Hg, Carbon-based materials) have been found to enhance the catalyst performance of 2 e$^-$ ORR.[62,63] However, the practical applications necessitate the rational design of specialised catalysts highly favourable for the 2e$^-$ ORR pathway, which still remains a challenge.[57,64]

2 e⁻ ORR pathway:

$$O_2 + 2H^+ + 2e^- \rightarrow H_2O_2 \ (E^o = 0.70\ V) \qquad \textbf{(Eq. 1.13)}$$

4 e⁻ ORR pathway:

$$O_2 + 4H^+ + 4e^- \rightarrow 2H_2O \ (E^o = 1.23\ V) \qquad \textbf{(Eq. 1.14)}$$

H_2O_2 Reduction and Decomposition (**Eq. 1.15-1.16**):

$$H_2O_2 + 2H^+ + 2e^- \rightarrow 2H_2O \qquad \textbf{(Eq. 1.15)}$$

$$2H_2O_2 \rightarrow 2H_2O + O_2 \qquad \textbf{(Eq. 1.16)}$$

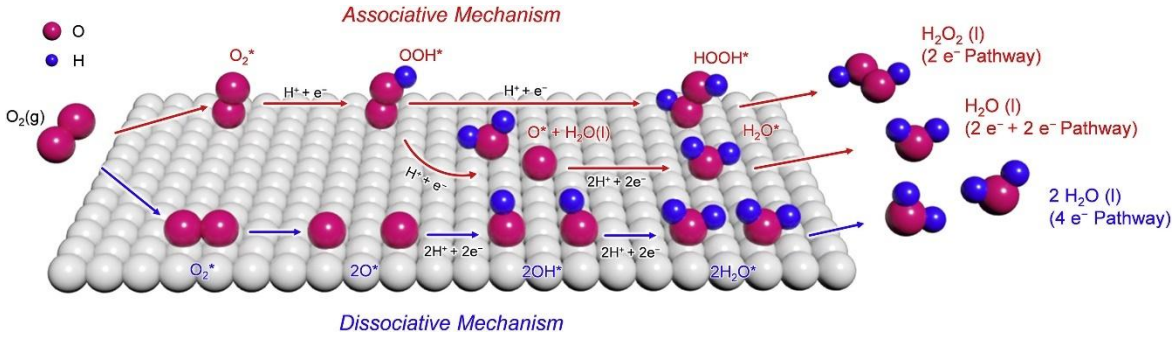

Figure 1.4. ORR mechanism.[64]

Compared to the ORR process, the WOR process does not involve a gas-phase reactant (e.g. O_2) but provides a new approach to electrochemically produce H_2O_2. Since the first report in 2004 on H_2O_2 synthesis using a carbon-based catalyst in NaOH via two-electron (2 e⁻) WOR,[65] numerous relevant studies have been developed by using metal oxides (e.g. WO_3, $BViO_4$, $CaSnO_3$, MnO_2, and ZnO)[56,66–69] and carbon-based catalysts (e.g. carbon catalyst coated with hydrophobic polymer).[70] Overall, three main pathways exist in the WOR process, illustrated in Figure 4, including 4 e⁻ WOR (**Eq. 1.17**), two-electron 2 e⁻ WOR (**Eq. 1.18**), and 1 e⁻ WOR (**Eq. 1.19**). In addition to the thermodynamically favourable 4 e⁻ WOR process or oxygen evolution reaction (OER) process, which has the lower equilibrium potential (E^o = 1.23 V_{RHE}). WOR can also occur via a two-electron pathway to in situ form H_2O_2 (E^o = 1.76 V_{RHE}), or through a one-electron pathway leading to the formation of ·OH (E^o = 2.38 V_{RHE}).[71]

4 e⁻ WOR pathway:

$$2H_2O \rightarrow O_2 + 4H^+ + 4e^- \ (E^o = 1.23\ V_{RHE}) \qquad \textbf{(Eq. 1.17)}$$

2 e⁻ WOR pathway:

$$2H_2O \rightarrow H_2O_2 + 2H^+ + 2e^- (E^o = 1.76\, V_{RHE}) \quad \textbf{(Eq. 1. 18)}$$

1 e^- WOR pathway:

$$H_2O \rightarrow OH^{\cdot -} + H^+ + e^- \; (E^o = 2.38\, V_{RHE}) \quad \textbf{(Eq. 1. 19)}$$

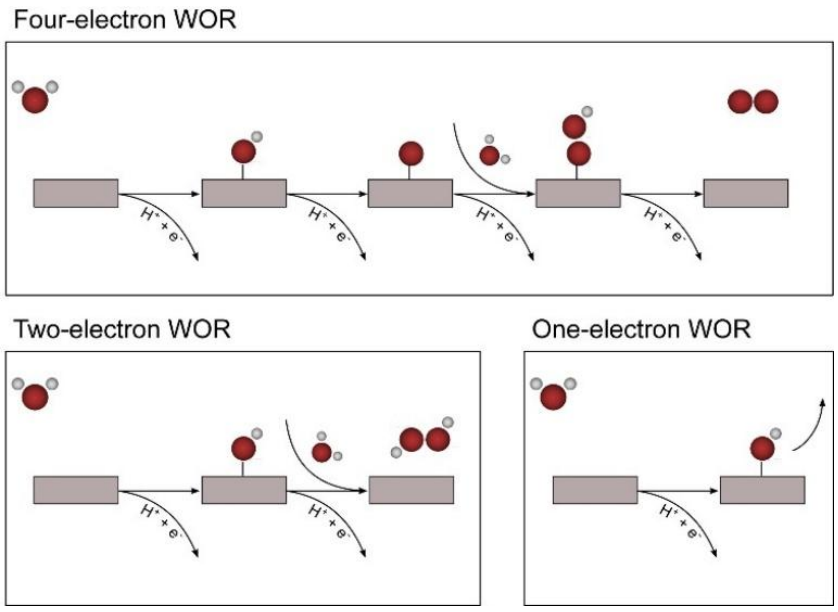

Figure 1.5. WOR mechanism: Different pathways for water oxidation over the catalyst surface.[71]

1.4.3.2 Photosynthesis of H_2O_2 from O_2

Photocatalytic H_2O_2 production has emerged as a promising and sustainable alternative to traditional methods due to its eco-friendliness, utilising H_2O, O_2 and light. This process leverages the photocatalytic properties of semiconductor materials to catalyse reactions under visible light, avoiding hazardous by-products common in conventional synthesis routes. Photocatalytic generation typically involves semiconductor excitation, electron-hole pair generation, and subsequent participation in redox reactions.[58] Effective photocatalysts, such as graphitic carbon nitride (g-C_3N_4), require carefully engineered electronic structures, suitable bandgap energies (1.8–2.9 eV), and optimised surface areas to enhance reaction efficiencies.[59]

Similar to the electrocatalysis of H_2O_2, the primary reaction mechanisms for photocatalytic H_2O_2 production also involve ORR and WOR. ORR pathways can proceed via a direct two-electron process, energetically favourable at +0.68 V vs. NHE, or through a less efficient sequential single-electron reduction, initially forming superoxide radicals ($O_2^{\cdot -}$). Conversely, WOR can occur directly via two-hole oxidation to yield H_2O_2 (+1.76 V vs. NHE) or

sequentially via ·OH intermediates (+2.73 V vs. NHE). Achieving an optimal balance of these reactions without sacrificial agents is essential for effective solar-driven photocatalytic systems [72]

Significant advancements in this field include materials like modified g-C_3N_4,[73] covalent organic frameworks (COFs),[74] and metal-free polymers,[75] enhanced through techniques such as defect engineering, facet modulation, and functionalization. For instance, g-C_3N_4 co-doped with sulphur has shown enhanced photocatalytic performance, producing H_2O_2 at a rate significantly higher than its pristine counterparts.[73] Despite these advancements, key challenges remain, including insufficient stability under operational conditions, undesired decomposition of H_2O_2 due to photocatalyst surface reactions, and limited scalability of the photocatalytic systems.[76]

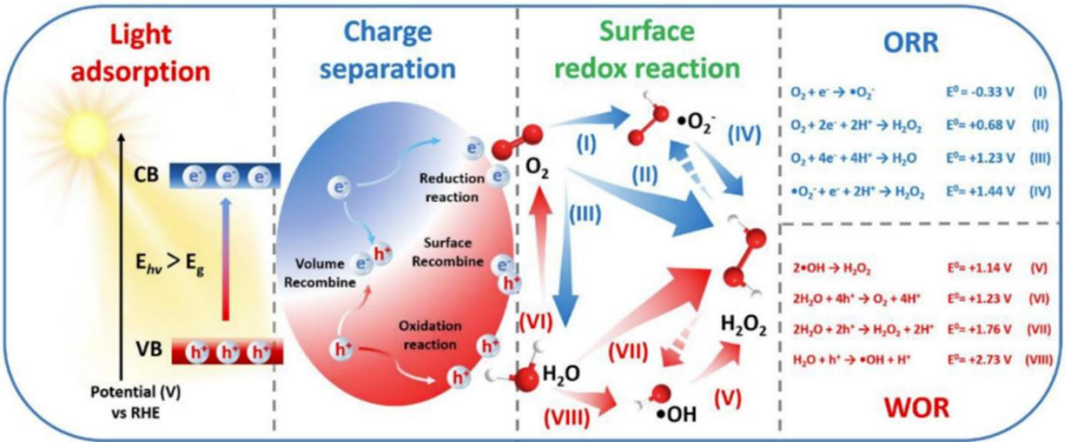

Figure 1.6. Schematic representation of the three basic processes in photocatalytic H_2O_2 production.[72]

1.4.3.3 Direct Synthesis of H_2O_2 from H_2 and O_2

Synthesising H_2O_2 directly from molecular H_2 and O_2 via catalytic reactions is desirable due to the potential for total atom efficiency and avoiding the use of additional reagents, providing a much greener and more environmentally sustainable route to H_2O_2 production.[52,53] This direct route was first found in 1914 by Henkel and Weber and has been widely studied since then.[77] It has not yet been fully commercialised due to the inherent challenges associated with the synthesis process, including various unfavourable water-forming side reactions resulting in a low H_2O_2 selectivity (**Figure 1.7**). 1) The active sites on the surface of the catalyst are responsible for the synthesis of H_2O_2 (**route 1**) but also responsible for further H_2O_2 hydrogenation (**route 2**) and decomposition (**route 3**). 2) The direct combustion of H_2 and O_2

(**route 4**) during the synthesis process. 3) The instability of the H_2O_2 molecule itself causes decomposition at the same time (route 3).[53,78]

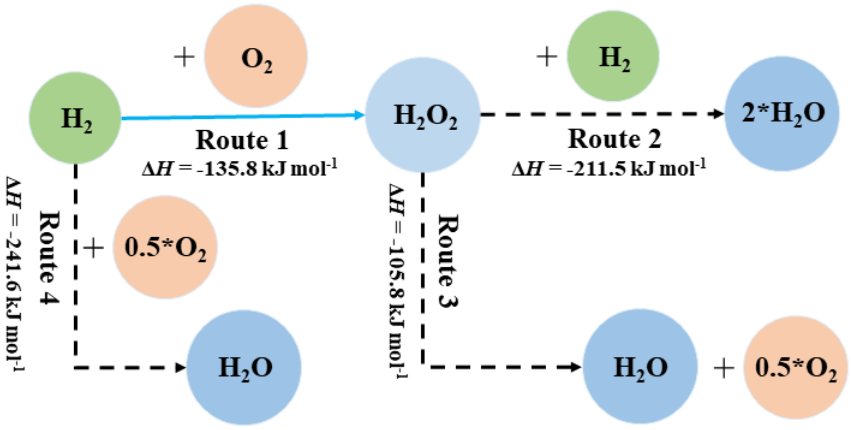

Figure 1.7. Reaction routes during the direct synthesis of hydrogen peroxide, based on the description from previous paper.[53]

Two-step O_2 hydrogenation is the well-accepted reaction mechanism for the direct synthesis of H_2O_2, while keeping the O-O bonds associated are critical for the H_2O_2 formation.[53] An early study by Lunsford and Dissanayake ran oxygen isotope experiments to determine whether the associated O-O bonds or dissociated O were involved in the formation of H_2O_2, and the results showed that only $H_2{}^{16}O_2$ and $H_2{}^{18}O$ were present on Raman spectra, with $H_2{}^{16}O^{18}O$ not observed. These results indicated that the production of H_2O_2 is from diatomic O_2.[79] Furthermore, Hutchings and coworkers,[80] hypothesised a possible mechanism in which H_2 is activated on the catalyst surface to form H*, and then interacts with O_2^* and O^* to form H_2O_2 (H_2O_2 formation reactions) and H_2O (H_2O formation reactions), respectively. Meanwhile, Wilson and Flaherty,[78] also proposed a proton-electron mechanism to explain this direct route over Pd catalysts, where the formation of H_2O_2 proceeds via sequential proton and electron transfer to O_2 with *OOH intermediates on the surface, while the formation of H_2O occurs when the O-O bond in *OOH breaks.

H_2O_2 formation reactions:

$$H_2 + 2^* = 2\,H^* \qquad \textbf{(Eq. 1.20)}$$

$$O_2 + 2^* = {O_2}^* \qquad \textbf{(Eq. 1.21)}$$

$$H^* + {O_2}^* = O_2H^* + * \qquad \textbf{(Eq. 1.22)}$$

$$H^* + O_2H^* = {H_2O_2}^* + * \qquad \textbf{(Eq. 1.23)}$$

$$H_2O_2{}^* = H_2O_2 + *$$ **(Eq. 1.24)**

H_2O formation reactions:

$$O_2 + 2^* = 2\,O^*$$ **(Eq. 1.25)**

$$H^* + O^* = OH^* + *$$ **(Eq. 1.26)**

$$H^* + OH^* = H_2O^* + *$$ **(Eq. 1.27)**

$$H_2O^* = H_2O + *$$ **(Eq. 1.28)**

Similar theoretical research of the direct synthesis of H_2O_2 on Pd catalyst was investigated by Staykov et al., using first-principle DFT methods (**Figure 1.8**).[81] In this model, the first step in H_2O_2 formation involves a superoxol species that interacts with a H atom adsorbed at the nearest threefold hollow site, generating the initial intermediate. A second H atom at an adjacent threefold site then reacts with this intermediate, yielding H_2O_2.

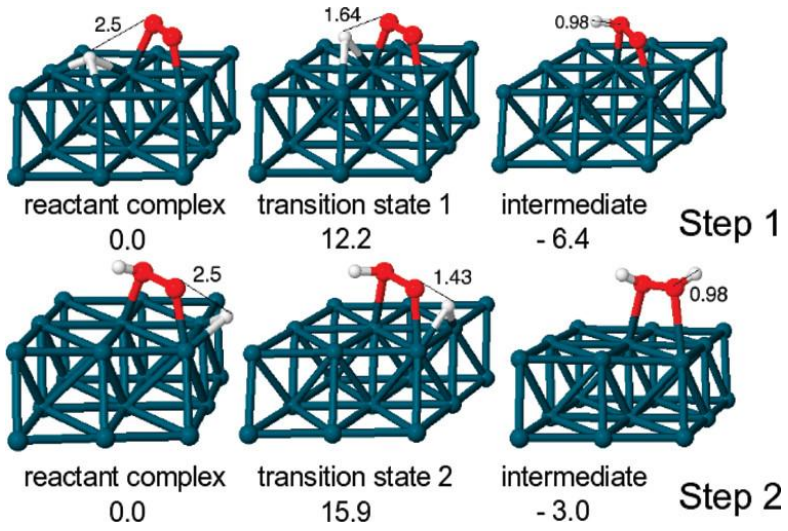

Figure 1.8. The reaction mechanism of direct H_2O_2 formation over the Pd surface.[81]

In the direct synthesis of H_2O_2, the thermodynamic analysis of the reaction pathways indicates that **routes 2-4** (**Figure 1.7**) are more favourable than **route 1** (**Figure 1.7**), showing that the water-forming side reactions represent a significant challenge that limits the complete and efficient utilisation of H_2 for the synthesis of H_2O_2. Besides, it is crucial to consider the safety aspects during the direct synthesis of H_2O_2. At the early stage, the highly pressured, dangerous, and explosive H_2/O_2 mixture used in the direct route presented inherent hazards that have prevented the commercialisation of this direct route for over a century, and further, DuPont found that the gas mixture (4% H_2/Air) was still flammable due to the high H_2 diffusion rate.

To address this safety concern, diluted reactant gases with an inert gas (e.g., N_2, CO_2, etc.) have been introduced to improve safety. Only less than 4% of H_2 is present in the diluted gas mixture (H_2/inert gas), and the H_2:O_2 ratio is 0.5, allowing work below the lower explosive limit, but also limiting the production of H_2O_2 simultaneously.[82] Most importantly, safety considerations are an essential aspect to consider in the optimisation of the direct synthesis of H_2O_2.

1.5 Palladium and Palladium-based Catalysts in the Direct Synthesis of H_2O_2

1.5.1 Monometallic Pd catalysts in H_2O_2 synthesis

The direct H_2O_2 synthesis from H_2 and O_2 is theoretically an atom-efficient alternative to the anthraquinone process and an enabling route for decentralised, on-demand oxidant supply. Among heterogeneous catalysts, Pd has been examined most intensively over decades due to its high catalytic activity towards both H_2 and O_2 activation under mild conditions, yet this same reactivity predisposes it to O-O bond scission of the intermediates ($*O_2$, *OOH) and the rapid subsequent hydrogenation/decomposition of H_2O_2. To mitigate inherent selectivity limitations, Pd catalysts are frequently operated in a "modified" solvent environment, with acidic media, in the presence of halide promoters, and the addition of alcohols, to suppress pathways responsible for H_2O_2 degradation and promote selective H_2O_2 production.[53]

In 1961, Pospelova et al. first reported that adding inorganic acids could inhibit H_2O_2 decomposition, plausibly by suppressing deprotonation of H_2O_2 to OOH^- and its subsequent breakdown.[83] Similarly, Lunsford and co-workers confirmed the benefits of using HCl to promote H_2O_2 formation but also emphasised that the use of acid could leach supported Pd, compromising catalyst stability and introducing homogeneous catalytic contribution.[79,84–86] The initial investigation into the homogeneous Pd colloid was utilising 5wt.% Pd/SiO_2 catalyst to produce H_2O_2 in situ from H_2 and O_2 in the HCl acidified water solution.[84] Experimental results showed that the main active sites for the direct H_2O_2 synthesis were not the supported Pd/SiO_2 catalyst, but the Pd colloid. As shown in **Figure 1.9 (A)**, H_2O_2 productivity remains constant after removing the solid Pd/SiO_2 phase when in either 1 M or 0.1 M HCl solutions, while H_2O_2 productivity ceased in the 0.01 M HCl solution under identical procedures. Further evidence given by Lunsford confirmed that the presence of both HCl and O_2 promoted the formation of Pd colloid, which was generated from the reduction of $PdCl_4^{2-}$ ions in acidic

aqueous solutions, while the presence of Pd depended on the reaction time and H_2/O_2 ratios. (**Figure 1.9 (B)**).[86]

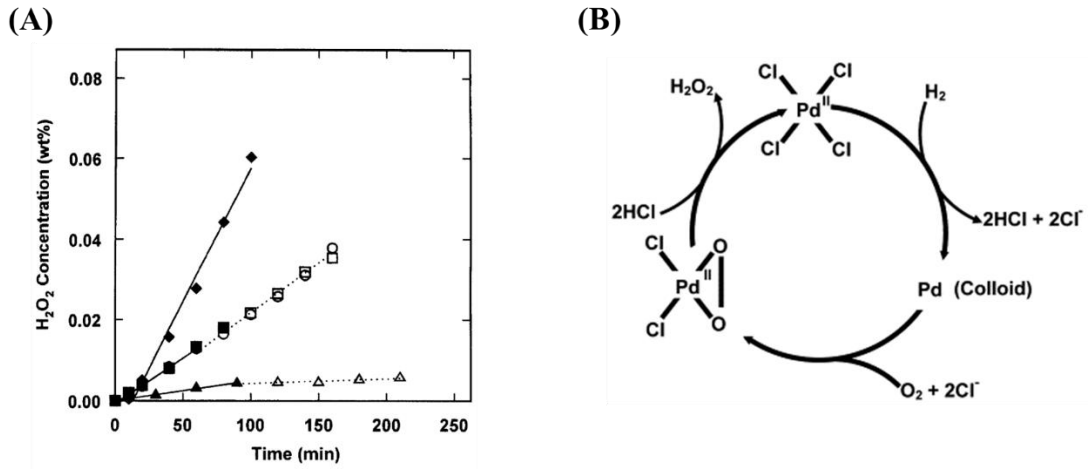

Figure 1.9. (A) Direct synthesis of H_2O_2 in an aqueous phase (H_2O only) before and after the removal of 2.2 mg of 5 wt% Pd/SiO_2: (■) before and (□) after the removal of the solid phase from a 1 M HCl solution; (●) before and (○) after the removal of the solid phase from an 0.1 M HCl solution; (▲) before and (△) after the removal of the solid phase from an 0.01 M HCl solution. Peroxide formation in a nominally 1.0×10^{-4} M $PdCl_4^{2-}$ solution containing 1 M HCl is depicted by (⧫)[84] and (B) the schematic plot of the reaction mechanism.[86]

Continue with the pure-water condition (i.e., in the absence of alcohols), Han et al.[87] further reported that no measurable H_2O_2 was formed in the H_2SO_4/H_2O system over 5 wt.% Pd/SiO_2 catalyst, even though the system maintained around 20% H_2 consumption, suggesting that the H_2O formation reaction dominated (**Figure 1.10 (A)**). This significant contrast pointed out the importance of the counterion of the acid, where the halide ion (e.g., Cl^-) seems a promoter for the H_2O_2 synthesis, while SO_4^{2-} was not involved in H_2O_2 synthesis. Chinta et al.[86] further confirmed that the introduction of Br^- into the HCl/H_2O system promoted H_2O_2 production by increasing the H_2O_2 selectivity, and experimental results also revealed that Br^- is more effective than Cl^-, in terms of the selectivity towards H_2O_2 production (**Figure 1.10 (B)**).

Indeed, these earlier studies provided no quantitative evidence that protons or mineral acids function as true co-reactants or co-catalysts in H_2O_2 formation. To answer the questions and hypotheses from early studies on how halide ions or counterions of these acids affect the H_2O_2 synthesis. Wilson and Flaherty found that the promoted H_2O_2 turnover rates/H_2O_2 formation rates could be attributed to the adsorption of counterions (i.e., Cl^-, SO_4^{2-}, HCO_3^-, and $H_2PO_4^-$) onto the Pd, which agrees with previous observations that strongly binding anions decrease H_2O formation rates during ORR, perhaps because the anions must be displaced from the

surface prior to O-O bond rupture.[78] Similarly, the kinetic analysis and DFT calculation by Deguchi et al.[88] suggested that the presence of H^+ and Br^- significantly decreased the more unsaturated sites, which are mainly responsible for the direct H_2O formation and H_2O_2 decomposition. Whereas the selective H_2O_2 synthesis occurs on the less unsaturated active sites. Experimental work by Biasi et al. found the poisoning effect of Br^- on Pd active sites which are responsible for H_2O_2 degradation. Complementary proposals emphasise electronic effects that halides can curb electron back-donation into the O_2 $2\pi^*$ antibonding orbitals, helping to preserve the O-O linkage and favour molecular H_2O_2 formation.[89] Together, site blocking, electronic modulation, and halide-driven structural reorganisation likely act in concert to boost selectivity towards H_2O_2 synthesis.

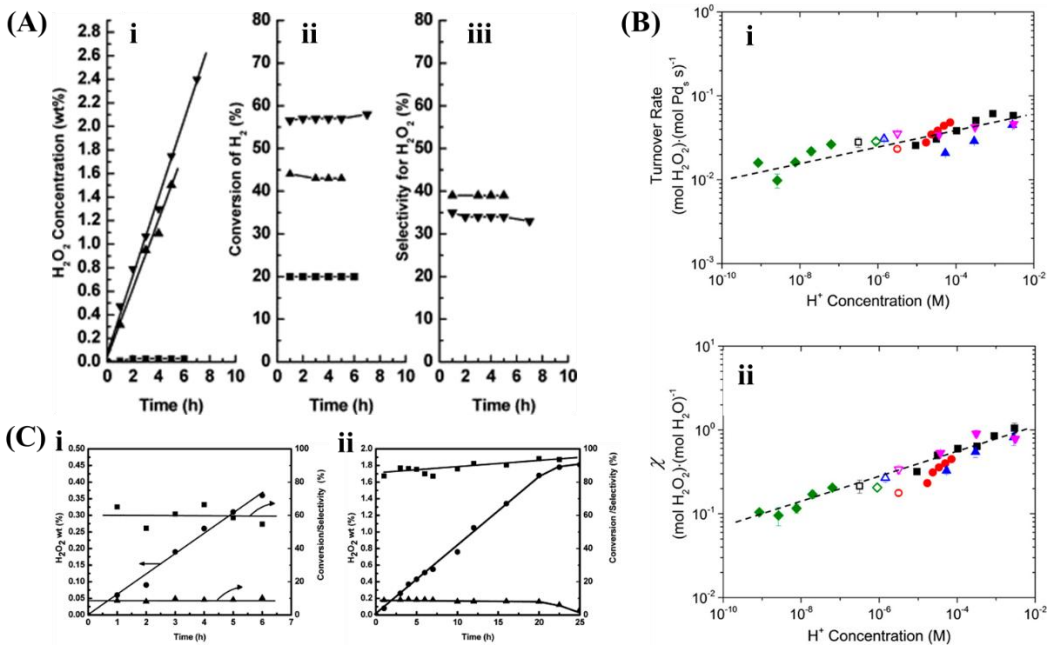

Figure 1.10. (A) Catalytic formation of H_2O_2 in the ethanol solution acidified to (▲) 0.12 N and (▼) 0.24 N in H_2SO_4, and (■) 0.24 N H_2SO_4/water: (i) concentration of H_2O_2, (ii) conversion of H_2, and (iii) selectivity for H_2O_2.[87] **(B)** (i) H_2O_2 turnover rates and (ii) ratio of the formation of H_2O_2 to that for H_2O on 0.7 nm Pd clusters as a function of H^+ concentration, which was controlled by the addition of a mineral acid or base including H_2SO_4 (black ■), H_3PO_4 (blue ▲), HCl (magenta ▼), $NaHCO_3$ (green ♦), or H_2CO_3 (red ●, by applying 0-0.7 MPa CO_2) (50 kPa H_2, 60 kPa O_2, 277 K, 10 cm^3 min^{-1} 20% v/v CH_3OH). Empty symbols represent measurements taken prior to the addition of each acid or base.[78] **(C)** Formation of H_2O_2, (i) in the absence of Br^- and (ii) in the presence of Br^- (0.01 M); (●) wt% H_2O_2, (▲) H_2 conversion, and (■) selectivity for H_2O_2. The solution was 0.1 N in HCl and the O_2/H_2 gas ratio was 4:1.[86]

The subsequent study conducted by Han and co-workers,[87] determined that the H_2 conversion rate and H_2O_2 concentration showed a positive correlation with the concentration of H_2SO_4 in the reaction mixture (H_2SO_4/ethanol) (**Figure 1.10 (C)**), suggesting that the presence of ethanol is also crucial to produce H_2O_2 in situ without the promotive effect from halide ions, which might be attributed to promote H_2 dissolubility and possibly, the surface acetate ions via the interaction between ethanol and O_2 over the Pd(110) phase,[87] suggesting that the rate dependencies and kinetic behaviour observed in alcohols and in aprotic solvents differ markedly from those in water, indicating that the solvent participates directly in the catalytic cycle, either as a co-reactant or as a cocatalyst, rather than serving merely as an inert medium. Moreover, measurable H_2O_2 production in non-aqueous systems without added halides demonstrates that halides are not intrinsically required for selective O_2 reduction to H_2O_2.

Nevertheless, a systematic study on the effect of organic cosolvents on both catalyst activity and selectivity is lacking. The addition of organic co-solvents also had a dramatic effect. Water-miscible solvents like ethanol and acetonitrile were found to improve selectivity, potentially by coordinating to the palladium catalyst and inhibiting the water-forming reaction. In contrast, water-immiscible solvents such as toluene and hexane increased H_2 conversion but resulted in very poor selectivity for H_2O_2,[90] which is consistent with the conclusion drawn from Krishnan et al.[91] who also found that the optimal selective H_2O_2 synthesis exists in a methanol or acetonitrile organic mixture (organic/H_2SO_4).

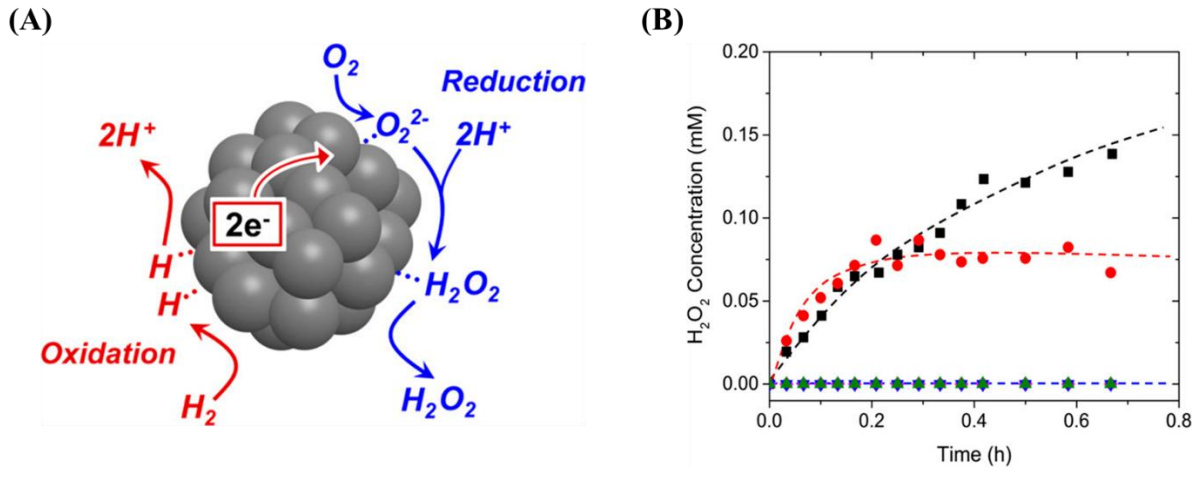

Figure 1.11. (A) The reaction mechanism of Pd clusters catalyses both heterolytic H_2 oxidation and O_2 reduction steps in order to form H_2O_2. (B) H_2O_2 concentrations as functions of time during direct synthesis in a well-mixed semi batch reactor using protic (methanol (black ■) and water (red ●)) or aprotic (dimethyl sulfoxide (green ▲), acetonitrile (blue ▼), and propylene carbonate (magenta ♦)) solvents (4.2 kPa H_2, 4.2 kPa O_2, 40 cm^3 solvent, 20 mg of 3.8 wt % Pd/SiO_2, 295 K).[78]

Indeed, these studies initially proposed the effect of proton-electron transfer on the direct synthesis of H_2O_2 over Pd catalysts, yet the reaction mechanism remained unclear. Recently, Wilson and Flaherty,[78] suggested that the Langmuir–Hinshelwood mechanism does not apply to the direct synthesis of H_2O_2 and proposed a new reaction mechanism for the direct H_2O_2 synthesis (**Figure 1.11 (A)**), where the sequential proton-electron transfer to O_2 and hydroperoxide intermediates is the key process for H_2O_2 generated in situ. Analysis over supported Pd catalysts (**Figure 1.11 (B)**) demonstrated that the presence of protons is key to H_2O_2 synthesis, with the H_2O_2 production rates in protic solvents (water and methanol) 10^3 times higher than in aprotic solvents (dimethyl sulfoxide, acetonitrile, and propylene carbonate) under the identical reaction conditions ((4.2 kPa H_2, 4.2 kPa O_2, 295 K, 3.8 wt % Pd–SiO_2). A kinetic study from Deguchi et al.[88] pointed out that increasing proton activity accelerates transformations involving the surface *OOH to H_2O_2 (*OOH + H* → H_2O_2* → H_2O_2) and competing reaction to H_2O (*OOH + H* → H_2O + O*), but the proton-driven rate enhancement is greater for the former reaction, shifting toward selective H_2O_2 formation. Wilson et al.[92] further proved the proton-electron theory by quantifying steady-state H_2O_2 and H_2O formation rates as functions of H_2 pressure, O_2 pressure, and proton activity in the liquid phase. The H_2O_2 rate increased approximately linearly with H_2 pressure up to 100 kPa and became sub-linear at higher pressures, and the H_2O rate also rose with H_2 pressure, while variations in O_2 pressure produced negligible changes in either rate over the range examined. In protonated media, bulk H_2O_2 accumulated over time, whereas in the absence of added protons, it remained effectively zero. DFT calculation by Chen et al.[93] demonstrated that high partial pressure of H_2 could enhance H_2O_2 selectivity, providing extra evidence that the proton-electron transfer is crucial in the direct synthesis of H_2O_2.

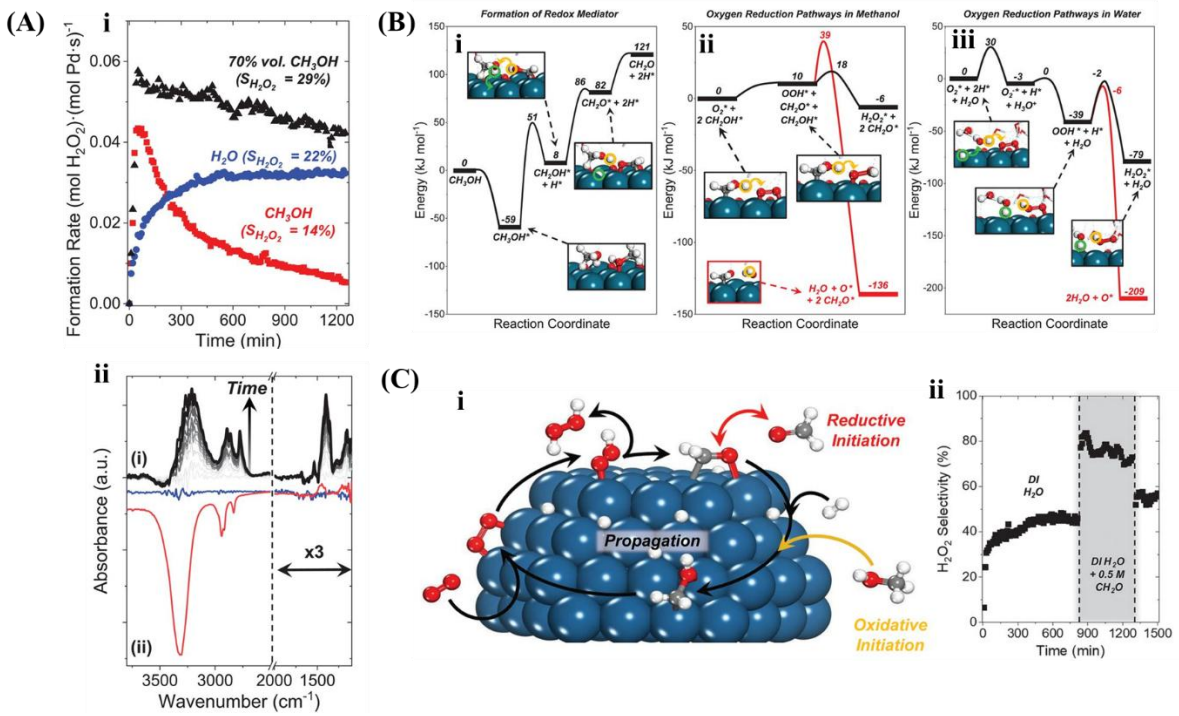

Figure 1.12. (A) (i) H_2O_2 formation rates over time in a fixed-bed reactor at 278 K with 60 kPa H_2 and 60 kPa O_2, comparing methanol red squares, water blue circles, and 70 vol% CH3OH in water black triangles. (ii) Time profiles of H_2O_2, H_2O, and CH_2O during direct synthesis in CH_3OH at 298 K with 4.8 kPa H_2 and 4.8 kPa O_2. (B) DFT energy diagrams. (i) Formation of the redox mediator from adsorbed CH_3OH or CH_2O. (ii and iii) Pathways for H_2O_2 and H_2O on Pd(111) in methanol and in water. The slab includes 1/3 ML O* and subsurface H* at 1/3 ML in water or 2/3 ML in methanol, consistent with operando EXAFS. Green circles mark the H atom oxidized to a proton, yellow circles mark the transferred proton. (C) (i) CH_2OH* forms by oxidative initiation of methanol or reductive initiation of formaldehyde and mediates O_2 and H_2 to give H_2O_2 and H_2O. (ii) Adding 0.5 M CH_2O to deionized water increases steady-state H_2O_2 selectivity at 278 K under 200 kPa H_2 and 60 kPa O_2.[94]

Although previous researchers have found the enhancement in the selective H_2O_2 synthesis in protic solvents (e.g. alcohols),[78,87,90,91] the mechanism of how these groups are involved in the H_2O_2 synthesis was, until recently, largely unknown. Based on the previously proposed proton-electron theory, Adam and Flaherty,[94] explained how solvent molecules modulate the H_2 and O_2 reaction on Pd nanoparticles. Kinetic analysis and calculations indicate cooperative catalysis by methanol and water through proton-electron transfer (**Figure 1.12 (A-C)**). Methanol forms adsorbed hydroxymethyl (CH_2OH*) species on the Pd surface that deliver H^+ and e^- to O_2, producing H_2O_2 and CH_2O. The formaldehyde then oxidises H_2 and regenerates CH_2OH*, closing a methanol-driven redox cycle during H_2O_2 synthesis. Water contributes via heterolytic H_2 activation that generates hydronium ions and electrons at the metal, which reduce O_2.

The state of Pd active sites towards effective H_2O_2 synthesis has been controversial for years, and the previous reports have mainly focused on whether it is the metallic (Pd^0) or the oxidation (Pd^{2+}) state that favours the synthesis of H_2O_2. Kanungo et al.[95] utilized in situ X-ray Absorption Spectroscopy (XAS) analysis and confirmed that Pd remained fully reduced during reaction, thus concluding that Pd^0 is the main active state for H_2O_2 synthesis. Liu et al. observed that, in ethanol with acid/halide promoters, fully reduced Pd^0/SiO_2 outperformed partially reduced samples, again pointing to Pd^0 as more conducive to H_2O_2 formation.[96] Conversely, several studies implicate Pd^{2+} as the operative phase rather than Pd^0. Evidence for oxidized Pd (e.g., Pd^{2+}) as a productive state includes studies by Choudhary et al.,[97] who argued that Pd^{2+} sites bind peroxide intermediates (e.g. *OOH, $*O_2$) while Pd^0 preferentially promotes H_2O_2 degradation. Wang et al.[98] found that the PdO(101) surface is more preferable for H_2O_2 synthesis compared to Pd(111) surface, showing higher productivity and selectivity. DFT calculation suggested that the *OOH species are less active on the PdO(101) surface, whereas Pd(111) surface with a higher d-band centre results in higher O-O splitting activity.

However, the active sites for H_2O_2 synthesis might not be simply assigned to metallic Pd (Pd^0) or oxidised Pd species (Pd^{2+}). The interaction between Pd and PdO due to Pd cycling through its oxidation states could be responsible for the reaction. Ouyang and Han studied the active sites over supported Pd/TiO_2 catalysts with Pd loading from 1 wt% to 5 wt% on the direct synthesis of H_2O_2.[99] Synthesised by the incipient wetness impregnation method, a series of Pd/TiO_2 catalysts remained similar particle size (ca. 2.4 nm in diameter) and crystallinity, but showed significantly different catalytic ability, where 1wt%Pd/TiO_2 performed highest H_2O_2 productivity at 2.99 $mol_{H2O2}\ g_{Pd}^{-1}\ h^{-1}$, H_2O_2 selectivity at 61%, and TOF at 630 h^{-1}, but lowest H_2 conversion at only 10.2 %. Whereas the highest H_2 conversion (31.1%) could be observed on the 5wt%Pd/TiO_2 catalysts, but the H_2O_2 productivity (2.99 $mol_{H2O2}\ g_{Pd}^{-1}\ h^{-1}$), H_2O_2 selectivity (41%), and TOF (296 h^{-1}) were relatively low. XPS analysis revealed that the co-existence of Pd^0 and Pd^{2+} in all Pd/TiO_2 catalysts was due to the oxidation by absorbed oxygen with the assistance of TiO_2, and further formed Pd-PdO interfaces for H_2 activation and undissociated activation of O_2. These interfaces were influenced by Pd loading as the Pd^0/Pd^{2+} ratios changed from 1.1 on 1wt%Pd/TiO_2 to 1.8 on 5wt%Pd/TiO_2, leading to a drop in H_2O_2 productivity and selectivity (**Figure 1.13**).

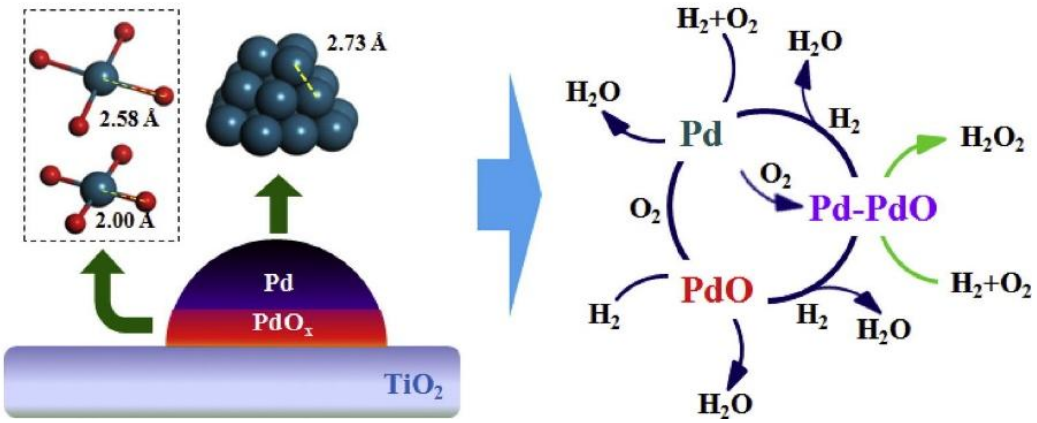

Figure 1.13. The reaction mechanism of Pd interface in the direct synthesis of H_2O_2.[99]

In addition to the Pd oxidation state, Pd particle size also matters to the catalytic performance of the direct synthesis of H_2O_2. Kim et al.[100] prepared Pd core–porous SiO_2 shell catalysts (Pd@SiO_2) with different Pd particle sizes, by controlling the weight ratio of polyvinylpyrrolidone (PVP) to Pd. The H_2O_2 productivity, H_2O_2 Selectivity, and H_2 conversion dropped when the Pd particle size decreased from 4.2 nm (Pd@SiO_2_PVP2) to 3.5 nm (Pd@SiO_2_PVP8) with the increased PVP. This might be due to the energetic sites (defects, corners, and edges), which are responsible for the O–O bond cleavage and water formation, increased on a Pd surface with the decreased mean Pd particle size, resulting in a low H_2O_2 production. A similar trend was found by Wilson et al.[78] who reported that H_2O_2 selectivity increases slightly as Pd clusters on SiO_2 grow from about 3.4 to 4.2 nm, likely due to ensemble effects that reduce O-O bond scission sites or electronic effects that lessen Pd back-donation into the π^* orbitals of the O-O bond..

However, Deguchi et al. reported a contrary trend. The catalytic activity of the Pd/C catalyst towards H_2O_2 synthesis increased with the decreasing Pd particle size due to the increasing Pd dispersion, whereas H_2O_2 formation selectivity decreased, probably due to the increasing density of more unsaturated sites.[88] Tian et al.[101] showed that the maximal H_2O_2 selectivity (94%) was observed over 0.5wt%Pd/ hydroxyapatite (HAp) catalysts with a size of 1.4 nm under mild conditions (atmospheric pressure, 283 K). Further experimental studies on a series of size-controlled Pd/HAP catalysts ranging from single sites (Pd clusters) to nanoparticles (dPd: ~30 nm) toward the H_2O_2 synthesis, together with Density functional theory (DFT) calculations revealed that Pd clusters of sub-nano size have the most effective active sites for the selective activation of O_2 hydrogenation, leading to a H_2O_2 productivity and selectivity. Whereas either Pd single sites (monodisperse Pd atoms), which lack active sites, or Pd

nanoparticles (>2.5 nm) with abundant Pd(111) facets, which were rather active for O_2 dissociative activation, were not favourable for the H_2O_2 formation (**Figure 1.14**).

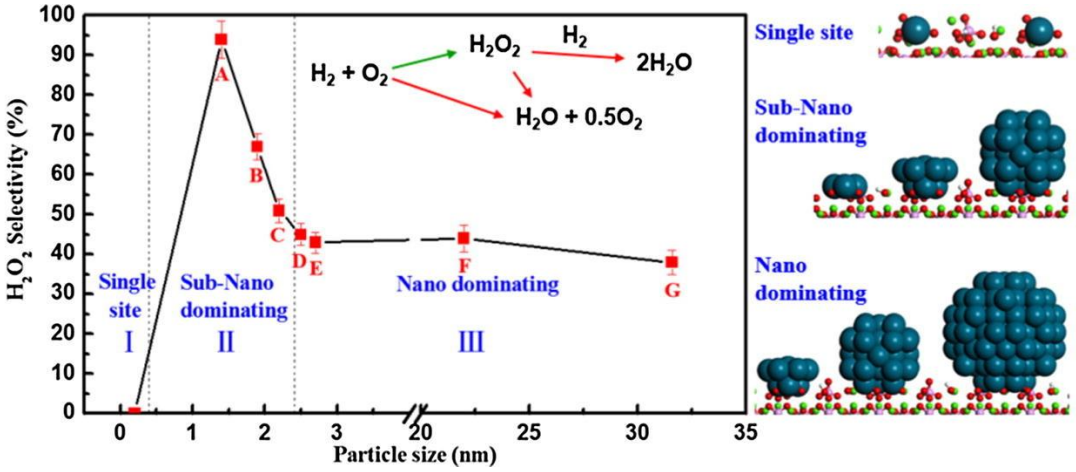

Figure 1.14. The correlation between Pd particle size and the catalytic selectivity towards H_2O_2 synthesis.[101]

However, scaling down the size even further to a single atom does not negatively affect H_2O_2 selectivity based on the schematic plot from **Figure 1.14.** Instead, single-atom Pd exhibited excellent activity and selectivity towards H_2O_2 production. Yu et al.[102] found that TiO_2-supported single-atom Pd catalysts with 0.1% Pd loading under calcined heat treatment in air (0.1%PdO/TiO_2) exhibited the highest H_2O_2 productivity (115 mol_{H2O2} g_{Pd}^{-1} h^{-1}) and H_2O_2 selectivity (99%) among a series of TiO_2-supported monometallic Pd catalysts with the Pd loading range from 0.05% to 3%. The dissociation energy barriers of O_2 and H_2 over a single Pd atom (1.89 eV & 0.22 eV) and Pd clusters (1.08 eV & 0.61 eV) were simulated and calculated using DFT calculations, indicating that the O_2 cleavage is not favourable, but H_2 is easily activated over single Pd atom sites.

Although the experimental results seemingly showed an opposite trend in terms of bigger the better or smaller the better, the H_2O_2 selectivity/productivity is highly associated with Pd ensemble, deficit density and Pd coordination. Pd particle size matters insofar as it tunes ensemble size and site coordination, on weakly interacting supports and in halide-free media, larger particles (fewer defects, larger terraces) tend to be more selective. In environments that stabilise *OOH and promote heterolytic H_2 activation, sub-nano clusters, and even single atoms can become optimal. The apparent contradictions across studies therefore reflect whether defect enrichment (small NPs) or site isolation (sub-nano/Pd or ensemble dilution) dominates under the chosen support, solvent, and promoter conditions.

1.5.2 Bimetallic AuPd catalysts in H_2O_2 synthesis

As discussed in the previous section, monometallic Pd catalysts have long been identified as the active materials for the direct H_2O_2 synthesis. However, for most cases, poor selectivity towards H_2O_2 formation in general hindered the practical application. While Pd surfaces are exceptionally efficient at dissociating H_2, they are also highly effective at catalysing the subsequent, undesired reaction pathways, including the hydrogenation of the newly formed H_2O_2 to H_2O and, more detrimentally, the direct dissociative chemisorption of O_2 followed by hydrogenation, which cleaves the crucial O-O bond and leads exclusively to the unwanted H_2O formation. This selectivity and activity challenge necessitated a fundamental rethinking of the catalyst design. The breakthrough arrived with the seminal work of Landon et al.,[103] who firstly reported the enhanced H_2O_2 productivity when introducing Au into Pd catalysts, compared to the monometallic Au and Pd analogues (**Table 1.1**),[103] where the bimetallic 2.5 wt% Au-2.5 wt% Pd/Al_2O_3 catalyst (4460 $mmol_{H2O2}$ Kg_{Cat}^{-1} h^{-1}) outperformed both monometallic 5wt% Au/Al_2O_3 (1530 $mmol_{H2O2}$ Kg_{Cat}^{-1} h^{-1}) and 5wt% Pd/Al_2O_3 (370 $mmol_{H2O2}$ Kg_{Cat}^{-1} h^{-1}), and this enhancement might be associated with the alloyed Au and Pd (**Figure 1.15**).[103]

Table 1.1. The catalytic performance of the direct H_2O_2 synthesis using Al_2O_3-supported AuPd series.[103]

Catalyst	H_2O_2 prodictivity / $mmol_{H2O2}$ Kg_{Cat}^{-1} h^{-1}	H_2O_2 concentration / wt%	H_2 Conversion / %	H_2O_2 selectivity / %
5 wt% Au/Al_2O_3	1530	0.031	6	53
5 wt% Pd/Al_2O_3	370	0.0008	80	1
2.5 wt% Au-2.5 wt% Pd/Al_2O_3	4460	0.09	63	14

Reaction conditions: catalyst: 0.05g, CH_3OH/H_2O co-solvent, 5% H_2/CO_2 and 25% O_2/CO_2 (O_2/H_2 molar ratio: 1.2), 2 °C, 0.5 hour.

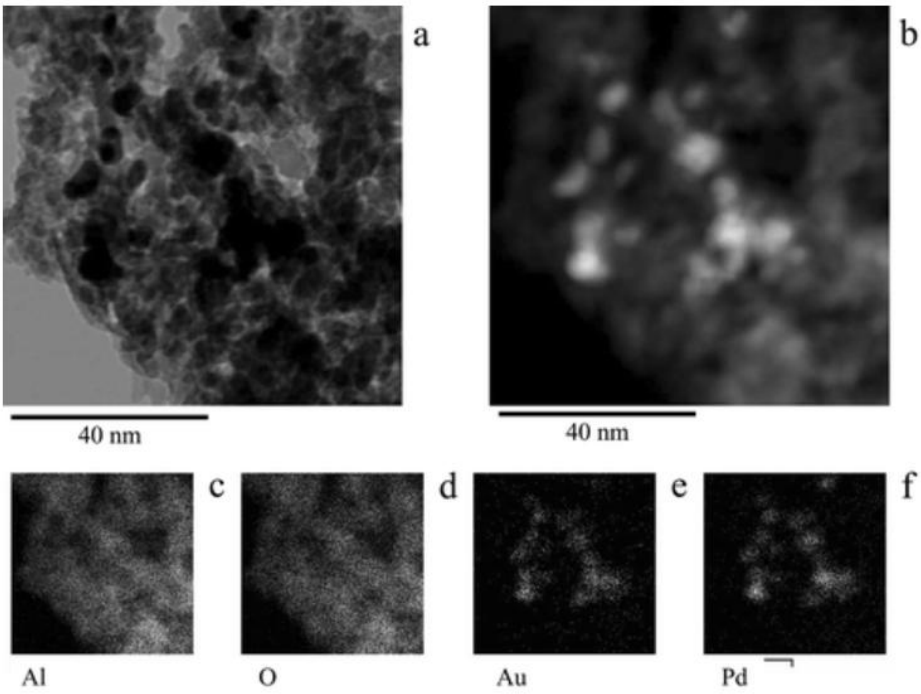

Figure 1.15. Bright field (top left) and annular dark field (top right) STEM images of the Au Pd/Al_2O_3catalyst. The lower montage shows a series of X-ray maps of the same area taken with Al Kα, O Kα, Au L and Pd L signals.[103]

The enhanced activity towards direct H_2O_2 synthesis was further explained by theoretical evidence proposed by the Yoshizawa group,[81,104] who gave possible reaction pathways of H_2O_2 synthesis over AuPd catalysts through theoretical calculations, and the reaction involving O-O bond dissociation is suppressed on the Au@Pd(111) surface due to the weaker existence of the O-Au bond, compared to the Pd(111) surface, where the side reaction (H_2O formation) dominates due to the stronger O-Pd bond, suggesting that the introduction of Au weakens the Pd−O interactions, leading to an enhanced selectivity towards the O−O bond (**Figure 1.16**). This is in a good argument with the work of Han and Mullins,[105] who found the dissociation barrier for O_2 steadily decreases with the increased Pd content or coverage, resulting increase in H_2O formation.

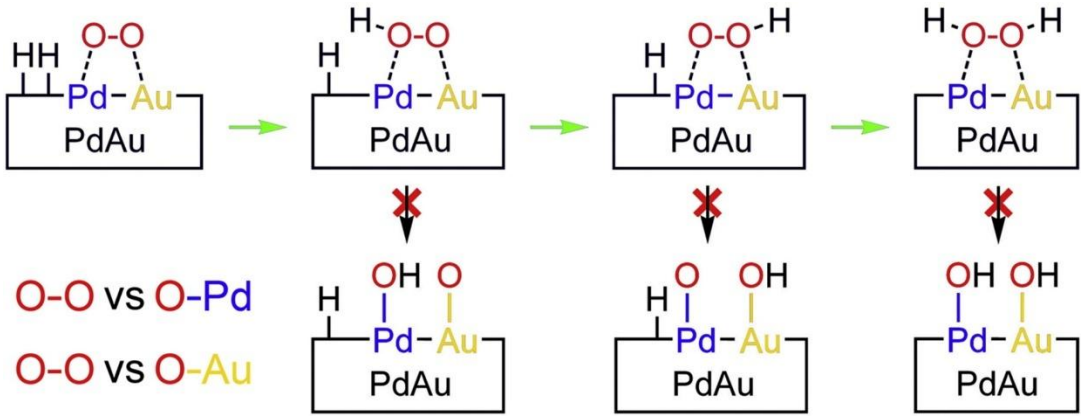

Figure 1.16. The proposed reaction mechanism of the direct synthesis of H_2O_2 over AuPd catalyst.[104]

Indeed, the synergistic mechanism of the bimetallic AuPd catalysts in the direct synthesis of H_2O_2 remained unclear. Arguments are around electronic modification, structural or segregation effects, and the synergistic effects observed experimentally may be the result of their combined action.[53] Han et al. first probed the modification of the Pd electronic structure by the addition of Au using diffuse reflectance infrared fourier transform spectroscopy (DRIFTS) spectra, indicating that the enhancement in activity and selectivity over AuPd alloy catalysts compared to monometallic Pd catalysts could be attributed to the surface structure changes by introducing Au into Pd catalysts (**Figure 1.17**).[106] Numerous studies into AuPd catalysts from Hutchings's group found the electron modification of Pd by the introduction of Au when analysing XPS or CO-DRIFTS spectra. Wilson et al.[107] pointed out that the electronic effects with the addition of Au contributed to the increased selectivity towards H_2O_2 formation over AuPd bimetallic surfaces, evidenced by the theoretical calculation and experimental results, showing that the increases in the Au:Pd ratio lead to the decreased turnover rate of H_2O formation reaction, compared to monometallic Pd.

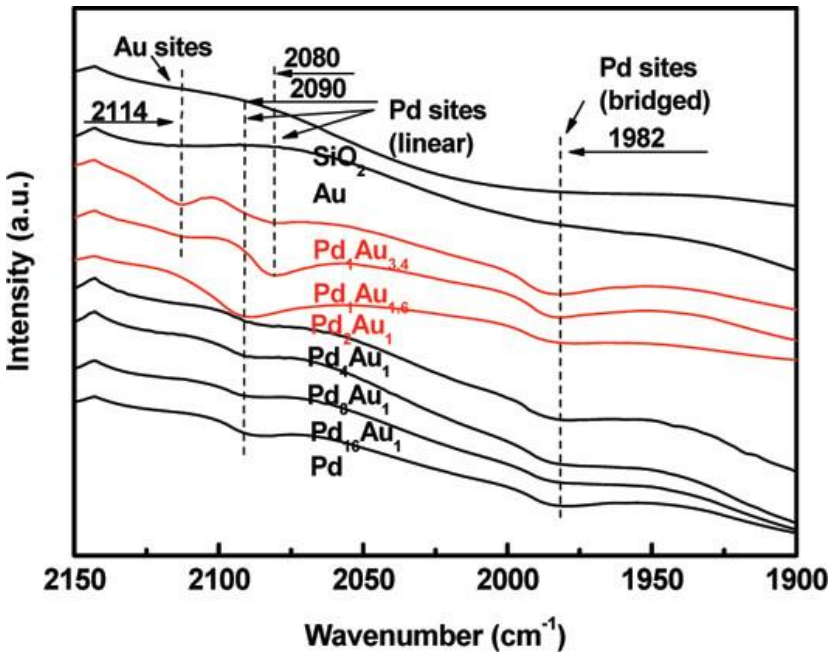

Figure 1.17. The electro modification effect with the introduction of Au into Pd catalysts as indicated by the DRIFTS study.[106]

On the other hand, the geometric effect in the AuPd alloy catalyst also played a vital role in the enhanced activity. Ouyang et al.[108] tuned the Au:Pd ratio in AuPd/TiO_2 catalysts and showed that Au restructures the Pd surface from contiguous Pd ensembles to isolated Pd monomers while subtly modifying Pd electronics, as indicated by CO-DRIFTS and XPS. This geometric dilution suppresses O-O scission, making Pd monomers surrounded by Au the primary sites for H_2O_2 formation, whereas contiguous Pd ensembles preferentially hydrogenate H_2O_2 and have lower selectivity towards H2O2 synthesis. As Au content increases, activity and selectivity follow a volcano with an optimum near $Pd_{2.0}Au_{1.0}$ (2330 $mmol_{H2O2}$ g_{metal}^{-1} h^{-1}, 48.1% selectivity) under mild conditions, compared with the monometallic Pd catalyst (1922 $mmol_{H2O2}$ g_{metal}^{-1} h^{-1}, 44.6% selectivity). Previous theoretical calculation works also confirmed that the superior H_2O_2 selectivity of AuPd alloys arises from Pd monomers embedded in Au, which curtail O-O bond scission compared with monometallic Pd and Au.[109] A following DFT-informed kinetic Monte Carlo model proposed by Svensson and Grönbeck,[110] found that the 100% H_2O_2 selectivity could be achieved when Pd monomer is embedded in the extended Au(111) surface, where the isolated Pd monomers dissociate H_2, while H_2O_2 forms predominantly on under-coordinated Au sites through a solution-mediated pathway in which solvated H^+ adds to O_2-derived surface species.

However, the beneficial effect of adding Au to Pd does not imply that more Au yields better performance. Instead, introducing an excessive amount of Au might result in low activity or even selectivity towards the direct H_2O_2 synthesis compared with the catalysts with optimal Au:Pd ratios, as previously reported by Ouyang et al.[108] and Wilson et al.[107] Kim and co-workers demonstrated that introducing excessive Au into Pd-core/Au-shell alloys leads to a loss of catalytic performance in both activity and selectivity toward direct H_2O_2 synthesis due to relaxation of Pd-induced compressive strain and charge-transfer in the Au overlayer, which weakens H_2 activation, thereby suppressing H_2O_2 formation and favouring H_2O (**Figure 1.18**).[111,112]

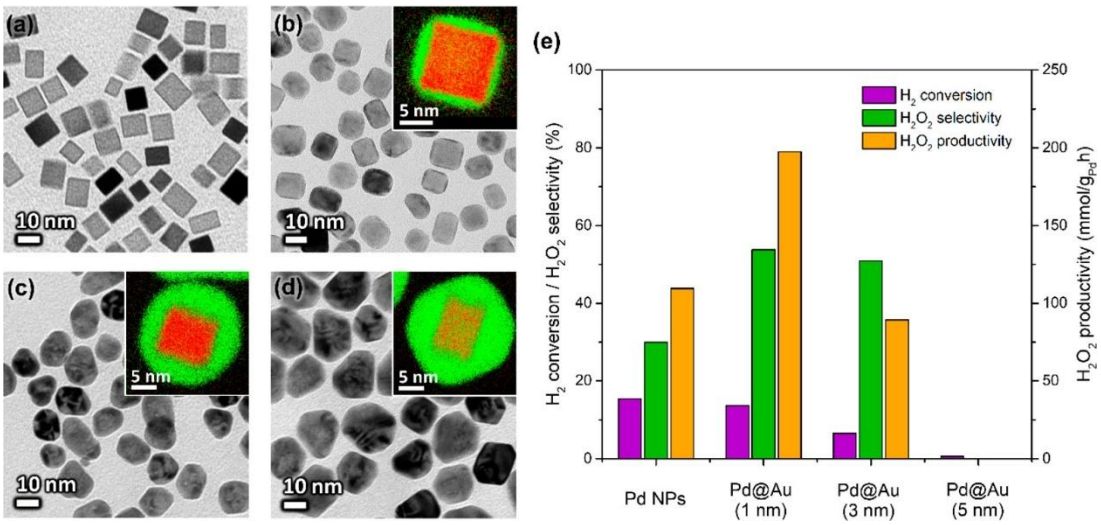

Figure 1.18. Morphologies of Pd and Pd@Au NPs along with their catalytic properties. Bright-field TEM images of (a) Pd, (b) Pd@Au (1 nm), (c) Pd@Au (3 nm), and (d) Pd@Au (5 nm). The insets of (b–d) are high-resolution EDS images (green: Au, red: Pd) recorded from each core–shell nanoparticle. (e) Catalytic properties evaluated from various NPs in terms of H_2 conversion, H_2O_2 selectivity, and H_2O_2 productivity.[112]

The effect of supports on the catalytic performance towards the direct H_2O_2 synthesis of the AuPd catalysts has been studied. Hutchings and co-workers systematically studied various supports, including Al_2O_3 supports,[103,113] TiO_2,[114] Fe_2O_3,[115] SiO_2, carbon,[116] MgO,[80] and linked performance to the support isoelectric point, with more acidic supports improving selectivity and thus increasing the net H_2O_2 yield by limiting hydrogenation and decomposition.[80,117] By proposing an acid pre-treatment strategy on the supported AuPd catalysts (e.g., on the SiO_2, TiO_2, C), [55,118,119] Edwards et al. reported that acid pretreatment of the carbon support for Au–Pd/C switches off H_2O_2 hydrogenation and decomposition, achieving >95% H_2 selectivity and up to >98% at 2 °C. Based on catalytic testing and STEM-XEDS/XPS results, the switching-

off effect is attributed to a redistribution toward small (2-5 nm) homogeneous AuPd nanoparticles that decorate and passivate support sites responsible for H_2O_2 loss, with no Au–Pd surface segregation, and to Au-induced modification of Pd that suppresses its hydrogenation function.[55]

Optimising the heat treatment process can tune the interfacial chemistry and catalyst stability toward H_2O_2 formation. Zhang et al.[120] examined AuPd–$AuPdO_x$ interfaces and showed that, for 3 wt% AuPd/TiO_2, pretreatment in H_2 at 575 K delivered the highest performance, with H_2O_2 productivity of 3116.4 $mmol_{H2O2}$ gPd^{-1} h^{-1} and selectivity of 87.7%. Raising the reduction temperature from 474 K to 673 K increased Au–Pd particle sizes from 2.8 nm to 4.2 nm, which exposed more Pd^0 sites and accelerated undesired hydrogenation. At higher temperatures, surface Pd and Au aggregated, eroding dispersion and depressing activity. The productivity fell below that of untreated catalysts when the treatment temperature was as high as 673 K. Pd–Au/TiO_2 also showed lower Au binding energies than pure Au, consistent with quantum size effects that shift the Au d-band toward the Fermi level and with electron transfer from Au^0 to Pd^0 and to TiO_2 (**Figure 1.19**). Early studies by Edwards et al. suggested that 400 °C calcination (in air) is needed to produce reliable and stable 5wt.% AuPd/TiO_2 catalysts as the untreated (>90% Pd loss and >80% Au loss) and low-temperature calcined (200 °C, >11% Au loss) samples faced significant Au and Pd metal loss after the first run of H_2O_2 synthesis, although the untreated sample exhibited much higher H_2O_2 productivity (202 mol_{H2O2} Kg_{Cat}^{-1} h^{-1}).[114] Similar to the acid-pretreated carbon support, experimental results and electron microscopy data showed that 400 °C calcination is required to enhance metal dispersion on the support, and this improved dispersion underpins the stability and reusability of the catalysts. XPS analysis suggested that the calcination process exposed more surface Pd^{2+} species and isolated Pd^0 sites that are mainly responsible for the subsequent H_2O_2 hydrogenation.[121]

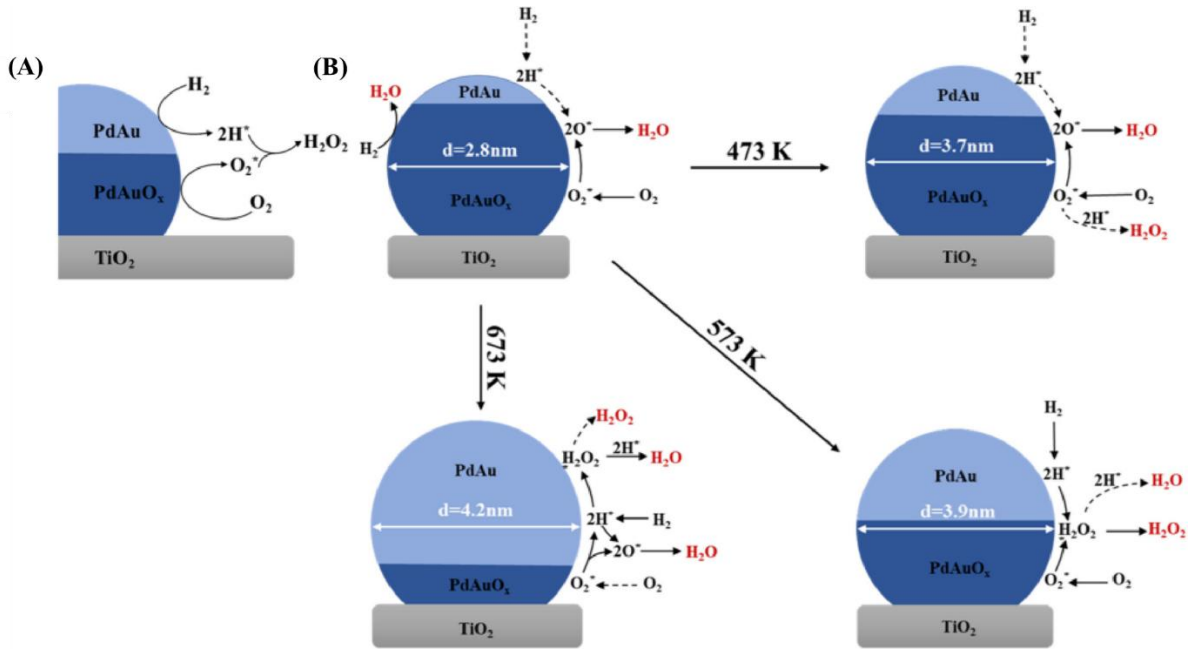

Figure 1.19. (A) The proposed reaction mechanism of H_2O_2 synthesis on $Pd_{2.0}Au_{1.0}/TiO_2$ catalysts. (B) The possible change of the structural model after reduction treatment.[120]

1.5.3 Other bimetallic Pd-based catalysts in H_2O_2 synthesis

Pd and Au alloy extremely well to form bimetallic Au-Pd catalysts for the direct synthesis of H_2O_2, exhibiting higher H_2O_2 productivity and selectivity compared to the monometallic Pd analogues under identical reaction conditions. Apart from adding Au into Pd catalysts, other noble metals, such as silver (Ag),[122–124] Platinum (Pt),[125,126] Ruthenium (Ru),[127] Rhodium (Rh)[128] and Iridium (Ir),[129] and some base metals and even non-metal elements have been attempted to be incorporated with Pd to improve the catalytic performance of the direct route for H_2O_2 production.

Gu et al.[122] synthesised active carbon (AC) supported bimetallic Pd-Ag catalysts and the optimal PdAg-40/AC catalyst achieved the highest H_2O_2 productivity of 7022 mol kg_{Pd}^{-1} h^{-1} among a series of Pd-Ag catalysts (PdAg-60/AC, PdAg-40/AC, PdAg-20/AC, PdAg-10/AC, where PdAg-10/AC contained the highest Ag loading). However, excessive Ag loading led to a decrease in H_2 conversion, resulting in a higher H_2O_2 selectivity but lower H_2O_2 productivity, which might be due to the blockage of Pd active sites by Ag, resulting in a lower reactant adsorption rate. Moreover, the addition of Ag decreased the number of contiguous Pd ensembles but increased monomeric Pd sites, preventing unwanted H_2O formation. The drop in H_2 conversion was also observed by Khan et al.,[123] when testing Pd-Ag/TiO_2 catalysts, the

blockage of Pd active sites by Ag might have happened and hindered reactant adsorption. Further XPS analysis and theoretical calculation on Pd-Ag nanoalloys during the direct H_2O_2 synthesis were conducted by Zhang et al.,[124] revealing that the introduction of Ag formed PdAg (100) active sites, where abundant Pd^0 sites were generated due to the electron transfer between Pd and Ag. DFT calculations revealed that PdAg (100) local squared lattice stabilised O_2 but separated H_2. The spontaneous charge transfer for both H and O_2 over PdAg(100) was much more energetic and favourable, leading to a rapid combination of 2 H^+ and O_2^{2-} by Coulombic attraction to finally form H_2O_2. With an optimal Ag loading, 5wt% PdAg-M NPs /TiO_2 (Ag:Pd=1.35) exhibited higher H_2O_2 productivity (80.4 mol kg_{cat}^{-1} h^{-1} vs 66.2 mol kg_{cat}^{-1} h^{-1}) and selectivity (82.1% vs 31.3%) than that of the 5wt% Pd/TiO_2, but showed higher H_2 conversion (24.2% vs 17.7%) compared to the excessive Ag loaded $PdAg_{1.5}$-M NPs /TiO_2 (Ag:Pd=1.48). The trend was consistent with previous research on Pd-Ag catalysts, which might also be due to the blockage of Pd active sites.

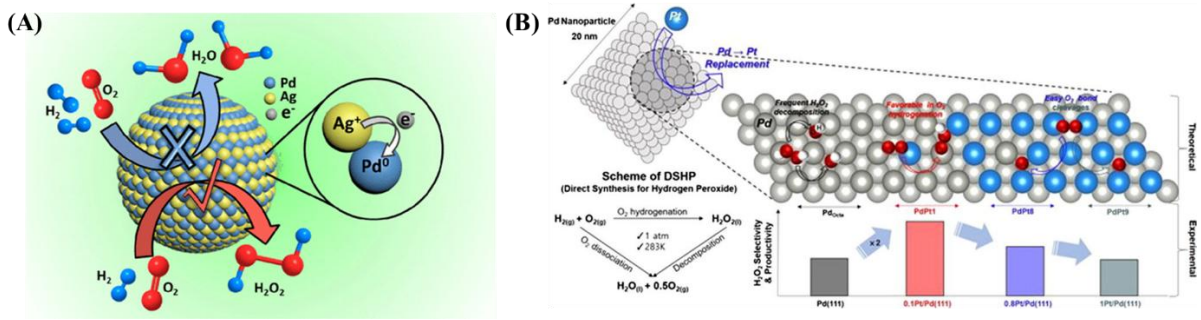

Figure 1.20. Reaction mechanism of PdAg and PdPt catalysts towards the direct H_2O_2 synthesis.[122,125]

The role of Pt atoms on Pd(1 1 1) facets among a series of octahedral monometallic Pd and bimetallic PdPt nanoparticles towards the direct H_2O_2 synthesis has been studied by Quon and co-workers (Figure 1.6.1 A).[125] 0.1Pt/Pd(111) exhibited far more effective H_2O_2 productivity (337.86 mmol·g_{metal}^{-1} h^{-1} vs 150.63 mmol·g_{metal}^{-1} h^{-1}) and selectivity (69.97% vs 37.17%) than those of Pd(111) analogous. Excessive Pt loading significantly decreased the H_2O_2 productivity (down to 184.12 mmol·g_{metal}^{-1} h^{-1}) and selectivity (down to 31.68%) but increased the H_2O_2 decomposition rate (up to 1973.66 mmol·g_{metal}^{-1} h^{-1}). As explained by DFT calculations, the lowest activation barrier for O_2 hydrogenation (E_a = 1.02 eV) and the highest one for H_2O_2 dissociation (E_a = 1.27 eV) were found over the 0.1Pt/Pd(111) surface, indicating that the minor substitution of Pt suppressed H_2O formation, thus enhancing H_2O_2 productivity and selectivity. Bader charge analysis also revealed that the outer Pt attracted electrons from the inner bulk Pd due to the different electronegativity, resulting in more electron-deficient Pd

species favourable for H_2O_2 synthesis. However, the amount of electron-deficient Pd species on the Pd(111) terrace could not be fully exposed due to the coverage by the randomly deposited Pt. To maintain the Pd–Pt alloy while maximising Pt domains, Han et al.[126] synthesised surface morphology controlled Pd@Pt core–shell nano-cubes with high-index faceted Pt on the corners and edges, while the Pd–Pt alloy on the terrace (Figure 1.6.1 B). H_2-temperature-programmed reduction (TPR) results demonstrated that the $Pd@Pt_7$ exhibited the highest H_2 absorption capacity and the most stable Pd-H formation. But $Pd@Pt_{20}$ formed less stable hydrides due to H_2 diffusion limitations through the encapsulating Pt shell. Experimental results further gave evidence that the increased Pt loading resulted in higher H_2 conversion and the highest rate was found over $Pd@Pt_7$ (19%), compared to the Pd cube (12%), due to the multifaceted properties of the Pd@Pt bimetal system in which the high-index Pt sites and high concentration of interstitial H atoms in Pd-H were favourable for fast H_2 dissociation. But excessive Pt loading also led to a drop in H_2 conversion, where $Pd@Pt_{20}$, with the surface fully covered by Pt, only showed around 8%. Indeed, the Pt/Pd ratio is crucial for Pd-Pt bimetallic catalyst to obtain high catalytic performance towards the direct H_2O_2 synthesis by regulating the surface morphology and composition.

Choudhary et al.[128] investigated the effect of Ru and Rh on the Pd particles by preparing Pd-Ru/ZrO_2 and Pd-Rh/ZrO_2 catalysts with various Ru/Pd (0-0.15) and Rh/Pd (0-0.15) ratios and found that the presence of Ru and Rh unfortunately hindered the H_2O_2 yield in both systems. In addition, Deguchi and co-workers[129] proposed that adding small amounts (0.5 atom%) of Ir to Pd-PVP colloid doubled the H_2O_2 productivity compared to the unmodified Pd-PVP catalyst in the presence of H_2SO_4 and NaBr. Kinetic analyses and DFT calculations revealed that Ir increased the rate of H_2-O_2 reaction, likely due to its high H_2 activating abilities, as the energy barriers for H_2 activation on Ir were lower than those on Pd. Interestingly, the movement of Ir atoms during the reaction was observed. Atomically dispersed Ir on the Pd surface rearranges to more stable positions over time, accounting for changes in reaction rate and selectivity during reactions.

Cost efficiency matters to the catalyst design and further application. Some base metal elements have also been used to synthesise bimetallic Pd-based catalysts to reduce the cost while maintaining high catalytic efficiency. Tran et al.[130] reported that bimetallic PdFe catalysts supported on optimal carbon material exhibited higher H_2O_2 selectivity (PdFe/GR-H: 68.8%) than the Pd analogous (Pd/GR-H: ~50%) due to the smaller Pd NPs size and higher Pd^{2+}/Pd^0 ratio. Wang et al.[131] demonstrated that the addition of Zn increased the isolated Pd^0-rich sites,

which are more favourable for H_2O_2 formation, leading to enhanced H_2O_2 productivity (25431 mol kg_{Pd}^{-1} h^{-1}) and selectivity (78.5%) on the 1Pd5Zn catalyst, compared to the Pd-only analogous (8533 mol kg_{Pd}^{-1} h^{-1}; 64.3%) and PdZn catalysts with lower Zn loading (from 19000 mol kg_{Pd}^{-1} h^{-1} to 23125 mol kg_{Pd}^{-1} h^{-1}; 76.6% to 77.1%).

PdPb Nano-rings (NRs) supported on TiO_2 with varying Pd:Pb ratios were synthesized by Cao et al.,[132] and the optimal Pd_6Pb NRs/TiO_2 exhibited the highest H_2O_2 productivity (170.1 mol kg_{cat}^{-1} h^{-1}), compared to the Pd NRs/TiO_2 (60 mol kg_{cat}^{-1} h^{-1}) and more Pb-loaded Pd_6Pb NRs/TiO_2 (~75 mol kg_{cat}^{-1} h^{-1}). H_2O_2 hydrogenation rates decreased from 421.5 mol kg_{cat}^{-1} h^{-1}on Pd NRs/TiO_2 to 85.2 mol kg_{cat}^{-1} h^{-1}on Pd_4Pb NRs/TiO_2 with the rise in Pb loading. Atomic resolution (AC)-STEM and X-ray adsorption spectroscopy (XAS) analysis suggested that the low-coordinated Pd atoms (edge) were replaced by the introduced Pb, leading to a decreased coordination number of Pd/Pb. DFT calculations further proposed a lower formation energy of *OOH (-0.16eV vs 0.052eV) but a higher formation energy of *O (-0.90 eV vs-1.18eV) on the Pd(111)-PbO(edge), comparted to the Pd(111), indicating that the formation of *OOH was more favourable on Pd(111)-PbO(edge) where the O-O cleavage was suppressed, resulting in a low H_2O_2 degradation rate, which was consistent with experimental results. Research on the acid-pretreated TiO_2 (s-TiO_2) supported shape-controlled Pd_3Pb nanocrystals (NCs) (cubic, cuboctahedra, spherical, and flowerlike aggregates) was carried out by Naina and co-workers.[133] Higher H_2O_2 productivity and selectivity were observed over Pd_3Pb NCs (except spherical nanocrystal), compared to monometallic Pd/s-TiO_2, in which the highest catalytic performance was showed on cubic NCs (7339 mol_{H2O2} kg_{Pd}^{-1} h^{-1}; 53%), which might be due to 1) the electron modification of Pd by the introduction of Pb; 2) the higher energy barrier for the adsorbed O_2 dissociation on cubic Pd_3Pb (200) than that on the Pd (111); 3) less Pd ensembles on the cubic Pd_3Pb NCs, which are responsible for the O-O cleavage and H_2O formation.

Hutchings's group reported that by implementing an appropriate heat treatment cycle (Oxidative-Reductive-Oxidative heat treatment), the result bimetallic PdSn catalysts achieved>95% H_2O_2 selectivity by encapsulating small Pd-rich particles while leaving larger PdSn alloys exposed (**Figure 1.21**).[134] The subsequent study within the group further examined one of the possibilities of replacing Au with Sn to synthesize the low-cost and sustainable bimetallic Pd-based catalysts for highly efficient H_2O_2 production, although a relatively large quantities of the secondary metal were required (0.25%Pd-2.25%Sn/TiO_2, H_2O_2 productivity: 92 mol_{H2O2} Kg_{Cat}^{-1} h^{-1}; H_2O_2 selectivity: 94%; H_2 conversion: 35%;) to rival the activity

observed over optimal Au-containing formulations (0.5%Pd-0.25%Au/TiO_2, H_2O_2 productivity: 90 mol_{H2O2} Kg_{Cat}^{-1} h^{-1}; H_2O_2 selectivity: 53%; H_2 conversion: 59%;)) under the identical reaction conditions.[135] Li et al.[136] also confirmed the excellent catalytic performance from the combination of Pd and Sn. The Pd oxide layered PdSn nanowires (PdL/PdSn-NW) exhibited superior H_2O_2 productivity at 528 mol Kg_{Cat}^{-1} h^{-1} and H_2O_2 selectivity over 95%, which could be attributed to the less O-O bond dissociation and weaker H_2O_2 adsorption on the Pd oxide layers.

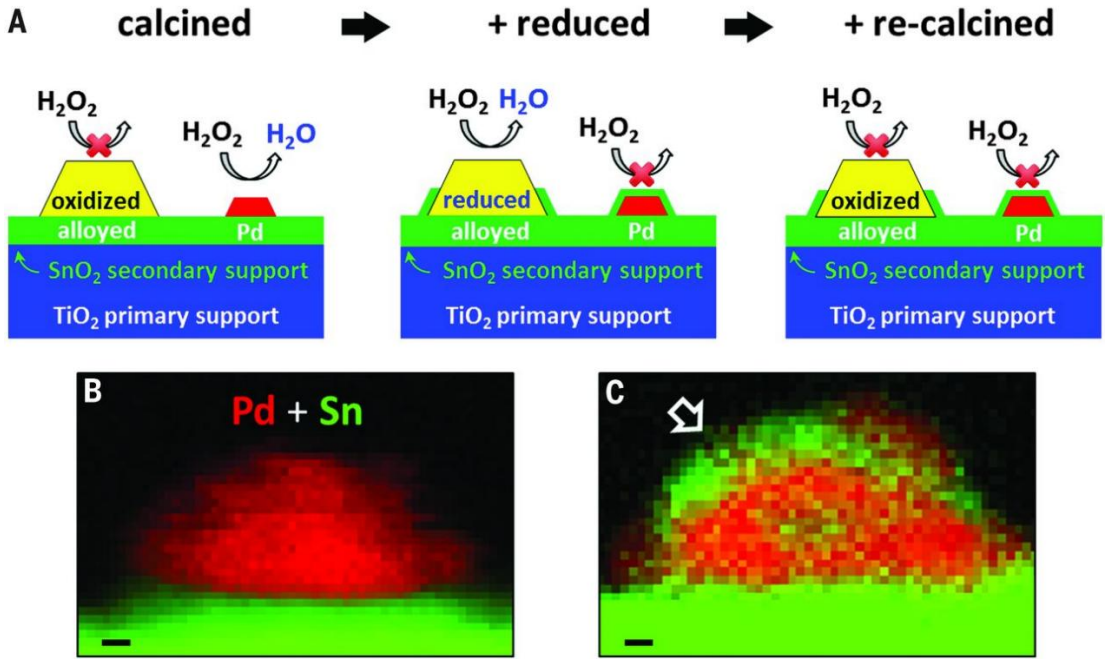

Figure 1.21. (A) Proposed mechanism for switching off H_2O_2 hydrogenation by small Pd-rich NPs through a strong metal-support interaction (SMSI). (B and C) STEM-EELS mapping of a 5 wt % Pd/SnO_2 model catalyst at the oxidized (B) and O-R-O (C) stages, showing partial encapsulation of the Pd NP (red) by SnOx (green) after the O-R-O heat treatment cycle.[134]

Doping some metalloid elements into Pd-based catalysts also affected H_2O_2 productivity and selectivity. Liu et al.[137] reported the presence of Boron (B) enhanced strong metal−support interaction (SMSI) between Pd and TiO_2, which led to the changes in Pd^0/Pd^{2+} ratio and Pd particle surface configuration. An appropriate loading of B at the Pd-TiO_2 interface increased Pd^{2+} sites, which are responsible for non-dissociated O-O activation, remarkably improved the H_2O_2 productivity and selectivity from 63.4% and 2.99 mol_{H2O2} g_{Pd}^{-1} h^{-1} to 80.1% and 3.65 mol_{H2O2} g_{Pd}^{-1} h^{-1} at 10°C and 0.1MPa, respectively. Ding et al.[138] found that the SbO_x layer partially encapsulated the Pd particle surface, suppressing the activation of H_2 and subsequent hydrogenation of H_2O_2, while also isolating contiguous Pd sites and increasing the number of

monomeric Pd sites that are favourable for H_2O_2 production. In addition, a remarkable enhancement in H_2O_2 productivity was observed over supported tellurium (Te)-modified Pd-Te/Al_2O_3 catalyst (2824 mmol $h^{-1}g_{Pd}^{-1}$), compared to the Pd analogous (2017 mmol $h^{-1}g_{Pd}^{-1}$). Tian et al.[139] further explained that the Te atoms located at the low-coordinated Pd (211) step sites blocked the unfavourable H_2O-forming reaction, thus improving the H_2O_2 production.

1.6 Synthesising H_2O_2 using trimetallic AuPd-based catalysts

Bimetallic AuPd formulation has been extensively studied over the years due to the synergistic effect between Au and Pd, promoting H_2O_2 production. However, using a third metal cooperation with AuPd catalyst to form a trimetallic formation is not yet well-studied. Despite this, it has been found that the addition of some noble (Ru, Pt, etc)[127,140] and even base metals (Cu, Zn, etc)[141,142] into AuPd catalyst enhanced the catalytic ability for efficient H_2O_2 production.

The addition of Ru into AuPd catalysts was studied by Ntainjua et al.[127] and the enhancement in H_2O_2 productivity by adding Ru to TiO_2-supported Au-based, Pd-based, and Au-Pd-based catalysts has been found. Synergistic effects were found between Au and Ru, where the 4.25 wt.%Ru-0.75wt.%Au/TiO_2 catalyst exhibited the highest H_2O_2 productivity among a series of 5wt.% AuRu/TiO_2 catalysts (69 mol_{H2O2} kg_{cat}^{-1} h^{-1}). With the presence of Pd, only a small amount of Ru was required to obtain the best catalytic performance, where 4.5wt.%Pd-0.5wt.%Ru/TiO_2 (143 mol_{H2O2} kg_{cat}^{-1} h^{-1}) and 4.5wt.%Pd-0.45wt.%Ru-0.05wt.%Au/TiO_2 (153 mol_{H2O2} kg_{cat}^{-1} h^{-1}) showed the highest H_2O_2 productivity in Pd-based and Au-Pd-based catalysts, respectively. The excellent cooperation between Ru and Au-Pd, resulting in enhanced H_2O_2 productivity, was consistent with the further catalyst design strategy proposed by Xu et al.,[143] where Ru has been nominated as one of the potential candidates for preparing a highly reactive trimetallic Au-Pd-based catalyst.

Meanwhile, Edwards et al.[140] further studied the effect of Pt on the Au-Pd for both H_2O_2 synthesis and decomposition by synthesizing CeO_2-supported trimetallic Au-Pd-Pt catalysts with total metal loadings of 5 wt% (**Figure 1.22 (A-B)**), and a small amount of Pt on the bimetallic AuPd/CeO_2 catalysts encouraged H_2O_2 productivity (up to 170 mol_{H2O2} Kg_{cat}^{-1} h^{-1}) and remarkably suppressed H_2O_2 hydrogenation (down to 11 mol_{H2O2} Kg_{cat}^{-1} h^{-1}). However, the excessive loading of noble metals might not be ideal to maintain a low-cost and sustainable approach for H_2O_2 synthesis. Gong et al.[144] developed trimetallic AuPdPt catalysts by scaling

down the metal loading with the total metal loading at 1wt.%, and the optimal $1\%Au_1Pd_1Pt_{0.01}/TiO_2$ catalysts exhibited the highest H_2O_2 productivity at 112 mol_{H2O2} Kg_{Cat}^{-1} h^{-1}, outperforming the bimetallic $1\%Au_1Pd_1/TiO_2$ (80 mol_{H2O2} Kg_{Cat}^{-1} h^{-1}) and Pt-rich trimetallic $1\%Au_1Pd_1Pt_1/TiO_2$ (30 mol_{H2O2} Kg_{Cat}^{-1} h^{-1}) catalysts.

These Ru and Pt-doped trimetallic AuPd catalysts exhibited excellent catalytic performance towards the direct H_2O_2 synthesis, as further evidenced by the DFT calculations and Sabatier analysis. Xu and co-workers proposed a strategy for synthesizing highly effective tri-metallic Au-Pd-based nanoparticles for the direct synthesis of H_2O_2.[143] Based on the catalyst structure evidence from previous studies, the core-shell models for the Au-Pd-based catalysts were introduced. **Figure 1.22 (C)** illustrates that the descriptor α ($\alpha = E_M/E_{Pd}$), based on the electronegativity of the dopant element (E_M) and Pd (E_{Pd}), is located within a specific range on Au-Pd-based catalysts (α ≈ 0.9-1.1), showing a higher *As* value for H_2O_2 synthesis and lower *As* for decomposition/hydrogenation. Through systematic research on the periodic table, several base metals, such as W, Pb, Mo, Pt/Rh, and Ru/Ir, would potentially cooperate well with Au-Pd particles for the direct synthesis of H_2O_2. Considering the reducibility of these elements, which might behave similarly to Sn after calcination heat treatment,[134] oxide layers might be potentially formed to encapsulate small Pd-rich particles, further improving the H_2O_2 selectivity and productivity.

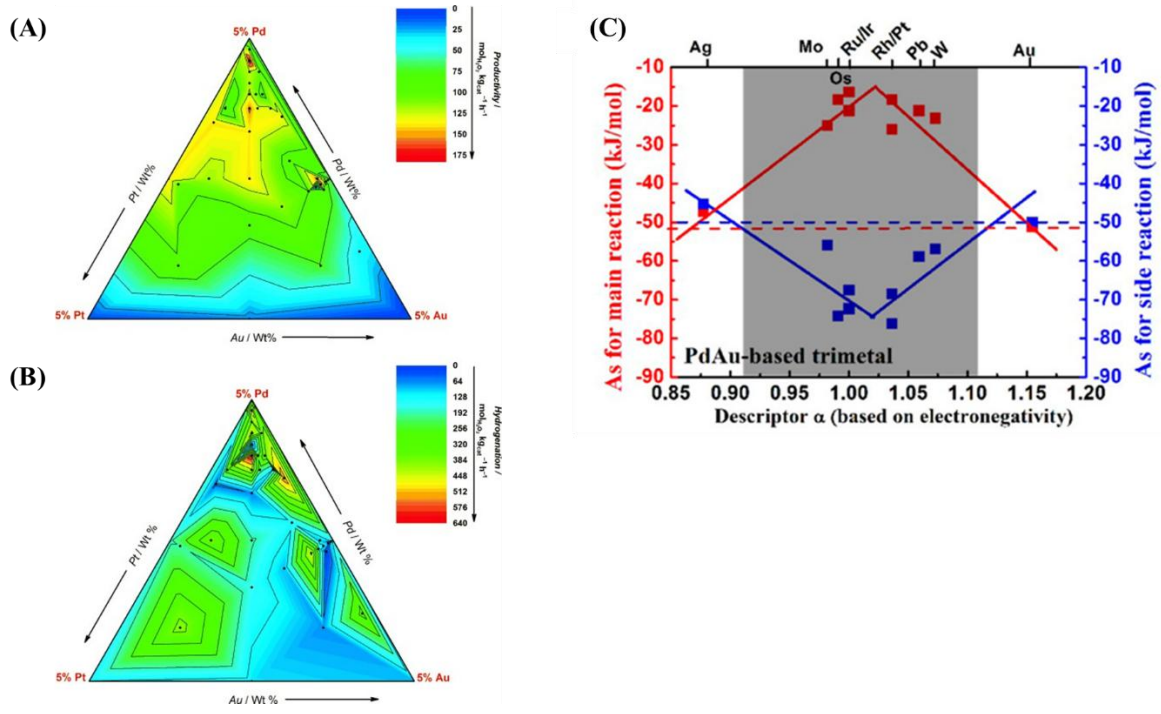

Figure 1.22. Rates of H_2O_2 synthesis and hydrogenation/decomposition for CeO_2 -supported 5 wt % Au/Pd/Pt catalysts presented as a contour diagram. (A) Productivity and (B) hydrogenation/decomposition.[140] (C) As values for the main and side reactions (Sabatier analysis) as a function of descriptor α based on the electronegativity of the doped element for PdAu-base ternary alloy clusters. The red and blue dotted lines represent the As values for the main and side reactions of $Au_{25}Pd_{30}$, respectively.[143]

Following up on the above prediction, Zhang et al.[145] conducted an investigation on the effect of electron modification of W on Pd catalysts. The synthesized Pd-W/Al_2O_3 with different W loading rates ranging from 1wt% (Pd-1wt%W/Al_2O_3) to 5wt% (Pd-5wt%W/Al_2O_3) were tested in H_2O/CH_3OH reaction medium under 2 °C and 4 MPa for the direct H_2O_2 synthesis. The highest H_2O_2 productivity (125.3 mol_{H2O2} kg_{cat}^{-1} h^{-1}) and selectivity (~60%) were observed over Pd-1wt%W/Al_2O_3, which was higher than that of Pd/Al_2O_3 (~69 mol_{H2O2} kg_{cat}^{-1} h^{-1} ;~35%) and Pd-5wt%W/ Al_2O_3 (93.9 mol_{H2O2} kg_{cat}^{-1} h^{-1}; ~20%), together with XPS results, indicating that the addition of W formed as WO_x on the Pd particle surface, regulated Pd^0/Pd^{2+} ratio. A small amount of optimization of the Pd^0/Pd^{2+} ratio to promote H_2O_2 productivity and hinder the subsequent H_2O_2 hydrogenation/decomposition simultaneously. Whereas the excessive W loading turned up more Pd^0, and also impeded the O_2 adsorption on the Pd surface, leading to a decrease in H_2O_2 synthesis. Based on the remarkable enhancement by the introduction of W onto Pd catalysts, Zhang et al. again introduced W to modify Au-Pd catalysts and found that the strong interaction between W and Au-Pd on TiO_2 was the key to the high catalytic ability towards the direct H_2O_2 synthesis.[146] Best performance was found when utilizing PdAu/3WO_3–TiO_2 catalyst, which introduced PdAu onto the W pre-loaded TiO_2 support, with H_2O_2 productivity and selectivity as high as 662.6 mol_{H2O2} kg_{cat}^{-1} h^{-1} and 85.5%, respectively, superior to the PdAu/TiO_2 catalyst (450.2 mol_{H2O2} kg_{cat}^{-1} h^{-1} and 73.9%). However, excessive W loading (e.g. PdAu/5WO_3–TiO_2) also led to a drop in both H_2O_2 productivity and selectivity. These indicated that a suitable amount of W partially wraps the PdAu particles, promoting the formation of Pd^{2+} species and improving the selectivity of H_2O_2. However, PdAu particles could be completely enclosed when W was loaded in excessive amounts, preventing the contact between PdAu active sites and reactants, and inhibiting the production of H_2O_2.

However, in addition to the highlighted metals from previous studies, other base metals also show catalytic potential in H_2O_2 synthesis when cooperating with AuPd catalysts. Barnes et al.[142] incorporated some base metals onto the TiO_2-supported AuPd nanoparticles to synthesise trimetallic 1wt%AuPd-M/TiO_2 (M=Cu, Ni, and Zn). Similar to the proposed relationship between Pt and AuPd,[140] the addition of a low concentration (0.025wt%) of these metals also

enhanced the H_2O_2 productivities (up to 107 mol_{H2O2} Kg_{Cat}^{-1} h^{-1}) compared to AuPd analogous (61 mol_{H2O2} Kg_{Cat}^{-1} h^{-1}) and metal-rich (>0.1 wt.%) trimetallic catalysts (<60 mol_{H2O2} Kg_{Cat}^{-1} h^{-1}). Barnes et al.[141] further applied this strategy by introducing Cu into ZSM-5 (SiO_2:Al_2O_3 = 30:1) supported AuPd catalyst, and a similar 'Volcano' trend was observed on H_2O_2 productivity with increased Cu loading, where the optimal trimetallic AuPdCu exhibited the H_2O_2 productivity at 115 $mol_{H2O2}kg_{cat}^{-1}h^{-1}$, 1.7 times higher than that of the bimetallic formulation (69 $mol_{H2O2}kg_{cat}^{-1}h^{-1}$). CO-DRIFTS spectra and XPS analysis revealed the changes in surface composition and Pd oxidation state by the introduction of Cu, resulting in the enhancement of H_2O_2 productivity. Similarly, Fu et al.[147] reported the Au_3Cu@AuPd core–shell catalysts (the actual Cu loading: ~0.49 wt.%) exhibited 94.8% H_2O_2 selectivity and 7600 $mmol_{H2O2}$ g_{Pd}^{-1} h^{-1} productivity by regulating the geometric effect of the surface Pd–Au alloy with an ordered Au_3Cu core, and the highly dispersed Pd atoms encircled by Au on the catalyst surface selectively activate O_2 via a non-dissociative pathway to form the key *OOH intermediate. In keeping with the earlier study conducted by Rahim and Hutchings[148] demonstrated that the introduction of large amount of Cu (>1 wt.%) inhibited the catalytic ability towards H_2O_2 synthesis on the TiO_2-supported AuPd catalysts under identical reaction conditions, where the bimetallic 2.5%Au-2.5%Pd/TiO_2 (83 $mol_{H2O2}Kg_{Cat}^{-1}$ h^{-1}) is far active than the 2.5% Au-2.5% Pd-2.5% Cu/TiO_2 (11 mol_{H2O2} Kg_{Cat}^{-1} h^{-1}) and 2.5%Au-2.5%Pd-1%Cu/TiO_2 (10 mol_{H2O2} Kg_{Cat}^{-1} h^{-1}), with previous DFT studies indicating that the formation of the intermediate hydroperoxyl species (*OOH) and subsequently H_2O_2 is thermodynamically unfavoured over Cu-containing precious metal surfaces[149]. Indeed, combining both experimental results and theoretical studies, the amount of the third meal introduced into AuPd catalysts is crucial for promoting catalytic performance towards H_2O_2 synthesis.

1.7 Utilising H_2O_2 in water treatment

1.7.1 The Challenge of Water Pollution

Water pollution is an increasingly critical global issue, exacerbated by rapid industrialisation, population growth, and urban expansion.[150] The continuous discharge of pollutants, ranging from suspended solids and heavy metals to recalcitrant organics and emerging contaminants, has led to the deterioration of freshwater resources.[151] Conventional pollutants, such as nutrients (e.g., nitrates and phosphates), and newer classes of contaminants, including

pharmaceuticals, personal care products, microplastics, and endocrine-disrupting compounds, have been detected with increasing frequency in surface and groundwater systems. These contaminants can exhibit toxicity, persistence, and bioaccumulate potential, threatening aquatic ecosystems and posing significant risks to public health through drinking water supplies and food chains.[150]

1.7.2 Overview of Various Techniques for Water Treatment

Traditional water and wastewater treatment systems, such as those employed in municipal and industrial plants, are typically designed to remove bulk contaminants through a combination of physical, chemical, and biological processes. These include screening, coagulation–flocculation, sedimentation, sand or membrane filtration, and disinfection (usually via chlorination or UV irradiation).[152,153] Additionally, biological treatments such as activated sludge processes and trickling filters are widely used for the removal of biodegradable organic matter and nutrients. However, these conventional systems often fall short when it comes to removing low-concentration, non-biodegradable, or toxic organic micropollutants. Many such contaminants are either poorly adsorbed onto sludge particles or remain largely unchanged due to their resistance to biological degradation and chemical oxidation under standard treatment conditions.[154]

As a result, Advanced Oxidation Processes (AOPs) have gained increasing attention as complementary or tertiary treatment strategies capable of degrading a wide spectrum of persistent and emerging pollutants. AOPs are defined by their capacity to generate reactive oxygen species (ROS), particularly hydroxyl radicals (·OH), which rank the second strongest oxidising agent after fluorine with a redox potential of approximately 2.8 E°/V vs SHE.[155] These radicals can rapidly attack and break down complex organic structures, including aromatic rings and conjugated systems, into smaller intermediates, eventually leading to complete mineralisation to CO_2 and water. The versatility and efficiency of AOPs have led to their application in the treatment of hospital effluents, industrial wastewater, landfill leachates, and even in potable reuse schemes.

A variety of AOPs have been developed and investigated for water and wastewater treatment applications. These include ozone-based systems (e.g., O_3, O_3/H_2O_2), UV-based systems (e.g., UV/H_2O_2, UV/O_3), photocatalysis (e.g., TiO_2/UV), electrochemical oxidation, and persulfate-based oxidation.[156,157] Each of these approaches offers distinct advantages and limitations

depending on the water matrix, target pollutants, operating conditions, and economic feasibility. For instance, UV/H_2O_2 processes are effective for transparent waters with low turbidity, while ozonation is particularly suitable for disinfecting and oxidising taste- and odour-causing compounds.[156,157] Despite their effectiveness, many AOPs require high energy input, precise control of reaction conditions, or specialised equipment, which can limit their large-scale adoption.

Among these techniques, Fenton-based processes have garnered particular attention due to their operational simplicity, low cost, and strong oxidative power. The classical Fenton reaction, which involves the catalytic decomposition of H_2O_2 in the presence of Fe^{2+}, is capable of generating ·OH under ambient conditions and has been applied to the treatment of various industrial wastewaters. However, while the core chemistry is well understood, the practical application of the conventional Fenton process can be constrained by issues such as sludge generation, narrow pH requirements, and reagent handling.[158]

As such, Fenton and Fenton-like systems are often further modified or integrated with other catalytic materials or process intensification strategies to enhance their efficiency, selectivity, and applicability across a wider pH range. These advancements, such as ex-situ Fenton systems and in situ Fenton systems, will be explored in subsequent sections.

1.7.3 Ex-situ Fenton Reaction and Its Application in Water Treatment

1.7.3.1 Homogeneous Fenton reaction

The first Fenton reaction was discovered and developed by French scientist Henry J. Fenton in 1894, that tartaric acid could be effectively oxidised by Fe^{2+}/H_2O_2 systems at a pH range of 2-3.[159] While the study was not initially aimed at environmental applications, it laid the foundation for a reaction that would later gain widespread relevance in the field of water and wastewater treatment. It was not until the mid-20th Century that the scientific community began to recognise the environmental utility of this reaction, particularly in the oxidative degradation of organic pollutants, when ·OH were identified as the key reactive species responsible for the observed oxidising power.

·OH is among the most potent oxidants in aqueous chemistry, possessing a redox potential of approximately 2.8 V. They are highly non-selective and capable of attacking a wide variety of organic molecules, including aromatic rings, aliphatic chains, and various functional groups.

In the classic Fenton system, these radicals are generated in situ through the catalytic decomposition of H_2O_2 by Fe^{2+} under acidic conditions, as shown in the primary reaction equations (**Eq. 1.29 – 1.33**).[160]

$$Fe^{2+} + H_2O_2 \rightarrow Fe^{3+} + \bullet OH + OH^- \ (k = 63 - 76\ M^{-1}S^{-1}) \quad \textbf{(Eq. 1.29)}$$

$$Fe^{3+} + H_2O_2 \rightarrow Fe^{2+} + HO_2\bullet + H^+ \ (k = 0.001 - 0.01\ M^{-1}S^{-1}) \quad \textbf{(Eq. 1.30)}$$

$$H_2O_2 + \bullet OH \rightarrow H_2O + HO_2\bullet \ (k = 1.7 - 4.5 \times 10^7\ M^{-1}S^{-1}) \quad \textbf{(Eq. 1.31)}$$

$$Fe^{3+} + HO_2\bullet \rightarrow Fe^{2+} + O_2 + H^+ \ (k = 0.33 - 2.10 \times 10^6\ M^{-1}S^{-1}) \quad \textbf{(Eq. 1.32)}$$

$$Fe^{2+} + \bullet OH \rightarrow Fe^{3+} + OH^- \ (k = 2.5 - 5 \times 10^8\ M^{-1}S^{-1}) \quad \textbf{(Eq. 1.33)}$$

This redox process oxidises Fe^{2+} to Fe^{3+} and simultaneously cleaves H_2O_2, producing ·OH and hydroxide ions (OH^-) (**Eq.1.29**). The Fe^{3+} formed can be reduced back to Fe^{2+} through reactions with excess H_2O_2 or other reducing agents, thereby sustaining a catalytic cycle, however with a much lower reaction rate (**Eq.1.30**), thus the reduction of Fe^{3+} is the rate-limiting step. Due to the rate-limiting step (**Eq.1.30**), maintaining a reasonable Fenton efficiency requires large doses of H_2O_2 (30–6000 mmol L^{-1}) and Fe^{2+} (18–410 mmol L^{-1}) to generate sufficient ·OH.[161] The mismatched two-step Fe redox cycle leads to the Fe^{3+} accumulation, Fe sludge formation, and low H_2O_2 utilisation efficiency. Excess H_2O_2 may also accelerate equipment corrosion and increase operating costs.[162] As a result, many optimisation efforts have been proposed to accelerate the Fe redox cycle, for example, by adding co-catalysts, including light irradiation (e.g., Ultraviolet and visible light),[163–165] organic (e.g., organic acids)[165–168] and inorganic (e.g., metal sulphides, Mo, Pd, etc.)[162,169–172] co-catalytic promoters.

Early studies utilised ultraviolet (UV) or visible light (Vis) irradiation to couple with a homogeneous Fenton system, and Fe^{3+} could be constantly converted into Fe^{2+} in the process of photo-assisted reaction. Herrera et al. demonstrated that visible light significantly accelerates the breakdown of the dyes Remazol Brilliant Blue R and Uniblue A using an acidic photo-homogeneous Fenton process. The rapid decolouration was entirely dependent on the presence of light, Fe^{3+}, and H_2O_2, and was most effective at the wavelengths of light the dyes themselves absorbed best. The core mechanism involves the dye and Fe first forming a D-Fe^{3+} complex, and Fe^{2+} would be generated after the photo dissociation reaction of this complex, which then reacts with H_2O_2 to produce ·OH that attacks and destroys the dye. Kinetic analysis showed that the direct breakdown of the dye-iron complex by light is the dominant initiation step, allowing a rapid Fe redox cycle between Fe^{3+} and Fe^{2+} to sustain the reaction.[163]

Subsequently, Ma and co-workers systematically investigated the effect of dyes on the degradation of organic pollutants in a photo Fenton system under visible light irradiation, showing that compared to the dyes (e.g. Malachite green) without quinone/hydroquinone structure, some dyes (e.g. Alizarin Violet 3B (AV)) with this unique structure could achieve the complete mineralization of salicylic acid, sodium benzenesulfonate, benzyl trimethylammonium chloride, and trichloroacetic acid. Investigation into the reaction mechanism suggested that AV acted as a co-catalyst after being irradiated by visible light and promoted the Fe redox cycle to facilitate the generation of Fe^{2+}, thus the classic Fenton reaction occurred to produce ·OH for organic pollutant degradation.[164]

The synergistic effect between light and some types of dyes in previous literature has been reported as a promoter for the efficient Fe^{3+} reduction and further promotes the catalytic Fenton reaction. However, the coupling effect of visible light and the unique structure (e.g., quinone/hydroquinone) remained unclear, and the reaction mechanism of how quinone/hydroquinone interacts with homogeneous Fe species needed further investigation. Following the previous study,[164] Ma et al.[165] discovered that the visible light (λ = 450 nm) and hydroquinone are essential in the Fe^{3+}/H_2O_2 system for the mineralisation of Malachite green. Similar observations later from Ma and co-workers,[173] confirmed that the involvement of hydroquinone in the Fe redox cycle promoted the Fe reduction (**Figure 1.23(A)**) and probed the existence of semi-quinone radicals generated during the Fenton reaction (**Figure 1.23 (B)**), which might be involved in the Fenton reaction process.

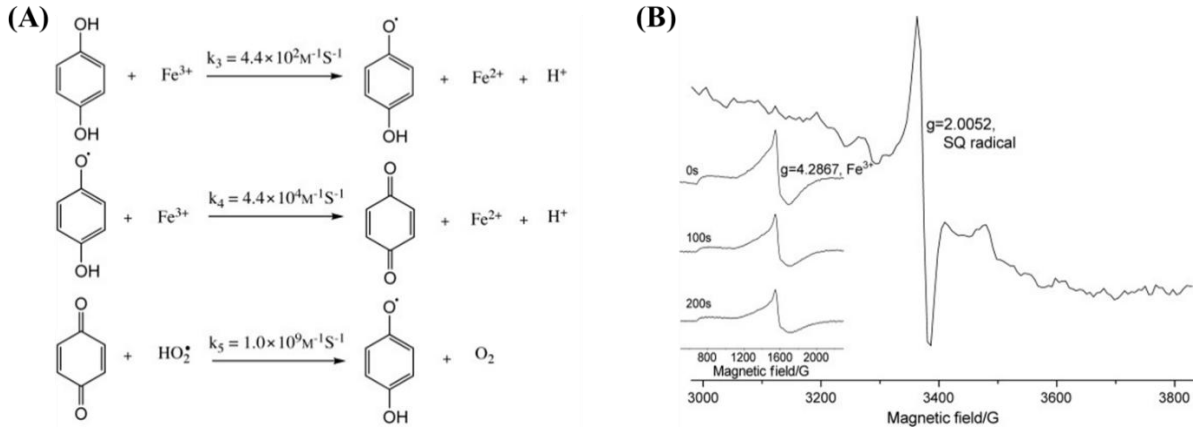

Figure 1.23. (A) The proposed reaction mechanism between hydroquinone and homogeneous Fe species. (B) EPR spectra (77 K) of the generated semi-quinone-like (SQ) radical from 4×10^{-5} M Fe^{3+} (50 mL) and 1 mg AVR under visible-light irradiation. Inset: the spectra-line-intensity change of Fe^{3+} with irradiation time.[173]

Without introducing an external energy source (eg., UV or Vis), adding some organic matter into the homogeneous Fenton system (Fe^{3+}/H_2O_2) could also form a co-catalytic environment for the pollutant degradation. For example, the ascorbic acid cycle (ascorbic acid ↔ dehydroascorbic acid) (**Figure 1.24 (A)**)[168] and cysteine cycle (cysteine ↔ cystine) (**Figure 1.24 (B)**)[174] coupled with Fe redox cycle (Fe^{3+} ↔ Fe^{2+}), promotively achieved 100% alachlor degradation and 96% Rhodamine B degradation, respectively, via the electron transfer between these two cycles (ascorbic acid vs Fe or cysteine vs Fe), thus facilitate rapid Fe^{3+}/Fe^{2+} cycle and enhancing ·OH generation for organic degradation. Meanwhile, introducing phenolic acids, like protocatechuic acid (PCA) **(Figure 1.24 (C))**[167] and gallic acid (GC) **(Figure 1.24 (D))**[166] into the homogeneous Fenton system have also been found the promotive effect in the oxidative degradation of alachlor (98% degradation with 43% TOC removal rate) and methyl orange (95% with 27& TOC removal rate), respectively, and this enhancement highly likely associated with the coupling effect (Fe complex formation) between quinone cycle and Fe redox cycle. However, not all phenolic acids have such a promotive effect. A previous study suggested that the coupling effect would tend to occur with those containing the catechol or galloyl moiety.[175]

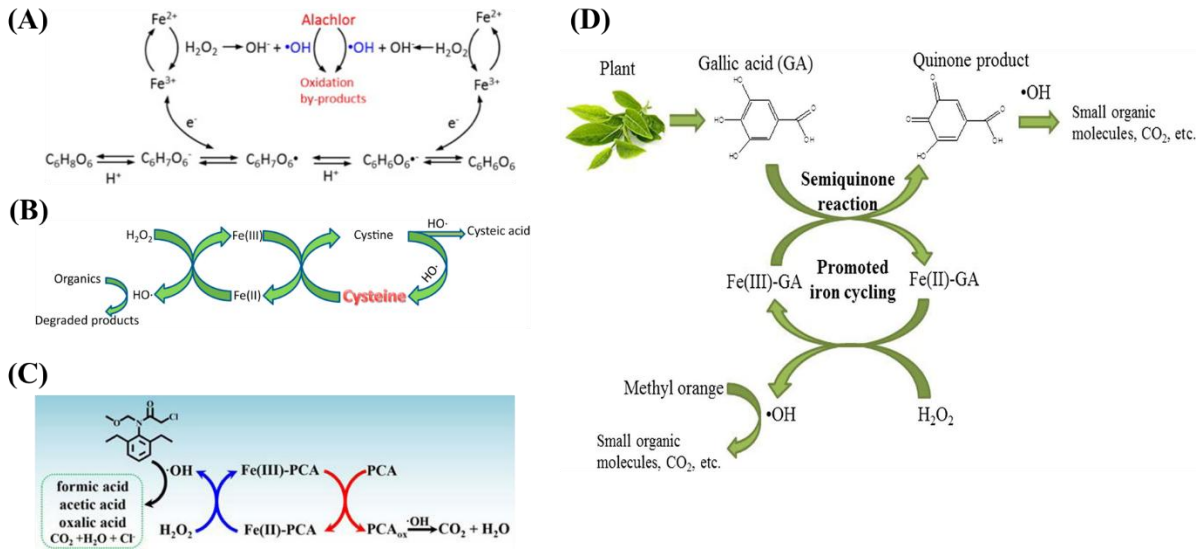

Figure 1.24. The proposed reaction mechanism in the Fe^{3+}/H_2O_2 Fenton systems with the introduction of organic matters, (A) ascorbic acid,[168] (B) cysteine,[174] (C) protocatechuic acid,[167] and (D) gallic acid.[166]

Although previous studies discussed the critical role of quinone/quinone-like structures in homogeneous Fenton reaction by forming a Fe-complex (quinone/hydroquinone) to facilitate electron transfer and promote the Fe redox cycle, introducing additional organic promoters

would increase the total organic carbon in the system[166,167] and result in a more complex effluent and possible secondary pollution.[176] Recent study by Chen et al.[177] confirmed that the self-co-catalytic mechanisms driven by the organic pollutants with phenolic moiety and homogeneous Fe species promoted the oxidative degradation of the organic pollutant itself without any external organic promoters. Using the state of art spectroscopy measurements, distinctive peaks were observed in the Fe^{3+}/Paracetamol (PCM)/H_2O_2 and Fe^{3+}/Bisphenol A (BPA)/H_2O_2 systems at 436 nm and 385 nm, respectively (**Figure 1.25 (A)-(B))**, with the structure under the graphs), while no peaks associated with complex could be observed in the Fe^{3+}/Naproxen (NPX)/H_2O_2 and Fe^{3+}/Caffeine (CAF)/H_2O_2 systems (**Figure 1.25 (C)-(D)**). Mössbauer spectrum (**Figure 1.25 (E))** and EPR analysis (**Figure 1.25 (F)**) confirmed that a phenolic ferric hydroperoxide complex forms in the Fe^{3+}/PCM/H_2O_2 system and that Fe^{3+} is rapidly reduced to Fe^{2+}, indicating phenolic ligation accelerates the Fe redox cycle and enhances ·OH generation. Based on the experimental results, a reaction mechanism was proposed in **Figure 1.25 (G)**. Phenolic pollutant (P) first chelates Fe^{3+} to form P-Fe^{3+} precursor, which subsequently reacts with H_2O_2 to form the high-spin HOO-Fe^{3+}-P complex. This complex then undergoes rapid homolysis that releases HO_2· and facilitates Fe^{3+} reduction to Fe^{2+}. The classic Fenton reaction occurs with the presence of H_2O_2 and Fe^{2+} to produce ·OH, which oxidises P to a quinone (Q), and the Q re-enters the cycle by binding Fe^{3+} and repeating the same steps, so the hydroperoxide loop and the quinone loop together sustain a fast Fe^{3+}/Fe^{2+} cycle and radical production.

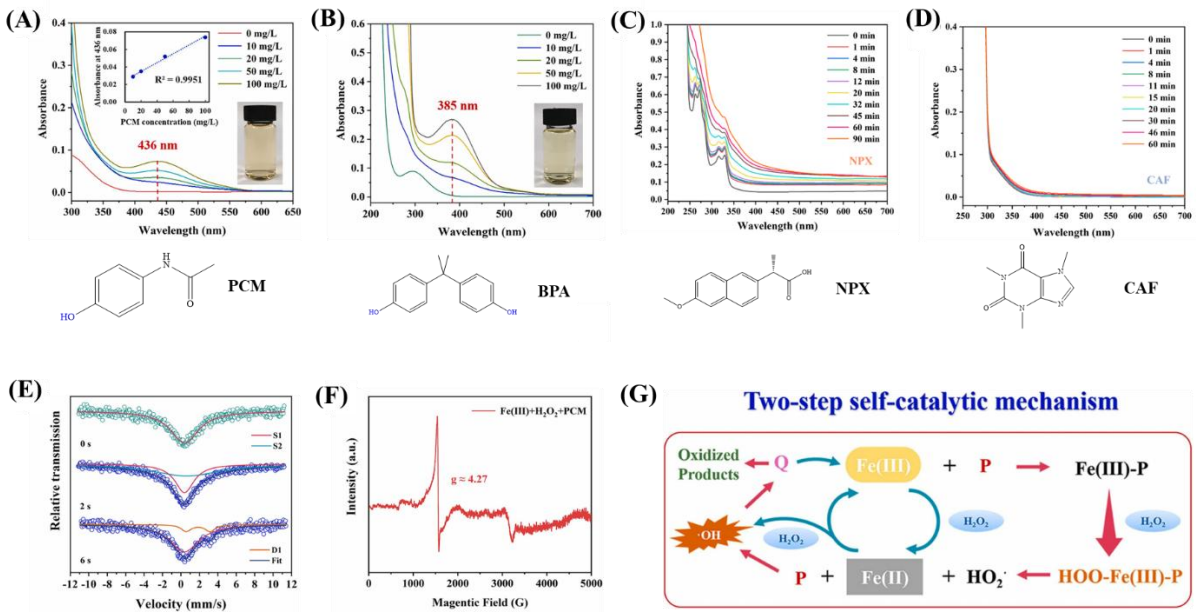

Figure 1.25. (A) UV–vis spectra of Fe^{3+}/H_2O_2/PCM system at different PCM concentrations, with a inset graph showing the relationship of absorbance at 436 nm to pollutant concentration at 4.0 min and photo shows the mixed solution colour of Fe^{3+}/H_2O_2/PCM system at 4.0 min; (B) UV–vis spectra of Fe^{3+}/H_2O_2/BPA system at different BPA concentrations, with a inset photo showing the mixed solution colour of Fe^{3+}/H_2O_2/BPA system at 4.0 min. UV-vis spectra of (C) Fe^{3+}/H_2O_2/NPX system and (D) Fe^{3+}/H_2O_2/CAF at different time. (E) Mössbauer spectrum of Fe^{3+} (green) and Fe^{3+}/H_2O_2/PCM mixture (blue) ([PCM]0 = 15 g L^{-1}, [Fe(III)]0 = 0.5 M, [H_2O_2]0 = 0.8 M), (F) Low-temperature (T = 98 K) EPR spectrum of Fe^{3+}/H_2O_2/PCM mixture, and (G) the proposed reaction mechanism. **For (A) to (D), reaction condition**: [Fe^{3+}]0 = 40.0 μM, [H_2O_2]0 = 2.0 mM, [NPX]0 = [CAF]0 = 100.0 mg L^{-1},[PCM] = 0-100 mg L^{-1}, [BPA] = 0-100 mg L^{-1}, pH 4.0, and T = 25 °C.

To mitigate the increased total organic carbon issue from organic promoters, utilizing inorganic materials as co-catalysts to facilitate the Fenton reaction has been reported. Xing et al.[162] innovated Mo-based co-catalyst, like MoS_2, effectively cooperated with Fe species and achieved 100% Rhodamine B degradation within 20s (in the $Fe^{2+}/MOS_2/H_2O_2$/Vis-light (λ > 420 nm) system) and elevated chemical oxygen demand (COD) removal rate of fine chemical (benzenoid) wastewater to 76.5%, remarkably outperformed the catalytic system without MoS_2 (12% COD removal rate). The enhanced catalytic performance could be attributed to the protonation of coordinatively unsaturated surface S, which generates H_2S and concomitantly oxidises surface $Mo^{4+}$to Mo^{6+}. This oxidation is coupled via interfacial electron transfer to Fe^{3+} reduction to Fe^{2+} (Eq. 6), which accelerates Fe^{2+} regeneration, the rate-limiting step in conventional AOPs. During subsequent Fenton turnover, H_2O_2 interacts with Mo^{6+} and reduces it back to Mo^{4+} (Eq. 7), thereby closing the MoS_2 cycle and sustaining rapid Fe redox cycling

and radical production (**Figure 1.26 (A)**). A similar promotive mechanism of MoS_2 was also reported by Zhu et al.,[169] who synthesized 3D-MoS_2 sponge loaded with MoS_2 nanospheres and graphene oxide (GO), where the exposed Mo^{4+} active sites on 3D-MoS_2 can maintain a stable Fe redox cycle and further promote the catalytic degradation efficiency up to 50 times compared to the system without a co-catalyst. Liu et al. employed this MoS_2-co-catalytic system for water disinfection, and the Escherichia coli K-12 remediation rate reached 83.37% in 1 min and 100% in 30 min.[170]

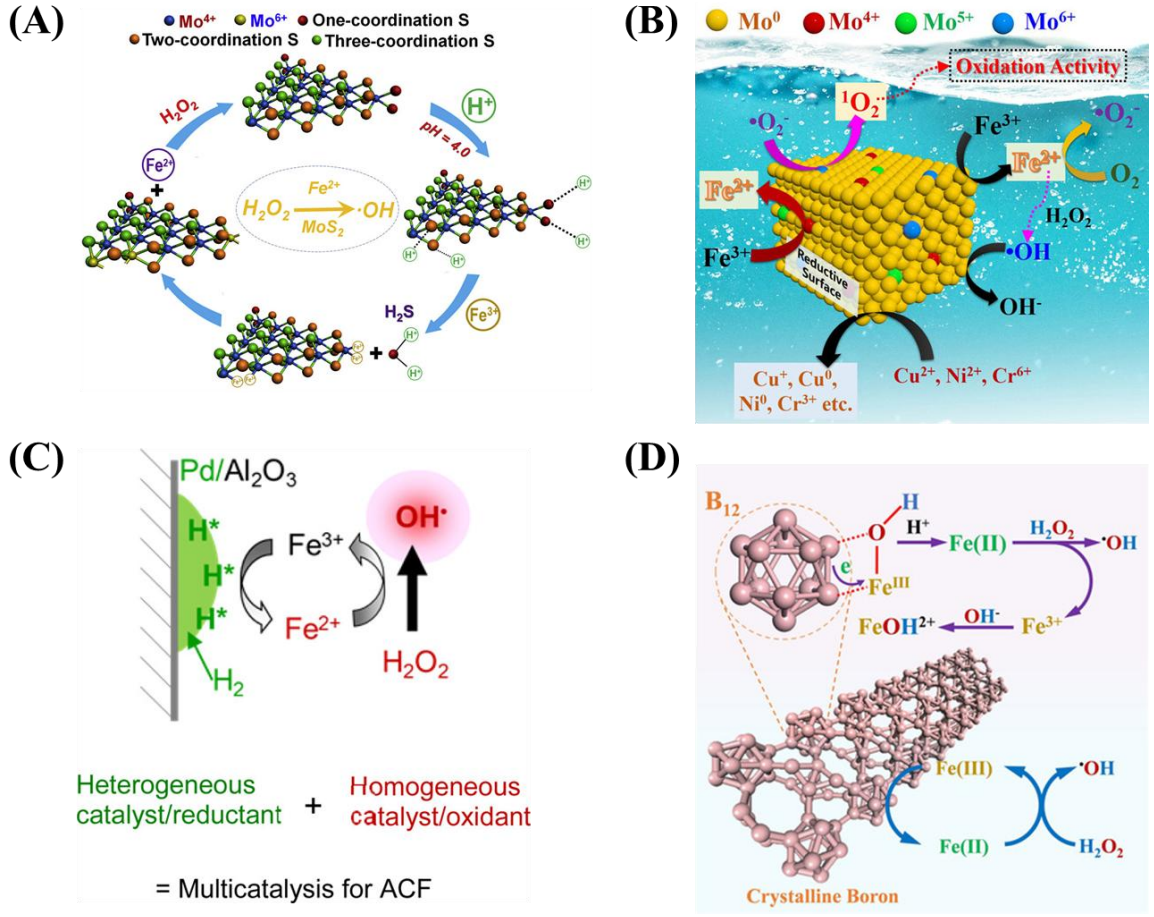

Figure 1.26. (A) Schematic illustration of the MoS_2/Fe^{2+} co-catalytic system.[162] (B) Mo powder used to promote the Fe redox cycle.[172] (C) Pd-assisted accelerated homogeneous Fenton system.[171] (D) B framework in homogeneous Fenton reaction.[178]

Yi et al. showed that adding molybdenum powder shifted ·OH pathways to a singlet oxygen ($^1O_2$) dominated non-radical pathway in the Fe^{2+}/H_2O_2 system. In the Mo-co-catalysed system, metallic Mo reduces Fe^{3+} to Fe^{2+} at the Mo surface, and the regenerated Fe^{2+} then reacts with O_2 to produce $O_2^{\bullet-}$. Metallic Mo consumes ·OH and Fe^{2+} provide a minor ·OH sink, removing the competing radical that masks $O_2^{\bullet-}$ to $^1O_2$ conversion. Surface Mo^{6+} sites subsequently drive

the $O_2^{\bullet-}$ to $^1O_2$ transformation by overcoming the thermodynamic barrier (**Figure 126 (B)**).[172] The hydrogenation ability of Pd has been noticed and further applied by Georgi et al., who proposed an accelerated catalytic Fenton (ACF) system by introducing Pd/Al_2O_3 catalyst into the Fe^{2+}/H_2O_2 Fenton system (**Figure 1.26 (C)**), where the Pd mainly facilitated the H_2 activation and the generated *H assisted Fe^{3+} to reduce back to Fe^{2+}.[171] Meanwhile, crystalline boron (C-boron) reported by Zhou et al.,[178] accelerates Fe^{3+}/Fe^{2+} cycling in C-boron/Fe^{2+}/H_2O_2 systems via the electron donation from surface B-B bonds and interfacial suboxide boron within B_{12} icosahedra, achieving 100% diethyl phthalate (DEP) degradation compared with the conventional Fenton system (Fe^{2+}/H_2O_2, 60% DEP degradation rate).

1.7.3.2 Heterogeneous Fenton reaction

Although advancements made in the application of the homogeneous Fenton reaction to promote Fe redox and reduced Fe sludge with the assistant of various co-catalytic promoter, the following disadvantages still exist in the application of homogeneous Fenton reaction, **1)** difficult recovery of homogeneous catalyst (homogeneous Fe^{2+} or Fe^{3+} species), **2)** narrow optimal pH range (2.5 - 3.5), and limitation arises from rapid hydrolysis of Fe^{3+} (10^5 - 10^6 L mol^{-1} s^{-1}) and Fe^{2+} (10^4 - 10^5 L mol^{-1} s^{-1}) at near-neutral to alkaline pH, while the reaction between Fe^{2+} and H_2O_2 is relatively slow (<10^2 L mol^{-1} s^{-1}), which promotes ferric hydroxide precipitation.[179]

In contrast, heterogeneous Fenton systems that employ solid iron-based catalysts can mitigate the limitations of homogeneous Fenton. A broad set of Fe phases has been studied, including ferrihydrite,[180,181] hematite (α-Fe_2O_3),[182,183] goethite (α-FeOOH),[184,185] magnetite (Fe_3O_4),[186–188] and pyrite (FeS_2).[189,190] Wang et al. reported that using α-FeOOH could efficiently degrade methyl orange with good reusability.[184] Magnetite nanoparticles synthesized by Zhang et al., exhibited 100% removal rates for phenol and aniline under near-neutral conditions while allowing magnetic recovery and reuse due to superparamagnetic.[188]

Immobilised Fe activates H_2O_2 and generates $^{\cdot}OH$ without bulk precipitation of ferric hydroxides. Fe leaching can still occur in the heterogeneous Fenton system, especially upon reuse, so most systems proceed through two concurrent pathways, namely leached Fe^{2+} reacting with H_2O_2 via the homogeneous Fenton route and surface or lattice $\equiv Fe^{3+}$ or $\equiv Fe^{2+}$ on the solid reacting with H_2O_2 via the heterogeneous route (**Figure 1.27**).[191]

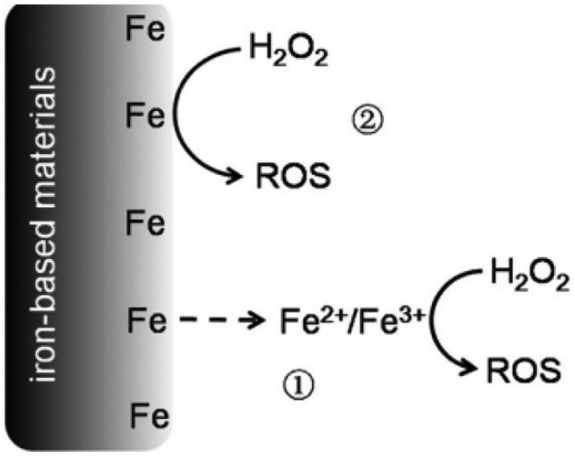

Figure 1.27. Two possible interfacial mechanisms of the Fe-based heterogeneous Fenton reaction.[191]

In heterogeneous Fenton catalysis, the redox cycling of surface Fe sites, typically denoted as $\equiv Fe^{3+}/\equiv Fe^{2+}$, is the principal determinant of catalytic activity.[192] Fe-based solids provide Lewis acidic centres that exhibit increasing hydroxide adsorption as pH rises, which shifts the particle zeta potential toward more negative values. Under neutral to alkaline conditions, the adsorbed hydroxide (OH^-) promotes hydrolysis of surface iron species and the formation of poorly soluble ferric hydroxide or oxyhydroxide phases. These precipitates block active sites, impede interfacial electron transfer, and progressively poison the catalyst. Maintaining appropriate surface iron speciation is therefore essential for sustained H_2O_2 activation and efficient radical generation.[192] Some strategies have been proposed for tailoring the interfacial microenvironment through proton management, competitive OH- modulation, and nanoscale confinement; by doing so, one can stabilise redox-active Fe centres, curb hydrolysis-driven deactivation, and couple radical paths.

Creating an acidic interfacial microenvironment offers one effective implementation to reduce the propensity of the surface to accumulate OH^-. $CoFe_2O_4/MoS_2$ catalyst synthesized by Yan et al.,[193] exhibited over 70% phenolic and 100% antibiotics degradation under neutral pH conditions (pH = 6.86). The high activity towards organic degradation could be attributed to the abundant unsaturated S edge sites on the surface of $CoFe_2O_4/MoS_2$ that capture protons and enrich H^+ near the interface surface, discouraging OH^- accumulation, promoting dissolution and outward diffusion of $\equiv Fe^{3+}$ toward the reaction zone, and stabilising catalytically competent Fe sites. In parallel, the exposed surface $\equiv Mo^{4+}/\equiv Mo^{6+}$ cycle couples with the $\equiv Fe^{3+}/\equiv Fe^{2+}$ cycle to facilitate rapid ROS generation (**Figure 1.28**). A similar microenvironment tactic was also reported by Li et al.,[194] a Fe-based carbon nitride (CN)

catalyst that cohosts single atoms (SA) and small clusters (SC) by tuning the CN/Fe ratio to maximise exposed Fe sites. The catalyst delivered ultrafast H_2O_2 activation and pollutant removal, achieving 100% methylene blue degradation in 20 s, and kept working under high pH and anion-rich conditions because SA and SC sites create a self-acidifying interfacial microenvironment that shifts neutral water into the acidic range around pH 3.8 to 5.5 and sustains ·OH generation.

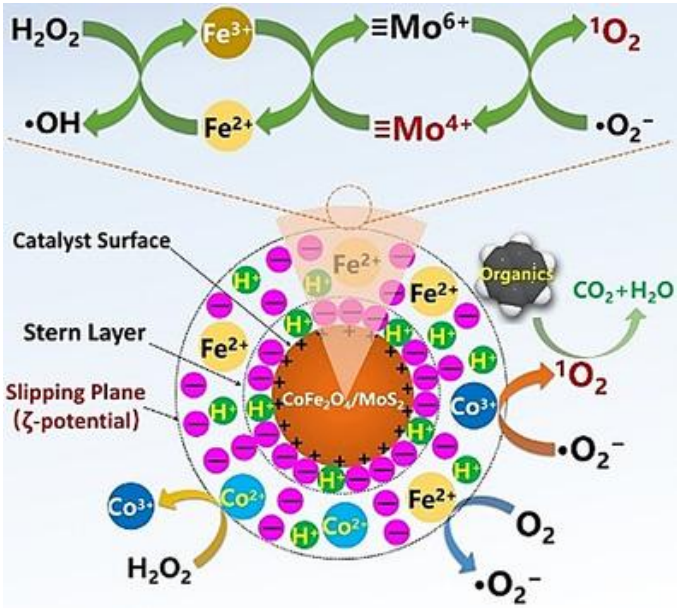

Figure 1.28. Catalytic microenvironment created near the $CoFe_2O_4/MoS_2$ surface.[193]

Microenvironment control can be strengthened further through nanoscale spatial confinement. Confining active sites and reactants within hollow or nanochannels lengthens pollutant residence times near the catalytic surface, increases encounter probabilities with short-lived oxidants, and reduces quenching pathways. Zheng et al. engineered nanoconfinement to keep Fe-oxide Fenton catalysts active at neutral pH conditions. Within 5 nm anodized-aluminium-oxide nanochannels, confined Fe_3O_4, FeOOH, $CuFe_2O_4$, and FeOCl achieved complete bisphenol A removal in under 10 s at pH 7, showing up to 310-fold higher kinetics after surface area normalization compared to the counterpart bulk reactions with suspension catalysts. Proton distribution simulations and experimental results indicated proton enrichment at the confined interface and a lowered in-pore pH that maintains reactive Fe sites and improves longevity (**Figure 1.29 (A)**).[195] Apart from the tube nanoconfined structure, Su et al. engineered Fe_3O_4@$MnSiO_3$ core–shell catalysts that implement hierarchical nanoconfinement. The $MnSiO_3$ shell selectively adsorbs tetracycline, enriching TC at the catalyst surface, while H_2O_2 is activated within the Fe_3O_4 cavity to generate concentrated ·OH. This synergistic confinement

places reactants and short-lived oxidants in proximity and improves their effective contact. Compared with the bulk Fe_3O_4/H_2O_2 Fenton system, the confined Fe_3O_4@$MnSiO_3/H_2O_2$ system increased the tetracycline degradation rate by 1.7 times and enhanced TOC removal by 60% (**Figure 1.29 (B)**).[196]

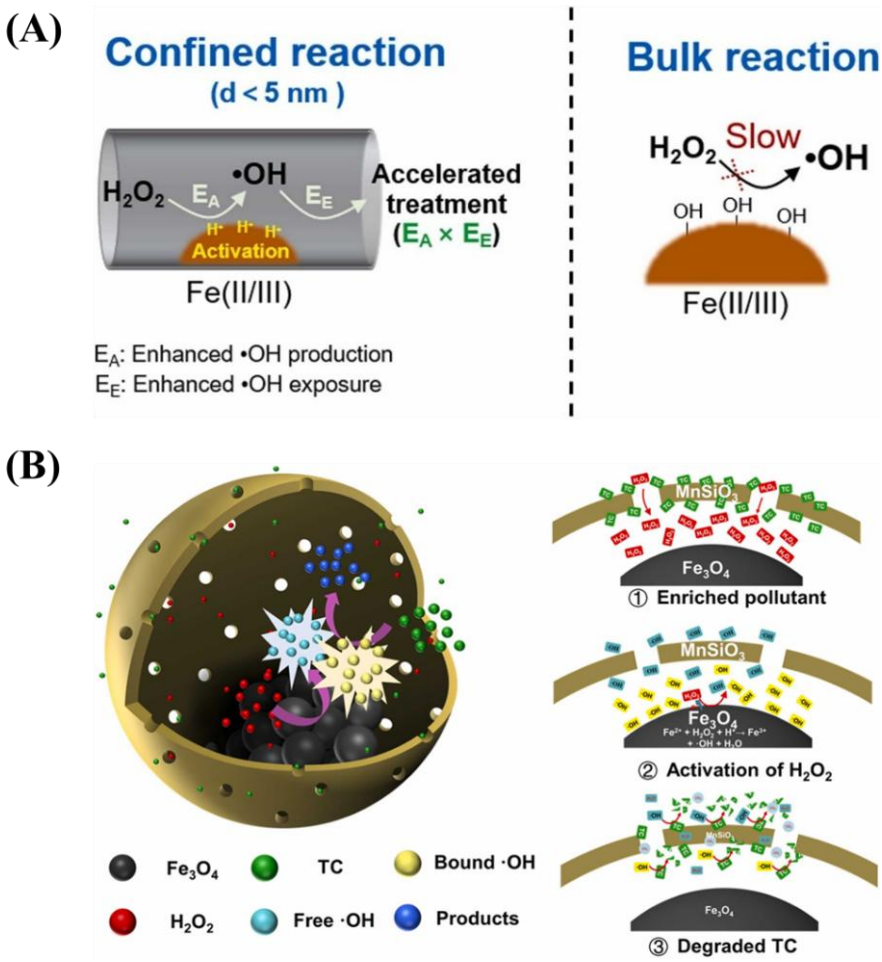

Figure 1.29. Tube-shaped and core-shell-shaped confined heterogeneous Fenton system.[195,196]

Interestingly, the nanoconfinement effect could also regulate the ROS generation, for example, from the radical pathway to the non-radical pathway. Yang et al.[197] confined approximately 2 nm Fe_2O_3 nanoparticles within approximately 7 nm carbon nanotubes (CNT), shifting the Fenton-like pathway from ·OH to $^1O_2$ and maintaining high activity up to pH 9.0. The nanoconfined catalyst degraded methylene blue 22.5 times faster than the nonconfined analogue and showed adsorption-dependent selectivity, with rates that follow how strongly cationic dyes bind inside the tubes. Mechanistically, confinement enriches and retains HO_2· and $O_2^{\bullet-}$ formed through the Haber–Weiss cycle, promoting $^1O_2$ generation and rapid pollutant oxidation.[197] Zhang et al.[198] found that the nanoconfinement effect could shut down the

conventional radical pathway assembled a nanoconfined Fenton reactor by immobilizing UiO-66-NH_2(Zr) within a graphene aerogel and coordinating isolated $\equiv Fe^{3+}$ atoms to the MOF nodes. The GA scaffold concentrates reductive intermediates and accelerates $\equiv Fe^{3+}$ to $\equiv Fe^{2+}$ cycling, which reshapes carbon fate during phenol treatment. The kinetically preferred ring-opening route is suppressed and the reaction is steered toward a thermodynamically favoured oligomerization pathway. This design delivers a 208-fold boost in the apparent first-order rate constant over the unconfined analogue.[198]

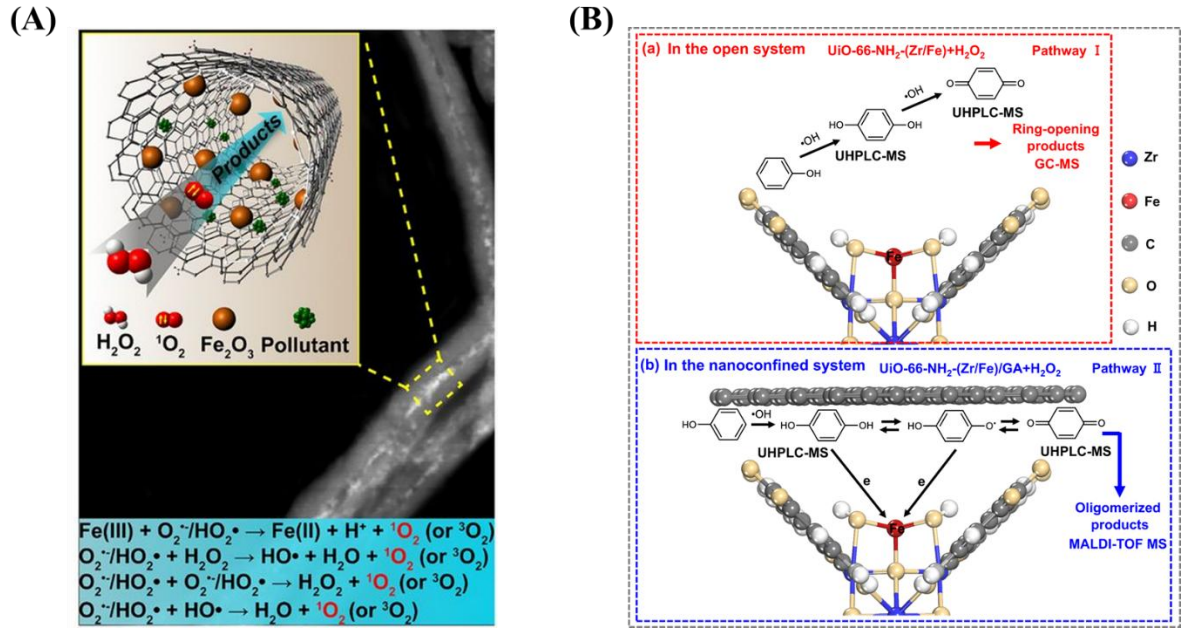

Figure 1.30. Illustration of (A) the possible mechanism of pollutant degradation in the Fe_2O_3@FCNT-H/H_2O_2 system[197] and (B) UiO-66-NH_2-(Zr/Fe) + H_2O_2 open system and UiO-66-NH_2-(Zr/Fe)/GA + H_2O_2 nanoconfined system.[198]

·OH (and related HO_2·, O_2·⁻. radicals) and $^1O_2$ are the reactive species that have been well documented in the Fenton system.[158,172,187,197] Other non-radical species, e.g., high valence metal-oxo species, were also limitedly reported in H_2O_2-based Fenton reactions, although most of the Fe^{IV}=O,[199] Co^{IV}=O,[200] Mn^{IV}=O[201] species have been well reported in peroxymonosulfate (PMS)-based AOPs. Li et al. reported the generation of Fe^{IV}=O species, probed by Dimethyl sulfoxide (DMSO), is associated with the synergistic effect between FeN_5 and Fe clusters during Fenton reaction, and selectively promotes oxidative degradation of contaminants (e.g. Tetracycline) containing electron-rich groups (e.g. amino groups) (**Figure 1.31**).[202]

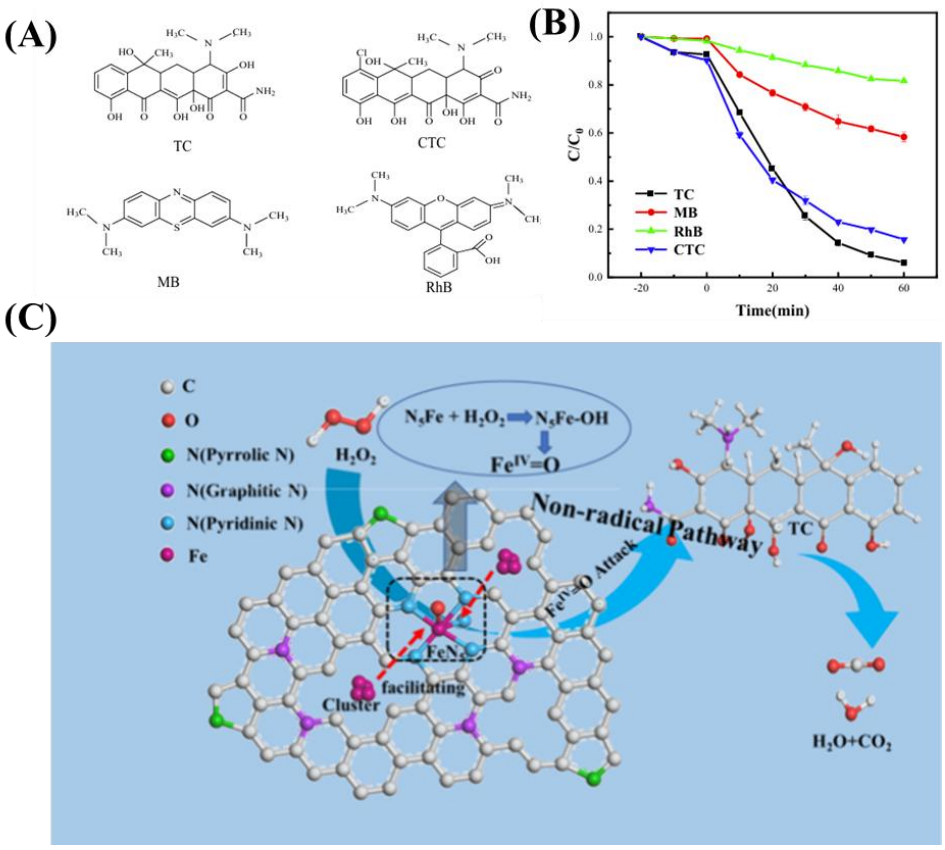

Figure 1.31. (A) Structures of TC, CTC, MB, and RhB. (B) Oxidative degradation of TC, CTC, MB, and RhB in the FeN_x/H_2O_2 system. (C) Reaction mechanism of the Fe^{IV}=O generated non-radical Fenton pathway.[202]

1.7.4 Fenton Reaction using the in situ generated H_2O_2

Adding H_2O_2 by bulk feeding is a common practice. However, it is associated with potential risks during the storage and transportation processes, as well as low utilization efficiency.[31] Consequently, the Fenton/Fenton-like processes, which involve in situ production of H_2O_2, have gained increasing attention in recent years.[203] Significant advancements have been made in the development of in situ H_2O_2 production strategies aimed at environmental remediation.[54] These approaches, spanning photocatalytic, electrocatalytic, and chemical routes (directly utilise H_2 and O_2), offer innovative pathways for generating reactive oxidative species critical for pollutant degradation.

1.7.4.1 In situ Photo-Fenton system for water treatment

Photocatalysis provides a clean route to convert sunlight into chemical energy and to form H_2O_2 at room temperature through O_2 photo-reduction ($O_2 + 2e^- + 2H^+ \rightarrow H_2O_2$ (0.68V vs.

NHE)) or H_2O photo-oxidation ($2H_2O + 2h^+ \rightarrow H_2O_2 + 2H^+$ (1.76V vs. NHE)).[54] Since seminal demonstrations of photocatalytic H_2O_2 generation in the 1990s and early 2000s, for example, on illuminated TiO_2 in 1994,[204] and mechanistic studies in 2003,[205] broad classes of semiconductors have been developed to accelerate photocatalytic efficiency in utilizing metal and carbon materials for efficient in situ H_2O_2 generation and the subsequent water treatment via Fenton or Fenton-like chemistry. **Table 1.2** below compiles representative systems together with light sources, H_2O_2 production, target pollutants, and Fenton efficiency to give an overview of the catalytic performance of this in situ Fenton system.

Table 1.2. Various in situ photo-Fenton systems for water treatment.

Photocatalysts	Light source	H_2O_2 Production	Pollutant	Removal Rate	Reference
$BaFe_{12}O_{19}/Ag_3PO_4$	300 W Xe arc lamp	~60 μmol L-1 h^{-1}	Bisphenol A, 20 mg L^{-1}	79.90%	206
FeOCl/Cdots	150 W Xenon lamp	337.2 μmol L^{-1}	p-chlorophenol, 5 mg L^{-1}	90.10%	207
CdS/Fe_{2+}	300 W xenon lamp	153.13 μmol L^{-1}	Sulfamethazine, 20 mg L^{-1}	99.73%	208
NH_2-MIL-88B(Fe)@$ZnIn_2S_4$	Xe-lamp	502 μmol h^{-1} g^{-1}	Bisphenol A, 10 mg L^{-1}	99.40%	209
$BN/Zn_3In_2S_6$	300 W Xe lamp	115.5 μmol L^{-1}	Oxytetracycline, 30 mg L^{-1}	84.50%	210
Mesoporous CN nanospheres	xenon lamp	N/A	Bisphenol A, 10 mg L^{-1}	100%	211
α-Fe_2O_3/g-C_3N_4	300 W Xenon lamp	12 μmol L^{-1}	Rhodamine B, 10 mg L^{-1}	96%	212
gCN-T	10 W LEDs	251 umol g_{cat}^{-1} h^{-1}	Phenol, 60 mg L^{-1}	76.30%	213
MIL-101(Fe)/g–C_3N_4	300 W Xenon lamp	4370 μmol h^{-1}	Methyl orange, mg L^{-1}	99%	214
ultra-thin g-C_3N_4 NS	400 nm≤λ≤760 nm	665.4 μmol h^{-1} g^{-1}	Tetracycline, 50 mg L^{-1}	90%	215

Two productive photochemical routes towards H_2O_2 formation via O_2 reduction (ORR) and H_2O oxidation (WOR).[216] However, the preferred branch in most practical systems is the 2e- ORR to H_2O_2 that proceeds through the *OOH intermediate at about 0.695 V versus NHE, while a complementary 2e- WOR has been considered difficult for solar-energy-driven to occur attributed to the robust thermodynamic kinetics (1.77 V vs. RHE).[217,218] So managing O_2 supply is critical as interfacial O_2 activity determines both rates for the in situ H_2O_2 and the downstream ROS formation. As reported by Ju and co-workers, a three-phase (gas–liquid–solid) reactors could enrich O_2 at the catalyst surface and shorten diffusion paths. A Z-scheme

MIL-101(Fe)/g-C_3N_4 photocatalyst immobilised on hydrophobic carbon cloth, which overcomes O_2 mass transfer limits and delivers in situ H_2O_2 production rate at 4370 μmol h^{-1} while achieving 99% methyl orange removal through rapid O_2 supply and improved charge separation. Mechanism studies indicated that photogenerated electrons in the conduction band of g-C_3N_4 reduce O_2 to H_2O_2, a process favoured because the conduction band potential is more negative than the $O_2/O_2^{\cdot-}$ redox couple. At the same time, holes in the valence band of MIL-101(Fe) oxidise water to produce ·OH. This spatial separation of reduction and oxidation sites promotes in situ H_2O_2 formation and its rapid conversion into reactive radicals, demonstrating that the three-phase photocatalytic design is a robust and sustainable route for oxidative pollutant removal and environmental remediation (**Figure 1.32**).[214]

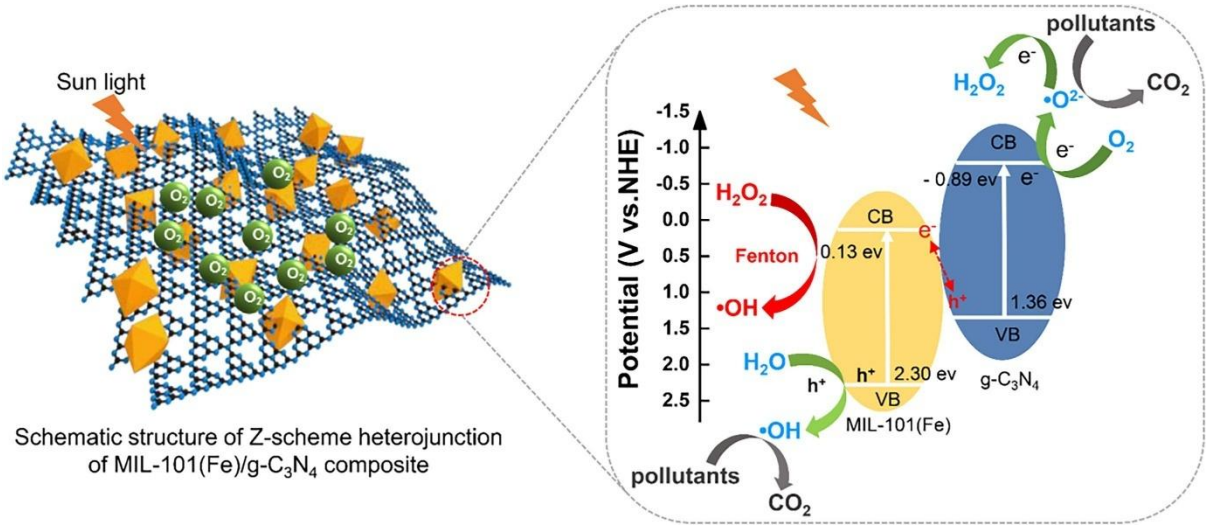

Figure 1.32. Schematic structure of MIL-101(Fe)/g–C_3N_4 composite and illustration of the photocatalytic mechanism.[214]

The selectivity towards $2e^-$ ORR pathway over the competing $4e^-$ route to H_2O is required to promote the in situ H_2O_2 synthesis and the subsequent ROS generation. Teng et al. demonstrated that some single-atom photocatalysts (e.g., In and Sn) on polymeric carbon nitride (M-SAPCs) are more favourable to selective H_2O_2 production under visible light. Theoretical calculation identified In(III) and Sn(IV) as optimal, lowering exciton binding, enhancing electron–hole separation, and localizing photoelectrons to favour end-on O_2 adsorption and the 2e- ORR (**Figure 1.33 (A)**).[217] Similarly, Zhang et al. reported an ultrathin carbon nitride bearing isolated Ni sites (NiCN-x, optimal NiCN-4) with an efficient visible-light photocatalyst for selective H_2O_2 production and pollutant removal. Under 400 nm irradiation, it delivers 27.11 mmol g^{-1} h^{-1} H_2O_2 with an apparent quantum yield of 8.56%,

reaches about 87% H_2O_2 selectivity in RRDE tests, and achieves 89.4% tetracycline degradation with good stability. Mechanistic evidence supports a two-electron oxygen reduction pathway that proceeds via end-on O_2 adsorption at Ni–N_x sites and a Ni-μ-peroxide intermediate, which suppresses O-O bond scission. DFT studies show that Ni–N_x coordination enriches interfacial charge density and tunes the local electronic structure, which benefits O_2 adsorption and its selective activation toward the two-electron route, thereby explaining the high activity and selectivity observed (**Figure 1.33 (B)**).[218]

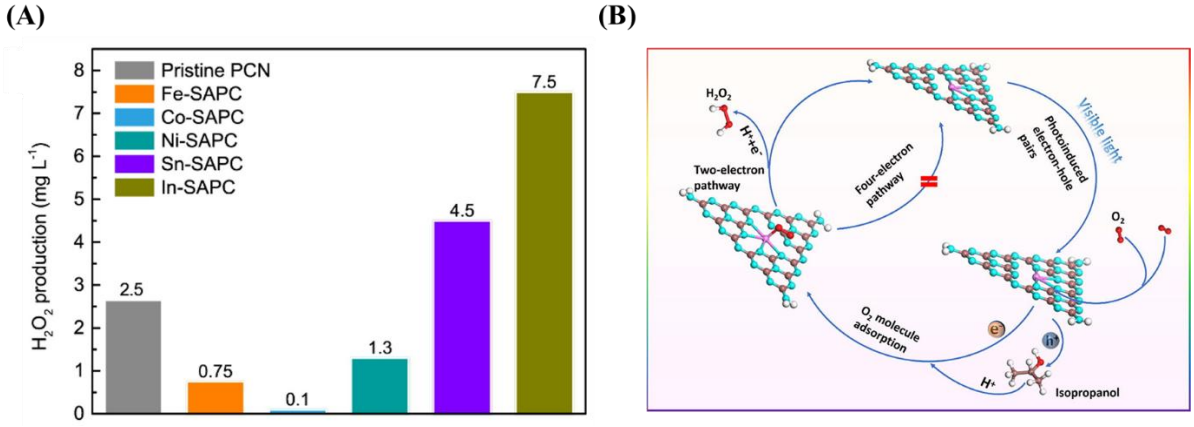

Figure 1.33. (A) Photocatalytic activities of pristine PCN and M-SAPCs for H_2O_2 production in 10% (v/v) ethanol aqueous solution..[217] (B) Schematic demonstration of photocatalytic H_2O_2 generation for NiCN-4 catalyst under visible light irradiation.[218]

Overall, solar-driven H_2O_2 generation coupled with pollutant removal is advancing quickly but still faces limits in H_2O_2 yield, $2e^-$ selectivity, and charge separation. Progress is most likely from semiconductors and heterostructures that harvest light more effectively, bias oxygen reduction toward the $2e^-$ path, suppress the $4e^-$ route, and maintain abundant interfacial O_2 through smart reactor design, with validation in real waters and air streams to guide deployment.

1.7.4.2 In situ Electron-Fenton system for water treatment

As one of the greenest and most efficient AOPs, the electro-Fenton (EF) process has received growing attention for environmental remediation over recent decades.[155,219] EF integrates electrochemistry with Fenton chemistry. Applying a voltage drives continuous reduction of dissolved O_2 at the cathode to electrically produce H_2O_2 in situ via 2 e^- ORR at the cathode ($O_2 + 2H^+ + 2e^- \rightarrow H_2O_2$) and then catalytic decomposition of the in situ generated H_2O_2 by M^{n+} (transition metals, e.g. Fe^{2+}, Cu^{2+}, Co^{2+}, Ag^+) occurs via the Fenton or Fenton-like pathway

($M^{n+} + H_2O_2 \rightarrow M^{(n+1)} + \cdot OH + OH^-$) to generate strongly oxidizing ·OH, enabling non-selective oxidation of toxic, refractory organic contaminants in water. After which, $M^{(n+1)}$ could be reduced back to Mn^{n+} via 1 e^- reduction, enabling a continuous $Mn^{n+}/M^{(n+1)}$ redox cycle (**Figure 1.34**, using Fe redox cycle as an example).[155,219,220]

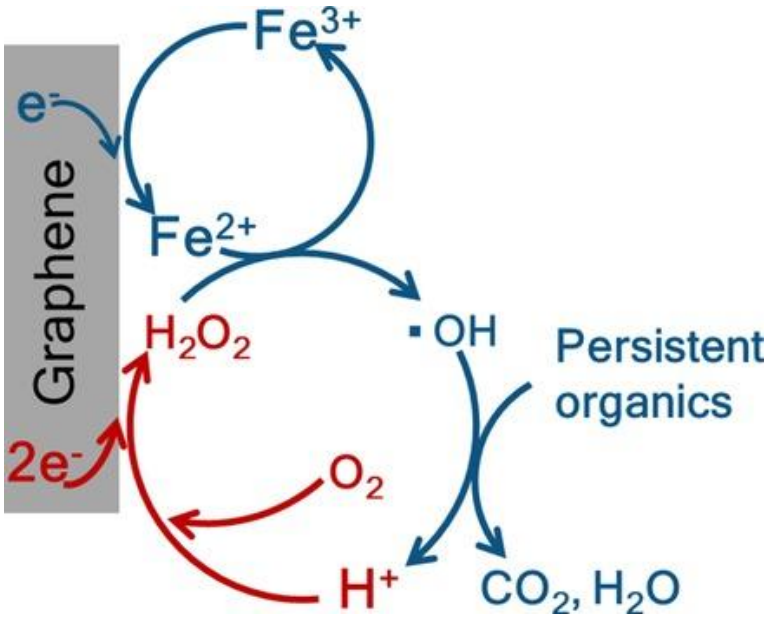

Figure 1.34. Illustration of electro-Fenton degradation catalysed by graphene-based electrocatalysts, using Fe^{3+}/Fe^{2+} redox cycle as an example.[220]

Electrode materials are critical to the O_2 reduction performance. As summarised in **Table 1.3**, pollutant degradation and H_2O_2 generation vary with the cathode used. High-performing options include various carbon materials, metal alloys, and others.[219,221–231] These materials typically offer a high H_2 evolution overpotential, low catalytic activity toward H_2O_2 decomposition, low cost, large specific surface area, and good corrosion resistance. Beyond selecting an appropriate substrate, researchers often apply targeted surface or structural modifications to enhance conductivity, increase active-site density, and improve adsorption of pollutants, thereby raising overall efficiency.[232]

Table 1.3. Properties of different electrode materials in the literature.

Cathodes	Anodes	Current Intensity or Potential	H_2O_2 Production	Pollutants	Removal Rate	Reference
ACFC	Pt	3.2 mA/cm^2	N/A	Wastewater from a textile dyeing plant	75.2% COD	221
C-PTFE-Ni	Pt	200 mA	N/A	Atrazine, 120 mg L^{-1}	Over 90% COD	222
HPC	Pt	4.6 mA/cm^2	47.5 mM/h	Perfluorooctanoate, 50 mg L^{-1}	90.7% TOC	219
3D-PCNS	Pt	−0.5 V	24 mg L^{-1}	Dimethyl phthalate, 50 mg L^{-1}	96%	223
Fe_3O_4-NP@CNF	Pt	−0.345 V	39.65 mmol/h/g	Carbamazepine, 1 mg L^{-1}	100% TOC	224
CMGF	N/A	−0.65 V	175.8 mg L^{-1}	p-nitrophenol, 50 mg L^{-1}	100%	225
EEGr-CF	Dimensionally stable anode	16.66 mA/cm^2	N/A	Imatinib, 0.07 mM	100%, TOC	226
PdFe alloy/CA	Graphite sheet	20 mA	46 mg L^{-1}	3-chlophenol, 50 mg L^{-1}	100%, TOC	227
Ni-CF	Ti/RuO_2-IrO_2	200 mA	~45 mg L^{-1}	Ciprofloxacin, 50 mg L^{-1}	81%, TOC	228
CFNFe	BDD	200 mA	~200 mg L^{-1}	Pymetrozine, 100 mg L^{-1}	90%, TOC	229
N-rGO/CF	Ti/PbO_2	500 mA	120 mg L^{-1}	Diuron, 40 mg L^{-1}	100%	230
AQS/PANI@CF	Pt	−0.5 V	83.3 μmol L^{-1}	Rhodamine B	98.80%	231

However, EF performance is often limited by the formation (via 2e$^-$ ORR) and subsequent activation of H_2O_2 (via 1e$^-$ Fenton). In recent years, researchers have advanced a 3e$^-$ ORR pathway that redirects O_2 reduction to the catalyst surface for immediate use, addresses both steps by generating ROS in situ, and reduces peroxide build-up and diffusion losses.[233–236] The process proceeds through an adsorbed H_2O_2 intermediate that is reduced in place, avoids release to bulk solution, and removes the need for a separate 1e$^-$ step, which improves mass transfer and overall efficiency compared with the 2e$^-$ route to free H_2O_2 and the 4e$^-$ route to water.

Realising this 3e$^-$ route requires a cascade electrochemical sequence in which O_2 and then H_2O_2 are reduced on the electrode without a classical Fenton cycle. Effective control comes from bifunctional catalysts that collocate H_2O_2-forming and ·OH-activating sites at a shared interface. The central challenge is to secure the initial 2e$^-$ step while suppressing over-reduction along

the competing $4e^-$ path to H_2O. This balance can be achieved by tuning oxidation state and coordination, increasing the density of accessible active sites, and pairing transition-metal centres such as Fe, Co, Ni, or Cu with non-metallic carbon sites to modulate selectivity and maintain tight coupling between H_2O_2 generation and activation.[236]

Two complementary strategies have been reported. The first builds metal-core, carbon-shell architectures (Metal@Nonmetal) that operate by sequential reduction on the shell followed by electron delivery from the core. For example, Xiao et al.,[234] proposed a core–shell FeCo alloy encapsulated by a carbon aerogel (FeCo@C) that delivers an efficient and selective $3e^-$ ORR pathway and achieves complete ciprofloxacin removal within 5 min (**Figure 1.35**). A graphitic shell enriched with carboxyl groups promotes the $2e^-$ formation of H_2O_2, while electrons supplied by the enclosed FeCo core tune the shell electronic environment and drive on-shell $1e^-$ activation of adsorbed H_2O_2 to yield surface ·OH, thereby bypassing classical Fenton cycling. DFT calculations support this mechanism, showing near-thermoneutral *OOH formation at $U^0(O_2/H_2O_2) = 0.70$ V with a minimum thermodynamic overpotential of about 0.13 V for $Fe_{0.5}Co_{0.5}C$ bearing -COOH groups, lower than Au, Pt, Pd, and carbon nitride comparators. The free-energy landscape identifies O_2 adsorption as the highest barrier at roughly 1.18 eV, with subsequent steps to *OOH and $*H_2O_2$ favourable, and indicates the conversion of $*H_2O_2$ to the surface ·OH is preferred over H_2O_2 desorption from the catalyst surface($\Delta G \approx -3.02$ eV versus −0.91 eV).

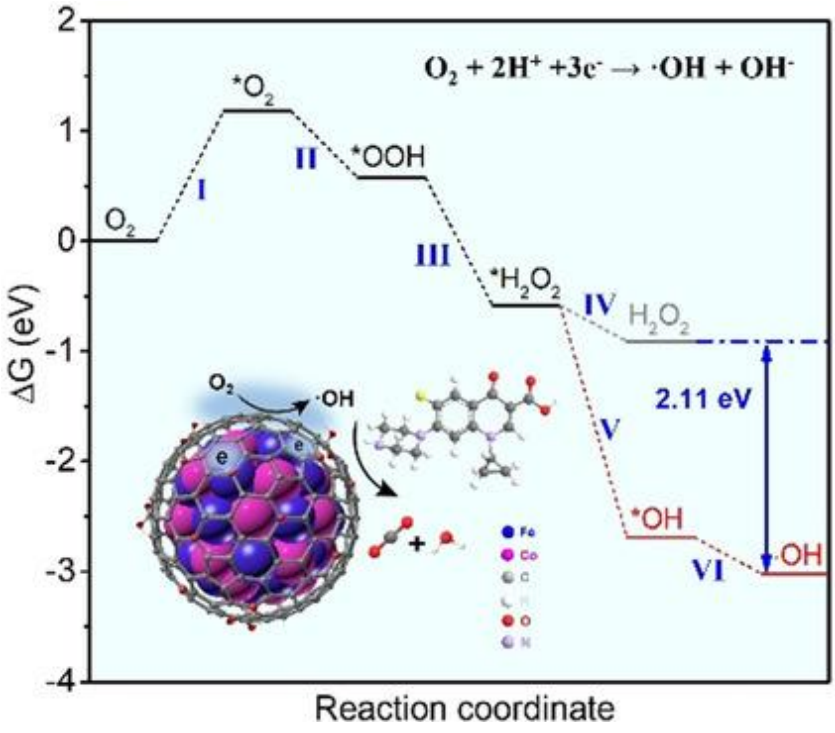

Figure 1.35. The proposed 3e- ORR mechanism for ciprofloxacin degradation.[234]

The second strategy exploits strong metal–support interactions. Xie and co-workers,[235] showed that strong metal-support interactions in Cu/$CoSe_2$/C bias oxygen reduction toward a three-electron pathway that generates surface ·OH for in situ Fenton-like oxidation with limited release of H_2O_2, whereas $CoSe_2$/C preferentially follows the two-electron route and produces more H_2O_2. Evidence for the $3e^-$ route included rotating ring-disk electrode (RRDE) measurements with an average electron-transfer number of about 2.75 and markedly lower ring currents for Cu/$CoSe_2$/C, together with direct quantification that found roughly 0.3 mM H_2O_2 in bulk for Cu/$CoSe_2$/C versus about 1.2 mM for $CoSe_2$/C. Operando Raman resolved a band near 1085 cm^{-1} attributed to adsorbed H_2O_2 on Cu/$CoSe_2$/C, EPR with DMPO detected ·OH only under O_2 and applied potential, and scavenger tests identified ·OH as the primary oxidant. Linear sweep voltammetry (LSV) in the presence of added H_2O_2 gave higher currents on Cu/$CoSe_2$/C than on $CoSe_2$/C, indicating superior H_2O_2 activation on the former. Complementary DFT free-energy analysis assigned H_2O_2 formation mainly to Co sites and its facile one-electron conversion to ·OH to interfacial Cu at Cu-Se-Co junctions, which explains both the limited accumulation of free H_2O_2 and the observed three-electron pathway (**Figure 1.36).**

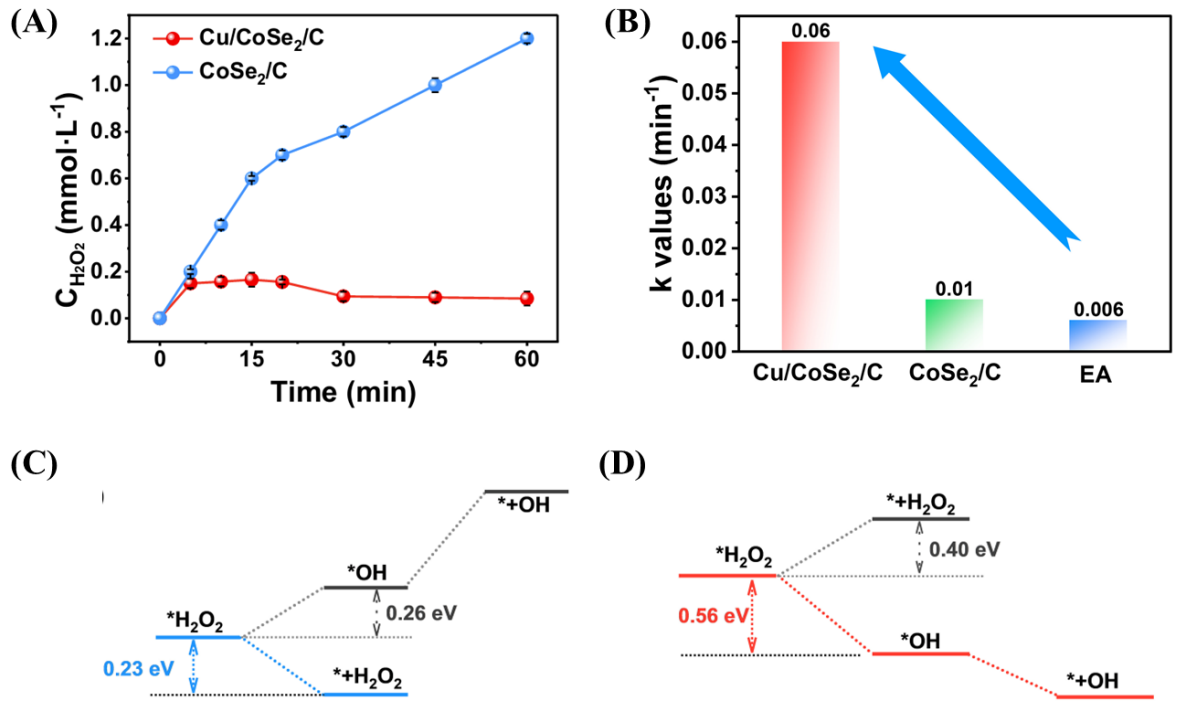

Figure 1.36. The catalytic performance of $Cu/CoSe_2/C$ and $CoSe_2/C$ towards (A) in situ H_2O_2 generation and (B) in situ ciprofloxacin (CIP) removal, and theoretical calculation for the key steps of ·OH production for (C) $CoSe_2/C$ and (D) $Cu/CoSe_2/C$.[235]

1.7.4.3 In Situ Fenton via the direct synthesis of H_2O_2 and ROS from H_2 and O_2

The in situ generation of H_2O_2 and the subsequent ROS directly from molecular H_2 and O_2 has emerged as a significant advancement in sustainable AOPs, particularly when combined with Fenton reactions for degrading persistent organic pollutants in wastewater streams. Traditional approaches utilising preformed H_2O_2 have substantial limitations, including storage, stability concerns, and transportation hazards, which impede practical implementation. The direct synthesis strategy, therefore, presents an advantageous decentralized solution, greatly simplifying operational logistics, enhancing safety, and enabling immediate generation and use at the treatment site.

In 2018, Underhill et al. [237] provided a detailed exploration of $Pd\text{-}Fe/TiO_2$ catalysts towards the oxidative degradation of phenol, which is a model organic pollutant representative of industrial waste streams (**Figure 1.37**). Phenol degradation rates approaching 80% were achieved over a bimetallic $2.5\%Pd\text{-}2.5\%Fe/TiO_2$ catalyst, outperformed the monometallic analogues, $2.5\%Fe/TiO_2$ and $2.5\%Pd/TiO_2$ (both >10%), as well as physically separated Pd and Fe combinations (35%) after 2 hours of reaction, suggesting that the effective phenol degradation requires the presence of both Pd and Fe and close contact or alloy effect is the key, as Pd active sites mainly facilitate the catalytic synthesis of H_2O_2 from molecular H_2 and O_2, while the Fe active sites subsequently interact with the in situ generated H_2O_2 to produce highly reactive ·OH for radical-mediated phenol degradation. Notably, the in situ route significantly outperformed traditional oxidation methods employing preformed H_2O_2 (0.5 wt.%), primarily due to the generation of a greater flux of reactive oxygen species responsible for phenol degradation by the PdFe interaction. The analysis between phenol conversion rate and Fe leach suggested that the catalyst stability is a concern, and it's primarily associated with the in situ generated byproducts, which may have been responsible for accelerated leaching of Fe from the catalyst.

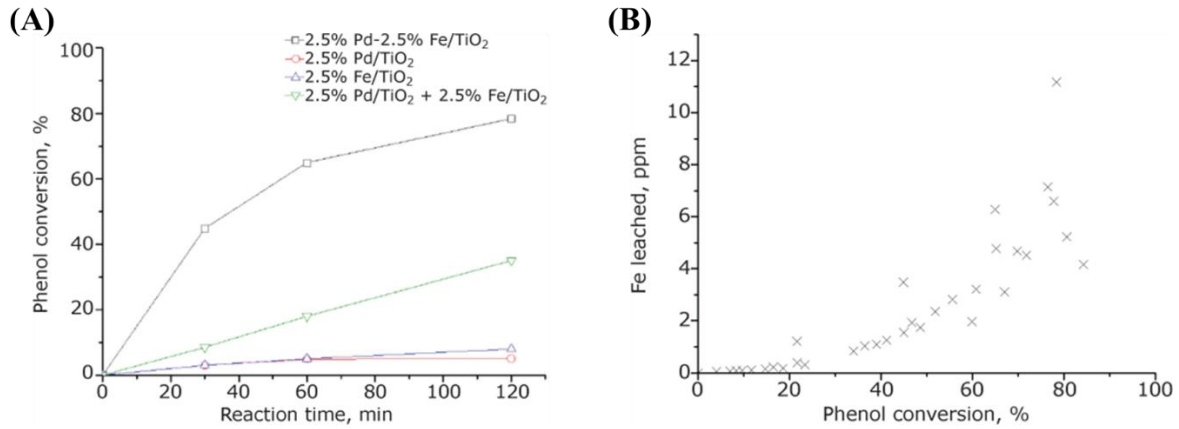

Figure 1.37. (A) A comparison of the catalytic performance towards in situ phenol degradation over the bimetallic PdFe (2.5%Pd-2.5%Fe/TiO_2), monometallic Pd (2.5%Pd/TiO_2) and Fe (2.5%Fe/TiO_2) and physically separated Pd and Fe combines (2.5%Pd/TiO_2 + 2.5%Fe/TiO_2). and (B) the correlation between phenol conversion and Fe leaching of the 2.5%Pd-2.5%Fe/TiO_2 catalyst. Reaction conditions: catalyst (0.01 g), phenol (1000 ppm, 8.5 g), 5% H_2/CO_2 (420 psi), 25% O_2/CO_2 (160 psi), 30°C, 2 h, 1200 rpm.[237]

Further investigation into the bimetallic PdFe catalysts was conducted by Santos et al.[238,239] , who evaluated a series of bimetallic PdFe catalysts on different supports (TiO_2 and ZSM-5) towards in situ phenol degradation. Similar to the previous study, the combination of Pd and Fe significantly enhanced the oxidative degradation of phenol towards phenolic intermediates and organic acids. Although the Fe leaching still remains, highly likely associated with the phenol byproducts. As the Fe leaching seems unavoidable in the situ oxidative system using Fe-contained catalysts, the degradation performance in the system is somehow attributed to the combination of heterogeneous (PdFe alloys) and homogeneous Fenton (the leached Fe). Thus, it's difficult to examine the contribution from heterogeneous or homogeneous Fenton systems solely.

A recent study by He et al.,[240] was proposed to investigate the catalytic activity towards organic degradation when combining heterogeneous H_2O_2 synthesis sites (Pd/TiO_2 and Pd-In/TiO_2) and homogeneous H_2O_2 activation sites (Fe^{2+}) together to further examine how homogeneous Fe species react within the in situ H_2O_2 synthesis environment. Unlike the previously reported PdFe systems where the phenol degradation rate is not positively correlated with H_2O_2 production, this hybrid system with heterogeneous H_2O_2 production and the sequential homogeneous Fenton reaction showed a good correlation between H_2O_2 production and tetracycline degradation, with highest H_2O_2 productivity (4.34 mol_{H2O2} g_{Pd}^{-1} h^{-1}) and tetracycline degradation rate (95.5%) achieved with In loading at 4 wt.% (**Figure 1.38 (A)** and

Figure 1.38 (B)), suggesting that a high rate of H_2O_2 generation is favourable for tetracycline degradation, which via the classic homo Fenton pathway ($Fe^{2+} + H_2O_{2(in\ situ)} \rightarrow Fe^{3+} + \cdot OH + OH^-$). EPR analysis (**Figure 1.38 (C)** and **Figure 1.38 (D)**) revealed ·OH and $O_2^{\cdot -}$ as primary oxidants when combining Pd-In/TiO_2 with homo Fe species, and a clear reaction mechanism was proposed where the H_2O_2 is mainly synthesised on the Pd-In active sites, and then the in situ generated H_2O_2 involved in the Fe redox cycle is activated to ROS (·OH and $O_2^{\cdot -}$) for the subsequent tetracycline degradation.

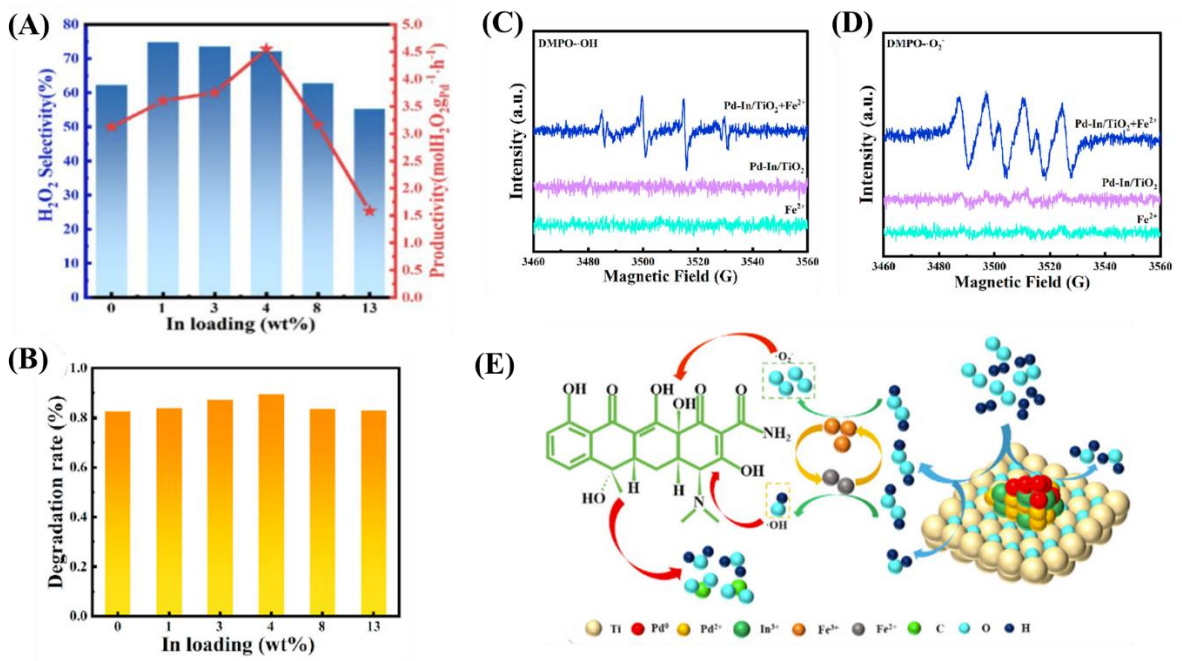

Figure 1.38. (A) The H_2O_2 productivity and selectivity in the direct synthesis of H_2O_2 over Pd-In/TiO_2 catalyst as a function of In loading (wt.%). (B) Catalytic performance towards tetracycline degradation over Pd-In/TiO_2 catalysts as a function of In loading (wt.%). Trapping experiments of active oxygen species in catalytic degradation of tetracycline in different catalytic systems using DMPO to prob (C) ·OH and (D) $O_2^{\cdot -}$. (E) Proposed reaction mechanism of the Pd-In/TiO_2 + Fe^{2+} system in the in situ degradation of tetracycline. Reaction conditions: **for H_2O_2 synthesis**: H_2 and O_2 directly synthesize H_2O_2 reaction conditions: 0.1 MPa, 283 K, the total gas flow rate was 60 mL min^{-1} (H_2 : O_2 : N_2 = 9 : 36 : 15, volume flow ratio), the stirring speed was 1000 r min^{-1}, the reaction solvent was 60 mL anhydrous ethanol and 0.38mL concentrated H_2SO_4, and the catalyst dosage was 50 mg; **For tetracycline degradation**: Initial tetracycline concentration (C0) = 50 mg/L, catalyst concentration (Cc) = 0.1 g/L, pH = 7, Fe^{2+}= 2 mg L^{-1}, T = 298 K.[240]

Beyond removing organic pollutants, the in situ Fenton system generated from H_2 and O_2 was applied to water disinfection with the aim of replacing sodium hypochlorite (NaClO) as a disinfectant. A recent study from the Hutchings group[241] reported that under similar conditions,

an optimal AuPd catalyst produced ROS identified by EPR (·OH, ·OOH, $O_2^{\cdot-}$) and achieved an 8.1 $\log_{10}$ E.coli reduction, whereas preformed H_2O_2 and NaClO each gave less than a 1 $\log_{10}$ E.coli reduction (**Figure 1.39 (A)** and **Figure 1.39 (B)**). This corresponds to a 7 to 8 order of magnitude greater inactivation than ex situ Fenton using preformed H_2O_2 or chlorination at the same oxidant dose and contact time. Varying the Au:Pd ratio showed that 0.5 wt%Au-0.5 wt%Pd/TiO_2 delivered the highest inactivation at 8.1 log10, outperforming monometallic Au at about 1.6 $\log_{10}$ E.coli reduction and Pd at about 2.6 $\log_{10}$ E.coli reduction (**Figure 1.39 (C)**). Despite similar residual H_2O_2 concentrations for the AuPd and Pd-only catalysts, 163 to 202 ppm (**Figure 1.39 (C)**), the superior E. coli inactivation with 0.5%Au-0.5%Pd/TiO_2 indicates that disinfection is not governed by bulk H_2O_2 alone. The results, together with EPR data, are consistent with a division of roles in which Pd sites generate ·OH and ·OOH at high rates, while Au sites facilitate desorption and release of ROS into solution, enabling rapid pathogen kill (**Figure 1.39 (D)**).

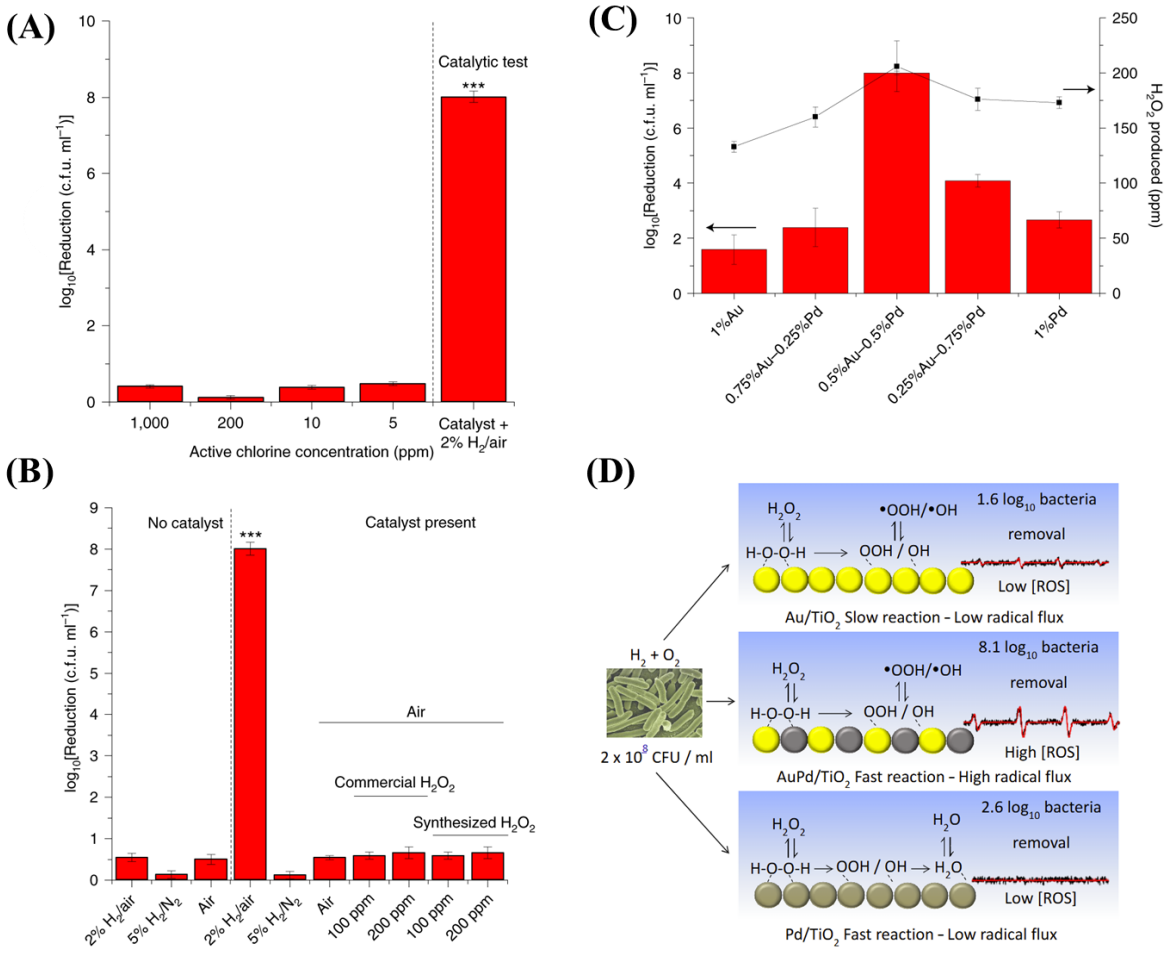

Figure 1.39. (A) Reduction in bacterial viability using a co-feed of aqueous NaOCl under flow conditions. (B) Reduction in bacterial viability after a single pass through the reactor system; the initial bacterial concentration was

2×10^8 c.f.u. ml^{-1}. (C) Observed steady-state H_2O_2 production (black squares) and bactericidal activity against E. coli K12 JM109 (red bars) of 1% AuPd/TiO_2 catalysts as a function of the Au:Pd ratio, at conditions relevant for water treatment. (D) Reaction mechanism of the AuPd series towards the in situ E.coli remediation. Reaction conditions: 10 bar, 2% H_2, 20% O_2, 78% N_2, total gas flow rate 42 mL min^{-1}; 120 mg of catalyst, liquid flow rate 0.2 mL min-^{1}, 2 °C.[241]

The proposed radical generation pathway from this work revealed a radical cascade reaction that turns adsorbed O_2 into ·OH and ·OOH by the initially generated H· from H_2 splitting, with the presence of H_2 and O_2 over the AuPd surface.[241] while Pd alone gives no detectable primary radicals. These radicals can be released from the surface and react in solution, which demonstrates that direct ROS formation might be through the H_2O_2 synthesis cycle rather than via decomposition of preformed H_2O_2. This radical pathway helps rationalise phenol oxidation trends in previous papers.[238,239] Under conditions optimised for H_2O_2 synthesis, 0.5%Au–0.5%Pd/TiO_2 gives higher H_2O_2 synthesis and degradation rates than 0.5%Pd–0.5%Fe/TiO_2, yet 0.5%Pd–0.5%Fe/TiO_2 achieved much higher phenol conversion (**Table 1.4**).[238] Phenol removal, therefore, might be associated with radical flux rather than bulk H_2O_2, suggesting that there might exist two cooperative routes over the PdFe surface during the in situ phenol degradation. First, transient H_2O_2 made on Pd active sites is then transferred to the adjacent Fe active site to be activated to ·OH via the Fenton pathway. Second, the reactive oxygen species are directly formed from H_2 and O_2 rather than the in situ synthesised H_2O_2. However, this second route still needs more evidence, e.g. EPR study or theoretical calculations to confirm that the direct ROS formation is more thermodynamically favourable on the PdFe surface rather than the direct H_2O_2 formation. Also, due to the uncontrolled Fe leaching during phenol degradation, the oxidative catalytic system will move to a mixture of heterogeneous and homogeneous Fenton reaction. Therefore, the determination of reaction mechanisms would be more difficult.

Table 1.4. Catalytic performance of monometallic Pd and bimetallic Pb-based catalysts towards the direct synthesis of H_2O_2, the subsequent H_2O_2 degradation, and in situ phenol degradation.[238]

Catalyst	H_2O_2 Productivity / $mmol_{H2O2}\ Kg_{Cat}^{-1}\ h^{-1}$	H_2O_2 Degradation / $mmol_{H2O2}\ Kg_{Cat}^{-1}\ h^{-1}$	Phenol Conversion / %
1%Pd/TiO_2	30	198	11
0.5%Au-0.5%Pd/TiO_2	97	258	12
0.5%Pd-0.5%Cu/TiO_2	11	80	6
0.5%Pd-0.5%Co/TiO_2	42	109	6
0.5%Pd-0.5%Fe/TiO_2	38	51	39

Reaction conditions: H_2O_2 direct synthesis reaction conditions: catalyst (0.01 g), H_2O (2.9 g), MeOH (5.6 g), 5% H_2/CO_2 (420 psi), 25% O_2/CO_2 (160 psi), 0.5 h, 2 °C, 1200 rpm. H_2O_2 degradation reaction conditions: catalyst (0.01 g), H_2O_2 (50 wt% 0.68 g) H_2O (2.22 g), MeOH (5.6 g), 5% H_2/CO_2 (420 psi), 0.5 h, 2 °C, 1200 rpm. Phenol degradation reaction conditions: catalyst (0.01 g), phenol (1000 ppm, 8.5 g), 5% H_2/CO_2 (420 psi), 25% O_2/CO_2 (160 psi), 2 h, 30 °C, 1200 rpm.

1.8 Challenges, aims and objectives of this thesis

A central challenge in applying the direct synthesis of H_2O_2 to water treatment lies in the intrinsic mismatch between H_2O_2 production and H_2O_2 utilisation. Catalysts optimised for high H_2O_2 synthesis rates often suppress pathways required for efficient activation of H_2O_2 into reactive oxygen species, whereas catalysts or conditions that favour rapid radical generation can simultaneously promote nonselective H_2O_2 decomposition, reducing overall oxidant efficiency. This imbalance is further complicated by the competing reactions inherent to the H_2 and O_2 system, including water formation and H_2O_2 hydrogenation, which limit net H_2O_2 availability, particularly on Pd rich surfaces. Together, these effects highlight that the key limitation is not solely H_2O_2 synthesis or utilisation in isolation, but the lack of integrated catalyst and process designs capable of synchronising H_2O_2 generation with controlled, selective utilisation for pollutant degradation, especially under conditions relevant to continuous water treatment systems.

In response to these challenges, this research aims to develop and optimise AuPd and AuPd-based heterogeneous catalysts via conventional wet co-impregnation and incipient wetness techniques for the in situ production of H_2O_2 and the subsequent reactive oxygen species (ROS), with application in both batch and continuous flow water treatment systems. The catalytic generation of oxidative species directly from molecular H_2 and O_2 presents a promising, cost-

effective alternative to conventional Fenton systems, while simultaneously mitigating the formation of harmful chemical residues typically associated with such treatments.

The aims of this thesis are outlined below:

1. **Develop novel Trimetallic AuPd-based Catalysts for the direct synthesis of H_2O_2**

Different amounts of the transition metals (e.g., Fe) will be introduced into AuPd catalysts to optimise the catalytic performance of trimetallic AuPd-based catalysts towards H_2O_2 synthesis and the H_2O_2 productivity, H_2O_2 selectivity and H_2 conversion will be evaluated. The optimised formulation will be benchmarked against previously reported AuPd-based trimetallic catalysts in short- and long-term H_2O_2 production tests, in terms of the accumulated H_2O_2 concentration (wt.%). Economic feasibility will be assessed by comparison with bimetallic AuPd and monometallic Pd systems to evaluate the industrial potential of the trimetallic formulations.

2. **Investigate the Efficacy of Pd/Pd-based and AuPd/AuPd-based catalysts for the in situ water treatment**

In situ water treatment tests will be conducted in a batch and continuous flow reactor, and the catalytic performance of Pd-based or AuPd-based catalysts towards the in situ H_2O_2 production and the subsequent ROS generation for the oxidation degradation of various organic pollutants will be examined to determine the degradation efficiency of the catalysts. The in situ pathway will be benchmarked against an ex situ Fenton process using commercial H_2O_2 to quantify efficiency. Long-term operation of organic pollutants degradation tests will be conducted in the flow condition to determine stability and industrial potential of the catalyst.

1.9 References

1. Anastas, P. T. Introduction: Green Chemistry. *Chem Rev* **107**, 2167–2168 (2007).
2. Anastas, P. & Eghbali, N. Green Chemistry: Principles and Practice. *Chem Soc Rev* **39**, 301–312 (2010).
3. Armor, J. N. A history of industrial catalysis. *Catal Today* **163**, 3–9 (2011).
4. Kumar, V. & Milewski, L. Humphrey Davy: At the vanguard of a new chemistry. *J Chem Educ* **62**, 397 (1985).
5. Wisniak, J. The History of Catalysis. From the Beginning to Nobel Prizes. *Educación Química* **21**, 60–69 (2010).
6. Roduner, E. Understanding catalysis. *Chem. Soc. Rev.* **43**, 8226–8239 (2014).
7. Ertl, G. Wilhelm Ostwald: Founder of Physical Chemistry and Nobel Laureate 1909. *Angewandte Chemie International Edition* **48**, 6600–6606 (2009).
8. Bravo-Suárez, J. J., Chaudhari, R. V & Subramaniam, B. Design of Heterogeneous Catalysts for Fuels and Chemicals Processing: An Overview. in *Novel Materials for Catalysis and Fuels Processing* vol. 1132 3–68 (American Chemical Society, 2013).
9. Cole-Hamilton, D. J. Homogeneous Catalysis--New Approaches to Catalyst Separation, Recovery, and Recycling. *Science (1979)* **299**, 1702–1706 (2003).
10. Pinault, N. & Bruce, D. W. Homogeneous catalysts based on water-soluble phosphines. *Coord Chem Rev* **241**, 1–25 (2003).
11. Costentin, C., Passard, G., Robert, M. & Savéant, J.-M. Ultraefficient homogeneous catalyst for the CO2-to-CO electrochemical conversion. *Proceedings of the National Academy of Sciences* **111**, 14990–14994 (2014).
12. Benkovic, S. J. & Hammes-Schiffer, S. A Perspective on Enzyme Catalysis. *Science (1979)* **301**, 1196–1202 (2003).
13. Long, C.-J. *et al.* Merging the Non-Natural Catalytic Activity of Lipase and Electrosynthesis: Asymmetric Oxidative Cross-Coupling of Secondary Amines with Ketones. *Angewandte Chemie* **134**, e202203666 (2022).
14. Salgado, C. A., dos Santos, C. I. A. & Vanetti, M. C. D. Microbial lipases: Propitious biocatalysts for the food industry. *Food Biosci* **45**, 101509 (2022).

15. Yang, Y., Cho, I., Qi, X., Liu, P. & Arnold, F. H. An enzymatic platform for the asymmetric amination of primary, secondary and tertiary C(sp3)–H bonds. *Nat Chem* **11**, 987–993 (2019).

16. Sheldon, R. A. & van Pelt, S. Enzyme immobilisation in biocatalysis: why, what and how. *Chem Soc Rev* **42**, 6223–6235 (2013).

17. Liang, S., Wu, X.-L., Xiong, J., Zong, M.-H. & Lou, W.-Y. Metal-organic frameworks as novel matrices for efficient enzyme immobilization: An update review. *Coord Chem Rev* **406**, 213149 (2020).

18. Schlögl, R. Heterogeneous Catalysis. *Angewandte Chemie International Edition* **54**, 3465–3520 (2015).

19. Huber, G. W., Iborra, S. & Corma, A. Synthesis of Transportation Fuels from Biomass: Chemistry, Catalysts, and Engineering. *Chem Rev* **106**, 4044–4098 (2006).

20. Rooke, J. C., Barakat, T., Siffert, S. & Su, B.-L. Total catalytic oxidation of toluene using Pd impregnated on hierarchically porous Nb2O5 and Ta2O5 supports. *Catal Today* **192**, 183–188 (2012).

21. Pu, X. & Shi, L. Commercial test of the catalyst for removal of trace olefins from aromatics and its mechanism. *Catal Today* **212**, 115–119 (2013).

22. Park, D. H. *et al.* Selective Petroleum Refining Over a Zeolite Catalyst with Small Intracrystal Mesopores. *Angewandte Chemie* **121**, 7781–7784 (2009).

23. Védrine, J. C. Metal Oxides in Heterogeneous Oxidation Catalysis: State of the Art and Challenges for a More Sustainable World. *ChemSusChem* **12**, 577–588 (2019).

24. An, Q., McDonald, M., Fortunelli, A. & Goddard, W. A. I. I. I. Controlling the Shapes of Nanoparticles by Dopant-Induced Enhancement of Chemisorption and Catalytic Activity: Application to Fe-Based Ammonia Synthesis. *ACS Nano* **15**, 1675–1684 (2021).

25. Fang, H. *et al.* Challenges and Opportunities of Ru-Based Catalysts toward the Synthesis and Utilization of Ammonia. *ACS Catal* **12**, 3938–3954 (2022).

26. Dey, S. & Chandra Dhal, G. Controlling carbon monoxide emissions from automobile vehicle exhaust using copper oxide catalysts in a catalytic converter. *Mater Today Chem* **17**, 100282 (2020).

27. Munoz, M., de Pedro, Z. M., Casas, J. A. & Rodriguez, J. J. Preparation of magnetite-based catalysts and their application in heterogeneous Fenton oxidation – A review. *Appl Catal B* **176–177**, 249–265 (2015).

28. Lin, J. *et al.* Functional Carbon Nitride Materials in Photo-Fenton-Like Catalysis for Environmental Remediation. *Adv Funct Mater* **32**, 2201743 (2022).

29. Duan, X., Sun, H. & Wang, S. Metal-Free Carbocatalysis in Advanced Oxidation Reactions. *Acc Chem Res* **51**, 678–687 (2018).

30. Kurian, M. Advanced oxidation processes and nanomaterials -a review. *Clean Eng Technol* **2**, 100090 (2021).

31. Miklos, D. B. *et al.* Evaluation of advanced oxidation processes for water and wastewater treatment – A critical review. *Water Res* **139**, 118–131 (2018).

32. Ross, J. R. H. Chapter 7 - The Kinetics and Mechanisms of Catalytic Reactions. in *Contemporary Catalysis* (ed. Ross, J. R. H.) 161–186 (Elsevier, Amsterdam, 2019). doi:https://doi.org/10.1016/B978-0-444-63474-0.00007-2.

33. Becker, C. From Langmuir to Ertl: The "Nobel" History of the Surface Science Approach to Heterogeneous Catalysis. in *Encyclopedia of Interfacial Chemistry* (ed. Wandelt, K.) 99–106 (Elsevier, Oxford, 2018). doi:https://doi.org/10.1016/B978-0-12-409547-2.13527-9.

34. Vogt, C. & Weckhuysen, B. M. The concept of active site in heterogeneous catalysis. *Nat Rev Chem* **6**, 89–111 (2022).

35. Zhao, D., Chen, J., Hu, X. & Zhang, S. Catalytic Antibodies: Design, Expression, and Their Applications in Medicine. *Appl Biochem Biotechnol* **195**, 1514–1540 (2023).

36. Logan, S. R. The origin and status of the Arrhenius equation. *J Chem Educ* **59**, 279 (1982).

37. Campos-Martin, J. M., Blanco-Brieva, G. & Fierro, J. L. G. Hydrogen Peroxide Synthesis: An Outlook beyond the Anthraquinone Process. *Angew. Chem. Int. Ed. Engl.* **45**, 6962–6984 (2006).

38. Ciriminna, R., Albanese, L., Meneguzzo, F. & Pagliaro, M. Hydrogen Peroxide: A Key Chemical for Today's Sustainable Development. *ChemSusChem* **9**, 3374–3381 (2016).

39. *Hydrogen Peroxide Market Size, Share & COVID-19 Impact Analysis*. (2021).

40. Sorokin, A. B. & Kudrik, E. V. Phthalocyanine metal complexes: Versatile catalysts for selective oxidation and bleaching. *Catal Today* **159**, 37–46 (2011).

41. Hâncu, D., Green, J. & Beckman, E. J. H2O2 in CO2/H2O Biphasic Systems: Green Synthesis and Epoxidation Reactions. *Ind Eng Chem Res* **41**, 4466–4474 (2002).

42. Uyanik, M. & Ishihara, K. Baeyer–Villiger Oxidation Using Hydrogen Peroxide. *ACS Catal* **3**, 513–520 (2013).

43. ten Brink, G.-J., Arends, I. W. C. E. & Sheldon, R. A. The Baeyer−Villiger Reaction: New Developments toward Greener Procedures. *Chem Rev* **104**, 4105–4124 (2004).

44. Crombie, C. M. *et al.* Enhanced Selective Oxidation of Benzyl Alcohol via In Situ H2O2 Production over Supported Pd-Based Catalysts. *ACS Catal* **11**, 2701–2714 (2021).

45. Huang, X. *et al.* Au–Pd separation enhances bimetallic catalysis of alcohol oxidation. *Nature* **603**, 271–275 (2022).

46. Yan, Q., Zhang, J. & Xing, M. Cocatalytic Fenton Reaction for Pollutant Control. *Cell Rep Phys Sci* **1**, 100149 (2020).

47. Shen, L. *et al.* Powdered activated coke for COD removal in the advanced treatment of mixed chemical wastewaters and regeneration by Fenton oxidation. *Chemical Engineering Journal* **371**, 631–638 (2019).

48. Wenderich, K. *et al.* Industrial feasibility of anodic hydrogen peroxide production through photoelectrochemical water splitting: a techno-economic analysis. *Sustain Energy Fuels* **4**, 3143–3156 (2020).

49. Mitraka, E. *et al.* Electrocatalytic Production of Hydrogen Peroxide with Poly(3,4-ethylenedioxythiophene) Electrodes. *Adv Sustain Syst* **3**, 1800110 (2019).

50. Gao, G. *et al.* Advances in the production technology of hydrogen peroxide. *Chinese J. Catal.* **41**, 1039–1047 (2020).

51. Samanta, C. Direct synthesis of hydrogen peroxide from hydrogen and oxygen: An overview of recent developments in the process. *Appl Catal A Gen* **350**, 133–149 (2008).

52. Flaherty, D. W. Direct Synthesis of H2O2 from H2 and O2 on Pd Catalysts: Current Understanding, Outstanding Questions, and Research Needs. *ACS Catal* **8**, 1520–1527 (2018).

53. Lewis, R. J. & Hutchings, G. J. Recent Advances in the Direct Synthesis of H2O2. *ChemCatChem* **11**, 298–308 (2019).

54. Ji, J., Wang, Z., Xu, Q., Zhu, Q. & Xing, M. In situ H2O2 Generation and Corresponding Pollutant Removal Applications: A Review. *Chemistry – A European Journal* **29**, e202203921 (2023).

55. Edwards, J. K. *et al.* Switching Off Hydrogen Peroxide Hydrogenation in the Direct Synthesis Process. *Science (1979)* **323**, 1037–1041 (2009).

56. Park, S. Y. *et al.* CaSnO3: An Electrocatalyst for Two-Electron Water Oxidation Reaction to Form H2O2. *ACS Energy Lett* **4**, 352–357 (2019).

57. Yang, X. *et al.* Tuning Two-Electron Oxygen-Reduction Pathways for H2O2 Electrosynthesis via Engineering Atomically Dispersed Single Metal Site Catalysts. *Advanced Materials* **34**, 2107954 (2022).

58. Liu, T. *et al.* Overall photosynthesis of H2O2 by an inorganic semiconductor. *Nat Commun* **13**, 1034 (2022).

59. Senthilnathan, S. *et al.* MoS2 modified g-C3N4 composite: A potential candidate for photocatalytic applications. *Journal of Saudi Chemical Society* **27**, 101717 (2023).

60. Siahrostami, S. H_2O_2 electrosynthesis and emerging applications, challenges, and opportunities: A computational perspective. *Chem Catalysis* **3**, (2023).

61. Yang, X. *et al.* Tuning Two-Electron Oxygen-Reduction Pathways for H2O2 Electrosynthesis via Engineering Atomically Dispersed Single Metal Site Catalysts. *Advanced Materials* **34**, 2107954 (2022).

62. Chen, S. *et al.* Defective Carbon-Based Materials for the Electrochemical Synthesis of Hydrogen Peroxide. *ACS Sustain Chem Eng* **6**, 311–317 (2018).

63. Siahrostami, S. *et al.* Enabling direct H2O2 production through rational electrocatalyst design. *Nat Mater* **12**, 1137–1143 (2013).

64. Lim, J. S., Sa, Y. J. & Joo, S. H. Catalyst design, measurement guidelines, and device integration for H2O2 electrosynthesis from oxygen reduction. *Cell Rep Phys Sci* **3**, 100987 (2022).

65. Ando, Y. & Tanaka, T. Proposal for a new system for simultaneous production of hydrogen and hydrogen peroxide by water electrolysis. *Int J Hydrogen Energy* **29**, 1349–1354 (2004).

66. Shi, X. *et al.* Epitaxial growth of WO3 nanoneedles achieved using a facile flame surface treatment process engineering of hole transport and water oxidation reactivity. *J Mater Chem A Mater* **6**, 19542–19546 (2018).

67. Shi, X., Zhang, Y., Siahrostami, S. & Zheng, X. Light-Driven BiVO4–C Fuel Cell with Simultaneous Production of H2O2. *Adv Energy Mater* **8**, 1801158 (2018).

68. Izgorodin, A., Izgorodina, E. & MacFarlane, D. R. Low overpotential water oxidation to hydrogen peroxide on a MnOx catalyst. *Energy Environ Sci* **5**, 9496–9501 (2012).

69. Kelly, S. R. *et al.* ZnO As an Active and Selective Catalyst for Electrochemical Water Oxidation to Hydrogen Peroxide. *ACS Catal* **9**, 4593–4599 (2019).

70. Xia, C. *et al.* Confined local oxygen gas promotes electrochemical water oxidation to hydrogen peroxide. *Nat Catal* **3**, 125–134 (2020).

71. Shi, X., Back, S., Gill, T. M., Siahrostami, S. & Zheng, X. Electrochemical Synthesis of H_2O_2 by Two-Electron Water Oxidation Reaction. *Chem* **7**, 38–63 (2021).

72. Chen, Z., Yao, D., Chu, C. & Mao, S. Photocatalytic H2O2 production Systems: Design strategies and environmental applications. *Chemical Engineering Journal* **451**, 138489 (2023).

73. Wang, Z. *et al.* Green and alcohol-free H2O2 generation paired with simultaneous contaminant treatment enabled by sulfur/cyano-modified g-C3N4 with efficient oxygen activation and proton adsorption. *Green Chemistry* **26**, 2730–2739 (2024).

74. Hao, J. *et al.* Robust Covalent Organic Frameworks for Photosynthesis of H2O2: Advancements, Challenges and Strategies. *Small* **20**, 2404139 (2024).

75. Wu, W. *et al.* Metal-free polymer photocatalysts for efficient gas-phase reduction of atmospheric CO2 and simultaneous H2O2 production. *Green Chemistry* **27**, 2766–2775 (2025).

76. Kumar, U., Pai, M. R. & Sinha, I. Evolution of H2O2 producing heterogeneous photocatalysts: A review. *J Environ Chem Eng* **13**, 117357 (2025).

77. Ma, S., Li, G. & Wang, X. Direct synthesis of hydrogen peroxide from H2/O2 and oxidation of thiophene over supported gold catalysts. *Chemical Engineering Journal* **156**, 532–539 (2010).

78. Wilson, N. M. & Flaherty, D. W. Mechanism for the Direct Synthesis of H2O2 on Pd Clusters: Heterolytic Reaction Pathways at the Liquid–Solid Interface. *J Am Chem Soc* **138**, 574–586 (2016).

79. Dissanayake, D. P. & Lunsford, J. H. The direct formation of H2O2 from H2 and O2 over colloidal palladium. *J Catal* **214**, 113–120 (2003).

80. Ntainjua N., E. *et al.* The role of the support in achieving high selectivity in the direct formation of hydrogen peroxide. *Green Chemistry* **10**, 1162–1169 (2008).

81. Staykov, A., Kamachi, T., Ishihara, T. & Yoshizawa, K. Theoretical Study of the Direct Synthesis of H2O2 on Pd and Pd/Au Surfaces. *The Journal of Physical Chemistry C* **112**, 19501–19505 (2008).

82. Ranganathan, S. & Volker Sieber. Recent Advances in the Direct Synthesis of Hydrogen Peroxide Using Chemical Catalysis—A Review. *Catalysts* **8**, 379 (2018).

83. Pospelova, T. A. & N. I. Kobozev. Palladium Catalyzed Synthesis of Hydrogen Peroxide from the Elements. 2. The Active Centers of Palladium in the Synthesis of H2o2. *Zhurnal Fizicheskoi Khimii* **35**, 535–542 (1961).

84. Dissanayake, D. P. & Lunsford, J. H. Evidence for the Role of Colloidal Palladium in the Catalytic Formation of H2O2 from H2 and O2. *J Catal* **206**, 173–176 (2002).

85. Lunsford, J. H. The direct formation of H2O2 from H2 and O2 over palladium catalysts. *J Catal* **216**, 455–460 (2003).

86. Chinta, S. & Lunsford, J. H. A mechanistic study of H2O2 and H2O formation from H2 and O2 catalyzed by palladium in an aqueous medium. *J Catal* **225**, 249–255 (2004).

87. Han, Y.-F. & Lunsford, J. H. Direct formation of H2O2 from H2 and O2 over a Pd/SiO2 catalyst: the roles of the acid and the liquid phase. *J Catal* **230**, 313–316 (2005).

88. Deguchi, T., Yamano, H. & Iwamoto, M. Kinetic and mechanistic studies on direct H2O2 synthesis from H2 and O2 catalyzed by Pd in the presence of H+ and Br− in water: A comprehensive paper. *Catal Today* **248**, 80–90 (2015).

89. Marshall, S. T. & Medlin, J. W. Surface-level mechanistic studies of adsorbate–adsorbate interactions in heterogeneous catalysis by metals. *Surf Sci Rep* **66**, 173–184 (2011).

90. Burch, R. & Ellis, P. R. An investigation of alternative catalytic approaches for the direct synthesis of hydrogen peroxide from hydrogen and oxygen. *Appl Catal B* **42**, 203–211 (2003).

91. Krishnan, V. V, Dokoutchaev, A. G. & Thompson, M. E. Direct Production of Hydrogen Peroxide with Palladium Supported on Phosphate Viologen Phosphonate Catalysts. *J Catal* **196**, 366–374 (2000).

92. Wilson, N. M. *et al.* Direct synthesis of H2O2 on PdZn nanoparticles: The impact of electronic modifications and heterogeneity of active sites. *J Catal* **368**, 261–274 (2018).

93. Chen, L., Medlin, J. W. & Grönbeck, H. On the Reaction Mechanism of Direct H2O2 Formation over Pd Catalysts. *ACS Catal* **11**, 2735–2745 (2021).

94. Adams, J. S. *et al.* Solvent molecules form surface redox mediators in situ and cocatalyze O2 reduction on Pd. *Science (1979)* **371**, 626–632 (2021).

95. Kanungo, S., van Haandel, L., Hensen, E. J. M., Schouten, J. C. & Neira d'Angelo, M. F. Direct synthesis of H2O2 in AuPd coated micro channels: An in-situ X-Ray absorption spectroscopic study. *J Catal* **370**, 200–209 (2019).

96. Liu, Q., Gath, K. K., Bauer, J. C., Schaak, R. E. & Lunsford, J. H. The Active Phase in the Direct Synthesis of H2O2 from H2 and O2 over Pd/SiO2 Catalyst in a H2SO4/Ethanol System. *Catal Letters* **132**, 342–348 (2009).

97. Choudhary, V. R., Sansare, S. D. & Gaikwad, A. G. Direct Oxidation of H2 to H2O2 and Decomposition of H2O2 Over Oxidized and Reduced Pd-Containing Zeolite Catalysts in Acidic Medium. *Catal Letters* **84**, 81–87 (2002).

98. Wang, F., Xia, C., de Visser, S. P. & Wang, Y. How Does the Oxidation State of Palladium Surfaces Affect the Reactivity and Selectivity of Direct Synthesis of Hydrogen Peroxide from Hydrogen and Oxygen Gases? A Density Functional Study. *J Am Chem Soc* **141**, 901–910 (2019).

99. Ouyang, L. *et al.* The origin of active sites for direct synthesis of H2O2 on Pd/TiO2 catalysts: Interfaces of Pd and PdO domains. *J Catal* **321**, 70–80 (2015).

100. Kim, S., Lee, D.-W., Lee, K.-Y. & Cho, E. A. Effect of Pd Particle Size on the Direct Synthesis of Hydrogen Peroxide from Hydrogen and Oxygen over Pd Core–Porous SiO2 Shell Catalysts. *Catal Letters* **144**, 905–911 (2014).

101. Tian, P. *et al.* The origin of palladium particle size effects in the direct synthesis of H2O2: Is smaller better? *J Catal* **349**, 30–40 (2017).

102. Yu, S. *et al.* High activity and selectivity of single palladium atom for oxygen hydrogenation to H2O2. *Nat Commun* **13**, 4737 (2022).

103. Landon, P., Collier, P. J., Papworth, A. J., Kiely, C. J. & Hutchings, G. J. Direct formation of hydrogen peroxide from H2/O2 using a gold catalyst. *Chemical Communications* 2058–2059 (2002) doi:10.1039/B205248M.

104. Li, J., Ishihara, T. & Yoshizawa, K. Theoretical Revisit of the Direct Synthesis of H2O2 on Pd and Au@Pd Surfaces: A Comprehensive Mechanistic Study. *The Journal of Physical Chemistry C* **115**, 25359–25367 (2011).

105. Han, S. & Mullins, C. B. Surface Alloy Composition Controlled O2 Activation on Pd–Au Bimetallic Model Catalysts. *ACS Catal* **8**, 3641–3649 (2018).

106. Han, Y.-F. *et al.* Au Promotional Effects on the Synthesis of H2O2 Directly from H2 and O2 on Supported Pd−Au Alloy Catalysts. *The Journal of Physical Chemistry C* **111**, 8410–8413 (2007).

107. Wilson, N. M., Priyadarshini, P., Kunz, S. & Flaherty, D. W. Direct synthesis of H2O2 on Pd and AuxPd1 clusters: Understanding the effects of alloying Pd with Au. *J Catal* **357**, 163–175 (2018).

108. Ouyang, L. *et al.* Insight into active sites of Pd–Au/TiO2 catalysts in hydrogen peroxide synthesis directly from H2 and O2. *J Catal* **311**, 129–136 (2014).

109. Ham, H. C., Hwang, G. S., Han, J., Nam, S. W. & Lim, T. H. On the Role of Pd Ensembles in Selective H2O2 Formation on PdAu Alloys. *The Journal of Physical Chemistry C* **113**, 12943–12945 (2009).

110. Svensson, R. & Grönbeck, H. Site Communication in Direct Formation of H2O2 over Single-Atom Pd@Au Nanoparticles. *J Am Chem Soc* **145**, 11579–11588 (2023).

111. Kim, I. *et al.* Studies on Catalytic Activity of Hydrogen Peroxide Generation according to Au Shell Thickness of Pd/Au Nanocubes. *ACS Appl Mater Interfaces* **10**, 38109–38116 (2018).

112. Kim, J.-S. *et al.* Catalytically Active Au Layers Grown on Pd Nanoparticles for Direct Synthesis of H2O2: Lattice Strain and Charge-Transfer Perspective Analyses. *ACS Nano* **13**, 4761–4770 (2019).

113. Landon, P. *et al.* Direct synthesis of hydrogen peroxide from H2 and O2 using Pd and Au catalysts. *Physical Chemistry Chemical Physics* **5**, 1917–1923 (2003).

114. Edwards, J. K. *et al.* Direct synthesis of hydrogen peroxide from H2 and O2 using TiO2-supported Au–Pd catalysts. *J Catal* **236**, 69–79 (2005).

115. Edwards, J. K. *et al.* Direct synthesis of hydrogen peroxide from H2 and O2 using Au–Pd/Fe2O3 catalysts. *J Mater Chem* **15**, 4595–4600 (2005).

116. Edwards, J. K. *et al.* Comparison of supports for the direct synthesis of hydrogen peroxide from H2 and O2 using Au–Pd catalysts. *Catal Today* **122**, 397–402 (2007).

117. Richards, T., Lewis, R. J., Morgan, D. J. & Hutchings, G. J. The Direct Synthesis of Hydrogen Peroxide Over Supported Pd-Based Catalysts: An Investigation into the Role of the Support and Secondary Metal Modifiers. *Catal Letters* **153**, 32–40 (2023).

118. Edwards, J. K. *et al.* Effect of acid pre-treatment on AuPd/SiO2 catalysts for the direct synthesis of hydrogen peroxide. *Catal Sci Technol* **3**, 812–818 (2013).

119. Edwards, J. K. *et al.* Direct Synthesis of H2O2 from H2 and O2 over Gold, Palladium, and Gold–Palladium Catalysts Supported on Acid-Pretreated TiO2. *Angew. Chem. Int. Ed. Engl.* **48**, 8512–8515 (2009).

120. Zhang, J. *et al.* Manipulation of the PdAu–PdAuOx interface on Pd-Au bimetallic catalysts for the direct synthesis of hydrogen peroxide. *Chinese Chemical Letters* 108446 (2023) doi:https://doi.org/10.1016/j.cclet.2023.108446.

121. Edwards, J. K. *et al.* The effect of heat treatment on the performance and structure of carbon-supported Au–Pd catalysts for the direct synthesis of hydrogen peroxide. *J Catal* **292**, 227–238 (2012).

122. Gu, J., Wang, S., He, Z., Han, Y. & Zhang, J. Direct synthesis of hydrogen peroxide from hydrogen and oxygen over activated-carbon-supported Pd–Ag alloy catalysts. *Catal Sci Technol* **6**, 809–817 (2016).

123. Khan Zainab, Dummer Nicholas F & Edwards Jennifer K. Silver–palladium catalysts for the direct synthesis of hydrogen peroxide. *Phil. Trans. R. Soc. A.* **376**, 1–12 (2018).

124. Zhang, J., Huang, B., Shao, Q. & Huang, X. Highly Active, Selective, and Stable Direct H2O2 Generation by Monodispersive Pd–Ag Nanoalloy. *ACS Appl Mater Interfaces* **10**, 21291–21296 (2018).

125. Quon, S. *et al.* Role of Pt atoms on Pd(1 1 1) surface in the direct synthesis of hydrogen peroxide: Nano-catalytic experiments and DFT calculations. *J Catal* **368**, 237–247 (2018).

126. Han, G.-H. *et al.* Tailored Palladium–Platinum Nanoconcave Cubes as High Performance Catalysts for the Direct Synthesis of Hydrogen Peroxide. *ACS Appl Mater Interfaces* **12**, 6328–6335 (2020).

127. Ntainjua, E. N., Freakley, S. J. & Hutchings, G. J. Direct Synthesis of Hydrogen Peroxide Using Ruthenium Catalysts. *Top Catal* **55**, 718–722 (2012).

128. Choudhary, V. R., Samanta, C. & Choudhary, T. V. Direct oxidation of H2 to H2O2 over Pd-based catalysts: Influence of oxidation state, support and metal additives. *Appl Catal A Gen* **308**, 128–133 (2006).

129. Deguchi, T., Yamano, H., Takenouchi, S. & Iwamoto, M. Enhancement of catalytic activity of Pd-PVP colloid for direct H2O2 synthesis from H2 and O2 in water with addition of 0.5 atom% Pt or Ir. *Catal Sci Technol* **8**, 1002–1015 (2018).

130. Tran, X. T., Vo, V. L. N. & Chung, Y.-M. Fast microwave-assisted synthesis of iron–palladium catalysts supported on graphite for the direct synthesis of H2O2. *Catal Today* **411–412**, 113821 (2023).

131. Wang, S., Gao, K., Li, W. & Zhang, J. Effect of Zn addition on the direct synthesis of hydrogen peroxide over supported palladium catalysts. *Appl Catal A Gen* **531**, 89–95 (2017).

132. Cao, K. *et al.* Efficient Direct H2O2 Synthesis Enabled by PdPb Nanorings via Inhibiting the O–O Bond Cleavage in O2 and H2O2. *ACS Catal* **11**, 1106–1118 (2021).

133. Naina, V. R. *et al.* Shape-Selective Synthesis of Intermetallic Pd3Pb Nanocrystals and Enhanced Catalytic Properties in the Direct Synthesis of Hydrogen Peroxide. *ACS Catal* **11**, 2288–2301 (2021).

134. Freakley, S. J. *et al.* Palladium-tin catalysts for the direct synthesis of H2O2 with high selectivity. *Science (1979)* **351**, 965–968 (2016).

135. Kovačič, D. *et al.* A comparative study of palladium-gold and palladium-tin catalysts in the direct synthesis of H2O2. *Green Chemistry* **25**, 10436–10446 (2023).

136. Li, H. *et al.* Layered Pd oxide on PdSn nanowires for boosting direct H2O2 synthesis. *Nat Commun* **13**, 6072 (2022).

137. Liu, S. *et al.* Understanding the Role of Boron on the Interface Modulation of the Pd/TiO2 Catalyst for Direct Synthesis of H2O2. *ACS Sustain Chem Eng* **10**, 3264–3275 (2022).

138. Ding, D. *et al.* Promotional effects of Sb on Pd-based catalysts for the direct synthesis of hydrogen peroxide at ambient pressure. *Chinese Journal of Catalysis* **39**, 673–681 (2018).

139. Tian, P. *et al.* Revealing the role of tellurium in palladium-tellurium catalysts for the direct synthesis of hydrogen peroxide. *J Catal* **385**, 21–29 (2020).

140. Edwards, J. K. *et al.* The Direct Synthesis of Hydrogen Peroxide Using Platinum-Promoted Gold–Palladium Catalysts. *Angew. Chem. Int. Ed. Engl.* **53**, 2381–2384 (2014).

141. Barnes, A., Lewis, R. J., Morgan, D. J., Davies, T. E. & Hutchings, G. J. Improving Catalytic Activity towards the Direct Synthesis of H2O2 through Cu Incorporation into AuPd Catalysts. *Catalysts* **12**, (2022).

142. Barnes, A., Lewis, R. J., Morgan, D. J., Davies, T. E. & Hutchings, G. J. Enhancing catalytic performance of AuPd catalysts towards the direct synthesis of H2O2 through incorporation of base metals. *Catal Sci Technol* **12**, 1986–1995 (2022).

143. Xu, H., Cheng, D. & Gao, Y. Design of High-Performance Pd-Based Alloy Nanocatalysts for Direct Synthesis of H2O2. *ACS Catal* **7**, 2164–2170 (2017).

144. Gong, X. *et al.* Enhanced catalyst selectivity in the direct synthesis of H2O2 through Pt incorporation into TiO2 supported AuPd catalysts. *Catal Sci Technol* **10**, 4635–4644 (2020).

145. Zhang, M. *et al.* Promoter role of tungsten in W-Pd/Al2O3 catalyst for direct synthesis of H2O2: Modification of Pd/PdO ratio. *Appl Catal A Gen* **628**, 118392 (2021).

146. Zhang, M., Xu, H., Luo, Y., Zhu, J. & Cheng, D. Enhancing the catalytic performance of PdAu catalysts by W-induced strong interaction for the direct synthesis of H2O2. *Catal Sci Technol* **12**, 5290–5301 (2022).

147. Fu, L. *et al.* Fabrication of the PdAu Surface Alloy on an Ordered Intermetallic Au3Cu Core for Direct H2O2 Synthesis at Ambient Pressure. *Ind Eng Chem Res* **61**, 11655–11665 (2022).

148. Ab Rahim, M. H. *et al.* Low temperature selective oxidation of methane to methanol using titania supported gold palladium copper catalysts. *Catal Sci Technol* **6**, 3410–3418 (2016).

149. Joshi, A. M., Delgass, W. N. & Thomson, K. T. Investigation of Gold−Silver, Gold−Copper, and Gold−Palladium Dimers and Trimers for Hydrogen Peroxide Formation from H2 and O2. *The Journal of Physical Chemistry C* **111**, 7384–7395 (2007).

150. Strokal, M. *et al.* Urbanization: an increasing source of multiple pollutants to rivers in the 21st century. *npj Urban Sustainability* **1**, 24 (2021).

151. Ahmed, M. *et al.* Recent developments in hazardous pollutants removal from wastewater and water reuse within a circular economy. *NPJ Clean Water* **5**, 12 (2022).

152. Kato, S. & Kansha, Y. Comprehensive review of industrial wastewater treatment techniques. *Environmental Science and Pollution Research* **31**, 51064–51097 (2024).

153. Sun, Y., Zhou, S., Chiang, P.-C. & Shah, K. J. Evaluation and optimization of enhanced coagulation process: Water and energy nexus. *Water-Energy Nexus* **2**, 25–36 (2019).

154. Abo, L. D. *et al.* Comprehensive review on co-integration of conventional systems and advanced oxidation processes for industrial and agricultural wastewater treatment applications. *Environmental Advances* **20**, 100638 (2025).

155. Brillas, E., Sirés, I. & Oturan, M. A. Electro-Fenton Process and Related Electrochemical Technologies Based on Fenton's Reaction Chemistry. *Chem Rev* **109**, 6570–6631 (2009).

156. Mortezazadeh, F., Ahmadi Nasab, M., Javid, A., Changani, F. & Dehghani, M. H. A review of UV-based advanced oxidation processes in wastewater treatment systems. *Desalination Water Treat* **323**, 101388 (2025).

157. Rekhate, C. V & Srivastava, J. K. Recent advances in ozone-based advanced oxidation processes for treatment of wastewater- A review. *Chemical Engineering Journal Advances* **3**, 100031 (2020).

158. Xiao, J., Guo, S., Wang, D. & An, Q. Fenton-Like Reaction: Recent Advances and New Trends. *Chemistry – A European Journal* **30**, e202304337 (2024).

159. Fenton, H. J. H. LXXIII.—Oxidation of tartaric acid in presence of iron. *Journal of the Chemical Society, Transactions* **65**, 899–910 (1894).

160. Bokare, A. D. & Choi, W. Review of iron-free Fenton-like systems for activating H2O2 in advanced oxidation processes. *J Hazard Mater* **275**, 121–135 (2014).

161. Fan, L. *et al.* Magnetically recoverable Fe3O4@polydopamine nanocomposite as an excellent co-catalyst for Fe3+ reduction in advanced oxidation processes. *Journal of Environmental Sciences* **92**, 69–78 (2020).

162. Xing, M. *et al.* Metal Sulfides as Excellent Co-catalysts for H_2O_2 Decomposition in Advanced Oxidation Processes. *Chem* **4**, 1359–1372 (2018).

163. Herrera, F., Kiwi, J., Lopez, A. & Nadtochenko, V. Photochemical Decoloration of Remazol Brilliant Blue and Uniblue A in the Presence of Fe3+ and H2O2. *Environ Sci Technol* **33**, 3145–3151 (1999).

164. Ma, J. *et al.* Fenton Degradation of Organic Compounds Promoted by Dyes under Visible Irradiation. *Environ Sci Technol* **39**, 5810–5815 (2005).

165. Ma, J. *et al.* Fenton Degradation of Organic Pollutants in the Presence of Low-Molecular-Weight Organic Acids: Cooperative Effect of Quinone and Visible Light. *Environ Sci Technol* **40**, 618–624 (2006).

166. Dong, H., Sans, C., Li, W. & Qiang, Z. Promoted discoloration of methyl orange in H2O2/Fe(III) Fenton system: Effects of gallic acid on iron cycling. *Sep Purif Technol* **171**, 144–150 (2016).

167. Qin, Y., Song, F., Ai, Z., Zhang, P. & Zhang, L. Protocatechuic Acid Promoted Alachlor Degradation in Fe(III)/H2O2 Fenton System. *Environ Sci Technol* **49**, 7948–7956 (2015).

168. Bolobajev, J., Trapido, M. & Goi, A. Improvement in iron activation ability of alachlor Fenton-like oxidation by ascorbic acid. *Chemical Engineering Journal* **281**, 566–574 (2015).

169. Zhu, L. *et al.* Designing 3D-MoS2 Sponge as Excellent Cocatalysts in Advanced Oxidation Processes for Pollutant Control. *Angewandte Chemie* **132**, 14072–14080 (2020).

170. Liu, J. *et al.* Molybdenum sulfide Co-catalytic Fenton reaction for rapid and efficient inactivation of Escherichia coli. *Water Res* **145**, 312–320 (2018).

171. Georgi, A., Velasco Polo, M., Crincoli, K., Mackenzie, K. & Kopinke, F.-D. Accelerated Catalytic Fenton Reaction with Traces of Iron: An Fe–Pd-Multicatalysis Approach. *Environ Sci Technol* **50**, 5882–5891 (2016).

172. Yi, Q. *et al.* Singlet Oxygen Triggered by Superoxide Radicals in a Molybdenum Cocatalytic Fenton Reaction with Enhanced REDOX Activity in the Environment. *Environ Sci Technol* **53**, 9725–9733 (2019).

173. Ma, J., Ma, W., Chen, C., Ji, H. & Zhao, J. An Efficient Anthraquinone–Resin Hybrid Co-Catalyst for Fenton-Like Reactions: Acceleration of the Iron Cycle Using a Quinone Cycle under Visible-Light Irradiation. *Chem Asian J* **6**, 2264–2268 (2011).

174. Li, T., Zhao, Z., Wang, Q., Xie, P. & Ma, J. Strongly enhanced Fenton degradation of organic pollutants by cysteine: An aliphatic amino acid accelerator outweighs hydroquinone analogues. *Water Res* **105**, 479–486 (2016).

175. Andjelković, M. *et al.* Iron-chelation properties of phenolic acids bearing catechol and galloyl groups. *Food Chem* **98**, 23–31 (2006).

176. Yan, Q., Zhang, J. & Xing, M. Cocatalytic Fenton Reaction for Pollutant Control. *Cell Rep Phys Sci* **1**, (2020).

177. Chen, C. *et al.* Overlooked self-catalytic mechanism in phenolic moiety-mediated Fenton-like system: Formation of Fe(III) hydroperoxide complex and co-treatment of refractory pollutants. *Appl Catal B* **321**, 122062 (2023).

178. Zhou, P. *et al.* Fast and Long-Lasting Iron(III) Reduction by Boron Toward Green and Accelerated Fenton Chemistry. *Angewandte Chemie International Edition* **59**, 16517–16526 (2020).

179. Cao, J. *et al.* Gambling of homogeneous and heterogeneous Fenton in wastewater treatment. *Cell Rep Phys Sci* **5**, (2024).

180. Chen, Y., Miller, C. J. & Waite, T. D. Heterogeneous Fenton Chemistry Revisited: Mechanistic Insights from Ferrihydrite-Mediated Oxidation of Formate and Oxalate. *Environ Sci Technol* **55**, 14414–14425 (2021).

181. Chen, X. *et al.* Bisulfite-assisted surface Fenton-like degradation of dimethyl phthalate by ferrihydrite-H2O2 system. *Chemical Engineering Journal* **452**, 139309 (2023).

182. Guo, L., Chen, F., Fan, X., Cai, W. & Zhang, J. S-doped α-Fe2O3 as a highly active heterogeneous Fenton-like catalyst towards the degradation of acid orange 7 and phenol. *Appl Catal B* **96**, 162–168 (2010).

183. Chen, F., Li, Y., Cai, W. & Zhang, J. Preparation and sono-Fenton performance of 4A-zeolite supported α-Fe2O3. *J Hazard Mater* **177**, 743–749 (2010).

184. Wang, Y., Gao, Y., Chen, L. & Zhang, H. Goethite as an efficient heterogeneous Fenton catalyst for the degradation of methyl orange. *Catal Today* **252**, 107–112 (2015).

185. Li, X., Huang, Y., Li, C., Shen, J. & Deng, Y. Degradation of pCNB by Fenton like process using α-FeOOH. *Chemical Engineering Journal* **260**, 28–36 (2015).

186. Chen, F., Xie, S., Huang, X. & Qiu, X. Ionothermal synthesis of Fe3O4 magnetic nanoparticles as efficient heterogeneous Fenton-like catalysts for degradation of organic pollutants with H2O2. *J Hazard Mater* **322**, 152–162 (2017).

187. Xu, L. & Wang, J. Fenton-like degradation of 2,4-dichlorophenol using Fe3O4 magnetic nanoparticles. *Appl Catal B* **123–124**, 117–126 (2012).

188. Zhang, S. *et al.* Superparamagnetic Fe3O4 nanoparticles as catalysts for the catalytic oxidation of phenolic and aniline compounds. *J Hazard Mater* **167**, 560–566 (2009).

189. Liu, W., Wang, Y., Ai, Z. & Zhang, L. Hydrothermal Synthesis of FeS2 as a High-Efficiency Fenton Reagent to Degrade Alachlor via Superoxide-Mediated Fe(II)/Fe(III) Cycle. *ACS Appl Mater Interfaces* **7**, 28534–28544 (2015).

190. Wang, M. *et al.* A crystallinity control strategy for controllable Heterogeneous-Homogeneous reaction and catalytic performance in wet-mechanochemical synthesized FeS2 Fenton system. *Sep Purif Technol* **355**, 129683 (2025).

191. He, J., Yang, X., Men, B. & Wang, D. Interfacial mechanisms of heterogeneous Fenton reactions catalyzed by iron-based materials: A review. *Journal of Environmental Sciences* **39**, 97–109 (2016).

192. Thomas, N., Dionysiou, D. D. & Pillai, S. C. Heterogeneous Fenton catalysts: A review of recent advances. *J Hazard Mater* **404**, 124082 (2021).

193. Yan, Q. *et al.* Constructing an Acidic Microenvironment by MoS2 in Heterogeneous Fenton Reaction for Pollutant Control. *Angewandte Chemie International Edition* **60**, 17155–17163 (2021).

194. Li, B. *et al.* Simple modulation of Fe-based single atoms/clusters catalyst with acidic microenvironment for ultrafast Fenton-like reaction. *Appl Catal B* **304**, 121009 (2022).

195. Zheng, J., Li, Y. & Zhang, S. Engineered nanoconfinement activates Fenton catalyst at neutral pH: Mechanism and kinetics study. *Appl Catal B* **343**, 123555 (2024).

196. Su, L. *et al.* Construction of Fenton-like systems based on hierarchical nanoconfinement for efficient antibiotic removal. *J Environ Chem Eng* **13**, 116427 (2025).

197. Yang, Z., Qian, J., Yu, A. & Pan, B. Singlet oxygen mediated iron-based Fenton-like catalysis under nanoconfinement. *Proceedings of the National Academy of Sciences* **116**, 6659–6664 (2019).

198. Zhang, X. *et al.* Nanoconfinement-triggered oligomerization pathway for efficient removal of phenolic pollutants via a Fenton-like reaction. *Nat Commun* **15**, 917 (2024).

199. Chen, T. *et al.* Robust Fe-N4-C6O2 single atom sites for efficient PMS activation and enhanced FeIV = O reactivity. *Nat Commun* **16**, 2402 (2025).

200. Li, C. *et al.* Self-suspending catalysts with Co-N4 sites in conjugated polymers for complete PMS-to-Co(IV)=O conversion to enhance ranitidine degradation. *Chemical Engineering Journal* **521**, 166564 (2025).

201. Miao, J. *et al.* Single-Atom MnN5 Catalytic Sites Enable Efficient Peroxymonosulfate Activation by Forming Highly Reactive Mn(IV)–Oxo Species. *Environ Sci Technol* **57**, 4266–4275 (2023).

202. Li, J., Le, Q. & Nan, Z. Boosting Fe Atom Density and Forming Fe(IV) via Fe–N5 Generation in the Catalyst for H2O2-Based Fenton Reaction. *Langmuir* **41**, 21728–21736 (2025).

203. Liu, Y., Zhao, Y. & Wang, J. Fenton/Fenton-like processes with in-situ production of hydrogen peroxide/hydroxyl radical for degradation of emerging contaminants: Advances and prospects. *J Hazard Mater* **404**, 124191 (2021).

204. Hoffman, A. J., Carraway, E. R. & Hoffmann, M. R. Photocatalytic Production of H2O2 and Organic Peroxides on Quantum-Sized Semiconductor Colloids. *Environ Sci Technol* **28**, 776–785 (1994).

205. Shiraishi, F., Nakasako, T. & Hua, Z. Formation of Hydrogen Peroxide in Photocatalytic Reactions. *J Phys Chem A* **107**, 11072–11081 (2003).

206. Xu, Y. *et al.* Fabrication of magnetic BaFe12O19/Ag3PO4 composites with an in situ photo-Fenton-like reaction for enhancing reactive oxygen species under visible light irradiation. *Catal Sci Technol* **9**, 2563–2570 (2019).

207. Zhang, J. *et al.* Carbon nanodot-modified FeOCl for photo-assisted Fenton reaction featuring synergistic in-situ H2O2 production and activation. *Appl Catal B* **266**, 118665 (2020).

208. Yang, Z. & Wang, J. Photo-Fenton degradation of sulfamethazine using self-assembled CdS nanorods with in-situ production of H2O2 at wide pH range. *Chemical Engineering Journal* **450**, 138024 (2022).

209. Liu, M. *et al.* An efficient photo Fenton system for in-situ evolution of H2O2 via defective iron-based metal organic framework@ZnIn2S4 core-shell Z-scheme heterojunction nanoreactor. *J Hazard Mater* **437**, 129436 (2022).

210. Fan, Q.-Q. *et al.* Insights into the role of reactive oxygen species in photocatalytic H2O2 generation and OTC removal over a novel BN/Zn3In2S6 heterojunction. *J Hazard Mater* **438**, 129483 (2022).

211. Chen, C.-B. *et al.* Cyano-rich mesoporous carbon nitride nanospheres for visible-light-driven photocatalytic degradation of pollutants. *Environ Sci Nano* **5**, 2966–2977 (2018).

212. Wang, Y. *et al.* A novel solar photo-Fenton system with self-synthesizing H2O2: Enhanced photo-induced catalytic performances and mechanism insights. *Appl Surf Sci* **512**, 145650 (2020).

213. Torres-Pinto, A., Sampaio, M. J., Silva, C. G., Faria, J. L. & Silva, A. M. T. Metal-free carbon nitride photocatalysis with in situ hydrogen peroxide generation for the degradation of aromatic compounds. *Appl Catal B* **252**, 128–137 (2019).

214. Ju, Y. *et al.* Solar-driven on-site H2O2 generation and tandem photo-Fenton reaction on a triphase interface for rapid organic pollutant degradation. *Chemical Engineering Journal* **430**, 133168 (2022).

215. Hu, J. *et al.* Screen superior ultra-thin g-C3N4 material for photocatalytic in-situ H2O2 production to remove tetracycline. *Appl Surf Sci* **576**, 151841 (2022).

216. Kumar, U., Pai, M. R. & Sinha, I. Evolution of H2O2 producing heterogeneous photocatalysts: A review. *J Environ Chem Eng* **13**, 117357 (2025).

217. Teng, Z. *et al.* Photoexcited single metal atom catalysts for heterogeneous photocatalytic H2O2 production: Pragmatic guidelines for predicting charge separation. *Appl Catal B* **282**, 119589 (2021).

218. Zhang, Y.-Z., Liang, C., Feng, H.-P. & Liu, W. Nickel single atoms anchored on ultrathin carbon nitride for selective hydrogen peroxide generation with enhanced photocatalytic activity. *Chemical Engineering Journal* **446**, 137379 (2022).

219. Liu, Y. *et al.* Efficient Mineralization of Perfluorooctanoate by Electro-Fenton with H2O2 Electro-generated on Hierarchically Porous Carbon. *Environ Sci Technol* **49**, 13528–13533 (2015).

220. Chen, C.-Y. *et al.* Oxygen Reduction Reaction on Graphene in an Electro-Fenton System: In Situ Generation of H2O2 for the Oxidation of Organic Compounds. *ChemSusChem* **9**, 1194–1199 (2016).

221. Wang, C.-T., Chou, W.-L., Chung, M.-H. & Kuo, Y.-M. COD removal from real dyeing wastewater by electro-Fenton technology using an activated carbon fiber cathode. *Desalination* **253**, 129–134 (2010).

222. Panizza, M. & Cerisola, G. Electro-Fenton degradation of synthetic dyes. *Water Res* **43**, 339–344 (2009).

223. Wang, Y. *et al.* Dimethyl phthalate degradation at novel and efficient electro-Fenton cathode. *Appl Catal B* **156–157**, 1–7 (2014).

224. Liu, K., Yu, J. C.-C., Dong, H., Wu, J. C. S. & Hoffmann, M. R. Degradation and Mineralization of Carbamazepine Using an Electro-Fenton Reaction Catalyzed by Magnetite Nanoparticles Fixed on an Electrocatalytic Carbon Fiber Textile Cathode. *Environ Sci Technol* **52**, 12667–12674 (2018).

225. Zhou, L., Zhou, M., Hu, Z., Bi, Z. & Serrano, K. G. Chemically modified graphite felt as an efficient cathode in electro-Fenton for p-nitrophenol degradation. *Electrochim Acta* **140**, 376–383 (2014).

226. Yang, W., Zhou, M., Oturan, N., Li, Y. & Oturan, M. A. Electrocatalytic destruction of pharmaceutical imatinib by electro-Fenton process with graphene-based cathode. *Electrochim Acta* **305**, 285–294 (2019).

227. Shen, X. *et al.* In Situ-Formed PdFe Nanoalloy and Carbon Defects in Cathode for Synergic Reduction–Oxidation of Chlorinated Pollutants in Electro-Fenton Process. *Environ Sci Technol* **54**, 4564–4572 (2020).

228. Liu, X.-C. *et al.* Cathode-Introduced Atomic H* for Fe(II)-Complex Regeneration to Effective Electro-Fenton Process at a Natural pH. *Environ Sci Technol* **53**, 6927–6936 (2019).

229. Fdez-Sanromán, A., Acevedo-García, V., Pazos, M., Sanromán, M. Á. & Rosales, E. Iron-doped cathodes for electro-Fenton implementation: Application for pymetrozine degradation. *Electrochim Acta* **338**, 135768 (2020).

230. Asgari, G. *et al.* Carbon felt modified with N-doped rGO for an efficient electro-peroxone process in diuron degradation and biodegradability improvement of wastewater from a pesticide manufacture: Optimization of process parameters, electrical energy consumption and degradation pathway. *Sep Purif Technol* **274**, 118962 (2021).

231. Gao, Y. *et al.* Anthraquinone (AQS)/polyaniline (PANI) modified carbon felt (CF) cathode for selective H2O2 generation and efficient pollutant removal in electro-Fenton. *J Environ Manage* **304**, 114315 (2022).

232. Ni, Y., Zhou, C., Xing, M. & Zhou, Y. Oxidation of emerging organic contaminants by in-situ H2O2 fenton system. *Green Energy & Environment* **9**, 417–434 (2024).

233. Qin, Y. *et al.* Ov-rich γ-MnO2 enhanced electrocatalytic three-electron oxygen reduction to hydroxyl radicals for sterilization in neutral media. *Nanoscale Horiz* **9**, 1999–2006 (2024).

234. Xiao, F. *et al.* Selective Electrocatalytic Reduction of Oxygen to Hydroxyl Radicals via 3-Electron Pathway with FeCo Alloy Encapsulated Carbon Aerogel for Fast and Complete Removing Pollutants. *Angewandte Chemie International Edition* **60**, 10375–10383 (2021).

235. Xie, L. *et al.* The strong metal–support interactions induced electrocatalytic three-electron oxygen reduction to hydroxyl radicals for water treatment. *Proceedings of the National Academy of Sciences* **120**, e2307989120 (2023).

236. Wang, Z., Hu, N., Wang, L., Zhao, H. & Zhao, G. In Situ Production of Hydroxyl Radicals via Three-Electron Oxygen Reduction: Opportunities for Water Treatment. *Angewandte Chemie International Edition* **63**, e202407628 (2024).

237. Underhill, R. *et al.* Oxidative Degradation of Phenol using in situ Generated Hydrogen Peroxide Combined with Fenton's Process. *Johnson Matthey Technology Review* **62**, 417–425 (2018).

238. Santos, A. *et al.* The degradation of phenol via in situ H2O2 production over supported Pd-based catalysts. *Catal Sci Technol* **11**, 7866–7874 (2021).

239. Santos, A. *et al.* The oxidative degradation of phenol via in situ H2O2 synthesis using Pd supported Fe-modified ZSM-5 catalysts. *Catal Sci Technol* **12**, 2943–2953 (2022).

240. He, J. *et al.* Direct synthesis of H2O2 over Pd-In/TiO2 and in situ activation toward tetracycline degradation. *Mater Res Bull* **192**, 113584 (2025).

241. Richards, T. *et al.* A residue-free approach to water disinfection using catalytic in situ generation of reactive oxygen species. *Nat Catal* **4**, 575–585 (2021).

Chapter 2 - Experimental

2.1 Materials and Reagents Used

All the chemical reagents and materials used during experiments (**Chapters 3 to 5)** in this thesis are listed below and were used as-recieved:

• $HAuCl_4.3H_2O$ (99.99% trace metals basis, 30 wt.% dil. HCl, Strem Chemicals)

• $PdCl_2$ (Reagent Plus®, 99.9% trace metals basis, Sigma Aldrich)

• $FeCl_2$ (Reagent Plus®, 99.9% trace metals basis, Sigma Aldrich)

• $FeCl_3$ (Reagent Plus®, 99.9% trace metals basis, Sigma Aldrich)

• $CuCl_2$ (Reagent Plus®, 99.9% trace metals basis, Sigma Aldrich)

• $NiCl_2$ (Reagent Plus®, 99.9% trace metals basis, Sigma Aldrich)

• $MnCl_2$ (Reagent Plus®, 99.9% trace metals basis, Sigma Aldrich)

• $CoCl_2$ (Reagent Plus®, 99.9% trace metals basis, Sigma Aldrich)

• TiO_2 (p25, Rutile: Anatase 85:15, 99.9% trace metals basis, 20 nm, Degussa)

• MeOH (HPLC grade, Sigma Aldrich)

• EtOH (HPLC grade, Sigma Aldrich)

• *tert*-Butanol (≥99.5%, Sigma Aldrich)

• Acetonitrile (HPLC grade, Sigma Aldrich)

• H_2O (HPLC grade, Sigma Aldrich)

• H_2O_2 (50 wt.%, stabilised, Sigma Aldrich)

• $Ce(SO_4)_2$ (Sigma Aldrich)

• $K_2TiO(C_2O_4)_2 \cdot 2H_2O$ (Sigma Aldrich)

• 1,10-Phenanthroline iron(II) sulfate (0.1 wt.% in H_2O, Sigma Aldrich)

• $(NH_4)_2SO_4.FeSO_4.6H_2O$ (99%, ACS reagent, Sigma Aldrich)

• HCl (37%, ACS reagent, Sigma Aldrich)

• H_2SO_4 (95%-98%, ACS reagent, Sigma Aldrich)

• SiC (coarse, 46 grit, Thermo Fisher Scientific)

• Hydrazine (35 wt.% in H_2O, Sigma Aldrich)

• Phenol (≥ 99%, Sigma Aldrich)

• Bisphenol A (≥ 99%, Supelco)

• Carbamazepine (Analytical standard, Supelco)

• Ibuprofen (Pharmaceutical Secondary Standard, Certified Reference Material, Supelco)

• Tetracycline hydrochloride (VETRANAL®, analytical standard, Supelco)

• 5-fluorouracil (≥ 99% purity (HPLC), poweder, Sigma Aldrich)

• Atrazine (PESTANAL®, analytical standard, Supelco)

• Quinmerac (PESTANAL®, analytical standard, Supelco)

• Clopyralid (PESTANAL®, analytical standard, Supelco)

2.2 Catalysts Preparation

2.2.1 Pd-based catalysts prepared by the wet impregnation method

A series of monometallic Au, Pd, Fe, bimetallic AuPd, PdFe, AuFe, and trimetallic AuPdFe catalysts were prepared by the wet co-impregnation method.[1] For investigation in the direct synthesis of H_2O_2 (catalysts used in **Chapter 3** and **Chapter 4**) and in situ degradation of phenol (catalysts used in **Chapter 4**).

The procedure to produce 2 g of $Au_{0.5}Pd_{0.5}Fe_2/TiO_2$ is outlined below. For Au and Pd precursors, the $HAuCl_4{\cdot}3H_2O$ was used as a gold precursor and was dissolved in deionised water to form a solution with a gold concentration of 12.4 mg mL^{-1}, and $PdCl_2$ was dissolved in deionised water with 1 ml of HCl (37%) and vigorous stirring to form a Pd precursor with a concentration of 5.84 mg mL^{-1}. Pd precursor (1.713 mL, 5.84 mg mL^{-1}) and Au precursor (0.806 mL, 12.4 mg mL^{-1}), and Fe precursor (0.1198 g $FeCl_3$) was dissolved in 10 mL deionised water and sonicated for 5 mins) were charged into a clean 50 mL round-bottom flask fitted with a magnetic stirrer bar. The volume of the solution was adjusted to 16 mL using deionised water. The flask was then immersed in an oil bath sitting on a magnetic stirrer hot plate. The solution was stirred (600 rpm), and the temperature of the oil bath was raised from room

temperature (20 ºC) to 65 °C. At 65 °C, TiO_2 (1.9796 g, P25) was added to the mixed solution with constant stirring. Following this, the temperature was raised to 85 °C for 16 h to complete water evaporation. The resulting solid was ground to a fine powder prior to heat treatment in a reductive atmosphere (flowing 5% H_2/Ar, 400 °C, 4 h, 10 °C min^{-1}).

2.2.2 Pd-based catalysts prepared by the incipient wetness method

A series of monometallic Au, Pd, bimetallic AuPd, PdFe, and trimetallic AuPdFe catalysts by the wet incipient method for the investigation in the direct synthesis of H_2O_2 and in situ oxidative degradation of various organic pollutants (catalysts used in **Chapter 5**).[2]

The procedure to generate 10 g of $Au_{0.5}Pd_{0.5}/TiO_2$ is outlined below. A TiO_2 (P25) to liquid mass ratio of 5:3.8 was used, corresponding to 7.52 g of total liquid per 9.9 g of TiO_2. For the preparation of 10 g of $Au_{0.5}Pd_{0.5}/TiO_2$, appropriate amounts of solid $HAuCl_4 \cdot 3H_2O$ (0.1 g) and $PdCl_2$ (0.083 g) were first weighed separately into individual vials. The precursors were subsequently combined and dissolved in a solution comprising 2.0 g of HCl and 5.52 g of deionised water to form a homogeneous AuPd precursor solution. Separately, 9.9 g of TiO_2 was weighed into a 250 mL glass beaker, into which the precursor solution was gradually introduced under continuous manual stirring using a glass rod. The resulting slurry was dried in an oven at 60 °C for 12 hours. Upon drying, the material was gently crushed to break down agglomerates and ground into a fine powder using an agate mortar. The powder was then dispersed in a freshly prepared 5% hydrazine solution (prepared by diluting concentrated 35% hydrazine as required) by mixing 10 mL of the 5% hydrazine solution in 240 mL of deionised water. This reducing solution was added to the powder and stirred until a uniform dark navy or black colour developed, indicative of the successful reduction of Au and Pd species. The suspension was left to settle for 30 minutes, followed by careful decantation of the supernatant. The washing procedure was repeated at least three times using 250 mL of deionised water to ensure the removal of residual hydrazine. Finally, the material was dried at 100 °C overnight (12 hours) and ground again to obtain fine powder, which was subsequently labelled and stored for catalytic testing.

2.3 Catalyst Testing

2.3.1 Batch Reactor-High Pressure Autoclave

The reactions associated with H_2O_2 synthesis and degradation took place within a Parr Instruments stainless steel autoclave, specifically designed with a capacity of 100 mL and a maximum operational pressure of up to 2000 psi (140 bar, gauged pressure). This autoclave is equipped with an overhead mechanical stirrer capable of rotating between 0 and 2000 rpm, facilitating the monitoring of both temperature and pressure. To maintain the desired temperature, a cooling jacket is employed, and gas introduction is facilitated by three lines connected to pre-mixed gas cylinders (CO_2 and CO_2 diluted gases: 5% H_2/CO_2, 25% O_2/CO_2, CO_2; N_2 and N_2 diluted gases: 5% H_2/N_2, 25% O_2/N_2, N_2). The procedural steps for the direct synthesis were adapted from previous literature in the field.[1,3,4] The detailed autoclave diagram, including the internal structure and external gas lines (using CO_2 and CO_2 diluted gases as an example), the structure of the autoclave (pressure panel, overhead stirrer, steel stirring bar, etc), and a liner, is shown in **Figure 2.1**.

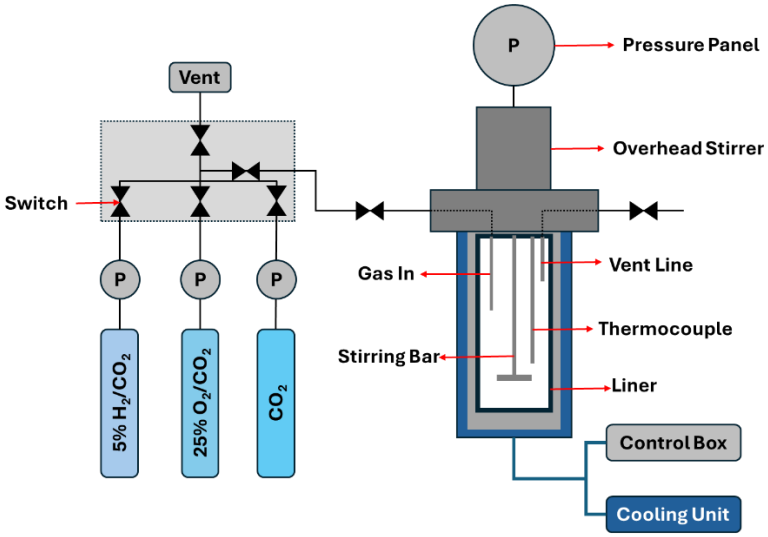

Figure 2.1. The schematic plot of the high-pressure autoclave reactor for the direct synthesis of H_2O_2, H_2O_2 degradation, and in situ phenol degradation using CO_2 and CO_2 diluted gases (**Chapters 3** and **4**). To run reactions using N_2 and N_2 diluted gases, simply change the gas cylinders. **Please note:** this plot was created by the author and is based on an actual high-pressure Parr Instruments stainless steel autoclave reactor.

2.3.2 Ideal Direct synthesis of H_2O_2 in a batch reactor

The ideal reaction conditions for H_2O_2 synthesis and degradation were previously determined by Santos et al.[3] A typical H_2O_2 synthesis in **Chapter 3** involves charging the PTFE liner in the autoclave with catalyst (0.01 g), solvent (mixed with 5.6 g CH_3OH and 2.9 g H_2O) and purging three times with 5% H_2/CO_2 (100 psi) before filling with 420 psi 5% H_2/CO_2 and 160 psi 25% O_2/CO_2, to give a H_2:O_2 ratio of 1:2. The reaction mixture was then cooled to the desired temperature (2 °C), before stirring commenced (1200 rpm) and the reaction time of 30 minutes began.After 30 mins, filter paper was used to separate solid catalyst and the post-reaction solutions. H_2O_2 yield was then determined by titrating filtered post-reaction solutions (0.5 g post-reaction solution mixed with 5% H_2SO_4 acidified ferroin indicator (1,10-phenanthroline iron(II) sulphate, 0.025M)) with acidified $Ce(SO_4)_2$ solution (ca. 8×10^{-3} M, the calibration procedure to determine the concentration of $Ce(SO_4)_2$ was outlined in **section 2.3.6**). The calculation of H_2O_2 yield was outlined in **Section 2.3.7**. Catalyst productivities are reported as mol_{H2O2} kg_{cat}^{-1} h^{-1}, with error bars being assigned based on a standard deviation of at least 3 repeat experiments.

If needed, the H_2 conversion rate (%) of the catalyst during the 30-minute reaction was determined by comparing the post-reaction H_2:CO_2 ratio, calculated using GC analysis on the post-reaction gas, with the initial H_2:CO_2 ratio obtained from a blank test. In the blank test, the reaction conditions remained the same for the direct synthesis of H_2O_2, except for the absence of a catalyst in the reactant mixture. The specific calculation method is presented in **Section 2.3.7**.

2.3.3 Ideal H_2O_2 degradation in a batch reactor

The reaction conditions for H_2O_2 degradation remained the same as H_2O_2 synthesis, apart from not feeding 25% O_2/CO_2 into the autoclave. In **Chapter 3**, a reactant solution contained 4 wt.% H_2O_2 (0.68 g 50 wt.% H_2O_2, 2.22 g H_2O, and 5.6 g CH_3OH). After mixing, weigh out 0.03 g and mix with acidified ferroin indicator (as before reaction samples) before mixing with the catalyst (0.01 g). Purge three times with 5% H_2/CO_2 (100 psi) and further fill to 420 psi with 5% H_2/CO_2 in the PTFE liner in the in the reactor. The reaction mixture was subsequently dropped to the target temperature of 2 °C, following which stirring was initiated at 1200 rpm for 30 minutes. H_2O_2 concentrations of before-reaction solutions and post-reaction solutions

were determined by titrating the solutions (0.03 g before-reaction/post-reaction solution, mixed with acidified ferroin indicator) with acidified $Ce(SO_4)_2$ solution (ca. 8×10^{-3} M). The degradation activity is reported as mol_{H2O2} kg_{cat}^{-1} h^{-1}, with error bars being assigned based on a standard deviation of at least 3 repeat experiments.

2.3.4 Non-Ideal direct synthesis of H_2O_2 in batch reactor

The non-ideal reaction conditions for direct H_2O_2 synthesis in **Chapter 4** involve charging the glass liner in the autoclave with catalyst (0.01 g), using pure water rather than water/methonal mixture (8.5 g H_2O) and purging three times with 5% H_2/CO_2 (100 psi) before filling with 420 psi 5% H_2/CO_2 and 160 psi 25% O_2/CO_2, to give a H_2:O_2 ratio of 1:2. The reaction mixture was then cooled to room temperature (20 °C), before stirring commenced (1200 rpm) and the reaction time of 30 minutes began. H_2O_2 yield was then determined by titrating filtered post-reaction solutions (0.5 g post-reaction solution mixed with 5%H_2SO_4 acidified ferroin indicator with acidified $Ce(SO_4)_2$ solution (ca. 8×10^{-3} M). Catalyst productivities are reported as mol_{H2O2} kg_{cat}^{-1} h^{-1}, with error bars being assigned based on a standard deviation of at least 3 repeat experiments. For the direct synthesis of H_2O_2 in **Chapter 5**, maintain the same reaction conditions except changing the CO_2-diluted gases (5% H_2/CO_2, 25% O_2/CO_2) to N_2-diluted gases (5% H_2/N_2, 25% O_2/N_2).

2.3.5 Non-Ideal H_2O_2 degradation in batch reactor

The non-ideal reaction conditions for H_2O_2 degradation in **Chapter 4** remained the same manner as the H_2O_2 synthesis in **Section 2.3.4**, apart from not feeding 25% O_2/CO_2 into the autoclave. A reactant solution contained 4 wt.% H_2O_2 (0.68 g 50 wt.% H_2O_2, 7.82 g H_2O), then mixed with catalyst (0.01 g) before being purged three times with 5% H_2/CO_2 (100 psi) and further filled to 420 psi with 5% H_2/CO_2. The reaction was subsequently conducted at a room temperature of 20 °C, following which stirring was initiated at 1200 rpm for 30 minutes. H_2O_2 yields of before-reaction solutions and post-reaction solutions were determined by titrating the solutions (0.03 g before-reaction/post-reaction solution, mixed with acidified ferroin indicator) with acidified $Ce(SO_4)_2$ solution (ca. 8×10^{-3} M). The degradation activity is reported as mol_{H2O2} kg_{cat}^{-1} h^{-1}, with error bars being assigned based on a standard deviation of at least 3 repeat experiments. For the H_2O_2 degradation tests in **Chapter 5**, maintain the same reaction conditions except changing the CO_2-diluted gases (5% H_2/CO_2) to N_2-diluted gases (5% H_2/N_2).

2.3.6 Preparation and Calibration of $Ce(SO_4)_2$ solution

The concentration of the H_2O_2 from the before or post-reaction solution of the direct synthesis tests was determined by the $Ce(SO_4)_2$ method, based on the following interaction between H_2O_2 and $Ce(SO_4)_2$, which has been extensively used in previous H_2O_2 synthesis studies (**Eq. 2.1**)[1,3–5]:

$$H_2O_2 + 2Ce(SO_4)_2 - Ce_2(SO_4)_3 + H_2SO_4 + O_2 \quad (\mathbf{Eq.\,2.1})$$

To prepare 2 L of $Ce(SO_4)_2$ solution, 6 g of $Ce(SO_4)_2$ was dissolved in 80 mL of H_2SO_4 (95%, ACS reagent, Sigma Aldrich), and the mixture was then topped up to 2 L with DI H_2O and string overnight before calibration. To accurately determine the concentration of acidified $Ce(SO_4)_2$ solution, Ammonium iron (II) sulphate 6-hydrate ($(NH_4)_2SO_4.FeSO_4.6H_2O$) was used. 0.02 g $(NH_4)_2SO_4.FeSO_4.6H_2O$ was dissolved in 2 mL of 2%H_2SO_4. Complete dissolution was ensured by sonicating each batch for 10 minutes. Subsequently, two drops of ferroin indicator were added to each of the 6 prepared solution mixtures, as well as 1 additional blank batch (only 2 ml of 2%H_2SO_4). The resulting solutions were then titrated individually against $Ce(SO_4)_2$ to quantitatively determine the concentration.

2.3.7 Calculating in the direct H_2O_2 synthesis and degradation tests

H_2O_2 productivity, degradation, selectivity, and H_2 conversion are considered vital factors for screening and identifying ideal catalysts among a series of them. Three samples were prepared, each mixed with filtered post-reaction solutions (0.5 g per sample) and two drops of acidified ferroin indicator. A titration was then conducted using acidified $Ce(SO_4)_2$ solution (ca. 8×10^{-3} M). This titration can be manipulated to produce a productivity/degradation value, together with the H_2 conversion rate, and further calculate H_2O_2 selectivity. The equations used to calculate these values are provided below:

2.3.7.1 Calculating H_2O_2 Productivity

Initially, the volume of $Ce(SO_4)_2$ solution (ml) consumed by the entire 8.5g post-reaction solution was obtained by converting the average volume of $Ce(SO_4)_2$ solution consumed by the titration of three 0.5 g post-reaction samples (**Eq. 2.2**):

$$Volume\ of\ Ce(SO_4)_2\ solution = \frac{(Sample\ 1 + Sample\ 2 + Sample\ 3)}{3} \times \frac{8.5}{Sample\ Mass} \quad (\mathbf{Eq.\,2.2})$$

The concentration of $Ce(SO_4)_2$ solution was calibrated in **Section 2.3.6** and the moles of $Ce(SO_4)_2$ could be calculated (**Eq. 2.3**):

$$Moles\ of\ Ce(SO_4)_2 = \frac{Volumn\ of\ Ce(SO_4)_2 \times Concentration\ of Ce(SO_4)_2}{1000} \quad (\mathbf{Eq.\ 2.3})$$

Based on the redox reaction, the stoichiometric ratio between $Ce(SO_4)_2$ and H_2O_2 in **Section 2.3.6**, the moles of H_2O_2 in the post-reaction solution could then be calculated (**Eq. 2.4**):

$$Moles\ of\ H_2O_2 = \frac{Moles\ of\ Ce(SO_4)_2}{2} \quad (\mathbf{Eq.\ 2.4})$$

Finally, the H_2O_2 productivity ($mol_{H2O2}\ Kg_{Cat}^{-1}\ h^{-1}$) could be calculated (**Eq. 2.5**):

$$H_2O_2\ Productivity = \frac{Moles\ of\ H_2O_2}{Mass\ of\ Catalyst\ \times Reaction\ Time} \quad (\mathbf{Eq.\ 2.5})$$

2.3.7.2 Calculating H_2O_2 Degradation

To obtain the difference of H_2O_2 concentration between the before- and post-reaction solutions, titrations for the before- and post-reaction solutions should be conducted. The main process is the same as the process to calculate H_2O_2 productivity, but the only difference is that the sample mass is 0.03 g (**Eq. 2.6**).

$$H_2O_2\ Degradation = \frac{Moles\ of\ H_2O_{2\ Before\ Reaction} - Moles\ of\ H_2O_{2\ Post\ Reaction}}{Mass\ of\ Catalyst\ \times Reaction\ Time} \quad (\mathbf{Eq.\ 2.6})$$

2.3.7.3 Calculating H_2 Conversion

The initial ratio (before reaction) and final ratio (post reaction) of H_2:CO_2 were obtained by Gas chromatography (GC). A similar process as H_2O_2 synthesis was implemented in the blank test, with the absence of the catalyst, and the conversion rate could be calculated (**Eq. 2.7**):

$$H_2\ Conversion\ (\%) = \frac{Initial\ Ratio - Final\ Ratio}{Initial\ Ratio} \times 100 \quad (\mathbf{Eq.\ 2.7})$$

2.3.7.4 Calculating H_2O_2 Selectivity

To further calculate H_2O_2 selectivity, the moles of H_2 charged into the autoclave should be calculated using the ideal gas law, $n = \frac{PV}{RT}$, where n_{H2} is the moles of H_2 in the autoclave, which

is outlined in the **section 2.3.7.5**, P is the pressure of 420 psi 5% H_2/CO_2, V is the volume of 420 psi 5% H_2/CO_2 in the autoclave, which is outlined in the **section 2.3.7.5**, R is the gas constant, and T is the temperature of the gas. Then, combining the H_2O_2 moles calculated in **Eq. 2.4** and the H_2 conversion rate in the E**Eq. 2.7** , the H_2O_2 selectivity could be calculated (**Eq. 2.8**):

$$H_2O_2\ Selectivity\ (\%) = \frac{Moles\ of\ H2O2}{H2\ Conversion\ \times n_{H2}} * 100 \qquad (\mathbf{Eq.\ 2.8})$$

2.3.7.5 Determination of total gas volume

The total gas volume in the autoclave is determined by water replacement method. Firstly charge the autoclave with 50 psi 5%H_2/CO_2 and then release the gas into a reversely positioned graduated cylinder (full of water). Finally measure the volume of released gas by reading the scale.

According to Boyle's Law, the volume of the autoclave (V_1) could be calculated via **Eq. 2.9**, based on the known parameters, including the pressure of 5%%H_2/CO_2(P_1), the volume of gas under atmospheric pressure (V_2) and the atmospheric pressure (P_2):

$$P_1 \times V_1 = P_2 \times V_2 \qquad (\mathbf{Eq.\ 2.9})$$

Then the volume of solvent ($V_{Solvent}$) and liner (V_{Liner}, which could be measured via water replacement method by determine the initial and end scale reading of the graduated cylinder when putting the liner into the cyclinder) need to be considered before calculating the total volume of the gas via **Eq. 2.10**:

$$V_{Gas} = V_1 - V_{Solvent} - V_{Liner} \qquad (\mathbf{Eq.\ 2.10})$$

According to ideal gas law, the mole of H_2 (n_{H2}, 420 psi 5%H_2/CO_2) in the autoclave could be calculated via **Eq. 2.11**, please note, the unit of P_{H2}, V_{Gas}, and T are atm, mL, and ^oC, respectively and R is 0.0821 L·atm/(mol·K) , while the unit of (273.15 + T) is K:

$$n_{H2} = \frac{P_{H2} \times (V_{Gas} \times 0.05)}{R \times (273.15 + T)} \qquad (\mathbf{Eq.\ 2.11})$$

To maximise the accuracy, this procedure needs to be conducted at least three times and the final average value could be used to determine the mole of H_2 (n_{H2}) in the reaction.

2.3.8 Worked Example for H_2O_2 Synthesis

H_2O_2 productivity, H_2O_2 selectivity, and H_2 conversion could be obtained when conducting the H_2O_2 synthesis experiment. Below is a detailed example for calculating these three values:

• The sample mass used was 0.5054 g, and the titration value returned as 8.2 mL.

• Values were substituted into **Eq. 2.2** as follows to calculate the volume of $Ce(SO_4)_2$ required to titrate against the total reaction solution:

$$(8.2 \times 8.5)/0.5054 = 137.68$$

• This value was then substituted into **Eq. 2.3** to calculate the moles of $Ce(SO_4)_2$:

$$(137.68 \times 0.008890)/1000 = 0.001224$$

• Using **Eq. 2.4**, this value was then divided by 2 to calculate the moles of H_2O_2:

$$0.001224/2 = 0.000612$$

• This value was then used to calculate the productivity value using **Eq. 2.5**:

$$0.000612/(0.00001 \times 0.5) = 123$$

• The initial H_2:CO_2 ratio was obtained by Blank Test, and the value of H_2 conversion rate was then calculated using **Eq. 2.7**:

$$((0.6831-0.4169)/0.6831 \times 100) = 39$$

• Combining the H_2 conversion rate and H_2O_2 moles, H_2O_2 selectivity was calculated using **Eq. 2.8**:

$$0.000612/((39/100) \times 0.004848)) \times 100=32$$

2.4 Oxidation degradation of Phenol in Batch Reactor

2.4.1 Time on line in-situ phenol degradation test

The time on line phenol degradation experiments was performed in a high-pressure autoclave at room temperature, in keeping with previous studies.[6,7] With 420 psi 5%H_2/CO_2 and 160 psi 25%O_2/CO_2 present. 8.5 g, 1000 ppm phenol solution was prepared before loading 0.01g Fe-doped AuPd or Pd catalysts. Then purging three times with 5% H_2/CO_2 (100 psi) before filling

with 420 psi 5% H_2/CO_2 and 160 psi 25% O_2/CO_2, to give a H_2:O_2 ratio of 1:2. The reaction was stopped after a certain time period by the cessation of stirring (from 5 mins to 360 mins). After moving the solid phase (catalysts), and 1 ml post-reaction aliquot solution was mixed with 0.5 mL CH_3OH, which is usually used as ·OH scavenger to quench the oxidation reaction.[8] The concentration of phenol is determined by HPLC, using 254/270 nm wavelength. The detailed HPLC method for phenol and its derivatives is illustrated in **Section 2.4.5**. The H_2 conversion rate during in situ phenol degradation test was measured by GC via the same procedure in **Section 2.3.7.3**. Due to the strong reddish colour that results from the formation of the aromatic oxidation products (catechol, hydroquinone, etc.), generated as a result of phenol oxidation, it's impossible to accurately measure residual H_2O_2 via standard titration or colorimetric procedures.

2.4.2. Ex-situ phenol degradation test using pre-formed H_2O_2

Ex-situ phenol degradation tests were conducted in the same manner as discussed above, except using 580 psi pure CO_2 gas and pre-formed H_2O_2 (50 wt.%, the amount of H_2O_2 is equivalent to 100% H_2 conversion, around 2.58 mmol). After 4 hours, vented the gas and ran HPLC to determine the concentration of phenol.

2.4.3. Re-use catalyst for the in-situ phenol degradation test

An identical procedure to the one above was done for the 4 hours in-situ Phenol degradation. The catalyst was then filtered using filter paper, washed with DI water and ethanol 2-3 times to remove any organic matter, and dried in a vacuum oven for 16 hours at 30 °C. Repeat the procedure three times to get a total of around 0.025 g used catalyst (considering the catalyst loss during recycling), before testing again following the procedure as discussed above for the in-situ phenol degradation test (**Section 2.4.1**).

2.4.4. Hot filtration experiments for the in-situ phenol degradation test

An identical procedure to that outlined above for the in-situ phenol degradation was followed for a reaction time of 2 hours. After stopping the reaction after 2 hours, the reactant gas mixture was vented prior to the removal of the solid catalyst via filtration. The post-reaction solution was returned to the reactor to identify the contribution of leached species to the observed

activity, with both steps of the reaction conducted at room temperature. To determine the effect of leached Fe and in-situ generated H_2O_2, 0.01 g of $Au_{0.5}Pd_{0.5}/TiO_2$ catalyst was added to the filtered post-reaction solution. To determine the effect of leached Fe and commercial H_2O_2, 2.58 mmol of 50wt.% commercial H_2O_2 (the measured H_2O_2 is the amount expected if all H_2 were selectively converted to H_2O_2) was added to the filtered post-reaction solution.

2.4.5. Quenching tests using tert-Butanol (TBA)

A radical quenching test was conducted by adding certain amounts of TBA (1-10 mM), which had been widely used as ·OH scavenger in the Fenton reaction, apart from MeOH,[9] into the reaction mixture with phenol and catalysts before starting the standard phenol degradation test outlined in **Section 2.4.1,** and the only difference is no need to add methanol after the reaction prior to the HPLC test. The initial phenol concentrations need to be retested with the presence of different amounts of TBA as introducing TBA into the mixture will further dilute the phenol concentration.

2.4.6. HPLC method for determining phenol and derivatives

The analysis of phenol and its derivatives (hydroquinone, catechol, resorcinol, para-benzoquinone, and organic acids) from post-reaction solution was carried out using an Agilent 1260 Infinity HPLC equipped with a reverse column (Agilent Poroshell 120 SB-C18, at 30 °C), flow gradient of mobile phase (HPLC grade water (0.1 wt. % H_3PO_4) to acetonitrile (CN-CH_3), 70%:30%) (0.50 mL min^{-1}) and employing a UV detector. The retention time and HPLC peaks for phenol and its derivatives are shown in **Table 2.1** and **Figures A2.1 to 2.5**, respectively.

Table 2.1. Wavelength and retention time of phenol and phenol derivatives for HPLC analysis. Test conditions: C18 column, column temperature 30 ºC, UV detector.

Analytes	Retention Time/min	Wavelength/nm
Phenol (PH)	7.24	210/254/270
Hydroquinone (HQ)	3.66	210/254/270
Catechol (CAT)	4.94	210/254/270
Para-benzoquinone (p-BQ)	5.12	210/254/270
Resorcinol (RS)	4.18	210/254/270

The formula to calculate phenol conversion (%) and derivatives selectivity/conversion (%) is shown in **Eq. 2.9-2.13** below:

$$PH\ Conversion\ (\%) = \frac{Initial\ [PH]mmol - After\ [PH]mmol}{Initial\ [PH]mmol} \times 100 \quad (\mathbf{Eq.\ 2.12})$$

$$Selectivity\ towards\ HQ = \frac{After[HQ]mmol}{Converted[PH]mmol} \times PH\ Conversion \quad (\mathbf{Eq.\ 2.13})$$

$$Selectivity\ \ towards\ CAT = \frac{After[CAT]mmol}{Converted[PH]mmol} \times PH\ Conversion \quad (\mathbf{Eq.\ 2.14})$$

$$Selectivity\ \ towards\ pBQ = \frac{After[pBQ]mmol}{Converted[PH]mmol} \times PH\ Conversion \quad (\mathbf{Eq.\ 2.15})$$

$$Selectivity\ \ towards\ RS = \frac{After[RS]mmol}{Converted[PH]mmol} \times PH\ Conversion \quad (\mathbf{Eq.\ 2.16})$$

2.5 Direct synthesis of H_2O_2 and in situ water treatment in a flow reactor

2.5.1 Brief introduction of the flow reactor

The direct synthesis and subsequent degradation of H_2O_2 and the degradation of organic pollutants were performed using a continuous flow reactor (**Figure 2.2 - schematic** and **Figure 2.3 - real picture**). Swagelok 316L 1/8 inch tubing was used as lines to connect each part of the reactor, with 316L 1/4 inch tubing being used for the catalyst bed, with the length of 15 cm and the total volume of 4.75 cm^3(Orange part in **Figure 2.2**). An Agilent HPLC pump was used to pump the mobile phase (DI H_2O or various organic solvents) and regulate the liquid flow rate (from 0.1 mL min^{-1} to 4 mL min^{-1}), and a Swagelok 120 mL gas-liquid separator (GLS) was attached at the end of the line for sample collection. During sample collection, a slight decrease in system pressure is observed, typically from 10 bar to approximately 9.5 bar (depending on duration of sample collection), after which the system rapidly repressurises to 10 bar. Two mass flow controllers (MFC) were used to regulate the gas flow rate (total volume from 30 mL min^{-1} to 90 mL min^{-1}) of the reactant gases (in this study, 5% H_2/N_2 and 25% O_2/N_2 were used, the ratio is 5:1). The maximal pressure in the flow reactor test is no higher than 11 bar and the operational pressure is 10 bar

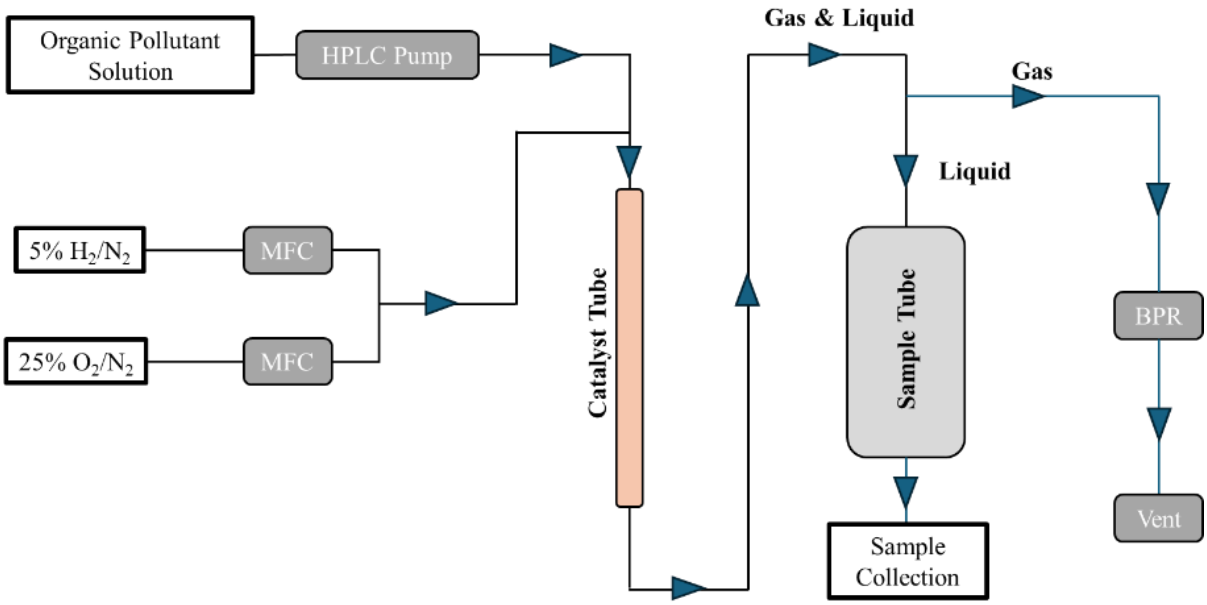

Figure 2.2. The schematic plot of the flow reactor system, which has been used for the direct synthesis of H_2O_2 and in situ water treatment. Illustration: The system is first pressurised to 10 bar by charging 5% H_2/N_2 and 25% O_2/N_2. The organic pollutant solution is then pumped into the catalyst tube, which is prepacked with a mixture of SiC and catalyst. The direct synthesis of H_2O_2 and the concurrent formation of oxygen based reactive species, as well as the in situ oxidative degradation of organic pollutants occur within the catalyst bed. The reactor effluent is subsequently separated into gas and liquid phases prior to the sampling stage, with the liquid collected in a sample tube for analysis and the gaseous stream safely vented. Please note: MFC-Mass flow controller, BPR: Back pressure regulator. **Please note:** this plot was created by the author and is based on an actual flow reactor in **Figure 2.3**.

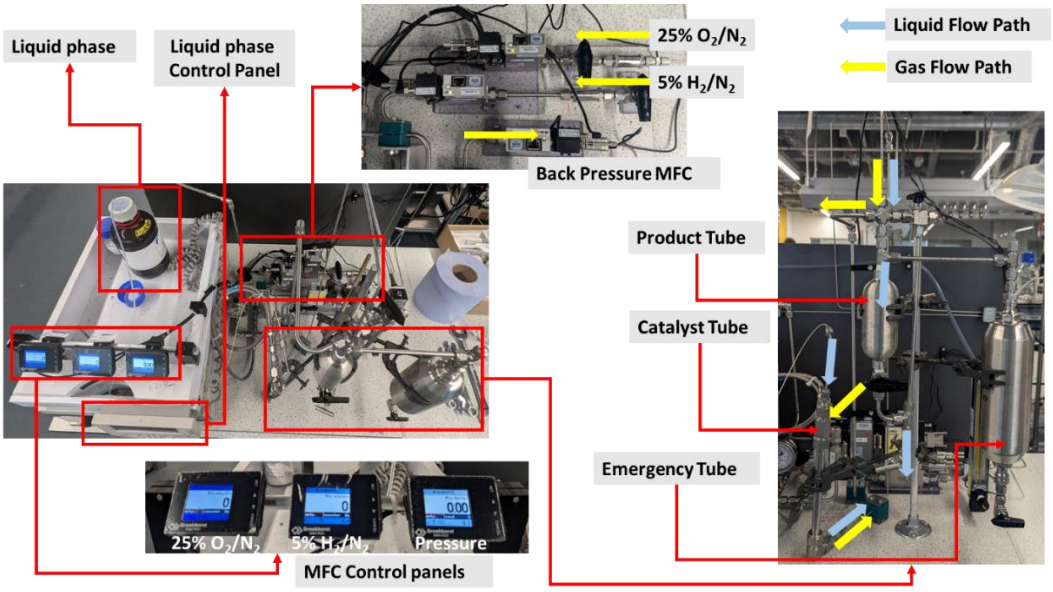

Figure 2.3. Pictures of the flow reactor, which has been used for the direct synthesis of H_2O_2 and in-situ water treatment.

2.5.2 Direct synthesis of H_2O_2 in the flow reactor

2.5.2.1 The general procedure for the H_2O_2 synthesis

The direct synthesis of H_2O_2 was conducted in a continuous flow reactor, and DI H_2O was used as the mobile phase. A synthesis reaction began with packing the union prior to the bed with cotton wool and then 0.12 g of catalyst, pelleted under 10 bar of pressure (up to 10 seconds), and sieved to a diameter of 425 - 250 microns (the catalyst size to catalyst tube size ratio is 0.04 to 0.07), was well mixed with 4.1 g of silicon carbide (SiC, 46 grit, ~0.4 mm) and no need to pre-wet the catalysts tube. The bed was then vertically attached to the lines and pressurised to 10 bar by seting gas flow rates to 42 mL min^{-1} (5% H_2/N_2 at 35 mL min^{-1} and 25% O_2/N_2 at 7 mL min^{-1}). Once the system is pressurized to 10 bar, double check if any gas leakage in the system using gas leak indicator, especially the joint, the, If no leakage, set the HPLC pump to pump the solvent from the reservoir at 0.2 mL $min^{-1,}$ and liquid samples were collected at a 30-minute interval. Please note, the volume of the liquid collected from the first 30 mins might below 6 mL due to the material adsorption. The reaction conditions and methodology for this synthesis of H_2O_2 in a continuous flow using a microreactor were modelled on work previously done by Freakley et al.[10] Error bars presented in the data are assigned based on the standard deviation of 3 repeat experiments.

2.5.2.2 Method to determine H_2O_2 concentration at lower level

The $Ce(SO_4)_2$ method (**Section 2.3.6**) is suitable to determine the H_2O_2 concentration at higher level, however, the H_2O_2 concentration of the post-reaction solution from the flow reactor is generally at a very low level (<10 ppm), so potassium titanium oxide oxalate dihydrate ($K_2TiO(C_2O_4)_2 \cdot 2H_2O$) was used to determine the H_2O_2 concentration.[11–13]

To prepare the acidified potassium titanium oxalate solution, begin by preparing an ice bath and keeping a second bucket of ice nearby. Weigh out 35.4 g of $K_2TiO(C_2O_4)_2 \cdot 2H_2O$ and transfer it into a 1 L volumetric flask, followed by approximately 300 mL of deionised water. Place the flask in the ice bath for 10 minutes to cool, swirling periodically. Measure out 272 mL of concentrated H_2SO_4 (95 %) in a clean, dry glass measuring cylinder. Slowly add the acid to the cooled solution over 5–10 minutes while stirring, ensuring the flask stays cold and topped up with ice as needed. Once all the acid is added, leave the flask in the ice bath for another 10 minutes, swirling occasionally. Remove the flask, top up to 1 L with deionised water, and return

it to the ice bath for 5–10 more minutes. Finally, remove the flask from the ice bath, add a stirrer bar, and stir the solution for 1 hour. Ensure no heating occurs before leaving the solution to stir unattended.

To determine the concentration of H_2O_2, mix 2 mL of the post-reaction solution (containing H_2O_2) and 2 mL of the as-prepared $K_2TiO(C_2O_4)_2 \cdot 2H_2O$ solution together before analysing the concentration using UV-vis analysis at a wavelength of 400 nm.

2.5.3 In situ water treatment in the flow reactor

Various organic contaminants were used as models to test the catalytic performance of AuPd series, PdFe series and AuPdFe series towards in-situ water treatment in the continuous flow reactor (Please note: PdFe and AuPdFe catalysts were only used in the preliminary tests of the in-situ phenol degradation tests). Similar to the H_2O_2 synthesis test, the organic degradation reaction began with packing the union prior to the bed with cotton wool, and then the catalyst, pelleted under 10 bars of pressure with a diameter of 425 - 250 microns, was well mixed with silicon carbide (SiC, 46 grit, ~0.4 mm), and the total amount of the mixture is 4.22 g (catalyst: 0.12 g, and SiC: 4.1 g) and no need to pre-wet the catalysts tube. The bed was then attached to the lines and pressurised to 10 bar by seting gas flow rates to 42 mL min^{-1} (5% H_2/N_2 at 35 mL min^{-1} and 25% O_2/N_2 at 7 mL min^{-1}). Once pressurised and leakage checked, then set HPLC pump to pump the solvent at various speeds, ranging from 0.1 mL min^{-1} to 1 mL min^{-1}, and samples were collected at a 30-minute interval before running HPLC analysis. Error bars presented in the data are assigned based on the standard deviation of 3 repeat experiments.

Similar to **Section 2.4.5**, tert-Butanol (TBA) was selected as a radical scavenger to determine the presence of ROS (especially ·OH) in the flow reaction. Mixing 200 ppm TBA and 20 ppm phenol solutions together to form a phenol solution with an initial concentration at 10 ppm (need to be tested in HPLC) and TBA solution with an initial concentration at 100 ppm, before conducting the standard in situ phenol degradation tests under the identical gas flow, liquid flow, and pressure reaction conditions.

A series of model organic contaminants, which have been widely reported in previous literature as common pollutants in the water stream, including phenolic group (Phenol, Bisphenol A),[14–16] Pharmaceuticals (Carbamazepine, Tetracycline, and 5-fluorouracil),[17–19] and pesticide (Atrazine, Quinmerac),[20,21] are selected for the in-situ oxidative degradation tests in a flow

regime, and the detailed HPLC method is listed in **Table 2.2**. and the structures of the listed organic contaminants are shown in **Figure 2.4**.

Table 2.2. Organic contaminants used in **Chapter 5**, alongside with the initial concentration and the HPLC analytical method

Organic Contaminants	Initial Concentration/ppm	Mobile Phase A	Mobile Phase B	Vol. A / Vol. B	Liquid Flow Rate (mL min^{-1})	Wavelength/nm
Phenol	10	0.1% H_3PO_4 acid solution	Acetonitrile	70% / 30%	0.5	254/270[14,15]
Bisphenol A	10	0.1% H_3PO_4 acid solution	Acetonitrile	70% / 30%	0.5	270[16]
Carbamazepine	10	0.1% H_3PO_4 acid solution	Acetonitrile	70% / 30%	0.5	286[17]
Tetracycline	10	0.1% H_3PO_4 acid solution	Acetonitrile	90% / 10%	0.5	360[18]
5-fluorouracil	10	0.1% H_3PO_4 acid solution	Acetonitrile	95% / 5%	0.5	262[19]
Atrazine	10	0.1% H_3PO_4 acid solution	Acetonitrile	80% / 20%	0.5	230[20]
Quinmerac	10	0.1% H_3PO_4 acid solution	Acetonitrile	85% / 15%	0.5	224[21]

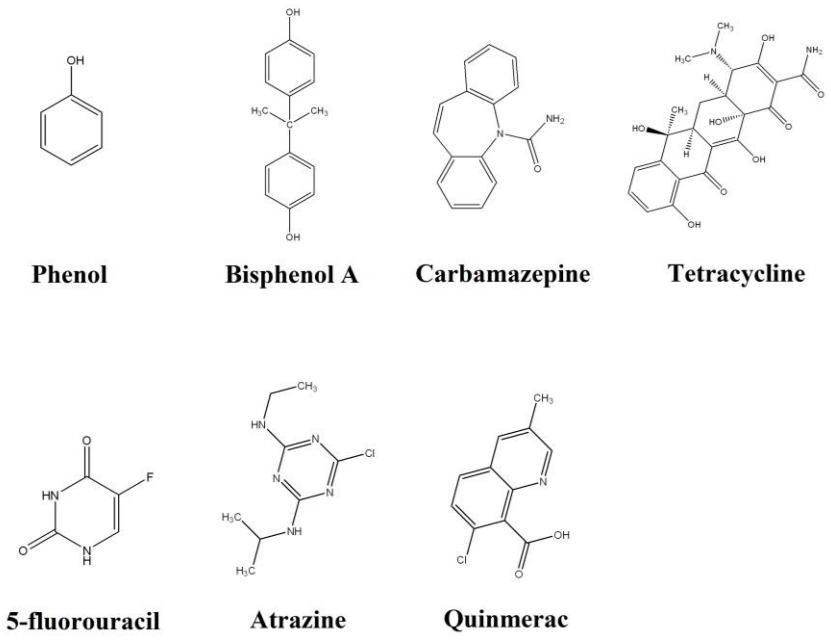

Figure 2.4. Chemical structures of the listed organic pollutants in **Chapter 5**.

2.6 Material Characterization

2.6.1 Powder X-ray Diffraction (XRD)

Powder X-ray diffraction (XRD) is a non-destructive and widely adopted technique for characterising the crystalline structure of solid materials, providing key information such as phase composition, crystallinity, average crystallite size, unit cell parameters, and the presence of amorphous phases. By comparing experimental patterns with reference databases or simulated models, phase identity and structural details can be determined with high accuracy.[22,23]

2.6.1.1 Background

XRD is based on the principle of elastic scattering of X-rays by atoms in a crystalline lattice.[22] In **Figure 2.4**, when a beam of monochromatic X-rays is incident on a crystalline material, the atoms arranged in periodic planes act as scattering centres. The intensity of the scattered X-rays is measured as a function of the scattering angle (2θ), producing a diffraction pattern characteristic of the atomic arrangement in the material. This diffraction pattern serves as a structural "fingerprint" for the identification of crystalline phases. The constructive interference of scattered X-rays occurs when the path difference between rays reflected from successive lattice planes satisfies the Bragg condition. This relationship can be derived from the geometry of X-ray reflection within a crystal. As the incident beam strikes the lattice planes, half of the wavelength travels toward the crystal, and the other half is scattered. By analysing the positions (2θ values) and intensities of the diffraction peaks, detailed information can be obtained regarding the crystal structure, unit cell dimensions, preferred orientation (texture), and phase composition. The technique is widely used for phase identification, estimation of crystallite size, and detection of structural defects in both single- and multi-phase materials.[22,23]

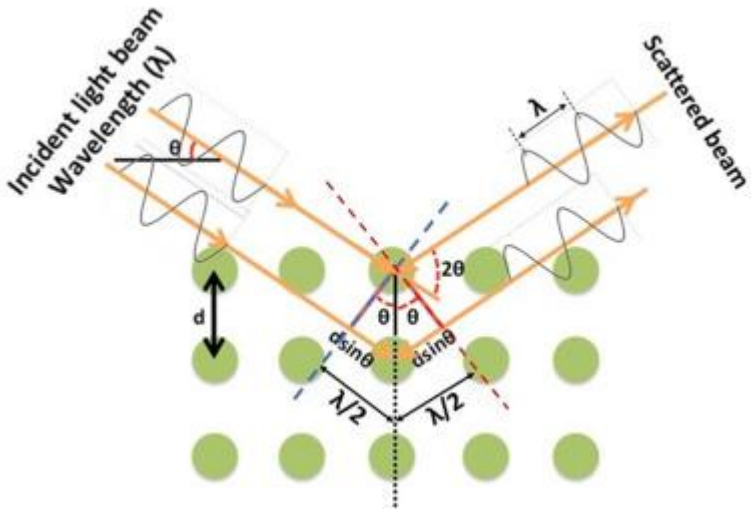

Figure 2.5. Working principle of XRD.[24]

2.6.1.2 Procedures and Software

XRD analysis was conducted by Dr. James Hayward using a X'Pert PRO instrument Phaser diffractometer equipped with a Cu Kα radiation source (λ = 1.5418 Å) operating at 30 kV and 10 mA. Powdered samples were gently ground and evenly spread on a zero-background silicon sample holder to ensure a smooth, flat surface. Data were collected in the 2θ range of 10–80°, with a step size of 0.02° and a count time of 1 s per step, unless otherwise stated. Diffraction patterns were processed using Bruker EVA software, and phase identification was carried out using the International Centre for Diffraction Data (ICDD). Crystallite size estimation for metal phases was performed using the Scherrer equation, applied to the most intense reflection peaks after baseline correction and background subtraction.

2.6.2 X-ray Photoelectron Spectroscopy (XPS)

X-ray Photoelectron Spectroscopy (XPS) is an analytical technique employed to investigate the surface properties of materials. It operates by exposing the material to X-ray radiation, causing the emission of photoelectrons. By measuring the kinetic energy of these emitted electrons, detailed information about the elemental composition, empirical structure, and the oxidation and electronic states of the surface atoms can be obtained. This method is particularly valuable for characterising surface chemistry and assessing the chemical environment of elements present at or near the material surface.

2.6.2.1 Background

In XPS, a focused beam of monochromatic X-rays, commonly Al Kα (1486.6 eV), irradiates the sample surface, causing core-level electrons to be emitted from atoms in the sample. The kinetic energy of these photoelectrons is measured and converted into binding energy values, which are characteristic of specific elements and their chemical states. The resulting spectra display peaks corresponding to core orbitals (e.g., Au 4f, Pd 3d, Fe 2p), with their positions and shapes influenced by the oxidation state, coordination environment, and any electronic interactions with surrounding atoms or support materials.

XPS allows quantitative surface analysis by comparing peak areas using known sensitivity factors. High-resolution scans enable the deconvolution of overlapping peaks, which is critical for distinguishing between different chemical species (e.g., Pd^0 vs Pd^{2+}). Because charging effects can shift peak positions in non-conductive samples, charge correction is typically performed using the C 1s peak from adventitious carbon (set to 284.8 eV).

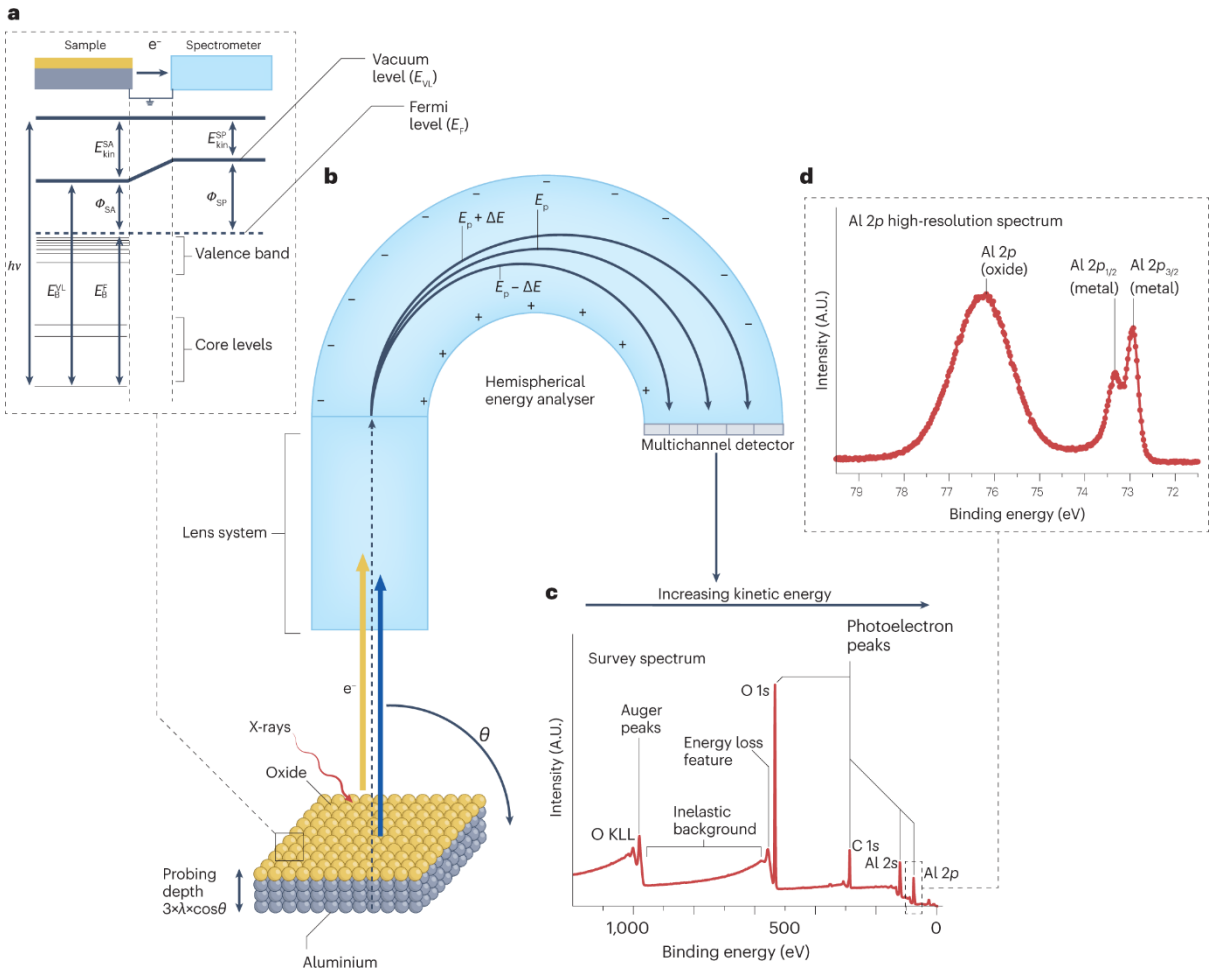

Figure 2.6. The overview of XPS techniques.[25]

2.6.2.2 Procedures

XPS measurements were performed by Dr. David John Morgan using a Kratos Axis Ultra DLD spectrometer, and the data were analysed in CasaXPS software. Samples were affixed to the sample holder using double-sided adhesive tape, and all spectra were acquired under monochromatic Al Kα radiation. A pass energy of 160 eV was applied for survey spectra, while high-resolution scans were conducted at 40 eV. Spectral calibration was referenced to the Ti 2p 3/2 peak at 458.5 eV from a blank P25 TiO_2 sample. The C 1s signal for adventitious carbon in the same reference sample was recorded at 284.8 eV and used for further energy calibration.

Binding energies for Pd 3d were assigned by referencing both metallic Pd^0 and oxidized Pd^{2+} states, supported by comparison with standard spectra and typical asymmetric or Gaussian peak shapes associated with bulk-phase materials. Similarly, Au binding energies were evaluated using the Au 4f signal, with bulk metallic Au expected near 83.9 eV. It is noted, however, that this value may shift to lower energies on TiO_2 due to possible charge transfer effects or coordination influences in small Au nanoparticles. The Au 4f and Pd 3d regions were analysed in detail to quantify the Au/Pd surface composition ratios.

2.6.3 Brunauer-Emmett-Teller (BET)

BET surface area analysis measures how much gas a solid can adsorb at cryogenic temperature and near equilibrium. From the adsorption isotherm, the monolayer capacity is obtained and converted to specific surface area using the known molecular cross section of the adsorptive. Nitrogen at 77 K is used most often. Argon at 87 K can be helpful for some oxides and for micro or mesoporous materials. BET analysis is widely used to characterise powders and porous solids and it supports interpretation of surface-dependent reactivity and transport.[26–28]

2.6.3.1 Background

The BET model extends the Langmuir approach to multilayer adsorption. It assumes identical surface sites, no lateral interactions, and a constant heat of adsorption for layers beyond the first. The linear BET plot is valid only over a limited range of relative pressure. For N_2 at 77 K, a typical working window is P/P_0 from about 0.05 to 0.30. The exact region should be chosen using the Rouquerol consistency criteria so that the intercept remains positive and the BET C constant is meaningful. The standard molecular cross-sectional area for N_2 is 0.162 nm^2. For

pore structure, the Barrett–Joyner–Halenda (BJH) method can be applied to the desorption branch to estimate mesopore size distributions.[29] Network effects and the tensile strength anomaly can influence the desorption path in some materials, so BJH results are best treated as estimates rather than absolutes.[26–28]

2.6.3.2 Procedure

BET surface area measurements for all TiO_2-supported catalysts were conducted using QUADRASORB EVO (Quantachrome Instruments). Prior to analysis, samples were degassed using FLOVAC Degasser under vacuum at 150°C for a minimum of 2 hours to remove adsorbed moisture and organic contaminants. Approximately 200 mg of sample was loaded into a sample tube and sealed for analysis. Nitrogen adsorption–desorption isotherms were recorded at 77 K over a relative pressure range of 0.01–0.99. The BET surface area was calculated using adsorption data in the linear region (typically P/P_0 =0.05 to 0.30). Pore size distribution and total pore volume were determined using the BJH method applied to the desorption branch of the isotherm.

2.6.4 Scanning Electron Microscopy (SEM)

Scanning Electron Microscopy (SEM) is a versatile and widely employed imaging technique that provides detailed information about the surface morphology, topography, and elemental composition of materials. Unlike Transmission Electron Microscopy (TEM), which relies on transmitted electrons through thin specimens, SEM utilises a focused electron beam that scans across the surface of bulk samples, making it particularly well-suited for characterising powders, films, and microstructure solids. SEM is frequently used in catalysis and materials science to investigate particle size, shape, aggregation, and support textures.[30,31]

2.6.4.1 Background

SEM is a method used to image surfaces and sub-surface areas of larger samples by exploiting different interactions (elastic and inelastic scattering) between an electron beam and the surface of the specimen. In SEM, a high-energy electron beam is aimed and systematically moved across the surface of a thick specimen. This process generates various signals, such as secondary electrons, Auger electrons, backscattered electrons, X-rays, and

cathodoluminescence. These signals are collected by specific detectors, each providing unique insights about the surface being studied. Because SEM requires samples to be electrically conductive, non-conductive materials such as ceramics or polymers are typically coated with a thin conductive layer (e.g. gold, platinum, or carbon) prior to imaging. SEM can achieve magnifications from 10× to over 100,000×, with spatial resolution down to a few nanometres depending on the accelerating voltage and working distance.

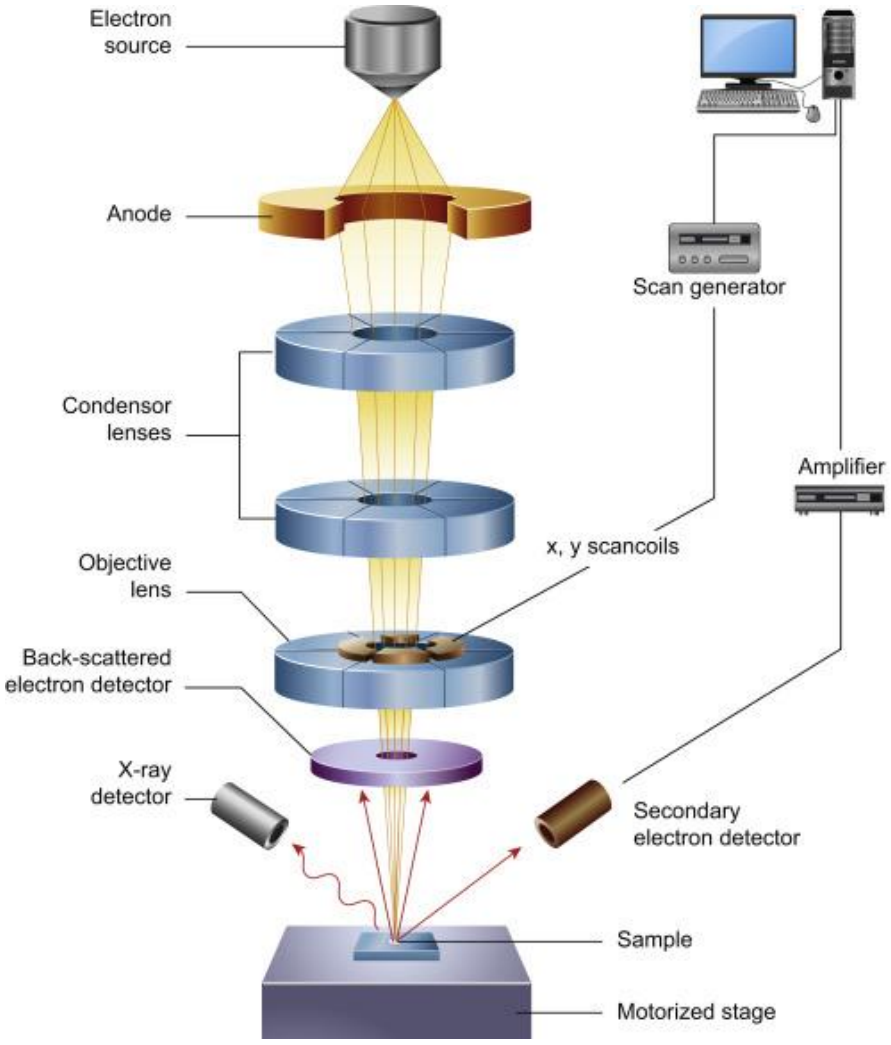

Figure 2.7. Schematic diagram of the core components of an SEM microscope.[30]

2.6.4.2 Procedure

SEM analysis was conducted using TESCAN FEG-SEM, operated under high vacuum conditions. Powdered catalyst samples were gently pressed onto conductive carbon tape mounted on standard aluminium SEM stubs. To minimise charging effects and enhance image quality, non-conductive samples were coated with a ~5 nm thin layer of gold using a sputter

coater (Quorum Q150T ES). Imaging was performed using secondary electron detection at accelerating voltages ranging from 5 kV to 15 kV, depending on the sample's conductivity and resolution requirements. Low magnification scans were used to survey particle dispersion and identify regions of interest, while higher magnifications provided detailed images of surface texture, porosity, and particle agglomeration. Backscattered electron imaging was used selectively to enhance compositional contrast, particularly in multi-metallic or supported catalyst systems. Elemental analysis was performed using an Oxford Instruments EDS system attached to the SEM. Point scans, line scans, and elemental mapping were conducted to identify elemental distribution across selected sample regions. Image analysis, including particle size measurements and morphology quantification, was carried out using ImageJ or proprietary SEM software.

2.6.5 Transmission electron microscopy (TEM)

Transmission Electron Microscopy (TEM) is a technique of imaging the internal structure of solids using a beam of high-energy electrons transmitted through the solid, which is a widely used analytical technique for characterising the structural, morphological, and crystallographic properties of materials at the nanoscale. Due to its exceptional spatial resolution—often below 0.2 nm—TEM is particularly valuable in catalysis research, enabling direct visualisation of catalyst particles, support structures, lattice fringes, and crystallographic defects. It provides both imaging and diffraction capabilities, making it a versatile tool for correlating structural features with catalytic performance.[30]

2.6.5.1 Background

In TEM, a high-energy electron beam (typically 100–300 kV) is transmitted through an ultrathin specimen, interacting with the sample as it passes through. The transmitted electrons are scattered depending on the sample's density, thickness, and atomic composition. These interactions generate image contrast, which is recorded by detectors or fluorescent screens to produce high-resolution images.

The technique utilises a series of electromagnetic lenses to focus and magnify the electron beam before and after it passes through the sample. Bright field (BF) imaging collects the directly transmitted electrons, allowing for contrast based on mass-thickness variations, while selected area electron diffraction (SAED) provides crystallographic information. High-

resolution TEM (HRTEM) can resolve lattice fringes, enabling analysis of crystal orientation and defects at the atomic level.[30]

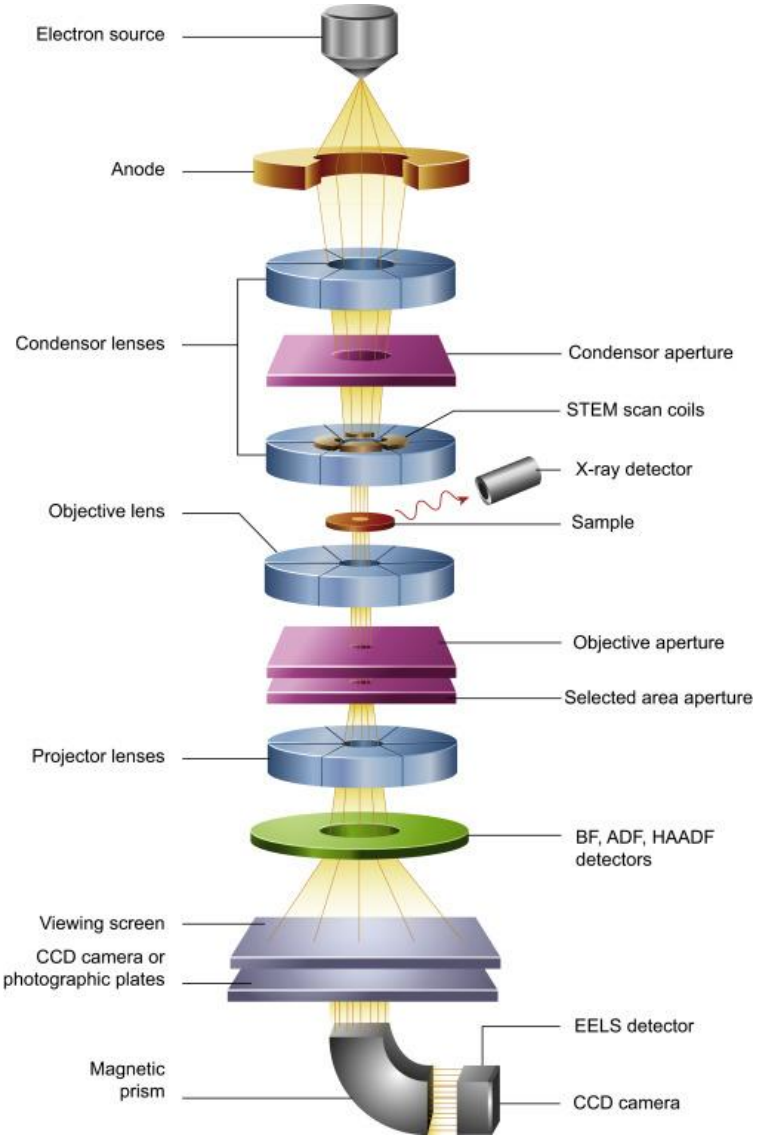

Figure 2.8. The schematic plot of TEM.[30]

2.6.5.2 Procedure

TEM imaging was performed using a JEOL 2100 transmission electron microscope operating at 200 kV. Samples were loaded directly onto a holey carbon-coated copper TEM grid. Bright field images were acquired to examine particle morphology and dispersion. Particle size and distribution were quantified using ImageJ software based on multiple TEM micrographs, and at least 200 nanoparticles were counted to ensure accuracy.

2.6.6 Scanning Transmission Electron Microscopy (STEM)

Scanning Transmission Electron Microscopy (STEM) is an advanced imaging technique that employs a high-energy focused electron beam to investigate the structural features of a sample, combining the principle of SEM and TEM. As the electrons interact with the material, they are scattered at high angles and detected using a high-angle annular dark field (HAADF) detector. This scattering provides contrast based on atomic number and mass-thickness variations. Through this interaction, detailed information on surface characteristics such as particle size, spatial distribution, and morphology can be obtained with high resolution.[32,33]

2.6.6.1 Background

A high-energy electron beam is essential for imaging in STEM, and this is generated using a cathode source. Typically, a hairpin-shaped tungsten filament serves as the electron emitter, surrounded by a negatively charged cathode cap. When a small current is applied, electrons are emitted and attracted towards an electronically grounded anode located below. These electrons pass through an aperture situated between the cathode and anode and are focused by condenser lenses onto the region of interest within the sample. The beam is then further refined by objective lenses, followed by intermediate and projector lenses to magnify the transmitted or scattered electrons and generate the final image.

High-angle annular dark-field (HAADF) imaging in STEM captures scattered electrons using detectors positioned at large angles. This method is particularly sensitive to atomic number (Z) contrast, as elements with higher Z values scatter electrons more strongly at high angles. The HAADF signal intensity is approximately proportional to $Z^{3/2}$, resulting in brighter contrast for heavier elements. This Z-contrast capability enables detailed imaging of compositional variations at the atomic scale, making HAADF-STEM a powerful tool for nanoscale structural and elemental analysis.[32,33]

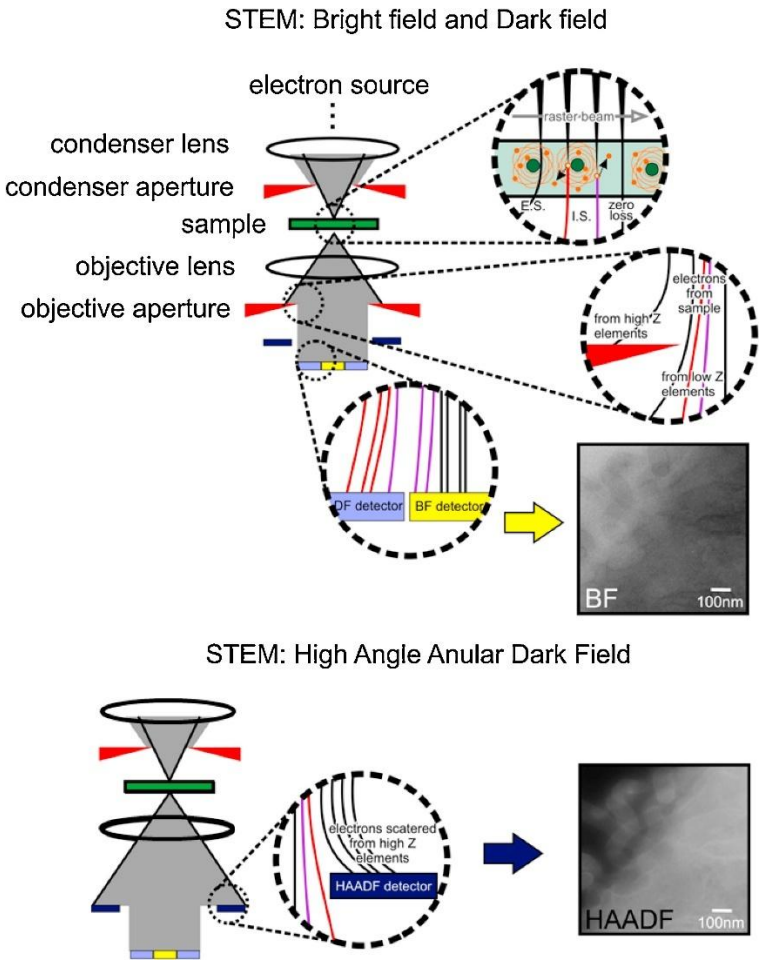

Figure 2.9. Simplified scheme of image formation in STEM mode.[34]

2.6.6.2 Procedure

STEM analysis was conducted by Dr. Thomas Davies and Ella Kitching using SPECTRA AC. Catalyst samples were prepared by dry dispersing the powder onto a holey carbon film supported on a 300-mesh copper TEM grid. Both bright field (BF) and high-angle annular dark field (HAADF) images were acquired to assess morphological and structural features. Particle size distribution was determined by analysing HAADF micrographs using ImageJ software. Elemental analysis was performed via energy-dispersive X-ray spectroscopy (EDX).

2.6.7 CO-Diffuse Reflectance Infrared Fourier Transform Spectroscopy (CO-DRIFTS)

CO-DRIFTS is a specialised in situ spectroscopic technique used to probe the surface chemistry of heterogeneous catalysts, particularly to investigate the electronic and coordination environment of metal active sites. By adsorbing CO as a molecular probe, the method enables

detailed characterisation of metal dispersion, oxidation state, and interaction with supports or promoters. CO-DRIFTS is especially valuable for supported noble metal catalysts (e.g., Au, Pd, Pt) due to the strong and well-defined infrared absorption features when bound to metal surfaces.

2.6.7.1 Background

In DRIFTS, infrared light is diffusely reflected from a powdered sample, and the resulting spectrum reveals molecular vibrational information. When CO is introduced, it adsorbs onto exposed metal sites in either linear or bridged configurations. These species display characteristic absorption bands, typically within the 2100–1800 cm^{-1} range. The exact wavenumber positions of these bands are sensitive to the metal electronic state and coordination geometry, allowing researchers to distinguish between metallic and oxidised species, or between isolated atoms and nanoparticles. The technique enables the monitoring of changes under controlled environments, making it highly suitable for operando or pre-/post-reaction characterisation.

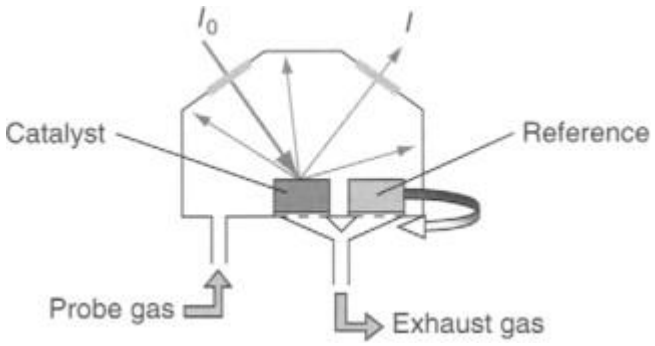

Figure 2.10. Schematic plot of DRIFTS.[35]

2.6.7.2 Procedure

CO-DRIFTS measurements were performed using a BRUKER INVEIO R instrument. Around 50-100 mg of finely powdered catalyst was loaded into a DRIFTS cell equipped with ZnSe windows and connected to a gas flow system. Samples were pretreated in situ with 5% H_2/Ar at 200 °C for 30 minutes to remove surface impurities and reduce metal species. After cooling to room temperature under flowing Ar, a dilute CO/Ar mixture (1–2% CO) was introduced for 10–15 minutes to allow CO adsorption onto the catalyst surface. The system was then purged with Ar to remove weakly adsorbed CO before spectrum acquisition. IR spectra were recorded

in the range 4000–1000 cm^{-1} at a resolution of 4 cm^{-1}, typically averaging 64 scans per measurement.

2.6.8 Mössbauer spectroscopy

Mössbauer spectroscopy measures tiny shifts in nuclear energy levels that reflect the local electronic and magnetic environment of Mössbauer-active nuclei. For iron-containing materials, the ^{57}Fe isotope is used most often. A ^{57}Co source emits γ-rays that are absorbed recoil-free by ^{57}Fe atoms in the sample as the source moves at a controlled velocity. The resulting spectrum is sensitive to oxidation state, spin state, coordination symmetry and magnetic ordering, so it is widely used in catalysis and oxide chemistry to distinguish Fe^{2+} and Fe^{3+}, assign crystallographic sites and detect small magnetic particles.[36,37]

2.6.8.1 Background

Routine interpretation relies on a small set of hyperfine parameters.[38] The isomer shift δ reflects the s-electron density at the nucleus and is the primary indicator for separating Fe^{2+} from Fe^{3+} and for tracking spin state. The quadrupole splitting ΔE_Q reports the asymmetry of the electric-field gradient at the nucleus and is therefore sensitive to coordination geometry, site distortion, and ligand environment. Magnetic hyperfine interactions produce a characteristic sextet when internal or applied fields are strong enough, and the derived hyperfine field helps to identify magnetically ordered phases or diagnose superparamagnetic. Spectra are recorded as absorption versus source velocity in mm s^{-1}. Velocities are calibrated against an α-Fe foil at room temperature, which defines zero for δ. The observed centre shift contains a small temperature-dependent second-order Doppler contribution, so measurements are best compared at the same temperature. Thin, homogeneous absorbers give reliable line shapes and areas, while overly thick layers broaden lines and bias relative areas. Low-temperature data are often collected to suppress relaxation effects and to sharpen magnetic splitting in small particles.[36–38]

2.6.8.2 Procedure

The Mössbauer spectroscopy analysis for the AuPdFe catalysts was undertaken by Dr. Iulian Dugulan (Delft University of Technology). Transmission ^{57}Fe Mössbauer spectra were

collected at 50 and 4.2 K with a conventional constant-acceleration spectrometer using a ^{57}Co(Rh) source. Velocity calibration was carried out using an α-Fe foil at room temperature. The Mössbauer spectra were fitted using the Mosswinn 4.0 program.[39]

2.7 Analytic techniques

2.7.1 High-Performance Liquid Chromatography (HPLC)

High Performance Liquid Chromatography (HPLC) is an analytical technique that utilises high-pressure pumps to pass a liquid mobile phase, containing the analyte of interest, through a column packed with a stationary phase. As the sample travels through the column, its components interact differently with the stationary and mobile phases based on their physicochemical properties. These differential interactions enable the separation of individual compounds, which can then be detected and quantified.[40]

2.7.1.1 Background

HPLC is a widely used analytical technique for separating, identifying, and quantifying components in complex mixtures. It operates by passing a liquid mobile phase through a packed column containing a stationary phase, with separation based on the differential interactions of analytes with these two phases. Depending on the analyte properties, HPLC can be tailored to separate compounds based on polarity, charge, or molecular size.

In polarity-based separations, analytes interact with the stationary phase, where polar compounds exhibit longer retention times on polar phases. Mobile phase gradients, typically involving water and organic solvents, are used to enhance resolution. Charge-based separations employ ion-exchange columns functionalised with ionic groups, enabling selective retention through electrostatic interactions. Size-based separations, or size-exclusion chromatography (SEC), rely on stationary phases with defined pore sizes to separate molecules by their hydrodynamic volume.

A standard HPLC system comprises a mobile phase reservoir, pump, injector, column, and detector. The system produces a chromatogram that reveals analyte retention times and relative concentrations. HPLC is flexible to change mobile phase composition, stationary phase

chemistry, and operating parameters, making it indispensable across fields such as pharmaceuticals, environmental monitoring, and biochemical analysis.

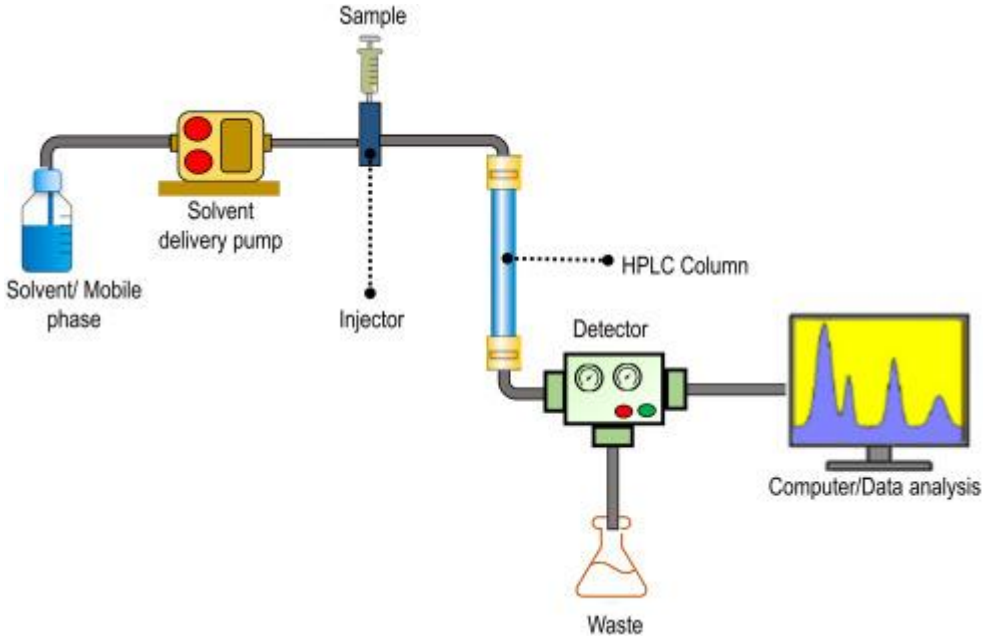

Figure 2.11. Configuration of an HPLC system.[40]

2.7.2.2 Procedure

Phenol and its derivatives were analysed using Agilent 1260 Infinity HPLC equipped with an ultraviolet detector and a reverse phase C18 column (250 mm x 4.6 mm) [19] at 30 °C. To determine phenol concentration (initial concentration 1000 mg L^{-1}), the post-reaction solution is filtered through a PTFE syringe filter and mixed with 0.5 ml CH_3OH before a 5 µL injection. The mobile phase (to determine phenol concentration) was an isocratic mixture of 0.1% H_3PO_4 solution (0.1% H_3PO_4 in HPLC Grade H_2O): Acetonitrile in a 70:30 ratio with a flow rate of 0.50 mL min^{-1}. The post-reaction solution detection peak at 254/270 nm was compared to an initial reactant detection peak and a calibration curve to allow the calculation of phenol concentration.

2.7.2 Gas Chromatography (GC)

Gas chromatography (GC) is a widely employed analytical method for separating and identifying volatile components within a gas-phase mixture. In this technique, the sample is introduced into a heated column coated with a stationary phase. As the analytes are carried through the column by an inert mobile phase, they interact with the stationary phase to varying

extents, resulting in differential retention and separation. Each analyte is subsequently detected as it elutes from the column, generating a measurable signal proportional to its concentration, thereby allowing both qualitative and quantitative analysis.

2.7.2.1 Background

Gas chromatography (GC) is a technique used to separate and analyse vaporised compounds within a gaseous mixture. The sample is introduced into the system through an injector and carried by an inert gas, such as helium or nitrogen, into a chromatographic column. Separation of analytes occurs as they interact with the stationary phase within the column. Two types of columns are commonly used: packed columns, typically filled with inert materials like diatomaceous earth or silica gel, and capillary columns, which are narrower and coated internally with either a liquid or solid stationary phase.

The separation process depends on the physicochemical interactions between the analytes and the stationary phase. Stronger interactions lead to longer retention times, while weaker interactions result in earlier elution. Columns are typically housed in an oven that maintains a constant or programmed temperature to influence analyte elution profiles.

Detection occurs as analytes exit the column, with common detectors including the Flame Ionisation Detector (FID) and Thermal Conductivity Detector (TCD). The FID operates by combusting the effluent with hydrogen and air, generating ions that produce a measurable current when attracted to an electrode. In contrast, the TCD detects changes in thermal conductivity between the carrier gas and analytes, generating a signal based on the energy required to maintain filament temperature as different gases pass over it.

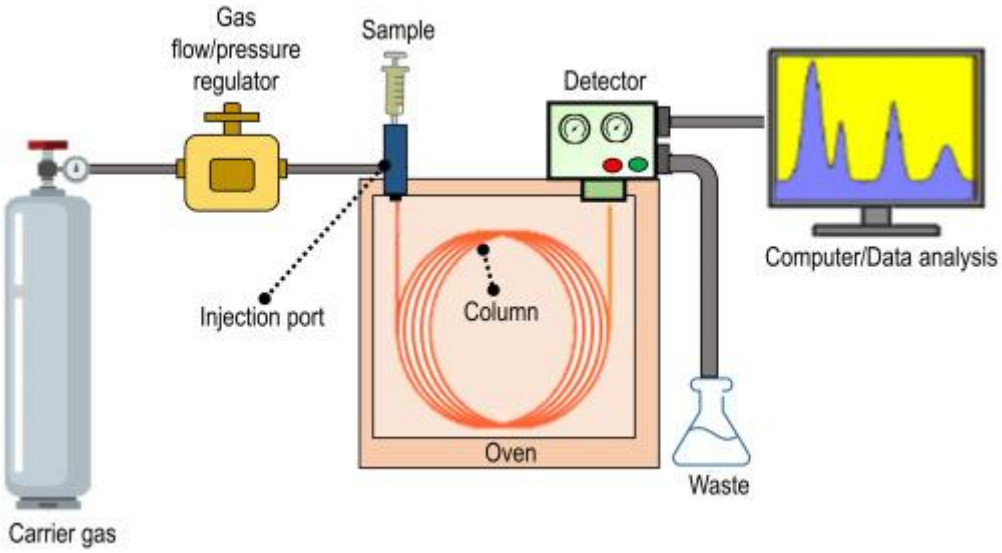

Figure 2.12. Scheme of a gas chromatograph.[40]

2.7.2.2 Procedure

Gas-phase products from the direct synthesis of H_2O_2 and the in situ phenol degradation reactions were analysed using a Varian 3800 GC equipped with a CP-Wax 52 CB column, maintained at 30 °C, and a thermal conductivity detector (TCD). This setup enabled the separation and quantification of the gas components (mainly for H_2 and CO_2), allowing the calculation of both H_2 conversion and H_2O_2 selectivity. Analyte peaks were integrated, and the H_2:CO_2 ratio from a blank experiment (without catalyst) was compared to that from catalysed reactions to determine H_2 conversion. H_2O_2 selectivity was subsequently derived by relating the moles of H_2O_2 formed, measured via titration, to the moles of H_2 consumed. Each run was conducted over a 22 minutes period to ensure complete passage of all relevant gases through the column.

2.7.3 Inductively Coupled Plasma Mass Spectroscopy (ICP-MS)

Inductively Coupled Plasma Mass Spectrometry (ICP-MS) is a powerful instrumental technique that couples a high-temperature plasma ionisation source with a mass spectrometer to enable rapid, sensitive, and multi-elemental analysis. It is capable of detecting most elements in the periodic table at concentrations ranging from milligrams per litre (mg L^{-1}) to nanograms per litre (ng L^{-1}). Due to its low detection limits, broad dynamic range, and high throughput,

ICP-MS is widely applied in environmental analysis, geochemistry, and materials science, particularly for quantifying metal content in catalyst materials and solution samples.[41,42]

2.7.3.1 Background

The ionisation source used in ICP-MS is an inductively coupled plasma, formed by supplying argon gas to a quartz torch surrounded by a radio frequency (RF) induction coil. When the RF generator energises the coil, it creates an oscillating electromagnetic field that ionises the argon gas, producing a high-temperature plasma (~6000 ºC). This plasma effectively atomises and ionises over 90% of the elements introduced into it.

Liquid samples are introduced into the plasma via a nebuliser and spray chamber system, which first converts the sample into a fine aerosol. Larger droplets are removed in the spray chamber, while smaller ones are carried into the plasma. As the aerosolised sample enters the high-temperature plasma, its constituent atoms are excited and ionised. These ions are directed through an interface composed of a sampler and skimmer cone, which operate under vacuum to extract ions from the plasma while minimising the transfer of neutral species and photons.

The extracted ions then pass through a cooled chamber and an electrostatic ion lens known as an ion optic system. Since all ions generated in the plasma are positively charged, they would otherwise repel each other. The ion optics focus the ion beam and guide it into the mass spectrometer. Before mass separation, the ions enter a quadrupole mass filter that separates them according to their mass-to-charge ratio (m/z). The quadrupole alternates electric fields to transmit only ions of a selected m/z value at any given moment. Detection is carried out using an electron multiplier, which amplifies the signal of each ion as it strikes a dynode surface. The resulting electrical signal is proportional to the number of ions detected and is used to quantify elemental concentrations. The system enables both qualitative identification and precise quantification of elements present in the sample, with high sensitivity and accuracy.

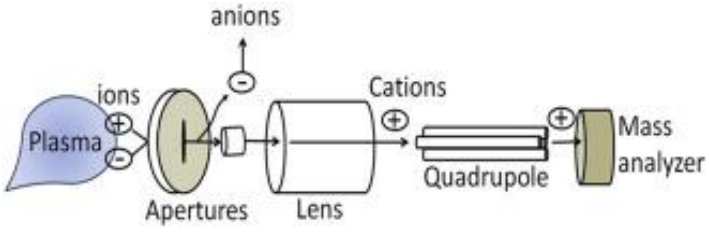

Figure 2.13. Components of inductivity coupled plasma (ICP) mass spectroscopy.[41]

2.7.3.2 Procedure

All ICP-MS analysis (metal leaching and metal loading) was undertaken by Mr. Simon Waller (Analytical Service, School of Chemistry, Cardiff University) using an Agilent 7900 ICP-MS instrument. For the metal loading test, the catalyst samples were digested using a microwave-assisted acid digestion protocol. Typically, 50 mg of catalyst was treated with a mixture of concentrated nitric acid and hydrochloric acid (aqua regia) and heated in sealed Teflon vessels at 180 °C for 30 minutes. The digests were then diluted with ultrapure water to a known volume and filtered to remove particulates. Calibration standards were prepared using certified multi-element solutions, covering the concentration range of interest. An internal standard (e.g., Sc, Rh, or In) was added to all samples and standards to correct for instrumental drift and matrix effects. Samples were introduced into the plasma via a concentric nebuliser and spray chamber, with standard operating parameters optimised for signal stability and sensitivity. Metal concentrations were reported in mg L^{-1} and converted to weight percent relative to the initial catalyst mass. All measurements were performed in triplicate to ensure reproducibility, and appropriate blanks were used to monitor background contamination. The detection limits for Au and Pd were reported as 0.0192 and 0.048 ug L^{-1}, respectively.

2.7.4 Microwave Plasma Atomic Emission Spectroscopy (MP-AES)

Microwave Plasma Atomic Emission Spectroscopy (MP-AES) is a multi-element analytical technique used for the quantitative determination of metals and select non-metals in liquid samples. It is especially suitable for trace metal analysis in catalytic materials and environmental matrices. MP-AES provides a robust, cost-effective, and flame-free alternative to traditional techniques such as Atomic Absorption Spectroscopy (AAS) and Inductively Coupled Plasma Optical Emission Spectroscopy (ICP-OES).[43]

2.7.4.1 Background

In MP-AES, a nitrogen plasma is sustained by a microwave energy source, which excites atoms in the sample to higher electronic states. As these atoms relax to their ground states, they emit characteristic wavelengths of light, which are measured by a spectrometer. The intensity of the emitted radiation is directly proportional to the concentration of the corresponding element in the sample.

Unlike ICP-based methods that require expensive argon gas, MP-AES uses nitrogen—typically generated from air—making it more economical and environmentally friendly. The technique offers good detection limits (ppm to sub-ppm range), high throughput, and the ability to perform multi-element analysis. MP-AES is commonly used in catalysis for quantifying metal loadings, verifying elemental ratios, and monitoring metal leaching from catalysts after reaction.[43]

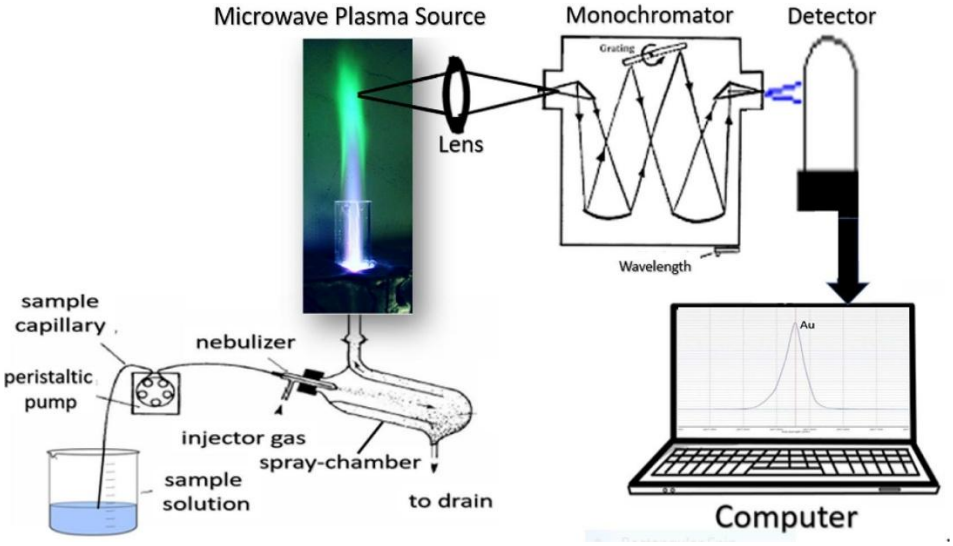

Figure 2.14. A schematic diagram explains the principle of MP-AES.[44]

2.7.4.2 Procedure

The concentrations of Au, Pd, and Fe precursors were detected using an Agilent 4100 MP-AES system equipped with a nitrogen gas generator. The precursor sample was first diluted 1000 times prior to the test (the unit changed from mg ml^{-1} to mg l^{-1}). For example, for Pd precursor (using $PdCl_2$), the calibration standards were prepared from certified Pd stock solutions (1000 mg l^{-1}) and matched to the expected analyte concentration range (10-30 mg l^{-1}). Wavelengths were selected based on the optimal emission lines for each target element (e.g., 340 nm and 363 nm for Pd). Samples and standards were introduced into the plasma using a pneumatic nebuliser and spray chamber system.

Data were acquired using Agilent's MP Expert software. Each measurement was performed in triplicate, and concentrations were calculated against the calibration curve. The final metal content was reported as weight percent relative to the initial sample mass.

2.7.5 Ultraviolet-visible (UV-vis) spectroscopy

Ultraviolet-Visible (UV-Vis) spectroscopy is a widely employed, cost-effective, and non-destructive analytical technique used to study the optical properties and electronic transitions of molecules. Owing to its simplicity, rapid response, and versatility, UV-Vis spectroscopy has found extensive application across numerous research disciplines, including environmental science, nanomaterials, catalysis, pharmaceuticals, food quality control, and polymer chemistry. It is especially suited for the analysis of organic compounds, coordination complexes, and select inorganic species that exhibit characteristic absorption in the UV (200-400 nm) or visible (400-800 nm) regions.[45,46]

2.7.5.1 Background

UV–Vis spectroscopy measures the absorbance or transmission of light as a function of wavelength, providing insight into electronic transitions such as $\pi \rightarrow \pi^*$ or $n \rightarrow \pi^*$ associated with various functional groups or chromophores. In catalysis and materials chemistry, UV-Vis is often used to monitor the formation of metal–ligand complexes, track molecular adsorption on surfaces, and evaluate nanomaterial optical properties.[45]

The technique is also widely applied to study nanomaterials (NMs), as their optical behaviour is sensitive to size, shape, aggregation state, and local dielectric environment. For instance, shifts in absorbance peaks (hypochromic or bathochromic shifts) can indicate nanoparticle growth, agglomeration, or surface modification. Similarly, UV-Vis is commonly employed in the design and evaluation of molecularly imprinted polymers (MIPs), where spectral changes reflect the interaction between templates, monomers, and cross-linkers. Though not as selective as fluorescence-based techniques, UV-Vis provides a rapid and economical approach for screening sensor materials and evaluating binding interactions.[45]

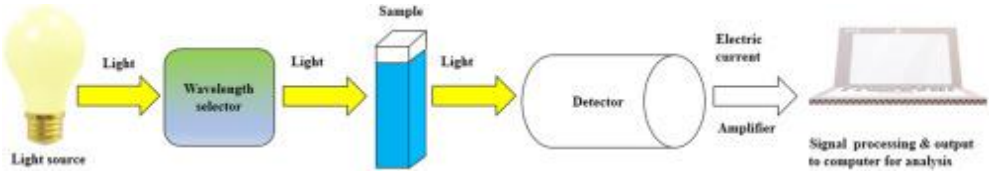

Figure 2.15. A schematic diagram of major components in a UV-Vis spectrophotometer.[45]

2.7.5.2 Procedure

UV–Vis measurements were carried out using a SHIMADZU UV-1900 spectrophotometer equipped with SHIMADZU CPS-100 Cell positioner. In this study, UV-Vis spectroscopy was specifically used to quantify H_2O_2 concentration in aqueous solutions via complexation with as-prepared $K_2TiO(C_2O_4)_2$ solution, which forms a stable yellow peroxotitanium complex exhibiting a strong absorbance at 400 nm.

2.8. Appendix

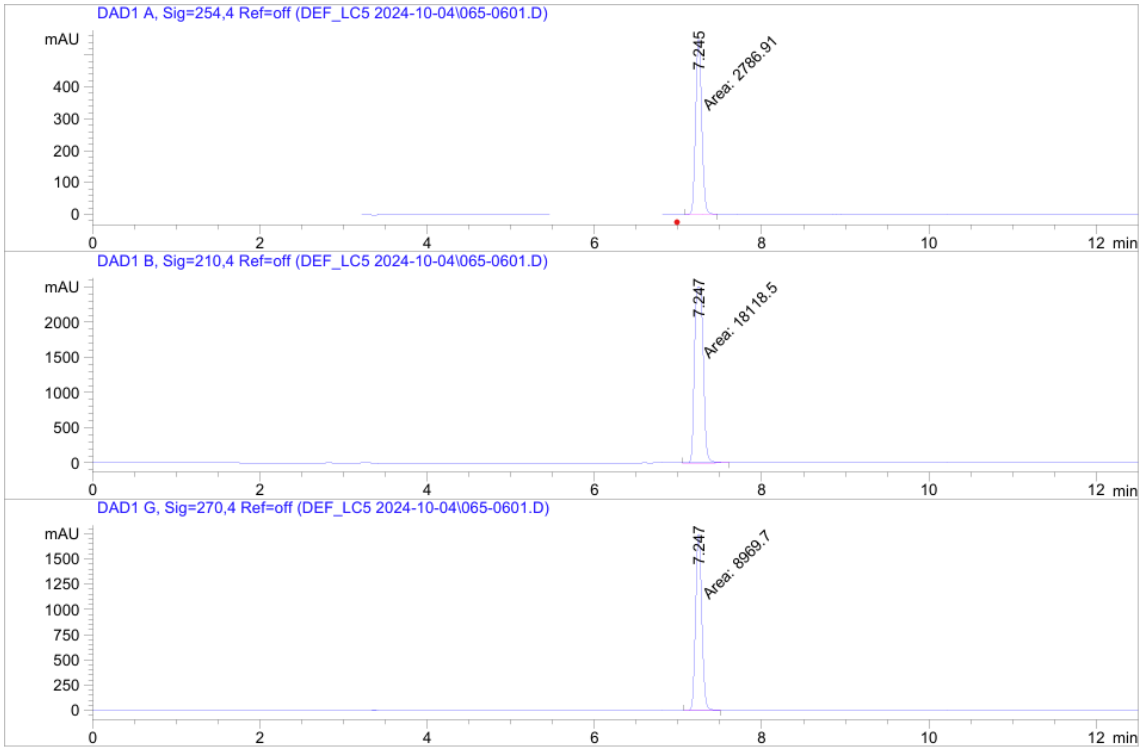

Figure A2.1. The HPLC peaks of phenol (1000 ppm) at 210 nm, 254 nm, and 270 nm, respectively.

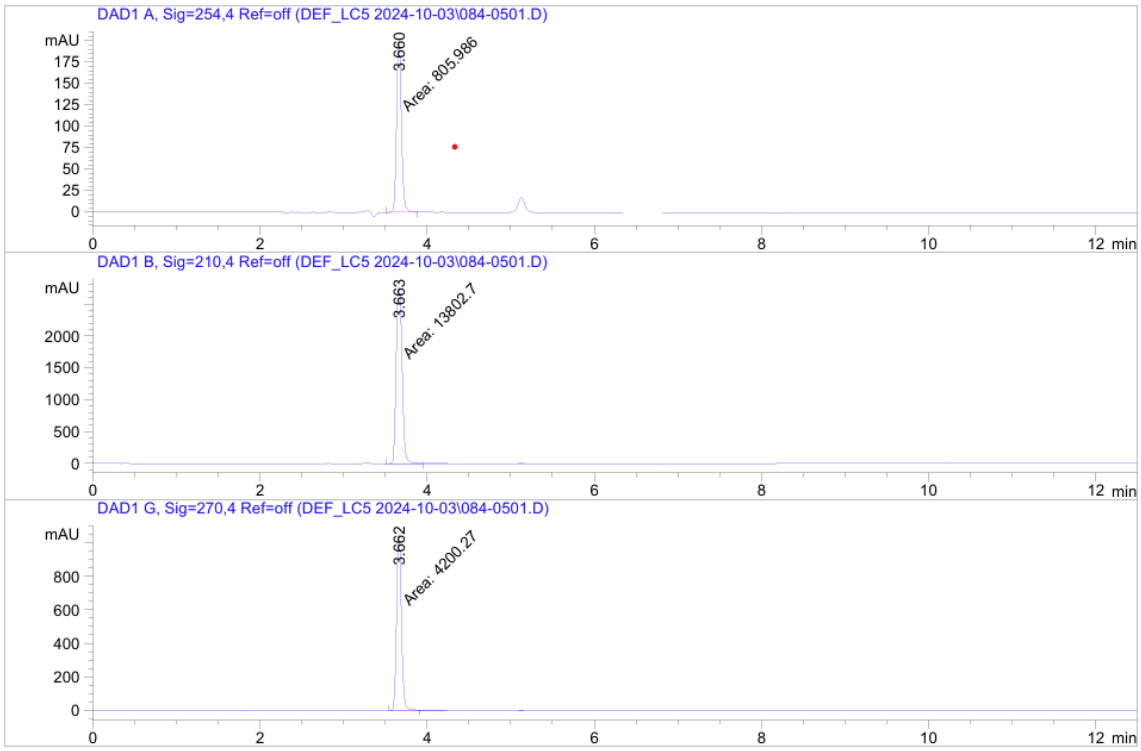

Figure A2.2. The HPLC peaks of hydroquinone (1000 ppm) at 210 nm, 254 nm, and 270 nm, respectively.

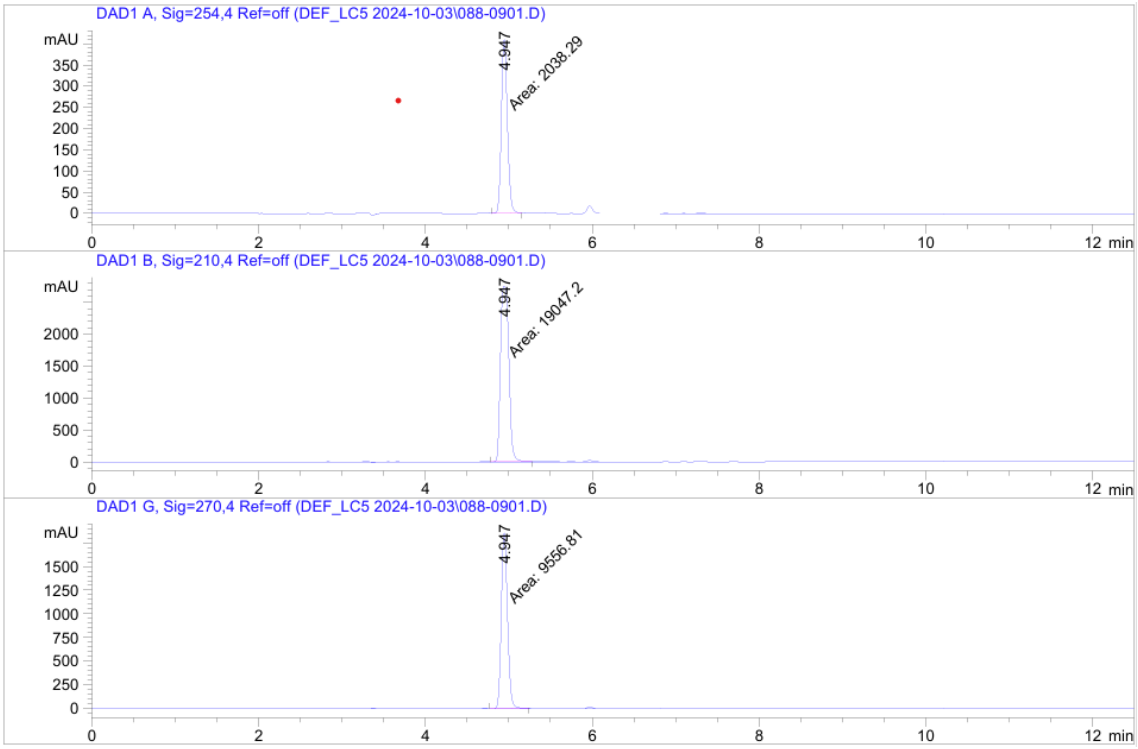

Figure A2.3. The HPLC peaks of catechol (1000 ppm) at 210 nm, 254 nm, and 270 nm, respectively.

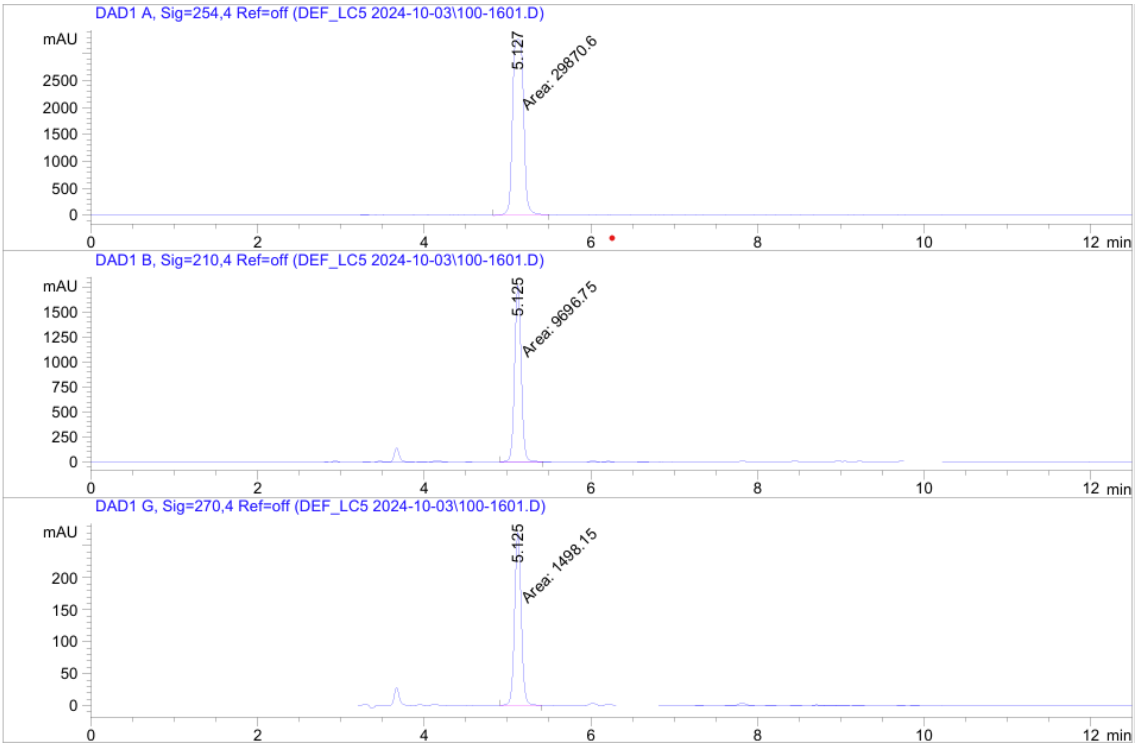

Figure A2.4. The HPLC peaks of para-Benzoquinone (1000 ppm) at 210 nm, 254 nm, and 270 nm, respectively.

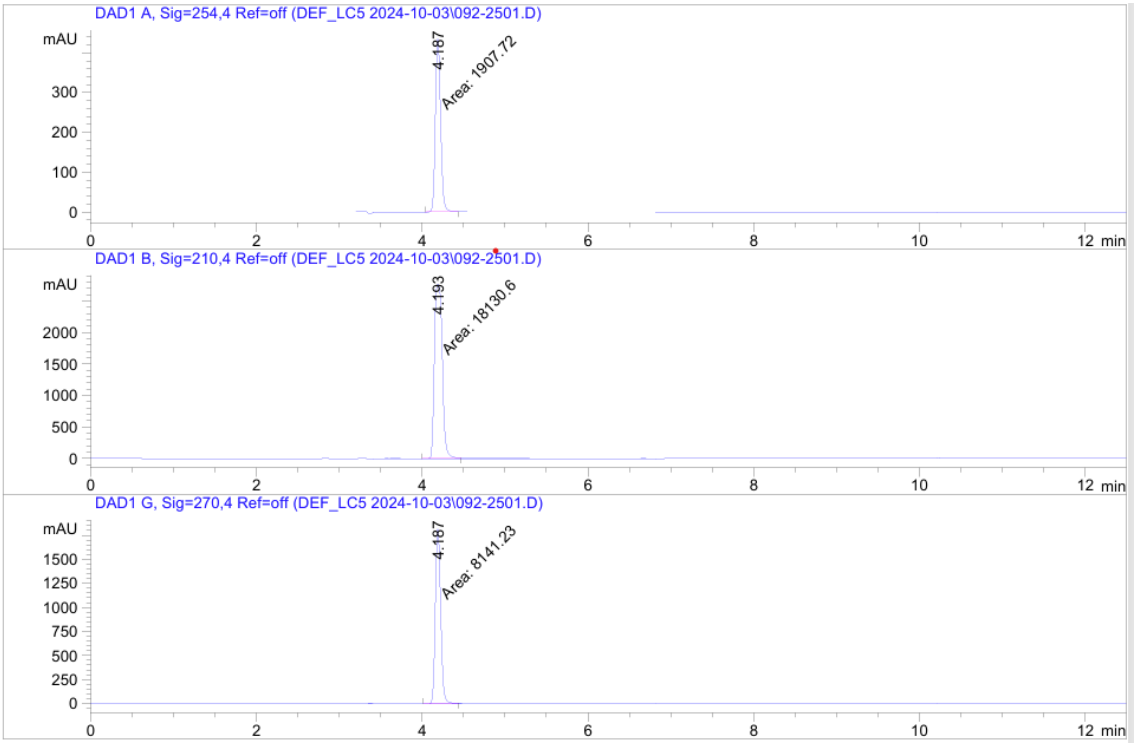

Figure A2.5. The HPLC peaks of resorcinol (1000 ppm) at 210 nm, 254 nm, and 270 nm, respectively.

2.9 References

1. Gong, X. *et al.* Enhanced catalyst selectivity in the direct synthesis of H2O2 through Pt incorporation into TiO2 supported AuPd catalysts. *Catal Sci Technol* **10**, 4635–4644 (2020).
2. Edwards, J. K., Carley, A. F., Herzing, A. A., Kiely, C. J. & Hutchings, G. J. Direct synthesis of hydrogen peroxide from H2 and O2 using supported Au–Pd catalysts. *Faraday Discuss* **138**, 225–239 (2008).
3. Santos, A. *et al.* Direct Synthesis of Hydrogen Peroxide over Au–Pd Supported Nanoparticles under Ambient Conditions. *Ind Eng Chem Res* **58**, 12623–12631 (2019).
4. Barnes, A., Lewis, R. J., Morgan, D. J., Davies, T. E. & Hutchings, G. J. Improving Catalytic Activity towards the Direct Synthesis of H2O2 through Cu Incorporation into AuPd Catalysts. *Catalysts* **12**, (2022).
5. Barnes, A., Lewis, R. J., Morgan, D. J., Davies, T. E. & Hutchings, G. J. Enhancing catalytic performance of AuPd catalysts towards the direct synthesis of H2O2 through incorporation of base metals. *Catal Sci Technol* **12**, 1986–1995 (2022).
6. Santos, A. *et al.* The degradation of phenol via in situ H2O2 production over supported Pd-based catalysts. *Catal Sci Technol* **11**, 7866–7874 (2021).
7. Santos, A. *et al.* The oxidative degradation of phenol via in situ H2O2 synthesis using Pd supported Fe-modified ZSM-5 catalysts. *Catal Sci Technol* **12**, 2943–2953 (2022).
8. Xie, J., Zhang, C. & Waite, T. D. Hydroxyl radicals in anodic oxidation systems: generation, identification and quantification. *Water Res* **217**, 118425 (2022).
9. Li, L. *et al.* Dual roles of MoS2 nanosheets in advanced oxidation Processes: Activating permonosulfate and quenching radicals. *Chemical Engineering Journal* **440**, 135866 (2022).
10. Freakley, S. J. *et al.* Effect of Reaction Conditions on the Direct Synthesis of Hydrogen Peroxide with a AuPd/TiO2 Catalyst in a Flow Reactor. *ACS Catal* **3**, 487–501 (2013).
11. Fu, J., Shao, Y., Wang, L. & Zhu, Y. Lysosome-controlled efficient ROS overproduction against cancer cells with a high pH-responsive catalytic nanosystem. *Nanoscale* **7**, 7275–7283 (2015).

12. Stenner, A. *et al.* Chemo-Enzymatic One-Pot Oxidation of Cyclohexane via in-situ H2O2 Production over Supported AuPdPt Catalysts. *ChemCatChem* **15**, e202300162 (2023).

13. Brehm, J. *et al.* Enhancing the Chemo-Enzymatic One-Pot Oxidation of Cyclohexane via In Situ H2O2 Production over Supported Pd-Based Catalysts. *ACS Catal* **12**, 11776–11789 (2022).

14. Dewidar, H., Nosier, S. A. & El-Shazly, A. H. Photocatalytic degradation of phenol solution using Zinc Oxide/UV. *J Chem Health Saf* **25**, 2–11 (2018).

15. Tian, N. *et al.* Biogenic manganese oxide: An efficient peroxymonosulfate activation catalyst for tetracycline and phenol degradation in water. *Chemical Engineering Journal* **352**, 469–476 (2018).

16. Liu, N., Lu, N., Yu, H., Chen, S. & Quan, X. Degradation of aqueous bisphenol A in the CoCN/Vis/PMS system: Catalyst design, reaction kinetic and mechanism analysis. *Chemical Engineering Journal* **407**, 127228 (2021).

17. Lee, Y.-Y., Fan, C. & Haque, F. Hybrid combination of advanced oxidation and biological processes for the micropollutant removal of carbamazepine. *NPJ Clean Water* **5**, 60 (2022).

18. Cao, J. *et al.* Degradation of tetracycline by peroxymonosulfate activated with zero-valent iron: Performance, intermediates, toxicity and mechanism. *Chemical Engineering Journal* **364**, 45–56 (2019).

19. de Melo Costa-Serge, N. *et al.* Fast degradation of 5-fluorouracil in urban wastewater by peroxymonosulfate activation using MgMnFe-layered double hydroxide. *J Mater Sci* **60**, 15567–15583 (2025).

20. Wu, S., Li, H., Li, X., He, H. & Yang, C. Performances and mechanisms of efficient degradation of atrazine using peroxymonosulfate and ferrate as oxidants. *Chemical Engineering Journal* **353**, 533–541 (2018).

21. N. Despotović, V. *et al.* Photocatalytic Degradation of Herbicide Quinmerac in Various Types of Natural Water. *Water Air Soil Pollut* **223**, 3009–3020 (2012).

22. Azam, M. A. & Mupit, M. Chapter 2 - Carbon nanomaterial-based sensor: Synthesis and characterization. in *Carbon Nanomaterials-Based Sensors* (eds. Manjunatha, J. G. &

Hussain, C. M.) 15–28 (Elsevier, 2022). doi:https://doi.org/10.1016/B978-0-323-91174-0.00015-9.

23. Iwashita, N. Chapter 2 - X-ray Powder Diffraction. in *Materials Science and Engineering of Carbon* (eds. Inagaki, M. & Kang, F.) 7–25 (Butterworth-Heinemann, 2016). doi:https://doi.org/10.1016/B978-0-12-805256-3.00002-7.

24. Azam, M. A. & Mupit, M. Chapter 2 - Carbon nanomaterial-based sensor: Synthesis and characterization. in *Carbon Nanomaterials-Based Sensors* (eds. Manjunatha, J. G. & Hussain, C. M.) 15–28 (Elsevier, 2022). doi:https://doi.org/10.1016/B978-0-323-91174-0.00015-9.

25. Greczynski, G., Haasch, R. T., Hellgren, N., Lewin, E. & Hultman, L. X-ray photoelectron spectroscopy of thin films. *Nature Reviews Methods Primers* **3**, 40 (2023).

26. Thommes, M. *et al.* Physisorption of gases, with special reference to the evaluation of surface area and pore size distribution (IUPAC Technical Report). **87**, 1051–1069 (2015).

27. Brunauer, S., Emmett, P. H. & Teller, E. Adsorption of Gases in Multimolecular Layers. *J Am Chem Soc* **60**, 309–319 (1938).

28. Barrett, E. P., Joyner, L. G. & Halenda, P. P. The Determination of Pore Volume and Area Distributions in Porous Substances. I. Computations from Nitrogen Isotherms. *J Am Chem Soc* **73**, 373–380 (1951).

29. Azam, M. A. & Seman, R. N. A. R. Chapter 4 - Analysis and characterization of graphene. in *Graphene, Nanotubes and Quantum Dots-Based Nanotechnology* (ed. Al-Douri, Y.) 67–89 (Woodhead Publishing, 2022). doi:https://doi.org/10.1016/B978-0-323-85457-3.00012-8.

30. Inkson, B. J. 2 - Scanning electron microscopy (SEM) and transmission electron microscopy (TEM) for materials characterization. in *Materials Characterization Using Nondestructive Evaluation (NDE) Methods* (eds. Hübschen, G., Altpeter, I., Tschuncky, R. & Herrmann, H.-G.) 17–43 (Woodhead Publishing, 2016). doi:https://doi.org/10.1016/B978-0-08-100040-3.00002-X.

31. Boote, C. *et al.* Scleral structure and biomechanics. *Prog Retin Eye Res* **74**, 100773 (2020).

32. Kumar, P. S., Pavithra, K. G. & Naushad, Mu. Chapter 4 - Characterization techniques for nanomaterials. in *Nanomaterials for Solar Cell Applications* (eds. Thomas, S., Sakho, E. H. M., Kalarikkal, N., Oluwafemi, S. O. & Wu, J.) 97–124 (Elsevier, 2019). doi:https://doi.org/10.1016/B978-0-12-813337-8.00004-7.

33. Jose Chirayil, C., Abraham, J., Kumar Mishra, R., George, S. C. & Thomas, S. Chapter 1 - Instrumental Techniques for the Characterization of Nanoparticles. in *Thermal and Rheological Measurement Techniques for Nanomaterials Characterization* (eds. Thomas, S., Thomas, R., Zachariah, A. K. & Mishra, R. K.) 1–36 (Elsevier, 2017). doi:https://doi.org/10.1016/B978-0-323-46139-9.00001-3.

34. da Cunha, M. M. L. *et al.* Overview of chemical imaging methods to address biological questions. *Micron* **84**, 23–36 (2016).

35. Lercher, J. A. & Jentys, A. Chapter 13 - Infrared and Raman Spectroscopy for Characterizing Zeolites. in *Studies in Surface Science and Catalysis* (eds. Čejka, J., van Bekkum, H., Corma, A. & Schüth, F.) vol. 168 435–476 (Elsevier, 2007).

36. Cohen, R. L. Mössbauer Spectroscopy: Recent Developments. *Science (1979)* **178**, 828–835 (1972).

37. Herber, R. H. Introduction to Mossbauer spectroscopy. *J Chem Educ* **42**, 180 (1965).

38. Rancourt, D. G. & Ping, J. Y. Voigt-based methods for arbitrary-shape static hyperfine parameter distributions in Mössbauer spectroscopy. *Nucl Instrum Methods Phys Res B* **58**, 85–97 (1991).

39. Klencsár, Z. Mössbauer spectrum analysis by Evolution Algorithm. *Nucl Instrum Methods Phys Res B* **129**, 527–533 (1997).

40. Arruda, T. R. *et al.* Chapter 2 - Emerging techniques for extraction and characterization of natural compounds. in *Green Products in Food Safety* (eds. Prakash, B. & Brilhante de São José, J. F.) 29–79 (Academic Press, 2023). doi:https://doi.org/10.1016/B978-0-323-95590-4.00009-6.

41. Singh, A. K. Chapter 4 - Experimental Methodologies for the Characterization of Nanoparticles. in *Engineered Nanoparticles* (ed. Singh, A. K.) 125–170 (Academic Press, Boston, 2016). doi:https://doi.org/10.1016/B978-0-12-801406-6.00004-2.

42. Brenner, I. (Joe). ICPMS Applications. in *Encyclopedia of Spectroscopy and Spectrometry (Second Edition)* (ed. Lindon, J. C.) 991–998 (Academic Press, Oxford, 2010). doi:https://doi.org/10.1016/B978-0-12-374413-5.00057-9.

43. Balaram, V. Microwave plasma atomic emission spectrometry (MP-AES) and its applications – A critical review. *Microchemical Journal* **159**, 105483 (2020).

44. Balaram, V. Microwave plasma atomic emission spectrometry (MP-AES) and its applications – A critical review. *Microchemical Journal* **159**, 105483 (2020).

45. Khalid, K., Ishak, R. & Chowdhury, Z. Z. Chapter 15 - UV–Vis spectroscopy in non-destructive testing. in *Non-Destructive Material Characterization Methods* (eds. Otsuki, A., Jose, S., Mohan, M. & Thomas, S.) 391–416 (Elsevier, 2024). doi:https://doi.org/10.1016/B978-0-323-91150-4.00021-5.

46. Quadri, T. W., Fayemi, O. E., Olasunkanmi, L. O. & Ebenso, E. E. Chapter 15 - Survey of different electrochemical and analytical techniques for corrosion measurements. in *Electrochemical and Analytical Techniques for Sustainable Corrosion Monitoring* (eds. Aslam, J., Verma, C. & Mustansar Hussain, C.) 293–323 (Elsevier, 2023). doi:https://doi.org/10.1016/B978-0-443-15783-7.00012-8.

Chapter 3 - Direct synthesis of H_2O_2 over trimetallic AuPdFe Catalysts

3.1 Introduction

The direct synthesis of H_2O_2 from molecular H_2 and O_2 represents a highly attractive alternative to the conventional industrial Anthraquinone Oxidation (AO) process.[1,2] Unlike the AO process, which involves multi-step redox cycling of anthraquinone derivatives,[2] the direct approach offers the potential for 100% atom economy, operational simplicity, and decentralised, on-demand H_2O_2 generation.[3,4] These characteristics are particularly advantageous for applications requiring continuous, low-level, in situ oxidant supply, such as water purification, green oxidation chemistry, and biomedical processes. In such contexts, the presence of proprietary stabilisers found in commercial H_2O_2 solutions produced via the AO process can be detrimental, rendering the direct synthesis route even more appealing.[3,5]

Despite its promise, the industrial adoption of the direct synthesis route has historically been hindered by several fundamental challenges, chief among them being the low selectivity towards H_2O_2. The undesired degradation of the product to water via both hydrogenation and decomposition pathways has been a major obstacle, as these side reactions significantly reduce process efficiency and pose difficulties in achieving economically viable concentrations of the target product.[3] However, in recent years, the development of increasingly sophisticated catalytic formulations has led to marked improvements in selectivity. Numerous studies have reported near-total H_2O_2 selectivity under mild conditions, primarily through the rational design of supported Pd-based catalysts with tailored surface compositions.[6–10]

To render the direct process commercially competitive with the AO method, however, it is necessary to achieve H_2O_2 concentrations of at least ~5 vol.%. This threshold is critical to minimise the energy-intensive downstream steps required for product separation and concentration. At present, such concentrations have only been attained under reaction conditions involving H_2/O_2 mixtures within the explosive regime conditions (<5%) that pose significant safety hazards and are impractical for scale-up or continuous industrial use.[11] This limitation has prompted continued research into strategies for improving catalyst productivity under safe operating conditions.

Among the most effective approaches to catalyst design has been the incorporation of secondary metal promoters into supported Pd-based systems.[9,12] Of these, AuPd bimetallic catalysts have emerged as particularly promising candidates.[13,14] The formation of AuPd nanoalloys has been shown to induce synergistic effects, attributed to a combination of electronic and geometric effects.[15] In particular, alloying Au with Pd disrupts extended Pd ensembles that are otherwise prone to cleaving O–O bonds in intermediates such as adsorbed peroxide (*H_2O_2), hydroperoxyl (*OOH), or molecular oxygen (*O_2), thereby suppressing the over-reduction of H_2O_2 to water and enhancing selectivity.

Despite the progress achieved with bimetallic systems, the potential of trimetallic catalysts in the direct synthesis of H_2O_2 has received comparatively limited attention. Initial studies in the Hutchings group revealed the promotive effect on H_2O_2 productivity when incorporating Ru or Pt into AuPd catalysts.[16–20] Such enhancement is further explained by Xu et al.,[21] who conducted a theoretical calculation combined density functional theory (DFT) calculations and Sabatier analysis, and determined that introducing certain elements (e.g. Pt, Ru, W, Pb, etc) into AuPd catalysts would enhance the H_2O_2 productivity. Following this theory, a subsequent study focused on introducing tungsten (W) into a supported AuPd catalyst, and experimental results showed 47% and 16% enhancement in H_2O_2 productivity and selectivity, respectively, compared to the bimetallic AuPd analogue.[22] Although some base metals were not mentioned in this theory,[21] the promotive effects have also been found in emerging studies that the use of very low-level earth-abundant transition metals (e.g. 0.025 wt.%), including Cu, Zn, and Ni, could enhance the activity or selectivity of H_2O_2 synthesis, compared to their bimetallic AuPd analogues.[5,23] The mechanistic basis for these improvements is still under investigation, but proposed explanations include modification of electronic properties, changes in nanoparticle morphology, and alteration of the adsorption/desorption energetics of key intermediates.

Building upon this body of work, in this Chapter, the present study turns its attention to the incorporation of Fe as a dopant within the AuPd catalyst framework. As an abundant, low-cost transition metal with multiple accessible oxidation states and redox flexibility, Fe presents a compelling candidate for catalytic promotion. However, its role in modulating the activity, selectivity, and stability of AuPd catalysts in the context of H_2O_2 synthesis remains underexplored. This study aims to systematically evaluate the influence of Fe on the performance of AuPd/TiO_2 catalysts, examining how subtle changes in Fe content affect catalytic behaviour and establishing structure–function relationships through detailed characterisation and kinetic analyses.

3.2. Initial Screening of the AuPdFe series towards Direct Synthesis of H_2O_2

Building on the foundational principles established in previously reported trimetallic AuPd-based catalysts,[5,19,23] the present investigation sought to explore the ability of dopant concentrations of Fe to promote the performance of AuPd-based catalysts towards H_2O_2 production and the subsequent H_2O_2 degradation (**Figure 3.1**). All catalysts were prepared via a wet co-impregnation method, and the actual metal loadings (wt.%) are presented in **Table A3.1**. Under conditions that have previously been optimised to ensure H_2O_2 productivity and stability,[14] the results from the initial screening revealed that the optimal $Au_{0.5}Pd_{0.5}Fe_{0.02}/TiO_2$ formulation achieved rates of H_2O_2 synthesis (122 mol_{H2O2} Kg_{Cat}^{-1} h^{-1}, 0.242 wt.% H_2O_2 concentration), significantly outperformed the bimetallic $Au_{0.5}Pd_{0.5}/TiO_2$ catalyst (70 mol_{H2O2} Kg_{Cat}^{-1} h^{-1}, 0.139 wt.% H_2O_2 concentration). In contrast, the high Fe-loaded $Au_{0.5}Pd_{0.5}Fe_1/TiO_2$ catalyst offered a declined H_2O_2 synthesis rate (65 mol_{H2O2} Kg_{Cat}^{-1} h^{-1}, 0.129 wt.% H_2O_2 concentration), falling slightly below that of the bimetallic analogue (70 mol_{H2O2} Kg_{Cat}^{-1} h^{-1}, 0.139 wt.% H_2O_2). The inverse relationship between Fe content and catalytic performance beyond the optimum loading (0.02 wt.%) threshold suggests that excessive Fe may reduce the net H_2O_2 yield by **1)** disrupting beneficial alloying effects or introducing structural/electronic changes that hinder H_2 activation and further reducing the reactivity towards H_2O_2 synthesis, and 2) the interaction between Fe and in situ generated H_2O_2 via Fenton pathway (e.g. $=Fe^{2+} + H_2O_2 \rightarrow =Fe^{3+} + \cdot OH + OH^-$), considering the Fe is one of the most popular Fenton metals.[24–26]

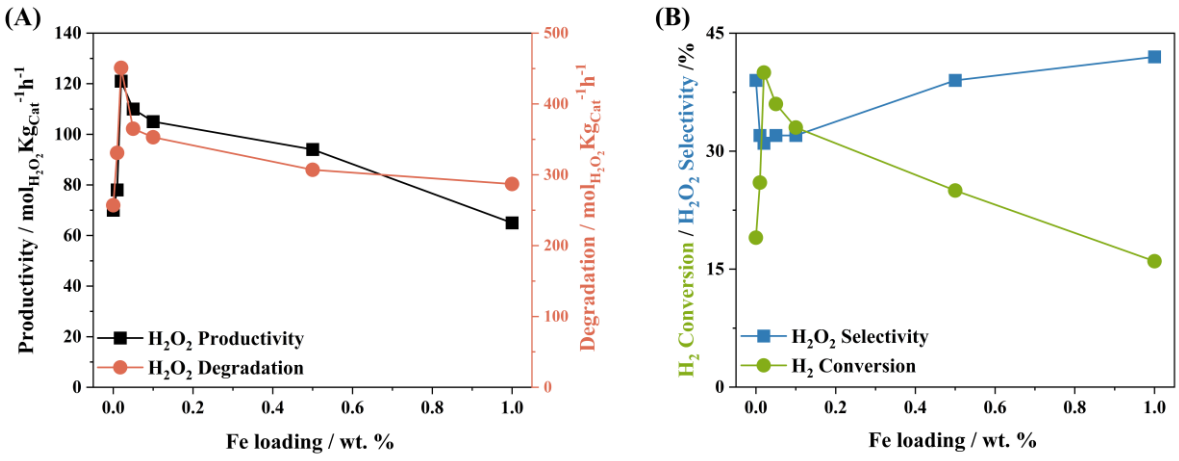

Figure 3.1. The effect of Fe loading on the performance of $Au_{0.5}Pd_{0.5}/TiO_2$ catalysts towards the direct synthesis and subsequent degradation of H_2O_2. **Key:** H_2O_2 synthesis (black squares), H_2O_2 degradation (orange circles), H_2 conversion (green circles), H_2O_2 selectivity (blue squares) **H_2O_2 direct synthesis reaction conditions:** Catalyst (0.01 g), H_2O (2.9 g), MeOH (5.6 g), 5% H_2/CO_2 (420 psi), 25% O_2/CO_2 (160 psi), 0.5 h, 2 °C 1200 rpm.

H_2O_2 degradation reaction conditions: Catalyst (0.01 g), H_2O_2 (50 wt% 0.68 g), H_2O (2.22 g), CH_3OH (5.6 g), 5% H_2/CO_2 (420 psi), 0.5 h, 2 °C, 1200 rpm. **Note:** Additional data is reported in **Table A3.2**.

Interestingly, catalytic activity towards H_2O_2 degradation (hydrogenation and decomposition) followed a similar trend to that observed for H_2O_2 synthesis. H_2O_2 degradation rate reached a maximum 451 $mol_{H2O2}\ kg_{Cat}^{-1}\ h^{-1}$ at a Fe loading of 0.02%, before decreasing considerably to 287 $mol_{H2O2}kg^{-1}cat^{-1}$ with the further incorporation of Fe up to 1 wt.%. Determination of catalytic selectivity towards H_2O_2 and H_2 conversion during H_2O_2 synthesis is presented in **Figure 3.1 (B)**. H_2 conversion rate drastically increased from 19% ($Au_{0.5}Pd_{0.5}/TiO_2$) to 40% ($Au_{0.5}Pd_{0.}5Fe_{0.02}/TiO_2$) before dropping down to 16% ($Au_{0.5}Pd_{0.5}Fe_1/TiO_2$) with excessive Fe loading. In contrast, H_2O_2 selectivity followed an opposing trend. The optimal formulation exhibited a relatively lower H_2O_2 selectivity at 31%, in comparison to the bimetallic $Au_{0.5}Pd_{0.5}/TiO_2$ (39%) and the Fe-rich $Au_{0.5}Pd_{0.5}Fe_1/TiO_2$ catalyst (42%). These experimental results suggest that **1)** the optimal trimetallic formulation ($Au_{0.5}Pd_{0.5}Fe_{0.02}/TiO_2$) is active towards both H_2O_2 synthesis and degradation, which might be due to the superior H_2 activation ability (**Figure 3.1 (B)**), and **2)** the higher Fe loading limit catalytic activity of the trimetallic AuPdFe catalysts by preventing H_2 conversion rather than promoting H_2O_2 degradation, which again may have been expected based on the previous hypothesis on the effect of Fenton pathway on the net H_2O_2 yield.

These measurements, alongside our evaluation of H_2O_2 synthesis and degradation activity (**Figure 3.1 (A)**), revealed that the improved performance that results from the introduction of dopant quantities of Fe could be primarily associated with increased rates of H_2 utilisation (an indicator of catalytic activity), rather than through an enhancement in H_2O_2 selectivity. The improved performance of the $Au_{0.5}Pd_{0.5}Fe_{0.02}/TiO_2$ catalyst is further highlighted through a comparison of the calculated initial rate of reaction (**Table A3.2**), at a reaction time (5 minutes), where it may be assumed **1)** that there is no or limited contribution from subsequent H_2O_2 degradation reactions and **2)** that the reaction is not limited by gaseous reagent availability. The rate of reaction over $Au_{0.5}Pd_{0.5}Fe_{0.02}/TiO_2$ ($3\times10^{\wedge3}$ $mmol_{H2O2}\ mmol_{metal}^{-1}\ min^{-1}$) was found to be 6 times that observed on $Au_{0.5}Pd_{0.5}Fe_1/TiO_2$ ($4.65\times10^{\wedge2}$ $mmol_{H2O2}\ mmol_{metal}^{-1}\ min^{-1}$) and 20% higher than the $Au_{0.5}Pd_{0.5}/TiO_2$ ($2.46\times10^{\wedge3}$ $mmol_{H2O2}\ mmol_{metal}^{-1}\ min^{-1}$).

The pronounced dependence of catalytic performance on Fe loading in the AuPdFe catalyst series prompted a more detailed investigation into the underlying structure–activity relationships. Notably, the enhanced catalytic activity of key formulations compared to those

previously reported in the literature (**Table A3.3**), thereby providing a strong rationale for selecting representative formulations ($Au_{0.5}Pd_{0.5}/TiO_2$, $Au_{0.5}Pd_{0.5}Fe_{0.02}/TiO_2$ and $Au_{0.5}Pd_{0.5}Fe_1/TiO_2$) for further investigation of the structure–activity relationships **Figure 3.1**) indicated that the incorporation of Fe resulted in a loss of selectivity towards H_2O_2, it is important to highlight that the catalytic series was not compared at near-equivalent rates of H_2 conversion.

Table 3.1. Comparison of catalytic selectivity towards H_2O_2 at iso-conversion.

Catalyst	Reaction time / min	H_2 Conv. / %	H_2O_2 Sel. / %	H_2O_2 Conc. / wt.%
$Au_{0.5}Pd_{0.5}/TiO_2$	10	8	50	0.08
$Au_{0.5}Pd_{0.}5Fe_{0.02}/TiO_2$	5	9	41	0.07
$Au_{0.5}Pd_{0.5}Fe_1/TiO_2$	10	8	37	0.06

H_2O_2 direct synthesis reaction conditions: Catalyst (0.01 g), H_2O (2.9 g), CH_3OH (5.6 g), 5% H_2/CO_2 (420 psi), 25% O_2/CO_2 (160 psi), 5 mins or 10 mins, 2° C, 1200 rpm.

Subsequent evaluation of H_2O_2 selectivity of key catalyst formulations at near iso-conversion is reported in **Table 3.1**, from which it is clear that the incorporation of dopant concentrations of Fe (0.02 wt.%) does indeed reduce catalytic selectivity (41% selectivity at 9% H_2 conversion), compared to that offered by the parent bi-metallic analogue (50% selectivity at 8% H_2 conversion). However, the extent of this reduction is not as substantial as that which may be inferred from the data reported in **Figure 3.1**. Such comparisons suggest that the enhanced performance of the $Au_{0.5}Pd_{0.5}Fe_{0.02}/TiO_2$ catalyst is indeed associated with increased activity, rather than a promotion of catalytic selectivity.

The further investigation of catalyst stability of the key formulations by the inductively coupled plasma-mass spectrometry (ICP-MS) in **Table 3.2** revealed negligible leaching of Au and Fe, with measured concentrations below the detection limit. In contrast, Pd was detected in all post-reaction filtrates, indicating minor but measurable leaching. For the bimetallic catalyst ($Au_{0.5}Pd_{0.5}/TiO_2$), Pd leaching was quantified at 3.3 ppb (0.06% of the total Pd loading), suggesting moderate stability under the reaction conditions. The addition of 0.02 wt% Fe to the trimetallic formulation resulted in a slight decrease in Pd leaching to 3.0 ppb (0.06%, within error), while maintaining negligible Fe dissolution. This suggests that trace Fe incorporation does not compromise structural stability and may slightly suppress Pd loss. However, when the Fe loading was increased to 1 wt%, Pd leaching increased to 6.3 ppb (0.12%), although Fe

remained undetectable in solution, indicating that excessive Fe content affects the interaction between metals and the support. The low extent of leaching in all cases confirms reasonable catalyst stability over short reaction times, but also highlights the need for further investigation of the catalyst stability over a prolonged reaction time.

Table 3.2. Catalyst stability after a 0.5 h H_2O_2 direct synthesis reaction, as determined by ICP analysis of post-H_2O_2 direct synthesis reaction solutions.

Catalyst	Au / ppb (%)	Pd / ppb (%)	Fe / ppb (%)
$Au_{0.5}Pd_{0.5}/TiO_2$	0.0 (0.0)	3.3 (0.06)	-
$Au_{0.5}Pd_{0.}5Fe_{0.02}/TiO_2$	0.0 (0.0)	3.0 (0.06)	0.0 (0.0)
$Au_{0.5}Pd_{0.5}Fe_1/TiO_2$	0.0 (0.0)	6.3 (0.12)	0.0 (0.0)

H_2O_2 direct synthesis reaction conditions: catalyst (0.01 g), H_2O (2.9 g), MeOH (5.6 g), 5% H_2/CO_2 (420 psi), 25% O_2/CO_2 (160 psi), 0.5 h, 2 °C, 1200 rpm.

3.3. Characterisation of the AuPdFe series

Preliminary investigations into the AuPdFe catalyst series for the direct synthesis of H_2O_2 have demonstrated that the incorporation of a trace amount of Fe (0.02 wt.%) into a bimetallic $AuPd/TiO_2$ system can lead to a remarkable enhancement in catalytic activity. This improvement is strongly associated with an increased H_2 conversion rate, suggesting that the introduction of Fe, even at such a minimal level, modifies the catalytic environment in a manner favourable to H_2 activation and subsequent H_2O_2 formation. While the beneficial effect of Fe addition is evident, the structural origin of this promotional behaviour remains to be fully elucidated. It is hypothesised that Fe incorporation alters key physicochemical parameters of the catalyst, thereby influencing its reactivity. In particular, three interrelated factors are believed to underpin the observed enhancement, **1)** the changes in the oxidation state of Pd, **2)** the modifications to the size, dispersion, and distribution of the metallic nanoparticles, which govern the availability and nature of catalytically active surface sites, and **3)** the extent and nature of alloy formation among Au, Pd, and Fe, which can modulate charge transfer.

To establish a structure–activity relationship and to gain insight into the role of Fe as a promoter, the following Section undertakes a comprehensive characterisation of the AuPdFe catalyst series. A combination of advanced analytical techniques is employed to probe the surface oxidation states, nanoparticle morphology, and alloying behaviour of the catalysts. These

characterisation results will be used to rationalise the enhanced catalytic performance observed and to provide a foundation for the informed design of next-generation trimetallic catalysts for efficient and selective H_2O_2 synthesis.

3.3.1. Characterisation of the AuPdFe catalyst series

X-ray diffraction (XRD) was first utilised to determine the structure of the TiO_2 supported AuPdFe series. From **Figure 3.2**, all samples display characteristic reflections corresponding to the anatase phase (*ICDD PDF File 00-021-1272*) and rutile phase (*ICDD PDF File 00-021-1276*) phases[27] and no new diffraction peaks or significant peak shifts are observed after the addition of Au, Pd, or Fe and the reductive thermal treatment, indicating that metal loading does not alter the crystalline structure of TiO_2. Such observations are perhaps, unsurprisingly, considering the relatively low metal loading (between 1 wt.% to 2 wt.% total metal), which is in keeping with previously reported bimetallic AuPd and trimetallic AuPd-based catalysts synthesised via a similar preparation method.[5,19]

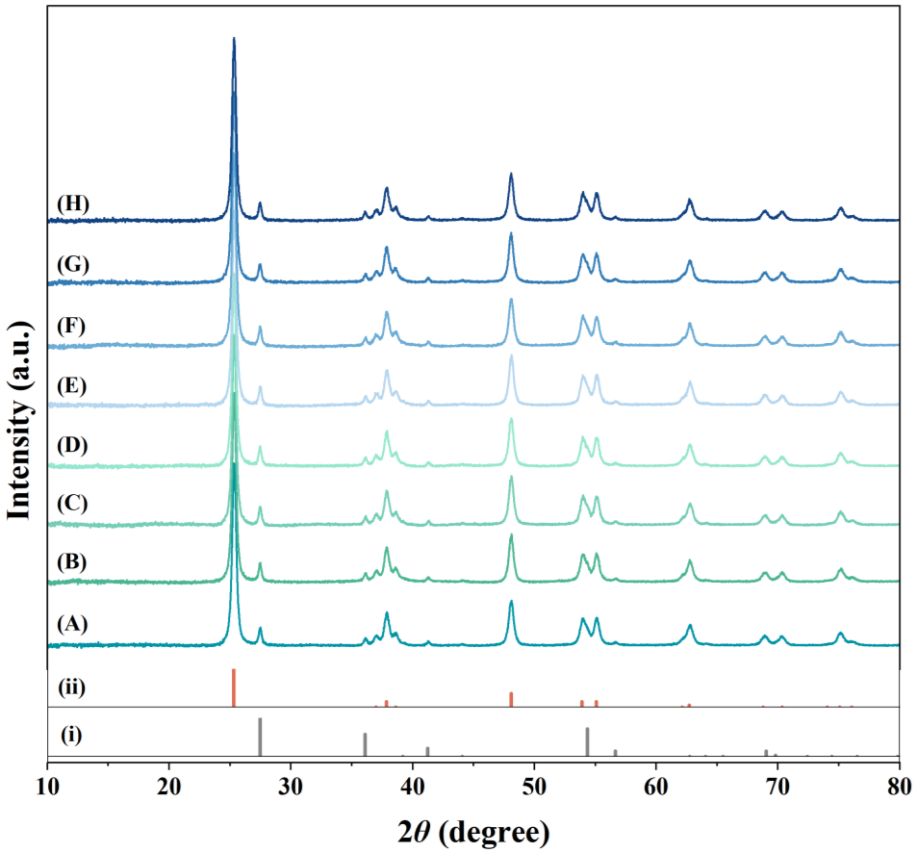

Figure 3.2. X-ray diffractograms of AuPdFe/TiO_2 catalysts. (A) TiO_2, (B) $Au_{0.5}Pd_{0.5}/TiO_2$, (C), $Au_{0.5}Pd_{0.5}Fe_{0.01}/TiO_2$, (D) $Au_{0.5}Pd_{0.5}Fe_{0.02}/TiO_2$, (E) $Au_{0.5}Pd_{0.5}Fe_{0.05}/TiO_2$, (F) $Au_{0.5}Pd_{0.5}Fe_{0.1}/TiO_2$, (G) $Au_{0.5}Pd_{0.5}Fe_{0.5}/TiO_2$, and (H)

$Au_{0.5}Pd_{0.5}Fe_1/TiO_2$ and with corresponding (i) Rutile (**ICDD PDF File 00-021-1276**) and (ii) Anatase phases (**ICDD PDF File 00-021-1272**). Note: Catalysts exposed to a reductive heat treatment (5%H_2/Ar, 400 °C, 4h, 10 °C min^{-1}). Support (TiO_2 P25), used as received.

Brunauer-Emmett-Teller (BET) analysis was taken to determine the potential changes in surface area after doping metal onto TiO_2 support (**Table 3.3**). The unmodified TiO_2 P25 support exhibited a surface area of 57 $m^2 g^{-1}$. Introduction of Au and Pd results in a slight reduction to 51 $m^2 g^{-1}$, likely due to partial pore coverage or blockage by the metal particles, in keeping with the previous observation.[13] Further incorporation of Fe causes subtle variations in surface area. No systematic trend is observed with increasing Fe loading, indicating that Fe addition has only a modest influence on the overall textural properties. The relatively small changes suggest that the mesoporous structure of the TiO_2 P25 support remains largely preserved across the catalyst series, with no significant sintering or pore collapse under the thermal reduction conditions used.

Table 3.3. BET analysis for the surface area of the AuPdFe series.

Catalyst	Surface Area / m^2g^{-1}
TiO_2	57
$Au_{0.5}Pd_{0.5}/TiO_2$	51
$Au_{0.5}Pd_{0.5}Fe_{0.01}/TiO_2$	45
$Au_{0.5}Pd_{0.5}Fe_{0.02}/TiO_2$	53
$Au_{0.5}Pd_{0.5}Fe_{0.05}/TiO_2$	49
$Au_{0.5}Pd_{0.5}Fe_{0.1}/TiO_2$	52
$Au_{0.5}Pd_{0.5}Fe_{0.5}/TiO_2$	55
$Au_{0.5}Pd_{0.5}Fe_1/TiO_2$	48

3.3.2. The effect of Fe on the particle size distribution

Particle size plays a critical role in determining the catalytic performance towards the direct H_2O_2 synthesis, in terms of the H_2O_2 selectivity and productivity, as illustrated by Tian et al.[12] Transition electron microscopy (TEM) was employed to evaluate the particle size distribution of the trimetallic AuPdFe series, as reported in **Table 3.4** (Representative micrographs are reported in **Figure A3.1** and **Figure A3.2**). For each catalyst, over 200 nanoparticles were

counted to maintain the accuracy of the mean size calculation. Across the series, the observed particle sizes remain within a narrow range of approximately 2 to 5 nm. The parent bimetallic $Au_{0.5}Pd_{0.5}Pd/TiO_2$ catalyst exhibits a mean particle size of 4.4 nm (according to the TEM particle size distribution analysis), while the Fe-modified trimetallic catalysts show only minor variations, with no consistent trend as a function of Fe content, suggesting that Fe incorporation at the investigated concentrations does not significantly influence particle growth or agglomeration during the thermal treatment process, which is also in agreement with the XRD analysis (**Figure 3.2**), showing no distinct diffraction peaks attributable to crystalline metallic phases. Also, there is no direct correlation between particle size and H_2O_2 productivity.

Table 3.4. The correlation between mean particle size and H_2O_2 productivity of the as-prepared $AuPdFe/TiO_2$ catalysts, as a function of Fe content.

Catalyst	Mean Particle Size (nm) /(Standard Deviation)	H_2O_2 Productivity (mol_{H2O2} Kg_{Cat}^{-1} h^{-1})
$Au_{0.5}Pd_{0.5}/TiO_2$	4.4 (1.7)	70
$Au_{0.5}Pd_{0.}5Fe_{0.01}/TiO_2$	4.6 (2.0)	78
$Au_{0.5}Pd_{0.}5Fe_{0.02}/TiO_2$	2.8 (1.1)	122
$Au_{0.5}Pd_{0.}5Fe_{0.05}/TiO_2$	4.0 (2.1)	110
$Au_{0.5}Pd_{0.}5Fe_{0.1}/TiO_2$	3.8 (2.1)	105
$Au_{0.5}Pd_{0.}5Fe_{0.5}/TiO_2$	3.2 (1.3)	94
$Au_{0.5}Pd_{0.}5Fe_{1}/TiO_2$	3.7 (1.9)	65

3.3.3. The effect of Fe on the catalyst morphology and alloys

Analysis of key catalyst formulations ($Au_{0.5}Pd_{0.5}/TiO_2$, $Au_{0.5}Pd_{0.}5Fe_{0.02}/TiO_2$ and $Au_{0.5}Pd_{0.5}Fe_1/TiO_2$) via scanning Transmission Electron Microscope (STEM), corroborated the earlier investigation by TEM (**Table 3.4**, **Figure A3.1** and **Figure A3.2**), which indicated the minimal variation in particle size across the wider catalyst series. Corresponding element mapping further revealed the intimate alloying of active metals (**Figure 3.3**). However, in the case of the $Au_{0.5}Pd_{0.}5Fe_{0.02}/TiO_2$ catalyst, no clear signal associated with Fe was measured, which may be attributed to the low metal loading, rather than the inability of the constituent metals to form alloyed structures, similar to the previous reported AuPdPt catalysts with the optimal Pt loading where Pt signal was not detectable by X-EDS mapping due to the ultra-low

loading.[19] The existence of Fe was clearly evidenced by analysis of the Fe-rich $Au_{0.5}Pd_{0.}5Fe_1/TiO_2$ catalyst, and notably, the immobilised metal nanoparticles were found to exist as random alloys, rather than the core-shell morphologies which have previously been reported for AuPd-based catalysts prepared on oxide supports, via similar impregnation methodologies.[28] However, such AuPd core–shell motifs are most commonly generated by oxidative heat treatment in air, which drives Pd to segregate to the surface and yields an Au-rich core with a Pd-rich shell.[29] Under oxidising conditions, the near-surface Pd readily forms PdO, so the outer layer is often Pd-oxide.[30] By contrast, the reductive H_2 treatment used in this study reduces Pd oxides and favours metallic surfaces or re-alloyed Au–Pd rather than Pd-oxide shells.[31,32]

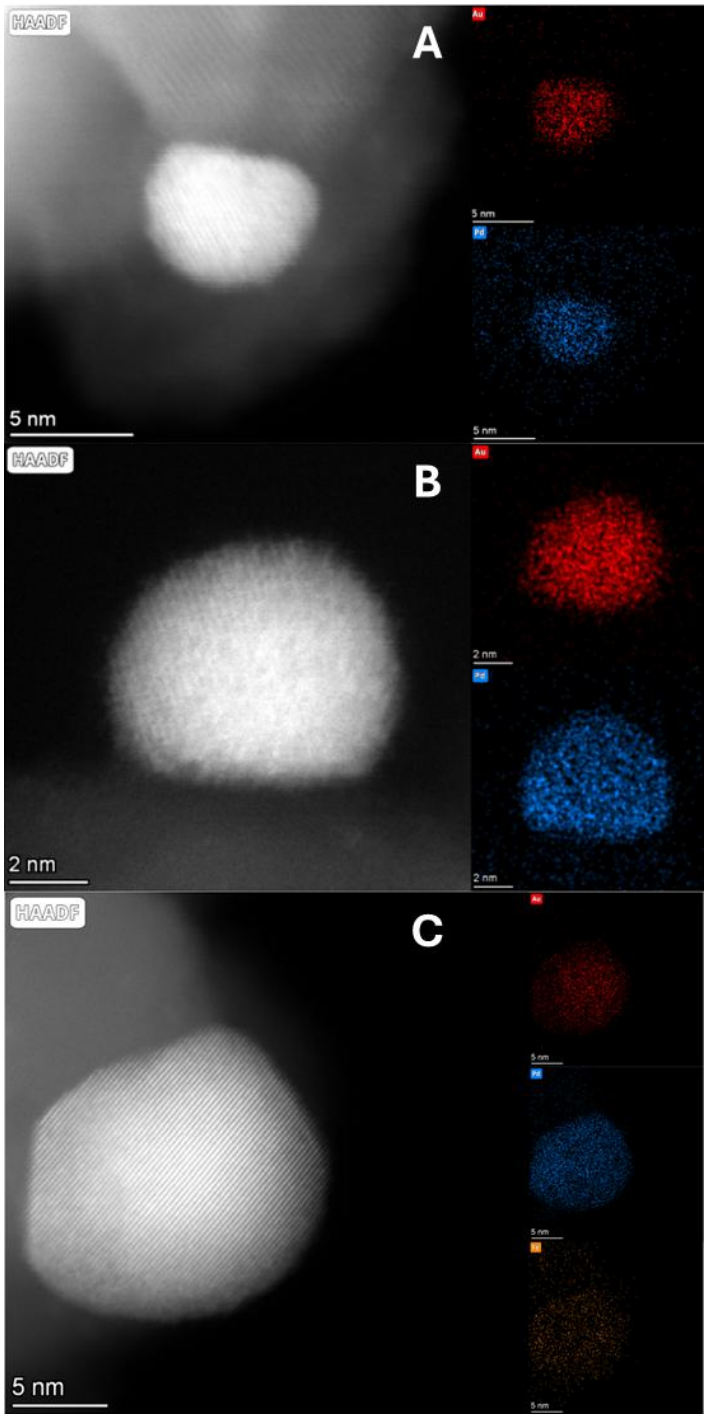

Figure 3.3. Representative HAADF-STEM micrographs and complementary EDX analysis of individual alloy nanoparticles in **(A)** $Au_{0.5}Pd_{0.5}/TiO_2$, **(B)** $Au_{0.5}Pd_{0.5}Fe_{0.02}/TiO_2$ and **(C)** $Au_{0.5}Pd_{0.5}Fe_1/TiO_2$. Element mapping key: Au-Red, Pd-Blue, Fe-Orange. **Note:** Catalysts exposed to a reductive heat treatment prior to use (5%H_2/Ar, 400 °C, 4h, 10 °C min^{-1}).

3.3.4. The electron modification of Pd by the introduction of Fe

The evaluation of the as-prepared AuPdFe/TiO_2 catalysts by X-ray photoelectron spectroscopy (XPS) is shown in **Figure 3.4** to gain a better understanding of the effect of Pd^{2+}/Pd^0 ratio on H_2O_2 synthesis. The presence of a significant proportion of Pd^{2+} for all formulations, despite the exposure of the catalysts to a relatively high-temperature reductive heat treatment (5%H_2/Ar, 400 °C, 4h, 10 °C min^{-1}), is likely due to preparation for analysis in standard laboratory conditions. However, it is evident the incorporation of Fe results in a clear shift in Pd speciation, towards Pd^{2+}, as shown in **Table 3.5**, and an overall increasing trend on the Pd^{2+}/Pd^0 ratio from 0.3 ($Au_{0.5}Pd_{0.5}/TiO_2$) to 1.5 ($Au_{0.5}Pd_{0.5}Fe_1/TiO_2$). Such observations align well with our earlier studies investigating the role of alternative transition metals as promoters for AuPd nanoalloys.[5,23] Notably, the performance of Pd-based catalysts towards H_2O_2 synthesis is well known to be highly dependent on Pd oxidation state, with domains of mixed Pd^{2+}-Pd^0 species typically offering improved performance compared to those with a predominance of Pd in either oxidation state.[33] As such, it is possible, at least in part, to attribute the improved activity, which results from the incorporation of dopant levels of Fe into AuPd alloys, to the control of Pd speciation.

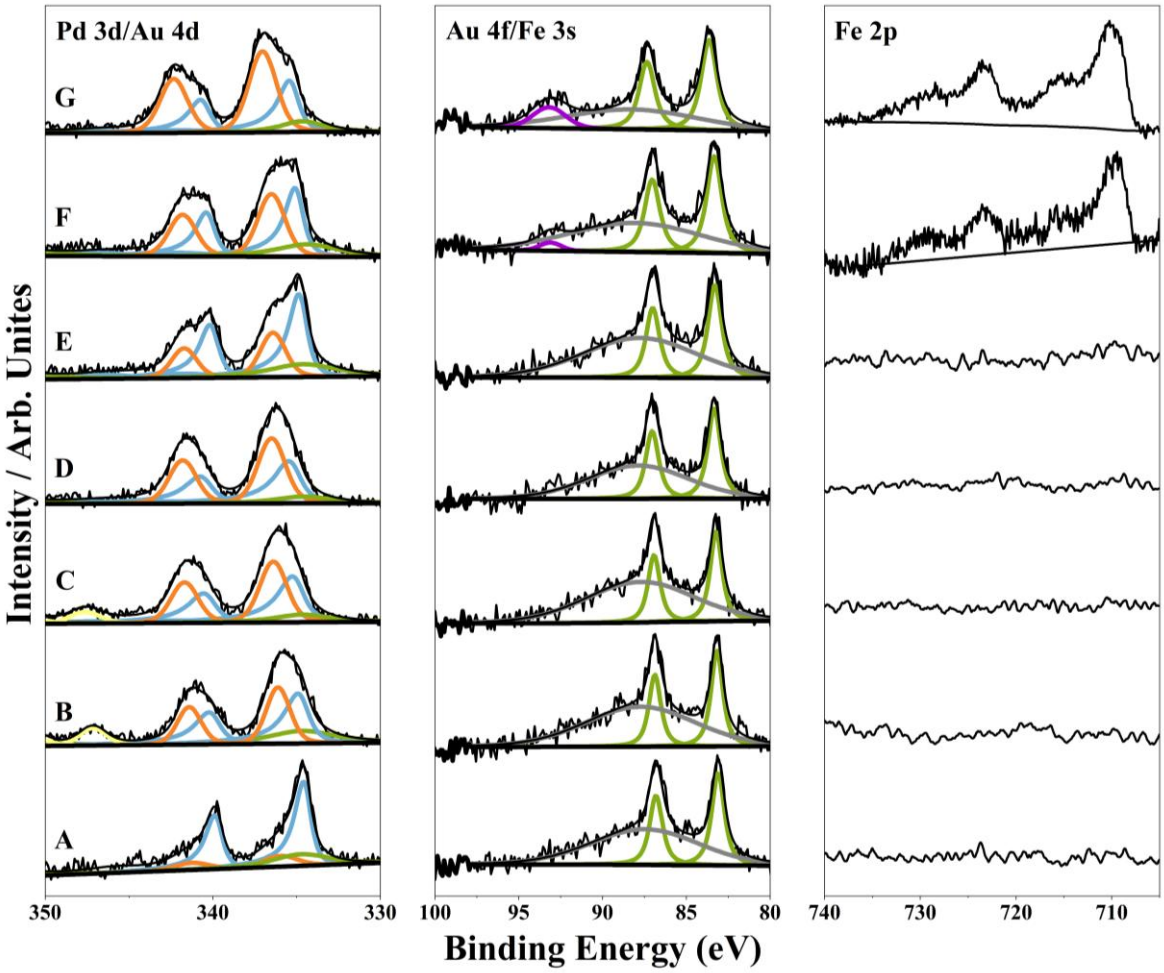

Figure 3.4. XPS analysis of the as-prepared AuPdFe/TiO_2 catalysts. **(A)** $Au_{0.5}Pd_{0.5}/TiO_2$, **(B)** $Au_{0.5}Pd_{0.5}Fe_{0.01}/TiO_2$, **(C)** $Au_{0.5}Pd_{0.5}Fe_{0.02}/TiO_2$, **(D)** $Au_{0.5}Pd_{0.5}Fe_{0.05}/TiO_2$, **(E)** $Au_{0.5}Pd_{0.5}Fe_{0.1}/TiO_2$, **(F)** $Au_{0.5}Pd_{0.5}Fe_{0.5}/TiO_2$ and **(G)** $Au_{0.5}Pd_{0.5}Fe_1/TiO_2$. **Key:** Au(4d) & Au(4f) (green); Fe(3s) (purple); Pd^0 (blue); Pd^{2+} (orange); loss structure (grey); Ca^{2+} (yellow). **Note 1:** Catalysts exposed to a reductive heat treatment prior to use (5%H_2/Ar, 400 °C, 4h, 10 °C min^{-1}). **Note 2:** Ca^{2+} signal results from the use of distilled water during catalyst preparation. **Please note**: the test and subsequent analysis were performed by Dr. David J. Morgan (Cardiff University; HarwellXPS).

In the case of the Fe speciation, only a distinct signal at a binding energy of 710.8 eV and satellite structure at *ca.* 719 eV, were observed[34] characteristic of Fe^{3+} on the Fe-rich trimetallic catalysts (Fe loading >=0.5 wt.%), while no Fe 2p signal could be detected on the trimetallic samples with lower Fe loading. However, the propensity of Fe to readily oxidise under ambient conditions and the surface sensitivity of XPS need to be highlighted. The broadness of the Fe 2p core-level spectra suggests a lower oxidation state could be present; as such, the presence of lower Fe oxidation states based on XPS analysis alone cannot be ruled out. It should also be noted that active metal speciation of the as-prepared materials is likely not fully representative of those under reaction conditions.

Table 3.5. The Pd^{2+}/Pd^{0} ratio of the as-prepared $AuPdFe/TiO_2$ catalysts.

Catalysts	Pd^{2+}/Pd^{0} Ratio
$Au_{0.5}Pd_{0.5}/TiO_2$	0.3
$Au_{0.5}Pd_{0.5}Fe_{0.01}/TiO_2$	0.7
$Au_{0.5}Pd_{0.5}Fe_{0.02}/TiO_2$	1
$Au_{0.5}Pd_{0.5}Fe_{0.05}/TiO_2$	1.2
$Au_{0.5}Pd_{0.5}Fe_{0.1}/TiO_2$	0.5
$Au_{0.5}Pd_{0.5}Fe_{0.5}/TiO_2$	1
$Au_{0.5}Pd_{0.5}Fe_{1}/TiO_2$	1.5

Similar to the STEM/EDX analysis, evaluation by XPS was unable to provide sufficient information about the nature of the Fe in the AuPdFe formulations with low Fe loading (<= 0.5wt%). We then subsequently employed ^{57}Fe Mössbauer spectroscopic analysis to gain further insight. Notably, these samples contain identical Fe loadings as analogues investigated for H_2O_2 synthesis but were prepared with $^{57}FeCl_3$ as the metal precursor, with comparisons made to a monometallic $^{57}Fe_{0.02}/TiO_2$ formulation (**Table 3.6** and **Figure 3.5**). Interestingly, the spectra of this monometallic Fe sample ($Fe_{0.02}/TiO_2$) were fitted with contributions of Fe^{2+} only, aligning with earlier works by Vanleerberghe et al.,[35] and indicative of the strong interaction between the immobilised Fe and TiO_2 support, possibly through the formation of iron titanates. By comparison, the spectra of the trimetallic $Au_{0.5}Pd_{0.5}Fe_{0.02}/TiO_2$ formulation is far more complex. In addition to the Fe^{2+} (iron titanate) species observed in the monometallic Fe sample, contributions indicative of a Fe-Pd(Au) phase (magnetic (sextuplet) contribution of 31.4 T), isolated Fe^{3+} species (paramagnetic doublet at 4.2 K) and Fe^{3+} oligomers (broad sextuplet) are also visible. Notably, these Fe^{3+} species were not present in the $Fe_{0.02}/TiO_2$ sample, further indicating the electronic interaction between Fe and the precious metals. Additionally, Au/Pd-Fe dimers (paramagnetic doublet) and Au-Pd-Fe oligomers (broad sextuplet) were also found to be present, aligning well with earlier investigations into AuFe structures.[36] Contrastingly, the spectra of the $Au_{0.5}Pd_{0.5}Fe_{1}/TiO_2$ sample was dominated by isolated and oligomeric Fe^{3+} species, in addition to contributions from the iron (Fe^{2+}) titanate species observed in alternative formulations, with minor contributions from Fe^{0}.

Table 3.6. The Mössbauer fitted parameters of the AuPdFe/TiO_2 samples, obtained at different temperatures.

Sample	*T (K)*	*IS (mm·s^{-1})*	*QS (mm·s^{-1})*	*Hyperfine field (T)*	*Γ (mm·s^{-1})*	*Phase*	*Spectral contribution (%)*
0.02%^{57}Fe/TiO_2	4.2	1.09	2.08	-	0.67	Fe^{2+}	37
		1.29	2.49	-	0.71	Fe^{2+}	63
$Au_{0.5}Pd_{0.5}{}^{57}Fe_{0.02}/TiO_2$	4.2	0.37	0.02	31.4	0.64	Fe-Pd(Au)	18
		1.32	2.62	-	1.20	Fe^{2+}	19
		0.59	-0.14	40.9	1.21	Fe^{3+} (oligomers)	41
		0.49	0.93	-	0.97	Fe^{3+} (isolated)	22
$Au_{0.5}Pd_{0.5}{}^{57}Fe_1/TiO_2$	4.2	0.13	0.00	34.0	0.36	Fe^0	6
		1.12	2.63	-	1.20	Fe^{2+}	14
		0.58	-0.15	37.7	1.27	Fe^{3+} (oligomers)	35
		0.51	0.79	-	0.70	Fe^{3+} (isolated)	45
$Au_{0.5}Pd_{0.5}{}^{57}Fe_1/TiO_2$	50	0.11	0.00	33.9	0.36	Fe^0	10
		1.10	2.51	-	0.71	Fe^{2+}	19
		0.50	0.78	-	0.60	Fe^{3+} (oligomers) + Fe^{3+} (isolated)	71

Experimental uncertainties: Isomer shift: I.S. ± 0.1 mm s^{-1}; Quadrupole splitting: Q.S. ± 0.2 mm s^{-1}; Line width: Γ ± 0.2 mm s^{-1}; Hyperfine field: ± 0.2 T; Spectral contribution: ± 5%. **Please note**: the test and subsequent analysis were performed by Dr. Iulian Dugulan (Delft University of Technology).

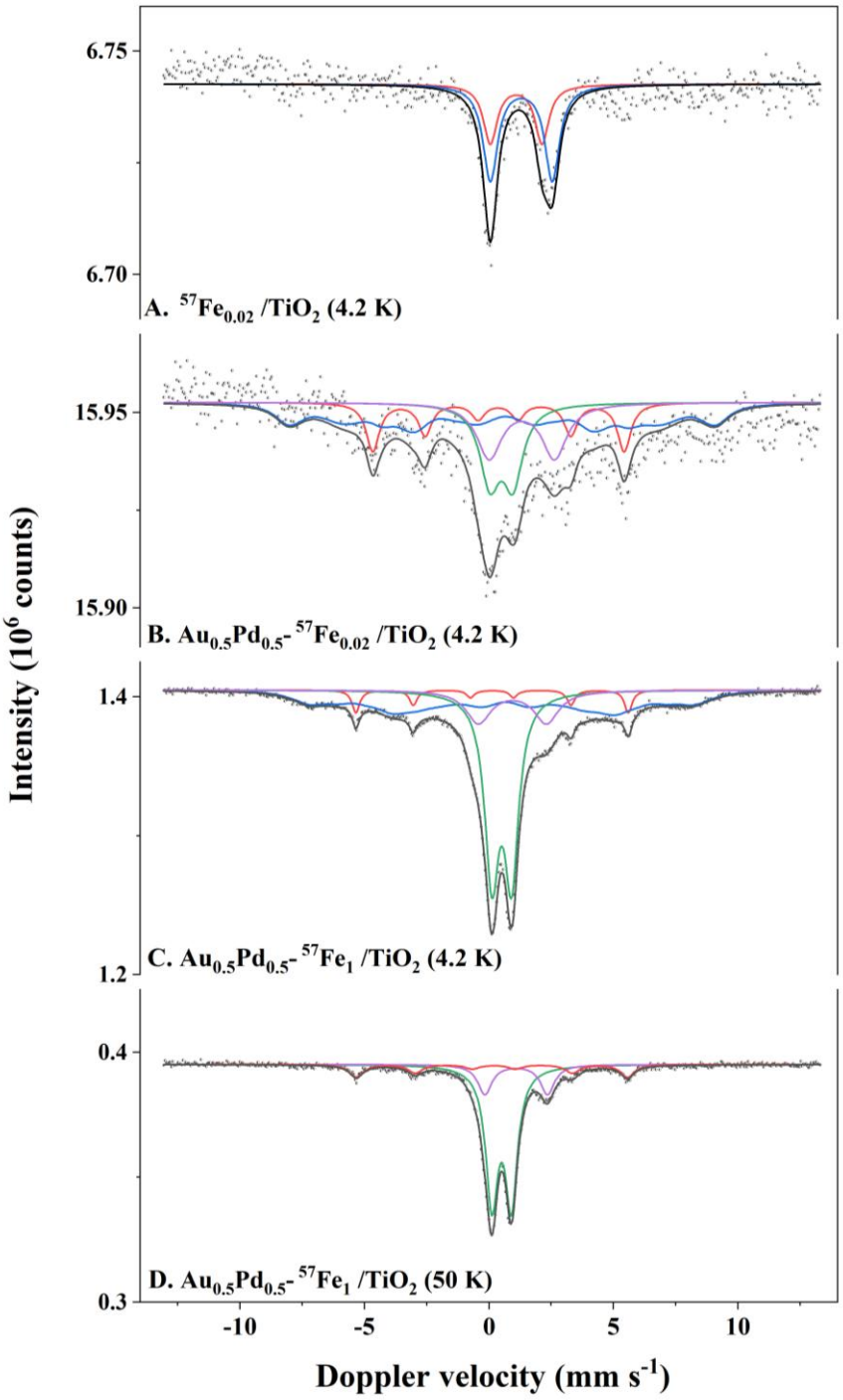

Figure 3.5. Mössbauer Analysis of the AuPdFe/TiO_2 samples at different temperatures together with the corresponding spectral illustrations, are presented in **Table 3.6**. **Please note**: the test and subsequent analysis were performed by Dr. Iulian Dugulan (Delft University of Technology).

Returning to the non-isotopically labelled samples CO- Diffuse Reflectance Infrared Fourier Transform Spectroscopy (DRIFT) was subsequently employed to further probe the electronic interaction that results from the incorporation of Fe into AuPd nanoalloys (**Figure 3.6**, which

includes CO-DRIFTS analysis of a Fe_1/TiO_2 catalyst for comparative purposes). Perhaps unsurprisingly, given the low loading of Fe in the $Au_{0.5}Pd_{0.5}Fe_{0.02}/TiO_2$ catalyst, no clear variation in the DRIFTS spectra was observed between the optimal trimetallic catalyst and bimetallic analogue, with both spectra dominated by Pd-CO bands. The bands observed at approximately 2060 cm^{-1} represent CO bonded linearly to low co-ordination Pd sites (i.e. edge or corner sites, denoted Pd–CO), while the broad feature, which is centred around 1925 cm^{-1} represents the 2- and 3-fold adsorption of CO on Pd.[37,38] Notably, no bands associated with the adsorption of CO onto the TiO_2 support (> 2200 cm^{-1} and previously reported by Cerrato et al.[39] and Green et al.[40]) or gaseous CO_2 (2350 cm^{-1})[41] were observed, likewise we do not observe bands which may be associated with the redox process of FeOx, (typically at 3700 cm^{-1}).[42] Interestingly upon the introduction of large quantities of Fe, a clear red-shift in the bands related to the linearly bonded CO on Pd and the bridging CO species can be observed, which may be attributed to charge-transfer to Pd d-orbitals, resulting in an enhanced back donation to 2π CO molecular orbitals, such observations align well with our earlier analysis by XPS which indicated the electronic modification of Pd species as a result of Fe incorporation. In keeping with the observations, Ouyang et al.[43] have previously reported a similar electron transfer upon the alloying of Au and Pd, which is associated with preventing O-O bond cleavage and enhancing catalytic performance towards the direct H_2O_2 synthesis.

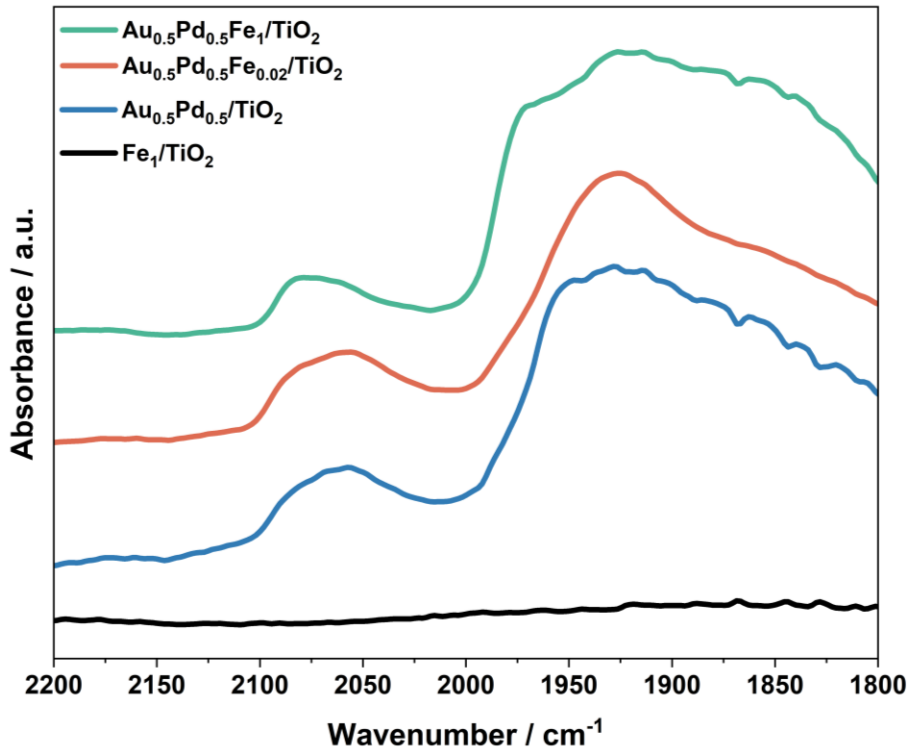

Figure 3.6. CO-DRIFTS spectra for AuPdFe/TiO_2 catalysts, with analysis of a Fe_1/TiO_2 formulation included for reference. **Note:** No bands which may be associated with the redox process of FeOx, (typically at 3700 cm^{-1}) were observed and the x-axis range has been restricted to allow for improved clarity of the Pd-CO region.[1]

3.4. Catalytic performance over prolonged reaction times

Time-on-line studies were conducted to evaluate the temporal evolution of catalytic performance across the key formulations, with reaction data collected over a period of 180 minutes. The results are summarised in **Figure 3.7**. It is important to note that, in these experiments, the gaseous reactants (H_2 and O_2) were not replenished throughout the reaction.

The $Au_{0.5}Pd_{0.5}Fe_{0.02}/TiO_2$ catalyst once again exhibited markedly superior activity compared to both the bimetallic $Au_{0.5}Pd_{0.5}/TiO_2$ and the Fe-rich $Au_{0.5}Pd_{0.5}Fe_1/TiO_2$ catalysts (0.3 wt%). After 60 minutes of reaction, the net H_2O_2 concentration achieved over the optimally doped catalyst was 35–45% higher than that observed over the alternative formulations (**Figure 3.7 (A)**), reinforcing the enhanced reactivity associated with low-level Fe incorporation. However, this performance advantage diminished progressively over extended reaction times. By 180 minutes, the net H_2O_2 concentrations for all three catalysts converged to similar values (~0.25 wt.%), suggesting that **1)** prolonged operation under static gas-phase conditions leads to either equilibrium limitations or the onset of secondary H_2O_2 degradation pathways that dominate at

low partial pressures of H_2 and O_2 and **2)** catalysts deactivation after long term operation might be due to either the loss of active metals or alloys agglomeration.

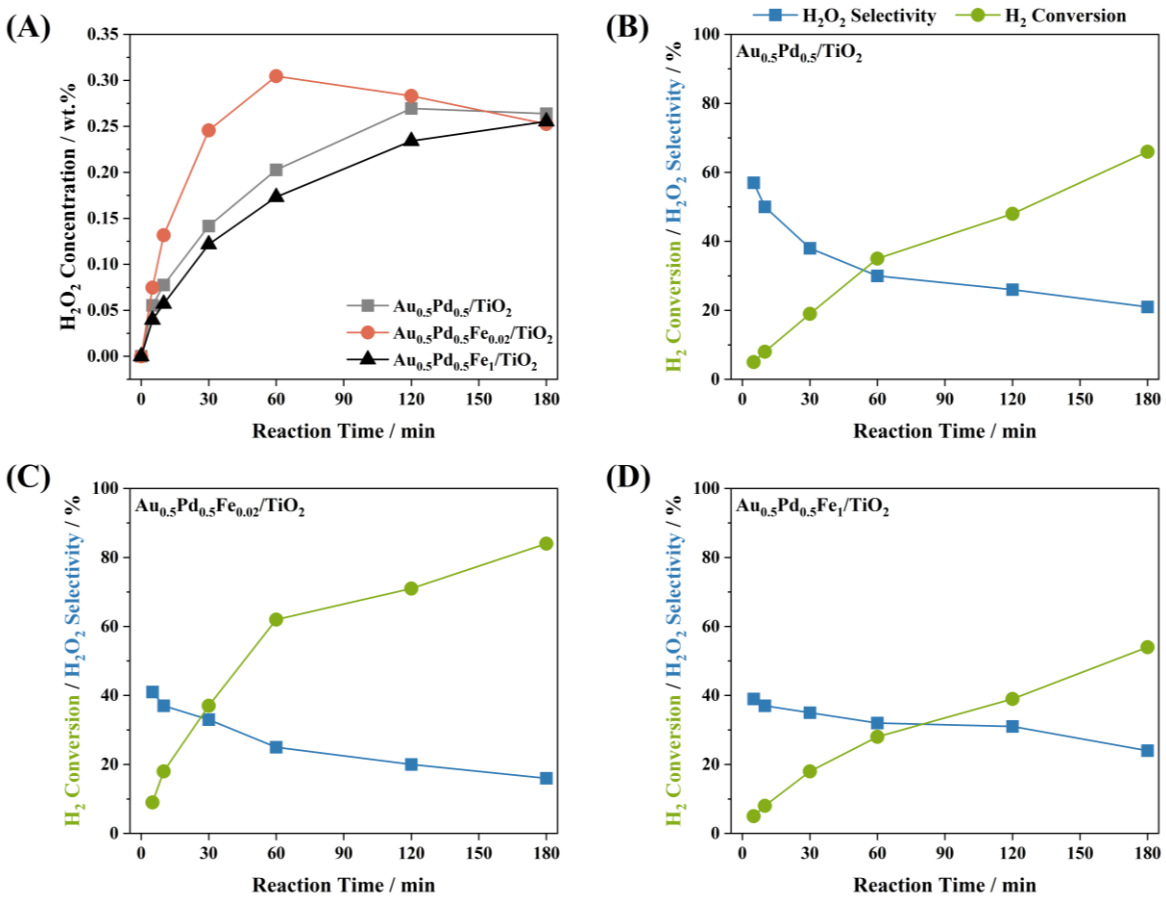

Figure 3.7. Comparison of catalytic activity towards the direct synthesis of H_2O_2, as a function of reaction time. **(A)** Catalytic activity based on net H_2O_2 concentration. Determination of H_2 conversion and H_2O_2 selectivity for the **(B)** $Au_{0.5}Pd_{0.5}/TiO_2$, **(C)** $Au_{0.5}Pd_{0.5}Fe_{0.02}/TiO_2$, and **(D)** $Au_{0.5}Pd_{0.5}Fe_1/TiO_2$ catalysts **Key:** $Au_{0.5}Pd_{0.5}/TiO_2$ (green squares), $Au_{0.5}Pd_{0.5}Fe_{0.02}/TiO_2$ (red circles), $Au_{0.5}Pd_{0.5}Fe_1/TiO_2$ catalysts (blue triangles) H_2 conversion (purple diamonds), H_2O_2 selectivity (black inverted triangles). **H_2O_2 direct synthesis reaction conditions:** catalyst (0.01 g), H_2O (2.9 g), MeOH (5.6 g), 5% H_2/CO_2 (420 psi), 25% O_2/CO_2 (160 psi), 2 °C, 1200 rpm.

To better understand the underlying causes of this convergence, the extent of H_2 conversion over the catalytic series was assessed (**Figure 3.7 (B)-(D)**) and reveals the near total utilisation of this reagent over the $Au_{0.5}Pd_{0.5}Fe_{0.02}/TiO_2$ catalyst (>80% H_2 conversion after 180 minutes on-line) compared to that of the alternative formulations (66 and 54% H_2 conversion after 180 minutes for the $Au_{0.5}Pd_{0.5}/TiO_2$ and $Au_{0.5}Pd_{0.5}Fe_1/TiO_2$ catalysts, respectively) under identical conditions. The excessively high rate of H_2 conversion and the continuously decreased H_2O_2 selectivity might indicate the undesired side reactions through the hydrogenation of in situ

generated H_2O_2, thereby reducing the overall H_2O_2 yield. This phenomenon is particularly evident in the case of the $Au_{0.5}Pd_{0.5}Fe_{0.02}/TiO_2$ catalyst, where a notable decline in H_2O_2 concentration is observed throughout the reaction. Specifically, the H_2O_2 concentration decreased from 0.30 wt.% at 60 minutes to 0.25 wt.% at 180 minutes, despite a continued increase in H_2 conversion from 60% to 80% over the same period. Concurrently, the H_2O_2 selectivity dropped markedly from 25% to 16%. These observations strongly suggest that the enhanced H_2 activation, while beneficial for overall catalytic activity, also facilitates competing hydrogenation pathways that consume the peroxide product, thereby limiting the maximum attainable concentration of H_2O_2 under extended reaction times. These findings are consistent with earlier observations (**Figure 3.1** and **Table 3.1**), which suggested that the superior performance of the optimally doped catalyst is primarily driven by enhanced intrinsic activity, namely, improved H_2 activation and utilisation, rather than a shift in selectivity towards H_2O_2 formation.

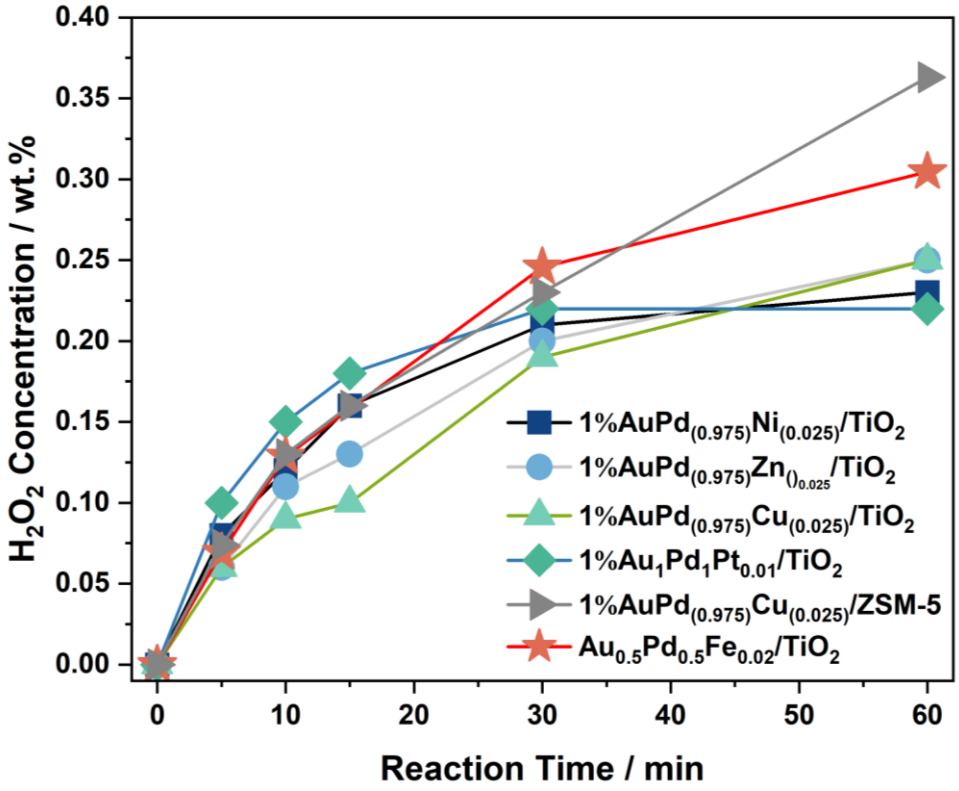

Figure 3.8. A comparison of catalytic performance towards the direct synthesis of H_2O_2, as a function of reaction time. **H_2O_2 direct synthesis reaction conditions:** Catalyst (0.01 g), H_2O (2.9 g), CH_3OH (5.6 g), 5% H_2/CO_2 (420 psi), 25% O_2/CO_2 (160 psi), 5 mins to 60 mins, 2 °C, 1200 rpm.[5,19,23]

To more comprehensively evaluate the long-term catalytic performance of the optimised $Au_{0.5}Pd_{0.5}Fe_{0.02}/TiO_2$ formulation in H_2O_2 production, a comparative analysis was conducted against previously reported AuPd-based trimetallic catalysts.[5,19,23] As illustrated in **Figure 3.8**, the AuPdFe catalyst developed in this study demonstrated superior performance relative to all other TiO_2-supported trimetallic systems examined under comparable reaction conditions, particularly at the 60-minute time point. Notably, the net H_2O_2 concentration achieved by this formulation approached 0.3 wt.%, exceeding that of the $1\%Au_1Pd_1Pt_{0.01}/TiO_2$ (0.22 wt.%),[19] $1\%AuPd_{(0.975)}Cu_{(0.025)}/TiO_2$ (0.25 wt.%),[5] $1\%AuPd_{(0.975)}Ni_{(0.025)}/TiO_2$ (0.25 wt.%),[5] and $1\%AuPd_{(0.975)}Zn_{(0.025)}/TiO_2$ (0.25 wt.%)[5] catalysts and reaching the similar level of net H_2O_2 offered by the $1\%AuPd_{(0.975)}Cu_{(0.025)}$/ZSM-5 system (0.35 wt.%)[23] previously investigated under identical reaction conditions.

The stability of the catalyst formulations over extended reaction periods was evaluated through ICP-MS analysis of post-reaction solutions collected at various time intervals over a total reaction time of 180 minutes. As reported in **Table 3.7**, the Au and Fe leach below the detection limits throughout the experiment. Notably, the inclusion of Fe, particularly at high concentrations, seems to lead to an enhancement in Pd leaching over time, from 6.3 ppb ($Au_{0.5}Pd_{0.5}/TiO_2$ after 180 mins reaction) to 15.2 ppb ($Au_{0.5}Pd_{0.5}Fe_1/TiO_2$ after 180 mins reaction). However, in all cases, the total loss of active species (e.g. Pd) is less than 0.3% of individual metal loadings, confirming the reasonable stability of the AuPdFe catalysts.

Table 3.7. Catalyst stability as a function of reaction time, as determined by ICP analysis of post-H_2O_2 direct synthesis reaction solutions.

Catalyst	Reaction time/min	Au / ppb (%)	Pd / ppb (%)	Fe / ppb (%)
$Au_{0.5}Pd_{0.5}/TiO_2$	5	0.0 (0.0)	1.9 (0.03)	-
	10	0.0 (0.0)	2.7 (0.05)	-
	30	0.0 (0.0)	3.3 (0.06)	-
	60	0.0 (0.0)	5.5 (0.10)	-
	120	0.0 (0.0)	6.0 (0.11)	-
	180	0.0 (0.0)	6.3 (0.12)	-
$Au_{0.5}Pd_{0.5}Fe_{0.02}/TiO_2$	5	0.0 (0.0)	1.7 (0.03)	0.0 (0.0)
	10	0.0 (0.0)	2.5 (0.05)	0.0 (0.0)
	30	0.0 (0.0)	3.0 (0.06)	0.0 (0.0)
	60	0.0 (0.0)	6.0 (0.11)	0.0 (0.0)
	120	0.0 (0.0)	6.7 (0.12)	0.0 (0.0)
	180	0.0 (0.0)	8.5 (0.16)	0.0 (0.0)
$Au_{0.5}Pd_{0.5}Fe_1/TiO_2$	5	0.0 (0.0)	3.1 (0.06)	0.0 (0.0)
	10	0.0 (0.0)	4.3 (0.08)	0.0 (0.0)
	30	0.0 (0.0)	6.3 (0.12)	0.0 (0.0)
	60	0.0 (0.0)	9.3 (0.17)	0.0 (0.0)
	120	0.0 (0.0)	13.2 (0.24)	0.0 (0.0)
	180	0.0 (0.0)	15.2 (0.28)	0.0 (0.0)

H_2O_2 direct synthesis reaction conditions: Catalyst (0.01 g), H_2O (2.9 g), MeOH (5.6 g), 5% H_2/CO_2 (420 psi), 25% O_2/CO_2 (160 psi), 2° C, 1200 rpm.

An in-depth evaluation of the electronic state of Pd within key catalytic formulations was carried out using XPS at various time points over the course of a 180-minute H_2O_2 direct synthesis reaction. As reported in **Figure 3.9** and **Table 3.8**, the Pd-speciation present within the as-prepared $Au_{0.5}Pd_{0.5}/TiO_2$ and $Au_{0.5}Pd_{0.5}Fe_{0.02}/TiO_2$ catalysts is maintained to a far greater extent than over the Fe-rich analogue. Indeed, a total shift towards Pd^0 was detected in the case of the $Au_{0.5}Pd_{0.5}Fe_1/TiO_2$ catalyst at a reaction time as short as 5 minutes, revealing the ability of Fe to promote the reduction of Pd.

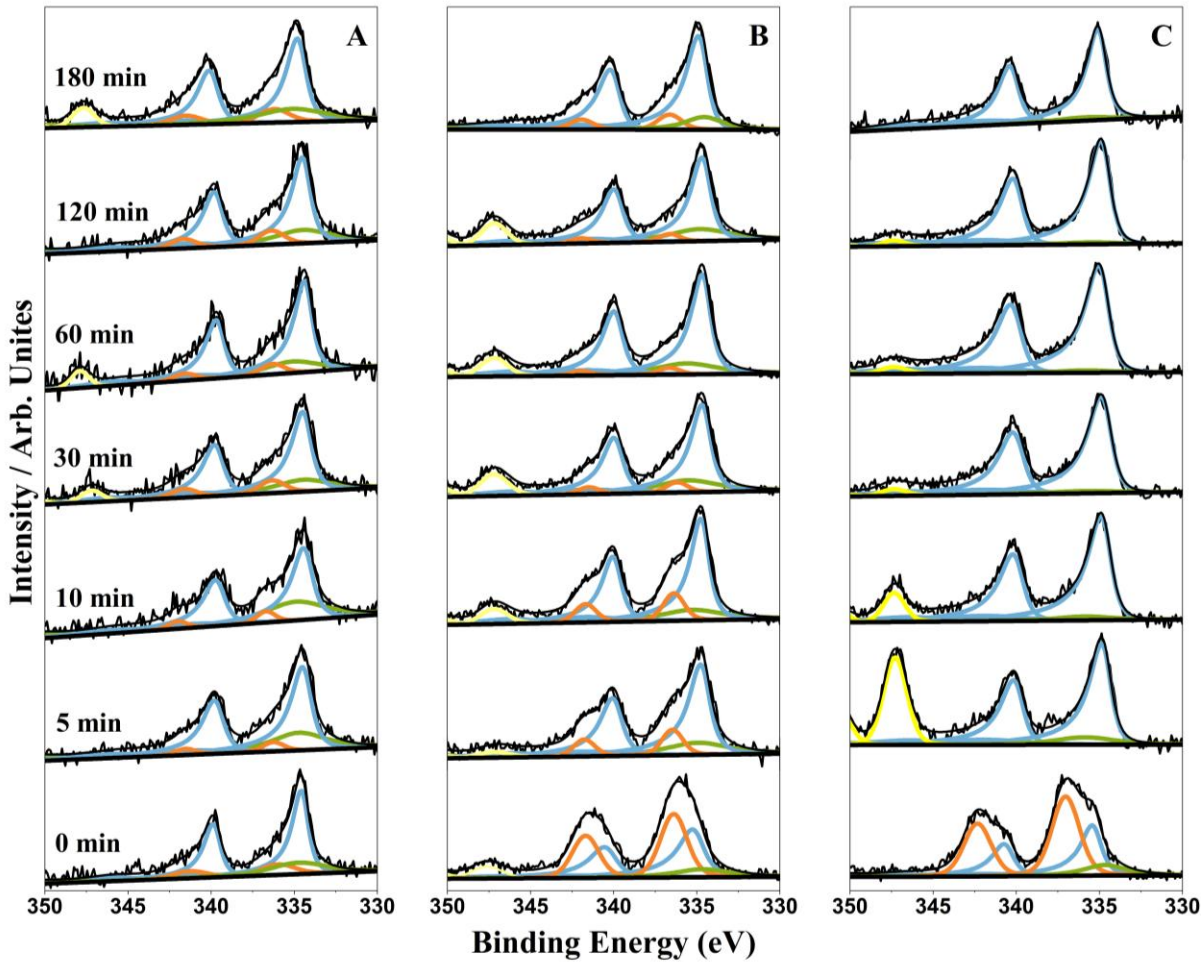

Figure 3.9. XPS analysis of the AuPdFe/TiO_2 catalysts, as a function of reaction time. **(A)** $Au_{0.5}Pd_{0.5}/TiO_2$, **(B)** $Au_{0.5}Pd_{0.5}Fe_{0.02}/TiO_2$ and **(C)** $Au_{0.5}Pd_{0.5}Fe_1/TiO_2$. **Key:** Au(4d) (green); Pd^0 (blue); Pd^{2+} (orange); Ca^{2+} (yellow). **Note:** Catalysts exposed to a reductive heat treatment prior to use (5%H_2/Ar, 400 °C, 4h, 10 °C min^{-1}). Spent catalysts were dried (30 °C, 16 h, under vacuum), prior to XPS analysis. **Please note**: the test and subsequent analysis were performed by Dr. David J. Morgan (Cardiff University; HarwellXPS).

Table 3.8. The changes of Pd^{2+}/Pd^{0} ratio of the selected catalysts during time on line H_2O_2 synthesis up to 3 hours.

Reaction Time	Pd^{2+}/Pd^{0} Ratio		
	$Au_{0.5}Pd_{0.5}/TiO_2$	$Au_{0.5}Pd_{0.5}Fe_{0.02}/TiO_2$	$Au_{0.5}Pd_{0.5}Fe_1/TiO_2$
0 mins	0.3	1.0	1.5
5 mins	0.1	0.2	All Pd^0
10 mins	0.1	0.2	All Pd^0
30 mins	0.2	0.1	All Pd^0
60 mins	0.2	0.1	All Pd^0
120 mins	0.2	0.1	All Pd^0
180 mins	0.2	0.1	All Pd^0

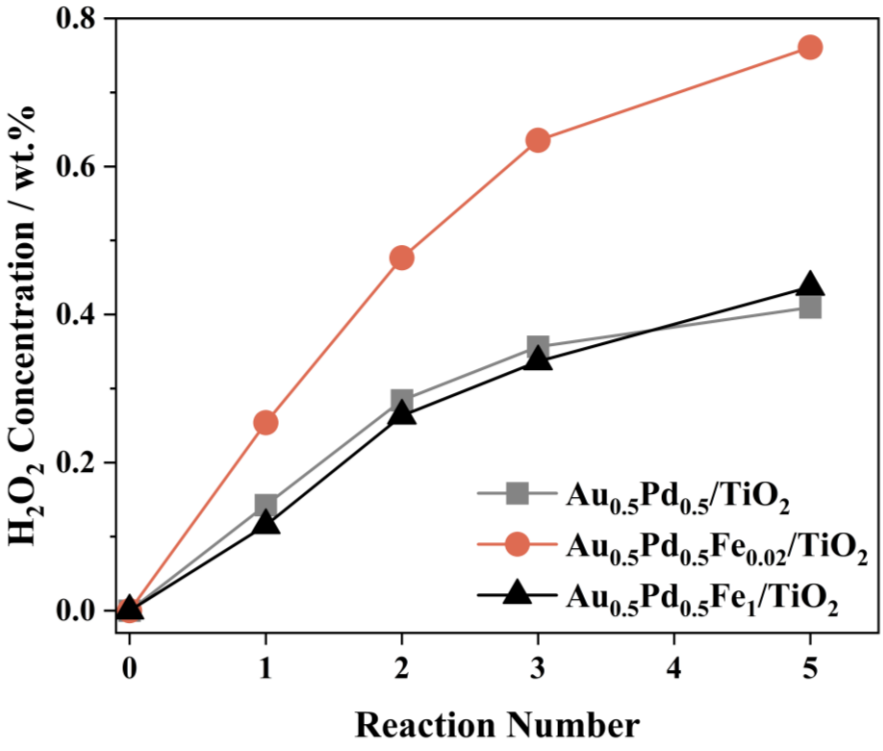

Figure 3.10. Comparison of catalytic activity over sequential H_2O_2 synthesis reactions. **Key:** $Au_{0.5}Pd_{0.5}/TiO_2$ (green squares), $Au_{0.5}Pd_{0.5}Fe_{0.02}/TiO_2$ (red circles), and $Au_{0.5}Pd_{0.5}Fe_1/TiO_2$ (blue triangles). **H_2O_2 direct synthesis reaction conditions:** catalyst (0.01 g), H_2O (2.9 g), MeOH (5.6 g), 5% H_2/CO_2 (420 psi), 25% O_2/CO_2 (160 psi), 0.5 h per reaction, 2 °C, 1200 rpm.

A notably high H_2 conversion rate was observed in the time-on-line tests for the optimally doped formulation, $Au_{0.5}Pd_{0.5}Fe_{0.02}/TiO_2$, reaching approximately 42% at 30 mins, 60% at 60 mins, and 80% at 180 mins in **Figure 3.10**. The high level of H_2 utilisation rate suggests that the reaction system may become increasingly limited by H_2 availability over time. In such scenarios, insufficient replenishment of H_2 could restrict the rate of H_2 activation, thereby suppressing the rate of in situ H_2O_2 formation and potentially allowing undesirable degradation pathways (such as H_2O_2 decomposition) to dominate. To investigate this hypothesis and better assess the sustained catalytic performance of the system under more favourable conditions, a series of sequential H_2O_2 synthesis experiments was conducted. In these tests, the reactant gases, H_2 and O_2 were periodically replenished at 30 mins intervals, and the reaction was continued over a total of five consecutive cycles.

Unsurprisingly, the improved performance of the $Au_{0.5}Pd_{0.5}Fe_{0.02}/TiO_2$ catalyst was again clear, offering a H_2O_2 concentration of 0.76 wt.% (equivalent to 7600 ppm) after five consecutive reactions, approximately 1.8 times greater than that offered by the bimetallic $Au_{0.5}Pd_{0.5}/TiO_2$ (0.41 wt.%, equivalent to 4100 ppm) or Fe-rich trimetallic $Au_{0.5}Pd_{0.5}Fe_1/TiO_2$ (0.44 wt.%, equivalent to 4400 ppm). Indeed, the net concentration of H_2O_2 offered by the $Au_{0.5}Pd_{0.5}Fe_{0.02}/TiO_2$ catalyst is comparable to that achieved by the previously reported and highly active AuPd formulation, which has been doped with Pt, when investigated under identical reaction conditions to those utilised in this work.[19] Indeed, the optimal Fe-containing formulation outperformed all of the alternative trimetallic catalysts in the gas replacement tests ($1\%AuPd_{(0.975)}Zn_{(0.025)}/TiO_2$,[5] $1\%AuPd_{(0.975)}Cu_{(0.025)}/TiO_2$,[5] $1\%AuPd_{(0.975)}Ni_{(0.025)}/TiO_2$,[5] $1\%AuPd_{(0.975)}Cu_{(0.025)}$/ZSM-5,[23] $1\%Au_1Pd_1Pt_{0.01}/TiO_2$[19]), when evaluated under identical reaction conditions (**Figure 3.11**).

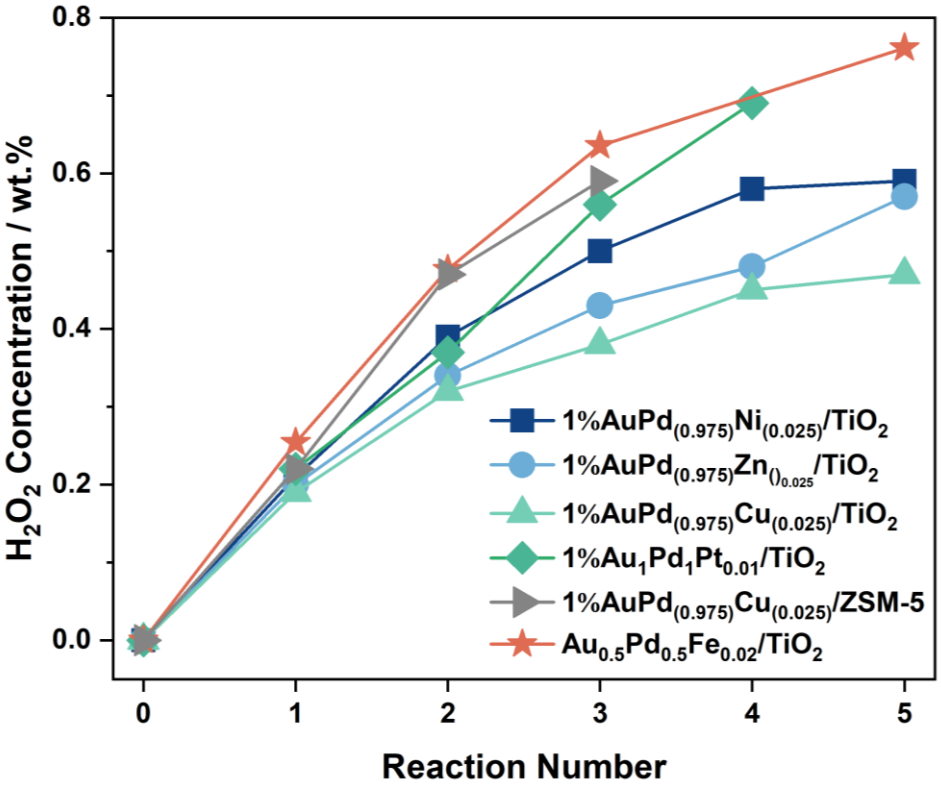

Figure 3.11. Comparison of the catalytic activity of various reported trimetallic catalysts in gas replacement tests.[5,19,23] **H_2O_2 direct synthesis reaction conditions:** catalyst (0.01 g), H_2O (2.9 g), MeOH (5.6 g), 5% H_2/CO_2 (420 psi), 25% O_2/CO_2 (160 psi), 0.5 hour per reaction, 2 °C, 1200 rpm.

3.5. Reusability test

Given that catalyst reusability is a fundamental principle in the development of sustainable catalytic systems aligned with green chemistry objectives, we next evaluated catalytic activity towards H_2O_2 synthesis and H_2O_2 degradation pathways, upon re-use (**Table 3.9**). All catalysts were washed multiple times using DI H_2O and dried in a vacuum at 30 °C overnight before use. Across all formulations, a notable decline in catalytic performance was observed upon re-use, with H_2O_2 production rates decreasing by approximately 32–42% relative to the initial run, accompanied by a corresponding reduction in H_2 conversion rates, suggesting that overall catalytic activity was impaired following the first reaction cycle. While catalyst deactivation is often attributed to the leaching of active metal species, particularly under liquid-phase conditions, previous ICP-MS analysis (**Table 3.2**) revealed that the extent of Pd leaching was minimal, and no detectable loss of Au or Fe was observed after a 0.5-hour reaction period, strongly suggesting that metal leaching is not the primary factor responsible for the observed deactivation.

Table 3.9. Re-usability of AuPdFe/TiO_2 catalysts towards the direct synthesis and subsequent degradation of H_2O_2.

Catalyst	Productivity / $mol_{H2O2}kg_{cat}^{-1}h^{-1}$		H_2 Conv. / %		H_2O_2 Sel. / %		Initial rate of reaction / $mmol_{H2O2}$ $mmol_{metal}^{-1}min^{-1}$*		Degradation / $mol_{H2O2}kg_{cat}^{-1}h^{-1}$	
	Use 1	Use 2	Use 1	Use 2	Use 1	Use 2	Use 1	Use 2	Use 1	Use 2
$Au_{0.5}Pd_{0.5}/TiO_2$	70	45	19	12	39	37	2.46 x10 3	$9.71x10^2$	208	169
$Au_{0.5}Pd_{0.5}Fe_{0.02}/TiO_2$	122	83	40	22	31	40	3.00 x10 3	$1.72 x10^3$	451	431
$Au_{0.5}Pd_{0.5}Fe_1/TiO_2$	65	38	16	11	42	36	4.65 x10 2	$1.91x10^2$	287	193

H_2O_2 direct synthesis reaction conditions: catalyst (0.01 g), H_2O (2.9 g), MeOH (5.6 g), 5% H_2/CO_2 (420 psi), 25% O_2/CO_2 (160 psi), 0.5 h, 2 °C, 1200 rpm. **H_2O_2 degradation reaction conditions:** catalyst (0.01 g), H_2O_2 (50 wt.% 0.68 g), H_2O (2.22 g), MeOH (5.6 g), 5% H_2/CO_2 (420 psi), 0.5 h, 2 °C, 1200 rpm. **Note:** reaction rates are calculated based on the as-determined metal content. Spent samples were dried (30 °C, 16 h, under vacuum), prior to re-use.

Post-reaction structural characterisation of the key catalytic formulations was performed using TEM, with the aim of identifying any changes in nanoparticle size arising from exposure to reaction conditions during the direct synthesis of H_2O_2. The quantitative particle-size data are summarised in **Table 3.10**, and representative TEM micrographs are presented in **Figure A3.3**. The TEM analysis revealed a modest but measurable increase in nanoparticle size for both the bimetallic $Au_{0.5}Pd_{0.5}/TiO_2$ catalyst (from an initial average particle size of 4.4 nm to 5.1 nm post-reaction) and the optimal trimetallic formulation, $Au_{0.5}Pd_{0.5}Fe_{0.02}/TiO_2$ (from 2.8 nm to 5.1 nm). This slight growth in particle size suggests minor agglomeration or sintering processes occurring under reaction conditions, potentially contributing to the moderate catalyst deactivation observed. In contrast, the Fe-rich trimetallic $Au_{0.5}Pd_{0.5}Fe_1/TiO_2$ catalyst exhibited remarkable structural stability, showing no significant change in particle size distribution (from 3.7 nm to 3.6 nm).

Table 3.10. Mean particle size of key AuPdFe/TiO_2 catalysts, after use in the direct synthesis of H_2O_2.

Catalyst	Mean Particle Size (nm) / (Standard Deviation)	
	Fresh	**Used**
$Au_{0.5}Pd_{0.5}/TiO_2$	4.4 (1.7)	5.1 (1.9)
$Au_{0.5}Pd_{0.5}Fe_{0.02}/TiO_2$	2.8 (1.1)	5.1 (1.4)
$Au_{0.5}Pd_{0.5}Fe_1/TiO_2$	3.7 (1.8)	3.6 (1.4)

H_2O_2 direct synthesis reaction conditions: Catalyst (0.01 g), H_2O (2.9 g), MeOH (5.6 g), 5% H_2/CO_2 (420 psi), 25% O_2/CO_2 (160 psi), 0.5 h, 2 °C 1200 rpm. **Note:** Catalysts exposed to a reductive heat treatment prior to use (5%H_2/Ar, 400 °C, 4h, 10 °Cmin^{-1}). Spent samples were dried (30 °C, 16 h, under vacuum)

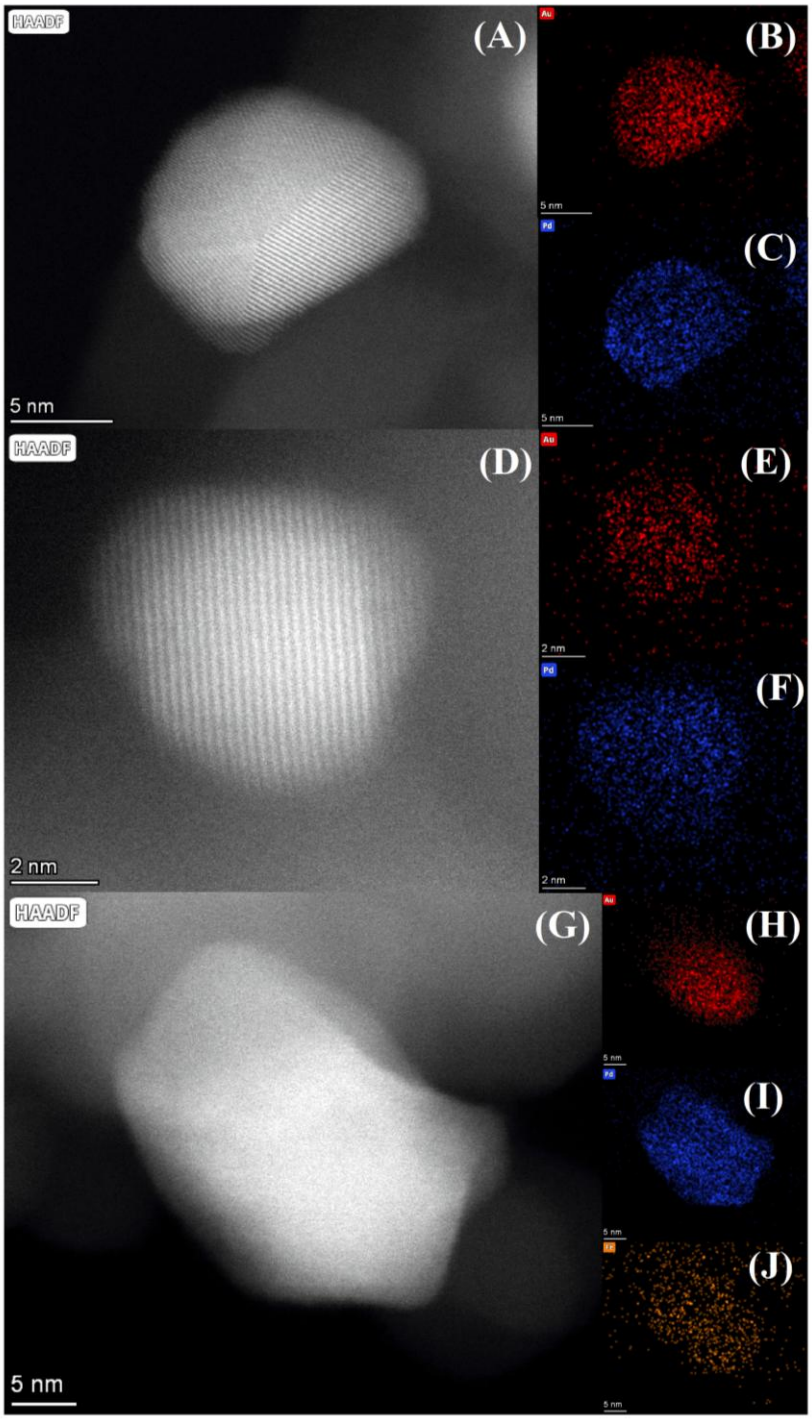

Figure 3.12. HAADF-STEM and corresponding EDX analysis of the (A-C) $Au_{0.5}Pd_{0.5}/TiO_2$, (D-F) $Au_{0.5}Pd_{0.5}Fe_{0.02}/TiO_2$, and (G-J) $Au_{0.5}Pd_{0.5}Fe_1/TIO_2$ catalysts after use in the direct synthesis of H_2O_2. **H_2O_2 direct synthesis reaction conditions:** Catalyst (0.01 g), H_2O (2.9 g), CH_3OH (5.6 g), 5% H_2/CO_2 (420 psi), 25% O_2/CO_2 (160 psi), 2° C, 1200 rpm. **Note:** Catalysts exposed to a reductive heat treatment prior to use (5%H_2/Ar, 400 °C, 4h, 10 °Cmin^{-1}). Spent samples were dried (30 °C, 16 h, under vacuum).

To further substantiate these findings, HAADF-STEM combined with energy-dispersive EDX spectroscopy analysis was employed to examine the spent catalysts. The resulting data, detailed in **Figure 3.12**, confirmed the stability of nanoparticle composition upon reaction. Specifically, the random alloy arrangement of Au, Pd, and Fe within the nanoparticles observed in the fresh catalysts is preserved in the spent materials, with no discernible segregation or compositional variation detected following exposure to reaction conditions.

Notably, XPS analysis of the spent catalysts (**Figure 3.9**) provided clear evidence of electronic changes in Pd species as a consequence of exposure to reaction conditions during the direct synthesis of H_2O_2. Specifically, a detectable shift in Pd oxidation states toward more Pd^0 species was observed post-reaction. Based solely on this observation and considering the established higher intrinsic activity, but typically lower selectivity of metallic Pd relative to oxidised Pd^{2+} species, one might initially expect an increase in H_2 conversion and enhanced rates of H_2O_2 degradation upon catalyst reuse. However, the opposite trend was experimentally observed, with a notable decrease in both H_2 conversion and H_2O_2 degradation rates during subsequent reaction cycles.

However, the analysis of spent materials by XPS revealed a significant loss in surface chloride content after use in the direct synthesis reaction (**Figure 3.13** and **Table 3.11**) and the surface Cl atomic concentration dropped from 0.2% for the $Au_{0.5}Pd_{0.5}/TiO_2$ and $Au_{0.5}Pd_{0.5}Fe_{0.02}/TiO_2$ catalyst, and from 1.12% for the $Au_{0.5}Pd_{0.5}Fe_1/TiO_2$ catalyst, to around 0.1% after 30 mins reaction. Halide ions are well-known promoters for the direct synthesis reaction,[13,44] and their use has typically been shown to result in improved catalytic performance, with this promotive effect often attributed to either the blocking of sites that promote O–O bond scission[45,46] or reducing the density of states near the Fermi level and consequently making metal surfaces less reactive for O–O cleavage.[47] More recently, Flaherty and co-workers,[48] proposed that the electronic modification of the solution at the liquid–solid interface induced by the presence of counterions is largely responsible for the improved activity observed in the presence of Cl^-. Such propositions are indeed compelling. However, regardless of the underlying cause for catalytic promotion in the presence of Cl^-, we can draw a direct correlation between these factors and indeed, such observations are in keeping with earlier studies into AuPd-based catalysts for H_2O_2 synthesis.[13]

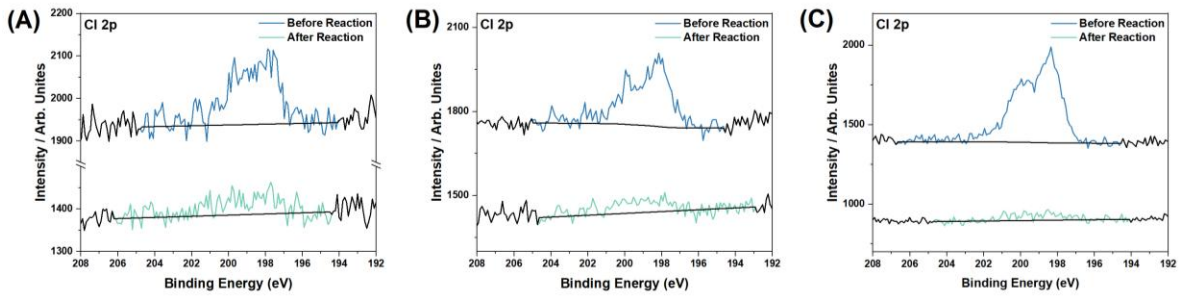

Figure 3.13. XPS analysis of Cl 2p before and after the direct H_2O_2 synthesis reaction on **(A)** $Au_{0.5}Pd_{0.5}/TiO_2$, **(B)** $Au_{0.5}Pd_{0.5}Fe_{0.02}/TiO_2$ and **(C)** $Au_{0.5}Pd_{0.5}Fe_1/TiO_2$. **$H_2O_2$ direct synthesis reaction conditions:** catalyst (0.01 g), H_2O (2.9 g), CH3OH (5.6 g), 5% H_2/CO_2 (420 psi), 25% O_2/CO_2 (160 psi), 0.5 h, 2 °C, 1200 rpm. **Please note**: the test and subsequent analysis were performed by Dr. David J. Morgan (Cardiff University; HarwellXPS).

Table 3.11. The Cl content before and after the direct synthesis of H_2O_2 reaction on $Au_{0.5}Pd_{0.5}/TiO_2$, $Au_{0.5}Pd_{0.5}Fe_{0.02}/TiO_2$ and $Au_{0.5}Pd_{0.5}Fe_1/TiO_2$ catalysts.

Catalyst	%Atom Concentration	
	Before	After
$Au_{0.5}Pd_{0.5}/TiO_2$	0.21	0.11
$Au_{0.5}Pd_{0.5}Fe_{0.02}/TiO_2$	0.27	0.1
$Au_{0.5}Pd_{0.5}Fe_1/TiO_2$	1.17	0.12

H_2O_2 direct synthesis reaction conditions: catalyst (0.01 g), H_2O (2.9 g), CH_3OH (5.6 g), 5% H_2/CO_2 (420 psi), 25% O_2/CO_2 (160 psi), 2 °C, 1200 rpm.

3.6. Techno-economic analysis for the trimetallic AuPdFe catalysts

Following the catalytic performance evaluations, an economic comparison was conducted to assess the viability of the optimised $AuPdFe/TiO_2$ catalyst relative to other well-established catalytic systems frequently reported in the literature, such as AuPdPt, bimetallic AuPd, and monometallic Pd-based catalysts. **Figure 3.14** and further supported by detailed numerical data in **Table A3.4** to **Table A3.13,** specifically considers the raw material costs associated with the production of 1 metric ton of H_2O_2 and tt should be emphasised that this analysis exclusively accounts for direct catalyst and reagent expenses, without incorporating ancillary process costs such as the separation and removal of promoter agents (e.g., halides and acids) or accounting for potential economic benefits related to improved reactor lifetimes achievable through avoiding such additives.[49]

The analysis indicates that, irrespective of catalyst composition, H_2 cost (represented in blue bars) consistently emerges as a significant contributor to the overall cost of H_2O_2 production, accounting for a substantial proportion of total expenditure. For the AuPdFe/TiO_2 catalyst, despite its relatively lower catalyst material costs (41 USD$/ton H_2O_2), the overall economic competitiveness is compromised by considerable costs associated with H_2 consumption, leading to a total material cost of approximately 609 USD$/ton H_2O_2. This figure compares closely with the AuPdPt catalyst (46 USD$/ton H_2O_2), which achieves similar total costs around 552 USD$/ton H_2O_2, highlighting the limited economic advantage conferred by substituting platinum with iron, primarily due to similar H_2 consumption levels.

Interestingly, the AuPd catalyst, despite the use of additional promoters such as H_2SO_4 and NaBr, presents the lowest overall material cost (282 - 412 USD$/ton H_2O_2), driven largely by reduced H_2 consumption. Conversely, Pd-based monometallic catalysts show significantly higher material costs, ranging from approximately 627 to 1016 USD$/ton H_2O_2, driven predominantly by the additional and substantial costs associated with the required solvent (MeOH or EtOH) and acid (H_2SO_4), as clearly illustrated by the increased proportion of these components (green bars).

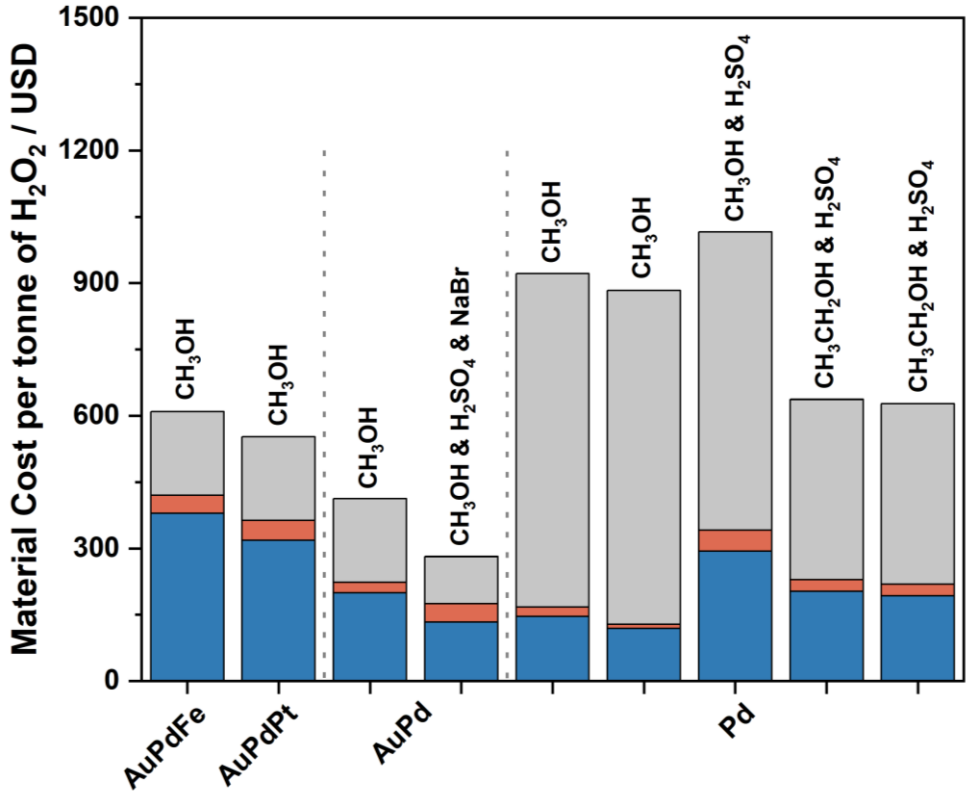

Figure 3.14. Techno-economic analysis of the direct synthesis of H_2O_2 over the optimal AuPdFe/TiO_2 catalysts and comparison to alternative formulations. Key: H_2 (Blue bar), catalyst (Orange bar), and organic component of reaction

solvent (Grey bar, ethanol or methanol as indicated), promoters utilised as indicated. Additional data is provided in **Table A3.4** to **Table A3.13**.

3.7. Conclusion

The selective formation of H_2O_2 remains a vital process for green chemical applications. This chapter demonstrates that strategic modification of AuPd-based catalysts with small amounts of third metals can significantly influence their performance, especially in reaction activity. Here, trimetallic catalysts were synthesised by incorporating Fe into AuPd/TiO_2 systems via a conventional co-impregnation method, followed by reductive heat treatment. The addition of Fe was found to deliver substantial enhancement in catalytic efficiency for direct H_2O_2 production. In particular, the catalyst $Au_{0.5}Pd_{0.5}Fe_{0.02}/TiO_2$ showed a near 1.9-fold improvement compared to the bimetallic $Au_{0.5}Pd_{0.5}/TiO_2$. Moreover, this Fe-modified catalyst exhibited performance levels comparable to those previously achieved by Pt-promoted AuPd systems, despite the absence of noble metal promoters.

To explore the role of Fe content, a series of catalysts with varying Fe loadings was evaluated. It was established that only a narrow compositional range yielded performance gains, beyond this optimal loading (0.02 wt.%), excess Fe led to a decreased catalytic performance. Further detailed characterisations, including CO-DRIFTS and XPS, revealed electronic restructuring and increased Pd oxidation states within the Fe-doped catalysts. These changes likely underpin the observed enhancement in H_2O_2 productivity of the optimal Fe-containing catalyst can be related to greater H_2 utilisation rather than an inhibition of competitive H_2O_2 degradation pathways, *i.e.* increased catalytic reactivity, rather than selectivity, is responsible for the improvements offered over the parent AuPd bimetallic catalyst.

Despite some concerns around long-term stability due to the Pd oxidation state change and the loss of Cl^-, the results here point to the strong potential of Fe-containing trimetallic catalysts for direct H_2O_2 synthesis. Their superior activity and lower reliance on expensive noble metal additives make them promising candidates for sustainable, in situ oxidative applications in environmental and industrial settings.

Tech-economic analysis further revealed that the future catalyst optimisation efforts must prioritise enhancements in selectivity towards H_2O_2 production, alongside reduced H_2 usage, to significantly reduce total costs and achieve economically viable and sustainable H_2O_2 production via the direct synthesis route. Only through such selectivity improvements, ensuring

that increased catalytic activity does not inadvertently enhance competing side reactions (such as hydrogenation and decomposition), can the AuPdFe/TiO_2 catalyst truly rival existing catalytic formulations.

3.8. Future work

The results in this chapter establish an investigation into the promotive effect in the direct H_2O_2 synthesis when doping a trace amount of base metal Fe into TiO_2-supported AuPd catalysts. Some further studies worth considering to trying new trimetallic formulations while promote the catalyst stability and gaining a clear understanding of the reaction mechanism in direct H_2O_2 synthesis.

- **Investigation on the new trimetallic AuPd-based catalysts**
  According to the theoretical DFT calculation work proposed by Xu et al.,[21] introducing certain metals (Ru, Pt, W, Pb, Rh, Ir, Os, Mo) could promote the activity or selectivity of the direct H_2O_2 synthesis. Experimental results from the Hutchings group and Zhang et al. confirmed the promising promotive effect in H_2O_2 productivity when adding Pt, Ru, and W into AuPd catalysts.[16–20,22] However, some other metals, including Pb, Rh, Ir, Os, and Mo, have not yet been reported in the field of direct H_2O_2 synthesis, and further investigations on the promotive effects of these proposed elements are warranted.
- **Improve catalyst stability and reusability by considering new catalyst preparation methods**
  Although the AuPdFe series in this chapter prepared via wet o-impregnation method (using Cl-based Au, Pd, and Fe precursors) was found to be superior in H_2O_2 productivity, the drop in catalytic activity upon the second reuse after cycling (including filtration and dry processes) suggested the catalysts are not stable enough for long term operation and investigation into the reason for the performance loss showed that the loss of chlorine through first use is associated with catalyst deactivation, as previously reported by Brehm et al.[13] Based on that, new catalyst preparation methods are needed to improve the catalyst stability.
- **Investigation of the reaction mechanism during the direct H_2O_2 synthesis**
  Previous studies and this chapter found that introducing trace amounts of third metals into supported AuPd-based catalysts could promote the activity or selectivity towards

the direct H_2O_2 synthesis. Although the XPS and CO-DRIFT analysis in these studies proposed that the promotive effect might be associated with the electron modification of Pd species upon the addition of these third metals, the reaction mechanism remains unclear how trace third-metal dopants reshape Pd species and mediate electron transfer during reaction. To clarify the mechanism, a systematic study of AuPd-based trimetallic catalysts that show a positive dopant effect should be undertaken, coupled with DFT to test whether the activation barrier for H_2O_2 formation is genuinely lower on these trimetallic systems than on bimetallic AuPd. Converging experimental kinetics and DFT would allow the promotive effect of the third metal to be explained.

3.9. Appendix

Table A3.1. Actual metal loading of AuPdFe/TiO_2 catalysts, as determined by ICP analysis of microwave-assisted aqua regia digested catalysts.

Catalyst	Actual metal loading / wt.%		
	Au	Pd	Fe
Au_1/TiO_2	1.01	-	-
Pd_1/TiO_2	-	0.91	-
$Au_{0.5}Pd_{0.5}/TiO_2$	0.48	0.46	-
$Au_{0.5}Pd_{0.5}Fe_{0.01}/TiO_2$	0.45	0.47	0.01
$Au_{0.5}Pd_{0.5}Fe_{0.02}/TiO_2$	0.48	0.49	0.02
$Au_{0.5}Pd_{0.5}Fe_{0.05}/TiO_2$	0.52	0.52	0.05
$Au_{0.5}Pd_{0.5}Fe_{0.1}/TiO_2$	0.48	0.47	0.11
$Au_{0.5}Pd_{0.5}Fe_{0.5}/TiO_2$	0.49	0.49	0.47
$Au_{0.5}Pd_{0.5}Fe_1/TiO_2$	0.55	0.53	0.99
$Au_{0.5}Fe_{0.02}/TiO_2$	0.46	-	0.03
$Pd_{0.5}Fe_{0.02}/TiO_2$	-	0.47	0.02
$Au_1Fe_{0.02}/TiO_2$	1.04	-	0.03
$Pd_1Fe_{0.02}/TiO_2$	-	0.97	0.03

Table A3.2. Catalytic performance towards the direct synthesis of H_2O_2, as a function of Fe loading.

Catalyst	Productivity / $mol_{H2O2}kg_{cat}^{-1}h^{-1}$	H_2O_2 Conc. / wt.%	H_2 Conv. / %	H_2O_2 Sel. / %	Initial rate of reaction / $mmol_{H2O2}$ $mmol_{metal}^{-1}min^{-1}$	Degradation / $mol_{H2O2}kg_{cat}^{-1}h^{-1}$
Au_1/TiO_2	4	0.008	3.0	14	1.76×10^2	28
Pd_1/TiO_2	50	0.100	13	41	9.99×10^2	224
$Au_{0.5}Pd_{0.5}/TiO_2$	70	0.139	19	39	2.46×10^3	208
$Au_{0.5}Pd_{0.5}Fe_{0.01}/TiO_2$	78	0.155	26	32	1.30×10^3	331
$Au_{0.5}Pd_{0.5}Fe_{0.02}/TiO_2$	121	0.242	40	31	3.00×10^3	451
$Au_{0.5}Pd_{0.5}Fe_{0.05}/TiO_2$	110	0.213	36	32	1.89×10^3	365
$Au_{0.5}Pd_{0.5}Fe_{0.1}/TiO_2$	105	0.210	33	32	2.26×10^3	353
$Au_{0.5}Pd_{0.5}Fe_{0.5}/TiO_2$	94	0.186	25	39	1.33×10^3	307
$Au_{0.5}Pd_{0.5}Fe_1/TiO_2$	65	0.129	16	42	4.65×10^2	287
$Au_{0.5}Fe_{0.02}/TiO_2$	3	0.006	2	16	3.18×10^2	52
$Pd_{0.5}Fe_{0.02}/TiO_2$	35	0.070	9	40	1.03×10^3	151
$Au_1Fe_{0.02}/TiO_2$	3	0.006	2	13	1.74×10^2	24
$Pd_1Fe_{0.02}/TiO_2$	41	0.082	11	38	7.24×10^2	233

H_2O_2 direct synthesis reaction conditions: Catalyst (0.01 g), H_2O (2.9 g), MeOH (5.6 g), 5% H_2/CO_2 (420 psi), 25% O_2/CO_2 (160 psi), 0.5 h, 2 °C, 1200 rpm. **H_2O_2 degradation reaction conditions:** Catalyst (0.01 g), H_2O_2 (50 wt.% 0.68 g), H_2O (2.22 g), MeOH (5.6 g), 5% H_2/CO_2 (420 psi), 0.5 h, 2 °C, 1200 rpm. **Note:** Initial reaction rate measured over a reaction time of 0.083 h, calculated based on actual metal loading.

Table A3.3. A comparison of the catalytic performance of trimetallic catalysts towards the direct synthesis of H_2O_2.

Catalyst	Productivity / $mol_{H2O2}kg_{cat}^{-1}h^{-1}$	Solvent	Temp / °C	Time / h	H_2O_2 Conc. / wt. %	H_2 Conv. / %	H_2O_2 Sel. / %	Rate of reaction / $mol_{H2O2}mol_{metal}^{-1}h^{-1}$	Reference
1% $Au_1Pd_1Pt_{0.01}/TiO_2$	112	H_2O/MeOH	2	0.5	0.22	43	37	1.70 x10^3	[19]
1%$AuPd_{(0.975)}Pt_{(0.025)}/TiO_2$	106	H_2O/MeOH	2	0.5	0.22	-	-	1.62 x10^3	[5]
1%$AuPd_{(0.975)}Ni_{(0.025)}/TiO_2$	107	H_2O/MeOH	2	0.5	0.22	32	41	1.56 x10^3	[5]
1%$AuPd_{(0.975)}Sn_{(0.025)}/TiO_2$	78	H_2O/MeOH	2	0.5	0.16	-	-	1.18 x10^3	[5]
1%$AuPd_{(0.975)}Cu_{(0.025)}/TiO_2$	94	H_2O/MeOH	2	0.5	0.19	31	40	1.38 x10^3	[5]
1%$AuPd_{(0.975)}Co_{(0.025)}/TiO_2$	71	H_2O/MeOH	2	0.5	0.14	-	-	1.04 x10^3	[5]
1%$AuPd_{(0.975)}In_{(0.025)}/TiO_2$	77	H_2O/MeOH	2	0.5	0.15	-	-	1.16 x10^3	[5]
1%$AuPd_{(0.975)}Ga_{(0.025)}/TiO_2$	70	H_2O/MeOH	2	0.5	0.14	-	-	1.03 x10^3	[5]
1%$AuPd_{(0.975)}Zn_{(0.025)}/TiO_2$	100	H_2O/MeOH	2	0.5	0.20	24	50	1.47 x10^3	[5]
1%$AuPd_{(0.975)}Cu_{(0.025)}$/ZSM-5	115	H_2O/MeOH	2	0.5	0.23	19	72	1.69 x10^3	[23]
1%$AuPd_{(0.975)}Ni_{(0.025)}$/ZSM-5	81	H_2O/MeOH	2	0.5	0.16	-	-	1.19 x10^3	[23]
1%$AuPd_{(0.975)}Zn_{(0.025)}$/ZSM-5	77	H_2O/MeOH	2	0.5	0.16	-	-	1.13 x10^3	[23]
2.4%Au-2.4%Pd-0.2%Pt/TS-1	167	H_2O/MeOH	2	0.5	0.33	-	-	4.67 x10^2	[16]
0.275%Au-0.275%Pd-0.11%Pt/TS-1	135	H_2O/MeOH	2	0.5	0.27	-	-	2.97 x10^3	[17]
2.4%Au-2.4%Pd-0.2%Pt/CeO_2	170	H_2O/MeOH	2	0.5	0.34	-	-	4.75 x10^2	[18]
0.5%Au-0.5%Pd-0.02%Fe/TiO_2	122	H_2O/MeOH	2	0.5	0.24	40	31	1.61 x10^3	This work

Reaction conditions: catalyst (0.01 g), H_2O (2.9 g), MeOH (5.6 g), 5% H_2/CO_2 (420 psi), 25% O_2/CO_2 (160 psi), 0.5 h, 2 °C, 1200 rpm.

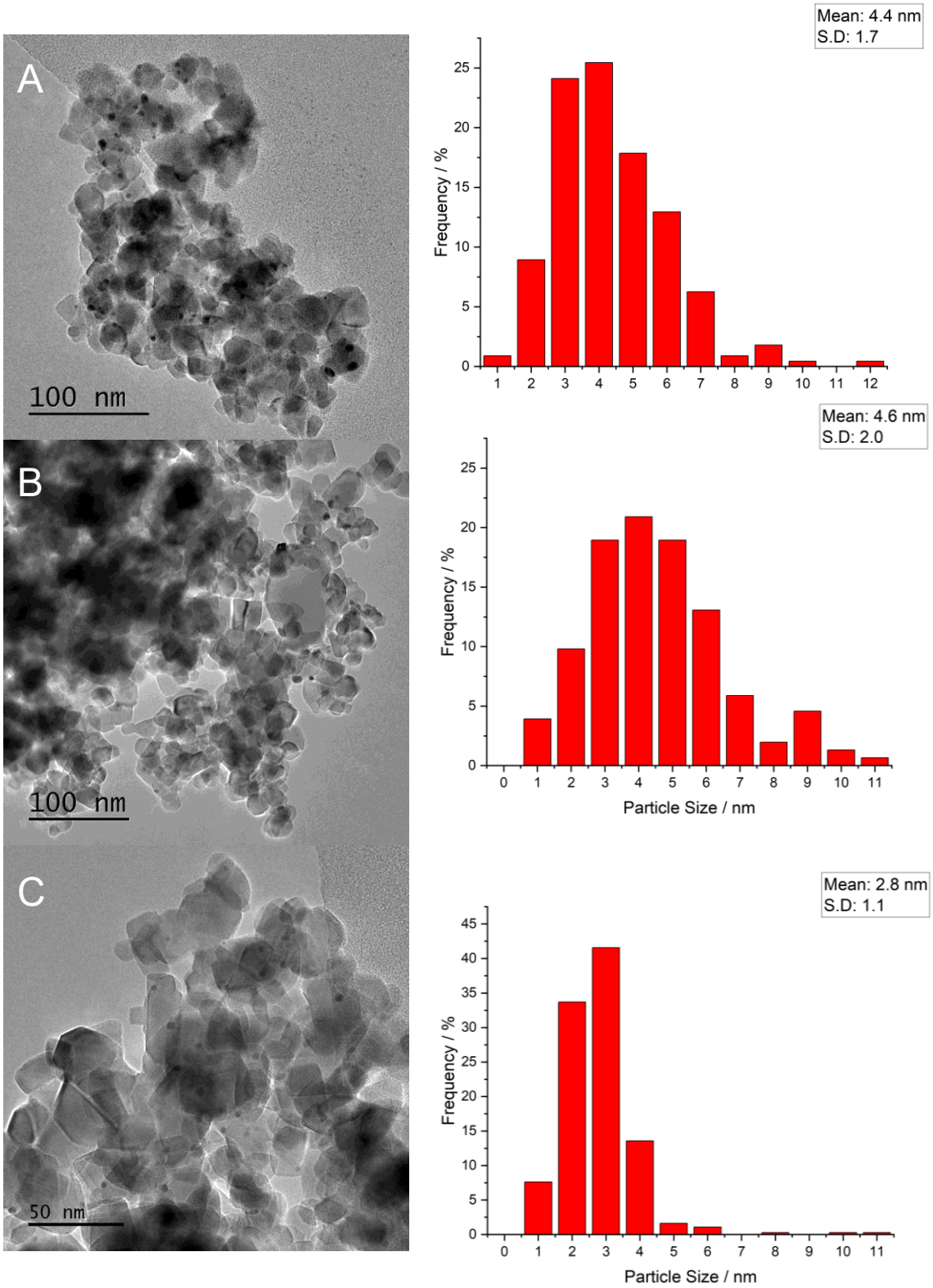

Figure A3.1. Representative bright field transmission electron micrographs and corresponding particle size histograms of (A) $Au_{0.5}Pd_{0.5}/TiO_2$ (B) $Au_{0.5}Pd_{0.5}Fe_{0.01}/TiO_2$ and (C) $Au_{0.5}Pd_{0.5}Fe_{0.02}/TiO_2$ catalysts. Note: All catalysts exposed to a reductive heat treatment (5%H_2/Ar, 400 °C, 4h, 10 °C min^{-1})

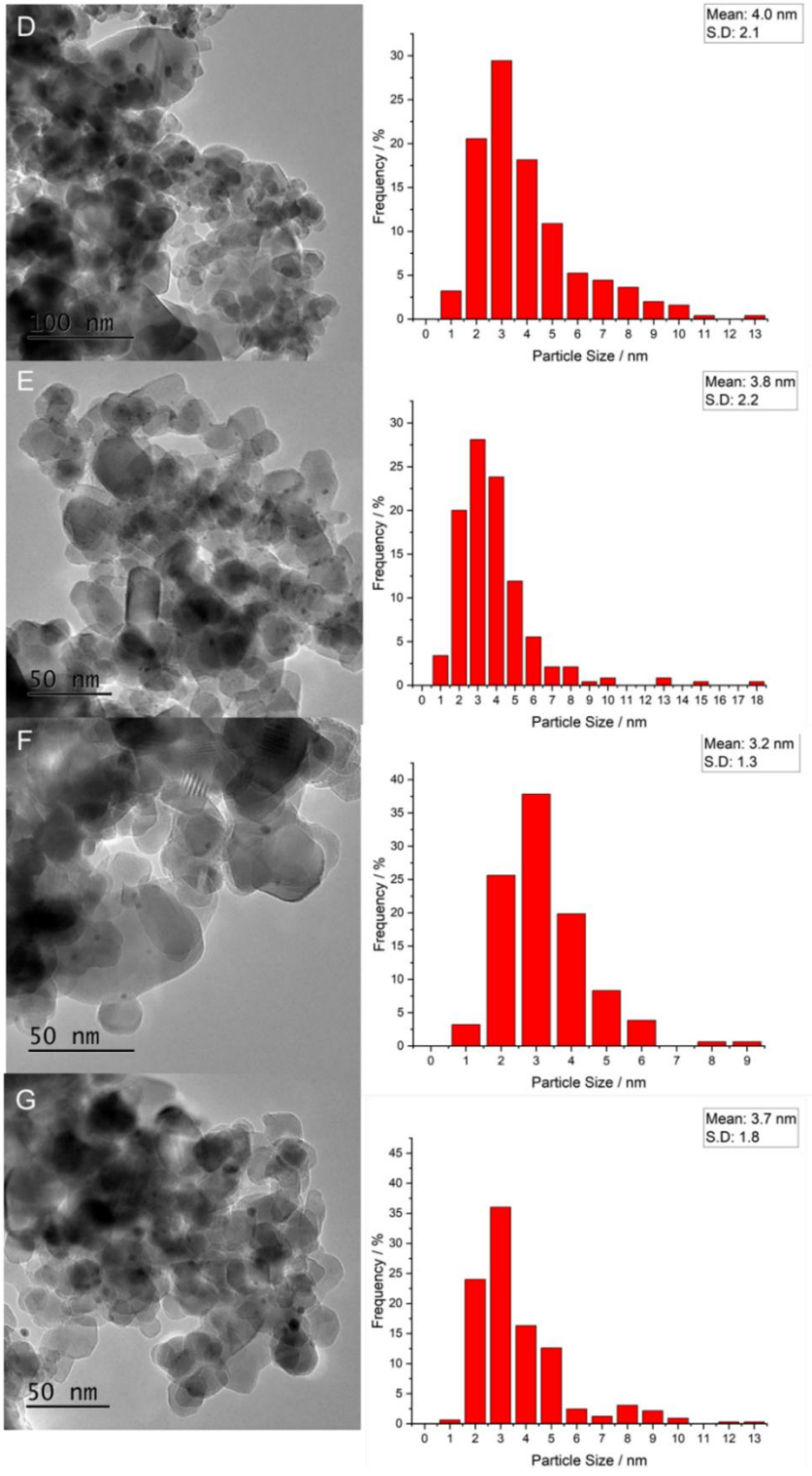

Figure A3.2. Representative bright field transmission electron micrographs and corresponding particle size histograms of (D) $Au_{0.5}Pd_{0.5}Fe_{0.05}/TiO_2$, (E) $Au_{0.5}Pd_{0.5}Fe_{0.1}/TiO_2$, (F) $Au_{0.5}Pd_{0.5}Fe_{0.5}/TiO_2$ and (G) $Au_{0.5}Pd_{0.5}Fe_1/TiO_2$ catalysts. Note: All catalysts exposed to a reductive heat treatment (5%H_2/Ar, 400 °C, 4h, 10 °C min^{-1})

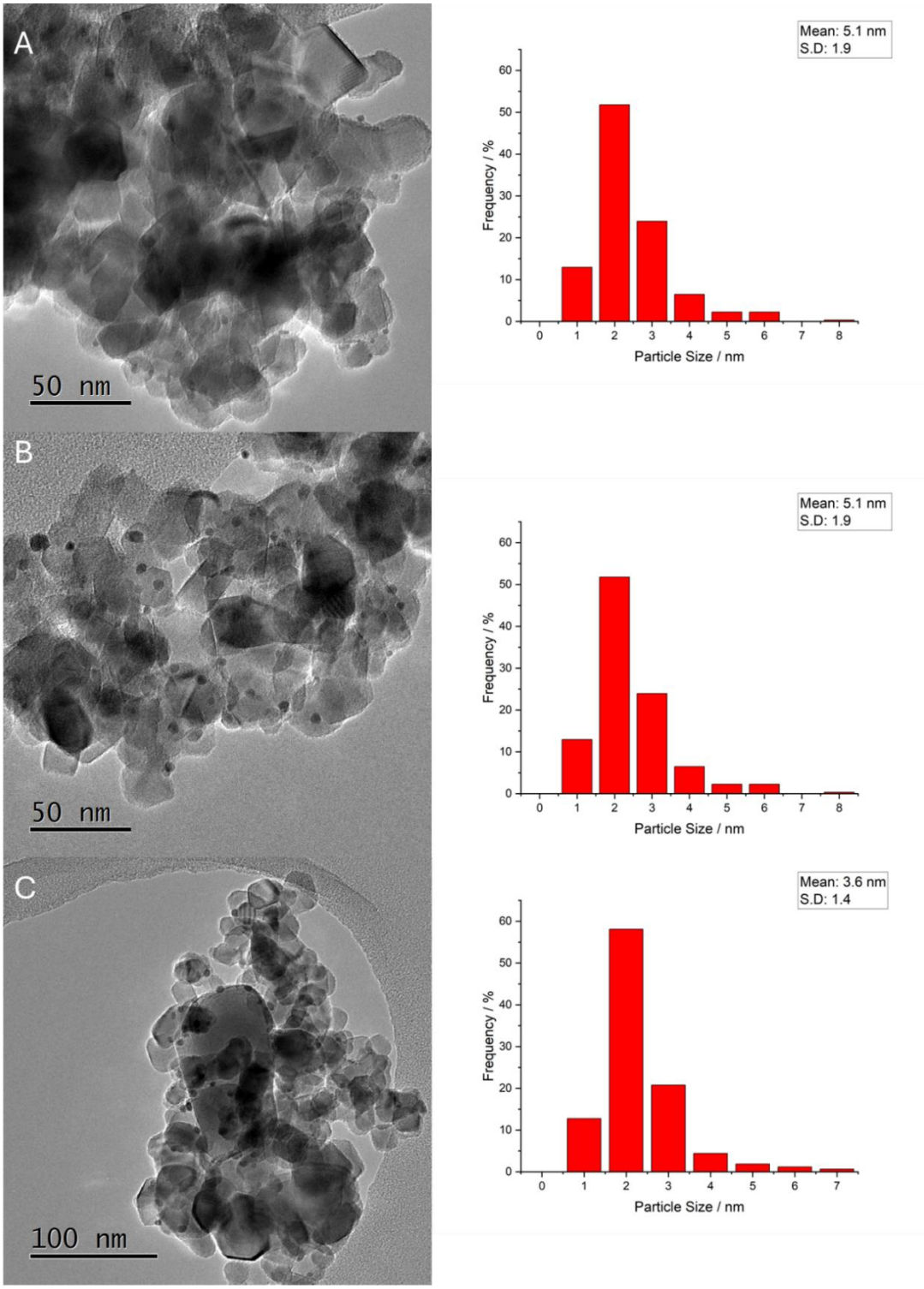

Figure A3.3. Representative bright field transmission electron micrographs and corresponding particle size histograms of (A) $Au_{0.5}Pd_{0.5}/TiO_2$ (B) $Au_{0.5}Pd_{0.5}Fe_{0.02}/TiO_2$ and (C) $Au_{0.5}Pd_{0.5}Fe_1/TiO_2$ catalysts after use in the direct synthesis of H_2O_2. **H_2O_2 direct synthesis reaction conditions:** Catalyst (0.01 g), H_2O (2.9 g), MeOH (5.6 g), 5% H_2/CO_2 (420 psi), 25% O_2/CO_2 (160 psi), 0.5 h, 2 °C, 1200 rpm. **Note:** Catalysts exposed to a reductive heat treatment prior to use (5%H_2/Ar, 400 °C, 4h, 10 °C min^{-1}). Spent samples were dried (30 °C, 16 h, under vacuum).

Table A3.4. Technoeconomic analysis of the direct synthesis of H_2O_2 over the $Au_{0.5}Pd_{0.5}Fe_{0.02}/TiO_2$ catalyst reported in this work.

Catalyst		**$Au_{0.5}Pd_{0.5}Fe_{0.02}/TiO_2$**	
Metal Loading / g	Au	5.00	
	Pd	5.00	
	Fe	0.20	
Support / g	TiO_2	989.80	
Catalyst: Solvent Ratio (wt/wt)		0.0018	
Solvent Usage / t		0.56	
H_2O_2 Selectivity / %		31.00	
H_2O_2 Productivity / $mol_{H2O2}\ Kg_{Cat}^{-1}\ h^{-1}$		122.00	
H_2 Usage / Kg		189.75	
	Unit	**USD / Unit**	**Cost / USD**
H_2	Kg	2	379.51
Methanol	t	336.99	188.71
TiO_2 (P25)	Kg	1.5	7.42
Au (metal)	g	96.9	24.23
Pd (metal)	g	37.2	9.30
Fe (metal)	t	104.62	0.0000010462
Catalyst	Kg		40.95
Total Cost/ USD			**609.17**

Table A3.5. Technoeconomic analysis of the direct synthesis of H_2O_2 over the $Au_{0.65}Pd_{0.35}Pt_{0.01}/TiO_2$ catalyst.

Catalyst		**$Au_{0.65}Pd_{0.35}Pt_{0.01}/TiO_2$**	
Metal Loading / g	Au	5.00	
	Pd	5.00	
	Pt	0.10	
Support / g	TiO_2	989.80	
Catalyst: Solvent Ratio (wt/wt)		0.0018	
Solvent Usage / t		0.56	
H_2O_2 Selectivity / %		37.00	
H_2O_2 Productivity / $mol_{H2O2}\ Kg_{Cat}^{-1}\ h^{-1}$		112.00	
H_2 Usage / Kg		158.98	
	Unit	**USD / Unit**	**Cost / USD**
H_2	Kg	2	317.97
Methanol	t	336.99	188.71
TiO_2 (P25)	Kg	1.5	7.42
Au (metal)	g	96.9	31.49
Pd (metal)	g	37.2	6.51
Pt (metal)	g	36.3	0.18
Catalyst	Kg		45.61
Total Cost/ USD			**552.29**

.

Table A3.6. Technoeconomic analysis of the direct synthesis of H_2O_2 over the $Au_{0.25}Pd_{0.25}/TiO_2$ catalyst.

Catalyst		**$Au_{0.25}Pd_{0.25}/TiO_2$**	
Metal Loading / g	Au	2.50	
	Pd	2.50	
Support / g	TiO_2	995.00	
Catalyst: Solvent Ratio (wt/wt)		0.0018	
Solvent Usage / t		0.56	
H_2O_2 Selectivity / %		59.00	
H_2O_2 Productivity / mol_{H2O2} Kg_{Cat}^{-1} h^{-1}		90.00	
H_2 Usage / Kg		99.70	
	Unit	**USD / Unit**	**Cost / USD**
H_2	Kg	2	199.40
Methanol	t	336.99	188.71
TiO_2 (P25)	Kg	1.5	7.46
Au (metal)	g	96.9	12.11
Pd (metal)	g	37.2	4.65
Catalyst	Kg		24.23
Total Cost/ USD			**412.34**

Table A3.7. Technoeconomic analysis of the direct synthesis of H_2O_2 over the $Au_{0.5}Pd_{0.5}/TiO_2$ catalyst.

Catalyst		**$Au_{0.5}Pd_{0.5}/TiO_2$**	
Metal Loading / g	Au	5.00	
	Pd	5.00	
Support / g	TiO_2	990.00	
Catalyst: Solvent Ratio (wt/wt)		0.0032	
Solvent Usage / t		0.32	
H_2SO_4 Usage / t		9.81×10^{-3}	
NaBr Usage / t		2.06×10^{-6}	
H_2O_2 Selectivity / %		88.00	
H_2O_2 Productivity / $mol_{H2O2}\ Kg_{Cat}^{-1}\ h^{-1}$		51	
H_2 Usage / Kg		66.84	
	Unit	**USD / Unit**	**Cost / USD**
H_2	Kg	2	133.69
H_2SO_4	t	85	0.83
NaBr	t	1734	3.57×10^{-3}
Methanol	t	336.99	106.66
TiO_2 (P25)	Kg	1.5	7.43
Au (metal)	g	96.9	24.23
Pd (metal)	g	37.2	9.30
Catalyst	Kg		40.95
Total Cost/ USD			**282.14**

Table A3.8. Technoeconomic analysis of the direct synthesis of H_2O_2 over the $Pd_{0.72}/TiO_2$ catalyst.

Catalyst		**$Pd_{0.72}/TiO_2$**	
Metal Loading / g	Pd	7.20	
Support / g	TiO_2	992.80	
Catalyst: Solvent Ratio (wt/wt)		0.0004	
Solvent Usage / t		2.24	
H_2O_2 Selectivity / %		80.50	
H_2O_2 Productivity / $mol_{H2O2}\ Kg_{Cat}^{-1}\ h^{-1}$		186	
H_2 Usage / Kg		73.07	
	Unit	**USD / Unit**	**Cost / USD**
H_2	Kg	2	146.15
Methanol	t	336.99	754.86
TiO_2 (P25)	Kg	1.5	7.45
Pd (metal)	g	37.2	13.38
Catalyst	Kg		20.84
Total Cost/ USD			**921.84**

Table A3.9. Technoeconomic analysis of the direct synthesis of H_2O_2 over the $Pd_{0.1}/TiO_2$ catalyst.

Catalyst		**$Pd_{0.1}/TiO_2$**	
Metal Loading / g	Pd	1.00	
Support / g	TiO_2	999.00	
Catalyst: Solvent Ratio (wt/wt)		0.0004	
Solvent Usage / t		2.24	
H_2O_2 Selectivity / %		99.00	
H_2O_2 Productivity / $mol_{H2O2}\ Kg_{Cat}^{-1}\ h^{-1}$		115	
H_2 Usage / Kg		59.42	
	Unit	**USD / Unit**	**Cost / USD**
H_2	Kg	2	118.84
Methanol	t	336.99	754.86
TiO_2 (P25)	Kg	1.5	7.49
Pd (metal)	g	37.2	1.86
Catalyst	Kg		9.35
Total Cost/ USD			**883.05**

Table A3.10. Technoeconomic analysis of the direct synthesis of H_2O_2 over the $Pd_{2.16}/TiO_2$ catalyst.

Catalyst		**$Pd_{2.16}/TiO_2$**	
Metal Loading / g	Pd	21.60	
Support / g	TiO_2	978.40	
Catalyst: Solvent Ratio (wt/wt)		0.0005	
Solvent Usage / t		2.00	
H_2SO_4 Usage / t		$3.92x10^{-3}$	
H_2O_2 Selectivity / %		41.00	
H_2O_2 Productivity / mol_{H2O2} Kg_{Cat}^{-1} h^{-1}		24	
H_2 Usage / Kg		147.06	
	Unit	**USD / Unit**	**Cost / USD**
H_2	Kg	2	294.12
H_2SO_4	t	85	0.33
Methanol	t	336.99	673.98
TiO_2 (P25)	Kg	1.5	7.34
Pd (metal)	g	37.2	40.18
Catalyst	Kg		47.51
Total Cost/ USD			**1015.95**

Table A3.11. Technoeconomic analysis of the direct synthesis of H_2O_2 over the $Pd_1/N\text{-}TiO_2$ catalyst.

Catalyst		**$Pd_1/N\text{-}TiO_2$**	
Metal Loading / g	Pd	10.00	
Support / g	TiO_2	990.00	
Catalyst: Solvent Ratio (wt/wt)		0.0011	
Solvent Usage / t		1200.00	
H_2SO_4 Usage / t		$4.11x10^{-3}$	
H_2O_2 Selectivity / %		58.0	
H_2O_2 Productivity / $mol_{H2O2}\ Kg_{Cat}^{-1}\ h^{-1}$		41	
H_2 Usage / Kg		101.42	
	Unit	**USD / Unit**	**Cost / USD**
H_2	Kg	2	202.84
H_2SO_4	t	85	0.35
Ethanol	L	0.34	408.00
TiO_2 (P25)	Kg	1.5	7.43
Pd (metal)	g	37.2	18.60
Catalyst	Kg		26.03
Total Cost/ USD			**637.21**

Table A3.12. Technoeconomic analysis of the direct synthesis of H_2O_2 over the Pd_1/TiO_2 catalyst.

Catalyst		**Pd_1/TiO_2**	
Metal Loading / g	Pd	10.00	
Support / g	TiO_2	990.00	
Catalyst: Solvent Ratio (wt/wt)		0.0011	
Solvent Usage / t		1200.00	
H_2SO_4 Usage / t		$4.11x10^{-3}$	
H_2O_2 Selectivity / %		61.0	
H_2O_2 Productivity / mol_{H2O2} Kg_{Cat}^{-1} h^{-1}		30	
H_2 Usage / Kg		96.43	
	Unit	**USD / Unit**	**Cost / USD**
H_2	Kg	2	192.86
H_2SO_4	t	85	0.35
Ethanol	L	0.34	408.00
TiO_2 (P25)	Kg	1.5	7.43
Pd (metal)	g	37.2	18.60
Catalyst	Kg		26.03
Total Cost/ USD			**627.24**

Table A3.13. Costings associated with key reagents utilised in the direct synthesis of H_2O_2, used to conduct the economic analysis reported in **Figure 3.14** and **Table A3.4** to **Table A3.12**.

	Unit	USD / Unit	Reference
H_2	Kg	2.00	[50]
H_2SO_4	t	85.00	[51]
NaBr	t	1734.00	[52]
Ethanol	L	0.34	[53]
Methanol	t	336.99	[54]
TiO_2 (P25)	Kg	1.50	[55]
Au (metal)	g	96.90	[56]
Pd (metal)	g	37.20	[57]
Pt (metal)	g	36.30	[58]
Fe (metal)	t	104.62	[59]

3.10. Reference

1. Crole, D. A. *et al.* The direct synthesis of hydrogen peroxide from H2 and O2 using Pd–Ni/TiO2 catalysts. *Philosophical Transactions of the Royal Society A: Mathematical, Physical and Engineering Sciences* **378**, 20200062 (2020).
2. Ciriminna, R., Albanese, L., Meneguzzo, F. & Pagliaro, M. Hydrogen Peroxide: A Key Chemical for Today's Sustainable Development. *ChemSusChem* **9**, 3374–3381 (2016).
3. Lewis, R. J. & Hutchings, G. J. Recent Advances in the Direct Synthesis of H2O2. *ChemCatChem* **11**, 298–308 (2019).
4. Flaherty, D. W. Direct Synthesis of H2O2 from H2 and O2 on Pd Catalysts: Current Understanding, Outstanding Questions, and Research Needs. *ACS Catal* **8**, 1520–1527 (2018).
5. Barnes, A., Lewis, R. J., Morgan, D. J., Davies, T. E. & Hutchings, G. J. Enhancing catalytic performance of AuPd catalysts towards the direct synthesis of H2O2 through incorporation of base metals. *Catal Sci Technol* **12**, 1986–1995 (2022).
6. Kovačič, D. *et al.* A comparative study of palladium-gold and palladium-tin catalysts in the direct synthesis of H2O2. *Green Chemistry* **25**, 10436–10446 (2023).
7. Yu, S. *et al.* High activity and selectivity of single palladium atom for oxygen hydrogenation to H2O2. *Nat Commun* **13**, 4737 (2022).
8. Edwards, J. K. *et al.* Switching Off Hydrogen Peroxide Hydrogenation in the Direct Synthesis Process. *Science (1979)* **323**, 1037–1041 (2009).
9. Li, H. *et al.* Layered Pd oxide on PdSn nanowires for boosting direct H2O2 synthesis. *Nat Commun* **13**, 6072 (2022).
10. Freakley, S. J. *et al.* Palladium-tin catalysts for the direct synthesis of H2O2 with high selectivity. *Science (1979)* **351**, 965–968 (2016).
11. Voloshin, Y., Halder, R. & Lawal, A. Kinetics of hydrogen peroxide synthesis by direct combination of H2 and O2 in a microreactor. *Catal Today* **125**, 40–47 (2007).
12. Tian, P. *et al.* The origin of palladium particle size effects in the direct synthesis of H2O2: Is smaller better? *J Catal* **349**, 30–40 (2017).

13. Brehm, J., Lewis, R. J., Morgan, D. J., Davies, T. E. & Hutchings, G. J. The Direct Synthesis of Hydrogen Peroxide over AuPd Nanoparticles: An Investigation into Metal Loading. *Catal Letters* **152**, 254–262 (2022).

14. Santos, A. *et al.* Direct Synthesis of Hydrogen Peroxide over Au–Pd Supported Nanoparticles under Ambient Conditions. *Ind Eng Chem Res* **58**, 12623–12631 (2019).

15. Liu, P. & Nørskov, J. K. Ligand and ensemble effects in adsorption on alloy surfaces. *Physical Chemistry Chemical Physics* **3**, 3814–3818 (2001).

16. Lewis, R. J. *et al.* The Direct Synthesis of H2O2 Using TS-1 Supported Catalysts. *ChemCatChem* **11**, 1673–1680 (2019).

17. Lewis, R. J. *et al.* Cyclohexanone ammoximation via in situ H2O2 production using TS-1 supported catalysts. *Green Chemistry* **24**, 9496–9507 (2022).

18. Edwards, J. K. *et al.* The Direct Synthesis of Hydrogen Peroxide Using Platinum-Promoted Gold–Palladium Catalysts. *Angew. Chem. Int. Ed. Engl.* **53**, 2381–2384 (2014).

19. Gong, X. *et al.* Enhanced catalyst selectivity in the direct synthesis of H2O2 through Pt incorporation into TiO2 supported AuPd catalysts. *Catal Sci Technol* **10**, 4635–4644 (2020).

20. Ntainjua, E. N., Freakley, S. J. & Hutchings, G. J. Direct Synthesis of Hydrogen Peroxide Using Ruthenium Catalysts. *Top Catal* **55**, 718–722 (2012).

21. Xu, H., Cheng, D. & Gao, Y. Design of High-Performance Pd-Based Alloy Nanocatalysts for Direct Synthesis of H2O2. *ACS Catal* **7**, 2164–2170 (2017).

22. Zhang, M., Xu, H., Luo, Y., Zhu, J. & Cheng, D. Enhancing the catalytic performance of PdAu catalysts by W-induced strong interaction for the direct synthesis of H2O2. *Catal Sci Technol* **12**, 5290–5301 (2022).

23. Barnes, A., Lewis, R. J., Morgan, D. J., Davies, T. E. & Hutchings, G. J. Improving Catalytic Activity towards the Direct Synthesis of H2O2 through Cu Incorporation into AuPd Catalysts. *Catalysts* **12**, (2022).

24. Zhu, Y. *et al.* Strategies for enhancing the heterogeneous Fenton catalytic reactivity: A review. *Appl Catal B* **255**, 117739 (2019).

25. Cao, J. *et al.* Gambling of homogeneous and heterogeneous Fenton in wastewater treatment. *Cell Rep Phys Sci* **5**, (2024).

26. Neyens, E. & Baeyens, J. A review of classic Fenton's peroxidation as an advanced oxidation technique. *J Hazard Mater* **98**, 33–50 (2003).

27. Wang, G., Xu, L., Zhang, J., Yin, T. & Han, D. Enhanced Photocatalytic Activity of TiO2 Powders (P25) via Calcination Treatment. *International Journal of Photoenergy* **2012**, 265760 (2012).

28. Edwards, J. K., Carley, A. F., Herzing, A. A., Kiely, C. J. & Hutchings, G. J. Direct synthesis of hydrogen peroxide from H2 and O2 using supported Au–Pd catalysts. *Faraday Discuss* **138**, 225–239 (2008).

29. Delannoy, L. *et al.* Surface Segregation of Pd from TiO2-Supported AuPd Nanoalloys under CO Oxidation Conditions Observed In situ by ETEM and DRIFTS. *ChemCatChem* **5**, 2707–2716 (2013).

30. Usoltsev, O. *et al.* Restructuring of Palladium Nanoparticles during Oxidation by Molecular Oxygen. *Small* **20**, 2401184 (2024).

31. Zhu, X. *et al.* Optimising surface d charge of AuPd nanoalloy catalysts for enhanced catalytic activity. *Nat Commun* **10**, 1428 (2019).

32. Ekborg-Tanner, P. & Erhart, P. Hydrogen-Driven Surface Segregation in Pd Alloys from Atomic-Scale Simulations. *The Journal of Physical Chemistry C* **125**, 17248–17260 (2021).

33. Ouyang, L. *et al.* The origin of active sites for direct synthesis of H2O2 on Pd/TiO2 catalysts: Interfaces of Pd and PdO domains. *J Catal* **321**, 70–80 (2015).

34. Liu, Y., Hu, S., Zhang, X. & Sun, S. p-n heterojunction constructed by γ-Fe2O3 covering CuO with CuFe2O4 interface for visible-light-driven photoelectrochemical water oxidation. *J Colloid Interface Sci* **639**, 464–471 (2023).

35. Vanleerberghe, R., de Grave, E., Vandenberghe E., R. & Robbrecht G., G. Fe57 MÖSSBAUER SPECTROSCOPY ON TITANIUM-RICH IRON TITANATES Fe3-xTixO4 (x = 1., 0.95, 0.9). *J. Phys. Colloques* **41**, C1-179-C1-180 (1980).

36. Cho, S.-J. *et al.* Characterization and magnetic properties of core/shell structured Fe/Au nanoparticles. *J Appl Phys* **95**, 6804–6806 (2004).

37. Brehm, J. *et al.* Enhancing the Chemo-Enzymatic One-Pot Oxidation of Cyclohexane via In Situ H2O2 Production over Supported Pd-Based Catalysts. *ACS Catal* **12**, 11776–11789 (2022).

38. Carter, J. H. *et al.* Synergy and Anti-Synergy between Palladium and Gold in Nanoparticles Dispersed on a Reducible Support. *ACS Catal* **6**, 6623–6633 (2016).

39. Cerrato, G., Marchese, L. & Morterra, C. Structural and morphological modifications of sintering microcrystalline TiO2: an XRD, HRTEM and FTIR study. *Appl Surf Sci* **70–71**, 200–205 (1993).

40. Green, I. X., Tang, W., Neurock, M. & Yates, J. T. Spectroscopic Observation of Dual Catalytic Sites During Oxidation of CO on a Au/TiO2 Catalyst. *Science (1979)* **333**, 736–739 (2011).

41. Dekkers, M. A. P., Lippits, M. J. & Nieuwenhuys, B. E. CO adsorption and oxidation on Au/TiO2. *Catal Letters* **56**, 195–197 (1998).

42. Zheng, B. *et al.* Role of the FeOx support in constructing high-performance Pt/FeOx catalysts for low-temperature CO oxidation. *Catal Sci Technol* **6**, 1546–1554 (2016).

43. Ouyang, L. *et al.* Insight into active sites of Pd–Au/TiO2 catalysts in hydrogen peroxide synthesis directly from H2 and O2. *J Catal* **311**, 129–136 (2014).

44. Ntainjua N., E. *et al.* The Effect of Bromide Pretreatment on the Performance of Supported Au–Pd Catalysts for the Direct Synthesis of Hydrogen Peroxide. *ChemCatChem* **1**, 479–484 (2009).

45. Lunsford, J. H. The direct formation of H2O2 from H2 and O2 over palladium catalysts. *J Catal* **216**, 455–460 (2003).

46. Choudhary, V. R. & Samanta, C. Role of chloride or bromide anions and protons for promoting the selective oxidation of H2 by O2 to H2O2 over supported Pd catalysts in an aqueous medium. *J Catal* **238**, 28–38 (2006).

47. Hohenegger, M., Bechtold, E. & Schennach, R. Coadsorption of oxygen and chlorine on Pt(111). *Surf Sci* **412–413**, 184–191 (1998).

48. Wilson, N. M. & Flaherty, D. W. Mechanism for the Direct Synthesis of H2O2 on Pd Clusters: Heterolytic Reaction Pathways at the Liquid–Solid Interface. *J Am Chem Soc* **138**, 574–586 (2016).

49. Gao, G. *et al.* Advances in the production technology of hydrogen peroxide. *Chinese J. Catal.* **41**, 1039–1047 (2020).

50. Kayfeci, M., Keçebaş, A. & Bayat, M. Chapter 3 - Hydrogen production. in *Solar Hydrogen Production* (eds. Calise, F., D'Accadia, M. D., Santarelli, M., Lanzini, A. & Ferrero, D.) 45–83 (Academic Press, 2019). doi:https://doi.org/10.1016/B978-0-12-814853-2.00003-5.

51. Sulphuric Acid Prices, Monitor, News, Analysis & Demand via www.chemanalyst.com/Pricing-data/sulphuric-acid-70 ((accessed 20.11.2024).).

52. Sodium Bromide Price Trend and Forecast via www.procurementresource.com/resource-center/sodium-bromide-price-trends (accessed 20.11.2024).

53. Trading Economics, Ethanol via www.tradingeconomics.com/commodity/ethanol (accessed 20.11.2024).

54. Trading Economics, Mehanol via www.tradingeconomics.com/commodity/methanol (accessed 20.11.2024) .

55. Degussa, P25 costing via www.daliantnn.en.made-in-china.com/product/WmkYHiDChpVo/China-Degussa-P25-Low-Price-Per-Kg-TiO2-Titanium-Dioxide-Rutile-Grade.html (accessed 20.11.2024).

56. Gold Prices - 100 Year Historical Chart via www.macrotrends.net/1333/historical-gold-prices-100-year-chart (accessed 20.11.2024).

57. Palladium Prices - Interactive Historical Chart via www.macrotrends.net/2542/palladium-prices-historical-chart-data (accessed 20.11.2024).

58. Platinum Prices - Interactive Historical Chart via www.macrotrends.net/2540/platinum-prices-historical-chart-data (accessed 20.11.2024).

59. Iron ore via www.tradingeconomics.com/commodity/iron-ore (accessed 20.11.2024).

Chapter 4 - In situ Phenol degradation over Fe-incorporated AuPd catalysts

4.1 Introduction

Water pollution, particularly caused by resistant organic pollutants, poses significant threats to ecological safety and public health globally.[1–3] Persistent organic contaminants, including dyes, pharmaceuticals, pesticides, and phenolic compounds, exhibit high chemical stability, strong bioaccumulation potential, and resistance to natural degradation processes.[4–6] Traditional water treatment techniques, such as biological processes,[7] adsorption,[8] coagulation-flocculation,[9] and membrane filtration mainly separates or transfers pollutants between phases rather than mineralising or often requiring additional handling and disposal.[10] Consequently, complete removal can be costly and may generate secondary pollution, highlighting the need for advanced, sustainable technologies that achieve destructive removal rather than mere phase transfer.[11]

Advanced oxidation processes (AOPs) have emerged as promising solutions for effectively degrading persistent organic pollutants.[12,13] Among the various AOPs, the Fenton reaction, employing homogeneous iron catalysts (Fe^{2+}/Fe^{3+}) and hydrogen peroxide (H_2O_2), has attracted substantial attention owing to its capability to generate hydroxyl radicals (•OH), possessing an oxidation potential of approximately 2.8 V.[14,15] However, the practical implementation of this method faces challenges due to its rate-limiting step, the slow Fe^{3+}/Fe^{2+} reduction reaction (rate constant: ~9.1×10^{-7} L mol^{-1} s^{-1}), which is significantly slower compared to the rapid Fe^{2+} oxidation step (rate constant: 40–80 L mol^{-1} s^{-1}).[11] Additionally, reliance on externally supplied commercial H_2O_2 elevates treatment costs[16] and results in poor utilisation efficiency.[13] The hazardous nature of concentrated H_2O_2, associated with storage and transport risks due to its explosive properties.[17] Currently, 95% of commercial H_2O_2 is predominantly produced through the anthraquinone auto-oxidation (AO) process, which consists of sequential hydrogenation and oxidation steps in an organic solvent, followed by extraction and further distillation, leading to substantial energy consumption and generating harmful organic by-products.[18,19] Thus, developing alternative, environmentally friendly methods to replace the AO-based synthesis of H_2O_2 has become a pivotal research direction.

Direct synthesis of H_2O_2 from molecular H_2 and O_2 represents an attractive alternative approach to producing H_2O_2 on-site, minimising safety risks associated with handling highly concentrated oxidants, avoiding the use of stabilising agents and the downstream purification process.[18] From this in situ water treatment perspective, a cascade reaction system integrating direct H_2O_2 synthesis and subsequent activation via the Fenton pathway can be established as a self-sufficient Fenton system, effectively addressing the limitations related to external H_2O_2 addition and poor utilisation efficiency. Richards and Hutchings demonstrated that the in situ generation of H_2O_2 and, importantly, related intermediate species (·OOH, ·OH etc) over bimetallic AuPd catalyst is 10^7 and 10^8 times more effective than the use of performed H_2O_2 and chlorination towards E. coli remediation under equivalent conditions, respectively. In this work, the authors conclude that the Pd active sites are mainly responsible for the in situ H_2O_2/reactive H_2O_2 intermediates production, while Au facilitates effective reactive oxygen species (ROS; ·OOH, ·OH $O_2^{\cdot-}$ etc) diffusion into the solution.[20] Later, highly reactive bimetallic Pd-based catalysts (e.g. PdFe formulations) were found to facilitate H_2O_2 synthesis, mainly on Pd active sites effectively, and subsequent H_2O_2 activation, mainly on the Fenton metal active sites, achieving an appreciable phenol degradation rate. However, the stability is an issue for these PdFe formulations to perform long-term use in the in situ phenol degradation.[21–23]

With these studies in mind, we now continue with the investigation on a series of TiO_2-supported AuPd-based trimetallic catalysts to further explore the catalytic potential in environmental application Although the catalytic performance of bimetallic PdFe catalysts have been investigated before, the catalytic performance and stability of the novel trimetallic AuPdFe catalysts still unknown. This chapter aims to combine the direct H_2O_2 synthesis activity of AuPd and the ability of the most popular Fenton metal, Fe, to generate reactive oxygen species through Fenton pathways for the in situ phenol degradation under more mild reaction conditions, e.g. pure water and room temperature, which are more close to the real-world water treatment conditions. Aim to establish the phenol degradation map via detailed intermediates analysis, build a relation between Fe loading and phenol conversion, and try to understand the differences between in situ Fenton system and ex situ Fenton system.

4.2 Direct synthesis and degradation of H_2O_2 over AuPdFe catalysts

Building upon the observation from **Chapter 3**, where the Fe-doped trimetallic AuPd-based catalyst demonstrated superior catalytic performance (120 $mol_{H2O2}\,kg_{cat}^{-1}\,h^{-1}$) compared to its bimetallic analogue (65 $mol_{H2O2}\,kg_{cat}^{-1}\,h^{-1}$) and Fe-rich trimetallic analogue (60 $mol_{H2O2}\,kg_{cat}^{-1}\,h^{-1}$) in the direct synthesis of H_2O_2 under idealised reaction conditions (CH_3OH+H_2O solvent mixture at 2 ºC). This chapter extends the investigation to evaluate the catalytic efficacy of these catalysts for phenol degradation using the in situ generated H_2O_2. To better represent conditions relevant to practical water treatment, reactions were conducted in pure water or aqueous phenol solutions without the addition of CH_3OH, which can act as a radical quencher such as for ·OH species, and the reaction temperature was increased from 2 °C to 20 °C.

A series of mono-, bi-, and trimetallic AuPdFe catalysts was synthesised via the co-impregnation method.[24] Detailed data regarding actual metal loading are summarised in **Table A4.1,** closely matching their theoretical values. While XRD spectra of the trimetallic AuPdFe series and the mono-, and bimetallic catalysts are provided in **Figure A4.1** and **Figure A4.2**, respectively, confirmed that metal introduction did not alter the crystal structure of the anatase (*ICDD PDF File 00-021-1272*) and rutile (*ICDD PDF File 00-021-1276*) phases of TiO_2 (P25), suggesting the relatively small particle dispersed on the surface of TiO_2. Brunauer-Emmett-Teller (BET) surface area measurements of key samples (and corresponding bare supports) are reported in **Table A4.2**, with a minor loss in surface area found to result from metal deposition and thermal treatment of the catalytic samples.

Under reaction conditions deemed sub-optimal for H_2O_2 production (i.e., ambient temperature and absence of the alcohol co-solvent typically employed to enhance H_2O_2 stability and gaseous reagent solubility),[25] yet relevant to real-world advanced oxidative treatments of aqueous waste streams, initial standard studies (30 mins) were conducted to assess the catalytic performance of a series of TiO_2-immobilised mono-, bi-, and trimetallic AuPdFe catalysts towards direct H_2O_2 synthesis and its subsequent degradation (**Table 4.1**).

Table 4.1 The effect of Fe loading on the performance of 1%AuPd/TiO_2 catalysts towards the direct synthesis and subsequent degradation of H_2O_2.

Catalyst	H_2O_2 Productivity / $mol_{H2O2}kg_{cat}^{-1}h^{-1}$	H_2O_2 Concentration / ppm	H_2 Conversion / %	H_2O_2 Selectivity / %	H_2O_2 Degradation / $mol_{H2O2}kg_{cat}^{-1}h^{-1}$
$Au_{0.5}Pd_{0.5}/TiO_2$	35	694	20	33	568
$Au_{0.5}Pd_{0.5}Fe_{0.1}/TiO_2$	31	613	22	27	1022
$Au_{0.5}Pd_{0.5}Fe_{0.5}/TiO_2$	31	611	23	26	853
$Au_{0.5}Pd_{0.5}Fe_1/TiO_2$	7	132	26	5	780
$Au_{0.5}Pd_{0.5}Fe_2/TiO_2$	2	33	30	1	589
$Au_{0.5}Pd_{0.5}Fe_3/TiO_2$	2	31	30	1	540
$Au_{0.5}Fe_2/TiO_2$	0	2	2	1	32
$Pd_{0.5}Fe_2/TiO_2$	7	148	33	4	288
$Au_{0.5}/TiO_2$	0	13	2	8	24
$Pd_{0.5}/TiO_2$	29	582	21	26	580
Fe_2/TiO_2	0	0	0	0	56

H_2O_2 direct synthesis reaction conditions: catalyst (0.01 g), H_2O (8.5 g), 5% H_2/CO_2 (420 psi), 25% O_2/CO_2 (160 psi), 0.5 h, 20 °C, 1200 rpm. H_2O_2 degradation reaction conditions: catalyst (0.01 g), H_2O_2 (50 wt% 0.68 g), H_2O (7.82 g), 5% H_2/CO_2 (420 psi), 0.5 h, 20 °C, 1200 rpm.

Consistent with previous studies, incorporating Au into a Pd-supported catalyst improved catalytic activity for H_2O_2 production. Specifically, the bimetallic $Au_{0.5}Pd_{0.5}/TiO_2$ catalyst exhibited a higher H_2O_2 synthesis rate (35 $mol_{H2O2}kg_{cat}^{-1}h^{-1}$) and H_2O_2 concentration (694 ppm) compared to the $Pd_{0.5}/TiO_2$ catalyst with the identical Pd content (29 $mol_{H2O2}kg_{cat}^{-1}h^{-1}$, 582 ppm), while the $Au_{0.5}/TiO_2$ catalyst (13 ppm H_2O_2) only has a minimal contribution towards H_2O_2 synthesis. This enhancement was primarily attributed to improved catalytic selectivity (33% for $Au_{0.5}Pd_{0.5}/TiO_2$ and 26% for $Pd_{0.5}/TiO_2$), rather than increased reactivity, as evidenced by similar H_2 conversion rates observed (20% for $Au_{0.5}Pd_{0.5}/TiO_2$ and 21% for $Pd_{0.5}/TiO_2$).

Aligning well with observations in **Chapter 3**, increasing the Fe loading in the AuPd-based catalysts resulted in significantly reduced H_2O_2 productivity and concentrations. Specifically, the H_2O_2 productivity declined progressively from 35 $mol_{H2O2}kg_{cat}^{-1}h^{-1}$ (694 ppm) for $Au_{0.5}Pd_{0.5}/TiO_2$ to a negligible value of 2 $mol_{H2O2}kg_{cat}^{-1}h^{-1}$ (31 ppm) for $Au_{0.5}Pd_{0.5}Fe_3/TiO_2$. This trend correlated with significantly enhanced H_2 conversion rates (from 20% to 30%) and

drastically diminished H_2O_2 selectivity (from 33% to 1%) as Fe content increased, and unsurprisingly, similar trend in H_2O_2 degradation as a function of Fe loading was observed, compared to previous work,[24] with the trimetallic AuPdFe catalyst with relatively lower Fe loading are active towards both H_2O_2 synthesis and degradation due to the electron modification of Pd by the introduction of Fe.

Although monometallic $Au_{0.5}/TiO_2$ catalysts demonstrated very limited H_2O_2 production (13 ppm after 30 minutes), Fe introduction drastically reduced the yield to only 2 ppm in the $Au_{0.5}Fe_2/TiO_2$ catalyst, accompanied by negligible H_2 conversion (2%) and very low selectivity (1%). Similarly, the bimetallic $Pd_{0.5}Fe_2/TiO_2$ catalyst yielded significantly lower H_2O_2 concentrations (148 ppm), a drastic decrease compared to the monometallic $Pd_{0.5}/TiO_2$ catalyst (582 ppm). The $Pd_{0.5}Fe_2/TiO_2$catalyst exhibited notably higher H_2 conversion (33%) yet considerably diminished selectivity (4%), suggesting the Fe addition promotes unselective H_2 oxidation pathways and increases catalytic degradation. Furthermore, the Fe-only catalyst (Fe_2/TiO_2) produced no detectable H_2O_2, consistent with negligible activity towards selective H_2O_2 generation.

Further evaluation of key catalytic formulations over extended reaction time (up to 6 hours) is reported in **Figure A4.3** to show the overall trend of H_2O_2 synthesis (including H_2O_2 concentration, H_2 conversion and H_2O_2 selectivity) and H_2O_2 degradation. Specifically, for the $Au_{0.5}Pd_{0.5}/TiO_2$ catalyst, the concentration of H_2O_2 reached a distinct peak within the initial 30–60 minutes, attaining approximately 700 ppm, before gradually declining due to concurrent H_2O_2 degradation processes. Comparatively, the initial 30-minute data presented earlier show that catalysts with lower Fe loading ($Au_{0.5}Pd_{0.5}Fe_{0.1}/TiO_2$ and $Au_{0.5}Pd_{0.5}Fe_{0.5}/TiO_2$) initially exhibited the H_2O_2 concentrations at around 600 ppm, but extended observation highlighted accelerated degradation and declining selectivity. The contrast becomes even more pronounced with catalysts of higher Fe loadings ($Au_{0.5}Pd_{0.5}Fe_1/TiO_2$, $Au_{0.5}Pd_{0.5}Fe_2/TiO_2$, and $Au_{0.5}Pd_{0.5}Fe_3/TiO_2$). While short-term (30 min) evaluations indicated lower initial H_2O_2 productivity, prolonged monitoring emphasised the rapid and sustained degradation activity of these Fe-rich catalysts.

With incremental Fe incorporation, notable changes in the catalytic behaviour emerged. For catalysts with low Fe loading ($Au_{0.5}Pd_{0.5}Fe_{0.1}/TiO_2$ and $Au_{0.5}Pd_{0.5}Fe_{0.5}/TiO_2$), the H_2O_2 concentration still achieved significant peaks around 600 ppm within the first hour, but exhibited accelerated degradation rates thereafter. Correspondingly, H_2 conversion rates were

enhanced moderately to approximately 22–23%, accompanied by decreased selectivity (27% and 26%, respectively). As Fe loading increased further ($Au_{0.5}Pd_{0.5}Fe_1/TiO_2$), the maximum H_2O_2 concentration significantly diminished to around 130 ppm, with substantially elevated H_2 conversion (26%) and notably lower selectivity (5%).

Catalysts with higher Fe contents ($Au_{0.5}Pd_{0.5}Fe_2/TiO_2$ and $Au_{0.5}Pd_{0.5}Fe_3/TiO_2$) exhibited minimal peak concentrations of H_2O_2 (below 35 ppm), with the majority of the produced H_2O_2 being rapidly degraded. H_2 conversion rates for these catalysts rose markedly to around 30%, reflecting significantly enhanced non-selective oxidation processes and minimal selectivity towards H_2O_2 formation (around 1%). These observations strongly indicate that higher Fe loading substantially promotes non-selective catalytic pathways, leading to immediate consumption of any generated H_2O_2.

Nevertheless, the observed gradual increase in the H_2 conversion rate with higher Fe loadings suggests an enhanced catalytic activity for H_2 activation compared to the bimetallic $Au_{0.5}Pd_{0.5}/TiO_2$ catalyst, excluding the effect of active site blockage by excessive Fe loading. Indeed, the H_2 conversion rate is highly associated with the Pd oxidation state, where H_2 could be easily activated on Pd^0 sites.[26] Therefore, the X-ray photoelectron spectroscopy (XPS) analysis was conducted and revealed the presence of a significant proportion of Pd^{2+} for all trimetallic formulations, despite the exposure of the catalysts to a relatively high-temperature reductive heat treatment (5%H_2/Ar, 400 °C, 4 h, 10 °C min^{-1}) (**Figure 4.1**).

The introduction of Fe resulted in a clear shift in Pd speciation toward Pd^{2+}, with such observations aligning well with our earlier studies investigating the role of alternative transition metals as promoters for AuPd nanoalloys.[24,27,28] Theoretically, the formation of mixed domains, consisting of Pd^0 and Pd^{2+}, was well reported to offer enhanced catalytic performance towards H_2O_2 synthesis, compared to purely Pd^0 or Pd^{2+} analogues.[26] However, such enhancement in H_2O_2 synthesis was not observed in this work. Indeed, the XPS analysis for the fresh catalyst could not fully represent the dynamic changes of the Pd oxidation state over time under reaction conditions, and the in situ X-ray absorption spectroscopy (XAS) technology might be beneficial to examine the Pd oxidation state more dynamically. In keeping with previous AuPdFe study in **Chapter 3**, the addition of Fe could also promote Pd reduction during H_2O_2 synthesis reaction and only Pd^0 species existed on the surface of Fe-rich trimetallic after 5 mins according to the time on line XPS analysis, thus forming more active metallic Pd^0 sites, which are likely responsible for effective H_2 activation despite the overall decline in H_2O_2 degradation

efficiency, whereas residual Pd^{2+} species persisted on bimetallic AuPd catalysts and trimetallic AuPdFe catalysts with less Fe content maintain a relatively higher H_2O_2 selectivity over time.[24] Regarding Fe speciation, a distinct signal at a binding energy of 710.7 eV and a satellite structure around 719 eV indicate the presence of Fe^{3+}. However, it is important to highlight the tendency of Fe to oxidise readily under ambient conditions, coupled with the surface sensitivity of XPS. Additionally, the broad Fe 2p core-level spectra suggest the coexistence of Fe^{2+}, likely formed during the reductive heat treatment.

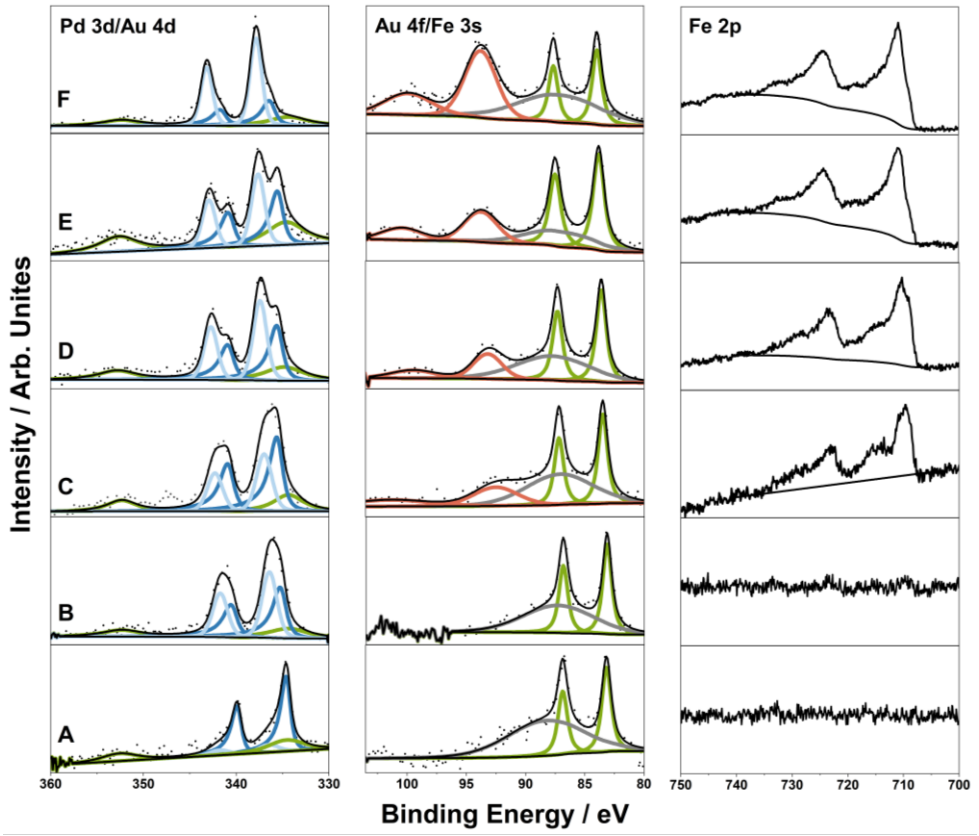

Figure 4.1. XPS analysis of the as-prepared AuPdFe/TiO_2 catalysts. (A) $Au_{0.5}Pd_{0.5}/TiO_2$, (B) $Au_{0.5}Pd_{0.5}Fe_{0.1}/TiO_2$, (C) $Au_{0.5}Pd_{0.5}Fe_{0.5}/TiO_2$, (D) $Au_{0.5}Pd_{0.5}Fe_1/TiO_2$, (E) $Au_{0.5}Pd_{0.5}Fe_2/TiO_2$, (F) $Au_{0.5}Pd_{0.5}Fe_3/TiO_2$. Key: Au(4d) & Au(4f) (green); Fe(3s) (orange); Pd^0 (dark blue); Pd^{2+} (light blue); loss of structure (grey). Note: catalysts exposed to a reductive heat treatment prior to use (5%H_2/Ar, 400 °C, 4 h, 10 °C min^{-1}). **Please note**: the test and subsequent analysis were performed by Dr. David J. Morgan (Cardiff University; HarwellXPS).

CO-DRIFTS experiments further provided deeper insights into electronic interactions induced by Fe incorporation into AuPd nanoalloys (**Figure 4.2**). DRIFTS spectra of the bimetallic and trimetallic AuPdFe (with low Fe content) samples were dominated by Pd–CO bands. The peaks near 1930 cm^{-1} and 1988 cm^{-1} could be attributed to the doubly and triply bridging (3-fold hollow) CO species.[29,30] The peaks at 2060 cm^{-1} and 2081 cm^{-1} were observed and can be

attributed to linear CO adsorption modes on low-coordinated Pd sites (edges or corners),[30,31] while the peaks in 1950-1960 cm^{-1} and in 1850–1900 cm^{-1} regions can be assigned to bridge and 3-fold adsorbed CO on metallic Pd species, respectively.[32,33] Upon introducing Fe (≤1 wt.%), significant shifts in the position of the linear and bridged Pd–CO bands occur, likely due to electron transfer to Pd d orbitals, enhancing back-donation into the CO 2π* orbital, consistent with the Pd oxidation state shift upon the addition of Fe as indicated by XPS (**Figure 4.1**). Further increasing Fe content up to 3 wt.% gradually diminishes and eventually eliminates peaks at 2060 cm^{-1} and 2081 cm^{-1}, which is consistent with the XPS results of the Pd electron loss due to the strong interaction between Fe and AuPd and the disappearance of the Pd sites at the corner or edge.[33,34]

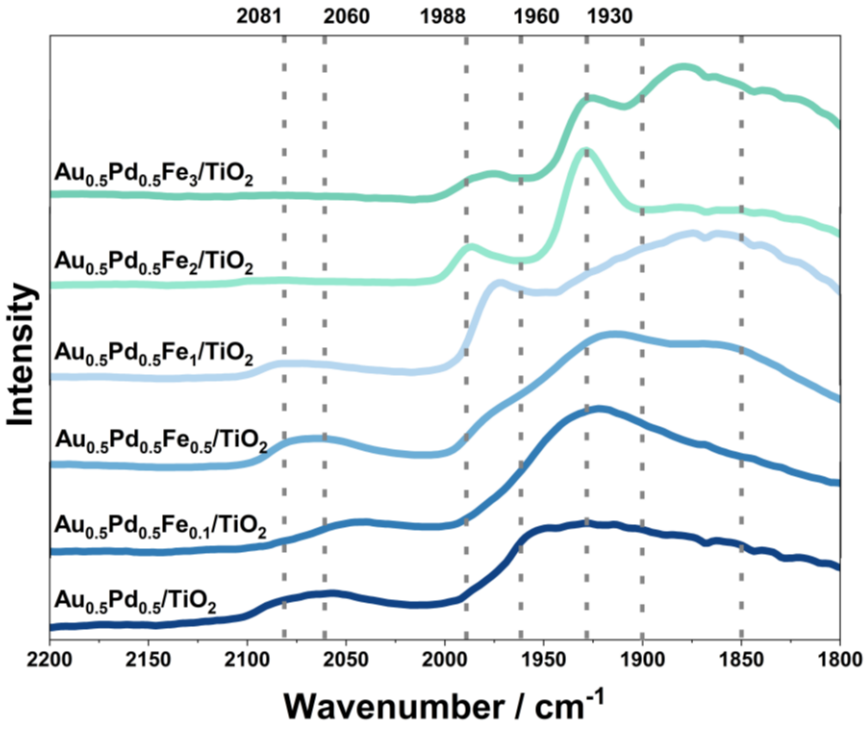

Figure 4. 2. CO-DRIFTS spectra of AuPdFe series.

With the strong correlation between catalytic selectivity towards the direct H_2O_2 synthesis and nanoparticle size well known,[35] the particle size distribution analysis based on Transmission electron microscopy (TEM) images were presented in **Figure A4.4**, **Figure A4.5** and **Table 4.2**, showing well dispersed nanoparticles with the mean particle size between 4 to 6 nm on the surface of TiO_2 and slightly increased mean particle size, with the increase in Fe content, from on the 4.4 nm (bimetallic $Au_{0.5}Pd_{0.5}/TiO_2$) to 6.1 nm ($Au_{0.5}Pd_{0.5}Fe_3/TiO_2$), showing a slight negative correlation to the H_2O_2 productivity and selectivity might be due to the strong

interaction between Fe and AuPd reducing availability of selective catalytic sites according to CO-DRIFTs analysis.

Table 4. 2. Corresponding mean particle size of the AuPdFe series.

Catalyst	Mean Particle Size / nm	S.D. / nm
$Au_{0.5}Pd_{0.5}/TiO_2$	4.37	1.65
$Au_{0.5}Pd_{0.5}Fe_{0.1}/TiO_2$	3.84	2.14
$Au_{0.5}Pd_{0.5}Fe_{0.5}/TiO_2$	3.21	1.24
$Au_{0.5}Pd_{0.5}Fe_1/TiO_2$	3.69	1.85
$Au_{0.5}Pd_{0.5}Fe_2/TiO_2$	4.88	2.05
$Au_{0.5}Pd_{0.5}Fe_3/TiO_2$	6.07	2.71

4.3 The catalytic activity of the AuPdFe series towards the in situ phenol degradation

4.3.1 The effect of Fe on the in situ phenol degradation

On the basis of evaluating the performance of a series of bi- and trimetallic catalysts for direct H_2O_2 synthesis, the influence of Fe loading on the subsequent in situ utilisation of H_2O_2 for phenol degradation was further systematically investigated, as illustrated in the **Figure. 4.3**, with the optimal $Au_{0.5}Pd_{0.5}Fe_2/TiO_2$ catalyst outperforming other formulations, in terms of phenol degradation rate. This optimal catalyst achieved the highest phenol conversion rate, exceeding 83%, which is nearly 10-fold greater than the bimetallic formulation (approximately 8%). Excessive Fe loading (3 wt.%) in the trimetallic formulation did not further enhance phenol degradation rate, but rather, the phenol degradation rate only reached 73%.

Detailed analysis of the phenolic intermediates (hydroquinone, catechol, resorcinol, para-benzoquinone, and others (organic acids, CO_2 etc)) generated during the phenol degradation reaction showed that very limited phenolic intermediates were observed in the $Au_{0.5}Pd_{0.5}/TiO_2$ and $Au_{0.5}Pd_{0.5}Fe_{0.1}/TiO_2$ systems, suggesting lower phenol degradation efficiency occurs in the absence or presence of only trace amounts of Fenton metals (e.g. Fe). While abundant hydroquinone and catechol, and a small amount of resorcinol were detected in the other trimetallic AuPdFe system, with the Fe loading ≥ 0.5 wt.%. These hydroxylated phenolic products (hydroquinone, catechol, resorcinol, etc.) seemingly suggested that ·OH is the main

reaction species generated in the reaction medium, in keeping with the similar phenol degradation via the radical pathway presented in previous studies.[22,23,36] Meanwhile, to examine if any post-oxidation of phenolic intermediates occurred, the degradation tests in **Figure A4.6 (A)** firstly showed a near complete conversion of para-benzoquinone within 30 mins with the presence of both H_2 and O_2, and the control experiments subsequently confirmed that this transformation only occurred with the presence of both H_2 and O_2, excluding the contribution from hydrogenation reaction (**Figure A4.6 (B)**). This high para-benzoquinone conversion might somehow explain the quick disappearance of para-benzoquinone through a fast and selective transformation to hydroquinone within a short period (**Figure 4.3**; For the trimetallic AuPdFe catalysts with Fe loading ≥ 0.5 wt.%) via the oxidation pathway.[37] Meanwhile, the conversion of other phenolic intermediates, hydroquinone (25%), catechol (18%), resorcinol (34%) was also observed in the in situ oxidation system, suggesting the post oxidation processes exist and highly likely leading to the continued oxidation and the generation of ring-opening products in "Others" (di-acids, inorganic carbon, and H_2O).[37]

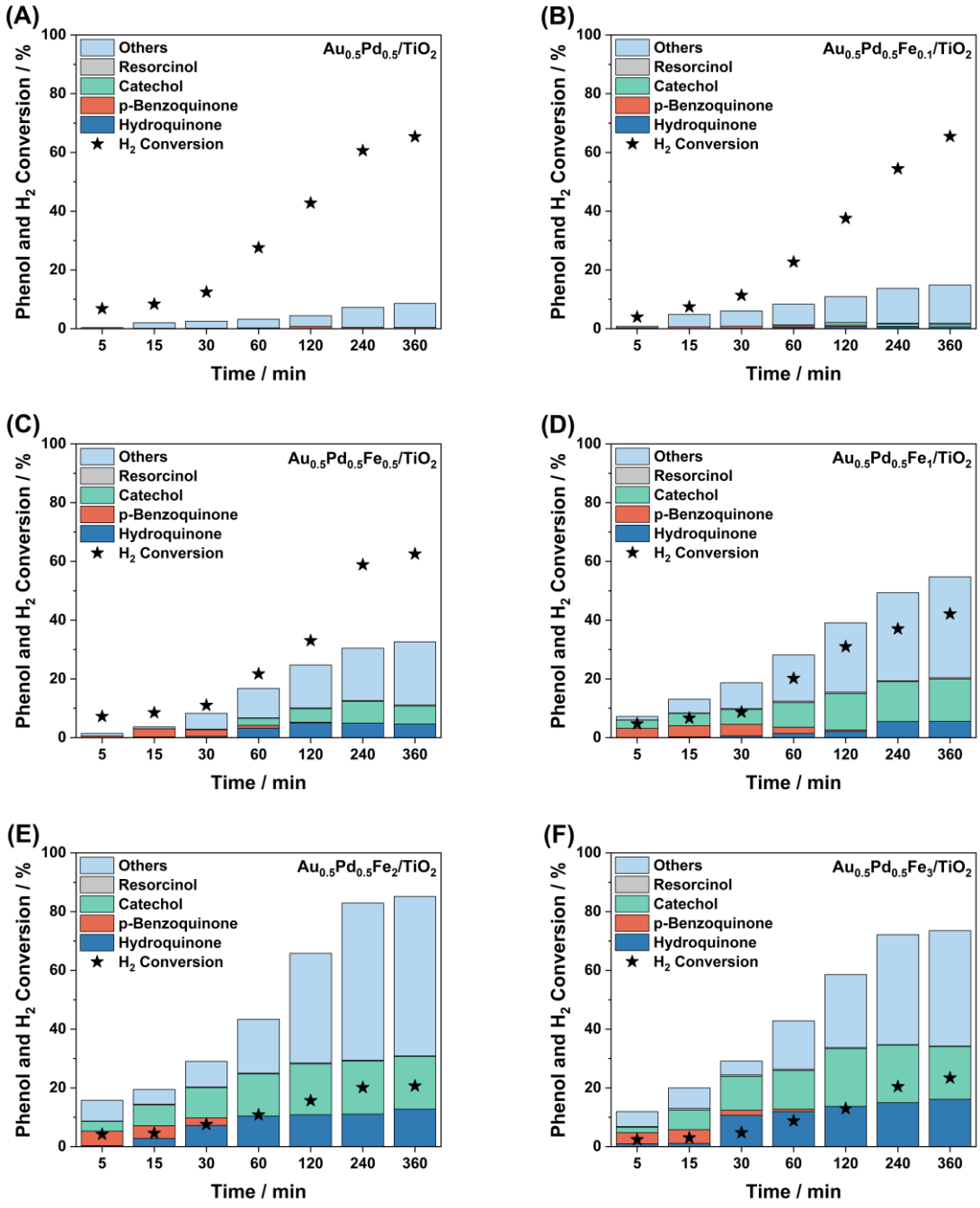

Figure 4.3. The activity of $Au_{0.5}Pd_{0.5}Fe_x/TiO_2$ catalysts towards the oxidation of phenol, where X = 0 to 3. Reaction conditions: catalyst (0.01 g), phenol (1000 ppm, 8.5 g), 5% H_2/CO_2 (420 psi), 25% O_2/CO_2 (160 psi), 20°C, 1200 rpm.

Furthermore, for the AuPdFe series, H_2 conversion during in situ phenol degradation shows the opposite dependence on Fe content compared with direct H_2O_2 synthesis (**Figure A4.3**). In H_2O_2 synthesis, the conversion increases with Fe content, whereas in phenol degradation it decreases. For example, the Fe-rich trimetallic (e.g. $Au_{0.5}Pd_{0.5}Fe_2/TiO_2$) reached 75% H_2

conversion after 4 hours in H_2O_2 synthesis, but only 20% H_2 utilisation after 4 hours phenol degradation test. By contrast, the bimetallic $Au_{0.5}Pd_{0.5}/TiO_2$ showed only a modest drop from 74% in H_2O_2 synthesis to 61% in phenol degradation after 4 hours. This drastic change in H_2 conversion over Fe-rich AuPdFe catalyst could be associated with the change in reaction medium, according to the intermediates analysis in **Figure 4.3**. For example, the in situ generated phenolic and ring-opening byproducts, leading to the deactivation of Pd or AuPd active sites, which might mainly be responsible for H_2 activation. The phenol degradation process ceased from 4 hours to 6 hours when the H_2 conversion reached a plateau over the $Au_{0.5}Pd_{0.5}Fe_2/TiO_2$ catalyst, as the effective phenol degradation relies on the in situ H_2O_2 generation from the first stage, and the effect of any residual H_2O_2 is minimal.

Pseudo-first-order kinetic analysis was conducted to quantitatively assess the reaction rates in each catalytic system, utilising data from the initial 4 hours of the reaction. Notably, the phenol degradation ceased after 4 hours in Fe-rich trimetallic systems due to catalyst deactivation. As demonstrated in **Figure 4.4,** the highest rate constant was observed for the optimal $Au_{0.5}Pd_{0.5}Fe_2/TiO_2$ catalyst (0.429 h^{-1}), which is approximately 25 times higher than that of the corresponding bimetallic catalyst ($Au_{0.5}Pd_{0.5}/TiO_2$, 0.017 h^{-1}). The reproducibility of the optimal formulation was triple-checked by preparing another two batches under the same procedure (**Figure A4.7**), and all three different batches exhibited similar level of phenol conversion (83% on average), H_2 conversion (20% on average), and even the selectivity towards phenolic derivatives (31% on average) and others (organic acids, CO_2 and H_2O, 52% on average).

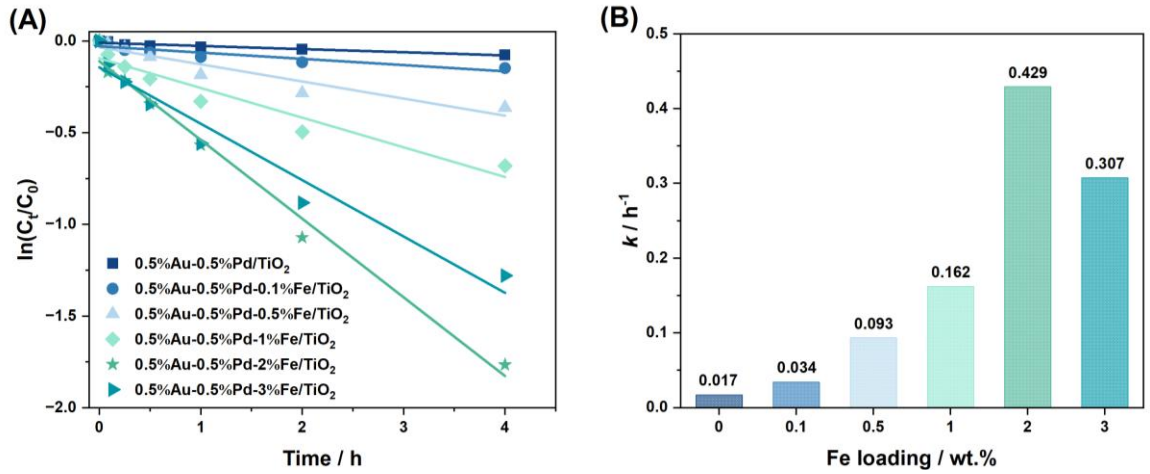

Figure 4.4. (A) Pseudo first-order kinetic analysis for the catalytic performance of AuPdFe series toward in situ phenol degradation. (B) The rate constant in each catalytic system for phenol degradation. Reaction conditions: catalyst (0.01 g), phenol (1000 ppm, 8.5 g), 5% H_2/CO_2 (420 psi), 25% O_2/CO_2 (160 psi), 25°C, 1200 rpm.

4.3.2 Comparing in situ with ex situ supplied H_2O_2

Although the possibility of phenol hydrogenation over Pd active sites was excluded in a previous PdFe study, where no hydrogenation products (e.g. cyclohexanol or cyclohexanone) could be seen via ^{1}H NMR analysis.[23] The new trimetallic AuPdFe is still worth checking due to the appreciable H_2 activation ability. In **Figure 4.5**, the "*Cat.*" test (CO_2 diluent only, no H_2 and O_2) indicates that the adsorption of phenol on the surface of the catalyst is negligible (<1% phenol conversion), suggesting that the phenol conversion is mainly attributed to the oxidative degradation process rather than physical adsorption. Single-reactant gas tests, 2% and 5% phenol conversion achieved in O_2-only ("*Cat.*+O_2") and H_2-only ("*Cat.*+H_2") systems, respectively, demonstrating that a single reactant gas alone cannot effectively trigger the oxidative degradation of phenol. A relatively higher phenol conversion was observed in the H_2 only reaction compared to the O_2 only reaction, with some phenolic intermediates observed after 4hours of reaction (e.g. Catechol and hydroquinone), suggesting that oxidative degradation of phenol occurred, and this can be mainly due to the presence of dissolved oxygen (DO) within the reaction medium.

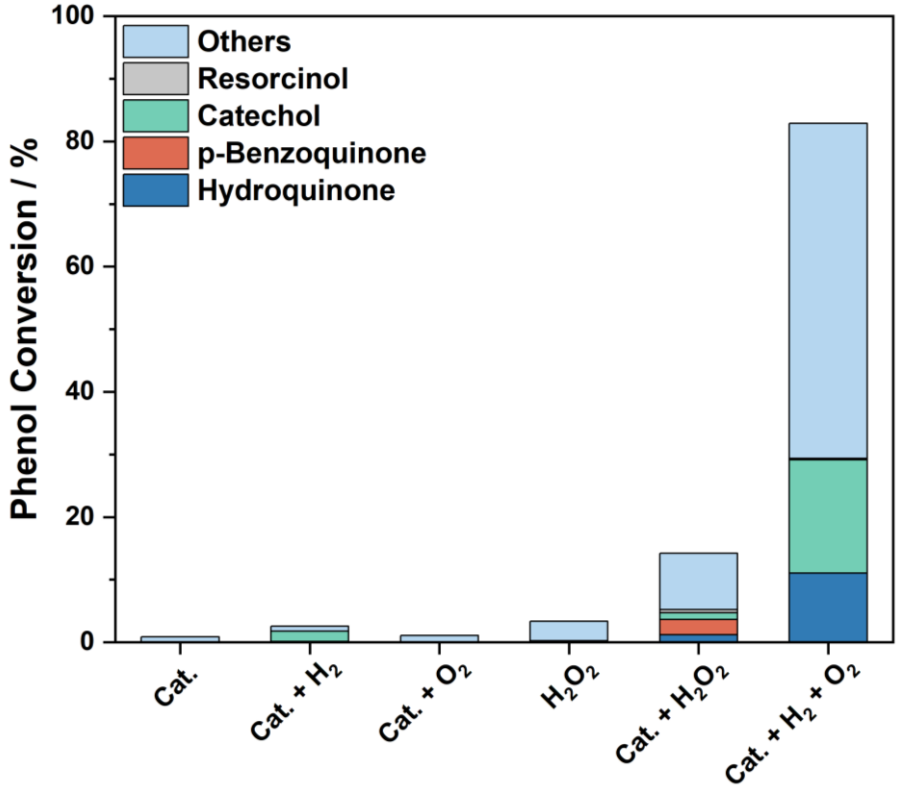

Figure 4.5. The effect of reactant gases and physical adsorption on phenol degradation using $Au_{0.5}Pd_{0.5}Fe_2/TiO_2$ catalyst. Reaction condition: No H_2 and O_2: 580 psi CO_2 charged; H_2 Only: 420 psi 5%H_2/CO_2 + 160 psi CO_2; O_2 Only: 420 psi CO_2 + 160 psi 25%O_2/CO_2; H_2+O_2: 420 psi 5%H_2/CO_2 + 160 psi 25%O_2/CO_2; Preformed H_2O_2: 2.58 mmol, which is equivalent to the amount of H_2O_2 converted from all H_2 with 100% selectivity. In all cases: catalyst (0.01 g), phenol (1000 ppm, 8.5 g), 25°C, 1200 rpm, 4hrs.

The required amount of pre-formed H_2O_2 for the ex-situ phenol degradation (8.5g, 1000 ppm) was added to determine the oxidative ability of H_2O_2 to break down phenol to CO_2 and H_2O. The reaction was carried out under a pure CO_2 atmosphere (580 psi), which is the diluent gas for H_2 and O_2 in standard phenol degradation and H_2O_2 synthesis tests. In the absence of any catalyst ("*H_2O_2*", H_2O_2 concentration equivalent to that which may be achieved if all the H_2 in the in-situ system was selectively converted to H_2O_2), phenol conversion remained extremely low (<3 %) with the interaction between only phenol and H_2O_2, suggesting limited oxidative efficiency of bulk H_2O_2 towards phenol degradation. Crucially, these experiments implicate highly reactive oxygen-based radical species as the primary drivers of the observed activity. Additional support for the central role of ROS in phenol oxidation comes from radical-quenching tests (**Figure A4.8**), where the addition of t-butanol, a widely used scavenger of oxygen-based radicals, leads to a substantial decrease in phenol conversion.[38]

The trimetallic AuPdFe catalyst showed a slight improvement in phenol conversion ("*Cat.* + H_2O_2", ~15 % conversion) in the ex-situ Fenton system when interacting with pre-formed H_2O_2 (H_2O_2 concentration equivalent to that which may be achieved if all the H_2 in the in-situ system was selectively converted to H_2O_2). But still far less efficient than that of the in situ supplied Fenton system ("*Cat.* + H_2 + O_2", 82%), suggesting that **1)** the H_2O_2 generated in situ throughout the time is a more efficient approach for the subsequent H_2O_2 activation rather than adding bulk H_2O_2 initially. Previous literature reported that continuous addition of H_2O_2 enhanced oxidative degradation of organic pollutants compared to batch operation (adding all H_2O_2 at the beginning), by avoiding the unnecessary H_2O_2 decomposition and the competitive scavenging reactions involving H_2O_2, and ·OH ($H_2O_2 + {\cdot}OH \rightarrow H_2O + HO_2{\cdot}$).[39–42] **2)** the direct involvement of reactive intermediates (e.g., *OOH, *OH, $*H_2O_2$) formed during the in situ synthesis of H_2O_2 in the phenol degradation process is a more efficient oxidation pathway than subsequent activation of stable H_2O_2 molecules. Experimental and theoretical findings from studies on the three-electron oxygen reduction reaction (3 e^- ORR) suggest that the direct generation of ·OH from O_2 via the intermediate route ($O_2 \rightarrow *H_2O_2 \rightarrow {\cdot}OH$) is more kinetically favourable than the alternative pathway involving stable H_2O_2 formation ($O_2 \rightarrow *H_2O_2 \rightarrow H_2O_2$),[43,44] which could potentially explain the contrasting trends observed in **Figures A4.3** and **Figure 4.3**, where the $Au_{0.5}Pd_{0.5}Fe_2/TiO_2$ catalyst demonstrates relatively poor performance for in situ H_2O_2 synthesis but exhibits the highest catalytic efficacy for phenol oxidative degradation when compared to both the bimetallic $Au_{0.5}Pd_{0.5}/TiO_2$ catalyst and its trimetallic counterparts with lower Fe content. However, such a hypothesis could not be determined in this study due to the lack of direct time-resolved, operando evidence for the putative surface-bound intermediates and the theoretical calculation on the activation energy of these two possible pathways.

4.3.2 In situ phenol degradation using mono-, and bimetallic AuPdFe catalysts

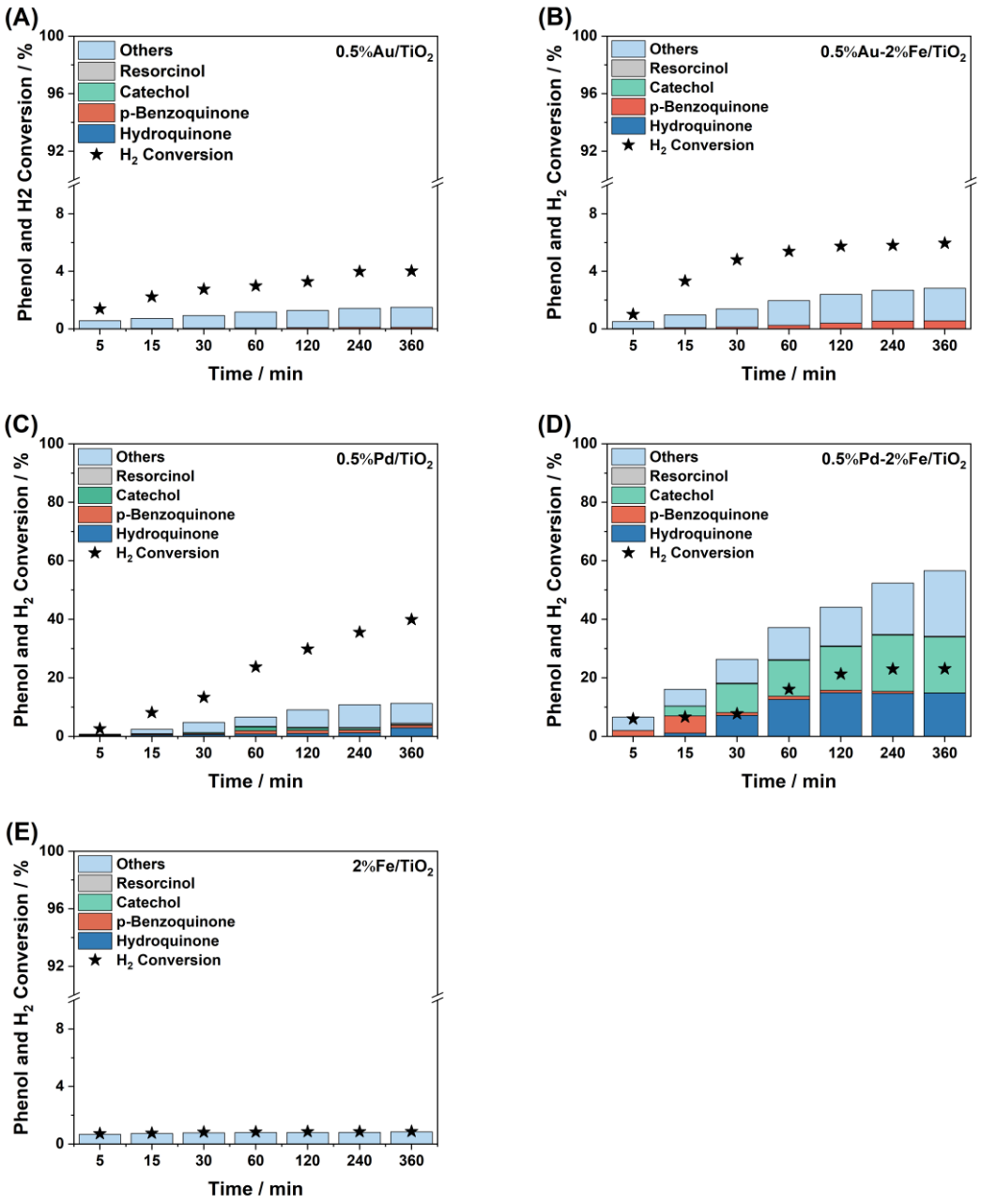

Figure 4.6. The activity of the mono-, bimetallic Au, Pd, Fe catalysts towards the oxidation of phenol. Reaction conditions: catalyst (0.01 g), phenol (1000 ppm, 8.5 g), 5% H_2/CO_2 (420 psi), 25% O_2/CO_2 (160 psi), 20°C, 1200 rpm.

Figure 4.6 shows the limited catalytic abilities of $Au_{0.5}/TiO_2$, Fe_2/TiO_2, and $Au_{0.5}Fe_2/TiO_2$ catalysts towards phenol conversion via in situ H_2O_2 generation, achieved only1.7%, 2.2%, and 2.7% after 4 hours of reaction, respectively, also <4 % H_2 conversion measurements suggested that limited H_2 activation resulting in a low H_2O_2 synthesis at the first stage. Indeed, only a

minimal amount of H_2O_2 was generated over $Au_{0.5}/TiO_2$ (13 ppm H_2O_2 after 30 mins) and $Au_{0.5}Fe_2/TiO_2$ (2 ppm H_2O_2 after 30 mins), while no H_2O_2 could be detected on Fe_2/TiO_2 (0 ppm H_2O_2 after 30 mins) under idealised reaction conditions for the direct H_2O_2 synthesis (**Table 4.1**). On the contrary, $Pd_{0.5}/TiO_2$ and $Pd_{0.5}Fe_2/TiO_2$ formulations achieved 10% and 53% phenol conversion after 4 hours of reaction, respectively. Considerably enhanced H_2O_2 synthesis rates for these formulations were also observed, with 582 ppm and 148 pm for the $Pd_{0.5}/TiO_2$ and $Pd_{0.5}Fe_2/TiO_2$, respectively (**Table 4.1**), suggesting that the first stage, the H_2 activation (to form H_2O_2 or reactive intermediates in situ), is the initial key for the subsequent phenol degradation. Trace amounts of hydroxylated phenolic intermediates were observed on the $Pd_{0.5}/TiO_2$ catalyst, showing the bifunctionality of Pd active sites in H_2O_2 synthesis and subsequent H_2O_2 activation. Still, the inefficient H_2O_2 utilisation via the Fenton pathway on the Pd active sites solely resulted in a limited amount of ROS generated in situ, or the diffusion of the generated ROS to the solution is poor, resulting in lower Fenton effeciency.[20] Unfortunately, the bimetallic $Pd_{0.5}Fe_2/TiO_2$ formulation (53% after 4 hours) was still not comparable to the trimetallic $Au_{0.5}Pd_{0.5}Fe_2/TiO_2$ catalyst (82% after 4 hours). Previous investigation into the remediation of *E. coli* via in situ H_2O_2 and associated ROS generation suggested that Au could promote the diffusion of ROS generated on the Pd surface into the solution, thus enhancing the reactive ability of the bimetallic formulation compared to the monometallic Pd catalyst.[20]

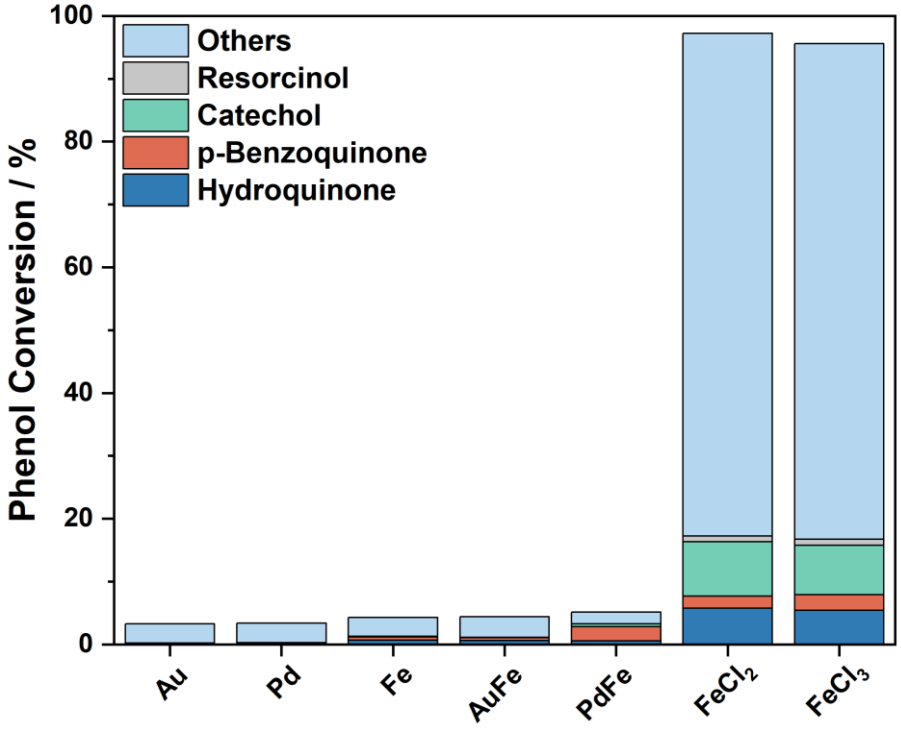

Figure 4.7. Ex-situ phenol degradation using TiO_2 supported monometallic $Au_{0.5}/TiO_2$, $Pd_{0.5}/TiO_2$, Fe_2/TiO_2, $Au_{0.5}Fe_2/TiO_2$, $Pd_{0.5}Fe_2/TiO_2$ and homogeneous Fe source, $FeCl_2$ and $FeCl_3$. Reaction conditions: catalyst (0.01 g), phenol (1000 ppm, 8.5 g), CO_2 (580 psi), 20°C, 1200 rpm

An ex situ Fenton reaction was also conducted to determine the H_2O_2 activation efficiency on Au, Pd, Fe, and Fe-contained formulations and further evidence the actual active sites for H_2O_2 activation. TiO_2-supported monometallic Au and Pd catalysts (**Figure 4.7**), yielded no statistically significant improvement in comparison to the "*H_2O_2*" (< 3 % conversion; in **Figure 4.5**), especially no real difference in the composition of intermediates, with only para-benzoquinone being dominant, suggesting that the Au and Pd active sites are not primarily responsible for H_2O_2 activation.

Further, the Fe-contained monometallic and bimetallic TiO_2-supported Fe, AuFe, and PdFe catalysts slightly enhanced the phenol conversion rate further (~5% conversion, **Figure 4.7**) compared to the pure Au or Pd catalysts. Detailed intermediate analysis showed the existence of hydroxylated phenol byproducts (e.g., hydroquinone and catechol), suggesting that the generation of •OH radicals undoubtedly occurs from the interaction between Fe active sites and pre-formed H_2O_2. Product speciation revealed small but detectable quantities of hydroquinone, p-benzoquinone, and catechol, together with an "Others" fraction representing further-oxidised, low-molecular-weight intermediates.

Adding homogeneous Fe species (Fe^{2+} and Fe^{3+}, and molar amounts equivalent to 100% Fe leaching from the 2wt.% Fe-loaded catalysts) resulted in > 95 % phenol conversion (**Figure 4.7**), leading to less than 20% of the phenolic intermediates, with the majority of phenol degraded into organic acids and inorganic carbon (CO_3^{2-}, HCO_3^-, etc) comprising over 80% of the total products. The nearly 100% removal underscores the critical role of Fe^{2+}/Fe^{3+} in catalysing the decomposition of pre-formed H_2O_2 to •OH, thereby overcoming the intrinsic inertness of phenol, indicating that Fe (especially homogeneous Fe) is the main active site responsible for effective H_2O_2 activation and ROS generation.

Surprisingly, both homogeneous Fe^{2+} and Fe^{3+} Fenton systems exhibited comparable phenol degradation rates after 4 hours, despite the known kinetic constraint of the Fe^{3+} to Fe^{2+} redox transition in the Fe^{3+}/H_2O_2 reaction system. This unexpected result strongly suggests the presence of an inherent reducing agent within the reaction medium, promoting rapid Fe^{3+} reduction and sustaining efficient Fe redox cycling. Such reducing agents are typically required and have been widely used in homogeneous Fe^{3+}/H_2O_2 systems, for example, bisulfites (HSO_3^-) were used to facilitate the Fe^{3+}/Fe^{2+} cycle to promote bisphenol A degradation via homogeneous Fenton reaction.[45] However, Fe^{3+} reduction might be associated with the in situ generated phenolic intermediates. Chen and Pignatello reported that the quinones play an important catalytic role in Fenton oxidation of aromatic compounds by facilitating Fe redox cycle[46] and Chen et al.[47] further identified and proved the existence of a self-catalytic mechanism between the Phenolic-Fe-OOH complexes and H_2O_2 in the ex-situ homogeneous Fenton reaction, whereby the progressive generation of hydroquinone intermediates from phenolic pollutant degradation markedly accelerated the release of Fe^{2+} and •OH, further boosting degradation performance.

4.3.3 The effect of physical separation on the in situ phenol degradation

To gain further insight into the mechanism underlying the Fenton interactions between Fe species (both heterogeneous and homogeneous) and AuPd, physically mixed bimetallic $Au_{0.5}Pd_{0.5}/TiO_2$, monometallic heterogeneous Fe_2/TiO_2, and homogeneous Fe species were evaluated. The amounts of Au, Pd, and Fe in these mixtures were equivalent to those present in the optimal $Au_{0.5}Pd_{0.5}Fe_2/TiO_2$ catalyst (**Figure 4.8**). Neither phenol nor H_2 conversion was detected when heterogeneous or homogeneous Fe species were tested independently. However, enhanced phenol conversion (22%), along with the formation of phenol hydroxylation

intermediates (e.g., hydroquinone and catechol), indicated increased catalytic oxidation activity when physically separated Fe_2/TiO_2 was present alongside $Au_{0.5}Pd_{0.5}/TiO_2$, compared to $Au_{0.5}Pd_{0.5}/TiO_2$ alone (8%). However, the phenol conversion rate still remained significantly lower compared to the $Au_{0.5}Pd_{0.5}Fe_2/TiO_2$ catalyst (83%), suggesting that the importance of close contact of Au, Pd, and Fe species, such proximity, restricts non-selective decomposition of H_2O_2 as it diffuses between catalytic sites responsible for its formation and subsequent degradation into reactive oxygen species, predominantly ·OOH and ·OH.

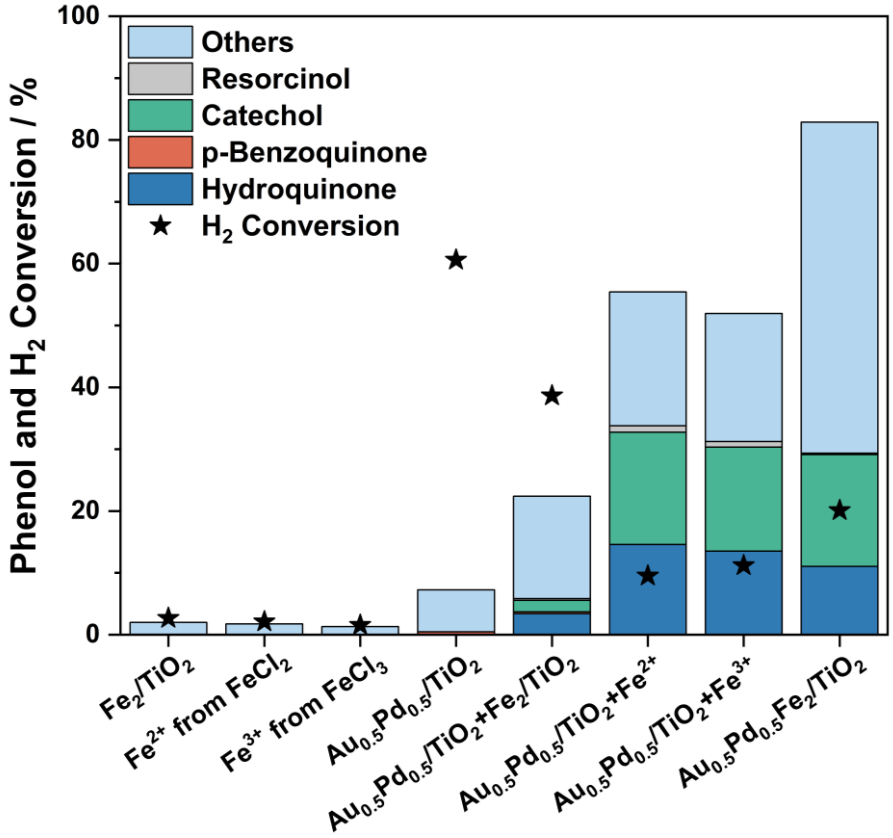

Figure 4.8. Physically mixed heterogeneous and homogeneous Fe species with AuPd catalyst. Reaction conditions: heterogeneous catalyst (0.01 g) or homogenous Fe solution for Fe^{2+} and Fe^{3+} (100 uL, 2mg mL^{-1}), phenol (1000 ppm, 8.5 g), 5% H_2/CO_2 (420 psi), 25% O_2/CO_2 (160 psi), 25°C, 1200 rpm, 4 hrs. Please note: 1) the amount of Fe (mole) in both heterogeneous and homogeneous formation is the same. 2) The dilution effect of the homogeneous Fe solutions is excluded.

Further experiments employing homogeneous Fe (Fe^{2+} and Fe^{3+}) species mixed physically with $Au_{0.5}Pd_{0.5}/TiO_2$ significantly enhanced phenol conversion rates, achieving 55% and 52% after 4 hours of reaction, respectively. This improvement underscores the critical role of homogeneous Fe species interacting directly with H_2O_2 generated in situ at the AuPd surface and subsequently diffusing into solution. Interestingly, the phenol degradation rates achieved

with Fe^{2+} and Fe^{3+} were remarkably similar, despite the known restricted Fe redox cycle, where the lower reaction rate of Fe^{3+} to Fe^{2+}, suggesting that the reduction of Fe^{3+} species occurred during the reaction. Apart from the self-catalytic mechanism via the phenolic-Fe-OOH complexes and H_2O_2, the presence of molecular H_2 might also be responsible for the rapid Fe^{3+} reduction in the ex situ Fenton reaction with the presence of heterogeneous catalysts. Georgi et al.[48] observed an accelerated Fenton system Pd/H_2 as a catalyst/reductant pair, where the reduction of Fe^{3+} occurred over the surface of Pd by the activated H_2, thus accelerating the Fe^{3+}/Fe^{2+} redox cycle.

However, the phenol conversions in these physically mixed systems still remain significantly below the performance of the integrated $Au_{0.5}Pd_{0.5}Fe_2/TiO_2$ catalyst (83%), despite containing equivalent total Fe loadings. Two factors may explain this discrepancy: firstly, although homogeneous reactions facilitated by Fe^{2+} and Fe^{3+} are significant, a crucial heterogeneous catalytic effect arising from the close proximity or alloyed structure of Fe and Pd on the integrated catalyst surface further promotes phenol degradation. Secondly, the comparatively lower H_2 conversion rates observed in the $Au_{0.5}Pd_{0.5}/TiO_2$ & homogeneous Fe systems (10% with Fe^{2+} and 12% with Fe^{3+}) limit the in situ generation of H_2O_2, thereby reducing the availability of reactive oxygen species necessary for phenol degradation, compared to the integrated $Au_{0.5}Pd_{0.5}Fe_2/TiO_2$ catalyst (20%). Additionally, a notable decline in H_2 conversion from 60% ($Au_{0.5}Pd_{0.5}/TiO_2$ only) to approximately 10-20% in the Fe-containing systems suggested a possible blockage or partial deactivation of active AuPd catalytic sites, potentially through adsorption or coordination of homogeneous Fe complexes formed in solution.

4.3.4 The reusability of $Au_{0.5}Pd_{0.5}Fe_2/TiO_2$ catalyst in the in situ phenol degradation

Reusability tests were undertaken to determine the catalytic activity loss after the first run (4 hours in situ phenol degradation). Unfortunately, the phenol degradation efficiency dropped 60%, from 83% (run 1) to 30% (run 2), highly likely due to the considerable loss of Fe (60%) in the initial 4 hours reaction (**Table A4.3**), resulting in insufficient Fe active sites for subsequent H_2O_2 activation (**Figure 4.9**) and clearly suggests that further catalyst and process design is necessary to achieve optimal catalyst performance and stability. With the extent of Fe loss correlating well with the extent of phenol conversion (**Figure A4.9**), which may be indicative of product-mediated leaching, and indeed, further experiments under ambient conditions reveal the role of formic, oxalic, and manolic acids, confirming the role of the highly

oxidised products in promoting catalyst deactivation (**Table A4.4**). Indeed, such observations are in keeping with previous investigations that established the ability of phenolic oxidative products to chelate to heterogeneous Fe species and promote their dissolution.[21–23] It is well known that the Fenton process is highly dependent on solution pH, with activity reduced at elevated pH due to the formation of inactive iron oxyhydroxides in addition to the increased decomposition of H_2O_2, while the acidic condition is always beneficial for the Fenton reaction.[21] The pH of the phenol solution at the starting point (after charging 420 psi H_2/CO_2 and 160 psi 25%O_2/CO_2, without catalyst) is around 4.3 (as determined by pH meter), due to the acidification of CO_2 diluent. The pH decreased over time from 4.3 to 2.9 in the $Au_{0.5}Pd_{0.5}Fe_2/TiO_2$ systems after 6 hours (**Figure A4.10**), which might explain the massive Fe leaching with the Fe dissolved in the acidic conditions over time due to the existence of intermediates generated via the deep oxidation of phenol. On the contrary, the pH changes in the $Au_{0.5}Pd_{0.5}/TiO_2$ system is minimal, from 4.3 to 4.0 after 6 hours (**Figure A4.10**), aligning well with the previous intermediates analysis as limited byproducts were generated in the system (**Figure 4.3**).

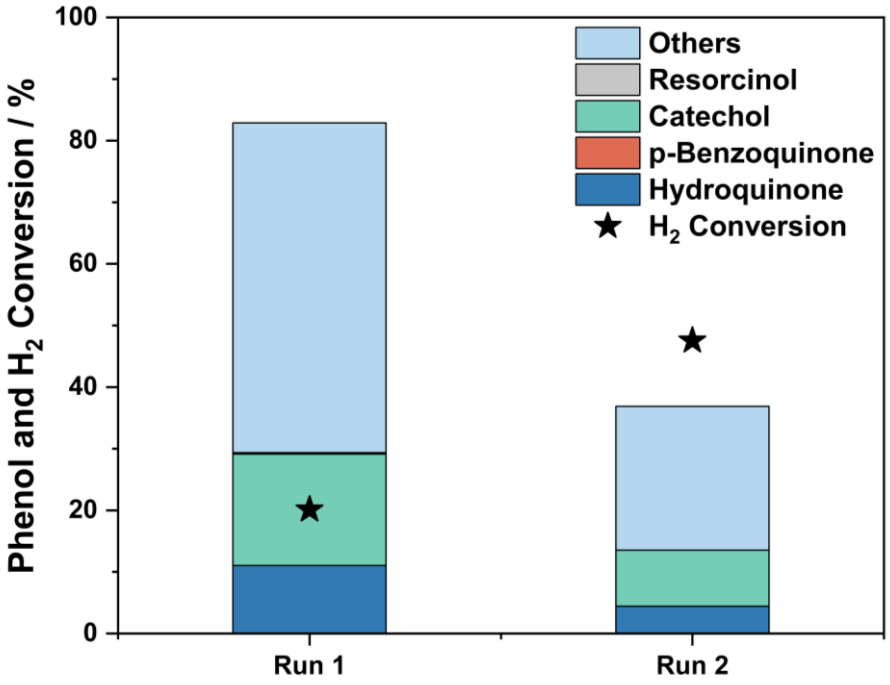

Figure 4.9. Reusability of the $Au_{0.5}Pd_{0.5}Fe_2/TiO_2$ catalyst towards phenol degradation. Reaction conditions: catalyst (0.01 g), phenol (1000 ppm, 8.5 g), 5% H_2/CO_2 (420 psi), 25% O_2/CO_2 (160 psi), 25°C, 1200 rpm, 4 hrs. **Please note**: after Run 1, the sample was washed at least three times using DI water and dried in the vacuum oven at 30 °C overnight before Run 2.

However, an increase in H_2 conversion was observed in the reusability test on the used catalyst for the in situ phenol degradation, and the H_2 conversion rate increased from 20% (run 1) to 48% (run 2) This increase in H_2 conversion rate might indicate the possibility of site blockage by reaction intermediates in run 1 and the boost in run 2 could be attributed to the loss of Fe or the homo Fe complex, leading to the presence of more active sites, which are responsible for H_2 activation and further H_2O_2 synthesis. **Figure A4.11** showed the improved H_2O_2 synthesis rate on the used (after 4 hours of phenol degradation reaction) $Au_{0.5}Pd_{0.5}Fe_2/TiO_2$ catalyst (17 mol_{H2O2} Kg_{Cat}^{-1} h^{-1}, 339 ppm) compared to the fresh $Au_{0.5}Pd_{0.5}Fe_2/TiO_2$ catalyst (2 mol_{H2O2} Kg_{Cat}^{-1} h^{-1}, 33 ppm). Such observations align well with the observed stability of the H_2O_2 synthesising component (i.e. Au and Pd) (**Table A4.3**), and the observed shift of Pd oxidation state towards Pd^0 (**Figure A4.12**), which is well known to offer improved H_2 conversion activity compared to the Pd^{2+} analogues.

HAADF-STEM and corresponding EDX analysis of the as-prepared and used $Au_{0.5}Pd_{0.5}Fe_2/TiO_2$ catalysts are presented in **Figure 4.10** (with additional data reported in **Figures A4.13-18**). Notably, the extent of intimate incorporation of Fe into the AuPd nanoalloys was limited, with considerable quantities of unalloyed Fe found in addition of AuPd-rich trimetallic alloys. Aligning well with earlier investigations into catalyst stability and the stability of the AuPd component. No meaningful change in particle size upon exposure of the catalyst to phenolic degradation conditions. However, aligning well with our ICP analysis of post-reaction solutions (**Table A4.3**), Fe-K edge EDX analysis (**Figure A4.18**) revealed a decrease in elemental intensity, further confirming the loss of Fe upon exposure to phenolic degradation conditions.

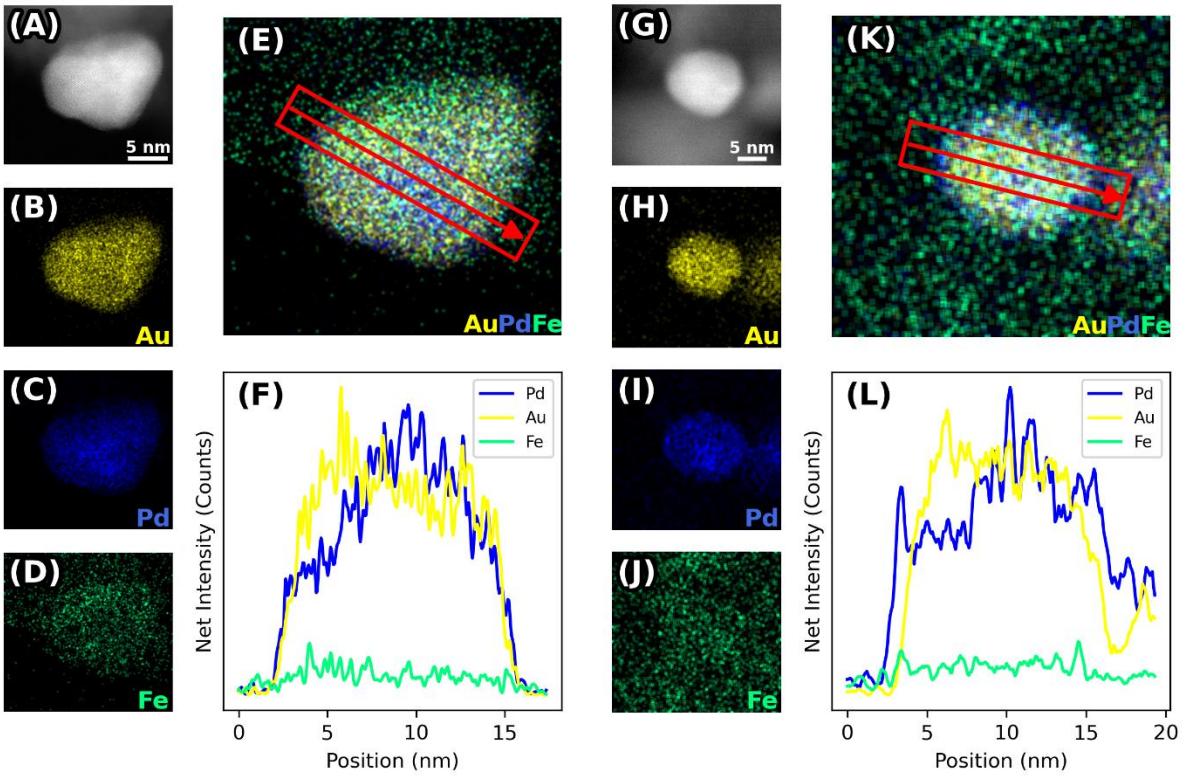

Figure. 4.10. Representative HAADF-STEM micrographs and complementary EDX analysis of individual alloy nanoparticles in (A-F) Fresh and (G-L) Used Au0.5Pd0.5Fe$_2$/TiO$_2$. Note: catalysts exposed to a reductive heat treatment prior to use (5%H$_2$/Ar, 400 °C, 4 h, 10 °C min^{-1}).

4.3.5 Hot-filtration experiment

With a particular focus on the optimal Au$_{0.5}$Pd$_{0.5}$Fe$_2$/TiO$_2$ catalyst, a series of hot-filtration experiments were conducted to identify the contribution of leached metal species or metal-phenolic complex towards phenol degradation (**Figure 4.11,** with detailed intermediates analysis and H$_2$ conversion in **Figure A4.19**). Additional phenol conversion (69%) was observed after the second 2 hours (Phase 2) reaction in the absence of heterogeneous catalyst (Au$_{0.5}$Pd$_{0.5}$Fe$_2$/TiO$_2$ + Blank), where the heterogeneous catalyst was removed by filtration after 2 hours prior to the post-reaction solution being returned to the reactor for a further 2 hours. This value was nearly identical to that observed for the Au$_{0.5}$Pd$_{0.5}$Fe$_2$/TiO$_2$ catalyst over a 2 h reaction (66%), with the limited additional conversion of phenol possibly attributed to the contribution from residual H$_2$O$_2$ generated in the initial 2 h reaction.

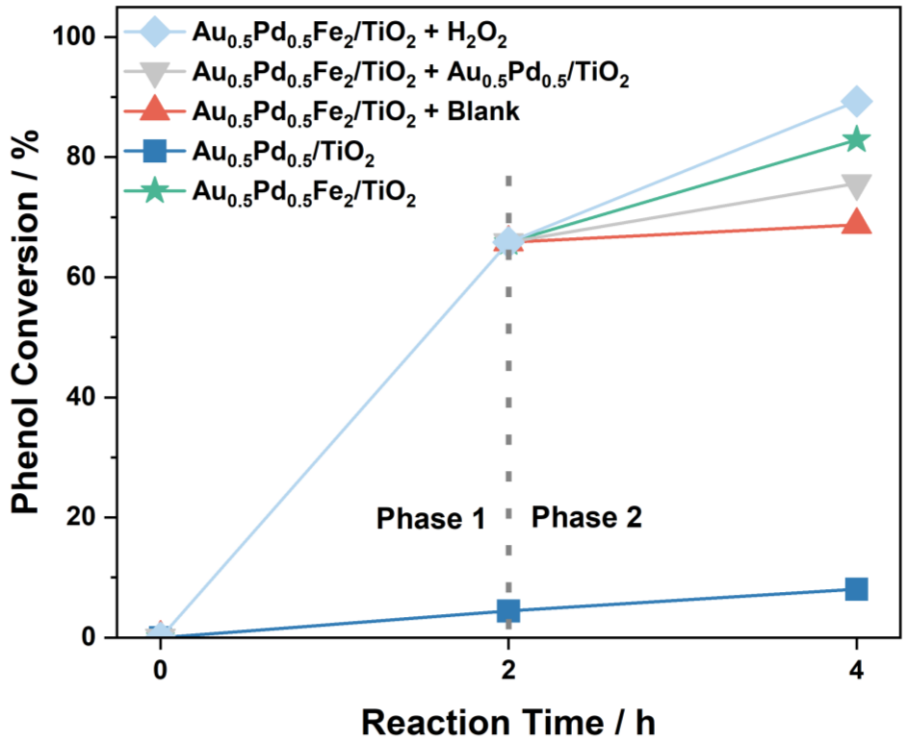

Figure 4.11. Efficacy of leached species in oxidative degradation of phenol as identified by a hot filtration experiment using the $Au_{0.5}Pd_{0.5}Fe_2/TiO_2$ catalyst. Phenol oxidation reaction conditions: catalyst (0.01 g), phenol (8.5g, 1000 ppm), 5% H_2/CO_2 (420 psi), 25% O_2/CO_2 (160 psi), 1200 rpm, 25 °C, 2 h for each phase. key: $Au_{0.5}Pd_{0.5}Fe_2/TiO_2$ catalysed reaction (Green Star); $Au_{0.5}Pd_{0.5}/TiO_2$ catalysed reaction (Dark blue square)); hot filtration reaction where the $Au_{0.5}Pd_{0.5}Fe_2/TiO_2$ catalyst is removed by filtration after 2 h (red triangles); hot filtration reaction where $Au_{0.5}Pd_{0.5}Fe_2/TiO_2$ catalyst removed by filtration after 2 h and replaced by $Au_{0.5}Pd_{0.5}/TiO_2$ catalyst for final 2 h of reaction (Grey inverted triangles), hot filtration reaction where $Au_{0.5}Pd_{0.5}Fe_2/TiO_2$ catalyst removed by filtration after 2 h and replaced by commercial H_2O_2 (concentration identical to that if all H_2 utilised in a standard in situ reaction was selectively converted to H_2O_2) catalyst for final 2 h of reaction (Light blue diamonds).

To determine if the inactivity observed in the $Au_{0.5}Pd_{0.5}/TiO_2$ catalyst hot-filtration experiment was due to the limited ability of the homogeneous component to synthesize H_2O_2, which may be reasonable given our previous studies which identified the stability of Pd during the phenol degradation reaction a further hot-filtration experiment was conducted whereby, after the initial 2 h reaction, the $Au_{0.5}Pd_{0.5}Fe_2/TiO_2$ catalyst was replaced with $Au_{0.5}Pd_{0.5}/TiO_2$ analogue, ensuring that the total moles of Au and Pd was equal to that in the $Au_{0.5}Pd_{0.5}Fe_2/TiO_2$ catalyst. Perhaps unexpectedly, given the ability of the $Au_{0.5}Pd_{0.5}/TiO_2$ catalyst to catalyse the oxidative degradation of phenol (**Figure 4.3**) an increase in phenol conversion was observed (75%), slightly over the sum of the $Au_{0.5}Pd_{0.5}Fe_2/TiO_2$ (66%) and $Au_{0.5}Pd_{0.5}/TiO_2$ (4%) components when they were used independently over 2 h. However, the extent of phenol conversion was

found to be slightly lower than that observed over the analogous two-part, 4 h duration experiment conducted over the $Au_{0.5}Pd_{0.5}Fe_2/TiO_2$ catalyst alone (83%). In theory, improved phenol conversion should be observed considering the homogeneous Fenton interaction between H_2O_2 generated from $Au_{0.5}Pd_{0.5}/TiO_2$ catalysts and the homogenous complex generated from Phase 1. However, previous experiments proposed a theory that the homo-Fe complexes might block the Pd or AuPd active sites, which are responsible for H_2 activation and H_2O_2 synthesis, further unfortunately inhibiting ROS generation for phenol degradation. H_2 conversion analysis of the $Au_{0.5}Pd_{0.5}/TiO_2$ catalyst in the reaction mixture after initial phenol degradation test using the $Au_{0.5}Pd_{0.5}Fe_2/TiO_2$ catalyst (2 hours) was conducted, with only 9% for the further 2 hours reaction (**Figure A4.19**), significantly lower than that of the $Au_{0.5}Pd_{0.5}/TiO_2$ catalyst in standard phenol degradation reaction (43% after 2 hours, **Figure 4.3**). Considering the different reaction mediums in those two systems, the H_2 activation ability severally inhibited by the possible presence of homo Fe complexes.

To investigate the contribution of homo Fe complex on phenol degradation, in the final experiment, after the initial 2 hours reaction utilizing the $Au_{0.5}Pd_{0.5}Fe_2/TiO_2$ catalyst, commercial H_2O_2, at a concentration equivalent to if all H_2 in the in situ reaction was selectively converted to H_2O_2, was added to the reaction mixture. After a further 2 h reaction (carried out in the presence of CO_2 diluent and the absence of a heterogeneous catalyst), a significant improvement in phenol conversion was observed (89%). In keeping with the excellent phenol conversion in the homogeneous Fenton reaction (Fe^{2+} and Fe^{3+}) with the presence of commercial H_2O_2 after 4 hours of reaction (**Figure 4.7**). Together, in addition to electronically close contact between heterogeneous AuPd and Fe, homogeneous components in these experiments played a non-negligible role in phenol conversion but might unfortunately be responsible for Pd/AuPd active site blocking.

4.4 Conclusion

In this Chapter, various mono-, bi-, and trimetallic AuPdFe catalysts were prepared via wet co-impregnation method and investigated for their catalytic ability towards the direct synthesis of H_2O_2 and the subsequent oxidative degradation of phenol in a batch reactor under ambient conditions (alcohol free, room temperature). Although the catalytic ability towards in situ H_2O_2 synthesis significantly declined compared to the ideal reaction conditions, in keeping with previous works focused on AuPd systems, the bimetallic benchmark $Au_{0.5}Pd_{0.5}/TiO_2$ still

surpasses monometallic $Pd_{0.5}/TiO_2$ catalyst at equal Pd loading through higher selectivity to H_2O_2 at comparable H_2 conversion (Table 4.1). Progressive incorporation of Fe into AuPd suppresses the selective H_2O_2 production by reducing the selectivity to H_2O_2 and increasing the overall H_2 consumption.

On the contrary, the efficacy of in situ phenol degradation rates as a function of Fe loading revealed an opposite trend than that of the in situ H_2O_2 synthesis. A clear volcano-type phenol degradation efficiency dependence on Fe loading, with an optimum at approximately 2 wt.%. At this composition, the trimetallic catalyst sustains the highest phenol conversion and the largest pseudo-first-order rate constant, exceeding the activity of the bimetallic analogue by over 10 times and 25 times, respectively. However, over-doping with Fe (e.g. 3 wt.%) reduced the performance. These trends show that maximum H_2O_2 titre or selectivity is not a reliable proxy for pollutant abatement under in-situ operation. Instead, activity reflects how well reactive intermediates are created and consumed at the catalyst solution interface.

Control experiments establish a coherent mechanistic picture. Adsorption of phenol is negligible, and feeds containing only H_2 or only O_2 did not drive meaningful conversion. A single batch addition of commercial H_2O_2, with or without the heterogeneous catalyst, is much less effective than the in-situ route. Product analysis is dominated at early times by hydroquinone and catechol, followed by ring-opening carboxylic acids, which is consistent with ·OH pathways. Together, these observations indicate that oxidising intermediates formed on the surface of AuPd (for example, hydroperoxyl and surface-bound peroxide species) are transferred over a very short distance to Fe active sites, where the Fenton reaction occurs or the presence of Fe promotes ROS desorption for the catalyst surface. Continuous, low-level oxidant generation limits both disproportionation of H_2O_2 and radical scavenging that are intrinsic to bulk dosing.

XPS analysis of fresh materials shows a significant fraction of Pd^{2+}. In combination with the reactivity trends, this points to rapid in-reaction reduction to Pd^0 in Fe-rich formulations, which explains efficient hydrogen activation even as selectivity to hydrogen peroxide falls (Figure 4.1). CO-DRIFTS reveal Fe-induced electronic perturbation of palladium at low iron contents and a loss of small metallic palladium ensembles at higher iron loadings, rationalising the decline in peroxide selectivity (**Figure 4.2**). TEM indicates well-dispersed nanoparticles in the range of four to six nanometres, with only a slight increase in mean size as iron content rises;

this geometric change is secondary to the dominant electronic and interfacial effects identified above.

Experiments that deliberately separate the catalytic functions underline the need for co-location. Physical mixtures of $Au_{0.5}Pd_{0.5}/TiO_2$ with Fe_2/TiO_2 provide only modest improvements relative to AuPd alone, and pairing AuPd with homogeneous Fe increases conversion further yet still falls well short of the integrated trimetallic material (**Figure 4.8**). Stability of the catalyst, however is a problem. Following one phenol-degradation run, activity falls markedly on reuse in parallel with substantial Fe loss. Notably, the used catalyst exhibits higher H_2 conversion in the in situ phenol degradation and a higher rate of H_2O_2 formation than the fresh sample, reflecting Pd reduction and the loss of Fe that had previously accelerated non-selective peroxide decomposition.

Hot-filtration tests show that the filtrate from an AuPdFe run retains substantial oxidative activity and responds strongly to added H_2O_2, confirming a non-negligible homogeneous Fe contribution. At the same time, reintroducing AuPd into such filtrates suppresses H_2 activation, which is consistent with the coordination or blocking of Pd/AuPd active sites by homogeneous Fe complexes. Thus, while homogeneous Fe can accelerate the Fenton reaction, uncontrolled leaching simultaneously undermines the upstream AuPd function that supplies oxidant via H_2 activation.

4.5 Future Work

The results in this Chapter establish a mechanistic basis for coupling oxidant generation on AuPd with Fenton activation on Fe active sites under alcohol-free, near-ambient conditions. To consolidate and extend these findings toward durable, scalable processes, the following avenues merit priority.

- **Time-resolved Electron paramagnetic resonance (EPR) to qualify ROSs**
  Although radical quenching experiments were conducted in this study, EPR with appropriate spin traps (for example, DMPO or TEMP) should be applied at defined reaction times during in situ H_2 and O_2 operation to detect ·OH, $O_2^{\cdot-}$, ·OOH and other related intermediates. Parallel measurements during direct H_2O_2 synthesis, in-situ phenol degradation (with the presence of H_2 and O_2), and control feeds (H_2 only, O_2 only, and commercial H_2O_2) would allow correlation between catalyst composition, gas

regime, and radical flux. Particular emphasis should be placed on comparing the bimetallic benchmark with the Fe-optimised trimetallic to verify whether the superior phenol abatement coincides with a higher steady-state concentration of short-lived species rather than bulk peroxide.

- **Liquid Chromatography-Mass Spectrometry (LC–MS) time-courses to map the degradation network**

  High-resolution LC–MS should be used to build time on line degradation profiles for phenol. Early phenolic intermediates (for example hydroquinone, catechol, para-benzoquinone), and ring-opened products (for example maleic acid, fumaric acid, muconic acid, oxalic acid, formic acids, etc), enable kinetic model construction and validation of the proposed pathway.

- **UV–vis spectroscopy to identify homogeneous phenolic-Fe complexes**

  Post-reaction solutions from the in situ systems using $Au_{0.5}Pd_{0.5}/TiO_2$ and $Au_{0.5}Pd_{0.5}Fe_2/TiO_2$, the ex-situ system with homogeneous Fe and pre-formed H_2O_2 should be probed for the homogeneous phenolic-Fe complex. According to Chen et al.,[47] the distinct phenolic-Fe complex shoulder peaks at around 400 nm (depending on the organic substrate, for example, 385 nm for the bisphenol A system while 436 nm for the paracetamol system), which could possibly provide strong evidence for the existence of the phenolic-Fe complex.

- **Investigation into the possible "3e$^-$" pathway**

  The reaction mechanism of the in situ Fenton pathway utilizing molecular H_2 and O_2 is not yet fully clear in terms of the generation of reactive oxygen species, from the activation of the in situ synthesised H_2O_2 ($H_2 + O_2 \rightarrow H_2O_2 \rightarrow \cdot OH + \cdot OOH$) or directly from the activation of H_2 ($H_2 + O_2 \rightarrow {}^*H_2O_2 \rightarrow \cdot OH + \cdot OOH$).[44] Density Function Theory (DFT) Calculation would be beneficial to figure out the changes in free energy/active energy during the O_2 activation process.

- **Chemical oxygen demand (COD) or Total Organic Carbon (TOC) metrics to quantify mineralisation**

  COD or TOC should be measured time on line series for the bimetallic and the Fe-optimised trimetallic under identical conditions. These measurements will differentiate transformation from true mineralisation and allow benchmarking against discharge targets. Pairing COD or TOC with LC–MS will help exam whether increasing iron

content shifts selectivity toward deeper oxidation rather than merely faster phenol degradation.

- **Mitigation of Fe loss**

  From previous studies and in this Chapter, the Fe leaching is somehow highly associated with phenol conversion rate/the types of intermediates.[21–23] To improve the catalyst stability, a new catalyst preparation method needs to be further investigated to alleviate unwanted Fe leaching.

4.6 Appendix

Table A4.1. Actual metal loading of the mono-, bi-, and trimetallic AuPdFe/TiO_2 catalysts, as determined by ICP analysis of Microwave-assisted aqua regia digested catalysts.

Catalyst	Au / wt%	Pd / wt%	Fe / wt%
$Au_{0.5}Pd_{0.5}/TiO_2$-R	0.46	0.48	-
$Au_{0.5}Pd_{0.5}Fe_{0.1}/TiO_2$-R	0.46	0.46	0.10
$Au_{0.5}Pd_{0.5}Fe_{0.5}/TiO_2$-R	0.46	0.47	0.49
$Au_{0.5}Pd_{0.5}Fe_1/TiO_2$-R	0.47	0.47	1.16
$Au_{0.5}Pd_{0.5}Fe_2/TiO_2$-R	0.47	0.48	1.88
$Au_{0.5}Pd_{0.5}Fe_3/TiO_2$-R	0.45	0.46	3.22
$Au_{0.5}Fe_2/TiO_2$-R	0.47	-	1.93
$Pd_{0.5}Fe_2/TiO_2$-R	-	0.49	1.89
$Au_{0.5}/TiO_2$-R	0.45	-	-
$Pd_{0.5}/TiO_2$-R	-	0.48	-
Fe_2/TiO_2	-	-	1.96

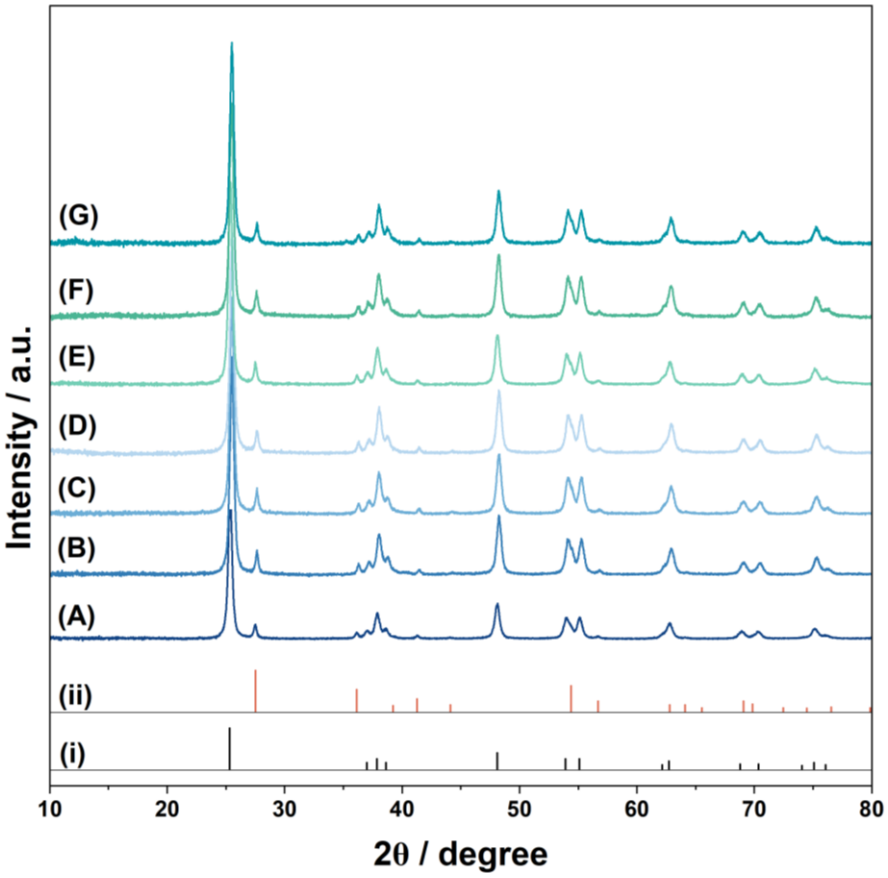

Figure A4.1. XRD Spectra for (A)TiO_2, (B) $Au_{0.5}Pd_{0.5}/TiO_2$, (C) $Au_{0.5}Pd_{0.5}Fe_{0.1}/TiO_2$, (D) $Au_{0.5}Pd_{0.5}Fe_{0.5}/TiO_2$, (E) $Au_{0.5}Pd_{0.5}Fe_1/TiO_2$, (F) $Au_{0.5}Pd_{0.5}Fe_2/TiO_2$, (G) $Au_{0.5}Pd_{0.5}Fe_3/TiO_2$, and the (i) anatase (ICDD PDF File 00-021-1272) and (ii) rutile (ICDD PDF File 00-021-1276) TiO_2 phases.

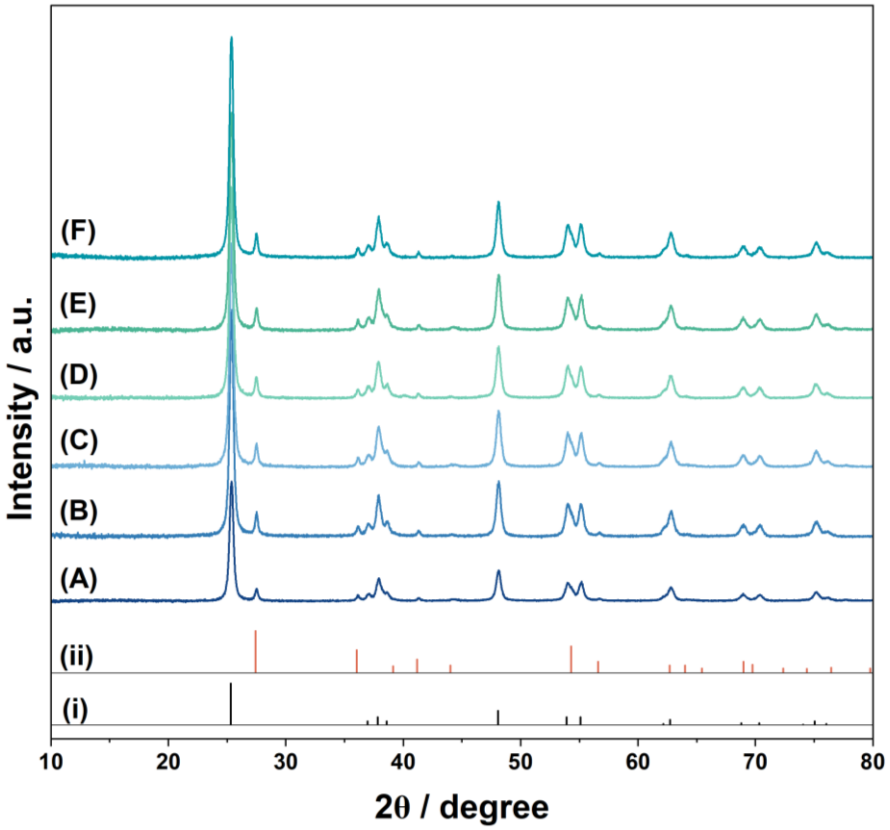

Figure A4.2. XRD Spectra for (A) TiO_2, (B) Fe_2/TiO_2, (C) $Au_{0.5}/TiO_2$, (D) $Au_{0.5}Fe_2/TiO_2$, (E) $Pd_{0.5}/TiO_2$, (F) $Pd_{0.5}Fe_2/TiO_2$, and the (i) anatase (ICDD PDF File 00-021-1272) and (ii) rutile (ICDD PDF File 00-021-1276) TiO_2 phases.

Table A4.2. BET Analysis for the AuPdFe series

Catalyst	Surface area / m^2g^{-1}
TiO_2	60
$Au_{0.5}Pd_{0.5}/TiO_2$	51
$Au_{0.5}Pd_{0.5}Fe_{0.1}/TiO_2$	52
$Au_{0.5}Pd_{0.5}Fe_{0.5}/TiO_2$	55
$Au_{0.5}Pd_{0.5}Fe_1/TiO_2$	48
$Au_{0.5}Pd_{0.5}Fe_2/TiO_2$	47
$Au_{0.5}Pd_{0.5}Fe_3/TiO_2$	47
$Au_{0.5}Fe_2/TiO_2$	48
$Pd_{0.5}Fe_2/TiO_2$	51
$Au_{0.5}/TiO_2$	55
$Pd_{0.5}/TiO_2$	54
Fe_2/TiO_2	57

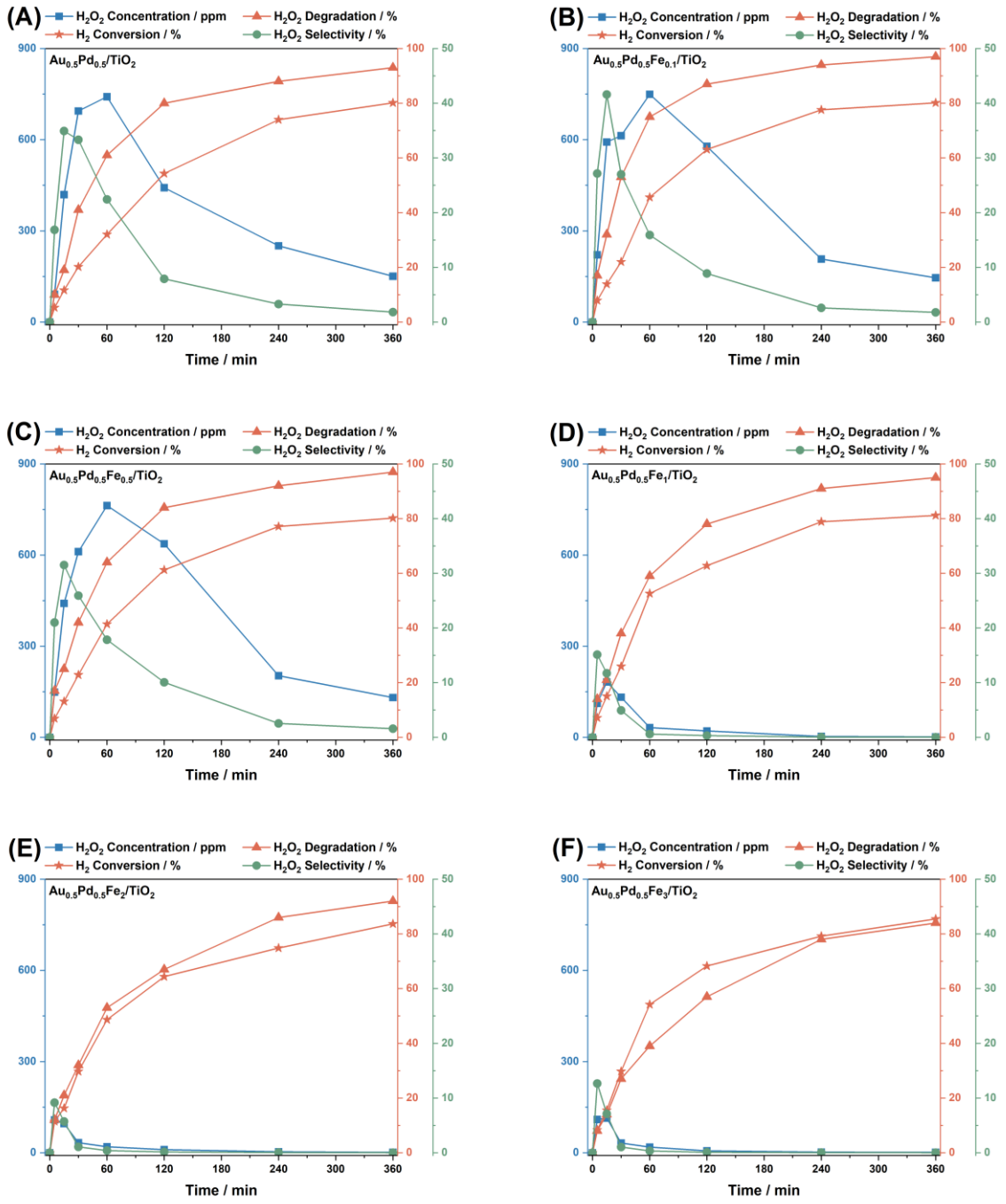

Figure A4.3. Time on line direct H_2O_2 synthesis over AuPdFe series up to 6 hours. Key: H_2O_2 concentration: Blue square; H_2 conversion: Orange triangle; H_2O_2 selectivity: Green circle; H_2O_2 degradation: Orange star. Reaction conditions: catalyst (0.01g), H_2O (8.5 g), 420 psi 5%H_2/CO_2, 160 psi 25%O_2/CO_2, 25ºC, 1200 rpm

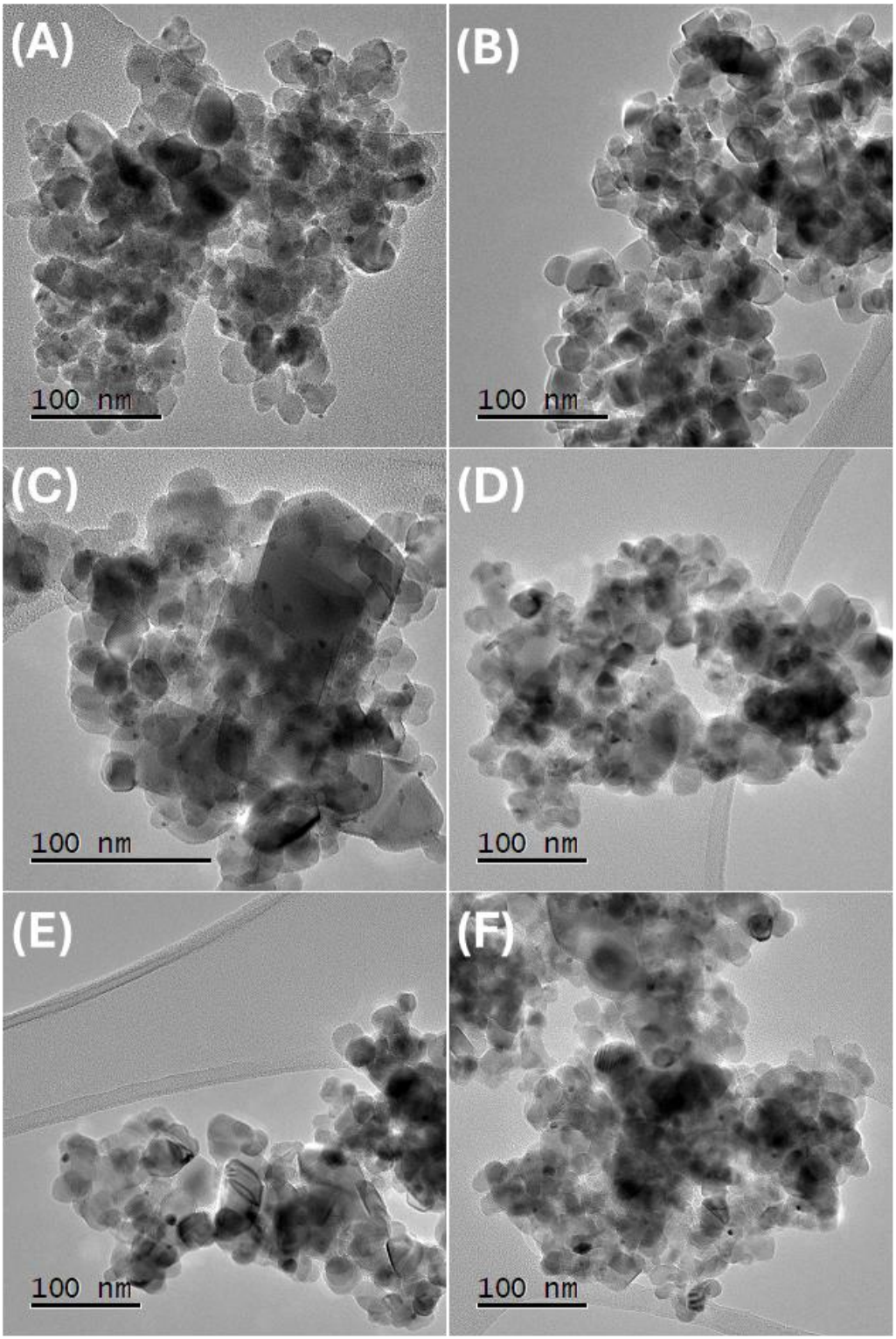

Figure A4.4. Representative bright field transmission electron micrographs of the AuPdFe series. (A) $Au_{0.5}Pd_{0.5}/TiO_2$, (B) $Au_{0.5}Pd_{0.5}Fe_{0.1}/TiO_2$, (C) $Au_{0.5}Pd_{0.5}Fe_{0.5}/TiO_2$, (D) $Au_{0.5}Pd_{0.5}Fe_1/TiO_2$, (E) $Au_{0.5}Pd_{0.5}Fe_2/TiO_2$, (F) $Au_{0.5}Pd_{0.5}Fe_3/TiO_2$.

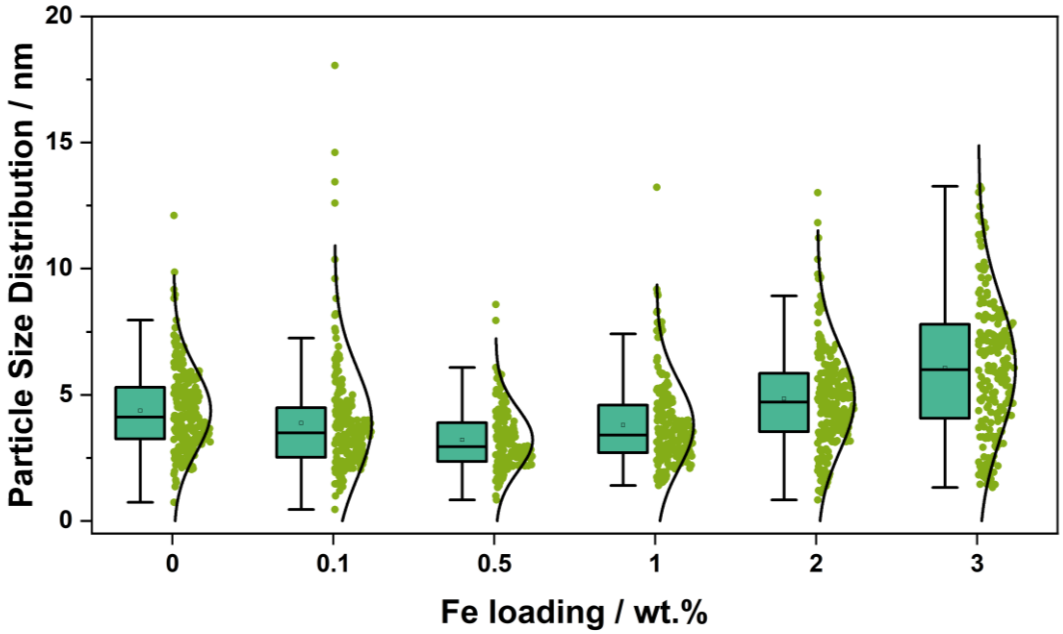

Figure A4.5. Corresponding particle size distribution of the AuPdFe series as a function of Fe loading (wt.%). **Please note**: over 200 nanoparticles were considered for PSD analysis for each catalyst to ensure accuracy.

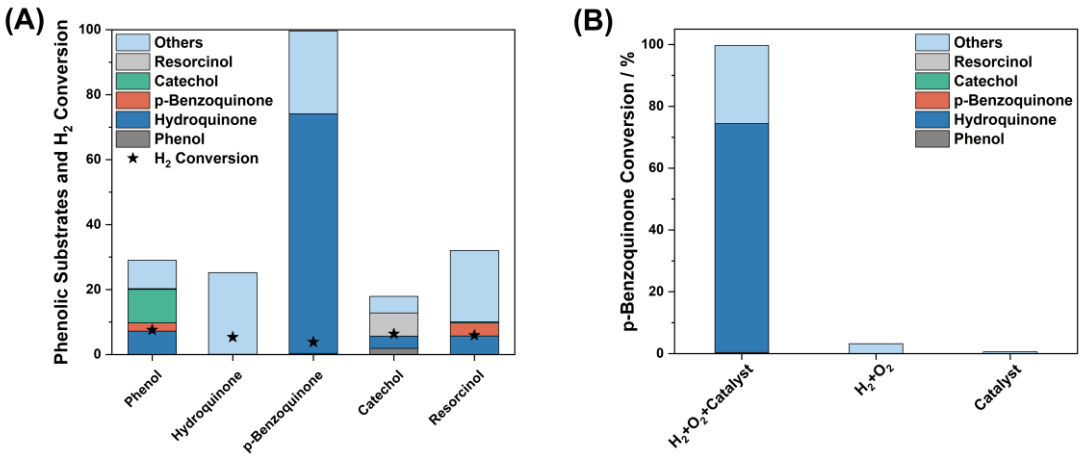

Figure A4.6. (A) The oxidative degradation of phenolic intermediates and (B) the effect of gas and catalyst on the degradation of pBQ. Reaction conditions: catalyst (0.01 g), phenolic intermediates (1000 ppm, 8.5 g), 5% H_2/CO_2 (420 psi), 25% O_2/CO_2 (160 psi), 25°C, 1200 rpm.

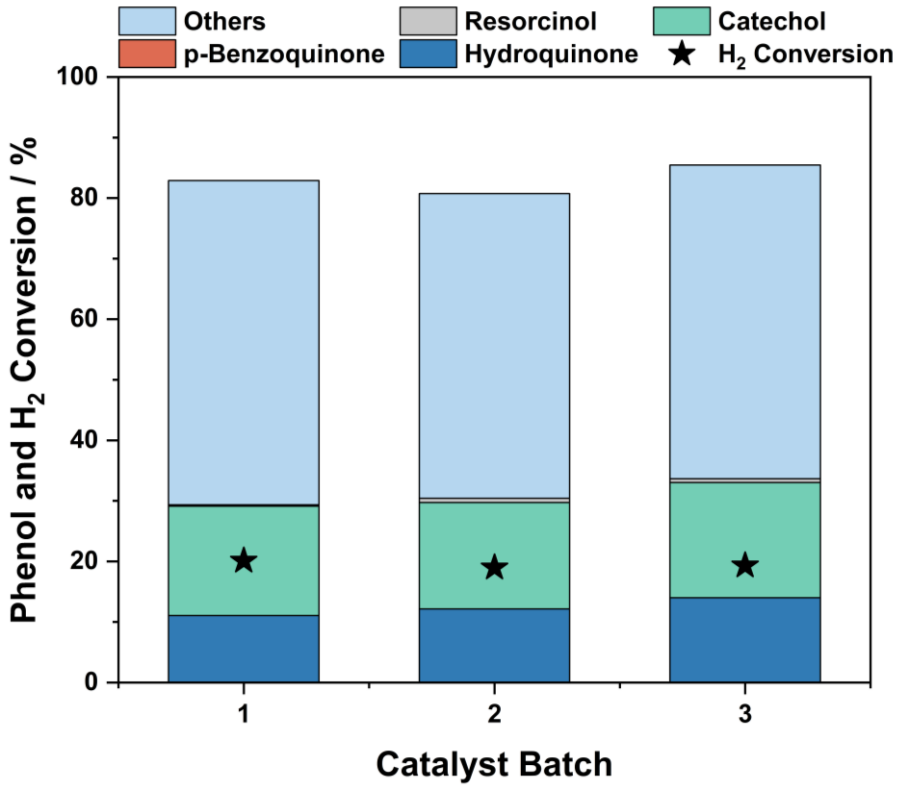

Figure A4.7. Reproducibility test for the optimal $Au_{0.5}Pd_{0.5}Fe_2/TiO_2$ catalyst. Reaction conditions: catalyst (0.01 g), phenol (1000 ppm, 8.5 g), 5% H_2/CO_2 (420 psi), 25% O_2/CO_2 (160 psi), 25°C, 1200 rpm. Please note: all three batches of catalysts were prepared under the same procedure.

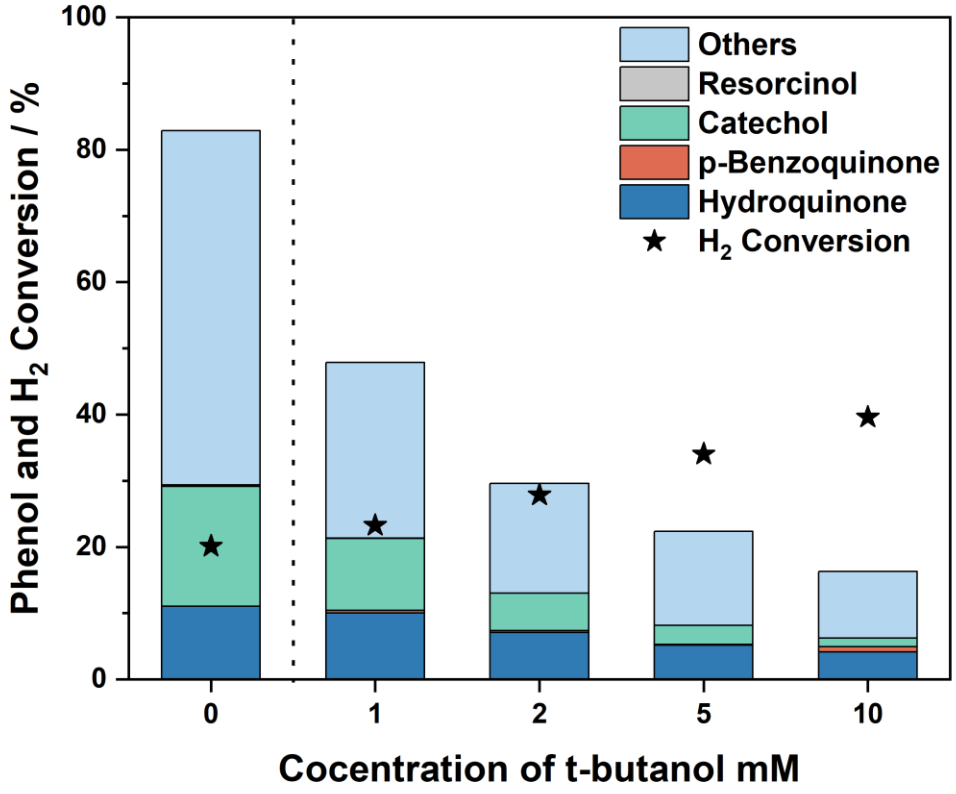

Figure A4.8. The effect of the radical quencher t-butanol on the oxidative degradation of H_2O_2 and associated reactive oxygen species over $Au_{0.5}Pd_{0.5}Fe_2/TiO_2$ catalyst. **Phenol degradation reaction conditions:** catalyst (0.01 g), phenol (1000 ppm, 8.5 g), t-butanol (0-10 mM), 5% H_2/CO_2 (420 psi), 25% O_2/CO_2 (160 psi), 20 °C, 2 h, 1200 rpm.

TableA4.3. Time on line leaching test of Au, Pd, and Fe for the $Au_{0.5}Pd_{0.5}Fe_2/TiO_2$ catalyst during phenol degradation test.

Catalyst	Reaction Time / min	Au leach (ppb/%)	Pd leach (ppb/%)	Fe leach (ppm/%)
$Au_{0.5}Pd_{0.5}Fe_2/TiO_2$	5	N. D	6.33 / 0.11	4.09 / 18.50
	15	N. D	9.28 / 0.16	7.3 / 33.01
	30	N. D	12.45 / 0.22	9.23 / 41.73
	60	N. D	13.14 / 0.23	11.51 / 52.03
	120	N. D	13.97 / 0.25	12.12 / 54.78
	240	N. D	14.34 / 0.25	14.08 / 63.67
	360	N. D	14.92 / 0.26	14.13 / 63.87

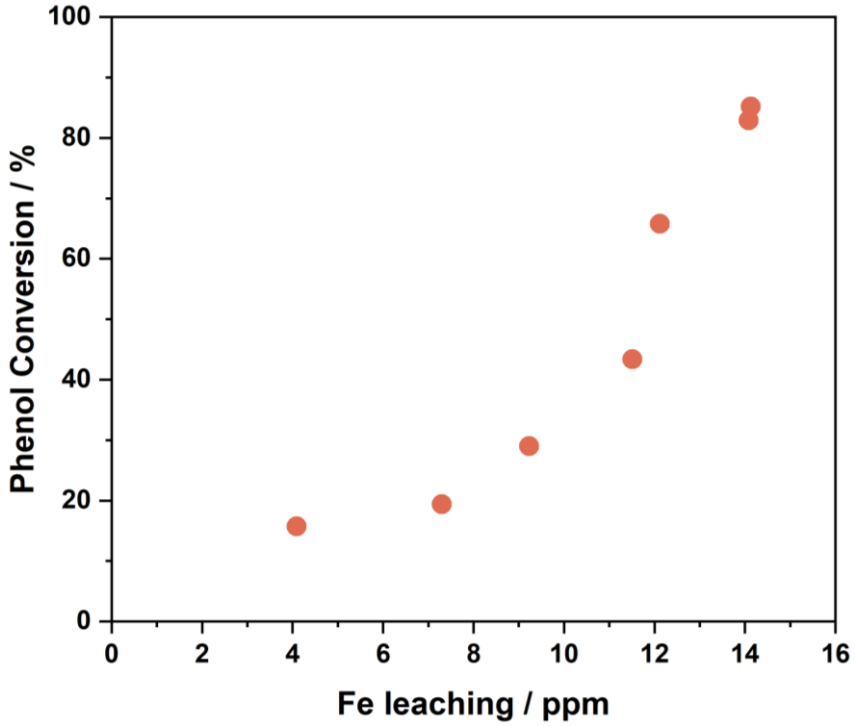

Figure A4.9. The correlation between Fe leaching and phenol conversion.

Table A4.4. Fe leaching test of the 1%AuPd-2%Fe/TiO_2 catalyst in various reaction solvents, as determined by MP-AES analysis of post-reaction solutions.

Solven	Fe leaching	
	ppm	%
H_2O	B.D.L	N/A
Phenol	B.D.L	N/A
Catechol	1.12	5.15
Resorcinol	B.D.L	N/A
Hydroquinone	1.63	7.50
P-Benzoquinone	B.D.L	N/A
Formic acid	17.37	79.90
Maleic acid	3.37	15.50
Fumaric acid	1.83	8.42
Oxalic acid	13.00	59.80
Manolic acid	7.30	33.58
Acetic acid	1.00	5.00
Muconic acid	1.58	7.27

Reaction conditions: catalyst (0.01 g), organics (1000 ppm, 8.5 g), 20 °C, 0.5 hr, 1200 rpm

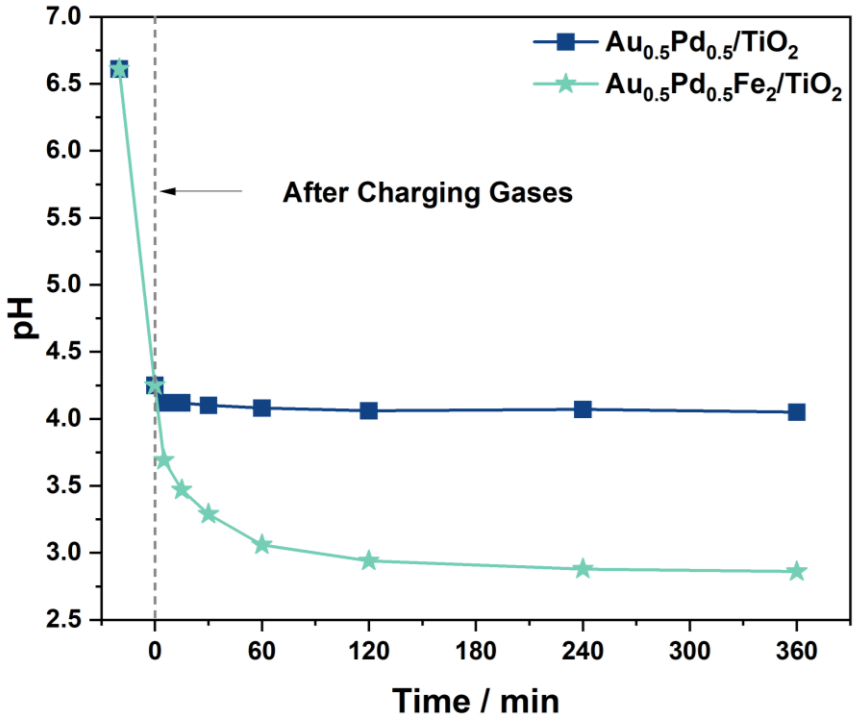

Figure A4.10. pH changes in the catalytic systems of $Au_{0.5}Pd_{0.5}/TiO_2$, and $Au_{0.5}Pd_{0.5}Fe_2/TiO_2$ catalysts during phenol degradation.

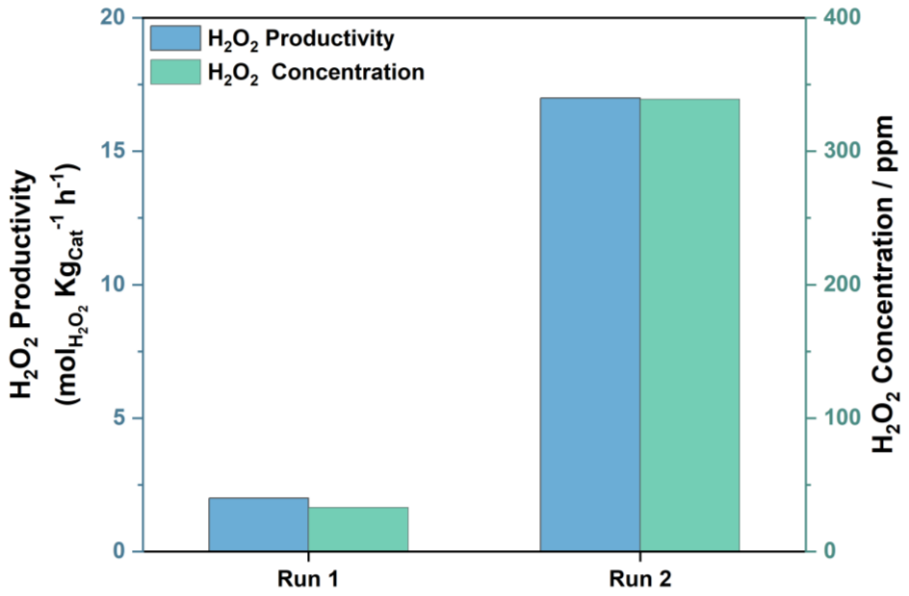

Figure A4.11. The direct synthesis of H_2O_2 using the fresh $Au_{0.5}Pd_{0.5}Fe_2/TiO_2$ catalyst and the used $Au_{0.5}Pd_{0.5}Fe_2/TiO_2$ catalyst (used after 4 hrs in-situ phenol degradation reaction). H_2O_2 direct synthesis reaction conditions: catalyst (0.01g), H_2O (8.5 g), 5%H_2/CO_2 (420 psi), 25%O_2/CO_2 (160 psi), 20 ºC, 1200 rpm.

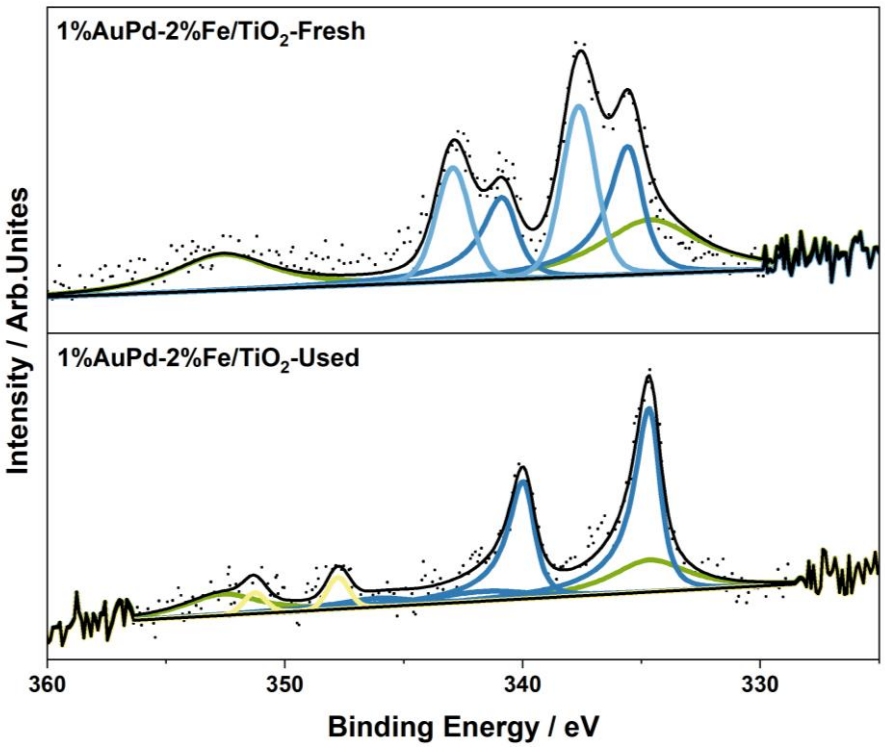

Figure A4.12. XPS analysis of the fresh and used $Au_{0.5}Pd_{0.5}Fe_2/TiO_2$ catalysts. Key: Au(4d) (green); Fe(3s) (orange); Pd^0 (dark blue); Pd^{2+} (light blue); Ca^{2+} (yellow). **Phenol degradation reaction conditions:** catalyst (0.01 g), phenol (1000 ppm, 8.5 g), 5% H_2/CO_2 (420 psi), 25% O_2/CO_2 (160 psi), 20 °C, 1200 rpm. **Please note**: the test and subsequent analysis were performed by Dr. David J. Morgan (Cardiff University; HarwellXPS).

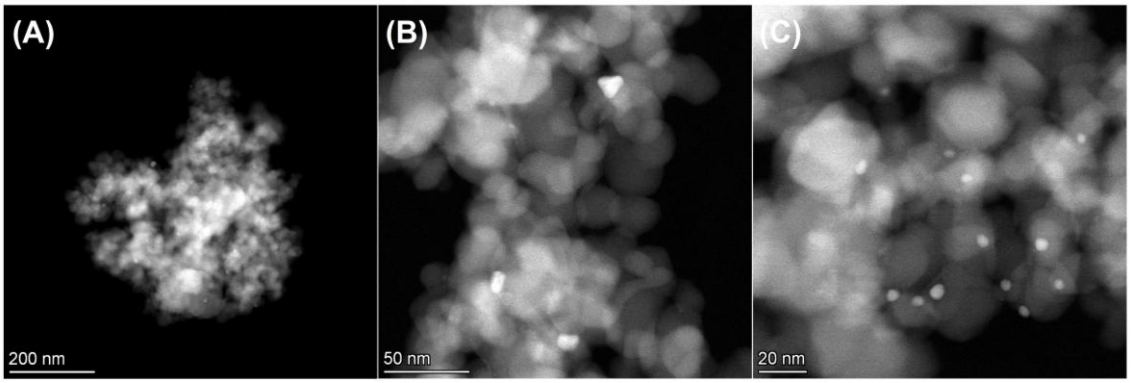

Figure A4.13. HAADF-STEM analysis of the fresh $Au_{0.5}Pd_{0.5}Fe_2/TiO_2$ catalyst.

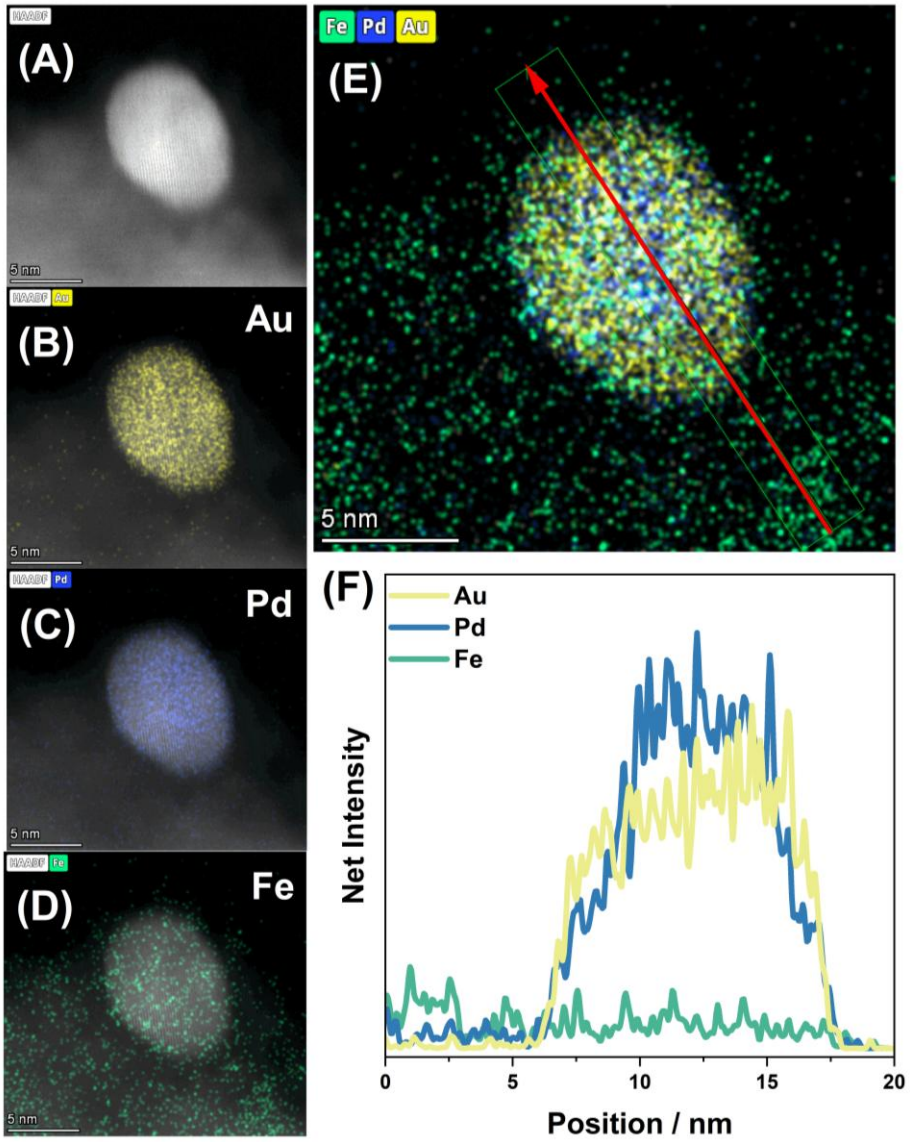

Figure A4.14. (**A**) HADDF-STEM and (**B-D**) EDX analysis with corresponding (**E-F**) line scan analysis of the as-prepared $Au_{0.5}Pd_{0.5}Fe_2/TiO_2$ catalyst.

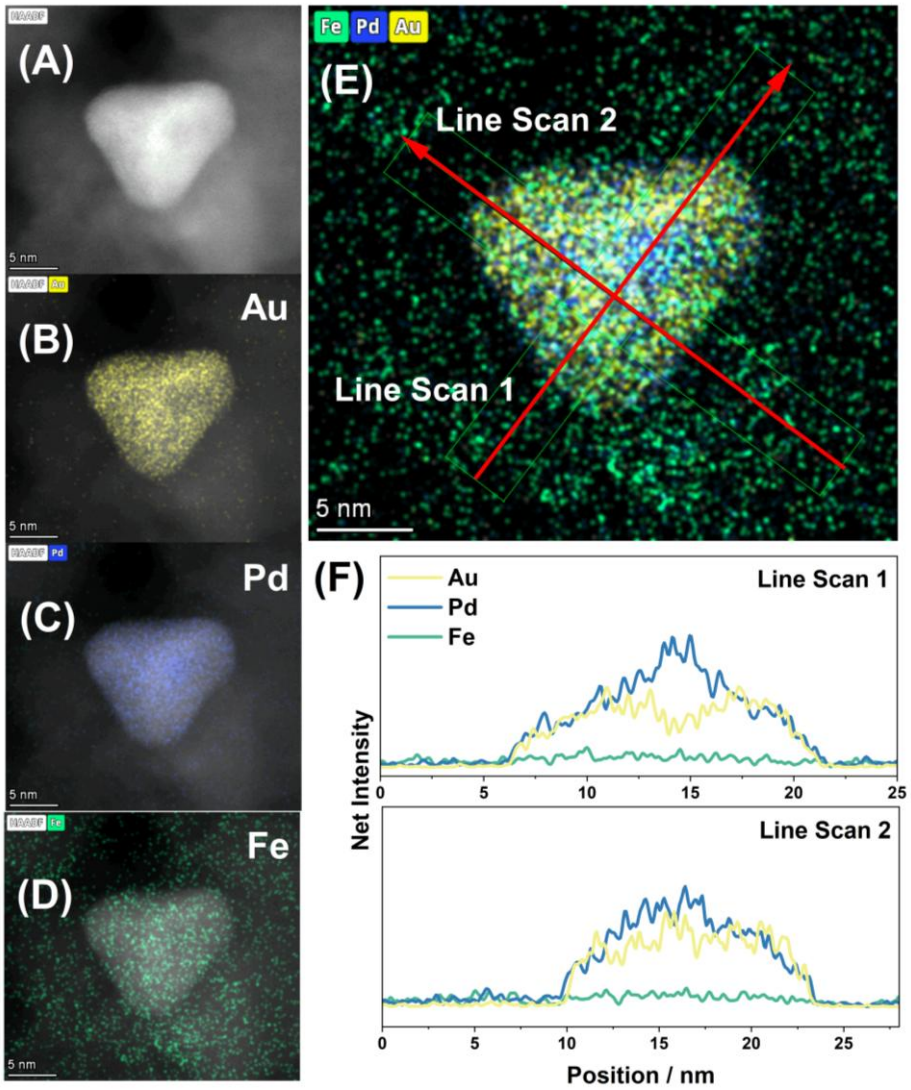

Figure A4.15. (**A**) HADDF-STEM and (**B-D**) EDX analysis with corresponding (**E-F**) line scan analysis of the as-prepared $Au_{0.5}Pd_{0.5}Fe_2/TiO_2$ catalyst.

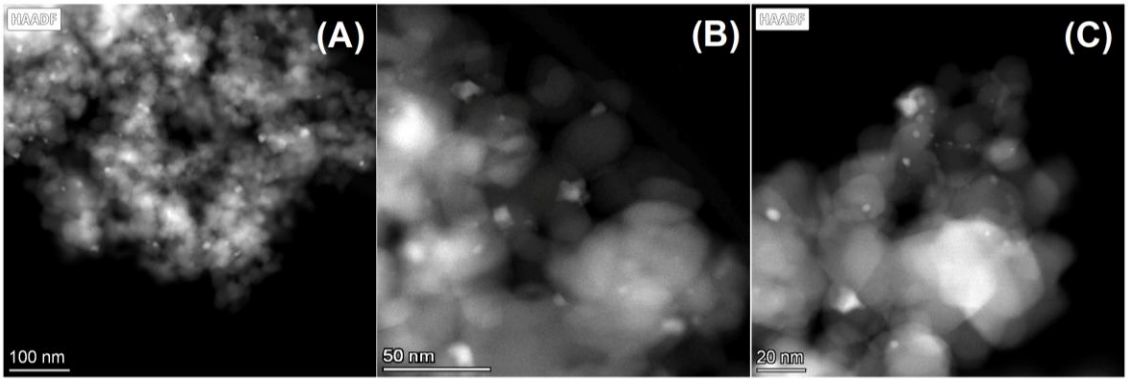

Figure A4.16. HAAD-STEM analysis of the used $Au_{0.5}Pd_{0.5}Fe_2/TiO_2$ after use in the in-situ degradation of phenol. **Phenol degradation reaction conditions:** catalyst (0.01 g), phenol (1000 ppm, 8.5 g), 5% H_2/CO_2 (420 psi), 25% O_2/CO_2 (160 psi), 20 °C, 4 h, 1200 rpm.

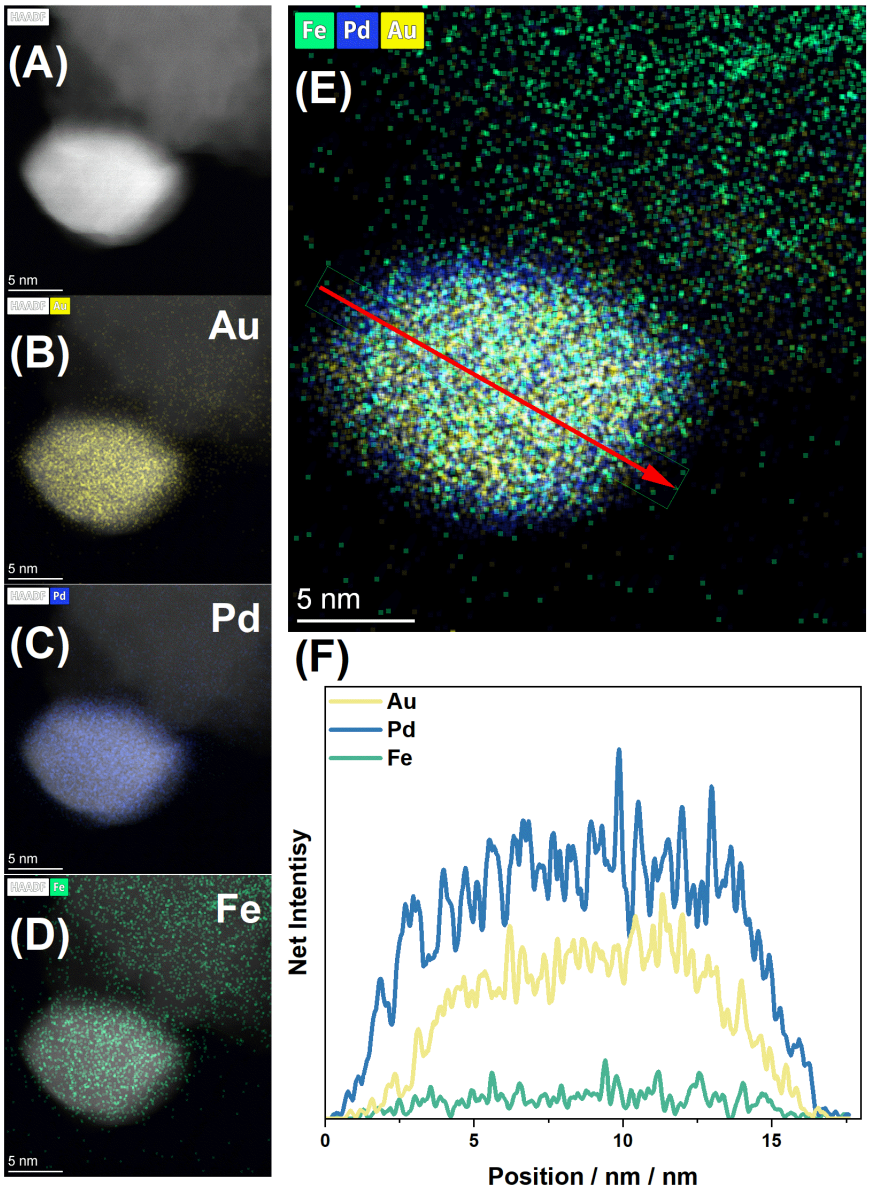

Figure A4.17. (**A**) HADDF-STEM, (**B-D**) STEM-EDX analysis and (**E-F**) line scan analysis of the $Au_{0.5}Pd_{0.5}Fe_2/TiO_2$ catalyst after 4 hour phenol degradation reaction. **Phenol degradation reaction conditions:** catalyst (0.01 g), phenol (1000 ppm, 8.5 g), 5% H_2/CO_2 (420 psi), 25% O_2/CO_2 (160 psi), 20 °C, 4 h, 1200 rpm.

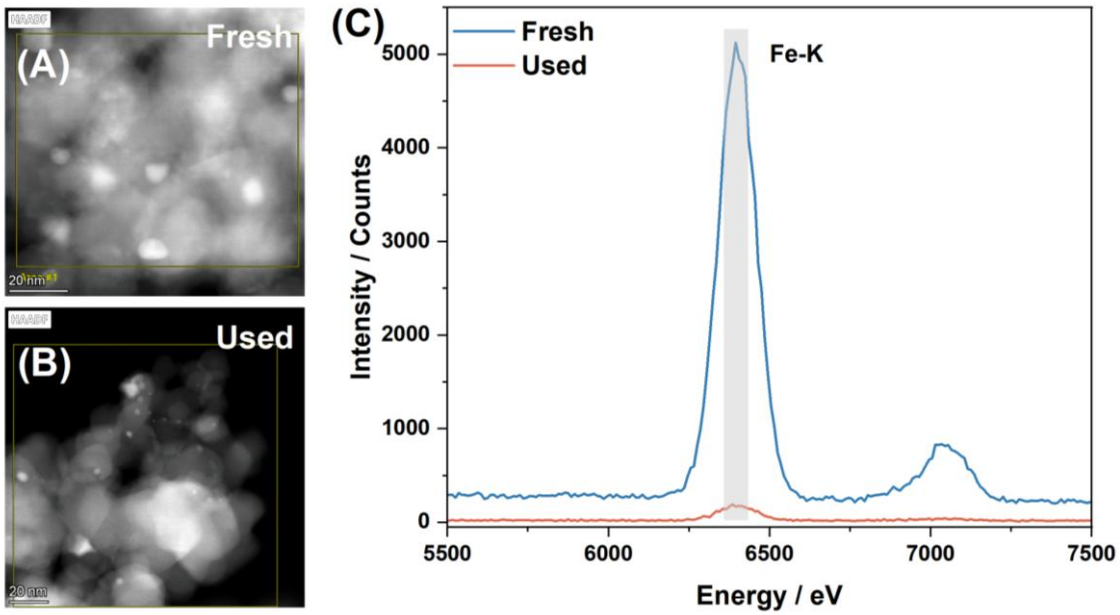

Figure A4.18. HADDF-STEM analysis of the (**A**) fresh and (**B**) used $Au_{0.5}Pd_{0.5}Fe_2/TiO_2$ catalyst, together with the (**C**) EDX analysis. **Phenol degradation reaction conditions:** catalyst (0.01 g), phenol (1000 ppm, 8.5 g), 5% H_2/CO_2 (420 psi), 25% O_2/CO_2 (160 psi), 20 °C, 4h, 1200 rpm. **Note:** The fresh catalyst was exposed to a reductive heat treatment prior to use (5%H_2/Ar, 400 °C, 4 h, 10 °C min^{-1}). The used sample was dried (30 °C, under vacuum, 16 h), prior to analysis.

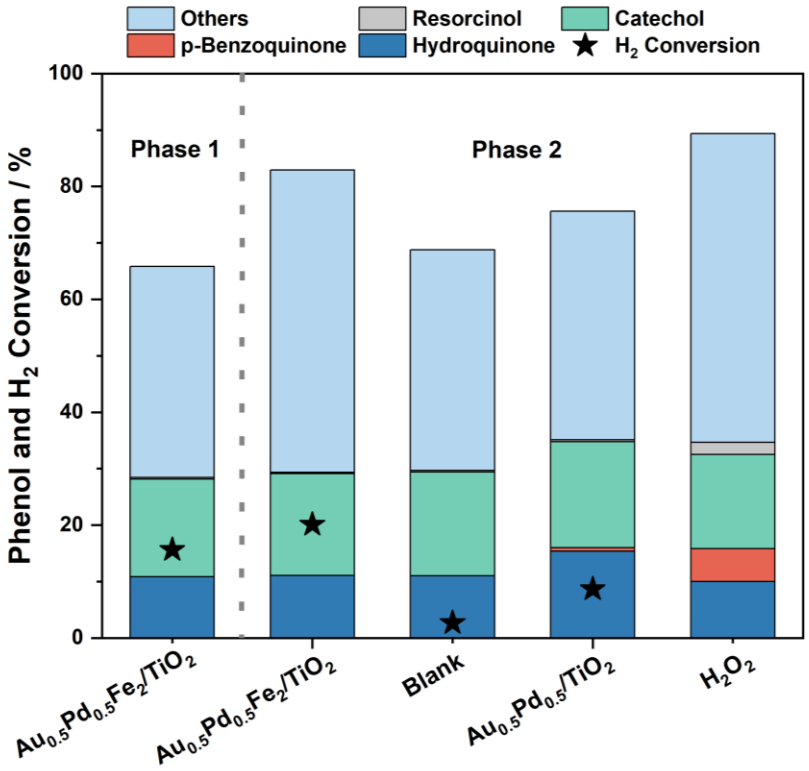

Figure A4.19. Detailed intermediate analysis for the hot-filtration experiments, including H_2 conversion. Phenol oxidation reaction conditions: catalyst (0.01 g), phenol (8.5g, 1000 ppm), 5% H_2/CO_2 (420 psi), 25% O_2/CO_2 (160 psi), 1200 rpm, 25 °C, 2 h for each phase. Key: **Phase 1 - $Au_{0.5}Pd_{0.5}Fe_2/TiO_2$** catalysed reaction for the initial 2 hours; **Phase 2 - $Au_{0.5}Pd_{0.5}Fe_2/TiO_2$** catalysed the continuous 2 hours reaction; **Blank:** hot filtration reaction where the $Au_{0.5}Pd_{0.5}Fe_2/TiO_2$ catalyst is removed by filtration after 2 hours and only homogeneous species left for the continuous 2 hours reaction; **$Au_{0.5}Pd_{0.5}/TiO_2$**: hot filtration reaction where $Au_{0.5}Pd_{0.5}Fe_2/TiO_2$ catalyst removed by filtration after 2 h and replaced by $Au_{0.5}Pd_{0.5}/TiO_2$ catalyst for final 2 h of reaction; **H_2O_2**: hot filtration reaction where $Au_{0.5}Pd_{0.5}Fe_2/TiO_2$ catalyst removed by filtration after 2 h and replaced by commercial H_2O_2 (concentration identical to that if all H_2 utilised in a standard in situ reaction was selectively converted to H_2O_2) catalyst for final 2 h of reaction.

4.7 References

1. Jamieson, A. J., Malkocs, T., Piertney, S. B., Fujii, T. & Zhang, Z. Bioaccumulation of persistent organic pollutants in the deepest ocean fauna. *Nat Ecol Evol* **1**, 0051 (2017).
2. Jones, E. R. *et al.* Current wastewater treatment targets are insufficient to protect surface water quality. *Commun Earth Environ* **3**, 221 (2022).
3. Larsen, T. A., Hoffmann, S., Lüthi, C., Truffer, B. & Maurer, M. Emerging solutions to the water challenges of an urbanizing world. *Science (1979)* **352**, 928–933 (2016).
4. Negrete-Bolagay, D. *et al.* Persistent organic pollutants: The trade-off between potential risks and sustainable remediation methods. *J Environ Manage* **300**, 113737 (2021).
5. Li, X., Shen, X., Jiang, W., Xi, Y. & Li, S. Comprehensive review of emerging contaminants: Detection technologies, environmental impact, and management strategies. *Ecotoxicol Environ Saf* **278**, 116420 (2024).
6. Svensson Grape, E. *et al.* Removal of pharmaceutical pollutants from effluent by a plant-based metal–organic framework. *Nature Water* **1**, 433–442 (2023).
7. Abu Hasan, H., Muhammad, M. H. & Ismail, N. 'Izzati. A review of biological drinking water treatment technologies for contaminants removal from polluted water resources. *Journal of Water Process Engineering* **33**, 101035 (2020).
8. Rashid, R., Shafiq, I., Akhter, P., Iqbal, M. J. & Hussain, M. A state-of-the-art review on wastewater treatment techniques: the effectiveness of adsorption method. *Environmental Science and Pollution Research* **28**, 9050–9066 (2021).
9. Zhao, C. *et al.* Application of coagulation/flocculation in oily wastewater treatment: A review. *Science of The Total Environment* **765**, 142795 (2021).
10. Hube, S. *et al.* Direct membrane filtration for wastewater treatment and resource recovery: A review. *Science of The Total Environment* **710**, 136375 (2020).
11. Wu, M. *et al.* Cascading H2O2 photosynthesis and Fenton reaction for self-sufficient photo-Fenton reactions: A review of recent advances. *Chemical Engineering Journal* **489**, 151091 (2024).
12. Wu, Z. *et al.* Long-range interactions driving neighboring Fe–N4 sites in Fenton-like reactions for sustainable water decontamination. *Nat Commun* **15**, 7775 (2024).

13. Chen, X. *et al.* Enhanced H2O2 utilization efficiency in Fenton-like system for degradation of emerging contaminants: Oxygen vacancy-mediated activation of O2. *Water Res* **230**, 119562 (2023).

14. Liang, Z. *et al.* Effective green treatment of sewage sludge from Fenton reactions: Utilizing MoS2 for sustainable resource recovery. *Proceedings of the National Academy of Sciences* **121**, e2317394121 (2024).

15. Pi, L. *et al.* Generation of H2O2 by on-site activation of molecular dioxygen for environmental remediation applications: A review. *Chemical Engineering Journal* **389**, 123420 (2020).

16. Zhu, Y. *et al.* Strategies for enhancing the heterogeneous Fenton catalytic reactivity: A review. *Appl Catal B* **255**, 117739 (2019).

17. Ni, Y., Zhou, C., Xing, M. & Zhou, Y. Oxidation of emerging organic contaminants by in-situ H2O2 fenton system. *Green Energy & Environment* **9**, 417–434 (2024).

18. Lewis, R. J. & Hutchings, G. J. Selective Oxidation Using In Situ-Generated Hydrogen Peroxide. *Acc Chem Res* **57**, 106–119 (2024).

19. Yang, S. *et al.* Toward the Decentralized Electrochemical Production of H2O2: A Focus on the Catalysis. *ACS Catal* **8**, 4064–4081 (2018).

20. Richards, T. *et al.* A residue-free approach to water disinfection using catalytic in situ generation of reactive oxygen species. *Nat Catal* **4**, 575–585 (2021).

21. Underhill, R. *et al.* Oxidative Degradation of Phenol using in situ Generated Hydrogen Peroxide Combined with Fenton's Process. *Johnson Matthey Technology Review* **62**, 417–425 (2018).

22. Santos, A. *et al.* The oxidative degradation of phenol via in situ H2O2 synthesis using Pd supported Fe-modified ZSM-5 catalysts. *Catal Sci Technol* **12**, 2943–2953 (2022).

23. Santos, A. *et al.* The degradation of phenol via in situ H2O2 production over supported Pd-based catalysts. *Catal Sci Technol* **11**, 7866–7874 (2021).

24. Li, R.-J. *et al.* Promoting H2O2 direct synthesis through Fe incorporation into AuPd catalysts. *Green Chemistry* **27**, 2065–2077 (2025).

25. Santos, A. *et al.* Direct Synthesis of Hydrogen Peroxide over Au–Pd Supported Nanoparticles under Ambient Conditions. *Ind Eng Chem Res* **58**, 12623–12631 (2019).

26. Ouyang, L. *et al.* The origin of active sites for direct synthesis of H2O2 on Pd/TiO2 catalysts: Interfaces of Pd and PdO domains. *J Catal* **321**, 70–80 (2015).

27. Barnes, A., Lewis, R. J., Morgan, D. J., Davies, T. E. & Hutchings, G. J. Improving Catalytic Activity towards the Direct Synthesis of H2O2 through Cu Incorporation into AuPd Catalysts. *Catalysts* **12**, (2022).

28. Barnes, A., Lewis, R. J., Morgan, D. J., Davies, T. E. & Hutchings, G. J. Enhancing catalytic performance of AuPd catalysts towards the direct synthesis of H2O2 through incorporation of base metals. *Catal Sci Technol* **12**, 1986–1995 (2022).

29. Thompson, S. T. & Lamb, H. H. Palladium–Rhenium Catalysts for Selective Hydrogenation of Furfural: Evidence for an Optimum Surface Composition. *ACS Catal* **6**, 7438–7447 (2016).

30. Thompson, S. T. & Lamb, H. H. Palladium-Rhenium Catalysts for Selective Hydrogenation of Furfural: Influence of Catalyst Preparation on Structure and Performance. *Catalysts* **13**, (2023).

31. Bahruji, H. *et al.* Pd/ZnO catalysts for direct CO2 hydrogenation to methanol. *J Catal* **343**, 133–146 (2016).

32. Spezzati, G. *et al.* Atomically Dispersed Pd–O Species on CeO2(111) as Highly Active Sites for Low-Temperature CO Oxidation. *ACS Catal* **7**, 6887–6891 (2017).

33. Fu, L. *et al.* Direct Synthesis of H2O2 over AuCu@AuPd Core–Shell Catalysts with Highly Dispersed Pd Sites. *Ind Eng Chem Res* **63**, 20144–20154 (2024).

34. Zhang, M., Xu, H., Luo, Y., Zhu, J. & Cheng, D. Enhancing the catalytic performance of PdAu catalysts by W-induced strong interaction for the direct synthesis of H2O2. *Catal Sci Technol* **12**, 5290–5301 (2022).

35. Tian, P. *et al.* The origin of palladium particle size effects in the direct synthesis of H2O2: Is smaller better? *J Catal* **349**, 30–40 (2017).

36. Zhang, X. *et al.* Nanoconfinement-triggered oligomerization pathway for efficient removal of phenolic pollutants via a Fenton-like reaction. *Nat Commun* **15**, 917 (2024).

37. Quintanilla, A., Casas, J. A., Mohedano, A. F. & Rodríguez, J. J. Reaction pathway of the catalytic wet air oxidation of phenol with a Fe/activated carbon catalyst. *Appl Catal B* **67**, 206–216 (2006).

38. Li, L. *et al.* Dual roles of MoS2 nanosheets in advanced oxidation Processes: Activating permonosulfate and quenching radicals. *Chemical Engineering Journal* **440**, 135866 (2022).

39. Zazo, J. A., Casas, J. A., Mohedano, A. F. & Rodriguez, J. J. Semicontinuous Fenton oxidation of phenol in aqueous solution. A kinetic study. *Water Res* **43**, 4063–4069 (2009).

40. Wang, F., Gu, Z., Hu, Y. & Li, Q. Split dosing of H2O2 for enhancing recalcitrant organics removal from landfill leachate in the Fe0/H2O2 process: Degradation efficiency and mechanism. *Sep Purif Technol* **278**, 119564 (2021).

41. Yamal-Turbay, E., Graells, M. & Pérez-Moya, M. Systematic Assessment of the Influence of Hydrogen Peroxide Dosage on Caffeine Degradation by the Photo-Fenton Process. *Ind Eng Chem Res* **51**, 4770–4778 (2012).

42. Chen, Z. *et al.* "Small amount for multiple times" of H2O2 feeding way in MoS2-Fex heterogeneous fenton for enhancing sulfadiazine degradation. *Chinese Chemical Letters* **33**, 1365–1372 (2022).

43. Wang, Z., Hu, N., Wang, L., Zhao, H. & Zhao, G. In Situ Production of Hydroxyl Radicals via Three-Electron Oxygen Reduction: Opportunities for Water Treatment. *Angewandte Chemie International Edition* **63**, e202407628 (2024).

44. Xie, L. *et al.* The strong metal–support interactions induced electrocatalytic three-electron oxygen reduction to hydroxyl radicals for water treatment. *Proceedings of the National Academy of Sciences* **120**, e2307989120 (2023).

45. Chen, M., Zhang, Z., Zhu, L., Wang, N. & Tang, H. Bisulfite-induced drastic enhancement of bisphenol A degradation in Fe3+-H2O2 Fenton system. *Chemical Engineering Journal* **361**, 1190–1197 (2019).

46. Chen, R. & Pignatello, J. J. Role of Quinone Intermediates as Electron Shuttles in Fenton and Photoassisted Fenton Oxidations of Aromatic Compounds. *Environ Sci Technol* **31**, 2399–2406 (1997).

47. Chen, C. *et al.* Overlooked self-catalytic mechanism in phenolic moiety-mediated Fenton-like system: Formation of Fe(III) hydroperoxide complex and co-treatment of refractory pollutants. *Appl Catal B* **321**, 122062 (2023).

48. Georgi, A., Velasco Polo, M., Crincoli, K., Mackenzie, K. & Kopinke, F.-D. Accelerated Catalytic Fenton Reaction with Traces of Iron: An Fe–Pd-Multicatalysis Approach. *Environ Sci Technol* **50**, 5882–5891 (2016).

Chapter 5 - In situ water treatment using AuPd catalysts in a Flow Reactor

5.1 Introduction

Growing pressure on the freshwater resources and the tightening of environmental standards have sharpened the focus on technologies that can effectively remove persistent organic contaminants from water with high efficiency, low secondary pollution, and credible routes to scale.[1] Among available options, advanced oxidation processes (AOPs) that generate reactive oxygen species (ROS), notably hydroxyl radicals (·OH) and superoxide ($O_2^{\cdot-}$), have attracted extensive attention over decades due to their ability to mineralize a wide spectrum of pollutants rather than merely transferring them to another phase.[2–7] Hydrogen peroxide (H_2O_2) is central to many AOPs (e.g., Fenton chemistry),[4,8,9] but conventional practice relies on bulk-manufactured H_2O_2 via the anthraquinone process, posing extra risks on transportation, storage, and dosing of concentrated H_2O_2.[10] This introduces liabilities related to cost, safety, and sustainability, including decomposition losses, hazards associated with concentrated oxidant inventories, and the addition of stabilisers or organic cosolvents that can complicate treatment trains or discharge permits.

The direct synthesis of H_2O_2 over supported catalysts has therefore emerged as a compelling alternative, offering on-demand generation of dilute H_2O_2 exactly where and when it's needed. In situ water treatment coupling the in situ H_2O_2 generation, along with associated ROS, which are formed as intermediates during H_2O_2 generation, has emerged as a promising strategy.[11–15] In contrast to alternative methods, including traditional Fenton-type systems that rely on homogeneous catalysts and commercial H_2O_2 (often resulting in significant sludge production),[16] the in situ, heterogeneous approach enables the controlled formation of low concentrations of highly reactive oxidative species.[14] This not only enhances reaction efficiency but also eliminates the need for downstream treatment associated with residual metal salts or stabilising additives commonly present in preformed H_2O_2 formulations.[10]

Previously reported bimetallic PdFe catalysts exhibited excellent catalytic potential in the in situ water treatment, where the Pd active sites are mainly responsible for the generation of H_2O_2 and the oxygen-based intermediates, while the subsequent H_2O_2 activation and ·OH production via the Fenton pathway mainly occurs on Fe active sites. However, catalyst stability is a real

concern with prior reports highlighting the limited stability of both noble metals (responsible for H_2O_2 generation) and non-noble, Fenton(-type) (responsible for ROS generation) in the presence of highly oxidised products of phenol degradation (oxalic acid, formic acid, maleic acid, etc.).[12,13,15] As a result, PdFe catalysts can suffer from extensive leaching that limit the suitability for extended operation in a continuous flow reactor.

In contrast, AuPd alloys are well established for selective direct H_2O_2 synthesis. Alloying Au with Pd dilutes and electronically modifies Pd ensembles, suppressing O-O bond scission and parasitic H_2O_2 decomposition while maintaining activity for H_2 and O_2 activation.[17–19] Initial study utilizing bimetallic AuPd catalysts in H_2O_2 synthesis in a continuous flow system was conducted by Freakley and Hutchings, showing promising catalytic activity towards H_2O_2 formation, as high as 760 ppm under optimal conditions.[20] Building on that, Hutching's group further demonstrated that AuPd catalysts can deliver powerful in situ oxidative capability in flow for water disinfection, achieving 8.1 $\log_{10}$ E.coli reductions, compared to the monometallic Au and Pd catalysts.[14]

Yet, despite this promise, the efficacy and durability of AuPd for degrading organics such as phenolic groups, pharmaceuticals, and pesticides, arguably the more demanding oxidation targets than microbial kill, remain underexplored in a multiphase flow system. In this chapter, a systematic study was conducted on the traditional AuPd series in the flow reactor to exam the catalytic reactivity and stability during long term, continuous phenol degradation tests, to understand the effect of each reaction parameters on the catalytic performance, to investigate the mechanism behind stable catalytic operation, and to expand the application range for a broad groups of organic pollutants.

5.2 Results and Discussion

5.2.1 Material characterisation

The introduction of Au into supported Pd nanoparticles has been well studied for a range of oxidative transformations, with the formation of AuPd nanoalloys often offering considerable enhancements in reactivity, selectivity, and stability compared to their monometallic analogues. Typically, these improvements are attributed to 'synergistic effects,' a catch-all term that encompasses electronic and structural changes, which result from the formation of bimetallic species.[21–23] The use of in-situ synthesised H_2O_2 and associated reactive oxygen species in chemical valorisation represents areas of considerable interest, where the synergy that results from Au-Pd alloy formation has been exploited to a considerable degree.[24,25] Building on these earlier works, we now turn our attention to the application of a series of 1%AuPd-based catalysts, immobilised on a TiO_2 (P-25) carrier, for the in-situ degradation of phenol, a widely studied model contaminant.[26]

Prior to their application in the oxidative degradation of phenol, the catalyst series was extensively characterised in order to identify potential structural-reactivity relationships. As expected with the impregnation method used for catalyst synthesis, the actual loadings of Au and Pd in the prepared 1%AuPd/TiO_2 formulations were close to their nominal values (**Table 5.1**).

Table 5.1. Metal loading of the as-prepared Au-Pd/TiO_2 catalysts, as established by ICP-MS analysis of aqua-regia digested samples.

Catalyst Formulation	Actual Au loading / wt. %	Actual Pd loading / wt. %
Au_1/TiO_2	1.00	-
$Au_{0.75}Pd_{0.25}/TiO_2$	0.72	0.24
$Au_{0.5}Pd_{0.5}/TiO_2$	0.43	0.46
$Au_{0.25}Pd_{0.75}/TiO_2$	0.28	0.76
Pd_1/TiO_2	-	0.96

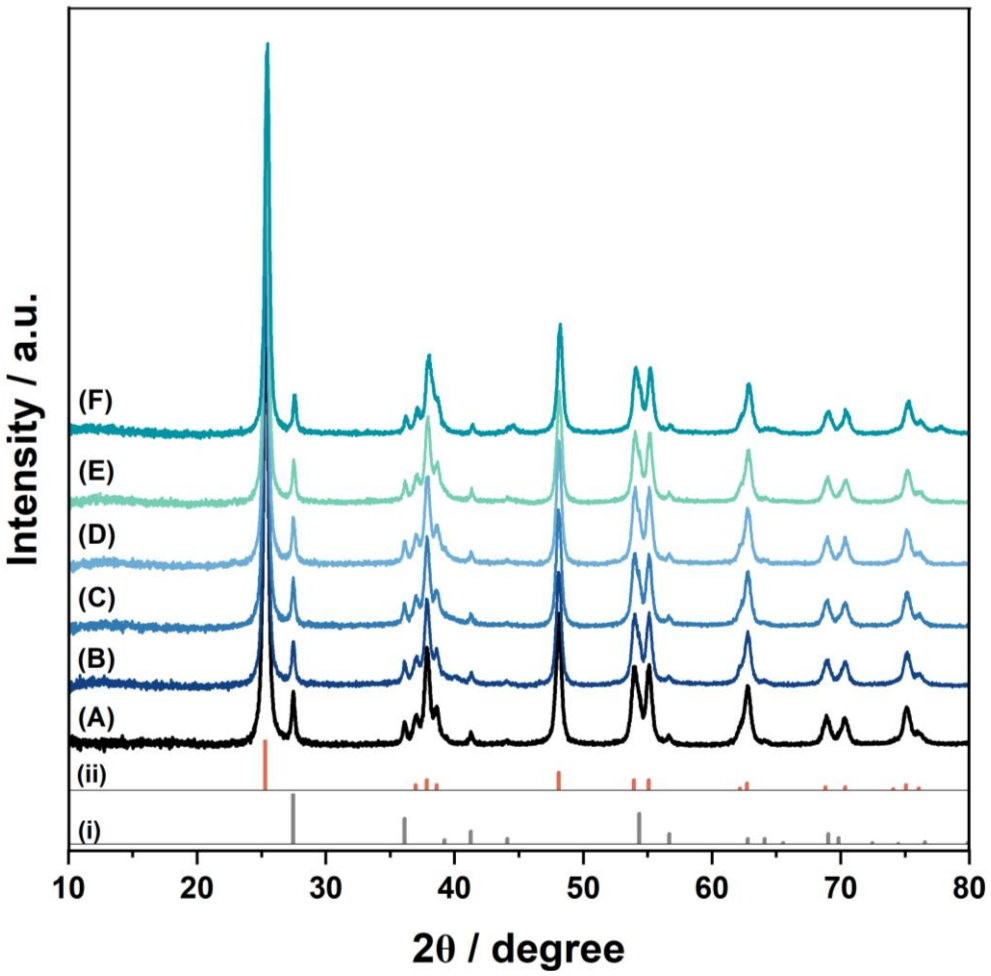

Figure 5.1. XRD spectra of the 1%AuPd/TiO_2 series. **(A)** TiO_2, **(B)** Pd_1/TiO_2, **(C)** $Au_{0.25}Pd_{0.75}/TiO_2$, **(D)** $Au_{0.5}Pd_{0.5}/TiO_2$, **(E)** $Au_{0.75}Pd_{0.25}/TiO_2$, and **(F)** Au_1/TiO_2 catalysts, with corresponding **(i)** Rutile (ICDD PDF File 00-021-1276) and **(ii)** Anatase phases (ICDD PDF File 00-021-1272).

With a strong correlation between catalytic selectivity and nanoparticle size well known,[27] the active sites dispersion was subsequently probed by X-ray diffraction (**Figure 5.1**). Unsurprisingly, due to the low metal loading, only the anatase (*ICDD PDF File 00-021-1272*) and rutile (*ICDD PDF File 00-021-1276*) phases of TiO_2 P25 could be observed across all AuPd formulations comparing to the bare TiO_2, with no clear reflections associated with Au or Pd were observed, which may indicate high dispersion or merely be a result of the relatively low loading of metals on the catalyst surface.

To provide a further indication of particle size, transmission electron microscopy (TEM) was employed, with mean particle sizes reported in **Table 5.2** (associated particle size distribution and micrographs are reported in **Figure A5.1-2**). A clear correlation between mean particle size and catalyst formulation was observed, with the Au-rich formulations (≥ 6.5 nm)

consisting of larger species compared to the Pd-rich analogues (≤ 4.5 nm), aligning well with earlier studies into AuPd-based materials prepared by a similar impregnation protocol.[28]

Table 5.2. Particle size of 1%AuPd/TiO_2 catalysts as determined by TEM.

Catalyst Formulation	Particle Size / nm (S.D)
Au_1/TiO_2	10.5 (8.3)
$Au_{0.75}Pd_{0.25}/TiO_2$	6.5 (3.9)
$Au_{0.5}Pd_{0.5}/TiO_2$	6.1 (2.8)
$Au_{0.25}Pd_{0.75}/TiO_2$	4.5 (1.8)
Pd_1/TiO_2	4.8 (2.1)

Further analysis via X-ray photoelectron spectroscopy (XPS) (**Figure A5.3,** with elemental surface ratios reported in **Table 5.3**) revealed that the formation of AuPd alloys significantly modifies Pd-oxidation state, with a shift towards Pd^{2+} observed with the introduction of relatively large quantities of Au (i.e. at Au loadings ≥ 0.5wt.%), with the Pd^{2+}/Pd^0 ratios from 0 to 0.13. Notably, Au is found to exist purely in the metallic state, with no cationic species observed (**Figure A5.4**).

Table 5.3. Au: Pd atomic ratio of 1%AuPd/TiO_2 catalysts as determined by XPS analysis.

Catalyst Formulation	Pd: Au	Pd^{2+} : Pd^0
Au_1/TiO_2	-	-
$Au_{0.75}Pd_{0.25}/TiO_2$	1.50	0.13
$Au_{0.5}Pd_{0.5}/TiO_2$	2.40	0.17
$Au_{0.25}Pd_{0.75}/TiO_2$	9.00	All Pd^0
Pd_1/TiO_2	-	All Pd^0

5.2.2 The direct H_2O_2 synthesis and degradation tests on the AuPd series

With the catalyst series extensively characterised, the investigation of the efficacy of these materials towards the direct synthesis and subsequent degradation of H_2O_2 was subsequently conducted. Under reaction conditions considered sub-optimal for H_2O_2 production (i.e. ambient temperature and in the absence of the alcohol co-solvent typically utilised to promote

H_2O_2 stability and gaseous reagent solubility), but relevant to the real world oxidative treatment of aqueous waste-streams (**Table 5.4**).

In keeping with earlier works, the incorporation of Au into a supported Pd catalyst was found to improve catalytic performance towards H_2O_2 production,[28–30] with accumulated H_2O_2 concentration (from 20 to 53 ppm), observed over the bimetallic series, greater than that offered by the Pd-only (12 ppm) and Au-only (6 ppm) catalysts after 30 mins of reaction. Notably, this improved performance can be related to enhancements in catalytic selectivity (6-19% H_2O_2 selectivity in the case of the bimetallic catalysts), rather than increased reactivity/H_2 utilization rate, as indicated by the near identical H_2 conversion rates (between 2-5 %) observed over these formulations.

Table 5.4. The effect of Au: Pd ratio on the activity of 1%AuPd/TiO_2 catalysts towards the direct synthesis and subsequent degradation of H_2O_2 in the batch reactor.

Catalyst	H_2O_2 Productivity / $mol_{H2O2}kg_{cat}^{-1}h^{-1}$	H_2O_2 Conc. / ppm	H_2 Conv. / %	H_2O_2 Sel. / %	H_2O_2 Degradation / $mol_{H2O2}kg_{cat}^{-1}h^{-1}$ (%)
Au_1/TiO_2	0.3	6	1	6	0 (0)
$Au_{0.75}Pd_{0.25}/TiO_2$	2.6	53	3	19	683 (33)
$Au_{0.5}Pd_{0.5}/TiO_2$	2.5	50	4	14	650 (32)
$Au_{0.25}Pd_{0.75}/TiO_2$	1.0	20	4	6	799 (39)
Pd_1/TiO_2	0.6	12	5	2	595 (28)

H_2O_2 direct synthesis reaction conditions: catalyst (0.01 g), H_2O (8.5 g), 5% H_2/N_2 (420 psi), 25% O_2/N_2 (160 psi), 0.5 h, 20 °C, 1200 rpm. **H_2O_2 degradation reaction conditions:** catalyst (0.01 g), H_2O_2 (50 wt.% 0.68 g), H_2O (7.82 g), 5% H_2/N_2 (420 psi), 0.5 h, 20 °C, 1200 rpm.

5.2.3 In situ phenol degradation using the AuPd series

Building on these studies, the catalytic performance of the AuPd series towards the in situ oxidative degradation of phenol, via the in situ synthesis of H_2O_2 and associated reactive oxygen species (ROS; ·OOH, ·OH, O_2^{-}), with these latter species generated as intermediates during H_2O_2 synthesis or via subsequent degradation of H_2O_2.[14]

A schematic of the flow reactor designed to evaluate catalytic performance is shown in **Figure A5.5.A,** with a photograph of the reactor shown in **Figure A5.5.B**. The detailed description is

in **Section 2.5.1** in **Chapter 2**. Briefly, the continuous fixed-bed reactor with 1/8 inch lines (3.2 mm outer diameter) and a 10 cm long stainless-steel tube (1/4 inch, 6.4 mm outer diameter) packed with catalyst/diluent was operated at 20 °C and 10 bar. 10ppm phenol solution (HPLC-grade water) was fed at 0.2 mL min^{-1} using an Agilent 1290 Infinity pump. Gas co-feeds were metered by mass flow controllers at 35 mL min^{-1} (5% H_2/N_2) and 7 mL min^{-1} (25% O_2/N_2), giving a total gas flow of 42 mL min^{-1} and an overall H_2:O_2 molar ratio of 1. Downstream check valves were installed, and the liquid hourly space velocity (LHSV) was calculated using the total packed bed volume (4.75 cm^3). At a liquid flow rate of 42 mL min^{-1}, the LHSV was 530.5 h^{-1} Pressure was maintained with a back-pressure regulator and safeguarded with relief valves. Effluents (post-reaction solutions) were sampled and analysed by HPLC (Agilent Poroshell 120 SB-C18).

As the SiC (4.1 g, 46 grit, ~0.4mm) was used as a catalyst diluent in the catalyst tube, the effects of SiC on the in situ H_2O_2 generation and phenol degradation were first determined in the absence of the catalyst. Negligible ability of the SiC to promote the degradation of H_2O_2, according to **Figure A5.6**, with less than 5% H_2O_2 loss over the first 60 mins, might be due to the interactions between impurities and H_2O_2 and/or the H_2O_2 adsorption on the surface of SiC. **Figure A5.7** showed a very limited impact of SiC on the phenol degradation with the presence of both H_2 and O_2, with a limited degree of phenol adsorption observed initially (5% at a reaction time of 0.5 h) and no further impact (<1%) at extended reaction time up to 3 hours.

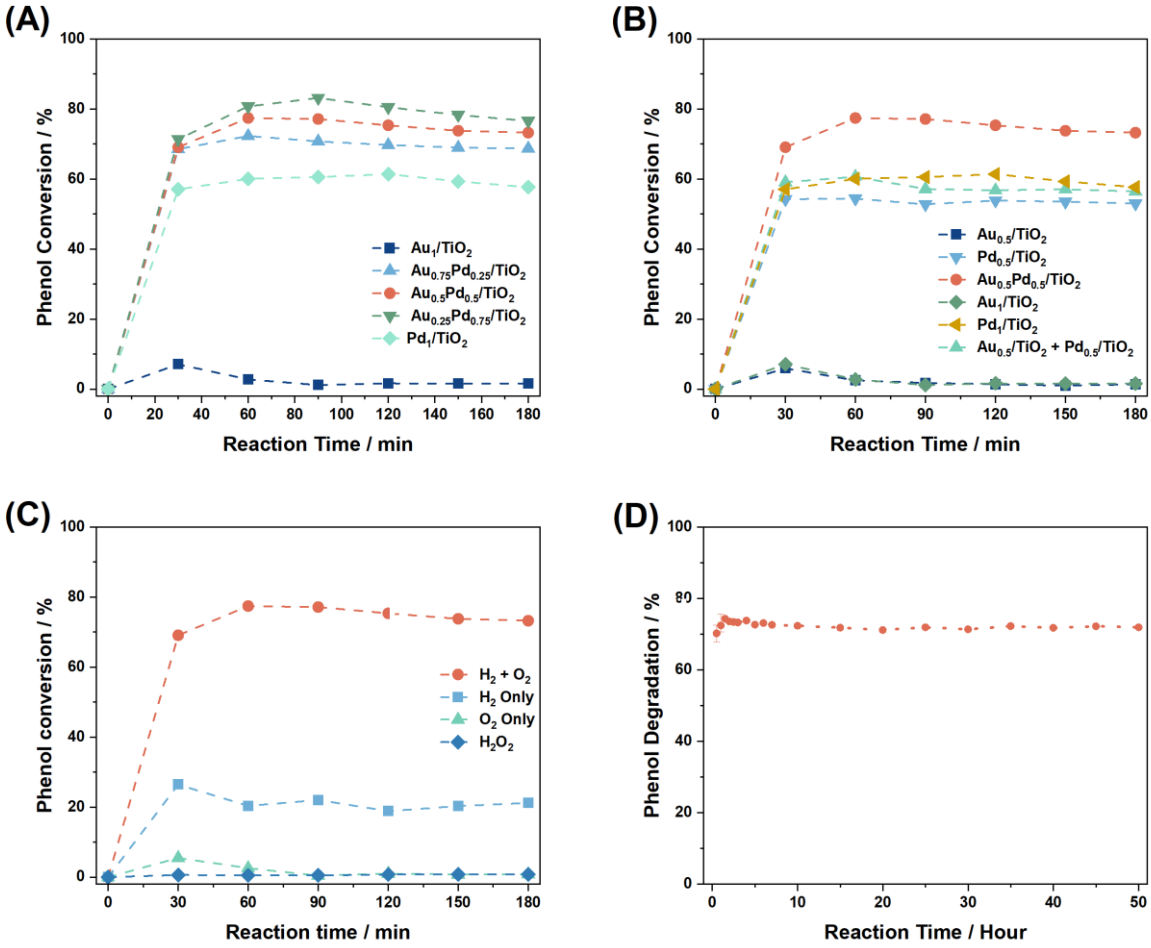

Figure 5.2. The performance of 1%AuPd/TiO_2 catalysts towards the degradation of phenol via the in-situ production of H_2O_2. (A) The effect of Au: Pd ratio on catalytic reactivity. (B) The requirement for Au-Pd alloys as established by comparison between bimetallic formulations and a physical mixture of monometallic analogues. (C) Control experiment demonstrating the contribution of the different reactants (H_2, O_2 and H_2O_2 (100ppm)). (D) The long-term stability of the $Au_{0.5}Pd_{0.5}/TiO_2$ catalyst. Reaction conditions: catalyst (0.12 g), SiC (4.1 g), phenol solution (10 ppm, in H_2O), total gas flow rate: 42 mL min^{-1} (H_2:O_2= 1), 10 bar, liquid flow rate: 0.2 mL min^{-1}, 20 °C.

After excluding the effect of catalyst diluent (SiC), subsequently, the efficacy of the series of 1%AuPd/TiO_2 catalysts towards the in-situ oxidative degradation of phenol, we set out to establish (**Figure 5.2.A**). A clear enhancement in reactivity was observed upon the formation of AuPd nanoalloys, with the bimetallic catalysts (68-80% phenol conversion steadily achieved) outperforming the monometallic analogues (58% and 2 % phenol conversion steadily achieved over the Pd_1/TiO_2 and Au_1/TiO_2 catalysts, respectively), where the activity of the $Au_{0.25}Pd_{0.75}/TiO_2$ formulation is particularly noteworthy, achieving rates of phenol conversion over 80%. Further evidence from radical quenching experiments suggested that ·OH is the primary reaction species responsible for the oxidation degradation of phenol, with the presence

of 100 ppm t-butanol, the phenol conversion rate significantly decreased from 73% to 20% (**Figure A5.8**).[31] This synergistic effect over the bimetallic AuPd catalysts is consistent with the previously reported AuPd series towards *E.Coli* remediation,[14] where the bimetallic AuPd catalyst showed 8.1 $\log_{10}$ E.coli reduction while only 2.6 $\log_{10}$ and 1.6 $\log_{10}$ reduction observed on the monometallic Pd and monometallic Au catalysts, respectively, revealing that the introduction of Au enhanced radical diffusion from the surface of Pd active sites, and further promoting the bactericidal efficiency.

The synergistic effect or close contact effect between Au and Pd in the in situ phenol degradation was further supported by the evaluation of a physical mixture of the monometallic materials, namely Au_1/TiO_2 and Pd_1/TiO_2 catalysts (**Figure 5.2.B**). This monometallic physical mixture steadily achieved phenol degradation rates around 56%, comparable to the sum of the individual components (60%, where 2% from Au_1/TiO_2 and 58% from Pd_1/TiO_2), but still, far less competitive than that of the bimetallic $Au_{0.5}Pd_{0.5}/TiO_2$ (73%), evidencing the enhanced performance which results from the formation of AuPd alloys.

The possibilities of phenol hydrogenation or oxidation from H_2 or O_2 alone were ruled out by determining phenol conversion using either reactant gas only. Similar to the reactant gas control experiments in **Chapter 4 (Figure 4.5**), relatively limited phenol conversion rates were observed when using either molecular H_2 (20% phenol conversion), or O_2 (<1% phenol conversion) alone (**Figure 5.2.C**). With the inevitably incomplete purging of dissolved oxygen (DO) from the reaction medium and the resulting production of low concentrations of H_2O_2, and related radical species, considered the primary cause for the observed conversion under a H_2 only atmosphere,[13] suggesting that the significant improvement in oxidative degradation may be achieved from the in-situ generation of H_2O_2 (and associated ROS).

Subsequent studies also indicated that a significant improvement in phenol conversion may be obtained via in-situ H_2O_2 production with the presence of both catalyst and reactant gases (H_2 and O_2), compared to that observed when using the catalyst and preformed oxidant (< 0.5 % conversion when co-feeding 100 ppm H_2O_2), with these latter experiments further implicating oxidative species other than H_2O_2 as primarily responsible for the observed reactivity (**Figure 5.2.C).**

Importantly, for all catalysts, no significant catalytic ability loss was observed over 3 hours on-stream, which aligns well with the metal leaching analysis of post-reaction solutions by ICP-MS (**Table A5.1**). The stability of Au in particular is noteworthy, with a small degree of Pd

lost (≤ 0.3 μgL^{-1} at 30 mins), over a short reaction time initially. However, no further Pd leaching was observed at extended reaction times. Indeed, with a particular focus on the $Au_{0.5}Pd_{0.5}/TiO_2$ catalyst, the catalyst stability towards long-term in-situ phenol degradation test was established. An over 70% phenol degradation rate was maintained up to 50 hours on-stream (**Figure 5.2.D**). ICP-MS analysis on the long-term samples (**Table A5.2**) showed the leached Pd or Au below detection limits on stream up to 50 hours, suggesting the reasonable stability of the bimetallic AuPd catalyst under long-term operational performance.

Scanning transmission electron microscope (STEM), element mapping and line-scan analysis confirmed the presence of Pd-rich bimetallic alloys on the surface of TiO_2 for the fresh and used (after 3 hours and after 50 hours phenol degradation tests) samples. Comparison between fresh and used samples indicated no discernible change in nanoparticle composition or structure after 3 hours and 50 hours on-stream (**Figure 5.3. A-C**), with no evidence of alloy decomposition, with all Pd-rich alloys. Notably, a degree of aggregation into chain-like structures was observed after exposure to reaction conditions (i.e. after 50 hours on-stream) and evidence of the formation of small Pd-only nanoparticles, after relatively short reaction times (with analysis performed after 3 hours of reaction) (**Figure A5.9**). The aggregation appears to have a very limited effect on catalytic performance, and we reiterate the continued presence of bimetallic particles after use. However, such analysis does indicate the need for further efforts to improve catalyst stability if the in-situ approach is to find large-scale application.

XPS analysis (**Figure A5.10**, with elemental surface ratios in **Table A5.3**) shows no meaningful changes in Pd oxidation state after 50 hours on-stream (Pd^{2+}/Pd^0 ratio: 0.19), with the Pd^{2+}/Pd^0 ratio comparable to that observed in the as-prepared catalyst (Pd^{2+}/Pd^0 ratio: 0.17), indicating a stable near-surface redox state under the reaction conditions. In parallel, the Au:Pd surface atomic ratios for the fresh (2.4), 3 h (2.8), and 50 h (3.0) samples are indistinguishable within quantification uncertainty, implying no measurable metal leaching or surface dealloying during the long-term in situ phenol degradation test, which is supportively consistent with the ICP-MS (**Table A5.2**) and STEM-EDX analysis (**Figure 5.3. A-C**).

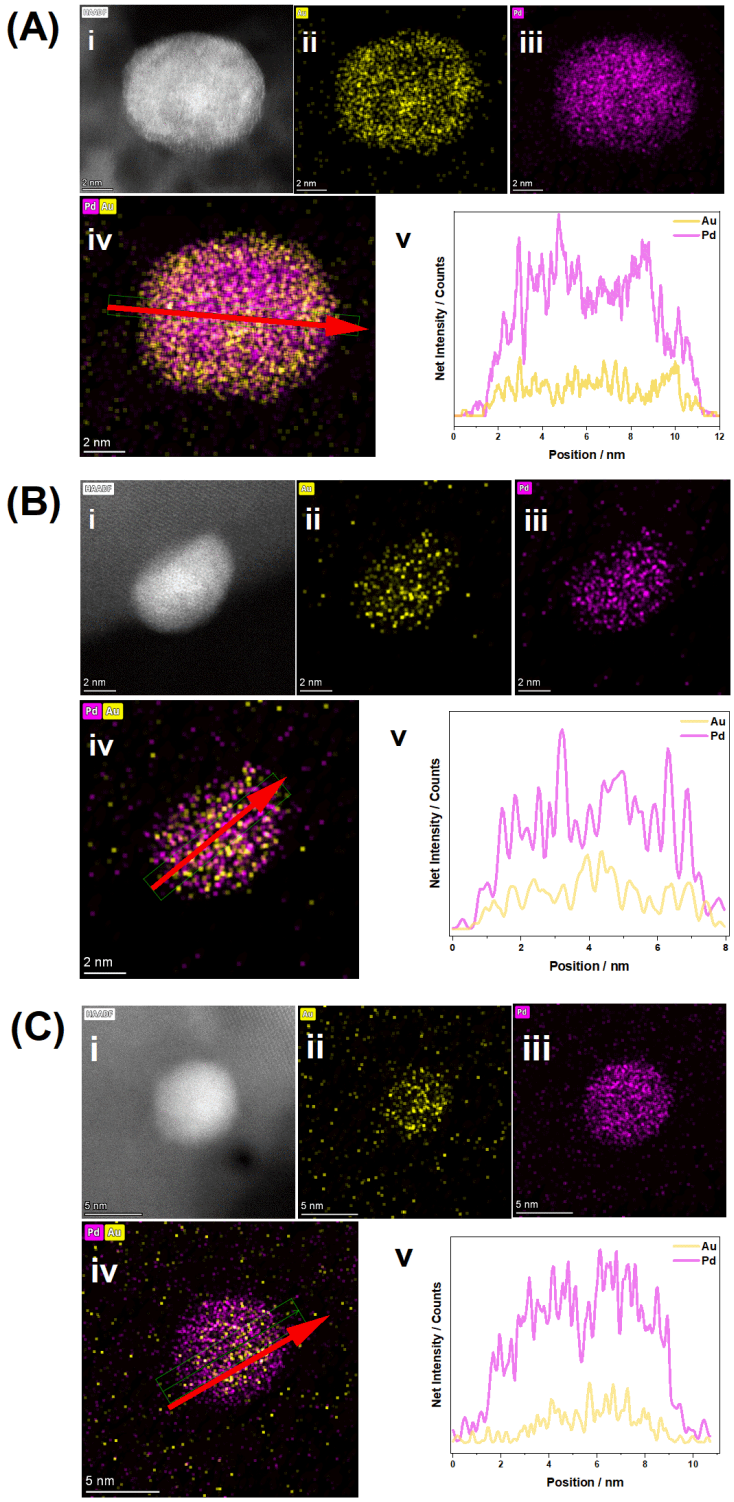

Figure 5.3. HAADF-STEM and corresponding EDX analysis of the $Au_{0.5}Pd_{0.5}/TiO_2$ catalyst (A) before, (B) after use in the oxidative degradation of phenol (3 h), and (C) after use in the oxidative degradation of phenol (50 h), with (i) HADDF image, (ii) Au EDX, (iii) Pd EDX, (iv) Line scan for the alloys, and (v) line scan of the Au and Pd signals. Key: Au (yellow), Pd (magenta). Reaction conditions: catalyst (0.12 g), SiC (4.1 g), phenol solution (10 ppm, in H_2O), total gas flow rate: 42 mL min^{-1} (H_2:O_2 = 1), 10 bar, liquid flow rate: 0.2 mL min^{-1}, 20 °C.

5.2.4 The effect of different reaction parameters on the in situ phenol degradation

A systematic series of experiments was undertaken to quantify how different parameters of reaction condition govern in-situ phenol removal over $Au_{0.5}Pd_{0.5}/TiO_2$ in the continuous flow reactor (**Figure 5.4. A-E)**.

A clear inverse correlation was found between phenol conversion and the contact time. Gas flow rate exerted a related but non-monotonic influence **(Figure 5.4.A).** At moderate total gas flows (from 30 to 48 mL min^{-1}), conversions remained high and comparatively insensitive, at around 71% conversion (on average) steadily achieved, indicating that interfacial mass transfer is adequate. Further increasing the gas flow shortened the effective contact time and marginally depressed conversion down to 49% at 60 mL min^{-1} and 32% at 90 mL min^{-1}, respectively. Similarly, lower liquid flow delivered the strongest effect **(Figure 5.4.B).** Phenol conversion decreased from 87% at a 0.1 mL min^{-1} flow rate to 25% at a 1 mL min^{-1} flow rate under the same gas flow rate (42 mL min^{-1}).

Increasing total pressure improved performance **(Figure 5.4.C).** Raising the pressure increases the solubility of H_2 and O_2, thereby elevating surface coverages of activated species and the steady-state H_2O_2 productivity. The positive correlation between pressure and conversion is consistent with the commonly reported near-first-order dependence of H_2O_2 formation on H_2 partial pressure. Practically, moving from low pressures (2–4 bar) to $\geqslant$6 bar shifts the reactor from oxidant-availability limitation toward kinetics-favoured conditions, delivering 70 to 80% conversion within the first hour under otherwise identical flows. Catalyst inventory provided a further lever on performance **(Figure 5.4.D).** Increasing the catalyst loading from 0.03 g to 0.24 g produced a near-linear rise in conversion from 30% to near 100%, reflecting the higher density of active sites for both H_2O_2 synthesis and its surface-mediated activation to ROS.

Legislation regulating phenolic compounds in water bodies is becoming increasingly stringent, with legal limits in the European Union ranging from 0.5 ppb in drinking water to 8 ppb in surface water.[32,33] Although the initial studies demonstrated effective phenol degradation at much higher concentrations (10 ppm) than those permitted by law, we were motivated to explore the limitations of this technology. With an aim to assess its potential for application in the treatment of chemical waste streams, where phenol concentrations are significantly higher, we evaluated system performance (with a fixed catalyst mass of 0.12 g) at levels of phenol as high as 50 ppm (i.e. 100000 times greater than that permitted in drinking water) (**Figure 5.4.**

E). Unsurprisingly, a reduction in phenol conversion was observed as phenol concentration increased. However, the in-situ approach was still able to achieve conversion rates as high as 40 % (at a phenol concentration of 50 ppm), with no loss in catalyst performance observed on-line. Notably, in these experiments (initial concentration: 50 ppm), the products of phenol degradation could be quantified (**Figure A5.11**), which was not feasible in earlier work at 10 ppm phenol because of analytical detection limits. The product slate shows relatively high selectivity toward highly oxidised species, namely the combined low-molecular-weight acids, CO_2, and H_2O (grouped as "others" in **Figure A5.11**), rather than toward phenolic derivatives such as catechol and resorcinol.

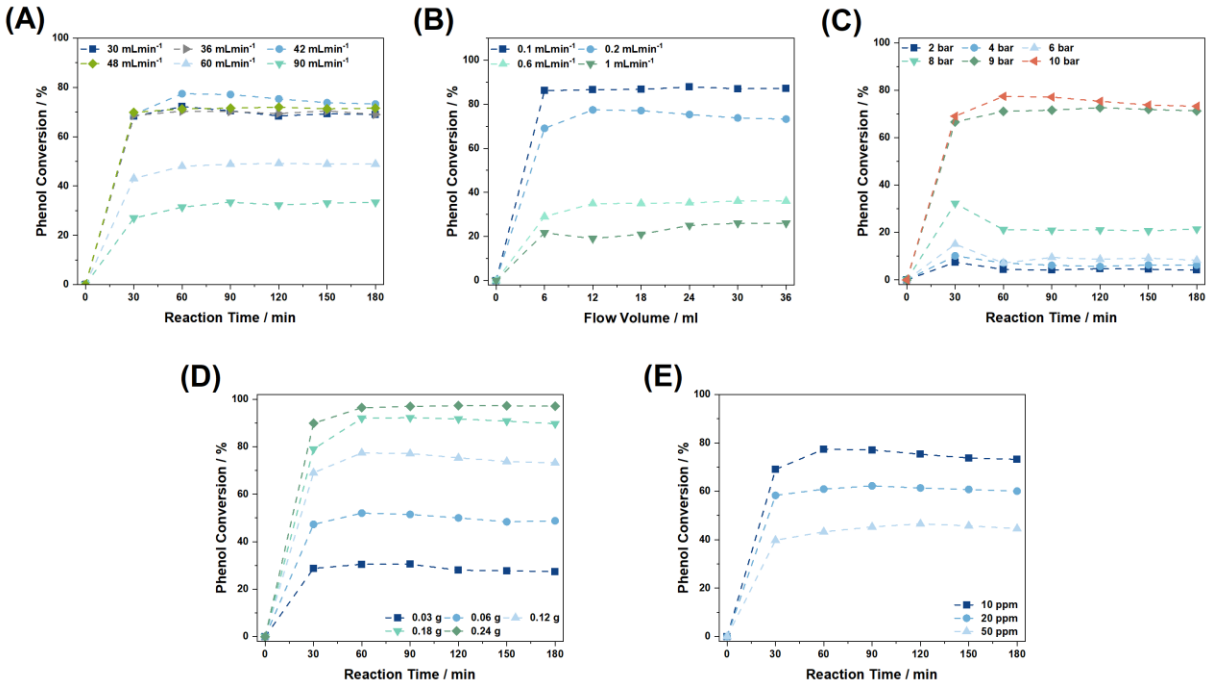

Figure 5.4. Optimisation of reaction conditions for the in-situ oxidative degradation of phenol over the $Au_{0.5}Pd_{0.5}/TiO_2$ catalyst. (A) The effect of gas and (B) liquid flow rates as well as (C) total gas pressure, (D) catalyst loading, and (E) phenol concentration on phenol degradation. Reaction conditions: catalyst (0.03 -0.24 g), SiC (4.1 g), phenol solution (10-50 ppm, in H_2O), total gas flow rate: 30-90 mL min^{-1}, total pressure 2-10 bar, total liquid flow rate: 0.1-1.0 mL min^{-1}, 20 °C.

5.2.5 Degradation of phenolic intermediates in the flow reactor using AuPd catalyst

With only 10 ppm initial phenol concentration used, the detection and analysis of phenolic intermediates became challenging than that of **Chapter 4**, where 1000 ppm phenol was utilized. With many of the phenolic derivatives posing greater health concerns than phenol itself, the catalytic efficacy towards the degradation of hydroquinone, catechol, benzoquinone, and

resorcinol was subsequently evaluated (**Figure 5.5**). Similar to previous observation in **Chapter 4 (Figure 4.5),** relatively high (>85% in general) rates of conversion were observed, somewhat higher than those observed for phenol itself, and clearly indicate the relative variation in the efficacy of reactive oxygen species towards the degradation of the various phenolic derivatives and the possible deep oxidation pathway.

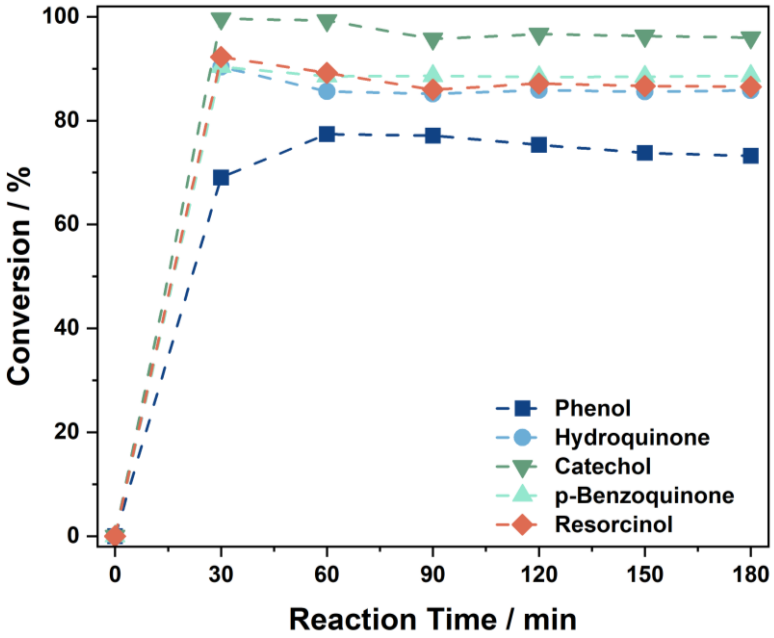

Figure 5.5. Catalytic activity towards the oxidative degradation of various phenolic intermediates over $Au_{0.5}Pd_{0.5}/TiO_2$ catalyst. **Reaction conditions:** catalyst (0.12 g), SiC (4.1 g), organic concentration (10 ppm), total gas flow rate: 42 mLmin^{-1} (H_2:O_2 = 1), 10 bar, liquid flow rate: 0.2 mL min^{-1}, 20 °C.

5.2.6 Degradation of other organic pollutants in the flow reactor using AuPd catalyst

To further examine the catalytic ability of the $Au_{0.5}Pd_{0.5}/TiO_2$ catalyst towards in situ water treatment. Some other organic components were selected as model pollutants for the continuous flow reactor tests. From **Figure 5.6** (with chemical structure presented) and **Table 5.5**, promising conversion rates steadily achieved across all organic components (phenol: 73%; Bisphenol A (BPA): 62%; Carbamazepine (CBZ): 98%; Tetracycline (TC): 99%; 5-fluorouracil (5-FU): 83%; Atrazine (ATZ): 100%; Quinmerac (QMRC): 99%) over 0.5%Au-0.5%Pd/TiO_2 catalyst with the presence of both H_2 and O_2.

Similar reactant gas control experiments were also conducted to further examine the contribution from either H_2 or O_2 only for these organic components. Several N-heteroaromatic/(halo)heterocyclic substrates underwent reduction/hydrogenation-dominated

reactions. CBZ, ATZ, and QMC reached 98%, 100% and 96% conversion under H_2 alone, respectively, while the contribution from O_2 alone is limited towards these components, with a maximal 4% conversion. König et al studied CBZ hydrogenation and revealed that on the surface of the platinum catalyst, the H-H bond of the sorbed H_2 molecule is weakened, and a syn-addition to the C=C double bond of the CBZ may occur.[34] Considering Pd is also a well-studied hydrogenation metal,[35,36] the hydrogenation reaction is highly likely to occur over the AuPd catalyst with the presence of H_2 only.

Other mixed-functionality pharmaceuticals show modest but reproducible co-feed gains relative to H_2 alone, BPA 62% (vs 51% H_2; 5% O_2), 5-FU 83% (vs 77% H_2; 7% O_2), and TC 99% (vs 93% H_2), with TC uniquely showing high conversion under O_2 only (87%), indicating intrinsic aerobic activatability on noble-metal surfaces even without a reductant.

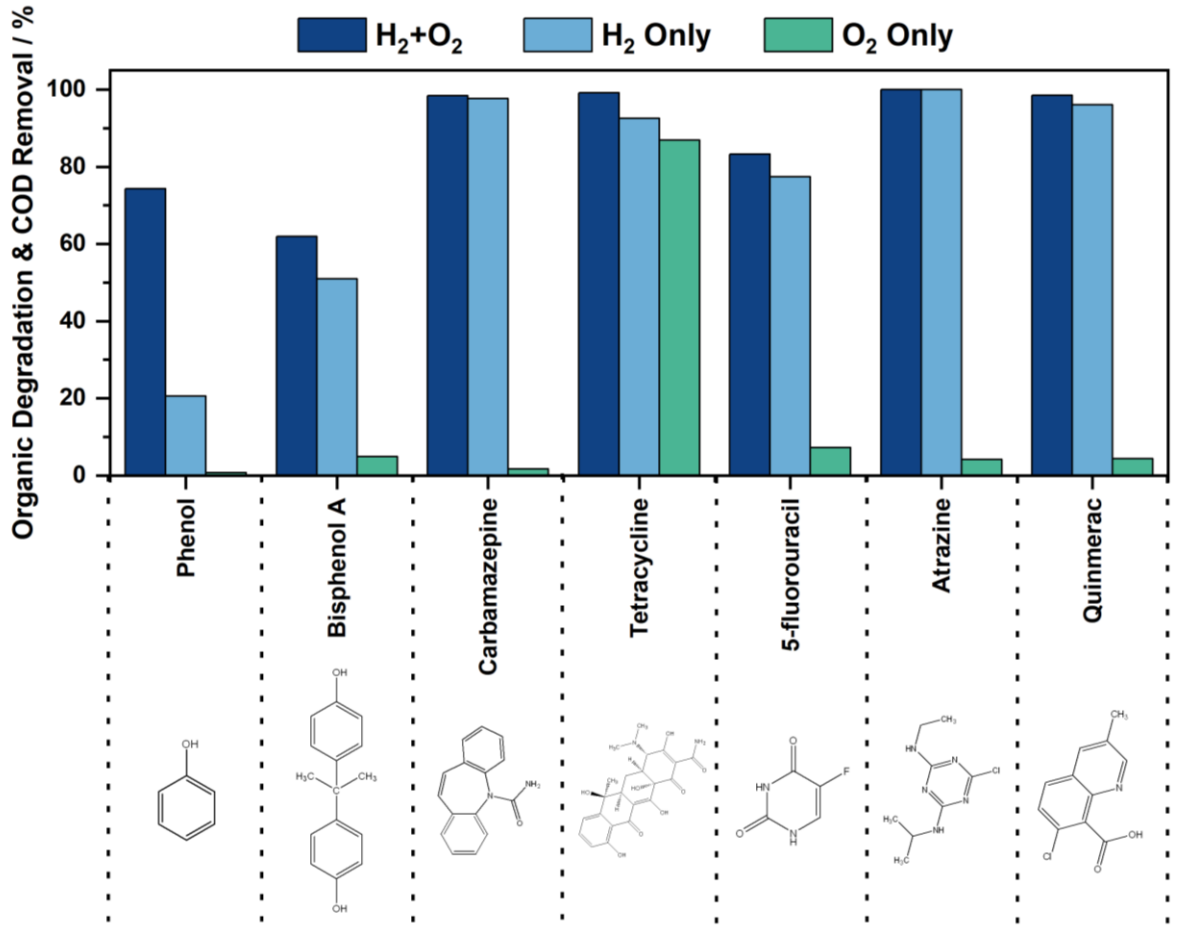

Figure 5.6. Catalytic activity towards the oxidative degradation of various organic pollutants over $Au_{0.5}Pd_{0.5}/TiO_2$ catalyst. Reaction conditions: catalyst (0.12 g), SiC (4.1 g), organic concentration (10 ppm), total gas flow rate: 42 mL min^{-1} (H_2:O_2 = 1), 10 bar, liquid flow rate: 0.2 mL min^{-1}, 20 °C.

Unfortunately, based on the reactant gas control experiments, the real contribution from H_2 and O_2 combined (i.e. the in situ route) could not be determined at this point due to the hydrogenation reaction being heavily involved. However, more evidence on the LC-MS would be supportive to illustrate the difference of intermediates between hydrogenation (with the presence of H_2 only) and oxidative degradation (with the presence of both H_2 and O_2). Chemical oxygen demand or total organic carbon analysis would be beneficial to distinguish the difference in organic carbon removal.

Table 5.5. Reactant gas control on the catalytic activity towards the oxidative degradation of various organic pollutants over $Au_{0.5}Pd_{0.5}/TiO_2$ catalyst. Reaction conditions: catalyst (0.12 g), SiC (4.1 g), organic concentration (10 ppm), total gas flow rate: 42 mL min^{-1} (H_2:O_2 = 1), 10 bar, liquid flow rate: 0.2 mL min^{-1}, 20 °C.

Organic Pollutants	$H_2 + O_2$	H_2 Only	O_2 Only
Phenol	73	20	1
Bisphenol A	62	51	5
Carbamazepine	98	98	2
Tetracycline	99	93	87
5-fluorouracil	83	77	7
Atrazine	100	100	4
Quinmerac	99	96	4

5.3 Conclusions

A series of TiO_2-supported AuPd catalysts was prepared via the incipient wetness method and utilised in a continuous flow reactor for long-term in situ water treatment with the presence of both H_2 and O_2 at room temperature. The introduction of Au into supported Pd catalysts shifted Pd oxidation state and enhanced catalytic performance, not only towards the direct synthesis of H_2O_2 but also the oxidative degradation of phenol via in-situ production of H_2O_2 and associated reactive oxygen species compared to the monometallic Au and Pd analogous.

Excellent phenol degradation performance requires intimate AuPd contact and true alloy formation when compared to the physically mixed Au and Pd. The reactant control experiment suggested the limited contributions from hydrogenation (via H_2 only), oxidation (via O_2 only), and preformed H_2O_2. Instead, the in situ oxidative degradation pathway dominated the phenol degradation in the presence of both H_2 and O_2.

Importantly, the optimal $Au_{0.5}Pd_{0.5}/TiO_2$ catalyst was found to be highly stable, with no loss in catalyst performance observed over 50 h on-stream towards phenol degradation. STEM-EDX and ICP-MS analysis revealed no alloy decomposition and metal leaching, respectively. We consider that these catalysts represent a promising basis for further exploration for the oxidative degradation of a range of recalcitrant.

Through optimisation of key reaction parameters, phenol degradation rates approaching 100 % may be achieved by altering the contact time, catalyst loading, and pressure. The high degradation efficacy towards the phenolic intermediates suggested the deep oxidation of phenol occurred. Meanwhile, the in situ oxidative degradation of other organic pollutants over AuPd catalyst was conducted. However, reactant gas control experiments could not exclude the contribution from H_2 only or O_2 only, and supportive evidence of the organic carbon removal rate could be potentially provided by chemical oxygen demand (COD) or total organic carbon (TOC) analysis.

5.4 Future Works

The results in this chapter establish a mechanistic basis for coupling oxidant generation and the subsequent activation over AuPd in a continuous flow system under mild reaction conditions. To consolidate and extend these findings toward durable, scalable processes, the following avenues merit priority.

- Qualify reaction oxygen species using electron paramagnetic resonance (EPR)
  EPR with appropriate spin traps (for example, DMPO or TEMP) should be applied at defined reaction times during in-situ H_2 and O_2 operation to detect $\cdot OH$, $O_2^{\cdot -}$, $\cdot OOH$ and other related intermediates.
- Liquid Chromatography-Mass Spectrometry (LC–MS) time-courses to map the oxidative degradation/hydrogenation/oxidation pathway of various organics
  High-resolution LC–MS should be used to build the degradation profiles for phenolic groups, pharmaceuticals, and pesticides in this Chapter. To determine the primary reaction that occurred in the flow reactor for different organics and to validate the proposed pathway.
- Chemical oxygen demand (COD) or Total Organic Carbon (TOC) metrics to quantify mineralisation

COD or TOC should be measured time on line series for the mineralisation of phenol and other organics over a bimetallic AuPd catalyst in the flow reactor. These assays differentiate transformation from true mineralisation, allowing comparison with discharge targets. Integrating COD or TOC with LC–MS will reveal whether added iron drives selectivity toward more complete oxidation rather than just faster phenol conversion.

- New preparation methods are needed to synthesize Fe-contained catalysts for the in situ flow reactor operation.

  Although Fe is one of the most famous Fenton metals in H_2O_2 activation to produce an extensive amount of reactive oxygen species, previous studies showed unsatisfactory catalyst stability during in situ phenol degradation due to the loss of Fe. Similarly, Fe-contained catalysts were synthesised and tested towards in situ phenol degradation in the flow system in this Chapter (**Figure A5.12**). The catalytic performance loss over time revealed that neither the co-impregnation nor the incipient wetness method is suitable for preparing Fe-contained catalysts for long-term use. New catalyst preparation methods are needed to stabilise Fe and maintain the high performance.

- Techno-economics and life-cycle assessment

  Quantify energy demand, gas consumption, catalyst cost, and greenhouse gas footprint of the flow reactor operation. Estimate the cost per cubic metre treated and compare with other continuous flow systems, for example, the continuous flow electron Fenton systems.[37,38]

5.5 Appendix

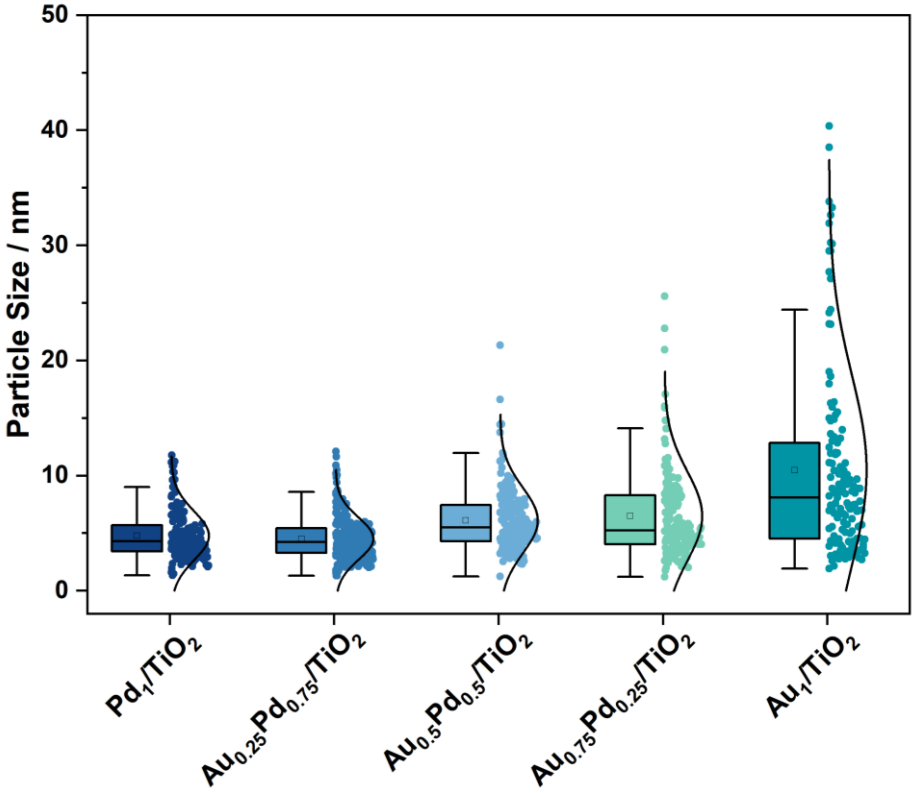

Figure A5.1. Particle size distribution of the as-prepared 1%AuPd/TiO_2 catalyst series.

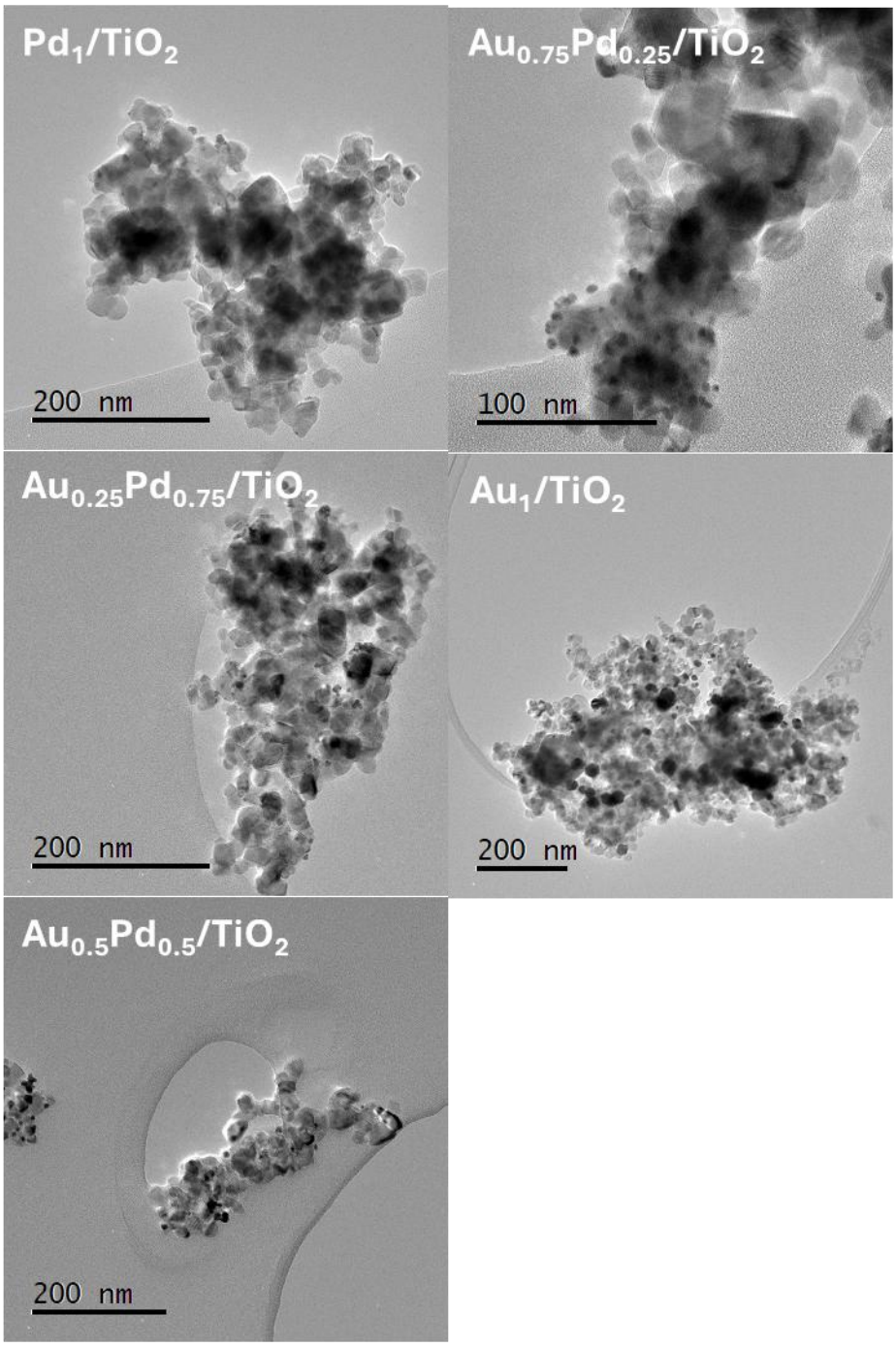

Figure A5.2. Representative bright field transmission electron micrographs of the as-prepared 1%AuPd/TiO_2 catalyst series.

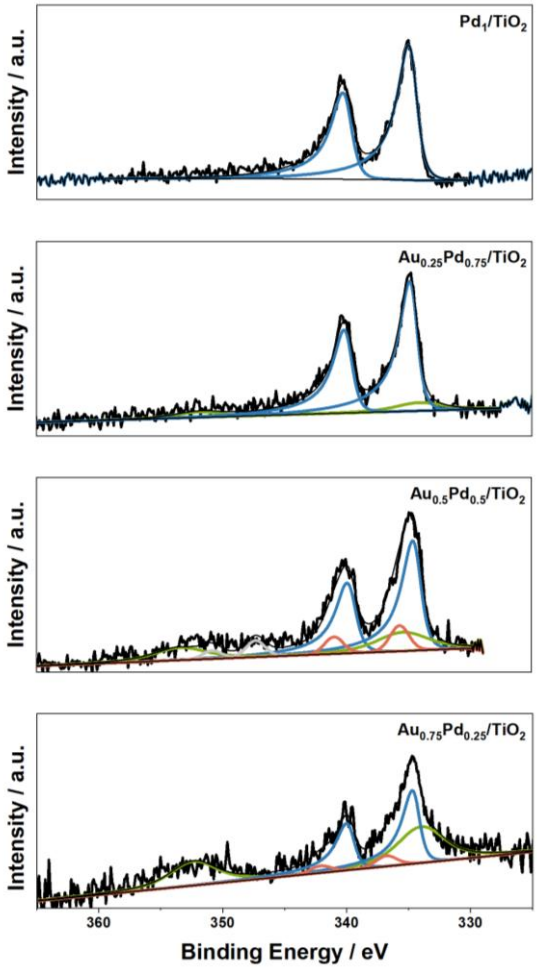

Figure A5.3. XPS spectra of Pd(3d) regions for the as-prepared 1%AuPd/TiO_2 catalyst series. ***Key*:** Pd^0 (*dark blue*), Pd^{2+}(*orange*), Au(4d) (*green*), Ca^{2+}(*grey*). **Please note**: the test and subsequent analysis were performed by Dr. David J. Morgan (Cardiff University; HarwellXPS).

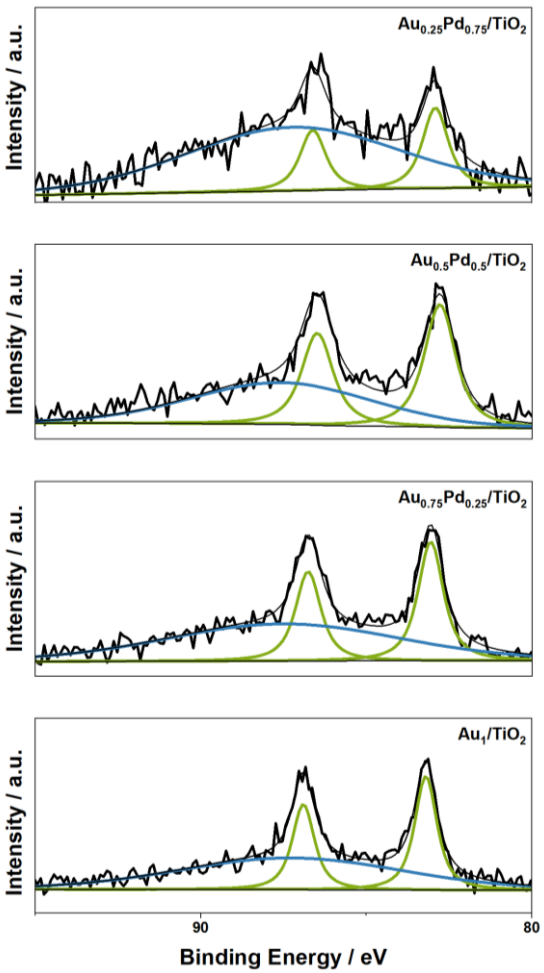

Figure A5.4. XPS spectra of Au(4f) regions for the as-prepared 1%AuPd/TiO_2 catalyst series. ***Key*:** Au(4f) (*green*), Pd(4s) and Ti loss *(blue)*. **Please note**: the test and subsequent analysis were performed by Dr. David J. Morgan (Cardiff University; HarwellXPS).

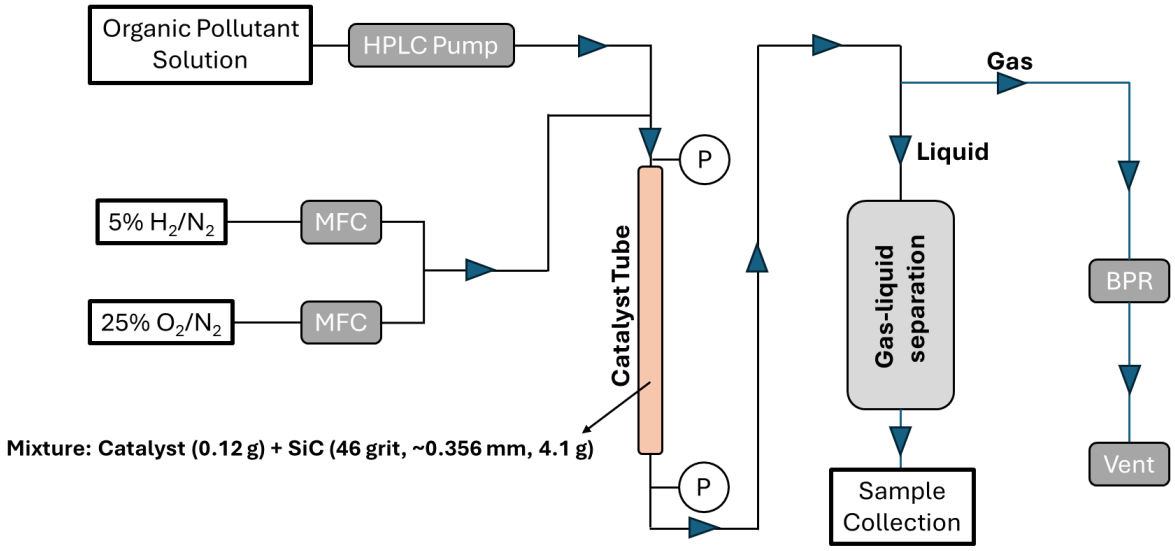

Figure A5.5.A. Schematic of the flow reactor used to evaluate catalytic performance towards the in-situ oxidative degradation of phenol. Please note: **P** = pressure gauge, **MFC** = mass flow controller, **BPR** = back pressure regulator.

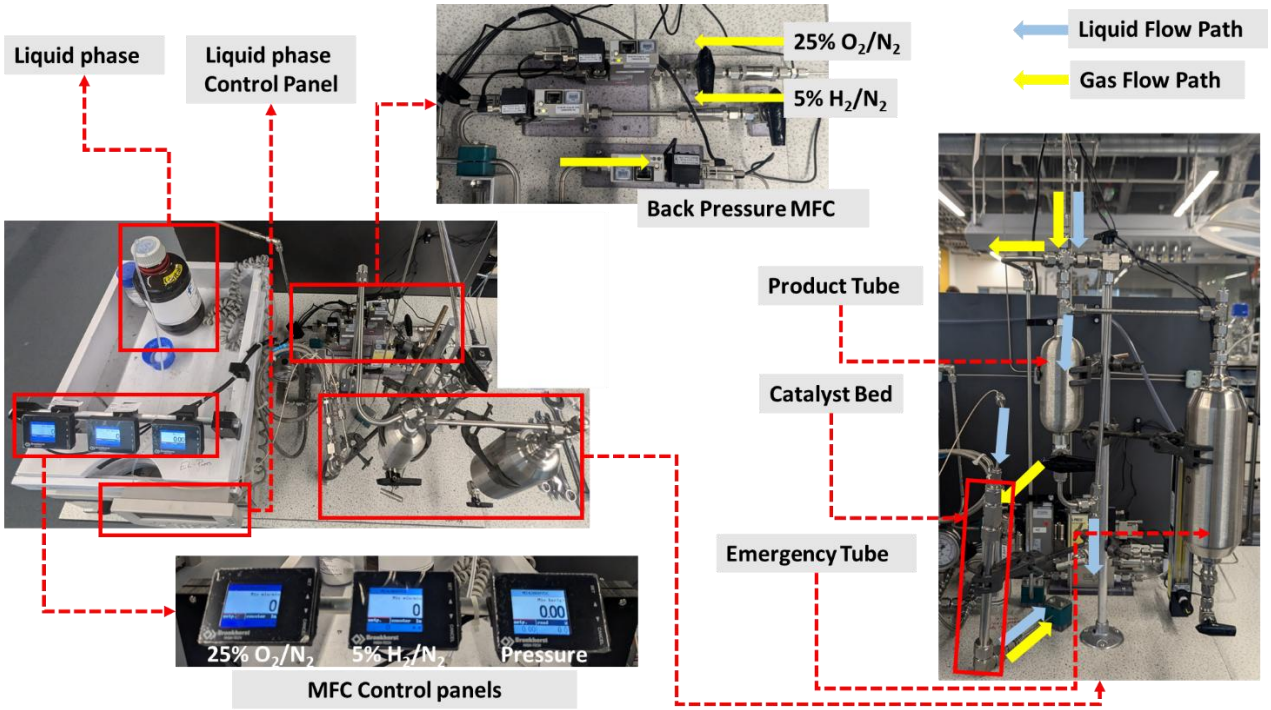

Figure A5.5.B. Annotated photograph of the flow reactor used to evaluate catalytic performance towards the in-situ oxidative degradation of phenol.

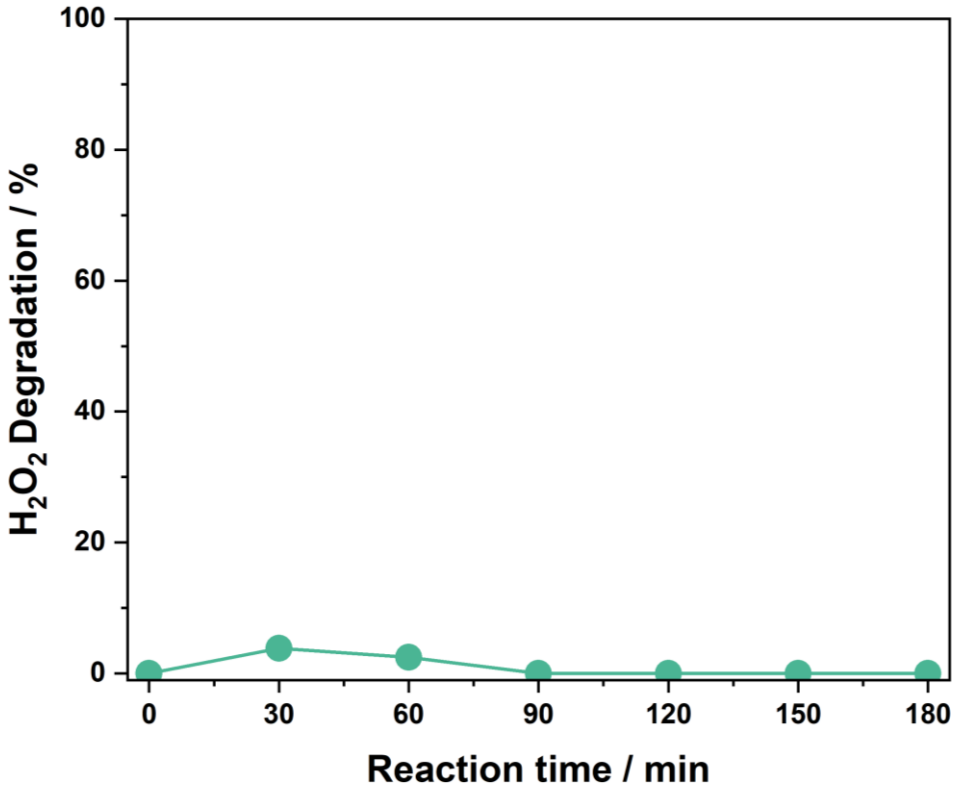

Figure A5.6. Control experiment demonstrating the negligible contribution of the SiC diluent to apparent degradation of H_2O_2. **Reaction conditions:** SiC (4.1 g), H_2O_2 (20 ppm, in H_2O), total gas flow rate: 42 mL min^{-1} (H_2:O_2 = 1), 10 bar, liquid flow rate: 0.2 mL min^{-1}, 20 °C.

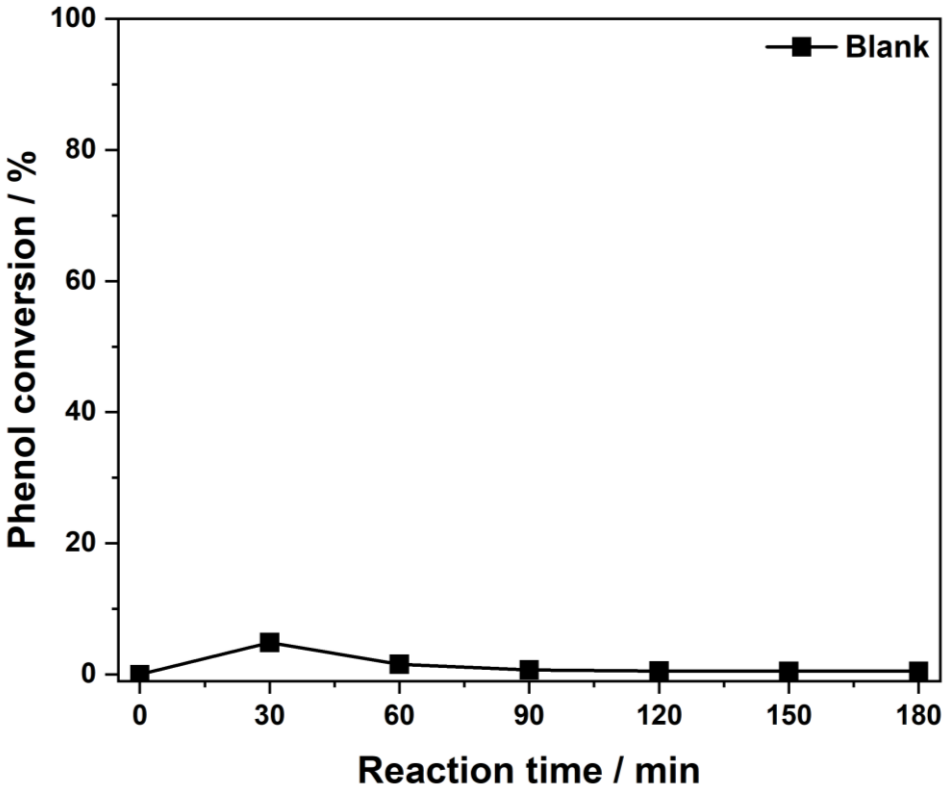

Figure A5.7. Control experiment demonstrating the negligible contribution of the SiC diluent to apparent phenol conversion. **Reaction conditions:** No catalyst, SiC (4.1 g), phenol solution (10 ppm, in H_2O), total gas flow rate: 42 mL min^{-1} (H_2:O_2 = 1), 10 bar, liquid flow rate: 0.2 mL min^{-1}, 20 °C.

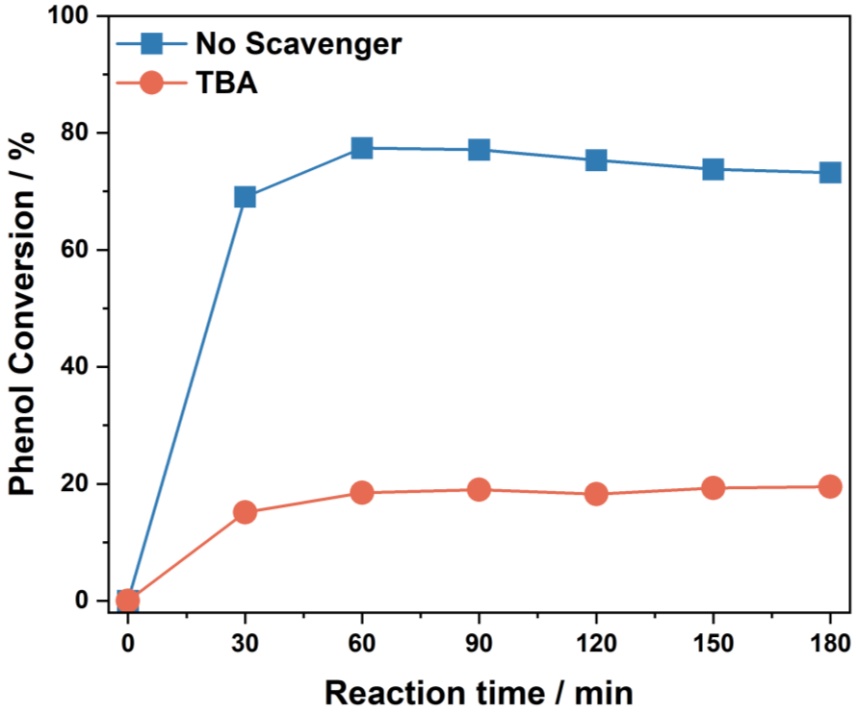

Figure A5.8. The effect of the radical quencher t-butanol on the oxidative degradation of phenol via the in-situ synthesis of H_2O_2 and associated reactive oxygen species. **Reaction conditions:** catalyst (0.12 g, $Au_{0.5}Pd_{0.5}/TiO_2$), SiC (4.1 g), phenol and tert-butanol (TBA) mixed solution (phenol: 10 ppm, TBA: 100 ppm), total gas flow rate: 42 mL min^{-1} (H_2: O_2 = 1), 10 bar, liquid flow rate: 0.2 mL min^{-1}, 20 °C.

Table A5.1. Catalyst stability during the in-situ oxidative degradation of phenol, as established by ICP-MS analysis of post-reaction solutions.

Catalyst	Leaching after 0.5 h		Leaching after 3 h	
	Au / μgL^{-1}	Pd / μgL^{-1}	Au / μgL^{-1}	Pd / μgL^{-1}
Au_1/TiO_2	0.0	-	0.0	-
$Au_{0.75}Pd_{0.25}/TiO_2$	0.0	0.1	0.0	0.0
$Au_{0.5}Pd_{0.5}/TiO_2$	0.0	0.1	0.0	0.0
$Au_{0.25}Pd_{0.75}/TiO_2$	0.0	0.3	0.0	0.0
Pd_1/TiO_2	0.0	0.3	0.0	0.0

Reaction conditions: catalyst (0.12 g), SiC (4.1 g), phenol solution (10 ppm, in H_2O), total gas flow rate: 42 mL min^{-1} (H_2:O_2 = 1), 10 bar, 0.2 mL min^{-1}, 20 °C.

Table A5.2. Catalyst stability of $Au_{0.5}Pd_{0.5}/TiO_2$ during the long-term in-situ oxidative degradation of phenol, as established by ICP-MS analysis of post-reaction solutions (up to 50 hours).

Reaction time / h	Au / ugL^{-1}	Pd / ugL^{-1}
0.5	0.0	0.1
3	0.0	0.0
5	0.0	0.0
10	0.0	0.0
20	0.0	0.0
30	0.0	0.0
40	0.0	0.0
50	0.0	0.0

Reaction conditions: catalyst (0.12 g), SiC (4.1 g), phenol solution (10 ppm, in H_2O), total gas flow rate: 42 mL min^{-1} (H_2:O_2 = 1), 10 bar, 0.2 mL min^{-1}, 20 °C.

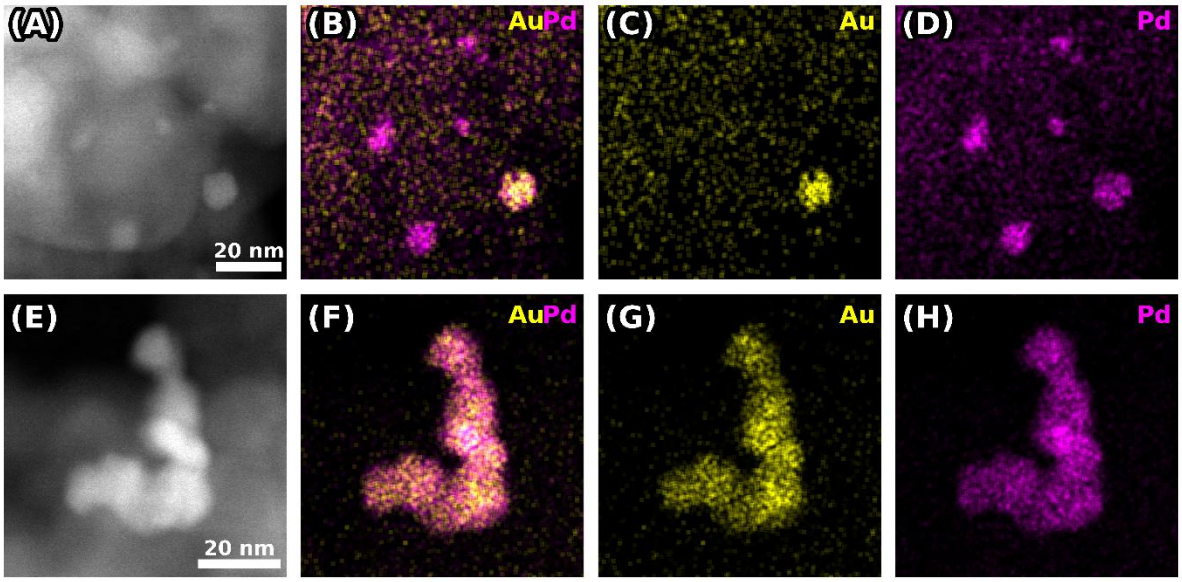

Figure A5.9. HAADF-STEM imaging and STEM-EDX mapping of (A-D) catalyst after 3 hours of reaction (showing development of individual Pd nanoparticles) and (E-H) catalyst after 50 hours of reaction (showing aggregation of AuPd nanoparticles) over $Au_{0.5}Pd_{0.5}/TiO_2$ catalyst. ***Key***: Au (*yellow*), Pd (*magenta*). **Reaction conditions:** catalyst (0.12 g), SiC (4.1 g), phenol solution (10 ppm, in H_2O), total gas flow rate: 42 mL min^{-1} (H_2:O_2 = 1), 10 bar, liquid flow rate: 0.2 mL min^{-1}, 20 °C.

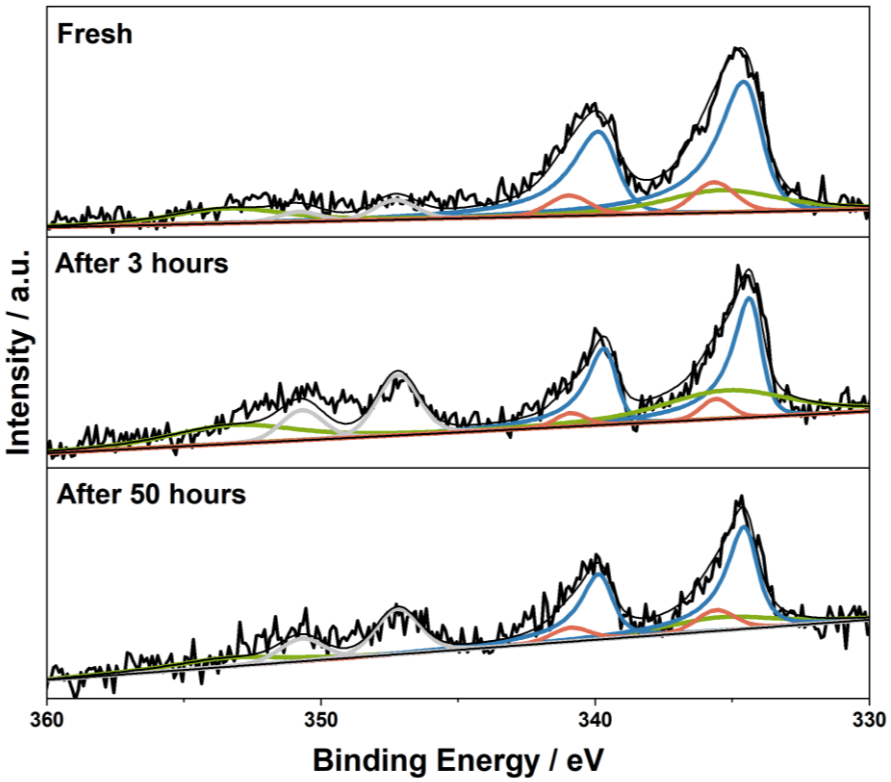

Figure A5.10. XPS spectra of Pd(3d) regions for the fresh and used (after3 hours and 50 hours) $Au_{0.5}Pd_{0.5}/TiO_2$ catalyst. ***Key*:** Pd^0 (*dark blue*), Pd^{2+}(*orange*), Au(4d) (*green*), Ca^{2+}(*grey*). **Please note**: the test and subsequent analysis were performed by Dr. David J. Morgan (Cardiff University; HarwellXPS).

Table A5.3. Au: Pd atomic ratio of the fresh and used (after 3 hours and 50 hours) $Au_{0.5}Pd_{0.5}/TiO_2$ catalysts as determined by XPS analysis.

Catalyst	Pd: Au	Pd^{2+} : Pd^0
Fresh	2.4	0.17
After 3 hours	2.8	0.13
After 50 hours	3.0	0.19

Reaction conditions: catalyst (0.12 g), SiC (4.1 g), phenol solution (10 ppm, in H_2O), total gas flow rate: 42 mL min^{-1} (H_2:O_2 = 1), 10 bar, liquid flow rate: 0.2 mL min^{-1}, 20 °C.

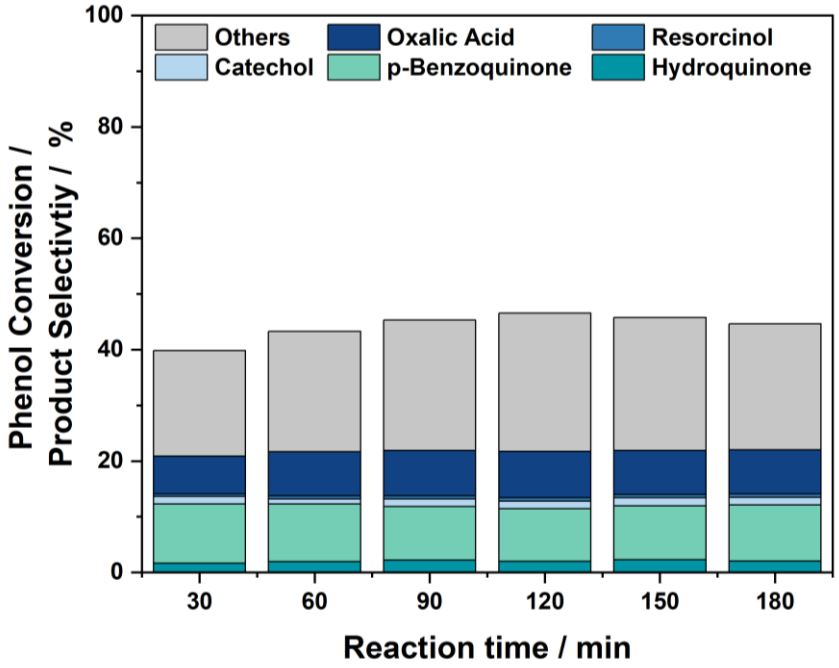

Figure A5.11. Quantification of the products of phenol degradation via the in-situ synthesis of H_2O_2 and associated ROS. **Reaction conditions:** catalyst (0.12 g, $Au_{0.5}Pd_{0.5}/TiO_2$), SiC (4.1 g), phenol solution (50 ppm, in H_2O), total gas flow rate: 42 mL min^{-1} (H_2:O_2 = 1), 10 bar, liquid flow rate: 0.2 mL min^{-1}, 20 °C.

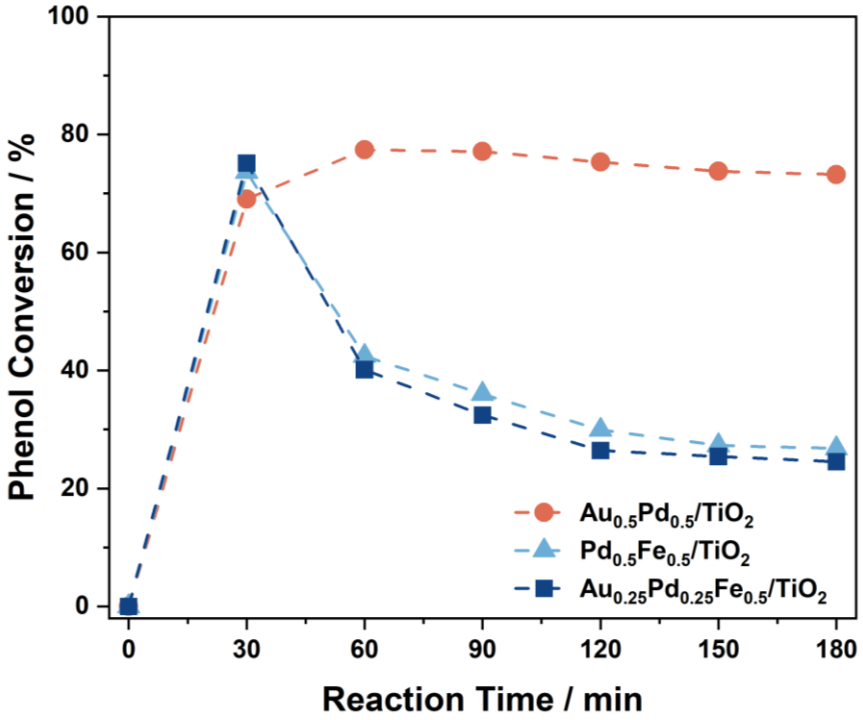

Figure A5.12. The performance of $Au_{0.5}Pd_{0.5}/TiO_2$, $Pd_{0.5}Fe_{0.5}/TiO_2$, and $Au_{0.25}Pd_{0.25}Fe_{0.5}/TiO_2$ catalysts towards the degradation of phenol via the in-situ production of H_2O_2. Reaction conditions: catalyst (0.12 g), SiC (4.1 g), phenol solution (10 ppm, in H_2O), total gas flow rate: 42 mL min^{-1} (H_2:O_2 = 1), 10 bar, liquid flow rate: 0.2 mL min^{-1}, 20 °C.

5.6 References

1. Johnson, A. C., Jin, X., Nakada, N. & Sumpter, J. P. Learning from the past and considering the future of chemicals in the environment. *Science (1979)* **367**, 384–387 (2020).

2. von Gunten, U. Oxidation Processes in Water Treatment: Are We on Track? *Environ Sci Technol* **52**, 5062–5075 (2018).

3. Ling, C. *et al.* Atomic-Layered Cu5 Nanoclusters on FeS2 with Dual Catalytic Sites for Efficient and Selective H2O2 Activation. *Angewandte Chemie* **134**, e202200670 (2022).

4. Hodges, B. C., Cates, E. L. & Kim, J.-H. Challenges and prospects of advanced oxidation water treatment processes using catalytic nanomaterials. *Nat Nanotechnol* **13**, 642–650 (2018).

5. Kato, S. & Kansha, Y. Comprehensive review of industrial wastewater treatment techniques. *Environmental Science and Pollution Research* **31**, 51064–51097 (2024).

6. Zhang, Q., Zheng, D., Bai, B., Ma, Z. & Zong, S. Insight into antibiotic removal by advanced oxidation processes (AOPs): Performance, mechanism, degradation pathways, and ecotoxicity assessment. *Chemical Engineering Journal* **500**, 157134 (2024).

7. Wu, J.-H. & Yu, H.-Q. Confronting the Mysteries of Oxidative Reactive Species in Advanced Oxidation Processes: An Elephant in the Room. *Environ Sci Technol* **58**, 18496–18507 (2024).

8. Xing, Y. *et al.* Fe/Fe3C Boosts H2O2 Utilization for Methane Conversion Overwhelming O2 Generation. *Angewandte Chemie* **133**, 8971–8977 (2021).

9. Xu, J. *et al.* Organic wastewater treatment by a single-atom catalyst and electrolytically produced H2O2. *Nat Sustain* **4**, 233–241 (2021).

10. Lewis, R. J. & Hutchings, G. J. Recent Advances in the Direct Synthesis of H2O2. *ChemCatChem* **11**, 298–308 (2019).

11. He, J. *et al.* Direct synthesis of H2O2 over Pd-In/TiO2 and in situ activation toward tetracycline degradation. *Mater Res Bull* **192**, 113584 (2025).

12. Underhill, R. *et al.* Oxidative Degradation of Phenol using in situ Generated Hydrogen Peroxide Combined with Fenton's Process. *Johnson Matthey Technology Review* **62**, 417–425 (2018).

13. Santos, A. *et al.* The degradation of phenol via in situ H2O2 production over supported Pd-based catalysts. *Catal Sci Technol* **11**, 7866–7874 (2021).

14. Richards, T. *et al.* A residue-free approach to water disinfection using catalytic in situ generation of reactive oxygen species. *Nat Catal* **4**, 575–585 (2021).

15. Santos, A. *et al.* The oxidative degradation of phenol via in situ H2O2 synthesis using Pd supported Fe-modified ZSM-5 catalysts. *Catal Sci Technol* **12**, 2943–2953 (2022).

16. Neyens, E. & Baeyens, J. A review of classic Fenton's peroxidation as an advanced oxidation technique. *J Hazard Mater* **98**, 33–50 (2003).

17. Ouyang, L. *et al.* Insight into active sites of Pd–Au/TiO2 catalysts in hydrogen peroxide synthesis directly from H2 and O2. *J Catal* **311**, 129–136 (2014).

18. Han, S. & Mullins, C. B. Surface Alloy Composition Controlled O2 Activation on Pd–Au Bimetallic Model Catalysts. *ACS Catal* **8**, 3641–3649 (2018).

19. Li, J., Ishihara, T. & Yoshizawa, K. Theoretical Revisit of the Direct Synthesis of H2O2 on Pd and Au@Pd Surfaces: A Comprehensive Mechanistic Study. *The Journal of Physical Chemistry C* **115**, 25359–25367 (2011).

20. Freakley, S. J. *et al.* Effect of Reaction Conditions on the Direct Synthesis of Hydrogen Peroxide with a AuPd/TiO2 Catalyst in a Flow Reactor. *ACS Catal* **3**, 487–501 (2013).

21. Wilson, N. M., Priyadarshini, P., Kunz, S. & Flaherty, D. W. Direct synthesis of H2O2 on Pd and AuxPd1 clusters: Understanding the effects of alloying Pd with Au. *J Catal* **357**, 163–175 (2018).

22. Gudarzi, D., Ratchananusorn, W., Turunen, I., Heinonen, M. & Salmi, T. Promotional effects of Au in Pd–Au bimetallic catalysts supported on activated carbon cloth (ACC) for direct synthesis of H2O2 from H2 and O2. *Catal Today* **248**, 58–68 (2015).

23. Edwards, J. K. *et al.* Direct Synthesis of H2O2 from H2 and O2 over Gold, Palladium, and Gold–Palladium Catalysts Supported on Acid-Pretreated TiO2. *Angewandte Chemie International Edition* **48**, 8512–8515 (2009).

24. Sharp, G. *et al.* Benzyl Alcohol Valorization via the In Situ Production of Reactive Oxygen Species. *ACS Catal* **14**, 15279–15293 (2024).

25. Sharp, G. *et al.* Highly efficient benzyl alcohol valorisation via the in situ synthesis of H2O2 and associated reactive oxygen species. *Green Chemistry* **27**, 5567–5580 (2025).

26. Garcia-Segura, S. & Brillas, E. Redesigning electrochemical-based Fenton processes: An updated review exploring advances and innovative strategies using phenol degradation as key performance indicator. *Applied Catalysis O: Open* **194**, 206980 (2024).

27. Tian, P. *et al.* The origin of palladium particle size effects in the direct synthesis of H2O2: Is smaller better? *J Catal* **349**, 30–40 (2017).

28. Brehm, J., Lewis, R. J., Morgan, D. J., Davies, T. E. & Hutchings, G. J. The Direct Synthesis of Hydrogen Peroxide over AuPd Nanoparticles: An Investigation into Metal Loading. *Catal Letters* **152**, 254–262 (2022).

29. Li, R.-J. *et al.* Promoting H2O2 direct synthesis through Fe incorporation into AuPd catalysts. *Green Chemistry* **27**, 2065–2077 (2025).

30. Kovačič, D. *et al.* A comparative study of palladium-gold and palladium-tin catalysts in the direct synthesis of H2O2. *Green Chemistry* **25**, 10436–10446 (2023).

31. Li, L. *et al.* Dual roles of MoS2 nanosheets in advanced oxidation Processes: Activating permonosulfate and quenching radicals. *Chemical Engineering Journal* **440**, 135866 (2022).

32. Jiang, H., Fang, Y., Fu, Y. & Guo, Q.-X. Studies on the extraction of phenol in wastewater. *J Hazard Mater* **101**, 179–190 (2003).

33. European Commission. Drinking water. Improving access to drinking water for all. (2023).

34. König, A. *et al.* Reductive transformation of carbamazepine by abiotic and biotic processes. *Water Res* **101**, 272–280 (2016).

35. Liu, Z. *et al.* Crystal facet engineering of Pd/TiO2 to boost the activity and selectivity for nitroarenes hydrogenation. *Chemical Engineering Journal* **503**, 158337 (2025).

36. Qiao, L. *et al.* Anion-Doping-Mediated Metal–Support Interactions in CeO2-Supported Pd Catalysts for CO2 Hydrogenation. *ACS Catal* **14**, 13181–13194 (2024).

37. Huang, Y. *et al.* A novel cost-effective flow-through electrode based on polyacrylonitrile carbon fiber for enhancing micropollutant degradation via electro-Fenton. *Chemical Engineering Journal* **477**, 147130 (2023).

38. Gao, M. *et al.* Fine-tune the electronic structure of single-atom Pd via halogen doping toward boosted Fenton-like reaction. *Applied Catalysis B: Environment and Energy* **371**, 125218 (2025).

Chapter 6 - Conclusion and Future Work

6.1 Conclusion

H_2O_2 is a green oxidant that has been widely used in different fields, for example, pulp/paper bleaching, textile, chemical synthesis, water treatment, etc.[1,2] Current large scale of H_2O_2 is produced from the auto-oxidation of anthraquinone, which involves in various toxic organic solvents during production and the downstream purification process.[3] Although batch production delivers highly concentrated H_2O_2, most end uses operate at far lower levels, e.g. under 30% in general and under 1% for wastewater treatment via the Fenton pathway.[4] The resulting requirements for extraction, stabilization, transport, and storage add cost and complexity that run counter to a green economy. As a more economical and environmentally friendly alternatives to the current industrial H_2O_2 production procedure via the auto-oxidation of anthraquinone, the direct synthesis of H_2O_2 from molecular H_2 and O_2 provides a direct route to produce H_2O_2 for on-site use.[2]

The direct synthesis of H_2O_2 has been well studied using supported bimetallic AuPd catalysts, which normally show the enhanced activity and selectivity towards H_2O_2 production due to the synergistic effect between Au and Pd, compared to the monometallic Pd catalysts.[2,5–10] Previous studies demonstrated that introducing a third element into the AuPd catalysts promotes H_2O_2 yield in situ (**Table 6.1**).[11–19] Initial studies on the use of precious metals like Ru and Pt were proposed by Hutchings group,[15,19] and subsequent studies by Lewis et al.,[16,17] and Gong et al.,[18] also found the promotive effect of Pt in the direct synthesis of H_2O_2 when cooperating with AuPd to form the trimetallic AuPdPt catalysts. Meanwhile, Barnes et al. also found the enhanced H_2O_2 productivity when introducing some non-precious based metals (e.g. Ni, Zn, Cu etc) with small quantities (0.025 wt.%) on different supports (TiO_2 and ZSM-5).[13,14]

Table 6.1 Catalytic performance of the AuPd-based trimetallic catalysts and their bimetallic AuPd analogues.

Catalyst	Productivity / $mol_{H2O2}kg_{cat}^{-1}h^{-1}$	H_2O_2 Conc. / wt.%	H_2 Conv. / %	H_2O_2 Sel. / %	Reference
1% Au_1Pd_1/TiO_2	81	0.16	39	31	[18]
1% $Au_1Pd_1Pt_{0.01}/TiO_2$	112	0.22	43	37	[18]
1%$AuPd/TiO_2$	61	0.13	12	59	[14]
1%$AuPd_{(0.975)}Pt_{(0.025)}/TiO_2$	106	0.22	-	-	[14]
1%$AuPd_{(0.975)}Ni_{(0.025)}/TiO_2$	107	0.22	32	41	[14]
1%$AuPd_{(0.975)}Sn_{(0.025)}/TiO_2$	78	0.16	-	-	[14]
1%$AuPd_{(0.975)}Cu_{(0.025)}/TiO_2$	94	0.19	31	40	[14]
1%$AuPd_{(0.975)}Co_{(0.025)}/TiO_2$	71	0.14	-	-	[14]
1%$AuPd_{(0.975)}In_{(0.025)}/TiO_2$	77	0.15	-	-	[14]
1%$AuPd_{(0.975)}Ga_{(0.025)}/TiO_2$	70	0.14	-	-	[14]
1%$AuPd_{(0.975)}Zn_{(0.025)}/TiO_2$	100	0.2	24	50	[14]
1%AuPd/ZSM-5	69	0.14	-	-	[13]
1%$AuPd_{(0.975)}Cu_{(0.025)}$/ZSM-5	115	0.23	19	72	[13]
1%$AuPd_{(0.975)}Ni_{(0.025)}$/ZSM-5	81	0.16	-	-	[13]
1%$AuPd_{(0.975)}Zn_{(0.025)}$/ZSM-5	77	0.16	-	-	[13]
2.5%Au-2.5%Pd/TS-1	100	-	-	-	[17]
2.4%Au-2.4%Pd-0.2%Pt/TS-1	167	0.33	-	-	[17]
0.33%Au-0.33%Pd/TS-1	104	-	-	-	[16]
0.275%Au-0.275%Pd-0.11%Pt/TS-1	135	0.27	-	-	[16]
2.5%Au-2.5%Pd/CeO_2	68	-	-	-	[15]
2.4%Au-2.4%Pd-0.2%Pt/CeO_2	170	0.34	-	-	[15]
$Au_{0.5}Pd_{0.5}/TiO_2$	70	0.14	19	39	Chapter 3
$Au_{0.5}Pd_{0.5}Fe_{0.02}/TiO_2$	122	0.24	40	31	Chapter 3

Reaction conditions: Catalyst (0.01 g), H_2O (2.9 g), MeOH (5.6 g), 5% H_2/CO_2 (420 psi), 25% O_2/CO_2 (160 psi), 0.5 h, 2 °C 1200 rpm

Inspired by these earlier works, in **Chapter 3**, a series of 1wt.%AuPd-xwt.%Fe/TiO_2 with different Fe loading (where X = 0, 0.01, 0.02, 0.05, 0.1, 0.5, 1) were prepared by the co-impregnation method and investigated for the catalytic performance towards the direct H_2O_2 synthesis and the subsequent H_2O_2 degradation, and a summary of the results for the AuPdFe series is presented in **Table 6.2.** A clear volcano-shaped trend was observed on the H_2O_2 productivity, where the trimetallic AuPdFe catalyst ($Au_{0.5}Pd_{0.5}Fe_{0.02}/TiO_2$) with the optimal small amount of Fe loading at 0.02 wt.% exhibited excellent catalytic activity towards the direct H_2O_2 production, with the highest H_2O_2 productivity (121 mol_{H2O2} Kg_{Cat}^{-1} h^{-1}), H_2O_2 concentration (0.242 wt.%) and H_2 conversion (40%), compared to the bimetallic $Au_{0.5}Pd_{0.5}/TiO_2$ catalyst (70 mol_{H2O2} Kg_{Cat}^{-1} h^{-1}; 0.139 wt.%;19%) and the Fe-rich trimetallic $Au_{0.5}Pd_{0.5}Fe_1/TiO_2$ catalyst (65 mol_{H2O2} Kg_{Cat}^{-1} h^{-1}; 0.129wt.%;16%). Although the

enhancement could be mainly associated with the increased catalytic activity toward H_2 activation rather than H_2O_2 selectivity based on the iso-conversion of 8% where the $Au_{0.5}Pd_{0.5}/TiO_2$ gave a H_2O_2 selectivity of 50% while $Au_{0.5}Pd_{0.5}Fe_{0.02}/TiO_2$ gave a H_2O_2 selectivity of 41% . A similar volcano-shaped trend was found on H_2O_2 degradation ($Au_{0.5}Pd_{0.5}/TiO_2$: 208 mol_{H2O2} Kg_{Cat}^{-1} h^{-1} ; $Au_{0.5}Pd_{0.5}Fe_{0.02}/TiO_2$: 451 mol_{H2O2} Kg_{Cat}^{-1} h^{-1}; $Au_{0.5}Pd_{0.5}Fe_1/TiO_2$: 287 mol_{H2O2} Kg_{Cat}^{-1} h^{-1}), suggesting that the optimal AuPdFe catalyst is active towards both H_2O_2 synthesis and the subsequent H_2O_2 degradation. Through the characterisation of the catalysts by X-ray photoelectron spectroscopy (XPS) and CO-DRIFTs, the enhanced catalytic performance could be attributed to the electron modification of Pd species with the introduction of a low quantity of Fe found to promote the formation of Pd^{2+}/Pd^0 mixed domains, which has been reported that it gives better H_2O_2 synthesis performance than that of the pure Pd^{2+} or Pd^0 domains,[20] and also the low Fe loading prevents the total reduction of Pd species to Pd^0 over time. Mössbauer spectroscopy and scanning transmission electron microscopy (STEM) found the surface modification of AuPd alloys upon the introduction of Fe with the formation of trimetallic AuPdFe alloys. Long term operational tests (time on line and gas replacement) on the key formulations ($Au_{0.5}Pd_{0.5}/TiO_2$, $Au_{0.5}Pd_{0.}5Fe_{0.02}/TiO_2$, $Au_{0.5}Pd_{0.5}Fe_1/TiO_2$) confirmed that the excellent catalytic ability of the optimal $Au_{0.5}Pd_{0.}5Fe_{0.02}/TiO_2$ towards H_2O_2 production, achieving 0.3 wt.% H_2O_2 concentration after 1 hour (in the time on line test) and 0.76 wt.% H_2O_2 concentration after 5 sequential reactions (in the gas replacement test). Meanwhile, the optimal trimetallic formulation outperformed most of the previously reported trimetallic catalysts in the time on line and gas replacement experiments under identical reaction conditions (**Figure 6.1 A and B**), showing promising and competitive catalytic ability towards direct H_2O_2 synthesis.[13,14,18] However, a drop in H_2O_2 productivity on the second use suggested that the loss of performance might be due to the loss of Cl^- during recycling process, evidence given by XPS analysis on Cl 2p, as it's well-known that the promote effect of halide ions on the activity and selectivity toward H_2O_2 synthesis.[10] Tech-economic analysis evaluated the cost of producing H_2O_2 using the selected trimetallic AuPdPt, AuPdFe, bimetallic AuPd, and monometallic Pd catalysts by calculating gas usage (H_2 and O_2), solvent cost, halide ions, but excluding the operational cost (e.g. electricity, labour etc).This analysis reveals that although the overall estimated cost of using AuPdFe catalysts to produce H_2O_2 compared to the monometallic Pd catalysts, yet no advantage for long term operation compared to the AuPdPt and bimetallic AuPd catalysts due to the limited H_2 or H_2O_2 selectivity, which associated with the cost of H_2.

Table 6.2. The catalytic performance of a series of AuPdFe catalysts towards the direct synthesis of H_2O_2 (including H_2O_2 concentration, H_2O_2 selectivity, H_2 conversion) and the subsequent H_2O_2 degradation.

Catalyst	Productivity / $mol_{H2O2}kg_{cat}^{-1}h^{-1}$	H_2O_2 Conc. / wt.%	H_2 Conv. / %	H_2O_2 Sel. / %	Degradation / $mol_{H2O2}kg_{cat}^{-1}h^{-1}$
$Au_{0.5}Pd_{0.5}/TiO_2$	70	0.139	19	39	208
$Au_{0.5}Pd_{0.5}Fe_{0.01}/TiO_2$	78	0.155	26	32	331
$Au_{0.5}Pd_{0.5}Fe_{0.02}/TiO_2$	121	0.242	40	31	451
$Au_{0.5}Pd_{0.5}Fe_{0.05}/TiO_2$	110	0.213	36	32	365
$Au_{0.5}Pd_{0.5}Fe_{0.1}/TiO_2$	105	0.210	33	32	353
$Au_{0.5}Pd_{0.5}Fe_{0.5}/TiO_2$	94	0.186	25	39	307
$Au_{0.5}Pd_{0.5}Fe_1/TiO_2$	65	0.129	16	42	287

H_2O_2 direct synthesis reaction conditions: Catalyst (0.01 g), H_2O (2.9 g), MeOH (5.6 g), 5% H_2/CO_2 (420 psi), 25% O_2/CO_2 (160 psi), 0.5 h, 2 °C 1200 rpm. **H_2O_2 degradation reaction conditions:** Catalyst (0.01 g), H_2O_2 (50 wt% 0.68 g) H_2O (2.22 g), CH_3OH (5.6 g), 5% H_2/CO_2 (420 psi), 0.5 h, 2 °C 1200 rpm.

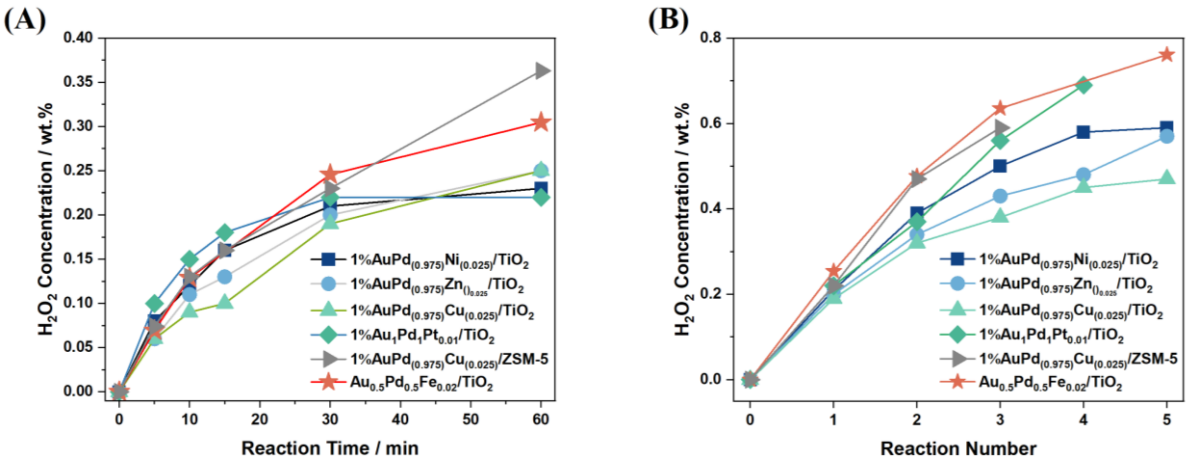

Figure 6.1. Catalytic performance comparison of a series of trimetallic AuPd-based catalysts in the (A) Time on line test and (B) gas replacement tests. Reaction conditions: Catalyst (0.01 g), H_2O (2.9 g), MeOH (5.6 g), 5% H_2/CO_2 (420 psi), 25% O_2/CO_2 (160 psi), 0.5 h, 2 °C 1200 rpm. **Reference:** $1\%AuPd_{(0.975)}Ni_{(0.025)}/TiO_2$,[14] $1\%AuPd_{(0.975)}Zn_{(0.025)}/TiO_2$,[14] $1\%AuPd_{(0.975)}Cu_{(0.025)}/TiO_2$,[14] $1\%Au_1Pd_1Pt_{0.01}/TiO_2$,[18] $1\%AuPd_{(0.975)}Cu_{(0.025)}/ZSM\text{-}5$,[13] $Au_{0.5}Pd_{0.5}Fe_{0.02}/TiO2$ (Chapter 3)

H_2O_2 has been widely used in many different chemical reactions as it's oxidative nature, for example, water treatment, via advanced oxidation processes (AOPs).[21] Appling Fenton system in water treatment has been extensively studied, mainly using homogeneous or heterogeneous catalysts to activate H_2O_2 to produce reactive oxygen species (ROS) for the organic pollutants decomposition and total mineralization.[22] Recent years, there is a growing interest in the in situ water treatment via the in situ generated H_2O_2 and ROS.[23] Richards et al. and Santos et al. reported highly reactive bimetallic Pd-based catalysts (e.g. PdFe formulations on different supports) were found to facilitate H_2O_2 synthesis, mainly on Pd active sites effectively, and subsequent H_2O_2 activation, mainly on the Fenton metal active sites, achieving an appreciable phenol degradation rates in situ. However, the stability is a great concern for these PdFe formulations to perform long-term operational test in the in situ phenol degradation.[24–26]

Building on these works, in **Chapter 4**, a series of mono, bi, and trimetallic AuPdFe catalysts was synthesized by co-impregnation method and evaluated the catalytic performance towards direct H_2O_2 synthesis and the subsequent oxidative degradation of phenol in a batch reactor operated at room temperature without alcohol. Unlike the H_2O_2 synthesis reaction under the ideal conditions (sub-ambient temperatures, presence of alcohol co-solvents etc), the activity for in situ H_2O_2 formation decreases, yet consistent with prior work on AuPd systems,[6,27,28] the bimetallic benchmark $Au_{0.5}Pd_{0.5}/TiO_2$ still outperforms $Pd_{0.5}/TiO_2$ at equal Pd loading through higher selectivity to H_2O_2 at comparable H_2 conversion. Introducing Fe progressively into AuPd suppresses selective H_2O_2 production by lowering selectivity and increasing overall H_2 consumption. In contrast, the rate of in situ phenol degradation exhibits the opposite dependence on Fe loading, with a clear volcano type trend that peaks at about 2 wt.% Fe, at which composition the trimetallic catalyst delivers the highest phenol conversion at 83%, exceeding the bimetallic analogue by more than ten-fold, while additional Fe loading up to 3 wt.% diminishes performance toward phenol degradation to 73%. Control experiments establish a coherent mechanism since phenol adsorption is negligible, feeds containing only H_2 or only O_2 show no meaningful conversion, and a single batch charge of commercial H_2O_2 with or without the heterogeneous catalyst is much less effective than the in situ route. The intermediate analysis revealed that the hydroxylated byproducts (e.g. hydroquinone and catechol) dominated, which is consistent with Fenton pathways mediated by ROS, particularly ·OH.

XPS analysis of fresh materials show a significant shift of Pd oxidation state to Pd^{2+} upon the addition of Fe and, taken together with the reactivity trends, point to rapid in reduction to Pd^0

in Fe-rich formulations, as evidenced in **Chapter 3**, while CO-DRIFTs reveals the electron modification of Pd species by the introduction of Fe. Experiments that deliberately separate functions confirm the need for colocation since physical mixtures of $Au_{0.5}Pd_{0.5}/TiO_2$ (mainly for the in situ H_2O_2 generation) with Fe_2/TiO_2 (mainly for H_2O_2 activation and radical generation) give only modest gains relative to AuPd alone and pairing AuPd with homogeneous Fe species increases conversion further yet still remains below the integrated trimetallic catalyst ($Au_{0.5}Pd_{0.5}Fe_2/TiO_2$). Catalyst stability is nevertheless a challenge with a remarkable loss of activity together with substantial Fe loss observed, and notably the used catalyst exhibits higher H_2 conversion in the in situ phenol degradation and a higher rate of H_2O_2 formation than the fresh sample, which reflects Pd reduction and the loss of Fe that had previously accelerated nonselective H_2O_2 decomposition. Hot filtration tests reveal that the filtrate from an AuPdFe run retains substantial oxidative activity and responds strongly to added H_2O_2, which confirms a non-negligible homogeneous Fe contribution, yet reintroducing $Au_{0.5}Pd_{0.5}/TiO_2$ into such filtrates suppresses H_2 activation consistent with coordination or blocking of Pd sites by homogeneous Fe complexes, so while homogeneous Fe can accelerate the Fenton step, uncontrolled leaching simultaneously undermines the upstream AuPd function that supplies oxidant through H_2 activation.[5]

To benchmark the catalytic performance of the in situ Fenton system, a comparison with other phenol oxidation systems was performed and is summarised in **Table 6.3**. Based on phenol degradation efficiency, the catalyst reported in this work achieves 2981 $mmol_{phenol}\ g_{Cat}^{-1}\ h^{-1}$, which is comparable with previously reported PdFe catalysts, including 2.5%Pd-2.5%Fe/TiO_2 (3522 $mmol_{phenol}\ g_{Cat}^{-1}\ h^{-1}$), 0.5%Pd-0.5%Fe/$TiO_2$ (1761 $mmol_{phenol}\ g_{Cat}^{-1}\ h^{-1}$), and 0.5%Pd-3 wt.%Fe/ZSM-5 (3161 $mmol_{phenol}\ g_{Cat}^{-1}\ h^{-1}$). In these studies, higher Fe loadings generally corresponded to higher apparent activity, which is consistent with reports of substantial Fe leaching during in situ phenol degradation tests. This suggests a noticeable contribution from dissolved iron via homogeneous Fenton chemistry, alongside the heterogeneous catalytic pathway.

Table 6.3. The comparison of catalytic performance towards in situ phenol degradation in the in situ Fenton systems.

Catalyst	Phenol degradation rate / %	H_2 conversion / %	Test time / hour	Phenol degradation efficiency / $mmol_{Phenol}\ g_{Cat}^{-1}\ h^{-1}$	Reference
2.5%Pd/TiO_2	4	n/a	2	181	[26]
2.5%Pd-2.5%Au/TiO_2	3.8	n/a	2	172	[26]
2.5%Pd-2.5%Cu/TiO_2	3.5	n/a	2	158	[26]
2.5%Pd-2.5%Mn/TiO_2	3.2	n/a	2	145	[26]
2.5%Pd-2.5%Fe/TiO_2	78	n/a	2	3522	[26]
1%Pd/TiO_2	11	n/a	2	497	[24]
0.5%Pd-0.5%Au/TiO2	12	n/a	2	542	[24]
0.5%Pd-0.5%Cu/TiO2	6	n/a	2	271	[24]
0.5%Pd-0.5%Co/TiO2	6	n/a	2	271	[24]
0.5%Pd-0.5%Fe/TiO2	39	38	2	1761	[24]
0.5%Pd/ZSM-5	38	70	2	1716	[25]
0.5%Pd-3%Fe/ZSM-5	70	48	2	3161	[25]
0.5%Au-0.5%Pd/TiO2	5	43	2	226	This work
0.5%Au-0.5%Pd-2%Fe/TiO2	66	16	2	2981	This work

Reaction conditions: catalyst (0.01 g), phenol (1000 ppm, 8.5 g), 5% H_2/CO_2 (420 psi), 25% O_2/CO_2 (160 psi), 20°C, 1200 rpm.

While considerable attention has been placed on the direct synthesis of H_2O_2 and the subsequent H_2O_2 activation for water treatment using batch regimes,[24–26] for application in real world water treatment, the use of a continuous flow system is likely to be more favourable. The initial flow reactor work within the Hutchings group, on the direct synthesis of H_2O_2 using bimetallic 1wt.%AuPd/TiO_2 catalysts was investigated by Freakley et al., by optimizing the reaction conditions, the highest H_2O_2 yield (760 ppm) was achieved over 30 mins on-stream with methanol as an organic co-solvent.[29] Building on this earlier study, Richard et al.[30] demonstrated that it is still possible to produce considerable amounts of H_2O_2 (202 ppm) using just water as the reaction medium, and further proposed the efficiency of the 1wt.% AuPd/TiO_2 towards the E.coli remediation via the in situ generated H_2O_2 and ROS. Experimental results confirmed that maximal 8.1 log_{10} E.coli remediation was observed over the 0.5%Au-0.5%Pd/TiO_2 catalyst, outperformed the monometallic Au (1.6 log_{10} E.coli) and Pd (2.6 log_{10} E.coli) analogous. The in situ E.coli remediation system is far more effective than using pre-formed commercial H_2O_2 and NaOCl (5 - 10000 ppm), which each gave $\leqslant$1 log10 reduction. Electron paramagnetic resonance (EPR) and spin-trapping reagents indicate that ROS (e.g. OH, $^{\cdot}$OOH) produced during H_2O_2 formation drive the kill, and based on the experimental

results, Au is required to release these radicals into solution, consistent with reports that Au promotes H_2O_2 release during direct synthesis.

Although the work reported in **Chapter 4** showed the excellent catalytic ability of the Fe-contained PdFe and AuPdFe catalysts towards efficient phenol degradation, the Fe leaching is a concern on the reusability and long-term operation. The initial experimental results reported in **Chapter 5** suggested that the PdFe and AuPdFe catalysts prepared via the wet-incipient method are also not suitable for long term phenol degradation in the flow regime. With the evidence given by the previous studies that the bimetallic AuPd is active towards both H_2O_2 synthesis and the subsequent bacterial remediation process,[30] the application of this continuous flow system on the in situ organic pollutants removal seems promising. A series of TiO_2 supported mono- and bimetallic AuPd catalysts were prepared via the incipient wetness method and pressed to pellet (0.25-0.425 mm) prior to use in the in situ water treatment in a flow regime in **Chapter 5**. Experimental results on the effect of Au:Pd ratio gave a similar conclusion to the previous E.coli work that synergistic effect between Au and Pd promotes the catalytic performance towards the in situ generation of H_2O_2 and ROS,[30] where the bimetallic AuPd catalysts (up to 80%) outperformed monometallic Au (2%) and Pd (58%) analogous, in terms of the 3 hours in situ phenol degradation on-stream. Minimal Pd leaching (≤ 0.3 μg L^{-1}) was observed at the initial 30 mins and no detectable metal leaching (for both Au and Pd) up to 3 hours across all AuPd series, suggesting the reasonable stability of the AuPd series prepared via the incipient wetness method. Further investigation using H_2 only, O_2 only, pre-formed H_2O_2, and the physical separation of metal components, suggested that the in situ generated H_2O_2 and ROS are the main effective source for the oxidative degradation of phenol, similar to the observation from **Chapter 4**. Long term stability test was conducted using the bimetallic $Au_{0.5}Pd_{0.5}/TiO_2$ catalyst for the in situ phenol degradation up to 50 hours, with no performance loss observed with a stable $\geq$ 70% phenol degradation rate achieved over 50 hours on-stream. XPS and STEM analysis on the fresh, after 3 hours and after 50 hours samples confirmed that the stable Pd oxidation state and minimal morphology changes might be the case for the long term stable operation. Further application of this oxidative flow system to various organic pollutants (pharmaceuticals, pesticides etc) confirmed the promising conversion rates steadily achieved across all organic components (phenol: 73%; Bisphenol A: 62%; Carbamazepine: 98%; Tetracycline: 99%; 5-fluorouracil: 83%; Atrazine): 100%; Quinmerac: 99%) over $Au_{0.5}Pd_{0.5}/TiO_2$ catalyst with the presence of both H_2 and O_2. However, reactant gas control experiments was found the H_2-mediated hydrogenation or O_2-mediated oxidation dominated

the conversion of the selected organics (excluding phenol), and it's unfortunate not be able to calculate the contribution from the oxidative reaction via the Fenton pathway.

6.2 Future work

The future work section was formulated based on the experimental results given by **Chapter 3-5**, mainly focused on the, **1)** improving catalyst stability and reusability for long term operation by exploring other catalyst preparation method, **2)** further investigation of the reaction mechanism in the in situ H_2O_2 synthesis and phenol degradation process, using advanced characterization techniques and theoretical calculation, **3)** future potential to apply the continuous flow system for various oxidative reactions.

The catalyst stability for both the direct synthesis of H_2O_2 and the in situ oxidative degradation of phenol in the batch regime has been identified as an issue throughout **Chapter 3** and **Chapter 4**, when using the catalysts prepared via the co-impregnation method. For **Chapter 3**, the metal leaching was under the detection limits for the selected formulations ($Au_{0.5}Pd_{0.5}/TiO_2$, $Au_{0.5}Pd_{0.5}Fe_{0.02}/TiO_2$, and $Au_{0.5}Pd_{0.5}Fe_1/TiO_2$) during direct synthesis of H_2O_2 up to 3 hours. However, the insufficient reusability of the key sample ($Au_{0.5}Pd_{0.5}Fe_{0.02}/TiO_2$) could be attributed to the loss of surface chloride during the initial use (evidence given by XPS-Cl 2p analysis), as demonstrated by Brehm et al.,[14] halide ions can act as a promotor in the H_2O_2 synthesis reaction. Also, for **Chapter 4**, substantial Fe leaching, greater than 60%, was detected on the key formulation ($Au_{0.5}Pd_{0.5}Fe_2/TiO_2$) in the in situ phenol degradation tests. Indeed, such high level of Fe leaching is associated with the harsh reaction conditions, namely the highly acidic reaction medium, as reported in **Chapter 4**, the pH dropped below 3 after 1 hour of reaction and remained up to 6 hours, driven by the in situ generated phenol byproducts (e.g. phenolic intermediates and organic acids), together with an extended retention time of up to 6 hours. Under more representative operating conditions with lower pollutant concentration and relatively shorter retention time, Fe leaching is expected to drop and the long term stability might not be a great concern. This finding indicates that the current co-impregnation method with chlorine based precursors such as $PdCl_2$ and $HAuCl_4$ is unlikely to support a stable long-term H_2O_2 production and the subsequent H_2O_2 activation via Fenton pathway, because residual halides can alter Pd or AuPd surface ensembles and promote both non selective H_2O_2 decomposition and metal leaching.[31,32] Although short term benefits from halide coordination have been reported under specific conditions, the difficulty of

controlling halide content during continuous operation makes chloride co-impregnation a durability risk.[31,33] Future efforts should prioritise halide free and reproducible syntheses, for example using nitrate or acetate salts and strong electrostatic adsorption to anchor cationic precursors with rigorous post washing to remove anions.[34] Sol or colloidal immobilisation with careful post treatments has also provided tight control over AuPd particle size and composition in direct H_2O_2 synthesis.[35] Acid assisted deposition and support pre acidification merit systematic evaluation because this route to catalyst synthesis offers suppression of the hydrogenation pathway together with control of Pd oxidation state and increased metal dispersion, improving activity and selectivity under chloride free conditions.[36] For the Fe component that activates H_2O_2 the priorities are resistance to leaching and rational spatial coupling with the H_2O_2 synthesis sites. Constructing Fe as isolated Fe sites coordinated by four nitrogen atoms on N doped carbons or as strongly bound FeO_x clusters on robust oxides such as TiO_2 can preserve high activity near neutral pH while greatly reducing Fe release and improving cycling stability.[37] Also, ultrathin conformal overlayers prepared by atomic layer deposition can be explored to pin Fe species and passivate dissolution prone sites while maintaining permeability to H_2O_2 and substrates.[38,39]

Experimental results from previously reported trimetallic AuPd-based catalysts and the trimetallic AuPdFe catalyst presented in **Chapter 3** found that doping a small amount (e.g. 0.02 wt.%) of the third metal (e.g. Pt, Cu, Zn, Ni, Fe etc) could effectively promote the activity or selectivity towards the direct H_2O_2 synthesis and according to the XPS and CO-DRIFTs analysis, the main cause proposed in these studies is the electron modification of Pd species.[13,14,18] However, it is still unclear how those small amount of third metals could significantly modify Pd species and regulate the electron transfer during reaction. To gain further insight into the reaction mechanism, a systematic study should be conducted focusing on AuPd-based trimetallic catalysts where a dopant promotive effect is observed, and utilizing theoretical calculation (e.g. density function theory (DFT)) to illustrate if the activation energy for H_2O_2 synthesis is truly lower on these trimetallic platforms compared to the bimetallic AuPd catalysts, with the experimental results and the theoretical evidence, the promotive effect of the third metal on the AuPd catalyst could hopefully be explained. Additionally, in situ X-ray absorption spectroscopy could be used to prob the dynamic change of Pd oxidation state,[40] e.g. during the H_2O_2 synthesis reaction provide insight into the effect of Fe on Pd oxidation state by comparing the bimetallic AuPd, PdFe, and the trimetallic AuPdFe catalysts, under reaction conditions.

Previous study has already utilized EPR to probe ROS (·OOH and ·OH) during the reaction in the AuPd system for E.coli remediation via the in situ generated H_2O_2 and ROS.[30] However, no further EPR analysis has been conducted in previous PdFe studies, focused on the remediation of chemical pollutants. Although the intermediate analysis in **Chapter 4** indicated the generation of hydroxylated phenolic intermediates and suggested that the ·OH is main reactive species based on the experimental results. However, the existence of other possible ROS (·OOH, $O_2^{\cdot-}$, $^1O_2$ and others) still remains unknown. In **Chapter 5**, due to the low concentration of phenol used in the in situ oxidation system, it was challenging to analyse the quantities of different intermediates thus it was not possible to qualify the main ROS in the system. Using EPR with spin trapping reagents such as 5,5-dimethyl-1-pyrroline N-oxide (DMPO, mainly for ·OH, $O_2^{\cdot-}$, ·OOH etc) and 2,2,6,6-Tetramethylpiperidine (TEMP, mainly for $^1O_2$),[41,42] at defined reaction times during in situ operation should quantify ROS, with parallel measurements during direct H_2O_2 synthesis, in situ phenol degradation with both gases present, and control feeds with H_2 only, O_2 only, and commercial H_2O_2, so that radical generation can be correlated with catalyst composition and gas regime. The contribution of homogeneous Fe species is non-negligible in the in situ phenol degradation process and a Fe redox cycle seems exist in the oxidation system. UV vis spectroscopy of post reaction solutions from in situ systems using $Au_{0.5}Pd_{0.5}/TiO_2$ and $Au_{0.5}Pd_{0.5}Fe_2/TiO_2$ and from an ex situ system with homogeneous Fe and pre formed H_2O_2 should test for homogeneous phenolic-Fe complexes, since distinct shoulders around 400 nm reported by Chen and co-workers for related systems would provide strong evidence of self-catalytic mechanism where the phenolic intermediates accelerate Fe redox cycle.[43] The reaction mechanism of the in situ phenol degradation system is not fully clear as the AuPd catalyst is favourable for H_2O_2 synthesis but less active towards phenol conversion while the opposite trend was found on the AuPdFe catalyst, similar experimental observation to the previously reported 3 e^- ORR work.[44,45] To clarify whether ROS originate mainly from activation of in situ generated H_2O_2 or form direct from activation of H_2 and O_2, targeted experiments should be coupled with DFT to map free energy and barriers along the O_2 activation sequence.[44]

In **Chapter 5**, the AuPd catalysts prepared via the incipient wetness method showed excellent stability towards the in situ degradation of phenol in a flow regime. A brief study on the Fe-contained PdFe and AuPdFe formulations prepared via the same procedure found that these catalysts are unusable in a flow condition, with a continuous loss of catalytic performance, although slightly higher phenol degradation rates were found at the initial 30 mins compared

to the AuPd catalyst. However, without determining the extent of leaching (via ICP-MS or similar) and XPS analysis, it's hard to examine the reason why these Fe-contained catalysts are not stable. But still, preparing a stable Fe-contained catalysts for the in situ water treatment in either batch or flow regime would be intriguing for a quick and deep oxidation of organic pollutants. Furthermore, the in situ generation of H_2O_2 and ROS in the flow regime shows a great potential for a continues water treatment and also could further be applied to other in situ oxidation reactions as the reaction parameters (gas feed, solvent feed, flow rate, pressure, temperature etc) could be easily modified to suit different reaction needs. For example, for those reaction that have already reported in the in situ oxidation reactions using the in situ generated H_2O_2 and ROS in the batch regime, including but not limited to, ketone ammoxidation,[46,47] alcohol oxidation,[48–50] C-H oxidation,[51] olefin oxidation.[52] Collectively, this work shows that the catalytic system developed here offers numerous promising opportunities for further study.

6.3 Reference

1. Ciriminna, R., Albanese, L., Meneguzzo, F. & Pagliaro, M. Hydrogen Peroxide: A Key Chemical for Today's Sustainable Development. *ChemSusChem* **9**, 3374–3381 (2016).
2. Lewis, R. J. & Hutchings, G. J. Recent Advances in the Direct Synthesis of H2O2. *ChemCatChem* **11**, 298–308 (2019).
3. Campos-Martin, J. M., Blanco-Brieva, G. & Fierro, J. L. G. Hydrogen Peroxide Synthesis: An Outlook beyond the Anthraquinone Process. *Angew. Chem. Int. Ed. Engl.* **45**, 6962–6984 (2006).
4. Wen, Y. *et al.* Electrochemical Reactors for Continuous Decentralized H2O2 Production. *Angewandte Chemie* **134**, e202205972 (2022).
5. Li, J., Ishihara, T. & Yoshizawa, K. Theoretical Revisit of the Direct Synthesis of H2O2 on Pd and Au@Pd Surfaces: A Comprehensive Mechanistic Study. *The Journal of Physical Chemistry C* **115**, 25359–25367 (2011).
6. Edwards, J. K. *et al.* Direct synthesis of hydrogen peroxide from H2 and O2 using Au–Pd/Fe2O3 catalysts. *J Mater Chem* **15**, 4595–4600 (2005).
7. Kanungo, S., van Haandel, L., Hensen, E. J. M., Schouten, J. C. & Neira d'Angelo, M. F. Direct synthesis of H2O2 in AuPd coated micro channels: An in-situ X-Ray absorption spectroscopic study. *J Catal* **370**, 200–209 (2019).
8. Burch, R. & Ellis, P. R. An investigation of alternative catalytic approaches for the direct synthesis of hydrogen peroxide from hydrogen and oxygen. *Appl Catal B* **42**, 203–211 (2003).
9. Wilson, N. M., Priyadarshini, P., Kunz, S. & Flaherty, D. W. Direct synthesis of H2O2 on Pd and AuxPd1 clusters: Understanding the effects of alloying Pd with Au. *J Catal* **357**, 163–175 (2018).
10. Brehm, J., Lewis, R. J., Morgan, D. J., Davies, T. E. & Hutchings, G. J. The Direct Synthesis of Hydrogen Peroxide over AuPd Nanoparticles: An Investigation into Metal Loading. *Catal Letters* **152**, 254–262 (2022).
11. Fu, L. *et al.* Fabrication of the PdAu Surface Alloy on an Ordered Intermetallic Au3Cu Core for Direct H2O2 Synthesis at Ambient Pressure. *Ind Eng Chem Res* **61**, 11655–11665 (2022).

12. Zhang, M., Xu, H., Luo, Y., Zhu, J. & Cheng, D. Enhancing the catalytic performance of PdAu catalysts by W-induced strong interaction for the direct synthesis of H2O2. *Catal Sci Technol* **12**, 5290–5301 (2022).

13. Barnes, A., Lewis, R. J., Morgan, D. J., Davies, T. E. & Hutchings, G. J. Improving Catalytic Activity towards the Direct Synthesis of H2O2 through Cu Incorporation into AuPd Catalysts. *Catalysts* **12**, (2022).

14. Barnes, A., Lewis, R. J., Morgan, D. J., Davies, T. E. & Hutchings, G. J. Enhancing catalytic performance of AuPd catalysts towards the direct synthesis of H2O2 through incorporation of base metals. *Catal Sci Technol* **12**, 1986–1995 (2022).

15. Edwards, J. K. *et al.* The Direct Synthesis of Hydrogen Peroxide Using Platinum-Promoted Gold–Palladium Catalysts. *Angew. Chem. Int. Ed. Engl.* **53**, 2381–2384 (2014).

16. Lewis, R. J. *et al.* Cyclohexanone ammoximation via in situ H2O2 production using TS-1 supported catalysts. *Green Chemistry* **24**, 9496–9507 (2022).

17. Lewis, R. J. *et al.* The Direct Synthesis of H2O2 Using TS-1 Supported Catalysts. *ChemCatChem* **11**, 1673–1680 (2019).

18. Gong, X. *et al.* Enhanced catalyst selectivity in the direct synthesis of H2O2 through Pt incorporation into TiO2 supported AuPd catalysts. *Catal Sci Technol* **10**, 4635–4644 (2020).

19. Ntainjua, E. N., Freakley, S. J. & Hutchings, G. J. Direct Synthesis of Hydrogen Peroxide Using Ruthenium Catalysts. *Top Catal* **55**, 718–722 (2012).

20. Ouyang, L. *et al.* The origin of active sites for direct synthesis of H2O2 on Pd/TiO2 catalysts: Interfaces of Pd and PdO domains. *J Catal* **321**, 70–80 (2015).

21. Wols, B. A., Hofman-Caris, C. H. M., Harmsen, D. J. H. & Beerendonk, E. F. Degradation of 40 selected pharmaceuticals by UV/H2O2. *Water Res* **47**, 5876–5888 (2013).

22. Cao, J. *et al.* Gambling of homogeneous and heterogeneous Fenton in wastewater treatment. *Cell Rep Phys Sci* **5**, (2024).

23. Ji, J., Wang, Z., Xu, Q., Zhu, Q. & Xing, M. In situ H2O2 Generation and Corresponding Pollutant Removal Applications: A Review. *Chemistry – A European Journal* **29**, e202203921 (2023).

24. Santos, A. *et al.* The degradation of phenol via in situ H2O2 production over supported Pd-based catalysts. *Catal Sci Technol* **11**, 7866–7874 (2021).

25. Santos, A. *et al.* The oxidative degradation of phenol via in situ H2O2 synthesis using Pd supported Fe-modified ZSM-5 catalysts. *Catal Sci Technol* **12**, 2943–2953 (2022).

26. Underhill, R. *et al.* Oxidative Degradation of Phenol using in situ Generated Hydrogen Peroxide Combined with Fenton's Process. *Johnson Matthey Technology Review* **62**, 417–425 (2018).

27. Han, Y.-F. *et al.* Au Promotional Effects on the Synthesis of H2O2 Directly from H2 and O2 on Supported Pd−Au Alloy Catalysts. *The Journal of Physical Chemistry C* **111**, 8410–8413 (2007).

28. Edwards, J. K. *et al.* Direct synthesis of hydrogen peroxide from H2 and O2 using TiO2-supported Au–Pd catalysts. *J Catal* **236**, 69–79 (2005).

29. Freakley, S. J. *et al.* Effect of Reaction Conditions on the Direct Synthesis of Hydrogen Peroxide with a AuPd/TiO2 Catalyst in a Flow Reactor. *ACS Catal* **3**, 487–501 (2013).

30. Richards, T. *et al.* A residue-free approach to water disinfection using catalytic in situ generation of reactive oxygen species. *Nat Catal* **4**, 575–585 (2021).

31. Plauck, A., Stangland, E. E., Dumesic, J. A. & Mavrikakis, M. Active sites and mechanisms for H2O2 decomposition over Pd catalysts. *Proceedings of the National Academy of Sciences* **113**, E1973–E1982 (2016).

32. Choudhary, V. R. & Samanta, C. Role of chloride or bromide anions and protons for promoting the selective oxidation of H2 by O2 to H2O2 over supported Pd catalysts in an aqueous medium. *J Catal* **238**, 28–38 (2006).

33. Richards, T., Lewis, R. J., Morgan, D. J. & Hutchings, G. J. The Direct Synthesis of Hydrogen Peroxide Over Supported Pd-Based Catalysts: An Investigation into the Role of the Support and Secondary Metal Modifiers. *Catal Letters* **153**, 32–40 (2023).

34. John Regalbuto. *Catalyst Preparation: Science and Engineering*. (CRC press, 2016).

35. Pritchard, J. *et al.* Direct Synthesis of Hydrogen Peroxide and Benzyl Alcohol Oxidation Using Au−Pd Catalysts Prepared by Sol Immobilization. *Langmuir* **26**, 16568–16577 (2010).

36. Edwards, J. K. *et al.* Switching Off Hydrogen Peroxide Hydrogenation in the Direct Synthesis Process. *Science (1979)* **323**, 1037–1041 (2009).

37. Yin, Y. *et al.* Boosting Fenton-Like Reactions via Single Atom Fe Catalysis. *Environ Sci Technol* **53**, 11391–11400 (2019).

38. Weimer, A. W. Particle atomic layer deposition. *Journal of Nanoparticle Research* **21**, 9 (2019).

39. Fonseca, J. & Lu, J. Single-Atom Catalysts Designed and Prepared by the Atomic Layer Deposition Technique. *ACS Catal* **11**, 7018–7059 (2021).

40. Yuan, N. *et al.* In situ XAS study of the local structure and oxidation state evolution of palladium in a reduced graphene oxide supported Pd(ii) carbene complex during an undirected C–H acetoxylation reaction. *Catal Sci Technol* **9**, 2025–2031 (2019).

41. Wu, J.-H., Chen, F., Yang, T.-H. & Yu, H.-Q. Unveiling singlet oxygen spin trapping in catalytic oxidation processes using in situ kinetic EPR analysis. *Proceedings of the National Academy of Sciences* **120**, e2305706120 (2023).

42. Wang, L., Fu, Y., Li, Q. & Wang, Z. EPR Evidence for Mechanistic Diversity of Cu(II)/Peroxygen Oxidation Systems by Tracing the Origin of DMPO Spin Adducts. *Environ Sci Technol* **56**, 8796–8806 (2022).

43. Chen, C. *et al.* Overlooked self-catalytic mechanism in phenolic moiety-mediated Fenton-like system: Formation of Fe(III) hydroperoxide complex and co-treatment of refractory pollutants. *Appl Catal B* **321**, 122062 (2023).

44. Xie, L. *et al.* The strong metal–support interactions induced electrocatalytic three-electron oxygen reduction to hydroxyl radicals for water treatment. *Proceedings of the National Academy of Sciences* **120**, e2307989120 (2023).

45. Wang, Z., Hu, N., Wang, L., Zhao, H. & Zhao, G. In Situ Production of Hydroxyl Radicals via Three-Electron Oxygen Reduction: Opportunities for Water Treatment. *Angewandte Chemie International Edition* **63**, e202407628 (2024).

46. Lewis, R. J. *et al.* Selective Ammoximation of Ketones via In Situ H2O2 Synthesis. *ACS Catal* **13**, 1934–1945 (2023).

47. Lewis, R. J. *et al.* Highly efficient catalytic production of oximes from ketones using in situ–generated H2O2. *Science (1979)* **376**, 615–620 (2022).

48. Sharp, G. *et al.* Benzyl Alcohol Valorization via the In Situ Production of Reactive Oxygen Species. *ACS Catal* **14**, 15279–15293 (2024).

49. Sharp, G. *et al.* Highly efficient benzyl alcohol valorisation via the in situ synthesis of H2O2 and associated reactive oxygen species. *Green Chemistry* **27**, 5567–5580 (2025).

50. Crombie, C. M. *et al.* Enhanced Selective Oxidation of Benzyl Alcohol via In Situ H2O2 Production over Supported Pd-Based Catalysts. *ACS Catal* **11**, 2701–2714 (2021).

51. Ni, F. *et al.* The direct synthesis of H2O2 and in situ oxidation of methane: An investigation into the role of the support. *Catal Today* **442**, 114910 (2024).

52. Lin, D. *et al.* Radical-constructed intergrown titanosilicalite interfaces for efficient direct propene epoxidation with H2 and O2. *Nat Commun* **16**, 5515 (2025).